Role of periosteum in bone regeneration and congenital pseudarthrosis of the tibia

Simon Perrin

Université Paris Cité

École doctorale Bio Sorbonne Paris Cité (562)

Groupe "Stem cells in musculoskeletal development, regeneration and diseases"
Laboratoire "Biology of the Neuro-Muscular System"
INSERM U955 – Institut Mondor de Recherche Biomédicale

Role of periosteum in bone regeneration and congenital pseudarthrosis of the tibia

Thèse de doctorat de Biologie Cellulaire et Moléculaire

Présentée par **Simon PERRIN**

Dirigée par Céline Colnot

Soutenue le 24 Novembre 2022

Devant un jury composé de

Rapportrice	Dr. Geert CARMELIET	Full professor, KU Leuven
Rapportrice	Dr. Farida DJOUAD	DR, Université de Montpellier
Examinatrice	Dr. Nadège BONDURAND	DR, Université Paris Cité
Examinateur	Dr. Eric PASMANT	PU-PH, Université Paris Cité
Examinateur	Dr. Olivier PEYRUCHAUD	DR, Université Claude Bernard Lyon 1
Directrice de thèse	Dr. Céline COLNOT	DR, Université Paris Est-Créteil

A Nathalie, Dominique et Lucie,

A Jeanne,

Acknowledgments

First, I would like to thank Dr. Geert Carmeliet and Dr. Farida Djouad for accepting to read and comment my thesis and Dr. Nadège Bondurand, Dr. Eric Pasmant, and Dr. Olivier Peyruchaud for accepting to evaluate my work.

My first lab experience was in the Civelek lab in 2017, and from that moment I knew I wanted to do research. I would like to thanks Dr. Mete Civelek, as well as Dr. Rédouane Aherrahrou and Jameson Hinkle for a great time in the Civelek lab and for all they taught me during this internship.

J'ai ensuite rejoint le laboratoire de Céline Colnot pour mon stage de Master 2, puis ma thèse. Céline, merci de m'avoir accueilli dans votre laboratoire et de m'avoir fait confiance en me donnant cet ambitieux projet que vous aviez imaginé. J'ai appris (et j'apprends encore) chaque jour à vos côtés. Je vous remercie pour vos conseils, votre intuition scientifique hors pair, votre confiance et votre disponibilité (je n'ose imaginer le nombre d'heures cumulées passées dans votre bureau). Vous avez su mettre la barre toujours un peu plus haute pour me permettre de continuellement progresser. Vous étiez le mentor dont le jeune scientifique que j'étais avait besoin. Pour tout cela, merci Céline.

Une thèse est un travail d'équipe. Je tiens donc à remercier chaleureusement les membres actuels et passés du Colnot Lab. Merci à Yasmine, Maria, Cassandre et Franceska pour votre soutien et patience ces derniers mois. Un merci particulier à mes deux prédécésseures, Oriane et Anais. Vous avez mis la barre très haute, j'espère que le Nain a réussi à maintenir le cap. Oriane, merci pour ces quelques mois passés ensemble et pour m'avoir transmis la "passion" des cultures de cellules de périoste. Anais, cette aventure que fut ma thèse n'aurait pas été la même sans toi, que ce soit au bureau d'à côté ou à 1544 km d'écart (distance IMRB – Karolinska selon Google). J'ai énormément appris à tes côtés (passion single cell). Je tiens surtout à te remercier pour tes milliers de conseils, encouragements et félicitations, et pour avoir su dire ce que j'avais besoin d'entendre. Tu es devenue une vraie amie. Et pour clore le débat, non, personne n'aime écouter Michel Sardou pendant des heures dans le bureau…

Attention Sanela, ce passage va être ta phobie. Le plus grand des mercis pour toi ma Sannie (ou Sanninounette selon les jours). Je te remercie pour le travail absolument incroyable que tu as accompli sur mes projets (tu es selon moi la reine de l'histologie). Je te remercie encore plus pour la collègue que tu as été, pour avoir supporté mes râleries, pour avoir apporté beaucoup de rires à mes longues journées de labo et pour m'avoir si souvent répété que j'étais vieux. Voir la petite stagiaire timide arrivée en 2020 repartir 2 ans plus tard en scientifique accomplie et prête à aller faire des miracles dans un autre laboratoire est pour moi une fierté.

J'ai eu la chance de côtoyer ou d'encadrer de nombreux stagiaires au cours de ces années de thèse. Merci à Anuya, Hadidja, Élise, Alexis, Sophie, Julie, Paul, Arianna et Gabriel pour votre travail, et pour avoir su ramener un peu de jeunesse et de fraîcheur dans le labo. Merci à Cécile-Aurore pour ton travail de bioinfo, ton stage fut une période très stimulante et j'ai

beaucoup aimé explorer les datas de single cell avec toi. Un merci tout spécial à toi Luka, pour tes goûts musicaux qui rendent l'été pêchu et un bœuf bourguignon resté dans les annales.

Je tiens à te remercier Béatrice pour notre collaboration très fructueuse. Merci pour ton implication, tes encouragements et ton didactisme hors pair (je sais maintenant expliquer les cnLOH grâce à toi). Merci également à Ingrid, Nicolas et Elena qui ont travaillé à tes côtés pour nous permettre d'obtenir tous ces résultats.

Je remercie également l'équipe de Piotr Topilko avec qui j'ai eu le plaisir de collaborer. Merci Piotr pour tous tes conseils avisés et de passionnantes discussions sur les cellules de Schwann et les boundary caps. Thanks to Kasia and Fanny for many great discussions and tips. Ce fut un plaisir de partager avec vous ce séjour à Philadelphie (et de briller en tant que Cheesy scientists). Merci également au reste de l'équipe, Myriam, Pernelle et Julie.

Je tiens également à remercier les Dr. Stéphanie Pannier et Philippe Wicart pour notre collaboration qui a permis de créer une des plus belles cohortes de patients de PCJ. Ce fut un plaisir d'assister à vos opérations toujours impressionnantes. Merci également au Dr. Smail Hadj-Rabia pour avoir contribué à l'étude et pour sa grande expertise sur la génétique des neurofibromatoses.

Les premiers pas de ma thèse ont eu lieu à l'Institut Imagine. Je tiens à remercier toutes les personnes des laboratoires et des plates-formes que j'ai pu côtoyer pendant mes 2 années passées à Imagine, et tout particulièrement Marcelo, Juliette, Iris, Clémentine, Cérane, Floriane, Clovis, Lisa, Émilie et Rachel.

Un immense merci à Marine et Brieuc, les 2 meilleurs d'Imagine (j'ai décidé que vous seriez ex-aequo pour ne pas faire de jaloux). Merci pour m'avoir si souvent accueilli dans votre bureau. J'aurais abandonné les expériences de single-cell (souvent ratées) si vous n'aviez pas été là pour me remonter le moral après chaque échec. Ce fut avec tristesse que je vous quittasse pour Créteil, mais je ne doutais pas que notre amitié perdurerait au-delà des murs de l'institut (le subjonctif imparfait est cadeau).

Nous avons ensuite rejoint l'Institut Mondor de recherche biomédicale, où je remercie notamment Adeline, Aurélie, Alice, Violaine et Dounia. Merci à Diana et Florine pour avoir su nous maintenir à flot, mais surtout pour des discussions et échanges de mails toujours savoureux. Mention spéciale pour Odile, pour des heures de discussions pendant que l'Influx travaille et tes pépites musicales à consommer sans modération (par contre, évite d'appuyer sur le bouton off stp).

I had the great chance to attempt several conferences during my PhD, and I want to thank everyone I met there for interesting discussions and feedbacks. A special thanks to Judith, Krystyna and Robin for an unforgettable week along the Californian coast, full of stories involving nerdy talks, lost notebooks and scale bars.

Je suis profondément reconnaissant envers tous mes amis pour leur soutien sans faille et pour m'avoir si souvent écouté râler sur ma thèse. Nos moments passés ensemble autour d'un verre, d'un repas, en week-end ou au téléphone ont été des moteurs pour moi, indispensable à ma thèse et à mon bien-être bien plus que vous ne pouvez l'imaginer. Un énorme merci à Camille, mon amour inconditionnel et comparse de kayak norvégien, à Elsa, ma plus ancienne amie, à Angeline, Alice et Elodie, les incroyables avions de chasse de la Patrouille de France, à Hélène, Alma et Aurélie, les reines des brunchs corréziens Karismatik, à Marine et Brieuc, qui méritent bien d'être remerciés deux fois, à Jessica et Valentin, les rescapés du monde de l'emballage cartonné, à Nathan, le voisin sur qui je peux toujours compter, à Raphael, le perdant au bingo fan de l'Oise, et à Joséphine, grâce à qui j'ai pu voir Brad Pitt. I also want to thanks Lisa, the 10/10 world explorer, Jac, the frenchiest American, and Marianna, my favorite Brazilian for their friendship and support, and for amazing trips together. Un merci spécial pour mon armée de docteures, Chloé, Marine, Pauline, Constance, Maithé, Maria et Lolita. Nous avons partagé ensemble ces dernières années intenses ainsi que les hauts et les bas de la vie de doctorant. Vous avez été pour moi une source de soutien et de motivation inégalable. Vous êtes un incroyable groupe d'amies et de scientifiques prêtes à conquérir le monde, et j'ai hâte de partager cela avec vous.

Un grand merci à toi Florent, pour avoir été un soutien de première ligne pendant ma thèse. Merci pour m'avoir remonté le moral après un énième échec et appris à célébrer les petites victoires du quotidien.

Je tiens à remercier chaleureusement ma famille pour leur soutien à toute épreuve et tout ce qu'ils ont pu m'apporter au quotidien au fil des années. Merci à mes grands-parents, tantes, oncles, cousins et cousines. Un merci spécial à Aline. Merci de croire en moi et de veiller sur moi comme tu le fais depuis toujours (en me rappelant qu'il faut se reposer de temps en temps). Je sais qu'auprès de toi, je trouverais toujours une oreille attentive et une porte ouverte. Merci Jeanne d'être mon rayon de soleil (et d'arriver à me piéger sur mes connaissances d'Harry Potter). Te voir grandir est sûrement la meilleure des expériences.

Je tiens également à remercier ma sœur, Lucie. Nous avons grandi ensemble, évolué ensemble et je ne serais pas la personne que je suis aujourd'hui sans toi. Merci de m'avoir soutenu et encouragé tout au long de mon parcours et de ma thèse (et je ne désespère pas, qu'un jour, tu arriveras à placer le mot périoste dans une phrase). J'espère que tu es fier de moi autant que je peux l'être de toi. J'ai hâte de nos prochaines aventures ensemble.

Et pour terminer, je veux remercier mes parents. Merci de votre soutien indéfectible et pour m'avoir toujours encouragé à aller plus loin et à donner le meilleur de moi-même. J'ai appris de vous de nombreuses qualités qui m'ont été indispensables pour cette thèse, comme la curiosité, le travail, la persévérance et l'engagement. Vous avez toujours fait votre possible pour que j'évolue dans les meilleures conditions et réussisse. Ce que je suis aujourd'hui et cette thèse, je vous le dois. Du fond du cœur, merci.

A tous, merci ! *Simon*

Table of Contents

Résumé

Rôle du périoste dans la régénération osseuse et la pseudarthrose congénitale de jambe

La régénération osseuse est un processus très efficace permettant aux os de réparer suite à une fracture. Ce processus repose sur l'activation et la différentiation de cellules souches/progénitrices osseuses (CSPO) recrutées localement depuis le périoste, la moelle osseuse, et muscle adjacent à la fracture. Le périoste, la membrane externe des os, est une source clé de CSPOs formant os et cartilage après une fracture. Cependant, les mécanismes de recrutement et de maturation des CSPOs du périoste (pCSPO) sont méconnus. De plus, le rôle du périoste dans les défauts de réparation osseuse est peu décrit, mais est suspecté dans le cas des pseudarthroses congénitales de jambe (PCJ), une atteinte osseuse sévère caractérisée par une fracture tibiale spontanée et une absence de consolidation. La PCJ est associée à la Neurofibromatose de type 1 (NF1), une maladie génétique causée par des mutations hétérozygotes du gène suppresseur de tumeur *NF1*. Certains symptômes de NF1, dont les tumeurs de la gaine des nerfs périphériques et les hyperpigmentations cutanées, sont dues à la perte biallélique de *NF1* dans des types cellulaires spécifiques i.e. les cellules de Schwann et les mélanocytes respectivement. L'inactivation biallélique de *NF1* a été identifiée dans les PCJ mais l'origine cellulaire de la pathologie reste à déterminer. Dans cette thèse, j'ai étudié les mécanismes de recrutement et de maturation des pCSPOs ainsi que l'implication du périoste dans la PCJ.

Dans la première partie de la thèse, j'ai utilisé le séquençage de l'ARN en cellule unique pour décrire la réponse des pCSPOs à la fracture. En s'activant, les pCSPO quittent leur état souche/progénitrice pour entrer en fibrogenèse puis en chondrogenèse. Ce schéma d'activation, équivalent à celui des CSPOs du muscle, est régulé par la voie de signalisation BMP.

Au cours de l'ossification endochondrale, le cartilage mature, s'hypertrophie et est remplacé par l'os, par apoptose ou transformation du cartilage en os. **Dans la seconde partie de la thèse**, le phénotype de souris portant une mutation suractivant le récepteur FGFR3 a été analysé et a montré que la transformation du cartilage en os est essentielle à la réparation osseuse. Les chondrocytes issus du périoste de souris mutantes pour *Fgfr3* ne sont pas capables de se transdifférencier en ostéoblastes et produisent du fibrocartilage, conduisant à une absence de réparation osseuse.

Dans la troisième partie de la thèse, j'ai combiné l'analyse d'échantillons de patients atteint de PCJ et du modèle murin *Prss56-Nf1 KO* portant une inactivation du gène *Nf1* dans une population spécifique de cellules de crêtes neurales, les capsules frontières (CP), et leurs dérivés. Nos résultats montrent que la PCJ est associée à l'inactivation biallélique de *NF1* chez l'homme au niveau du périoste au site de pseudarthrose et à la présence de pCSPO pro-fibrotiques dans le périoste pathologique. J'ai identifié un phénotype de pseudarthrose après fracture du tibia dans les souris *Prss56-Nf1 KO*. Les dérivés des CPs sont localisés dans le périoste, où ils correspondent à des pCSPOs et des cellules de Schwann. Les pCSPOs mutées pour *Nf1* présentent un défaut intrinsèque de différentiation bloquant leur transition de la fibrogenèse à la chondrogenèse. De plus, les cellules de Schwann mutantes ont un effet paracrine pro-fibrotique sur les CSPOs non-mutées et l'inhibition du facteur pro-fibrotique TGFβ corrige le phénotype de pseudarthrose chez les souris *Prss56-Nf1 KO*. Dans l'ensemble, cette thèse apporte une

meilleure compréhension sur le rôle des pCSPO au cours de la régénération osseuse et montre comment une déficience du périoste conduit à un défaut de régénération sévère dans la PCJ.

Mots-clés : périoste – régénération osseuse – cellules souches/progénitrices osseuses – pseudarthrose congénitale du tibia – Neurofibromatose de type 1

Abstract

Role of periosteum in bone regeneration and congenital pseudarthrosis of the tibia

Bone repair is a highly efficient process allowing bones to fully regenerate without scarring after fracture. It relies on the activation and differentiation of skeletal stem/progenitor cells (SSPCs) recruited locally from the periosteum, the bone marrow, and the skeletal muscle adjacent to bone. The periosteum, the outer layer of bones, is a major source of SSPCs contributing to cartilage formation after bone injury. The identity of periosteal SSPCs (pSSPCs) and their mechanisms of activation after fracture remains poorly described. Moreover, the role of the periosteum in bone repair defects is unknown, but is suspected in congenital pseudarthrosis of the tibia (CPT), a severe disorder characterized by spontaneous tibial fracture and fibrous non-union. CPT is associated with the genetic disorder Neurofibromatosis Type 1 (NF1), caused by heterozygous mutations in the tumor suppressor gene *NF1*. NF1 symptoms such as nerve sheath tumors and skin hyperpigmentation are due to *NF1* biallelic inactivation in specific cell types i.e. Schwann cells and melanocytes respectively. *NF1* biallelic inactivation was also reported in CPT but the cellular origin of the disease remains to be determined. In the thesis, I investigated the mechanisms of pSSPCs recruitment and maturation, and the role of periosteum in CPT.

In the first part of the thesis, I used single-cell RNAseq technology to characterize pSSPC response to fracture. Upon activation, periosteal SSPCs leave their stem/progenitor stage to become fibrogenic before undergoing chondrogenic differentiation. This activation pattern, common with skeletal muscle SSPCs, is regulated by BMP signaling.

During endochondral ossification, cartilage undergoes maturation, hypertrophy and is replaced by bone, via chondrocyte apoptosis or cartilage-to-bone transformation. **In the second part of the thesis**, the phenotype of mice carrying an overactivating mutation of FGF Receptor 3 was analyzed and showed that this step of cartilage-to-bone transformation is essential for bone repair. Periosteum-derived chondrocytes in *Fgfr3*-mutant fail to transdifferentiate into osteoblasts and produce fibrocartilage, thus leading to callus fibrosis and fracture non-union.

In the third part of the thesis, I combined analyses of bone samples from CPT patients and *Prss56-Nf1 KO* mice carrying *Nf1* inactivation in neural crest-derived boundary cap (BC) cells and their derivatives. The results show that CPT is linked to *NF1* biallelic inactivation in human pathological periosteum and the presence of profibrotic pSSPCs. I identified a fibrous pseudarthrosis phenotype following tibial fracture in *Prss56-Nf1 KO* mice. BC derivatives are located in adult periosteum, where they give rise to pSSPCs and Schwann cells. *Nf1*-deficient pSSPCs have an intrinsic differentiation impairment and fail to transition from fibrogenesis to chondrogenesis, thus forming fibrosis. Additionally, *Nf1*-deficient Schwann cells exert a profibrotic paracrine effect on wild type SSPCs, which can be prevented by TGFβ inhibition to allow bone

union. Overall, the thesis provides new insights into the role of pSSPCs during bone repair and how periosteum dysfunction can lead to severe bone repair deficiencies.

Keywords: periosteum – bone regeneration – skeletal stem/progenitor cells – congenital pseudarthrosis of the tibia – Neurofibromatosis type 1

Abbreviations

αSMA: alpha Smooth muscle actin
BC: Boundary cap
BDNF: Brain-Derived Neurotrophic Factor
BMD: Bone mineral density
BMP: Bone morphogenetic protein
BMU: Basic Multicellular Unit
CALM: Café-Au-Lait Macules
CAR cell: CXCL12 Abundant Reticular cell
CCL: Chemokine (C-C motif) Ligand
CFU-F: Colony forming unit fibroblast
CGRP: Calcitonin gene-related peptide
cnLOH: Copy neutral loss of heterozygosity
CNV: Copy number variant
cNF: Cutaneous neurofibromas
CPT: Congenital pseudarthrosis of the tibia
ColX: Collagen type X
COX2: Cyclooxygenase 2
CSRD: Cystein-serin rich domain
CTD: C-terminal domain
CTSK: Cathepsin K
CXCL12: C-X-C motif chemokine 12
DIO: Diet induced obesity
ECM: Extracellular matrix
EMT: Epithelial - Mesenchymal transition
Eph: Erythropoietin-producing human hepatocellular receptor
FDA: Food and Drug administration
FGF: Fibroblast growth factor
GAP: GTPase activating protein
GDNF: Glial cell line-derived neurotrophic factor
GDP: Guanosine diphosphate
GEF: Guanine nucleotide exchange factor
GFAP: Glial fibrillary acidic protein
GRD: GAP-related domain
GTP: Guanosine triphosphate
HH: Hedgehog
IGF: Insulin-like growth factor
ISCT: International Society for Cell & Gene Therapy
LOH: Loss of heterozygosity
MAPK: Mitogen-activated protein kinase
MMP: Matrix metalloproteinase
MPNST: Malignant peripheral nerve sheath tumor
MSC: Mesenchymal stem cell
mSC: Myelinating Schwann cells
mTOR: Mammalian target of rapamycin
nAG: Newt-anterior gradient
NC: Neural crest
NCAM: Neural Cell Adhesion Molecule
NCC: Neural crest cell
NF: Neurofibroma
NF1: Neurofibromatosis type 1
NF1: *NF1* human gene
***Nf1*:** *Nf1* mouse gene
***Nf1*$^{-}$**: Knock-out *Nf1* mouse gene
***Nf1*^{fl}**: Floxed *Nf1* mouse gene
NGF: Nerve Growth Factor
NRG1-III: Neuregulin 1 type III
nmSC: Non myelinating Schwann cell
OPG: Optic pathway glioma
OSM: Oncostatin M
OSX: Osterix
PA: Pseudarthrosis
PDGF: Platelet-derived growth factor
pNF: Plexiform neurofibroma
pSSPC: Periosteal skeletal stem/progenitor cell
PTH: Parathyroid hormone
repSC: Repair Schwann cell
scNF: Subcutaneous neurofibroma
SCP: Schwann cell precursor
scRNAseq: Single-cell RNA sequencing
snRNAseq: Single-nuclei RNA sequencing
SDF1: Stromal cell-derived factor 1

SKP: Skin-derived neural progenitor

SNP: Single polymorphism nucleotide

SSPC: Skeletal stem/progenitor cell

TBD: Tubulin-binding domain

TGFβ: Transforming growth factor beta

TH: Tyrosine Hydroxylase

TNFα: Tumor necrosis factor alpha

VEGF: Vascular endothelial growth factor

WT: Wild-type

List of figures

List of tables

Introduction

Chapter 1: The skeleton and bone regeneration

Humans, as all vertebrates, are defined by the presence of an internal skeleton. The human adult skeleton is composed of 206 bones playing crucial functions, such as supporting the body, anchoring, and protecting the soft and sensitive tissues[1–3]. Connected to the skeletal muscle by tendons, bones allow movement. The skeleton is also a reservoir of minerals, such as calcium and phosphorus, and has an endocrine function. Finally, bones are the site of hematopoiesis, the formation of blood and immune cells[4,5].

1. The skeleton

1.1. Types of bones

The 206 bones forming the human skeleton can be divided into different categories depending on their shape: long, short, flat, irregular, and sesamoid bones (Figure 1A).

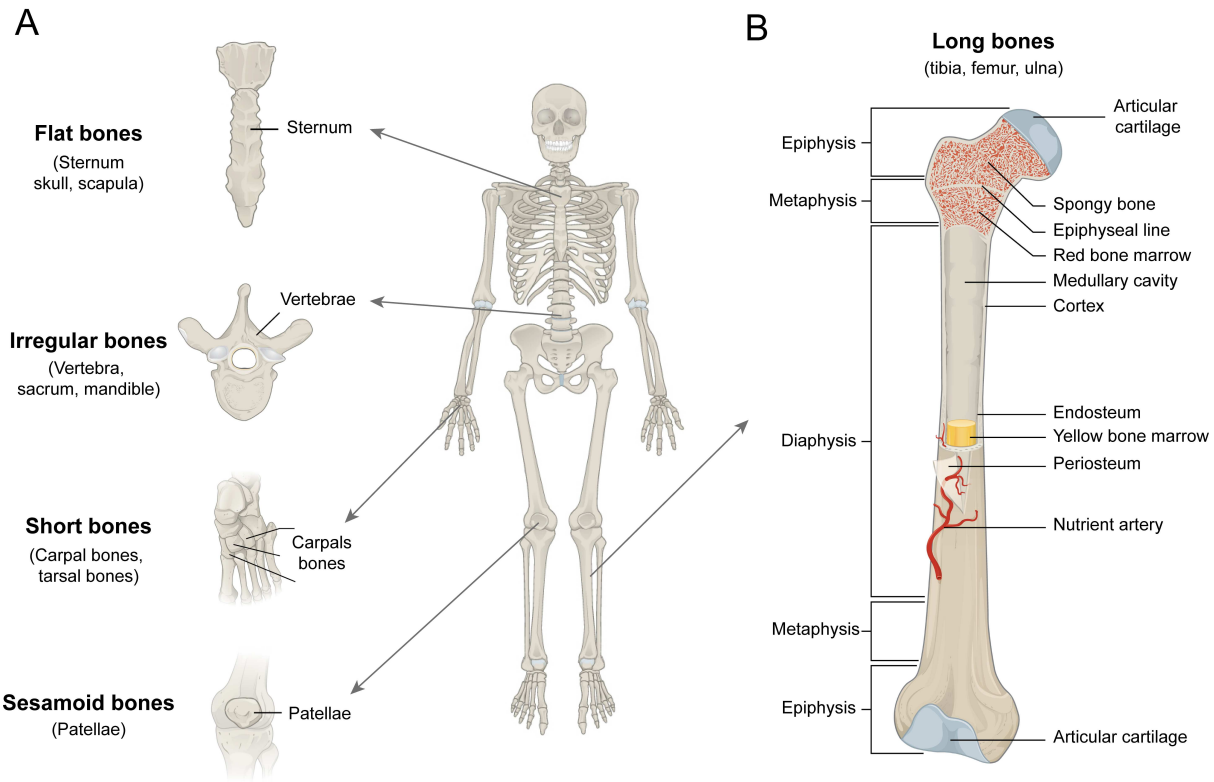

Figure 1: Types of bones (A) and structure of long bones (B). Adapted from [3]

1.1.1. Long bones

Long bones are characterized by their cylindrical shape and include bones found in the arm (humerus, ulna, radius), leg (femur, tibia, fibula), fingers, and toes. Long bones share a common 3 part-structure: epiphysis, metaphysis, and diaphysis (Figure 1B)[1–3]. Epiphyses are located at both extremities of the bone, and are composed of a thin layer of compact bone enclosing spongy trabecular bone rich in bone

marrow. The outer surface of the epiphyses is covered by a layer of articular cartilage. Below the epiphyses is located the metaphysis, a small region that contains the growth plate or epiphyseal line, a region of cartilage that is the site of bone growth during embryonic development and post-natal stages. The metaphysis is highly vascularized and contains cancellous bone, skeletal stem/progenitor cells (SSPCs), and blood vessels. At adult stage in human, the growth plate closes and is replaced by the epiphyseal line. The longest part of the bone is the diaphysis, which has a long tubular shape made of compact bone, named cortex. Within the diaphysis is located the marrow cavity, composed of red bone marrow in children and progressively replaced by adipogenic (or yellow) bone marrow in adult. The inner surface of the cortex is covered by a fibrous layer, the endosteum. The outer surface of the bones is covered by another fibrous layer, named periosteum.

1.1.2. Short, flat, irregular, and sesamoid bones

Short bones are cuboid bones that provide stability and support. They are the carpal and tarsal bones found in the ankles and wrists. Flat bones are thin bones like the sternum, cranial bones, and ribs. They protect internal organs (heart, brain) and serve for muscle attachment. Due to their complex shape, the vertebrae and some bones of the face are classified as irregular bones. They play a central role in protecting sensitive organs such as the spine. Finally, sesamoid bones such as the patellae are small round bones located in the tendons[1–3].

1.2. Composition of the bone tissue

Bones are composed of organic (cells and extracellular matrix) and inorganic (minerals) components[6]. The organic component include different cell types, such as the bone-forming cells or osteoblasts, that can mature to become osteocytes, embedded into the bone matrix[7]. Bones also contain immune-derived osteoclasts which can degrade the bone matrix. The bone matrix is composed of a rich network of extracellular matrix (ECM) proteins, that represent 35% of the bone weight. Collagens type I (90% of overall collagen), III, and V are the most abundant components of the organic ECM[8,9]. Proteoglycans (biglycan, asporin)[10,11], glycoproteins (osteonectin, thrombospondins)[12–14], small integrin-binding ligand N-linked glycoproteins (osteopontin, bone sialoprotein)[15,16] and osteocalcin[17] are also part of the organic ECM. The inorganic fraction of the bone matrix corresponds to 65% of its mass. It is composed of hydroxyapatite crystals ($Ca_5(PO_4)_3(OH)$), formed by the combination of calcium phosphate and calcium carbonate[18,19]. Hydroxyapatite can incorporate additional inorganic minerals like magnesium, fluoride, and sulfate. The crystals are deposited along collagen fibers and give bones their strength and stiffness.

1.3. The periosteum

The periosteum (from Greek peri- meaning "surrounding", and -osteon, meaning "bone") is a thin fibrous membrane covering the outer surface of bones, apart from sesamoid bones. The thickness of the periosteum varies with age, young individuals have a thick periosteum that becomes thinner with age.

The periosteum is attached to the bone cortex by strong collagen fibers called Sharpey's fibers and acts as an anchor for ligaments and tendons[20–23]. The periosteum is a bi-layered membrane (Figure 2)[24–26]. The outer layer is a fibrous layer, composed of fibroblasts and dense extracellular matrix, containing matrix proteins such as elastin and collagens. The inner layer, named cambium layer, is heterogenous and contains osteoblasts, fibroblasts, and skeletal stem/progenitor cells (SSPCs)[27,28]. The periosteum is highly vascularized and acts as a major source of blood supply for bones[29–32]. It is densely innervated by sensory fibers (expressing calcitonin gene-related peptide or CGRP) and sympathetic fibers (expressing Tyrosine Hydroxylase or TH)[33,34]. The periosteum also hosts resident and osteal macrophages (osteomacs)[35]. The exact composition and heterogeneity of the cell populations within the periosteum remain to be further described.

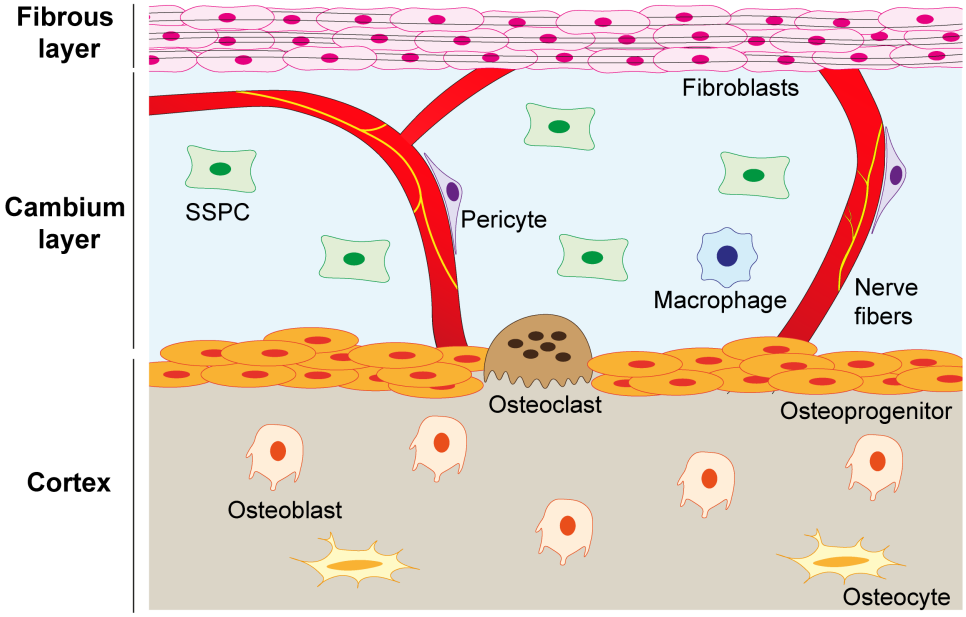

Figure 2: **Composition of the periosteum.**

2. Bone development and physiology

2.1. Bone development

Bone formation starts from 4 weeks after fecundation in human and at embryonic day 11.5 (E11.5) in mice. Bone-forming cells have different embryonic origins (Figure 3). Bones in the anterior part of the skull, in the face and the mandible are derived from the neural crest, the cell population that delaminates from the border of the neuroectoderm at the time of neural tube closure. The other bones have a mesodermal origin. The posterior part of the skull and axial skeleton are derived from the paraxial mesoderm (somites in the trunk) and the appendicular skeleton from the lateral plate mesoderm. A recent study from Xie *et al.* shows that Schwann cell precursors (SCPs), derived from the neural crest, give rise to mesenchymal cells, chondrocytes, and osteoblasts in the cranial and axial skeleton in mice and zebrafish[36]. This study suggests that mesoderm-derived bones can also contain cells with neural crest origin.

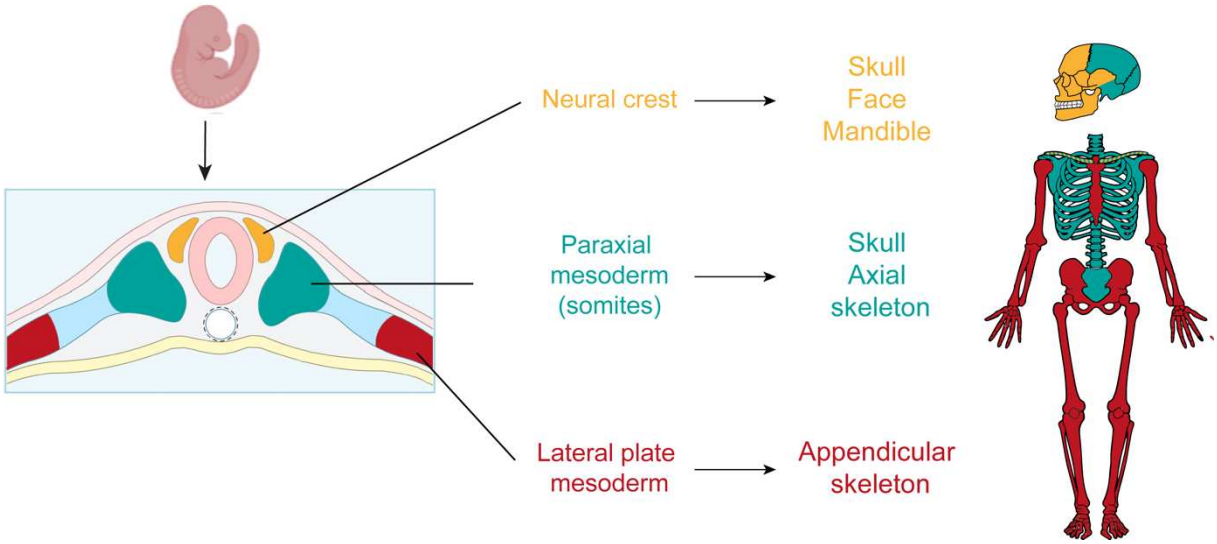

Figure 3: Embryonic origin of bones. The anterior part of the skull, bones of the face and the mandible are derived from the neural crest (orange), the posterior part of the skull and the axial skeleton are derived from the paraxial mesoderm (green) and the appendicular skeleton is derived from the lateral plate mesoderm.

Bone develops through two ossification processes. Bones of the skull, flat bones of the face, and part of the clavicle form by intramembranous ossification, or direct bone formation. The rest of the axial skeleton and the appendicular skeleton form by the endochondral ossification, a process that requires an intermediate cartilage step.

2.1.1.Intramembranous ossification

The first step of intramembranous ossification is the migration of mesodermal or neural crest-derived progenitors to the site of bone formation. The progenitors proliferate and condense to form a shape similar to the future bone. Skeletal progenitors start expressing *Dlx5*, which induces the expression of *Runx2*, the master regulator of osteogenesis[37]. Cells engage in osteogenesis, expressing genes such as *Alpl* and Osterix (Osx or *Sp7*), and become osteoblasts[38]. The newly formed osteoblasts produce a Collagen type I rich matrix and mineralize it. Some osteoblasts are entrapped in the bone matrix and further differentiate into osteocytes (Figure 4)[39,40].

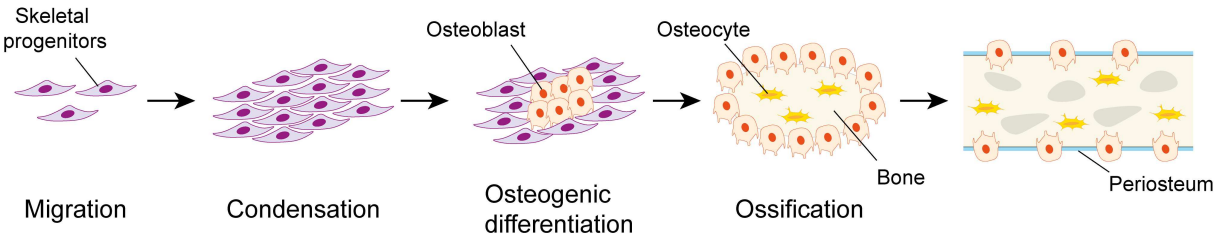

Figure 4: Intramembranous ossification

2.1.2. Endochondral ossification

Endochondral bone formation is also initiated by the migration and condensation of mesenchymal precursors (Figure 5). Cells at the periphery of the condensation align to form the perichondrium, a membrane surrounding the cartilage template. Cells inside the condensation start expressing *Sox9*, the master regulator of chondrogenesis, and differentiate into chondrocytes[41,42]. The early chondrocytes proliferate and express cartilage matrix proteins, such as Collagen type II and Aggrecan. Progressively, chondrocytes stop proliferating and mature by enlarging to become hypertrophic chondrocytes. This stage is characterized by the expression of a specific protein, collagen type X (ColX), and the expression of osteogenic genes such as *Runx2* and *Sp7* (Osterix). Hypertrophic chondrocytes also express Vascular Endothelial Growth Factor (VEGF) that promotes blood vessel invasion of the cartilaginous matrix[43]. The newly formed vessels allow the migration of osteoprogenitors and hematopoietic cells in the cartilage template and the formation of the primary ossification center. The nervous system also plays a role in the establishment of the primary ossification center[44,45]. Perichondrial cells express Nerve Growth Factor, required for embryonic bone innervation, vascularization, and ossification[46]. Several studies aimed to understand the origin of osteoprogenitors during endochondral bone development[47]. The absence of systemic recruitment was shown using ectopic renal capsule transplantation[48]. Lineage analysis showed that the perichondrium and the cartilaginous template itself are sources of osteoprogenitors for bone formation[49]. Perichondrial cells start expressing osteogenic markers, such as Osx, and migrate along blood vessels into the cartilaginous template, where they can give rise to bone cells as well as stromal cells[50–52]. While hypertrophic chondrocytes in cartilaginous template undergo cell death at the cartilage-to-bone junction[53,54], some terminal hypertrophic chondrocytes can transdifferentiate into osteoblasts. This mechanism of transdifferentiation was shown using chondrocytes specific-CRE lines (*Col10a1*^{CreERT}, *Col2a1*^{CreERT}, *Acan*^{CreERT}) to trace chondrocytes able to generate osteoblasts and stromal cells[55–59]. The relative contribution of cells from the perichondrium and the cartilage still needs to be further studied. At the end of the fetal stage, most of the cartilage has been replaced by bone, and the perichondrium becomes the periosteum. Cartilage remains at the metaphysis, where it forms the growth plate, that will support bone growth at post-natal stages [60].

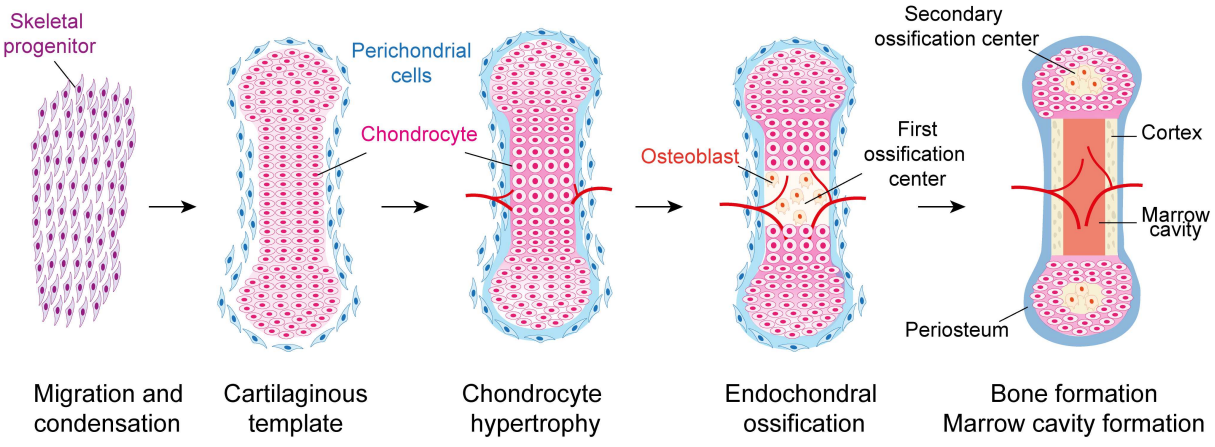

Figure 5: Endochondral ossification.

2.2. Bone growth and remodeling

2.2.1. Bone growth

Bone lengthening occurs at the growth plate during post-natal stages and adolescence. The growth plate is divided in 3 regions: the resting zone, the proliferative zone, and the hypertrophic zone (Figure 6)[61,62]. The resting zone hosts populations of stem cells, expressing PTHrP and FoxA2[63,64]. These stem cells give rise to chondrocytes, which will form columns through the growth plate. Chondrocytes proliferate before maturing to reach the hypertrophic stage. As during bone development, hypertrophic chondrocytes can undergo either apoptosis or transdifferentiation into osteoblasts or bone marrow stromal cells[47]. A population of chondrocytes located at the periphery of the growth plate, the borderline chondrocytes, is also an important source of cells during post-natal growth[65,66]. Borderline chondrocytes do not reach hypertrophy but undergo a transient skeletal precursor step before differentiating into osteoblasts or stromal cells.

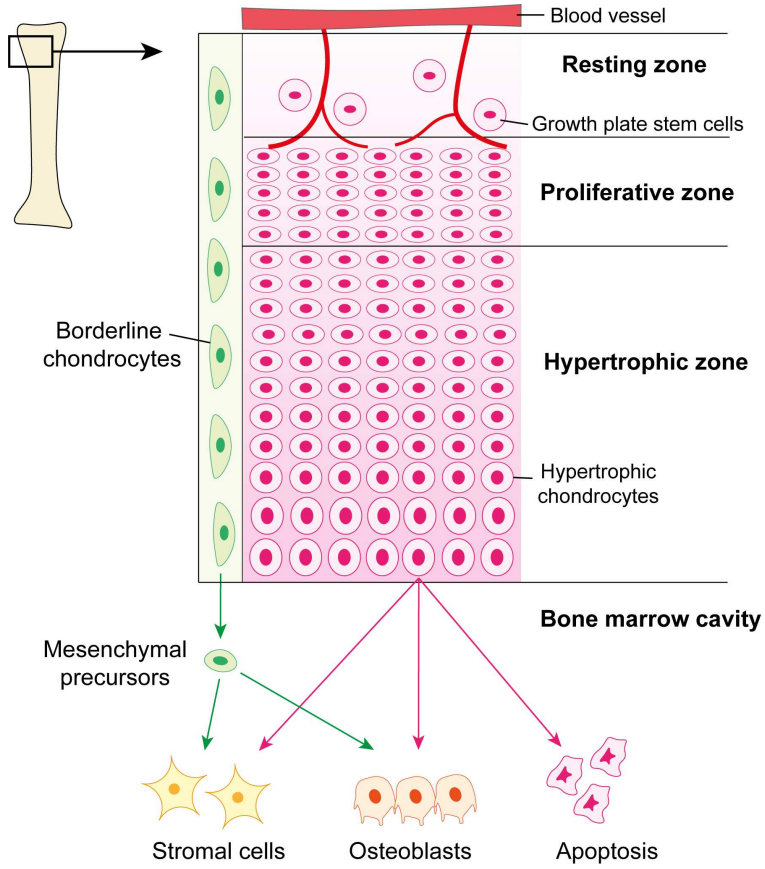

Figure 6: Bone formation at the growth plate. Osteoblasts and bone marrow stromal cells derive from hypertrophic chondrocytes (pink) and borderline chondrocytes (green).

Bone growth in width is independent of bone lengthening and can occur throughout the entire life to adapt bones to stimuli and mechanical constraints. Thickening of the bone cortex relies on local bone formation and resorption. Bone deposition occurs beneath the periosteum, increasing the diameter of the bone cortex. In parallel, bone resorption in the medullary cavity allows enlargement of the marrow space.

2.2.2. Bone remodeling

Throughout life, bones are constantly challenged. The skeleton controls its own maintenance by bone remodeling, a process by which old or damaged bone is replaced by new bone[67,68]. This process is regulated by a Basic Multicellular Unit (BMU), composed of osteoclasts, osteoblasts, and blood capillaries. Bone remodeling is composed of 5 steps (Figure 7). The first step, or activation, corresponds to the recruitment of osteoclast precursors at the surface of damaged bone. Several signals promote the formation of remodeling sites like local paracrine factors secreted by damaged osteocytes[69–71] or systemic hormonal changes, such as increased parathyroid hormone (PTH) blood level[72,73]. The phase of resorption starts with the differentiation of osteoclasts, which bind to the bone surface and progressively degrade the bone matrix[74–76]. The reversal phase corresponds to the switch from bone resorption to bone formation. Macrophages and bone lining cells eliminate debris from the resorption phase and osteoblasts, the bone-forming cells, are recruited[77,78]. The signals regulating the switch from bone resorption to bone formation remain debated. During the formation phase, osteoblasts produce extracellular matrix, rich in collagen type 1, before mineralization by deposing hydroxyapatite crystals in the matrix network. Finally, during the phase of termination, bone formation is complete, and osteoblasts undergo apoptosis or mature into osteocytes or bone lining cells. Bone remodeling is a complex multicellular process and is tightly regulated by many signaling pathways, such as Wnt and RANKL/RANK/OPG, and paracrine factors, including PTH, Vitamin D, and sex-hormones[73,79–82]. The balance between bone resorption and bone formation is critical to maintain bone homeostasis. Dysregulation of this balance leads to osteoporosis, a common clinical disorder affecting 1 in 3 women and 1 in 5 men in Europe and resulting in an increased fracture prevalence[83,84].

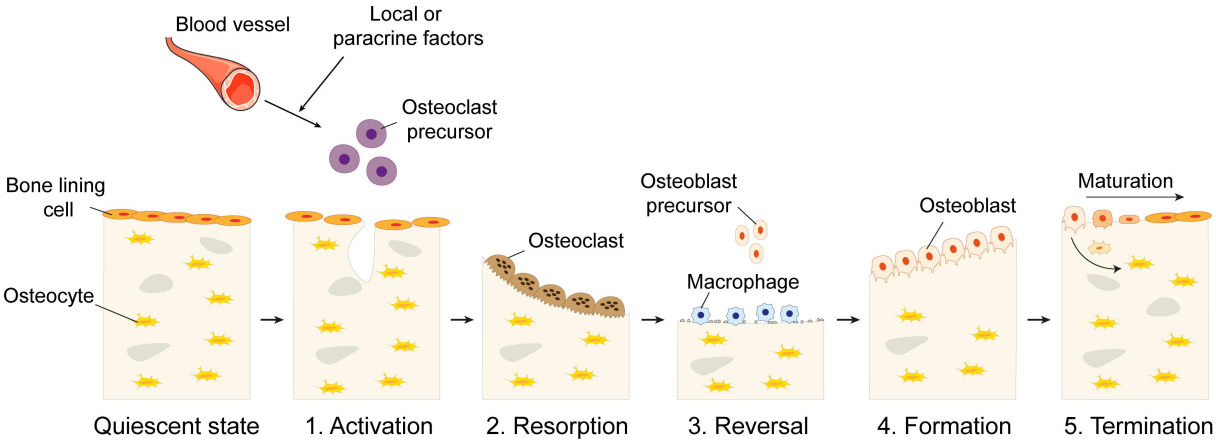

Figure 7: Bone remodeling cycle

2.3. Bone regeneration

Despite their remarkable strength, bones can be injured or fractured. Bone injury initiates the process of bone repair, which is a highly efficient regeneration process, allowing bones to fully regenerate without scarring. Bone repair is a 4-step process that resembles bone development and requires both endochondral and intramembranous ossification. Bone repair starts with an inflammation phase when

an acute immune response allows clearance of debris from the injury site and recruitment of skeletal stem/progenitor cells (SSPCs). During the second phase of healing, SSPCs differentiate into fibrogenic cells and chondrocytes to form a fibrocartilaginous callus (*i.e.* the regeneration area). The callus is progressively ossified during the bony callus phase, and finally, during the final phase, bone remodeling allows the bone to regain its initial shape (Figure 8)[85].

The first phase of bone repair corresponds to the formation of the hematoma concomitant to the acute inflammatory response[86,87]. The fracture causes the immediate rupture of blood vessels, leading to blood clot formation by platelets. This fibrin-clot and degranulation of platelets release cytokines and paracrine factors (CCL2, …) to recruit inflammatory cells, such as macrophages, neutrophils, and lymphocytes at the site of injury[88–90]. Recruited immune cells come from the circulation or are recruited locally (osteomacs)[35]. Immune cells clear the injury site from dead cells, debris, and necrotic tissues and secrete pro-inflammatory cytokines including Interleukin 1(IL-1), IL-6, IL20, TNFα[91–95]. Following the pro-inflammatory phase, the immune response engages in an anti-inflammatory phase to terminate the first step of bone repair. Secretion of IL-13 and IL-4 promotes the switch of pro-inflammatory macrophages, usually named M1 macrophages, to anti-inflammatory macrophages, or M2[96–99]. M2 macrophages secrete anti-inflammatory factors such as Transforming Growth Factor beta (TGFβ) and IL-10. The resolution of the immune response is necessary for healing, as persistent inflammation impairs bone healing[100–102]. During the inflammatory phase, many growth factors are secreted to recruit SSPCs. Among those factors are CXCL12 (or SDF1), Platelet Derived Growth Factors (PDGFs), Fibroblast Growth Factors (FGFs), Nerve Growth Factor (NGF), and Bone Morphogenetic Proteins (BMPs)[103–110]. SSPCs are recruited from different sources: the bone marrow compartment, the periosteum, and the skeletal muscle surrounding the fracture site[27,28,111–114]. SSPCs activate, proliferate, migrate at the injury site and differentiate to form the fibrocartilaginous callus. During this fibrocartilaginous phase of repair, the fibrotic tissue first found in the center of the callus is progressively replaced by cartilage, where mechanical instability is high. At the periphery of the callus, where mechanical instability is low, SSPCs differentiate directly into osteoblasts via intramembranous ossification. As during bone development, chondrocytes mature to become hypertrophic and express ColX as well as pro-angiogenic factors such as VEGF to promote vascular invasion. The invasion of blood vessels marks the beginning of cartilage resorption, by the action of osteoclasts and matrix metallopeptidases (MMPs)[115–117]. A specific subtype of blood vessel-associated osteoclasts, named septoclasts, has been recently described as mediating cartilage resorption[118,119]. Hypertrophic chondrocytes undergo apoptosis or transdifferentiation into osteoblasts[56,120,121]. Osteoblasts progressively ossify the callus and form the bony callus. The last phase of healing corresponds to the remodeling phase[122]. The bony callus is progressively remodeled to allow the replacement of the woven bone into mature cortical bone and the reconstitution of the bone marrow cavity. This step is mediated by the action of osteoclasts and osteoblasts, and can last several months after the injury. Finally, the bone has regained its shape and exhibits the same mechanical properties as unfractured bone.

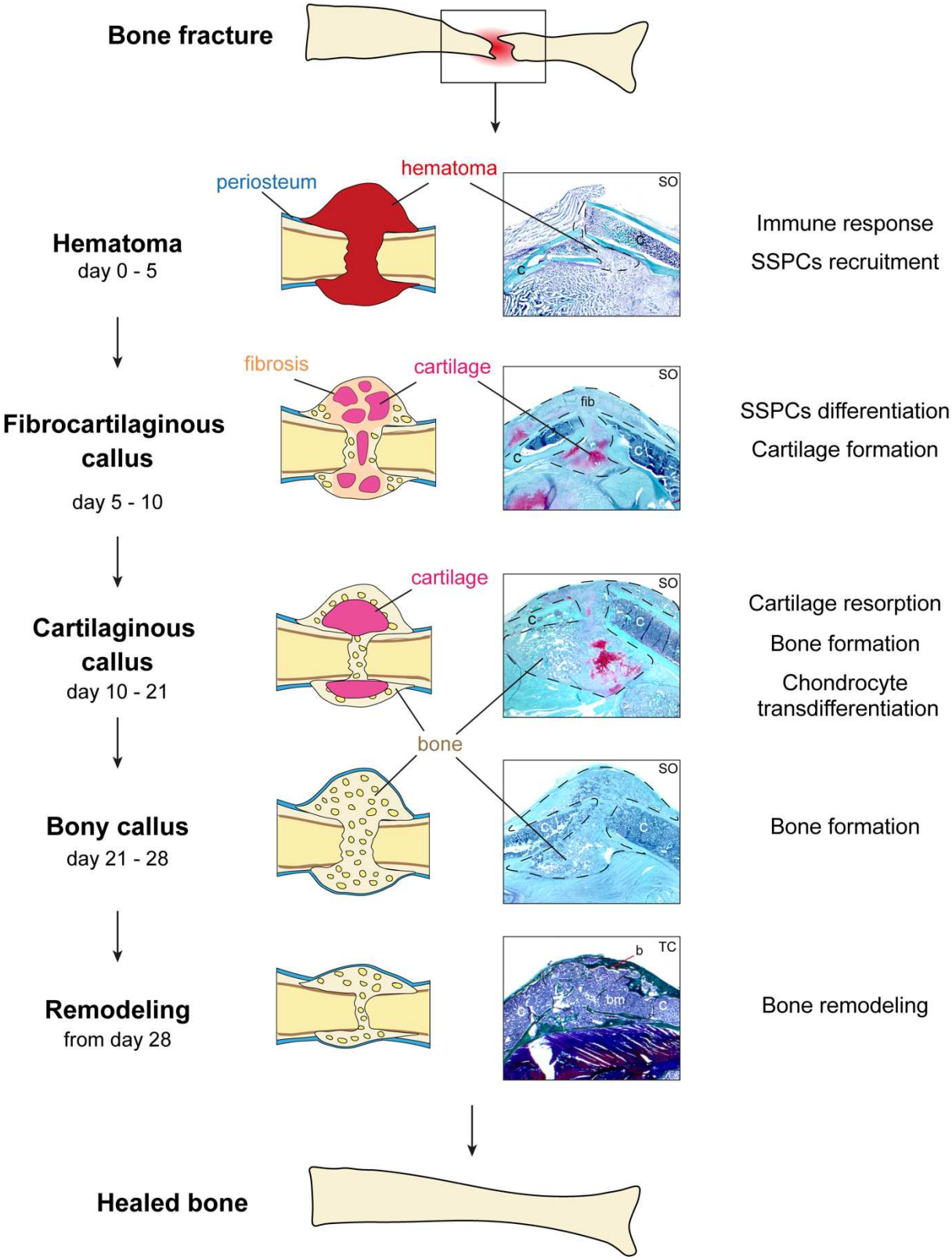

Figure 8: Steps of bone regeneration. Left: steps and timing of bone regeneration in mouse. Middle: scheme of bone regeneration steps and longitudinal callus sections stained by Safranin'O (SO), showing cartilage in pink, or Masson's Trichrome (TC), showing bone in green. fib: fibrosis. c: cortex. bm: bone marrow.

Chapter 2: Skeletal stem and progenitor cells

1. Diversity of cell sources for bone healing

1.1. From mesenchymal stem cells to skeletal stem/progenitor cells

In the 19th century, a first study from Cohnheim suggested that the bone marrow contains a population of cells that could give rise to fibroblasts[123]. In 1970, Alexander Friedenstein described bone marrow non-hematopoietic cells with in vitro osteogenic potential. These cells were adherent to plastic, formed clonogenic colonies, and were named colony-forming unit-fibroblasts (CFU-F). Further analysis showed their osteochondral potential and their capacity to reconstitute a marrow niche environment after ectopic transplantation. In 1991, Caplan proposed the term “mesenchymal stem cells”, or MSCs, to define these populations[124]. In 2006, the International Society for Cellular Therapy (ISCT) defined a list of 3 criteria to define MSCs to increase consistency among laboratories[125]. The criteria are (i) adherence to plastic in standard culture conditions, (ii) expression of specific cell surface markers (positive to CD105, CD73, CD90, and negative for hematopoietic and endothelial markers), and (iii) in vitro trilineage mesenchymal differentiation potential (adipogenic, osteogenic and chondrogenic) (Figure 9).

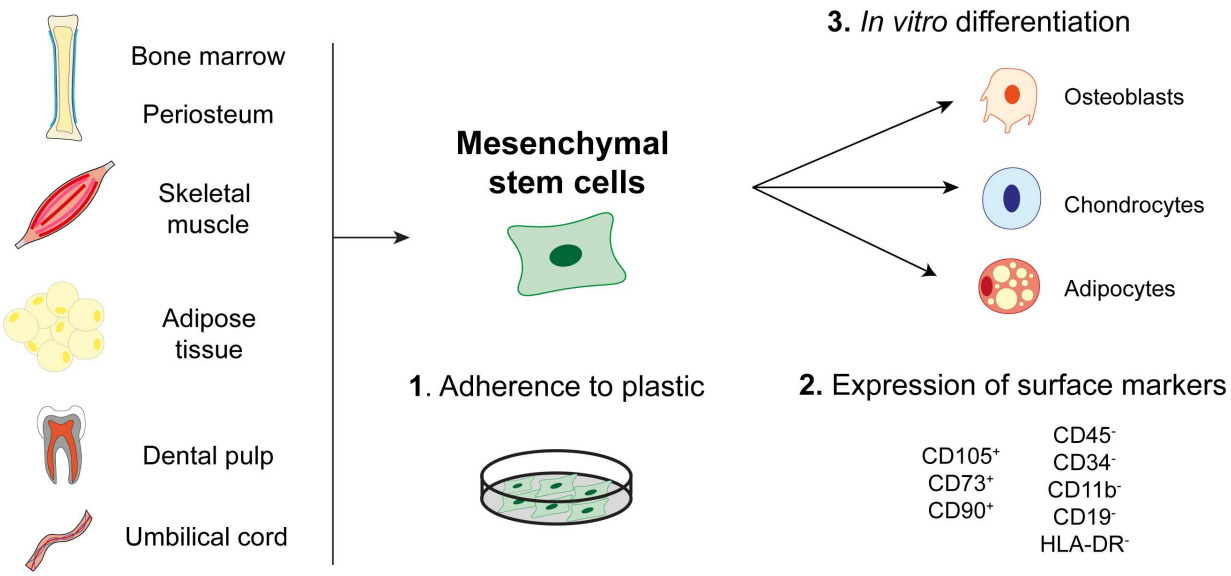

Figure 9: Criteria to define Mesenchymal Stem Cells from the ISCT in 2006.

However, the term “mesenchymal stem cells” has several limitations and its accuracy is questioned [126–128]. One concern is the use of the term mesenchymal. The mesenchyme is the embryonic tissue giving rise to many tissues, including skeletal tissue, muscle, blood vessels, and hematopoietic cells. There is no evidence of the presence of cells with this multipotent capacity in adult tissues and MSCs are only defined based on their adipogenic, osteogenic, and chondrogenic potentials. A second concern is the criterion of stemness for MSCs. Self-renewal potential is considered a hallmark of stem cell identity[129]. However, self-renewal potential is not a criterion to characterize MSCs according to the ISCT in 2006. In vitro clonal experiments are usually used to study stemness but the correlation with in vivo self-

renewing potential is limited. Finally, the term MSC is used to describe stromal populations in many tissues, including bone marrow, periosteum, adipose tissue, skeletal muscle, umbilical cord blood, and dental pulp. Despite sharing common characteristics, MSCs from different tissue origins exhibit differences in phenotype, function, and differentiation potential. Even within a given tissue, recent studies highlighted a strong heterogeneity of mesenchymal populations[130–134]. For these reasons, there is a need for an alternative terminology and nomenclature to define these populations.

Nowadays, the skeletal research field is progressively moving away from the MSC terminology to use the term skeletal stem/progenitor cells, or SSPCs. In vivo lineage tracing using transgenic mouse models allowed a better understanding of the role and fate of SSPCs. However, their identity remains debated. In 2015 and 2018, Chan *et al.* proposed a hierarchy model, based on the expression of cell surface markers, to define the mouse skeletal stem cell ($CD45^-$ $TER119^-$ $TIE2^-$ $CD51^+$ $THY1^-$ $6C3^-$ $CD105^-$) and human skeletal stem cell ($CD45^-$ $CD235^-$ $CD31^-$ $TIE2^-$ $PDPN^+$ $CD146^-$ $CD164^+$)[135,136]. As described before for the hematopoietic system, this model supports the idea of a unique stem cell population giving rise to different committed progenitors forming bone, cartilage, or stroma. However, this model is still highly debated. In 2019, Ono, Balani, and Kronenberg suggested that "*The notion that one or a few types of omnipotent skeletal stem cells can orchestrate the entire process of skeletal development and regeneration might be too simplistic. The current notion rather supports the hypothesis that multiple distinct types of skeletal stem and progenitor cells collaborate and cooperatively establish the network of the skeletal system*"[137]. Overall, the identity and heterogeneity of SSPCs remain elusive and their function during bone development, growth, remodeling, and repair is still highly investigated.

The concept that SSPCs represent heterogenous populations of cells is supported by the heterogeneity of markers identified to characterize them. Additionally, SSPCs present heterogeneity in their tissue location. After fracture, systemic recruitment of SSPCs is minimal[27,138]. SSPCs are recruited locally from the bone marrow, the skeletal muscle, and the periosteum (Figure 10).

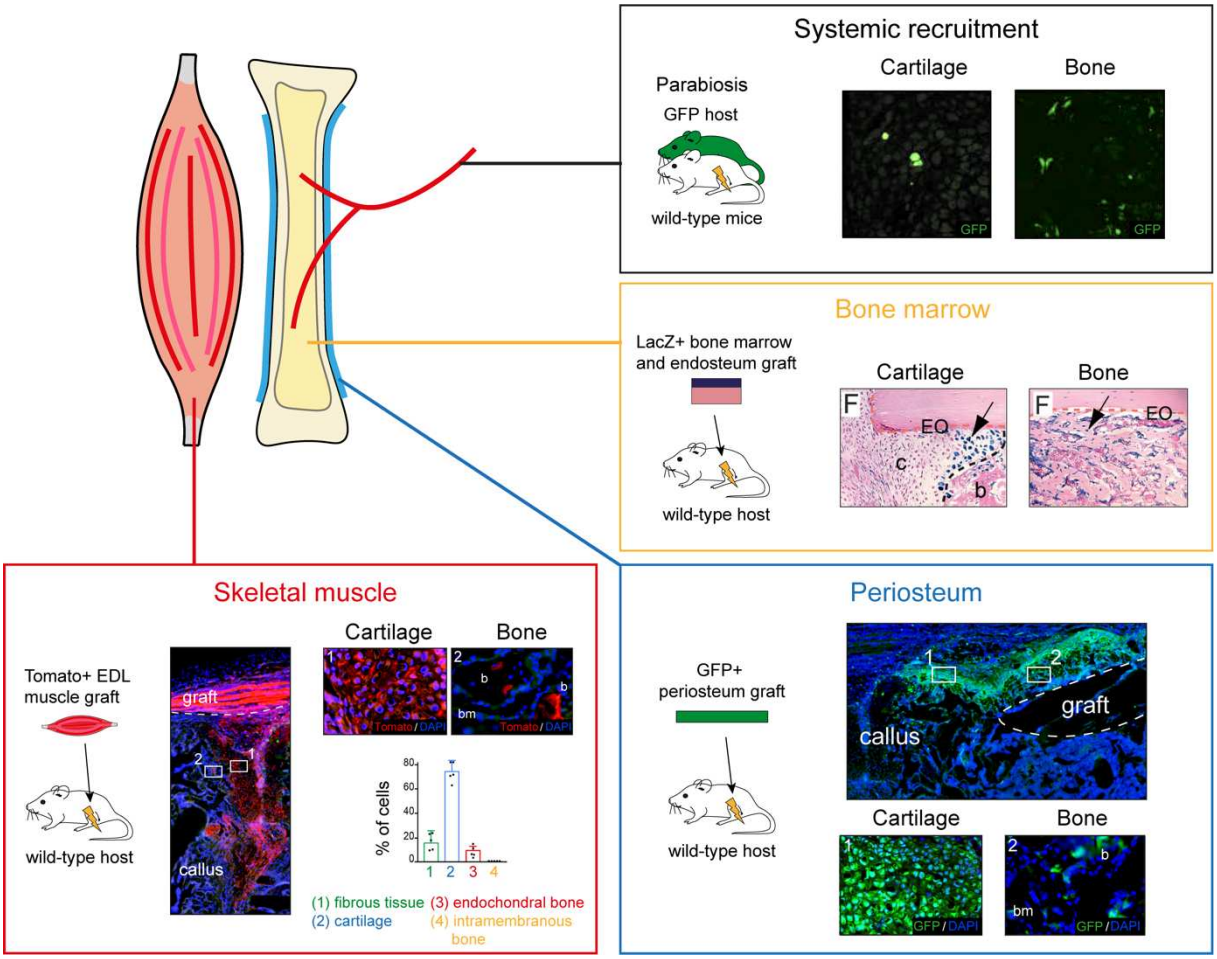

Figure 10: Tissue origin of skeletal stem/progenitor cells during bone repair. Black box: Systemic recruitment was assessed in parabiosis experiments between a GFP+ and a wild-type mouse. A fracture was induced in the wild-type mice and rare GFP+ cells were detected in the callus cartilage and bone. **Yellow box**: the contribution of the bone marrow compartment was assessed by grafting endosteum or bone marrow from a LacZ+ mouse at the site of fracture of a wild-type mouse. LacZ+ cells were detected in the intramembranous bone and only few in the cartilage. **Blue box**: the contribution of the periosteum was assessed by grafting periosteum from a GFP+ mouse at the site of fracture of a wild-type mouse. GFP+ cells were detected in the cartilage and bone in endochondral and intramembranous regions of the callus. **Red box**: the contribution of skeletal muscle was assessed by grafting EDL muscle from a Tomato+ mouse at the site of fracture of a wild-type mouse. Tomato+ cells were detected in the cartilage and bone. Quantification of the contribution showed that muscle-derived cells were only contributing to the endochondral process. Adapted from[111,112,138]

1.2. Skeletal stem and progenitor cells from the bone marrow

Due to their role in supporting hematopoiesis, the stromal cells of the bone marrow have been widely studied. The use of in vivo tracing tools, like the CRE/Lox system, increased the knowledge of the identity, location, and role of the different bone marrow stromal populations. Different markers have been identified for bone marrow SSPCs such as LEPR, CXCL12, GREM1, NESTIN, and MX1[139–143]. In the last decade, progress in high throughput sequencing at single-cell resolution led to a better photography of the bone marrow heterogeneity[131–133,144–148]. Different subpopulations of cells were defined, such as CXCL12-abundant reticular cells (CAR cells), expressing CXCL12 and LepR. CAR cells can be divided in Adipo-CAR and Osteo-CAR cells depending on the expression of adipogenic (*Adipoq, Lpl*) or osteogenic (*Bglap, Runx2*) genes. Using the *Cxcl12*^{CreERT}, Matsushita *et al.* described

the AdipoCAR population *in situ* and showed its role during cortical defect injury[113]. After injury, Adipo-CAR activate and differentiate into a pre-osteogenic state marked by expression of stemness markers and activation of the Wnt pathway, before engaging in osteogenesis. Additionally, many fibroblast populations were identified in the bone marrow, but their role and heterogeneity are poorly described.

The contribution of bone marrow SSPCs to bone repair is long known. However, tissue graft approaches and lineage tracing showed that bone marrow SSPCs were mostly contributing to bone formation and had a minimal chondrogenic potential after fracture[111]. Duchamp *et al.* showed that, despite their common embryonic origin with periosteum SSPCs, bone marrow SSPCs display a reduced colony forming efficiency, proliferation, and differentiation potential in vitro compared to periosteal cells. In vivo cell transplantation at fracture site showed that bone marrow SSPCs have a low efficiency to contribute to the callus compared to periosteal cells[27]. Bone marrow SSPCs are widely studied for cell-based orthopedic therapies. Although bone marrow SSPCs display a limited direct contribution to bone formation when transplanted, they exert paracrine and immunomodulatory roles that promote the resolution of the inflammatory phase of bone repair and the recruitment of SSPCs[149–152].

1.3. Skeletal stem and progenitor cells from the skeletal muscle

The role of skeletal muscle during bone repair as a mechanical support and source of factors is long known[153–157]. Recently, the skeletal muscle has been also described as a source of SSPCs for bone repair. Using lineage tracing and muscle graft approaches, Julien *et al.* showed that the muscle contains a population of SSPCs that migrate at the fracture site to form the callus [112]. In vitro, satellite cells and non-myogenic mesenchymal cells from adult skeletal muscle can form osteoblasts [158,159]. However, in vivo, only the non-myogenic interstitial cells derived from the Prx1-expressing limb bud mesenchyme are contributing to the callus. Skeletal muscle-derived cells are mostly contributing to cartilage. Single-cell RNAseq of skeletal muscle Prx1-derived cells showed that they correspond to a heterogenous population, predominantly composed of fibro-adipogenic progenitors / mesenchymal progenitors (FAP/MP). This population express markers such as PDGFRα, SCA1, CD34, and CD90 (THY1), and display adipogenic, osteogenic, and chondrogenic potentials in vitro. After fracture, the FAP/MP population leaves a stem/progenitor state to engage in fibrogenesis, characterized by an active extracellular matrix production, before undergoing chondrogenic differentiation. The skeletal muscle SSPCs are involved in several pathological conditions. Bone formation in the muscle, or heterotopic ossification, is observed in mice or patients with a muscle injury concomitant with a second systemic injury (skin burn, lung trauma)[160,161]. In musculoskeletal trauma, when a fracture is combined with a muscle injury, the accumulation of muscle-derived fibrotic tissue is observed at the fracture site and leads to non-union[112].

2. Periosteal skeletal stem and progenitor cells

The capacity of the periosteum to form bone after a fracture was first described in 1845 by Alexander Watson[162]. The periosteum displays a remarkable ability to regenerate bones and is indispensable to achieve bone healing. Indeed, its removal at the time of fracture can cause altered healing and non-union in experimental models as the periosteum is a key source of SSPCs for bone repair[163–167].

2.1. Characterization of periosteal stem and progenitor cells

Studying the periosteum and periosteal SSPCs (pSSPCs) is challenging due to its inaccessibility and thinness. Human pSSPCs have been isolated by scrapping or peeling away the periosteum from the cortex, followed by enzymatic digestion or explant culture[168]. In animal models, similar techniques have been employed. In addition, protocols have been developed to directly isolate cells by enzymatic digestion of the bone surface or by whole bone explant culture [169–172]. The presence of cells within the periosteum corresponding to the "mesenchymal stem cells" criteria was described in the 1980s[173–176]. Analysis of cell surface markers showed that pSSPCs are negative for hematopoietic and endothelial markers and express canonical mesenchymal markers such as CD90, CD105, CD51, CD29, and Sca1 in mice and CD90, CD105, CD73 in human [27,169,177–179]. The SSPC populations defined by the markers from Chan *et al.* were also identified in freshly isolated mouse and human bones [114,135,180]. Periosteal SSPCs exhibit multipotency in vitro with tri-lineage differentiation capacity towards osteogenesis, chondrogenesis, and adipogenesis [178,181]. The multipotency and differentiation potential of pSSPCs was confirmed by in vivo ectopic transplantation experiments [182,183]. Both mouse and human pSSPCs display self-renewal potential in serial CFU or ectopic transplantation assays [28,107].

2.2. Fate of periosteal stem and progenitor cells during bone regeneration

The direct contribution of the periosteum to bone regeneration is well established. The periosteal response to bone fracture is characterized by periosteum thickening near the site of injury within few days after fracture. Activated periosteal SSPCs proliferate and migrate at the fracture site, and participate in both intramembranous and endochondral ossification [27,111]. This ability of pSSPCs to form cartilage and bone after fracture is unique to the periosteum as SSPCs from bone marrow mostly contribute to bone and SSPCs from skeletal muscle contribute to cartilage [27,27,28,113]. The steps of activation of pSSPCS are still poorly described and were investigated in the first aim of the thesis. The regulation of fate decision of pSSPCs towards osteogenesis or chondrogenesis is also poorly understood. A recent study by Van Gastel *et al.* showed that pSSPCs can be directed towards chondrogenesis after fracture by blocking vascular ingrowth to prevent nutrient availability [184]. Activated pSSPCs with sufficient lipid intake can maintain sufficient levels of fatty acid oxidation and differentiate into osteoblasts. However, in regions with low lipid availability, reduced fatty oxidation leads to FOXO activation, SOX9 expression, and chondrogenic differentiation[184]. Periosteal-derived chondrocytes undergo maturation and hypertrophy. The second aim of the thesis focused on understanding the importance of periosteal-derived chondrocytes maturation and cartilage-to-bone transition for bone

repair. Finally, during the late stages of repair, pSSPCs can self-renew to reconstitute a new periosteum at the periphery of the callus. The in vivo self-renewal capacity of pSSPCs during bone repair was revealed using periosteum graft and serial fracture, showing that the periosteum maintains a pool of stem cells able to contribute to a subsequent injury[27].

2.3. Genetic lineage tracing of periosteal stem and progenitor cells during bone repair

To understand the endogenous role and fate of pSSPCs during bone regeneration, in vivo approaches using transgenic mouse models are still one of the most useful tools. These studies take advantage of the CRE/LOX system to label and trace pSSPCs during bone repair based on the expression of different markers listed in Table 1. Due to their mesenchymal origin, pSSPCs in long bones can be tracked from developmental stages using the limb bud mesenchymal marker PRX1. The non-inducible *Prrx1*^{Cre} model labels not only SSPCs in the periosteum but also SSPCs in the bone marrow and skeletal muscle[27,112]. In adult bone, pSSPCs still express *Prrx1* but the inducible *Prrx1*^{CreERT} model does not allow efficient labeling of pSSPCs [27,185]. The Platelet-Derived Growth Factor α (PDGFRα) has been described as a marker of mesenchymal cells from various tissue origins. Studies using the *Pdgfra*^{CreERT} model showed that PDGFRα marks pSSPCs with osteochondral potential during bone healing but is not restricted to the periosteum [114,186–188].

Debnath *et al.* combined the markers described by Chan *et al*. with the marker Cathepsin K (CTSK) and identified a population of pSSPCs involved in intramembranous ossification[28]. CTSK+ pSSPCs, traced in the non-inducible *Ctsk*^{Cre} model, display self-renewing capacity and osteochondral potential in calvarial or femoral injury models. scRNAseq analysis of sorted CTSK+ pSSPCs showed heterogeneity within this population, with cell clusters expressing chondrogenic genes (*Col2a1, Sox9*), osteogenic markers (*Kera, Alpl*), stemness markers (*Ly6a, Cd34*), and *Acta2* [28]. CTSK+ and CD200+ periosteal cells were also detected in human periosteum[28].

The protein alpha-Smooth Muscle Actin (αSMA), encoded by the *Acta2* gene, labels cells in the periosteum[189,190]. αSMA+ periosteal cells, traced using the *Acta2*^{CreERT} mouse line, are a heterogenous population of osteochondroprogenitors, with self-renewing potential and required for efficient bone healing[114]. Ortinau et colleagues described a sub-population of αSMA+ cells, using the pIpC inducible Mx1Cre line[191]. αSMA+ Mx1+ pSSPCs display self-renewal potential and are required for callus formation after tibial and calvarial injury [191].

Several other markers have been identified, such as the Wnt downstream target AXIN2, the receptor PDGFRβ, and HOX11[192–194]. Markers, such as Leptin receptor and Nestin, used to characterize bone marrow self-renewing SSPCs also label cells in the periosteum[107,195]. Tournaire *et al.* reported that Nestin-GFP+ periosteal cells in Nestin-GFP transgenic mice correspond to unipotent osteoprogenitors, with limited contribution to callus formation and no stemness properties[195]. Lineage tracing in the *Nes*^{CreERT} model revealed an osteogenic and self-renewing potential of Nestin+ periosteal cells[107]. GLI1 labels populations of SSPCs, including in the periosteum, forming chondrocytes and osteoblasts after

fracture[196,197]. Osteochondrogenic markers such as SOX9 (*Sox9*^{CreERT} model) and Osterix (*Osx*^{Cre} model) both label populations of periosteal progenitors contributing to cartilage and bone formation after fracture [193,198].

Markers	Mouse model	Injury model	Contribution	Comment	Used in
PRX1	*Prrx1* ^{Cre}	Non stabilized tibial fracture	Cartilage / Bone	Labels all SSPCs	Duchamp et al.
	Prrx1 ^{CreERT}	Non stabilized ulna fracture	Cartilage / Bone	Low cell labelling	Kawanami et al.
PDGFRα	*Pdgfra* ^{CreERT}	Non stabilized forelimb fracture	Bone / Cartilage		Xu et al.
CTSK	*Ctsk* ^{Cre}	Semi stabilized femoral fracture	Bone / Cartilage		Debnath et al.
		Calvarial cortical defect	Bone		
αSMA	*aSMA* ^{CreERT}	Semi stabilized tibial fracture	Bone / Cartilage		Matthews et al.
	aSMA-GFP	Calvarial cortical defect	Bone		Ortinau et al.
MX1	*Mx1* ^{Cre}	Non stabilized tibial fracture	Bone / Cartilage	Requires pIpC injection to induce Cre recombination	Ortinau et al.
		Tibial periosteal defect	Bone		
		Tibial cortical defect	Bone		
		Calvarial cortical defect	Bone		
AXIN2	*Axin2* ^{CreERT}	Tibial cortical defect	Bone		Ransom et al.
PDGFRβ	*Pdgfrb* ^{Cre}	Semi stabilized femoral fracture	Bone / Cartilage		Bohm et al.
HOX11	*Hoxa11* ^{CreERT2}	Non stabilized ulnar fracture	Bone / Cartilage	Restricted to zeugopod bone	Pineault et al.
GLI1	*Gli1* ^{CreERT1}	Semi stabilized femoral fracture	Bone / Cartilage		Shi et al.
		Semi stabilized tibial fracture	Bone / Cartilage		Xia et al.
Nestin	*Nes-GFP*	Semi stabilized tibial fracture	Bone	Marks bone marrow SSPCs	Tournaire et al.
	Nes ^{CreERT}	Tibial cortical defect	Bone	Marks bone marrow SSPCs	Gao et al.
LEPR	*Lepr* ^{Cre}	Tibial cortical defect	Bone	Marks bone marrow SSPCs	Gao et al.
SOX9	*Sox9* ^{CreERT}	Semi stabilized femoral fracture	Bone / Cartilage		He et al.
		Rib bone resection	Bone / Cartilage	Labelling is increased when induced after fracture	Kuwahara et al.
OSX	*Osx* ^{Cre}	Semi stabilized tibial fracture	Bone / Cartilage		Bohm et al.

Table 1: Markers and mouse lines labeling pSSPCs. Adapted from[199]

Overall, periosteal SSPCs populations defined by these different markers and CRE models display similar proprieties, such as the expression of stem/progenitor markers, osteochondral fate after fracture, and self-renewing capacity. It remains unclear how these populations overlap and differ in their identity and potential, and whether the periosteum encompasses several populations of SSPCs. A major challenge to study pSSPCs remains the absence of a marker fully specific to the periosteum as most of them are expressed also by cells localized in the bone marrow, skeletal muscle, or stromal cells in other tissues [27,188,200].

2.4. Molecular regulation of periosteal stem and progenitor cells

During bone repair, pSSPC proliferation, migration, and differentiation are governed by several signaling pathways including Bone morphogenic protein (BMP), Wnt, Notch, Fibroblast growth factor (FGF), Platelet-derived growth factor (PDGF), Transforming growth factor β (TGFβ), and Hedgehog (HH) signaling (Figure 11).

The Bone Morphogenetic protein (BMP) signaling is one of the major pathways regulating bone development, growth, remodeling, and repair[201,202]. There are 9 BMP ligands known to be involved in bone physiology. They bind to BMP receptors composed of two alpha or beta subunits, encoded by the *Bmpr1a*, *Bmpr1b,* and *Bmpr2* genes. The BMP signaling is active in the first days after bone injury. Increased BMP ligand and receptor expression, as well as activated downstream SMAD effectors, are observed in the activated periosteum at day 3 post-fracture[203]. Several studies investigated the importance of BMP ligand expression by SPPCs during bone repair. BMP2 inactivation in Prx1-derived SSPCs prevents periosteal activation bone repair showing the necessity of endogenous BMP production [110,204]. BMP4 and BMP7 inactivation in SSPCs did not show an impact on bone healing[205,206]. BMP2 can also play a role in pSSPC fate decision but the exact role of BMP signaling in pSSPC activation remains elusive[207].

Notch and Wnt signaling are 2 well-known mediators of the activation of SSPCs. Notch plays a role in the early activation of pSSPCs before they commit to the chondrogenic or osteogenic lineage, while expression of the Wnt pathway peaks between 5- and 10-days post-fracture [208–211]. In the early steps, Notch signaling promotes pSSPC activation and proliferation [208]. Inhibition of Notch signaling by Wnt marks the end of the pSSPC activation phase and the initiation of osteogenic differentiation[211,212]. Wnt regulates the differentiation of SSPCs by promoting osteogenic differentiation over chondrogenesis through SOX9 repression [213].

Fibroblast growth factors (FGFs) are a family of growth factors composed of 22 ligands that bind to 4 receptors coded by the *Fgfr1, Fgfr2, Fgfr3,* and *Fgfr4* genes[214]. FGFs are involved in the development and homeostasis of many tissues (heart, brain, lung) and are essential regulators of skeletal development[215–219]. Indeed, overactivation of the FGF signaling by mutation of the *FGFR3* gene is responsible for achondroplasia or dwarfism[220–222]. After fracture, FGFs are expressed during pSSPCs activation, during which FGF2 promotes the proliferation and chondrogenic differentiation of pSSPCs through BMP2 signaling [223–225]. FGFs are also expressed during cartilage formation and maturation (FGF16, FGF18), and during ossification (FGF1, FGF17), suggesting their involvement through all stages of repair[223].

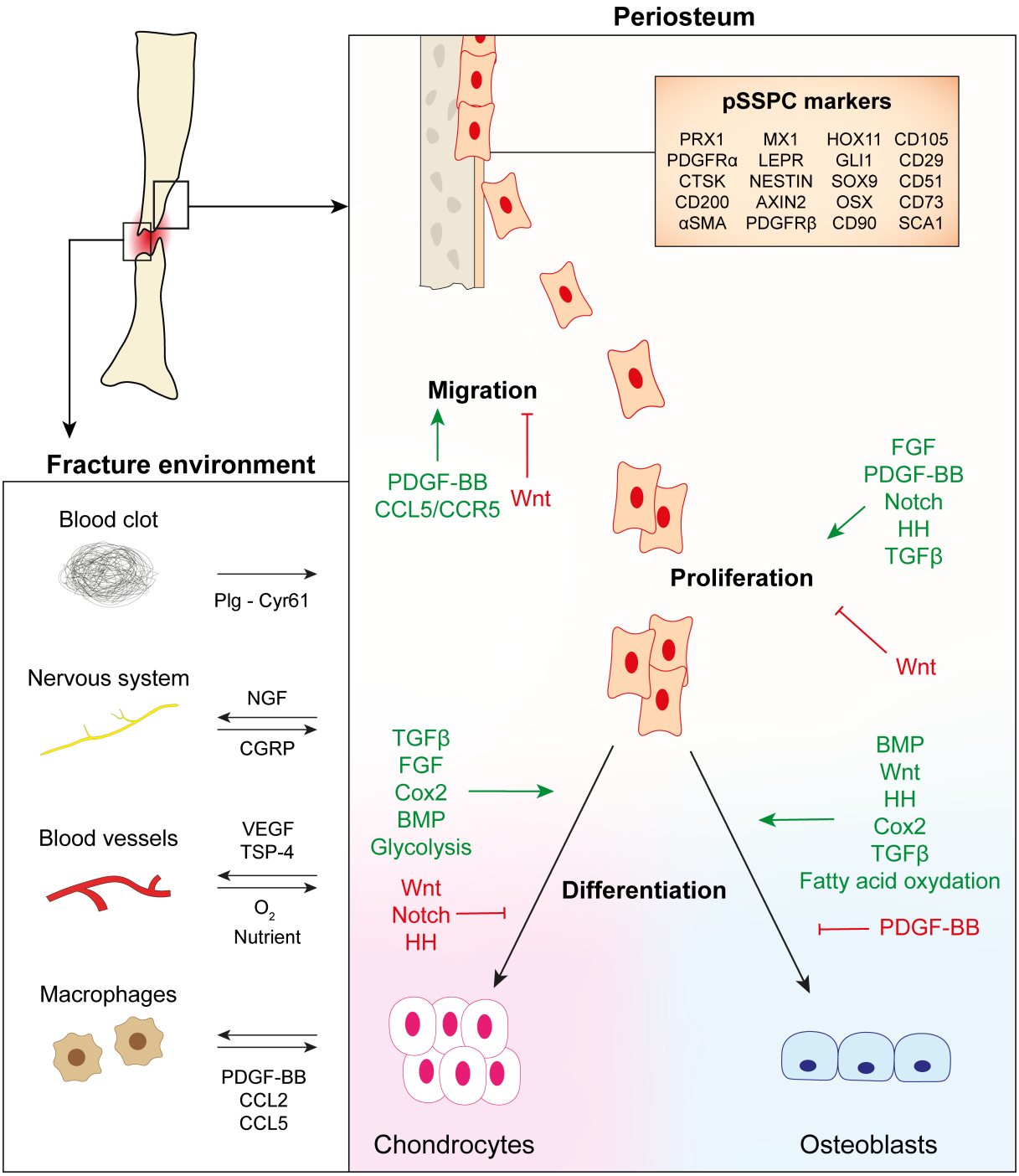

Figure 11: **Fate and regulation of periosteal stem/progenitor cells during bone repair.**
After fracture, periosteal stem/progenitor cells (pSSPCs), labeled by several markers (orange box) migrate to the site of injury, proliferate and differentiate into chondrocytes or osteoblasts. These steps are controlled by several signaling pathways (activation in green and inhibition in red). The fate of pSSPCs is also influenced by their interactions with the fracture environment, including the blood clot, nerve fibers, blood vessels, and macrophages (left box). Adapted from[199]

Several other growth factors and signaling pathways have been investigated. Transforming growth factor beta (TGFβ) encompasses 3 ligands (TGFβ1, TGFβ2, TGFβ3)[226]. TGFβ is known for its central role in fibrosis tissue formation in many tissues (skin, lung, heart) [227–231]. During bone repair, increased TGFβ expression is observed and regulates pSSPCs proliferation and osteogenic differentiation[197,232,233]. Platelet-derived growth factor BB (PDGF-BB), and Hedgehog are required for

pSSPC proliferation and differentiation [172,234–238]. Additionally, PDGF-BB stimulates pSSPCs migration and angiotropism while inhibiting apoptosis [107,193]. Cyclooxygenase 2 (COX2) is essential for the initiation of the periosteal response to cortical bone injury by modulating several key pathways such as Hif, PI3K-Akt, and Wnt [239–241]. In sum, many signaling pathways and growth factors must act in coordination to control pSSPC activation and subsequent steps of differentiation.

2.5. Influence of the fracture environment on periosteal stem and progenitor cells

Bone fracture creates a major perturbation of bone tissue homeostasis with the rupture of blood vessels and nerve fibers, and an acute inflammatory response occurring shortly after fracture. This multicellular environment plays a crucial role in the activation and fate decision of pSSPCs (Figure 11). The disruption of blood vessels causes immediate bleeding and subsequent blood clot formation. The blood clot is progressively degraded by the action of enzymes such as plasminogen which plays a paracrine role in the activation of pSSPCs through the matrix-associated growth factor Cyr61[242,243]. Vascular disruption at the fracture site subsequently causes hypoxia, HIF1α expression by pSSPCs, and the secretion of proangiogenic factors required for angiogenesis and bone healing[169,244–246]. Periosteum removal reduces blood vessel density at the injury site[184]. The role of the periosteum in the revascularization of the fracture site and especially the interplay between blood vessels and pSSPCs requires further investigation.

During the inflammatory phase of bone healing, the periosteum becomes invaded with osteomacs and activated macrophages [35]. Macrophages secrete factors involved in the recruitment and activation of pSSPCs. Gao *et al.* showed that TRAP+ periosteal macrophages secrete PDGF-BB, which binds to PDGFRβ expressed by pSSPCs and stimulates Periostin expression, a critical regulator of pSSPC response to injury and self-renewal [27,107]. Periosteal SSPCs are responsive to different chemokines, such as CCL2-MCP1[88,89]. The CCL5-CCR5 axis is necessary to induce the migration of murine and human pSSPCs[191]. In vitro osteogenic induction of periosteal cells can modulate macrophage polarization and promote M2 phenotype by secreting chemokines suggesting a crosstalk between macrophages and pSSPCs[247,248].

The disruption of nerve fibers in the periosteum triggers rapid nerve sprouting from both sympathetic and sensory fibers in the first day post-bone injury. Nerve sprouting is concomitant with NGF expression in periosteal cells and macrophages, and occurs prior to revascularization [249]. Nerves subsequently regulate pSSPCs activation by releasing neuropeptide calcitonin gene-related peptide (CGRP), that binds to the CALCRL-RAMP1 receptor and stimulates Osterix expression [250]. The implication of Schwann cells, the glial cells of peripheral nerves, in bone healing and its potential interactions with pSSPCS is still unknown. A study from Jones *et al.* described the requirement of innervation for mandibular injury healing and suggest that Schwann cells are a source of secreted factors for bone healing[251].

2.6. Clinical applications of periosteal stem and progenitor cells for bone repair

As the periosteum is an essential actor of bone healing, pSSPC deficiencies can have direct consequences on repair. Metabolic dysregulation in mice with induced type 1 diabetes reduces callus formation, correlated with decreased pSSPC proliferation and osteogenic differentiation [252]. Mice with diet-induced obesity (DIO) and subsequent type 2 diabetes also exhibit impaired fracture healing[253,254]. Periosteal SSPCs isolated from DIO mice show reduced osteochondral and adipogenic differentiation potential in vitro [254]. Aging is a long-known factor affecting bone repair in human and animal models partially due to a reduction of pSSPC potential and number [255,256]. Two reports indicate abnormal extracellular matrix deposition and proliferation of periosteal cells isolated from 1-year-old mice and reduced chondrogenic potential when isolated from 2-year-old mice [257,258]. Aging is frequently linked to osteoporosis. Mice with estrogen or glucocorticoid-induced osteoporosis display an abnormal periosteal response to scratch injury, caused by a reduced cartilage formation and maturation[259]. Overall, dysfunctions of pSSPCs are still poorly described but could be of major interest to understand bone healing impairment.

Periosteum flap or allografts are frequently used in orthopedic surgery to promote bone repair with convincing results in animal models and patients[260–262]. Periosteal SSPCs are therefore considered for cell-based therapies. Transplanted pSSPCs can improve bone healing in aged mice and critical size defects[263,264]. Bone tissue engineering aims to replace autograft approaches, by using cultured SSPCs embedded in a 3D matrix containing growth factors[265]. The choice of the optimal cell source is key for successful bone tissue engineering and the periosteum rise as a promising source of cells. Compared to other cell sources, such as bone marrow, adipose, or dental pulp-derived cells, pSSPCs display higher clonogenicity, proliferation, osteogenic, and chondrogenic differentiation[27,265,266]. Moreover, the potential of pSSPCs can be increased depending on the harvesting site and by using pre-treatment with BMP2 or FGF2[180,267,268]. The development of periosteum-like matrix, that mimics the structural organization and cellular composition of the periosteum is also explored with encouraging results[269]. Growth factors can be added to the scaffold to stimulate endogenous pSSPCs or promote angiogenesis of the grafted bioengineered tissue (VEGF)[265,270].

Chapter 3: Neurofibromatosis type 1

Neurofibromatosis type 1, or NF1, is an autosomal dominant disorder, affecting 1 in 3000 individuals worldwide, without differences between gender or ethnicity[271,272]. The first suspected case of NF1 is Cro-Magnon 1, a 30,000-years old skeleton discovered in France in 1868 that presents clinical features of the disease[273]. First reports of NF1 symptoms were made during the 1300s[274,275] and the first description of NF1 as a multisystemic disease was performed by Friedrich von Recklinghausen in 1882[276,277]. NF1 is a progressive multi-systemic disease with cutaneous, neurologic, and orthopedic manifestations. The increasing description of NF1 clinical features led to the publication of a list of criteria to define NF1 in 1987 by the NIH Consensus Development Conference[278]. The NF1 diagnostic criteria were revised in 2021[279]. NF1 is characterized by a high heterogeneity of manifestations, severity, and prognosis between patients. NF1 treatment remains highly challenging and patients have a decreased quality of life and life expectancy of 10-20 years[280–283].

1. *NF1* gene and neurofibromin

1.1. *NF1* gene

The gene responsible for Neurofibromatosis type 1 was identified in 1990[284]. This gene, named *NF1*, is one of the longest in the human genome (287 kbp) and is located on chromosome 17 (region 17q11.2). *NF1* is composed of 57 exons, with 4 alternative spliced exons (11alt12, 12alt13, 30alt31, 56alt57)(Figure 12)[285,286]. *NF1* gene is highly conversed among species with high homology (98% of homology between human and murine sequences)[286]. The messenger RNA (mRNA) from *NF1* is 11 to 13 kbp, with around 8.5 kbp of open reading frame and 3.5 kbp of untranslated region. *NF1* expression is highly regulated at the level of transcription and translation by several proteins and non-coding RNA[287–289]. *NF1* is ubiquitously expressed, with a strong expression detected in the nervous system and glial cells[290]. In bone, *NF1* is expressed in most cell types, including osteoblasts, osteocytes, osteoclasts, chondrocytes, periosteal cells, and bone marrow stromal cells[291,292].

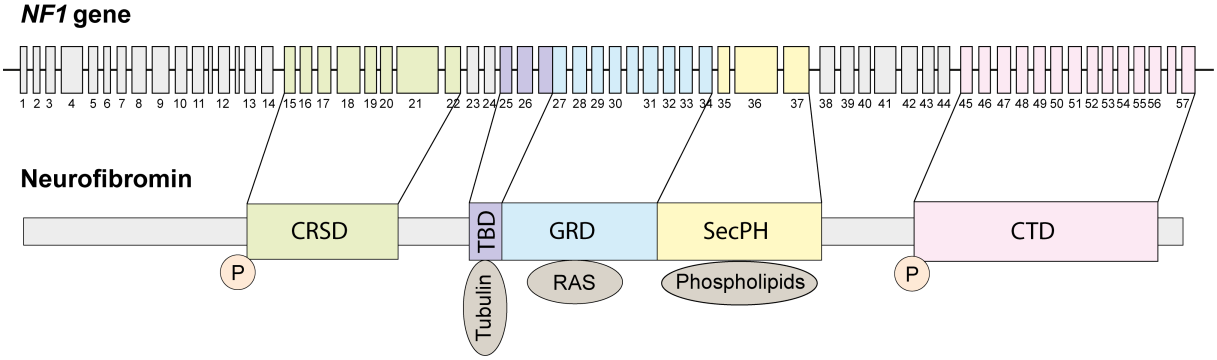

Figure 12: Structure of the *NF1* gene and the neurofibromin. Unlabeled exons correspond to alternatively spliced exons. CSRD: cysteine-serine-rich domain; TBD: tubulin-binding domain; GRD: GAP-related domain; SecPH: phospholipid- and protein-interaction domain; CTD: C-terminal domain; P: phosphorylated domains. Adapted from[286,293,294]

1.2. Neurofibromin and downstream effectors

The *NF1* gene codes for a large multi-domain protein, the neurofibromin[295,296]. It is a 250kDa protein composed of an N-terminal cysteine-serine-rich domain (CSRD), a tubulin-binding domain (TBD), a GAP-related domain (GRD), a phospholipid- and protein-interaction domain (SecPH), and a C-terminal domain (CTD)[297–299] (Figure 12). The different domains provide different functions to the protein. The CSRD and CTD domains can be phosphorylated by protein kinases A and C to regulate the activity and cellular localization of neurofibromin[300–303]. The TBD and SecPH domains allow interactions with the tubulin cytoskeleton and cytosolic membrane lipids[304–306]. The GRD domain binds to RAS proteins, binary molecules that switch from an active form bonded to GTP to an inactive GDP-bonded form (Figure 13)[307–310]. RAS proteins are activated in response to the binding of ligands to their tyrosine kinase receptors, such as PDGF and FGF receptors[311]. Ligand binding activates kinases/phosphatases, such as GRB2 and SHP2 to activate nucleotide exchange factors (GEFs), like SOS. GEFs convert RAS-GDP in its active form, RAS-GTP. RAS-GTP activates many signaling pathways, including the mitogen-activated protein kinase (MAPK) cascade and the PI3 kinase/Akt/mammalian target of rapamycin (mTOR) pathway. The MAPK cascade corresponds to a succession of 3 kinases, phosphorylating each other and regulating different transcription factors (Elk-1, c-Jun, ATF2, and p53)[312,313].

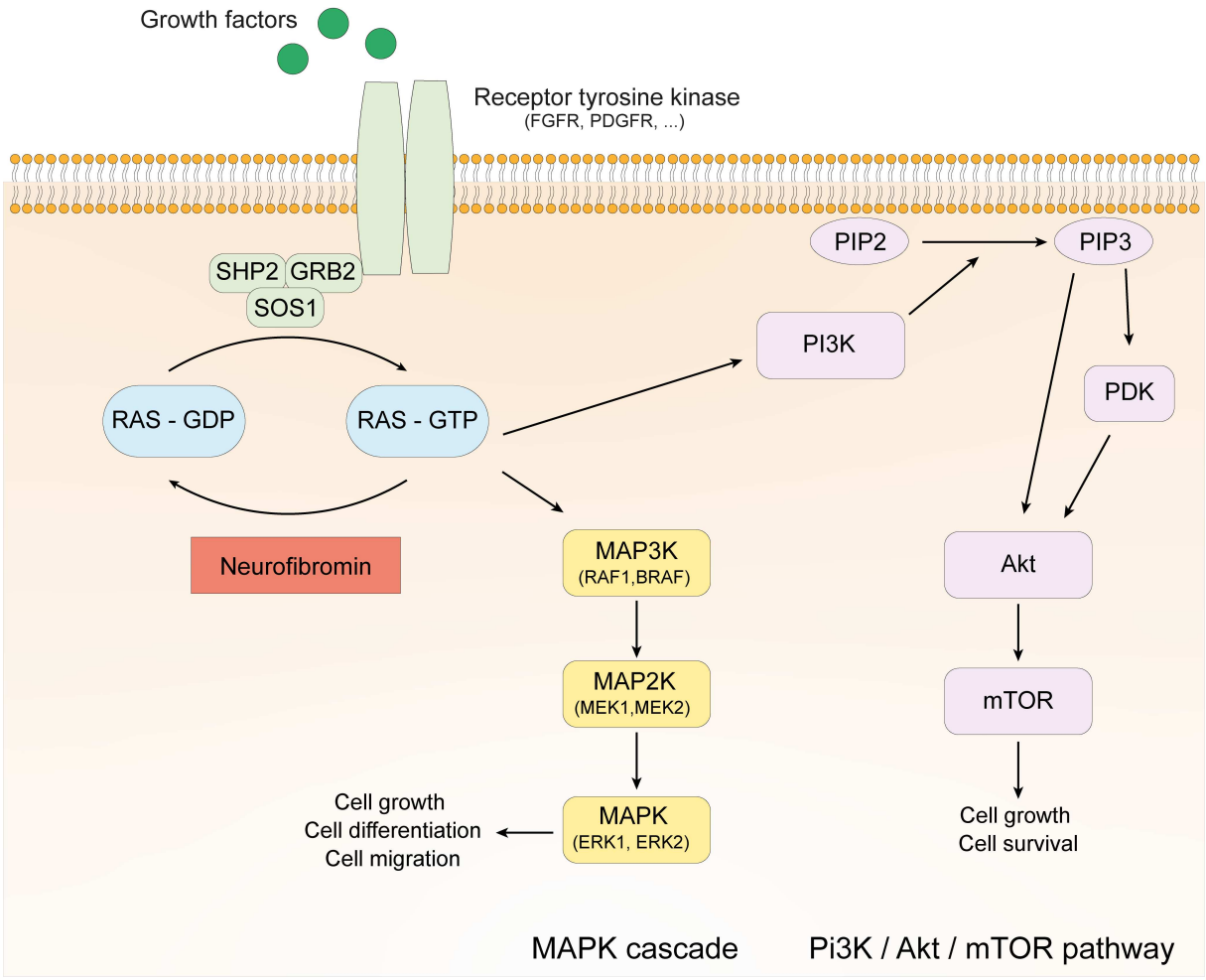

Figure 13: Signaling pathways regulated by RAS and neurofibromin

The MAPK cascade is involved in the regulation of many critical cell functions, including proliferation, differentiation, migration, senescence, and apoptosis[312,314]. Active RAS-GTP also activates the PI3 Kinase by its subunit p110. PI3K phosphorylates phosphatidylinositols causing the activation of PDK-1 and Akt kinases and downstream activation of the mTOR complex. The PI3K/Akt/mTOR signaling is involved in the regulation of cell growth and survival[315,316]. The regulation of RAS is highly sensitive and allows a tight regulation of the RAS signaling depending on incoming signals. This regulation relies on phosphatase and GTPase activating proteins (GAPs) such as neurofibromin. GAPs activate the GTPase function of RAS and induce the cleavage of GTP to obtain inactive RAS-GDP. The neurofibromin, as a negative regulator of the RAS proteins, regulates cell growth and survival. Its inactivation leads to an increased active RAS-GTP intracellular level, an overactivation of the downstream signaling pathways, and over proliferation. Thus, the *NF1* gene is classified as a tumor suppressor gene. There are several isoforms of neurofibromin, RAS (HRAS, KRAS, NRAS), and its downstream kinases. The presence of signaling networks or interactions specific to some cell types or mutations is one of the hypotheses that could explain NF1 phenotypic heterogeneity. In addition, neurofibromin also has functions in cell signaling independent of RAS, via the regulation of cAMP or interactions with the cytoskeleton [297].

2. Symptoms of Neurofibromatosis type 1

NF1 is characterized by a wide range of manifestations with high heterogeneity, severity, and prognosis between patients[271,272]. NF1 symptoms manifest progressively through all lifespan, but a full penetrance is observed from 8 years old (Figure 14-15).

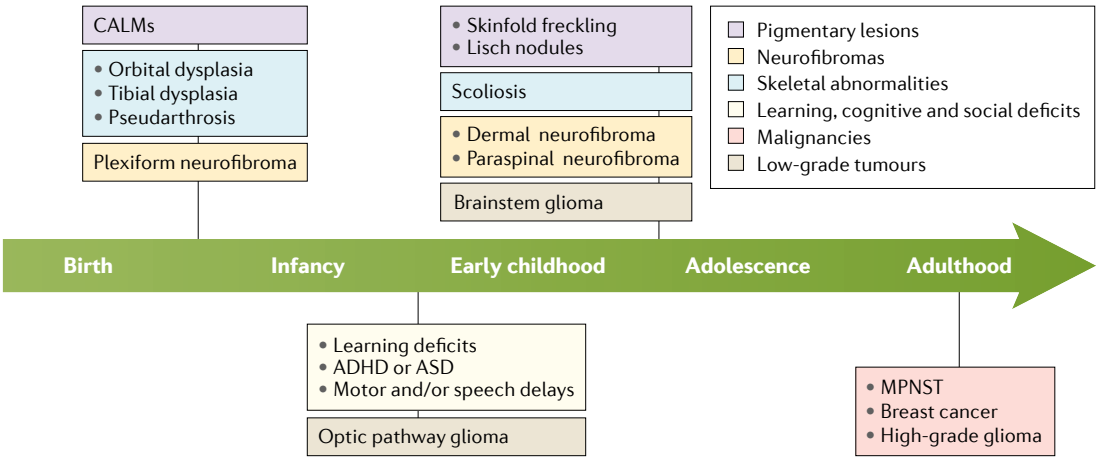

Figure 14: Progressive development of NF1 symptoms from birth to adulthood. From[271]

2.1. NF1, a multisystemic disease

Neurofibromas and Malignant Peripheral Nerve Sheath Tumors.

The hallmark of NF1 is the development of benign nerve sheath tumors, named neurofibromas (NFs). Almost all NF1 patients develop neurofibromas but the number, size, and age of appearance are highly

heterogenous between patients. These tumors are located along nerves and are composed of Schwann cells, axons, fibroblasts, immune cells, endothelial cells, and perineurial cells[271]. Based on their location, they are usually divided between cutaneous neurofibromas (cNFs), subcutaneous neurofibromas (scNFs), and plexiform neurofibromas (pNFs). cNFs are located on the skin and correspond to soft round tumors, usually hyperpigmented. cNFs are rare during early childhood and develop in almost all NF1 patients during late childhood and adolescence. These tumors are only benign and cannot transform into malignant tumors. scNFs are located in the dermis and affect around 20% of patients. Subcutaneous NFs rarely transform into malignant tumors[317]. pNFs are detected in 60% of NF1 patients and are located along peripheral nerves within the body[318]. They can have a paraspinal location and affect nerve roots. pNFs have an early onset but they grow during childhood and adolescence. Around 20 to 30% of pNFs can undergo a transformation to form malignant tumors, called Malignant Peripheral Nerve Sheath Tumors (MPNSTs)[319,320]. This transformation is usually caused by additional mutations in tumor-suppressor genes such as *TP53*, *CDKN2A,* or *SUZ12*[321–324]. MPNSTs can vary in severity but are associated with a poor prognosis and a high risk of metastasis[325].

Malignant tumors and cancer. As *NF1* is a tumor-suppressor gene, patients with NF1 have an increased risk of cancer and malignancies, with a lifetime cancer risk of 60%[326]. They present a 50-fold increase of risk to develop high-grade tumors[327]. NF1 patients exhibit a high incidence of many cancers, including malignant brain tumors, endocrine cancer, connective tissue malignancies, breast cancer, and leukemia[328–331].

Dermatological manifestations. One of the most common features of NF1, affecting 95% of patients, is the presence of benign pigmentary lesions, named café-au-lait macules (CALMs)[332,333]. CALMs are dense flat plaque of melanocytes on the epidermis that develop during infancy. NF1 patients also present skinfold freckling, small dark spots on the skin, that are distinguishable from CALMs by their reduced size and specific location at the axilla and inguinal regions[332].

Optic manifestations. Lisch nodules were firstly described in 1937 by K. Lisch. They are round fibrous hamartoma at the iris surface, specific to the NF1 disease and asymptomatic. They develop with time, only 10% of patients exhibit Lisch nodules before 6, while 90% after 16 years of age[334,335]. Optic pathway gliomas (OPG) are benign tumors of the optic nerves, frequently found in NF1 patients (15%). OPGs are composed of nervous cells, including astrocytes, oligodendrocytes, neurons, and microglia[336,337]. OPGs can progressively alter vision and chemotherapy can be used in this case, but only few cases of vision improvement were reported[338].

Cognitive manifestations. Patients affected with NF1 can present cognitive dysfunctions, including learning disabilities, attention deficits, and social perception problems[339–342]. One third of NF1 children display symptoms of autism spectrum disorder[343,344]. These disabilities have a strong deleterious impact on the patient's quality of life and 90% of NF1 children show altered school performances[345–347]. Additional symptoms such as epilepsy and sleep disturbance were documented for NF1 patients[348–351].

Other manifestations. Several other manifestations were described in NF1, but are rare. NF1 patients can be affected with hypertension and cardiovascular anomalies[352,353]. Between 2 and 6% of NF1 children exhibit cerebrovascular diseases as occlusive disease and vascular dilatation[354,355].

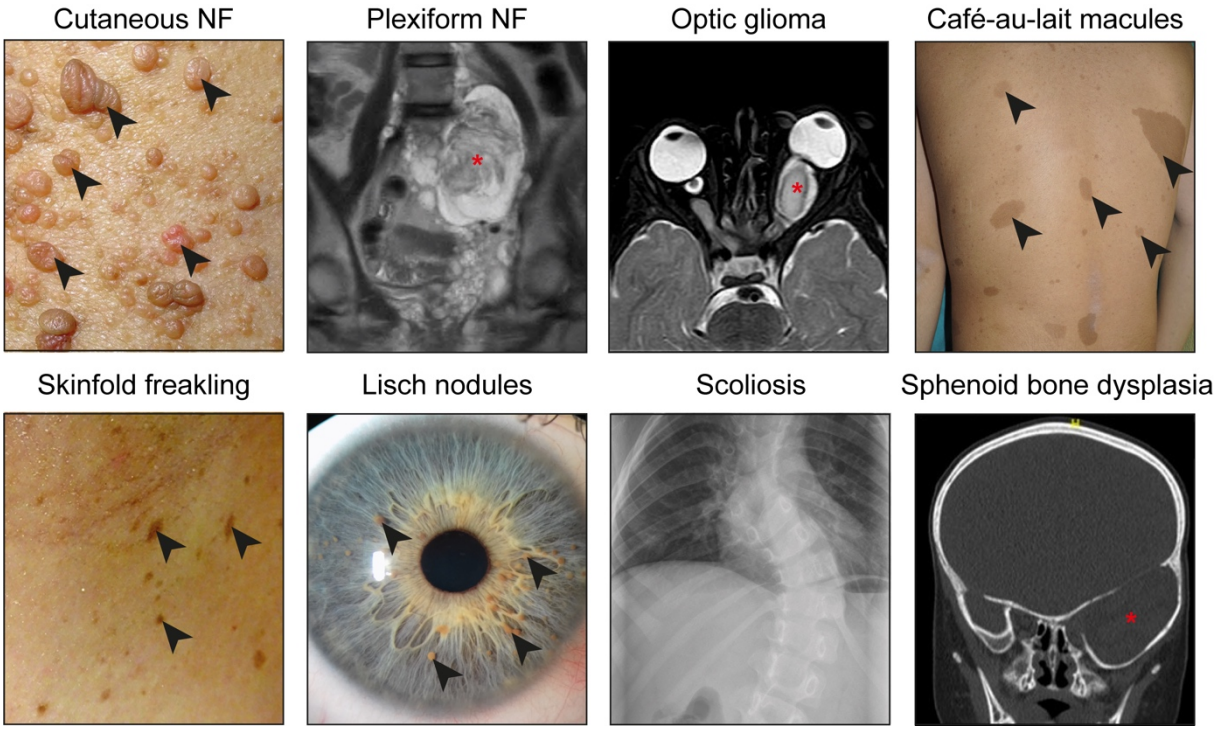

Figure 15: Neurofibromatosis type 1 symptoms. Images from [271,335,356–359]

2.2. NF1 bone manifestations

Around half of NF1 patients exhibit an orthopedic manifestation. These symptoms can be classified as either generalized manifestations, usually mild and common, or focal manifestations, rare but severe[360,361]. The generalized manifestations correspond to osteopenia/osteoporosis, shortness of stature, and macrocephaly. 50% of NF1 patients exhibit a reduced bone mineral density (BMD) leading to an increased incidence of osteopenia and osteoporosis (30% of patients)[362–365]. This is correlated with an increased bone remodeling, changes in circulating factors (Vitamin D), and an increased incidence of fracture[366–368]. NF1 patients can also present a reduced size compared to their family members in 20 to 30% of cases, due to reduced growth during puberty [369,370]. Increased head circumference, leading to macrocephaly in 25% of cases (head circumference >2 standard deviation above the mean) is also observed in NF1 individuals [370]. Focal manifestations, such as spine deformities, sphenoid bone, or long bone dysplasia, are rare but cause severe morbidity. The most frequent are spinal deformities, which affect 10 to 30% of NF1 patients[371]. Mild spine curvatures (curve under 20°) with progressive onset are classified as non-dystrophic scoliosis and are usually treated by bracing. Severe spine deformities (curve over 40°), with presence of bone abnormalities and rapid progression despite treatment, are classified as dystrophic scoliosis[372–375]. The treatment of dystrophic scoliosis is

complex and requires extensive surgical procedures to stabilize the deformation. Paraspinal pNFs can be associated with dystrophic scoliosis, but are not the only cause of spine deformities[376,377]. The pathogenesis of NF1-related spine deformities is still poorly understood. Cranial defects due to sphenoid bone dysplasia are also observed in a subset of NF1 patients. Sphenoid bone dysplasias are suspected to be caused by abnormalities in the adjacent soft tissues (presence of pNF, dural ectasia, …)[378–380]. Some cases of cystic osseous lesion and dental abnormalities were reported but the prevalence is low[381–383]. Finally, around 5% of NF1 patients exhibit long bone dysplasia or congenital pseudarthrosis of the tibia.

2.3. Congenital pseudarthrosis of the tibia

2.3.1. Description

Among NF1 bone manifestations, the congenital pseudarthrosis of the tibia (CPT) is one of the most severe[384,385]. CPT is a rare pediatric orthopedic disease affecting 5% of NF1 patients and overall, 1 in 150,000 to 200,000 children worldwide[371,386,387]. The link between CPT and NF1 is known since 1950, and NF1 patients represent between 40 and 80% of CPT cases[388–390]. No differences in prognosis and severity were observed between isolated and NF1-related CPT[391–393]. CPT is characterized by an anterolateral bowing or a spontaneous fracture of the tibia at young age, with absence of consolidation (Figure 16). CPT is mostly unilateral, rare bilateral cases were described[394]. Since 1973, several classifications were proposed (Anderson, Boyd, Crawford, Apoil) [389,395–397]. The most commonly used is the descriptive Crawford's classification from 1986[389]. CPT is divided in four types: Type I marked by a bowing with dense medullary canal, Type II marked by a bowing with abnormal medullary cavity, Type III marked by a cystic lesion, which may be fractured and Type IV marked by a bowing with fracture and pseudarthrosis. The prognosis progressively decreases from type I to type IV.

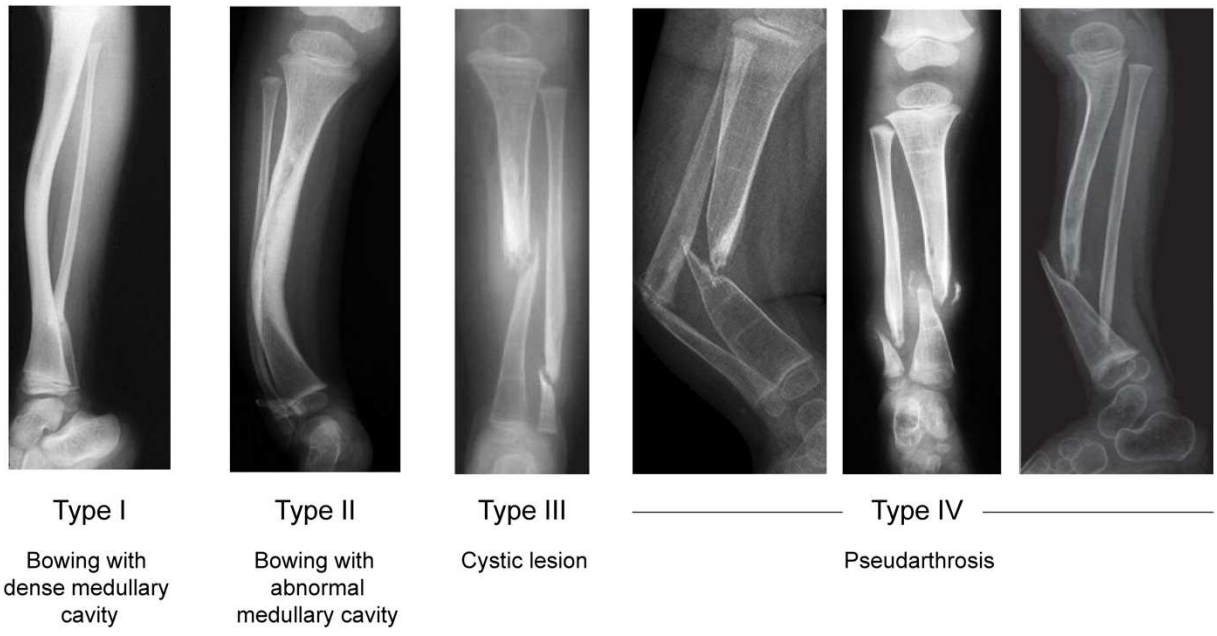

Figure 16: Congenital pseudarthrosis of the tibia according to Crawford classification. X-ray images from[360,384,398]

Histological analysis showed that the pseudarthrosis (PA) site is composed of a fibrous hamartoma (aberrant overgrowth of local cells that resembles local tissue) [399,400]. This hamartoma is rich in fibroblasts and extracellular matrix and can also contain fibrocartilage. The presence of giant osteoclasts was also reported[401]. The periosteum at the bone ends is considered pathological. It is described as thick, rich in fibroblasts with a reduced extracellular matrix and contains neural-like cells[391,402]. The periosteum also displays an impaired vascularization[402]. Several hypotheses have been suggested to understand the pathogenesis of CPT, like a mechanical blocking by the fibrous hamartoma and reduced vascularization, but overall, the origin of the CPT remains poorly understood.

2.3.2. Surgical treatment for congenital pseudarthrosis of the tibia

CPT is one of the most challenging orthopedic conditions to treat and the risk of failure is high. The treatment of CPT is only surgical and aims to consolidate the tibia while restoring its axis and limiting size inequality between legs. Even after consolidation, the risk of fracture remains high until skeletal maturity is reached. Three surgical techniques are traditionally used to treat CPT with similar success rates. An approach described by Charnley consists in the resection of the pseudarthrosis site and the combination of stable intramedullary nailing and a bone graft[403]. The vascularized bone transfer technique consists in an important resection of the pseudarthrosis and the grafting of a healthy bone (contralateral fibula or rib)[404]. The Ilizarov technique relies on the use of an external fixator combined with a resection of the pseudarthrosis site[405]. New surgical approaches have been described to treat CPT. The induced membrane technique, or Masquelet technique, was described at the end of the 1990s by Alain-Charles Masquelet to treat large diaphyseal defects[406]. This surgical procedure is also used to treat CPT and shows encouraging results[407]. The induced membrane technique is usually a 2 step-surgery procedure (Figure 17)[408–411]. During the first surgery, the pseudarthrosis site is resected to create an environment free of necrotic, non-viable, or pathological tissues. Intramedullary nailing is used to provide mechanical stability and a polymethylmethacrylate cement spacer is placed between the 2 bone fragments. The cement spacer creates a foreign body reaction that leads to the formation of a membrane at the cement surface, called induced membrane[412,413]. Six- to ten-weeks later, the second surgery consists in the removal of the cement spacer while preserving the induced membrane. An autogenous graft, composed of bone, spongy bone, and periosteum collected from the iliac crest, is placed within the induced membrane. One of the interests of this surgical approach is the presence of the induced membrane[414]. The membrane creates a favorable environment for the consolidation, as it prevents fibrous tissue invasion, allows quick vascularization of the graft, and protects it from resorption[414,415]. The induced membrane is a highly vascularized tissue organized in layers of epithelial cells, fibroblasts, mesenchymal cells, and extracellular matrix[416–419]. The presence of immune cells and osteoclasts was reported[420]. The induced membrane is also a source of growth factors such as TGFβ, VEGF, and BMP2[412,417,421,422]. Animal models of the induced membrane technique have been developed to study the induced membrane and its role to promote bone healing[417,418,423–425]. Overall, despite progress in surgical procedures, CPT remains a highly-challenging condition with an important risk of

failure and amputation can be performed as a last resort[426–428]. There is a current need for a better understanding of the pathological mechanisms causing CPT to improve therapeutical approaches.

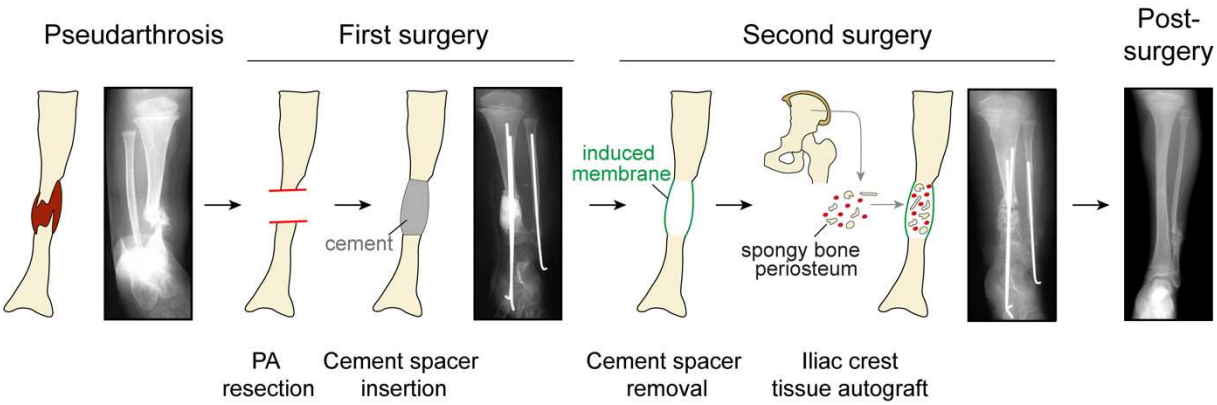

Figure 17: Induced membrane surgical technique. X-rays from a 30-month-old patient, before surgery (left), at the end of the first surgery (middle), the second surgery (right), and 6 years post-surgery (right). PA: pseudarthrosis. X-ray images from [407].

3. Genetic basis of Neurofibromatosis type 1

NF1 is an autosomal dominant disorder caused by mutations or pathogenic variants (PV) in the *NF1* gene. Half of NF1 patients inherited a mutation from a parent and half present a *de novo* mutation. *NF1* exhibits a very high mutation rate ($1x10^{-4}$ per gamete per generation), 10 to 100 times higher than other genes. *NF1* gene size is not sufficient to explain its high mutation rate. Around 3000 *NF1* PVs have been currently described, distributed all along the *NF1* gene without a "hotspot" region [293,429]. Large *NF1* deletions account for about 5 to 10% of the cases. Around 80% of the PVs cause a truncation of the neurofibromin, due to missense/nonsense variants or insertion/deletion, or abnormal splicing causing a frameshift and premature end of transcription. The remaining 10% of *NF1* PVs correspond to missense variants leading to an alteration of the activity of the protein[293]. A challenge in the clinical care of NF1 patients is the rare genotype-phenotype correlations[430–433]. Severe phenotypes, including facial dysmorphism and cardiovascular features, are associated with large *NF1* deletions[434–436]. Few PVs are associated with mild phenotypes, like the c2970-2972 delAAT that leads to the absence of cutaneous neurofibromas[437]. However, these correlations remain rare and suggest that PVs are not the origin of phenotypic heterogeneity between patients. This idea is reinforced by reports of clinical heterogeneity between patients within the same family and carrying the same variant[438,439]. NF1 also exists in mosaic forms. Mosaic NF1 is due to *NF1* mutation at postzygotic stage and leads to segmental development of symptoms. Mosaic NF1 patients develop similar symptoms as NF1 patients but the frequency and severity are reduced[440,441] The affected body regions are extremely variable and dependent on the timing and cellular distribution of the mutation.

In 1971, Alfred Knudson, studying retinoblastoma, describe the "2-hit hypothesis"[442,443]. This hypothesis suggests that both alleles of a tumor-suppressor gene must be inactivated for cellular tumoral transformation to occur. A patient inherits a germline mutation from a parent and acquires a second

mutation at post-fertilization stages. This second-hit or somatic mutation is the critical event leading to tumorigenesis[443,444]. *NF1* is an autosomal dominant disorder. Thus, patients carry a first *NF1* germline PV at heterozygous state. The *NF1* gene, as a negative regulator of the MAPK cascade and PI3K/Akt/mTOR pathway, regulates cell proliferation and is classified as a tumor-suppressor gene. Consistent with Knudson's two-hit hypothesis, a second *NF1* PV was identified in tumors in patients with NF1. In detail, *NF1* biallelic inactivation was identified in plexiform neurofibromas, cutaneous neurofibromas, MPNSTs, optic pathway glioma, and other tumors in NF1 patients[445–450]. NFs are composed of several cell types, including Schwann cells, fibroblasts, and immune cells, but only Schwann cells are harboring the *NF1* somatic PV[451]. This second somatic event in Schwann cells is required for NF formation. Interestingly, while Knudson's two-hit hypothesis was initially described for tumor development, the presence of a second *NF1* hit has also been described in non-tumoral NF1 manifestations. Melanocytes composing CALMs harbor 2 mutated *NF1* alleles[452,453]. In one study, *NF1* sequencing was performed on cNF Schwann cells and CALM melanocytes from the same patient and showed the same somatic event in the 2 cell populations, suggesting a common origin of these symptoms. For bone manifestations, the presence of *NF1* biallelic inactivation was detected for CPT and scoliosis[401,454]. Several studies showed the presence of a second *NF1* mutation in the fibrous tissue from the PA site[401,455–457]. Recently, Brekelmans *et al.* showed the presence of *NF1* biallelic inactivation in periosteum-derived cells from the PA site, suggesting the involvement of periosteum in CPT[458].

Different types of somatic mutations can lead to *NF1* biallelic inactivation, such as a second punctual PV or loss of heterozygosity (LOH) by deletion or isodisomy (Figure 18). As an autosomal dominant disorder, NF1 patients carry a germline PV that is detected at 50% of *NF1* sequences (heterozygote state) in a control tissue such as blood. A new point punctual PV affecting the remaining WT *NF1* allele leads to the presence of 2 non-functioning *NF1* alleles in the same cell. During sequencing, the germline mutation remains detected at 50% of *NF1* sequences and the second PV is detected up to 50% depending on the percentage of cells in the tissue carrying the *NF1* biallelic inactivation. In around 30% of cases, the *NF1* germline PV is detected at a frequency above 50%[373,459]. In this case, the heterozygous state is lost (loss of heterozygosity or LOH). LOH can be due to a deletion of the WT *NF1* allele. In this case, a reduced number of *NF1* copies (copy variant number, CVN) compared to control genes is detected during sequencing. After deletion, a DNA repair process can be performed by cells, by copying the remaining chromosome. Duplication of chromosome 17 harboring pathogenic *NF1* variant can also be the consequence of abnormal chromosomal segregation during mitosis. In these cases, the copy of the chromosome carrying the mutated version leads to the presence of 2 *NF1* alleles carrying the same PV. During sequencing, the frequency of the germline is above 50% and the CVN will be normal, thus this type of event is named copy neutral LOH (cnLOH). The study of allele frequency balance and informative single nucleotide polymorphisms (SNPs) are essential tools to validate LOH.

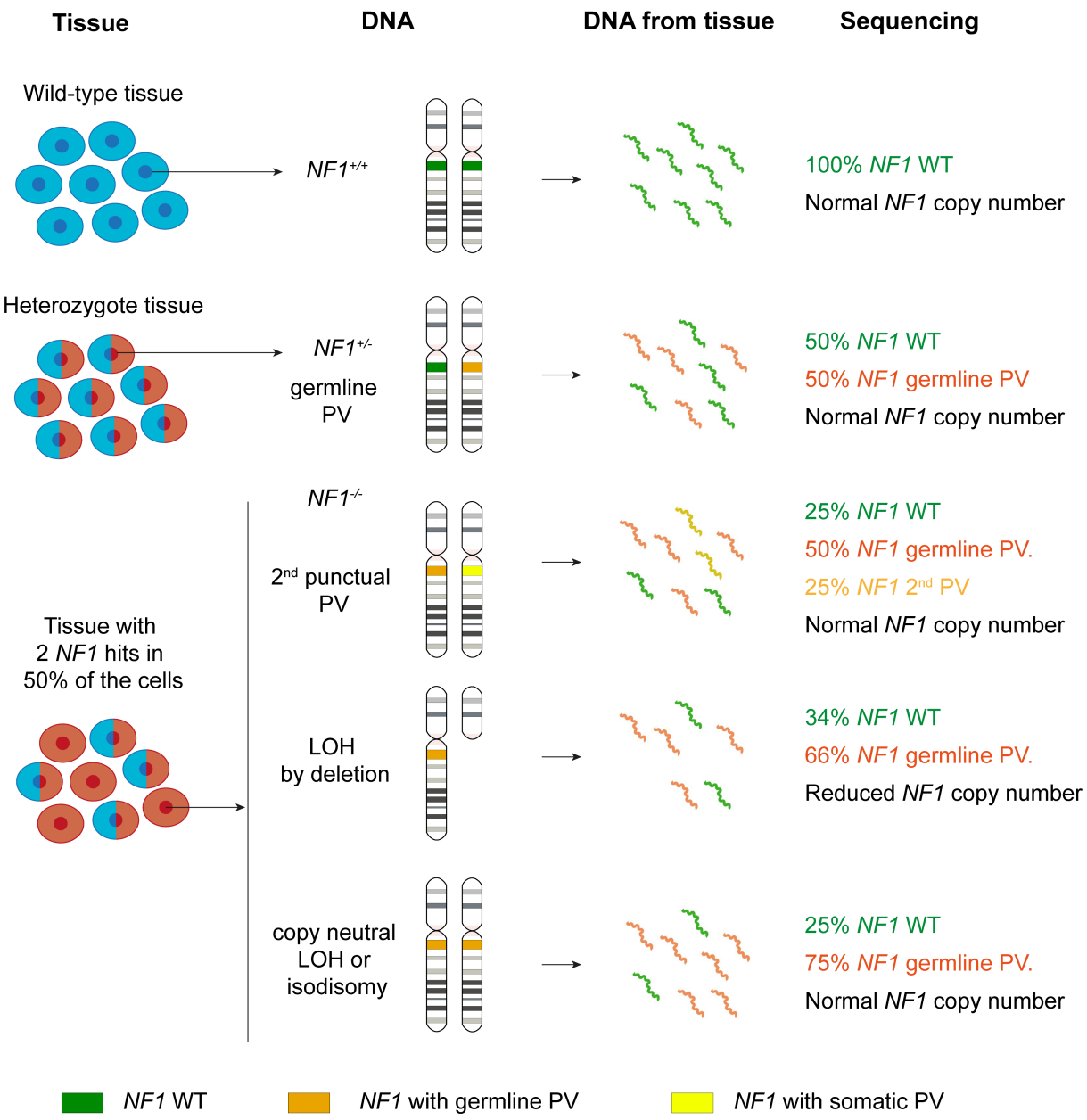

Figure 18: Detection of *NF1* biallelic inactivation by sequencing. In a wild-type tissue, all cells are carrying 2 *NF1* WT alleles (*NF1*$^{+/+}$), and only the WT *NF1* is detected during sequencing. In a heterozygote tissue, cells carry one WT *NF1* allele and one *NF1* allele (*NF1*$^{+/-}$) with the germline pathogenic variant (PV). Half of *NF1* sequences correspond to the WT allele and half to the allele carrying the germline PV. In a tissue where 50% of the cells are carrying *NF1* biallelic inactivation, three options are possible. In the case of a 2nd punctual PV, the tissue is composed of heterozygote cells and cells carrying the germline mutation and a somatic PV. During sequencing, the germline PV is detected at 50%, and the WT allele and somatic PVs are detected at 25%. In the case of loss of heterozygosity (LOH) by deletion, the tissue is composed of heterozygote cells and cells carrying only one NF1 allele, that carry *NF1* germline PV. During sequencing, the germline PV is detected at 66%, and the number of *NF1* copies is reduced. In the case of copy-neutral LOH, the tissue is composed of heterozygote cells and cells carrying two *NF1* alleles with the germline PV. During sequencing, the germline PV is detected at 75%, and the number of *NF1* copies is normal.

4. NF1 diagnosis and treatments

4.1. Clinical diagnosis

As NF1 is a progressive disease with a high heterogeneity, the clinical diagnosis can be challenging. A first list of criteria to diagnose NF1 was established in 1987 and was revised in 2021 to better differentiate NF1 from similar diseases (NF2, Legius Syndrome)[278,279]. Currently, NF1 diagnosis is given to a patient with at least 2 of the following criteria (Figure 19)[279]:

- Six or more café-au-lait macules (>5mm before puberty and >15mm after puberty)
- Two or more neurofibromas or one plexiform NF
- Skin freckling
- Optic pathway glioma
- Two or more Lisch nodules or choroidal abnormalities
- One bone lesion: sphenoid dysplasia, anterolateral bowing, or pseudarthrosis of a long bone
- A heterozygous pathogenic *NF1* variant with a variant allele fraction of 50% in normal tissue
- A parent with an NF1 diagnosis

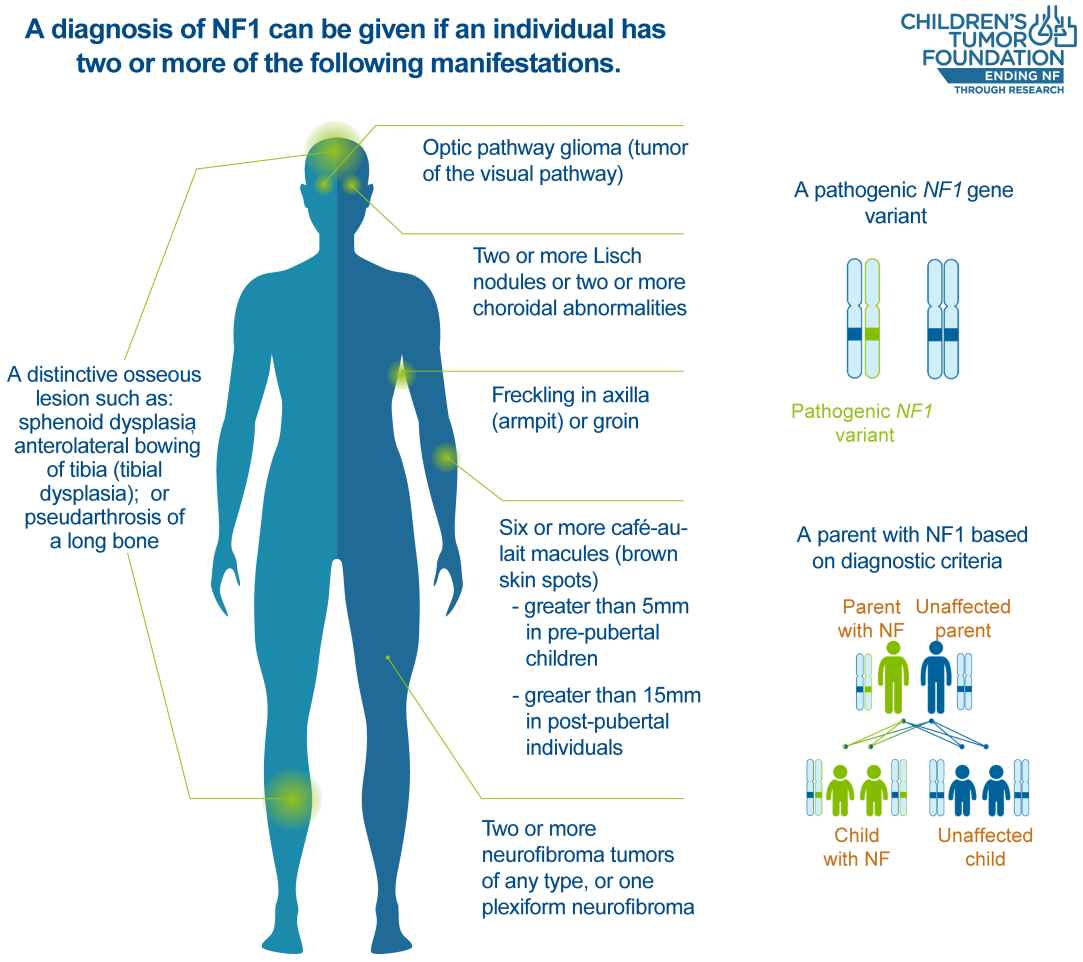

Figure 19: Criteria to define NF1 from the International Consensus Group on Neurofibromatosis Diagnostic Criteria. From[279]

4.2. Treatments

Currently, there is no global treatment to prevent the development of NF1 manifestations. NF1 patients have frequent clinical follow-ups and symptoms are treated independently and based on their severity. For tumoral manifestations, surgical approaches are the most frequent. They can be combined with chemotherapy. The Food and Drug Administration (FDA) recently approved the use of the MEK inhibitor Selumetinib for the treatment of inoperable pNFs in children[460,461]. Several other MEK inhibitors are currently in clinical trials (Cabozantinib, Trametinib, Binimetinib), raising the hope of an improved prognosis and treatment for NF1 patients.

The current management of bone manifestations also relies on surgical approaches when required. The use of pharmaceutical approaches is considered but remains at preliminary state. The use of Lovastatin, which displays RAS inhibitory properties, on bone manifestations in an NF1 mouse model did not show promising results[462]. MEK inhibition was combined with local delivery of BMP2 and led to an improvement of bone repair phenotype in NF1-mouse model[463,464]. A recent clinical trial using BMP2 on CPT was launched to investigate its clinical interest but was stopped due to low recruitment. The challenge in the use of MEK inhibitors for CPT or scoliosis is the strong toxicity of these molecules, specifically for a pediatric cohort. The current perspectives are the use of local delivery approaches, the combination of molecules with synergic effects, the use of MEK inhibitors with bone-specific effect (Ponatinib can target the osteoblastic MEKK2) or the use of molecules non-targeting the MAPK cascade (Asfotase-α plays a role on PPi and inorganic phosphate)[462,465,466].

5. Animal models to identify the cellular origin of NF1 symptoms

Animal models have been generated to study NF1, including zebrafish, minipigs, dogs, and rodents[467–469]. Genetically engineered mice are the predominant model. The first attempt to generate a mouse model of NF1, by generating the *Nf1* knock-out allele (*Nf1*$^{-}$), gave disappointing results. Homozygous *Nf1*$^{-/-}$ mice are lethal during development due to cardiac malformations, while the heterozygote *Nf1*$^{+/-}$ mice do not develop tumors and have a normal life expectancy[470,471]. Mice do not recapitulate the spontaneous *NF1* biallelic inactivation observed in human and required for the development of NF1 manifestations[469]. To overcome this problem, conditional *Nf1* inactivation, using the CRE/LOX system with the *Nf1* floxed allele (*Nf1*^{fl}), was used where *Nf1* is inactivated in specific subsets of cells. These cell-specific approaches aimed to understand the cells of origin of NF1 manifestations and the pathological mechanisms caused by *Nf1* biallelic inactivation.

5.1. Mouse models to study NF1 tumoral manifestations

Neurofibromas are tumors composed of Schwann cells and fibroblasts. Genetic studies showed that only Schwann cells are carrying *NF1* biallelic inactivation, suggesting that SCs are the cell of origin of neurofibromas[451]. In 2002, Zhu *et al.* showed that *Nf1* inactivation in Schwann cells using the *Krox20*^{Cre}

mouse model leads to the development of pNFs[472]. pNFs were also induced in mice where *Nf1* is inactivated in *P0A*^{Cre}- and *Dhh*^{Cre}-traced Schwann cells, confirming that SCs are responsible for pNF development[473,474]. The importance of the timing of *Nf1* inactivation for pNFs was studied by using the inducible *Plp*^{CreERT} model[475,476]. Overall, pNFs develop predominantly when *Nf1* is inactivated at embryonic stages in Schwann cell precursors (SCPs) from the nerve roots. While many models recapitulate pNFs, these models did not recapitulate cNFs[472–475]. Few studies focused on the cell of origin of cNFs. Le *et al.* showed that the cells of origin of cNFs are located within the skin. They applied tamoxifen on the skin of neonatal *CMV*^{CreERT2}*; Nf1*$^{fl/-}$ mice, where CRE-ERT2 is expressed in all cells, resulting in cNF formation at the site of treatment[477]. They identified skin-derived neural progenitors (SKPs) as the population responsible for cNF development, but SKPs are a heterogenous population[477]. The identification of nerve root SPCs and SKPs as the cells of origin for pNFs and cNFs respectively led to 2 hypotheses: either pNFs and cNFs have distinct origins or there is a population of cells giving rise to SCPs and SKPs at the origin of both pNFs and cNFs[478]. Two recent mouse models, using the *Hoxb7*^{Cre} and *Prss56*^{Cre}, recapitulate pNFs and cNFs (diffuse cNFs for *Hoxb7*^{Cre})[479,480]. Hobx7 marks neural crest derivates from the dorsal nerve roots as well as SKPs[480,481]. Prss56 marks a specific population of neural crest derivatives, called boundary cap cells, that can give rise to SCPs and SKPs, showing a possible common embryonic origin of cNFs and pNFs[479,482]. The *Prss56-NF1 KO* model will be detailed in the next chapter. The different mouse models also allowed a better understanding of the pathophysiology of NFs. NF development is highly dependent on the microenvironment as the presence of a heterozygous background is required for pNF development in some models[472,473,483–485]. Immune cells, including neutrophils, macrophages, dendritic cells, and T cells, trigger NF formation by secreting factors promoting tumorigenesis and fibroblast accumulation, such as TGF-β, CXCL10, CSF-1, and CCL2[483–489]. Skin and nerve injuries also promote NF tumorigenesis[479,490].

Optic pathway gliomas (OPGs) are tumors formed of glial cells, including astrocytes. Several CRE models were generated to study the cellular origin and timing of *Nf1* inactivation in OPG[337]. *Nf1*-somatic mutation in neural stem/progenitor cells, using the *Gfap*^{Cre} or *Blbp*^{Cre}, leads to OPG development by 3 months[491–493]. The timing of the mutation is also critical, as *Nf1* loss in Prom1-expressing cells after postnatal day 1 cannot induce tumorigenesis. These models allowed progress in the understanding of OPG development and recent studies showed the contribution of neuronal excitation as a key factor in OPG development[494,495].

5.2. Mouse models to study NF1 bone manifestations

The cellular origin of bone manifestations is a challenging question as the cell type(s) carrying *NF1* somatic mutation in patient bones and CPT is still unknown. To better understand the impact of *Nf1* inactivation on bone homeostasis and repair, several mouse models were used. Some models were not cell-type specific, such as the *Nf1*$^{+/-}$ model or the use of Adenovirus-CRE on *Nf1*$^{fl/fl}$ mice, while other models were specific to mesenchymal-derived cells (*Prx1*^{Cre}), osteoblasts (*Osx*^{Cre}*, Col1.1*^{Cre}), osteocytes (*Dmp1*^{Cre}) and chondrocytes (*Col2a1*^{Cre}).

5.2.1. Bone homeostasis

As the *Nf1*$^{-/-}$ mice are embryonically lethal, the skeletal tissue was not studied in this model. The first model studied was the heterozygote *Nf1*$^{+/-}$, which exhibit a mild phenotype[496]. This model presents a slight decrease in bone mineral density (BMD), associated with an increased number of osteoclasts and a reduced number of osteoblasts. Additional studies showed that *Nf1*$^{+/-}$ osteoblasts exhibit reduced osteogenic activity in vitro and *Nf1* heterozygote osteoclasts have an increased resorption activity in vitro and in vivo [497–499]. NF1 generalized manifestation such as osteoporosis could be explained by *Nf1* heterozygosity but severe skeletal manifestation, as pseudarthrosis and scoliosis, requires a second *Nf1* mutation. *Nf1* was inactivated in the Prx1 lineage, which gives rise to most of bone cells, including SSPCs, osteoblasts, and chondrocytes. This model recapitulates a severe bone phenotype, with reduced mineralization and increased porosity causing reduced length, tibial bowing, and joint malformations[500]. The role of *Nf1* in osteoblasts was studied by using osteoblast-specific CRE lines, such as *Osx*^{Cre} and *Col1a1*^{Cre} (using the *Col2.3*^{Cre} labeling mature osteoblasts). *Osx*^{Cre}*; Nf1*$^{fl/fl}$, and *Col1a1*^{Cre}*; Nf1*$^{fl/fl}$ mice develop a similar phenotype, with a reduced BMD and bone volume[464,465,496,501]. This phenotype is due to (i) an increased production of extracellular matrix by osteoblasts combined with a delay in mineralization and (ii) an overproduction of RANKL by osteoblasts, that stimulate the osteoclastogenesis[502]. *Nf1* was also inactivated in osteocytes, using the *Dmp1*^{Cre}. In this model, mice display a severe bone phenotype with accumulation of non-mineralized areas, increased porosity, and reduced osteoblast number[466,503]. Around 40% of *Dmp1*^{Cre}*; Nf1*$^{fl/fl}$ mice showed spontaneous fracture[503]. *Nf1* inactivation in chondrocytes, using the *Col2a1*^{Cre}, leads to major bone developmental defects. *Col2a1*^{Cre}*; Nf1*$^{fl/fl}$ exhibit short stature, tibial bowing, scoliosis, and spine structural defect as well as skull structure anomalies[504]. Overall, *Nf1* is required for bone development, growth, and maintenance, and *Nf1* biallelic inactivation in skeletal cells affects bone physiology (Table 2).

	BMD	Bone volume	Osteobl. number	Osteocl. number	Bone porosity	Bone length	Bowing
Nf1$^{+/-}$							
Prrx1^{Cre}							
Col1.1^{Cre}							
Osx^{Cre}							
Dmp1^{Cre}							
Col2a1^{Cre}							

Decrease Increase

Table 2: Effect of *Nf1* inactivation in bone cells using genetically engineered mice on bone physiology. BMD: bone mineral density. Osteobl: osteoblast. Osteocl: osteoclast.

5.2.2. Bone repair

Nf1 heterozygote mice display a mild bone repair phenotype, with a delay in bridging and cartilage resorption. This phenotype was observed in 50% of cases and only after distal tibial fracture[505]. This suggests that *Nf1* biallelic inactivation is required to induce pseudarthrosis in mice. The injection of Adenovirus with a CRE transgene to $Nf1^{fl/fl}$ mice at the site of fracture causes impaired healing with reduced cartilage and bone and presence of fibrotic tissue[506,507]. This model was used to test therapeutical approaches but does not allow to identify the cellular origin and mechanisms of CPT. $Prrx1^{Cre}$; $Nf1^{fl/fl}$ mice exhibit impaired bone healing with reduced cartilage and bone formation and accumulation of fibrotic tissue, suggesting that *Nf1*-deficient SSPCs have an impaired fate after fracture[508]. Osteoblast-specific inactivation of *Nf1* causes delayed healing, with delayed cartilage resorption, decrease osteoblast differentiation, and increased osteoclastogenesis[464,465,504,509]. Spontaneous fractures observed in $Dmp1^{Cre}$ do not lead to a pseudarthrosis phenotype, but healed bones show decreased stiffness and strength[503]. Overall, the mouse models of *Nf1* inactivation in bone cells showed altered bone healing with various severity (Table 3). These models were broadly used to test pharmacological approaches but as the cell population(s) carrying *NF1* biallelic inactivation in CPT is still unknown, the correlation with patients remains limited. The cellular origin and molecular mechanisms of NF1-related bone repair defects remain unknown. Furthermore, studies are needed to understand if CPT is a bone-specific lesion independent of other NF1 features or if it has a common origin with NF1 symptoms, such as NFs.

	Bone healing	Callus size	Bone volume	Cartilage volume	Fibrosis volume	Minera-lization	Osteobl. number	Osteocl. number
$Nf1^{+/-}$	Decrease			Increase	Increase			Increase
Ade-CRE	Decrease	Decrease	Decrease	Decrease	Increase	Decrease	Decrease	Increase
$Prrx1^{Cre}$		Decrease		Decrease	Increase	Decrease		Increase
$Col1.1^{Cre}$	Decrease	Increase	Decrease	Increase				Increase
Osx^{Cre}		Decrease				Decrease		

Table 3: Effect of *Nf1* inactivation in bone cells using genetically engineered mice on bone repair. Osteobl: osteoblast. Osteocl: osteoclast.

Overall, many models have been developed and allowed advances in the understanding of the origin and pathological mechanisms of NF1 symptoms. These models using mostly cell-type specific CRE models exhibit one or few features of NF1 but they fail to recapitulate the diversity of symptoms observed in patients. A new model, the *Prss56-Nf1 KO* model, has been recently generated and recapitulates several features of the disease[479]. This model will be described in the next chapter.

Chapter 4: Neural crest cells, Schwann cells, and boundary cap cells

1. Neural crest cells and their derivatives

The neural crest (NC) is an early embryonic multipotent cell population described in 1868 by Whilem His and considered at the fourth embryonic layer[510]. The NC is a major source of cells for vertebrate development. Neural crest cells (NCCs) form a transient population that emerges from the neural tube at the time of closing and migrates through the embryo to give rise to more than 30 cell types (Figure 20). Understanding the fate and contribution of NCCs has been possible by using several animal models (chick, xenopus, zebrafish, rodent) and techniques, including cell labeling, genetic fate-mapping, and cell/tissue ablation or transplantation[511–515].

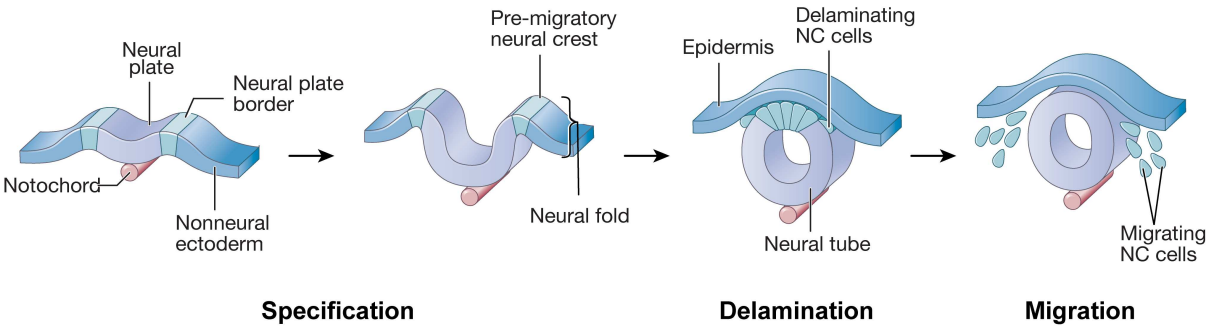

Figure 20: Neural crest development. Neural crest cells (NCCs) are specified in the neural plate borders. NCCs delaminate at the time of neural tube closure, before migrating. Adapted from Developmental Biology, Eleventh Edition (2016).

1.1. Specification, delamination, and migration of neural crest cells

The neural crest formation begins during gastrulation. The specification of the NC starts with the formation of specific domains within the ectoderm, the neural plate borders, that are located between the neural plate and the non-neural ectoderm. The formation of the neural plate borders is regulated by signals, including Wnt and FGFs, secreted by the surrounding tissues (neural plate, non-neural ectoderm, underlying mesodermal layer)[516–519]. The specification is characterized by the progressive expression of transcription factors such as Snail/Slug, Twist, and FoxD3[515,520–522]. In parallel, the neural plate folds to form the neural tube. At the time of closure, neural plate border cells undergo an epithelial-to-mesenchymal transition (EMT), leading to their delamination from the neuroepithelium. EMT is a strong phenotypical change, marked by a decrease in the expression of adhesion molecules (type 1 Cadherins) as well as morphological modifications[515,523,524]. These steps are regulated by the expression of specific transcription factors, named “neural crest specifiers” and induced by Notch, BMP, and Wnt[515,525,526]. Differences in EMT regulation are observed along the anteroposterior axis. After EMT, NCCs acquire a migratory phenotype and start migrating in the cephalic region before progressing on the anteroposterior axis following several streams (Figure 20)[527–529]. Cranial NCCs migrate in two waves: cells forming the cranial ganglia migrate to a dorsal position while cells forming the skeletal elements of

the face migrate to a ventral position and invade branchial arches. Trunk NCCs form three paths of migration as they can migrate (i) ventrally in the intersomitic space and migrate following the ventrolateral pathway, (ii) through the sclerotome and follow the ventromedial pathway, or (iii) by the dorsolateral pathway, between the dorsal ectoderm and the dermomyotome. The regulation of NCC migration is complex and relies on signals from cell-to-cell contact, secreted molecules, and interactions with the ECM[529]. These signals can have attractive or repulsive effects. Neuropilin/Semaphorin and the Erythropoietin-producing human hepatocellular (Eph) receptors/Ephrin axis are among the most important signaling pathways involved in the regulation of NCC migration[529–532].

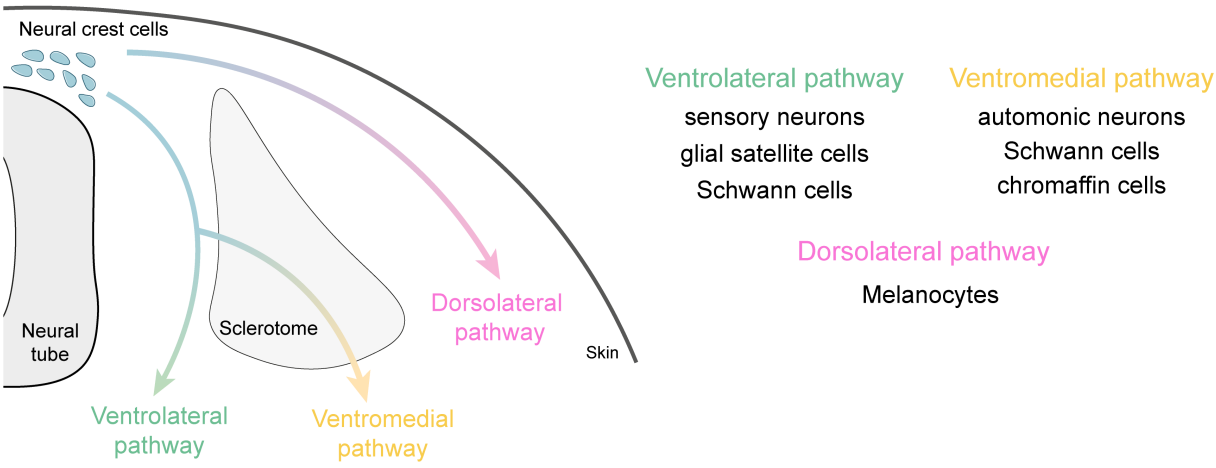

Figure 21: Pathways of trunk NCC migration. Adapted from[529]

After migration, NCCs finally undergo differentiation. NCCs are present all along the anteroposterior axis of the embryo and are usually divided in 4 subpopulations: the cranial neural crest (cephalic region to the 6th rhombomere), the vagal crest (7 first somites), the trunk crest (from the 8th to the 24th somite) and the sacral neural crest (from the 25th somite) (Figure 22). The different populations display specific cell fate, migratory pathway, gene expression, and regulation. While all NCC populations contribute to melanocytes and glial cells, cranial NCCs give rise to the skeletal elements of the face, vagal NCCs to the cardiac outflow tract, trunk NCCs to sensory neurons and adrenomedullary cells, and sacral NCCs to the enteric nervous system[511,528,533–535]. The differences in potential between NCC populations could be due to intrinsic differences between subpopulations or distinct environmental factors at different levels of the neural tube. Heterotopic transplantation experiments showed that NCCs can form neural and glial cells as well as melanocytes regardless of their axial level of origin. However, only cranial NCCs exhibit mesenchymal potential. Cranial NCCs transplanted in the sacral region form ectopic cartilage, while sacral NCC grafted in the cranial region will not form cartilage[511,536]. These experiments showed intrinsic heterogeneity between NCC subpopulations.

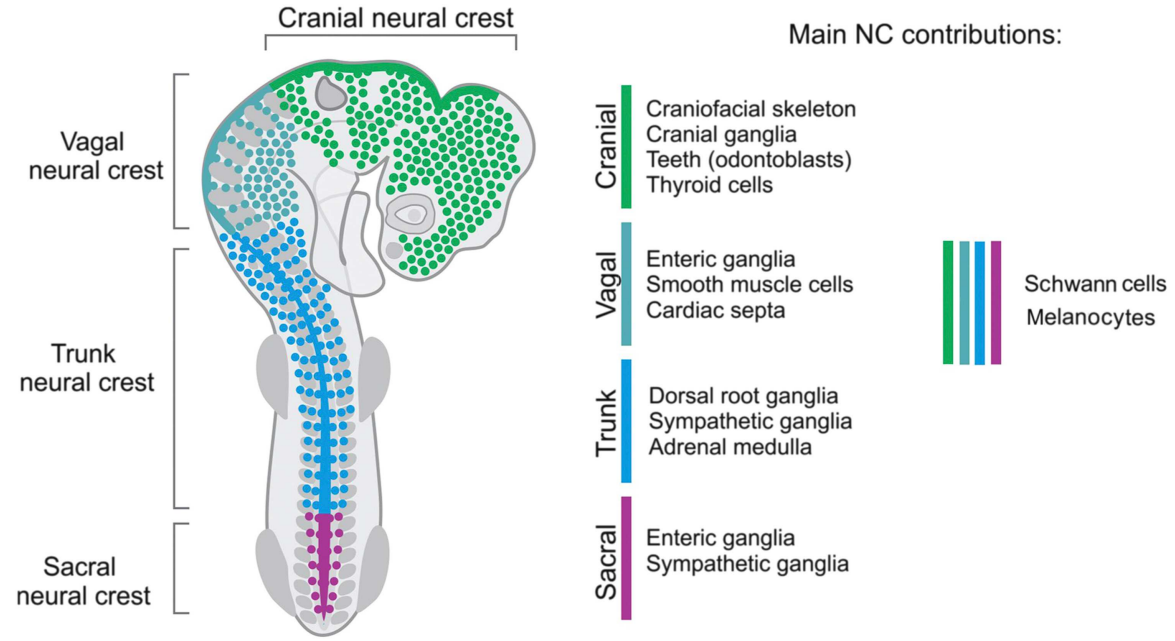

Figure 22: Distribution and fate of neural crest cell subpopulations. Adapted from[511]

1.2. Schwann cell precursors and immature Schwann cells

Schwann cells are derived from the neural crest, by a progressive specialization from NCCs before E10.5, to Schwann Cell precursors (SCPs) from E10.5 to E13.5, immature Schwann cells around E15.5, and finally mature SCs, myelinating or non-myelinating (Figure 23)[537,538].

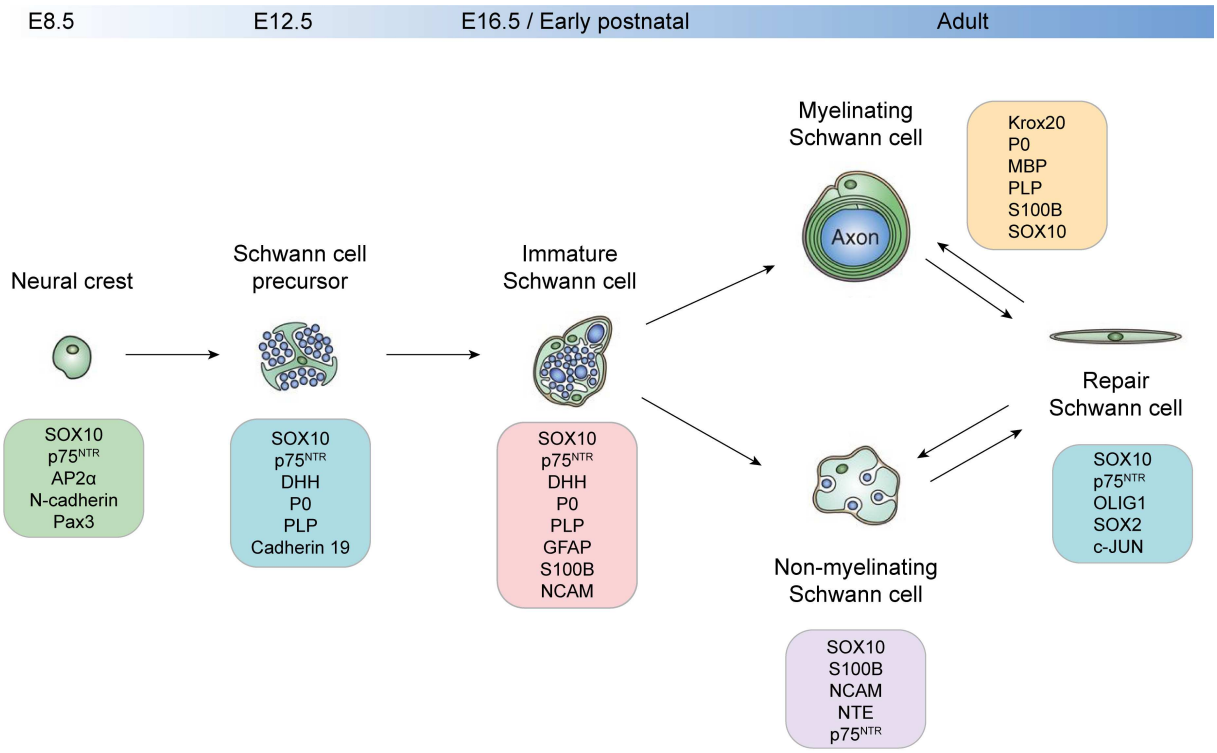

Figure 23: Schwann cell development. Markers expressed at each stage are listed in the boxes. Adapted from[537,539,540]

Schwann cell precursors arise from NCCs around E10.5. SCPs require neuregulin 1 type III (NRG1-III) signaling from axonal binding to survive and can migrate through embryonic tissues using nerves[541]. They differ from NCCs by the expression of glial genes, like *Dhh* and *Plp*[537]. SCPs play different functions, including guiding nerve endings and promoting the survival of DRG neurons and motoneurons[542–544]. SCPs were initially considered as glial-lineage restricted, but studies in the last decade revealed the multipotentiality of this population (Figure 24)[545,546]. SCPs form a significant proportion of endoneurial fibroblasts in peripheral nerves and melanocytes in the skin[547,548]. SCPs are also able to differentiate into osteoblasts and chondrocytes in the axial and cranial skeleton, dental mesenchymal cells, chromaffin cells, and autonomic neurons (enteric and parasympathetic cells)[36,549–555]. SCPs are considered as "secondary supply of neural crest-like cells" during development, providing cells to organs forming after neural crest migration. In addition, SCPs are involved in the regulation of tissue development. In the skin, SCPs secrete paracrine factors, such as VEGF and CXCL12, to promote vascular differentiation and coordinate blood vessel and nerve networks[556,557]. The presence of SCP-like cells in adult tissue remains unknown.

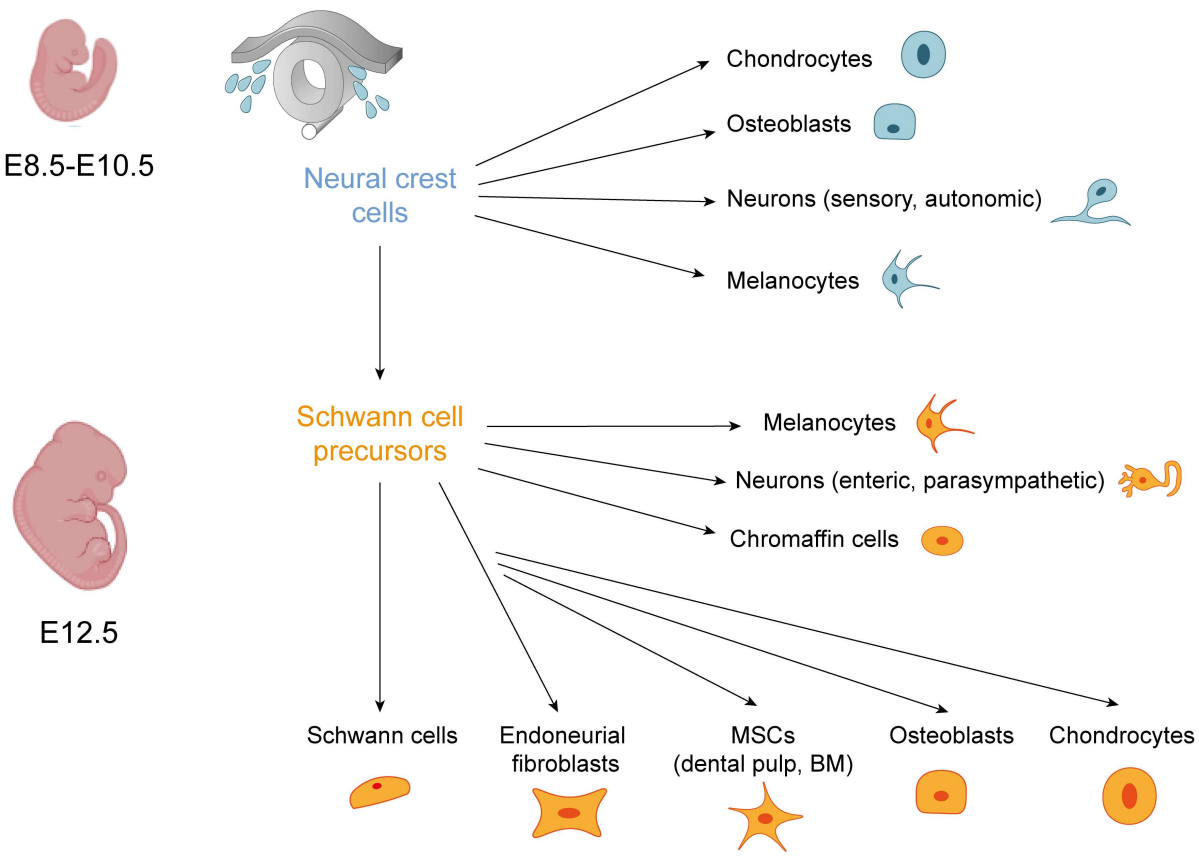

Figure 24: Fate of neural crest cells and Schwann cell precursors during development. BM: bone marrow. MSCs: mesenchymal stem cells. Adapted from[545,546]

SCPs differentiate into immature Schwann cells around E15.5-E16.5[538]. This transition is regulated by *Nrg1*, *Notch1,* and *Edn*[558,559]. Immature SCs differ from SCPs as they are non-migrating cells and no longer require axonal factors to survive. Instead, immature SCs establish an autocrine loop by secreting paracrine factors promoting their survival, including insulin-growth factor 2 (IGF2), PDGF-B, and

NT3[560,561]. Immature SCs play 2 crucial roles: they promote structural changes in embryonic nerves and separate the axons for myelination in a process called radial sorting. During early development, SCPs and axons are the only components of nerves. Immature SCs induce changes in the structure of nerves by secreting factors, such as Dhh that recruits mesenchymal cells to form perineurial and epineural nerve sheath, ephrin-B to interact with endoneurial fibroblasts and VEGF to recruit endothelial cells and promote nerve vascularization[538,547,562,563]. Radial sorting starts at perinatal stages and is active during the first 10 postnatal days. This process separates axons with a large caliber that require myelination from axons with a small caliber that do not require myelination[564]. Groups of 3 to 8 immature Schwann cells form bundles of axons by creating a common basal lamina around them. Schwann cells progressively form cytoplasmic processes to detect large caliber axons and place them at the periphery of the bundle. SCs proliferate and allow large axons to exit the bundle, acquire a 1:1 relationship with a pro-myelinating SC and become myelinating. As axonal separation progress, the axon bundle reduces in size, and only contains small caliber axons, which do not require myelination. The remaining structure will form a Remak bundle with non-myelinating SCs[537,564,565]. Radial sorting is highly dependent on the interactions of SCs with axons and the ECM (laminin, collagens)[537,564,566,567].

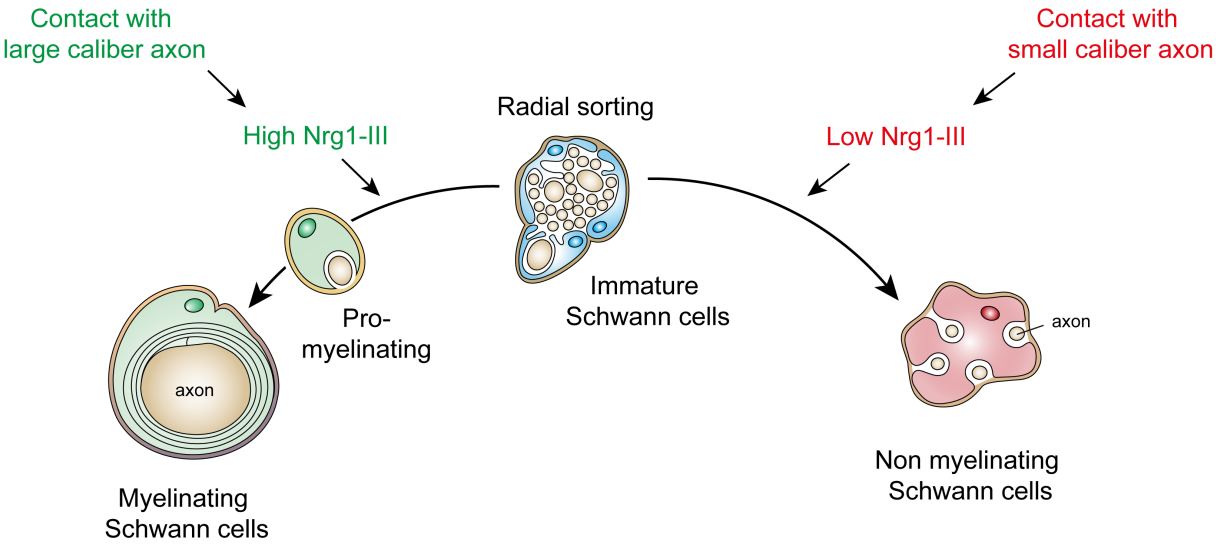

Figure 25: Radial sorting regulates the last step of Schwann cell differentiation. Adapted from [537,560]

1.3. Schwann cells

1.3.1. Identity and functions

Based on their ability to produce myelin, Schwann cells are divided in 2 types: myelinating (mSC) and non-myelinating Schwann cells (nmSC). Immature Schwann cells have the potential to differentiate into both myelinating and non-myelinating SCs and their fate is decided during radial sorting. Among the signaling promoting myelinating fate, Nrg1-III from axons is one of the most important[568,569]. Nrg1-III is expressed by axons proportionally to their size, thus SCs around large caliber axons differentiate into mSCs and SCs around small caliber axons differentiate into nmSCs. Overexpression of Nrg1-III in non-myelinated sympathetic neurons leads to their myelination. mSCs differentiate into a promyelinating

stage, with expression of genes including *Sox10, Pou3f1, Pou3f2*[570,571]. These factors induce the expression of *Krox20*, the master regulator of myelination, as it drives the transcription of the myelin structural proteins and factors involved in myelin lipid synthesis[572–574]. SCs progressively sheath the axon with myelin, composed mostly of lipids and proteins (Myelin basic protein, PLP, P0). The myelin sheath insulates axons and allows increased speed of neuronal signals.

Non-myelinating SCs are associated with small caliber axons, including C fiber nociceptors, preganglionic sympathetic, and neuromuscular junctions[575]. They are usually associated with several axons and their number can vary depending on the fiber type. Surprisingly, nmSCs can be immunocompetent cells, expressing pattern recognition receptors such as Toll-like receptors[576,577]. Non myelinating SCs can also contribute to the niche of adult stem cells, including bone marrow hematopoietic stem cells[578].

1.3.2. Schwann cells in tissue regeneration

Schwann cells play a crucial role in adult nerve regeneration. While the central nervous system fails to regenerate following injury, peripheral nerves can regrow. SCs are active players in peripheral nerve repair (Figure 26)[579–581]. Following injury, SCs detach from nerves and reprogram to become repair Schwann cells (repSCs). This process is characterized by SC demyelination, with down-regulation of pro-myelinating genes such as *Krox20*, Myelin basic protein (*Mbp*), and Myelin protein zero (*Mpz*). In parallel, genes expressed during SC development are upregulated, including neural cell adhesion molecule (*Ncam*), p75 neurotrophin receptor (*Ngfr*), and glial fibrillary acidic protein (*Gfap*)[582,583]. While repSCs seem to undergo dedifferentiation to an immature stage, they also express genes specific to the repair process, like *Olig1*, growth factors such as brain-derived neurotrophic factor (BDNF), glial cell-derived neurotrophic factor (GDNF), NGF or VEGF, and immune factors (IL-1α, IL-1B, TNFα, MCP-1)[584–588]. Repair SCs contribute to the removal of the distal part of the damaged axon and the myelin debris in collaboration with macrophages[589–593]. After clearance of the injury site, repSCs align to form a structure named the band of Büngner and express trophic factors to guide axon regrowth[588,594]. After axon regeneration, repSCs proliferate and redifferentiate into myelinating or non-myelinating SCs by repressing regeneration-related genes and upregulating genes involved in myelination and quiescence. Nerve regeneration is a multicellular process. Macrophages and blood vessels are essential as a source of trophic factors and scaffold for SC migration[593,594]. The transition of mature SCs to repSCs is tightly regulated by many signaling pathways. Two key signalings are c-Jun and the MAPK cascade. c-Jun is expressed at a low level in SCs and is not essential for nerve development and physiology. After injury, c-Jun is highly upregulated in SCs and drives the transition to repSC by repressing myelination[584,595–597]. c-Jun inactivation in SCs leads to decreased neuronal survival and limited regeneration. The MAPK cascade is also activated in SCs after injury and induces demyelination and inflammatory response[598,599]. Different MAP kinases are involved in this process, including ERK, p38MAPK, and JNK, and the specific role of each kinase remains to be further studied[579,600–602]. C-Jun is known to be regulated by the MAPK, indicating a possible connection between MAPK and c-Jun in response to injury.

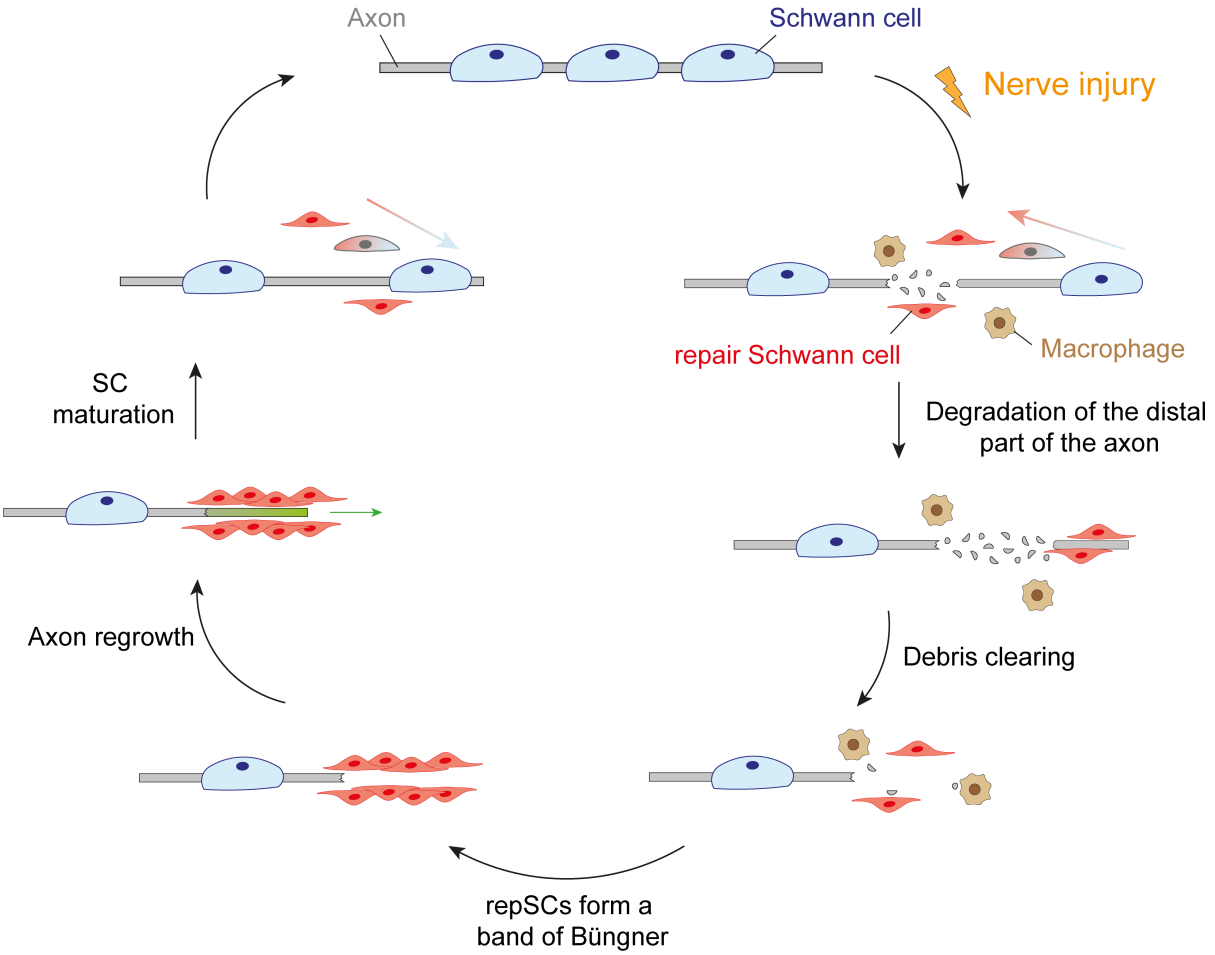

Figure 26: Role of Schwann cells during nerve regeneration.

In addition to their role in nerve repair, Schwann cells also participate in the regeneration of other tissues, including the digit tip, the mandible, and the skin (Figure 27)[251,603,604]. One example of the critical role of SC for tissue healing is limb regeneration in salamanders. Salamanders can fully regenerate a limb after amputation, by the formation of a blastema of undifferentiated cells[605]. Kumar *et al.* showed that innervation, and more precisely Schwann cells plays a crucial role in this process. SCs provide a trophic factor, the newt anterior gradient protein (nAG), required for blastema formation and maintenance[606,607]. In mammals, the function of SCs was described during digit tip regeneration. Amputation of the distal part of a phalangeal element can regenerate with reconstitution of the bone, nail, neurovascular network, and connective tissue[608–610]. Like salamander limb regeneration, digit tip repair relies on the formation of a blastema, composed of PDGFRA+ mesenchymal precursors[611]. Digit tip regeneration is nerve-dependent, as denervation inhibits blastema formation causing impaired healing. Johnston *et al.* showed that amputation is followed by differentiation of SCs into SOX2+ repSCs. SOX2-deficient SCs fail to become repSCs causing impaired blastema formation and digit tip regeneration. Using interactome analyses, they identified 2 factors, PDGF-AA and oncostatin-M (OSM) as essential trophic factors secreted by repSCs, to promote blastema formation, proliferation, and differentiation[603,612]. Additionally, after skin injury, SCs dedifferentiate to become SOX2+ repSCs secreting TGFβ that promotes myofibroblast proliferation and wound healing[613,614].

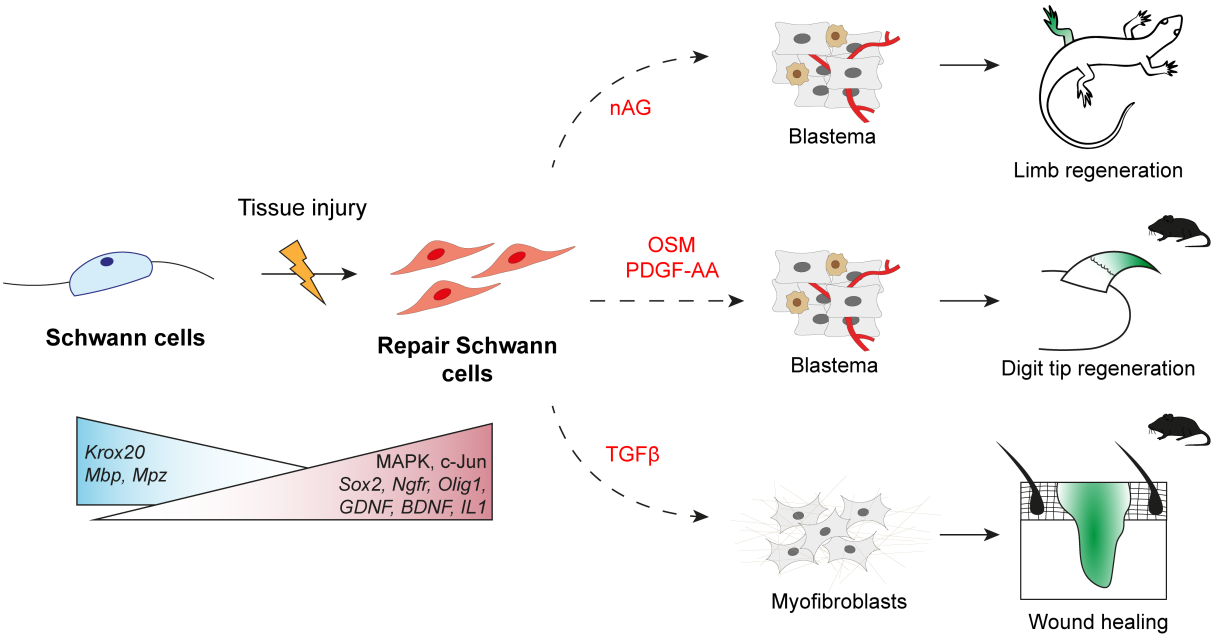

Figure 27: Schwann cells are a source of paracrine factors for tissue repair. After tissue injury, Schwann cells differentiate into repair Schwann cells, marked by the activation of the MAPK and c-Jun pathways and changes in gene expression. Repair Schwann cells express newt anterior gradient (nAG) protein during salamander limb regeneration, OSM and PDGF-AA during murine digit tip regeneration, and TGFβ during murine wound healing. Adapted from [603]

2. Boundary caps

2.1. Identity and functions

In addition to the derivatives described in the section above, neural crest cells give rise to a specific population of cells, called boundary caps (BCs). BCs are a transient cluster of cells, located along the developing spinal cord, at the region of the dorsal root entry zones and motor exit points[615]. The neural crest origin of dorsal BCs was confirmed using chick to quail transplantation, but the origin of ventral BCs is still debated as they could also contain cells derived from the ventral neural tube[615–618]. The gene *Krox20* (*EGFR2* in human) was the first marker identified to label BC cells[572]. In 2009, Coulpier *et al.* used Krox20-GFP mice to perform comparative transcriptomic analyses of BC cells, NCCs, and Schwann cell precursors and identified several markers to label BC cells (*Krox20, Prss56, Wif1, Sema6A, Hey2, Npr3)*[619]. Among them, *Krox20* and *Prss56* (also named L20) are the most specific to BCs and are expressed by both dorsal and ventral BCs (Figure 28). *Prss56* and *Krox20* are expressed in BC from E10.5 to E16.5, confirming that BCs are transient structures.

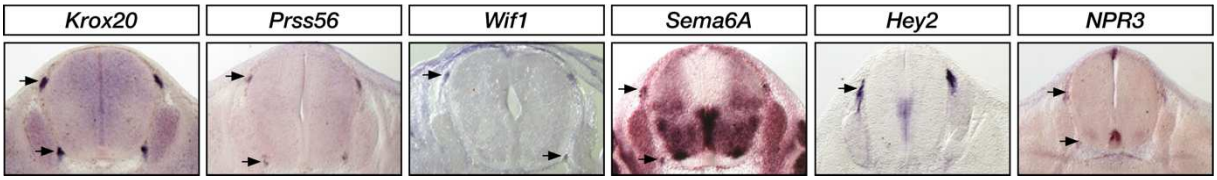

Figure 28: Markers to identify boundary caps. *In situ* hybridization on E12.5 mouse embryo shows that only *Krox20* and *Prss56* specifically mark dorsal and ventral BCs. Adapted from[619]

The formation of BCs coincides with the stage of exit of the motor axons from the neural tube. BCs are involved in motoneuron connection as the depletion of Krox20-expressing BC cells leads to the exit of motoneuron cell bodies from the neural tube and their death[620,621]. This “gatekeeping” function of BCs relies on the action of Semaphorin 6A and Netrin 5[621–623].

To understand the fate of BC cells, lineage tracing analyses using the *Krox20*^{Cre} and *Prss56*^{Cre} were performed[479,482,624]. While Prss56-derived cells can be traced until adult stages, *Krox20* is expressed in immature Schwann cells from E16.5, limiting lineage tracing using the *Krox20*^{Cre} after E16.5. These analyses showed that BC cells exit boundary caps and migrate along peripheral nerves to give rise to several cell populations (Figure 29).

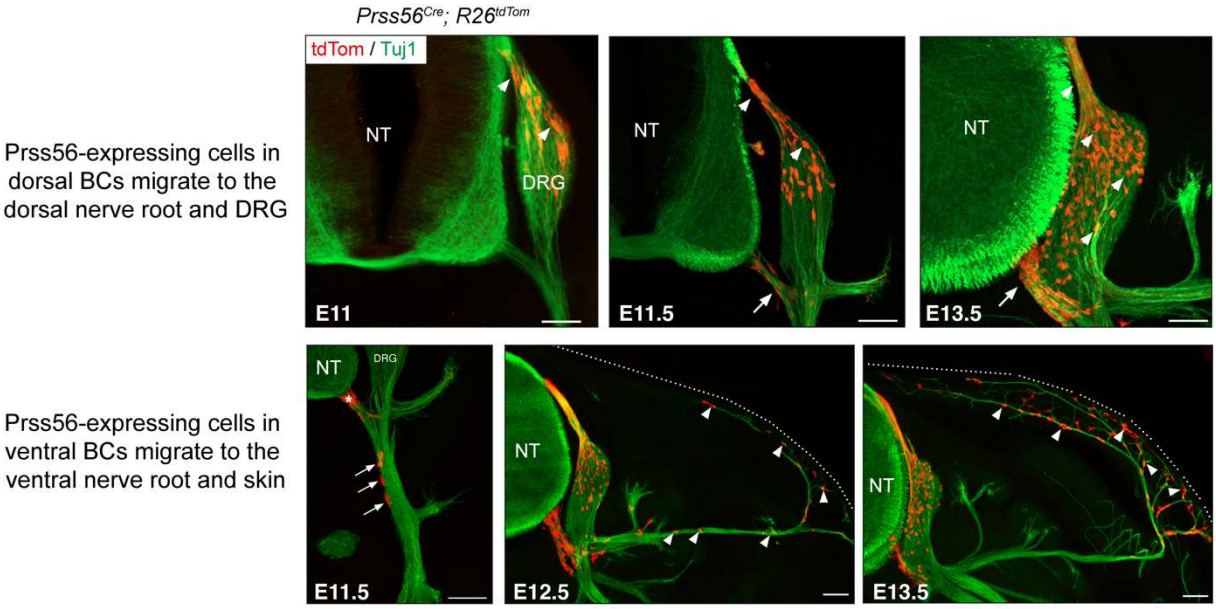

Figure 29: Migration of Prss56-expressing cells from the dorsal and ventral nerve roots. NT: Neural tube, DRG: Dorsal root ganglia. Adapted from [482].

Both dorsal and ventral BC cells give rise to Schwann cells and endoneurial fibroblasts in nerve roots. Dorsal BC cells migrate to the dorsal root ganglia (DRG) where they can form sensory neurons. Interestingly, while both Krox20- and Prss56-derived cells can give rise to nociceptive neurons, only Prss56-derived cells form mechanoceptive and proprioceptive neurons. Ventral BC cells exit BC from E11.5 and migrate until E13 along peripheral nerves to reach peripheral tissue, including the skin. In the skin, Prss56-derived cells differentiate into glial cells, predominantly non-myelinating SCs, associated with nerve fibers, around hair follicles, or free-nerve ending of nociceptive neurons, as well as melanocytes (Figure 30). BC derivatives in the skin also correspond to a population of multipotent skin-derived neural progenitors (SKP). Gresset *et al.* showed the pluripotency of skin Prss56-derived BC cells as they can differentiate into neurons, Schwann cells, fibroblast, adipocytes, melanocytes, and chondrocytes in vitro[482]. Pluripotency was also observed in vivo using DRG and injured sciatic nerve injection[482]. Krox20-derived cells from ventral BC also migrate along nerves to reach the skin but, between E12.5 and 13.5, these cells delaminate from the nerves and migrate along blood vessels. This switch is accompanied by repression of their glial identity and the expression of pericytic genes[625].

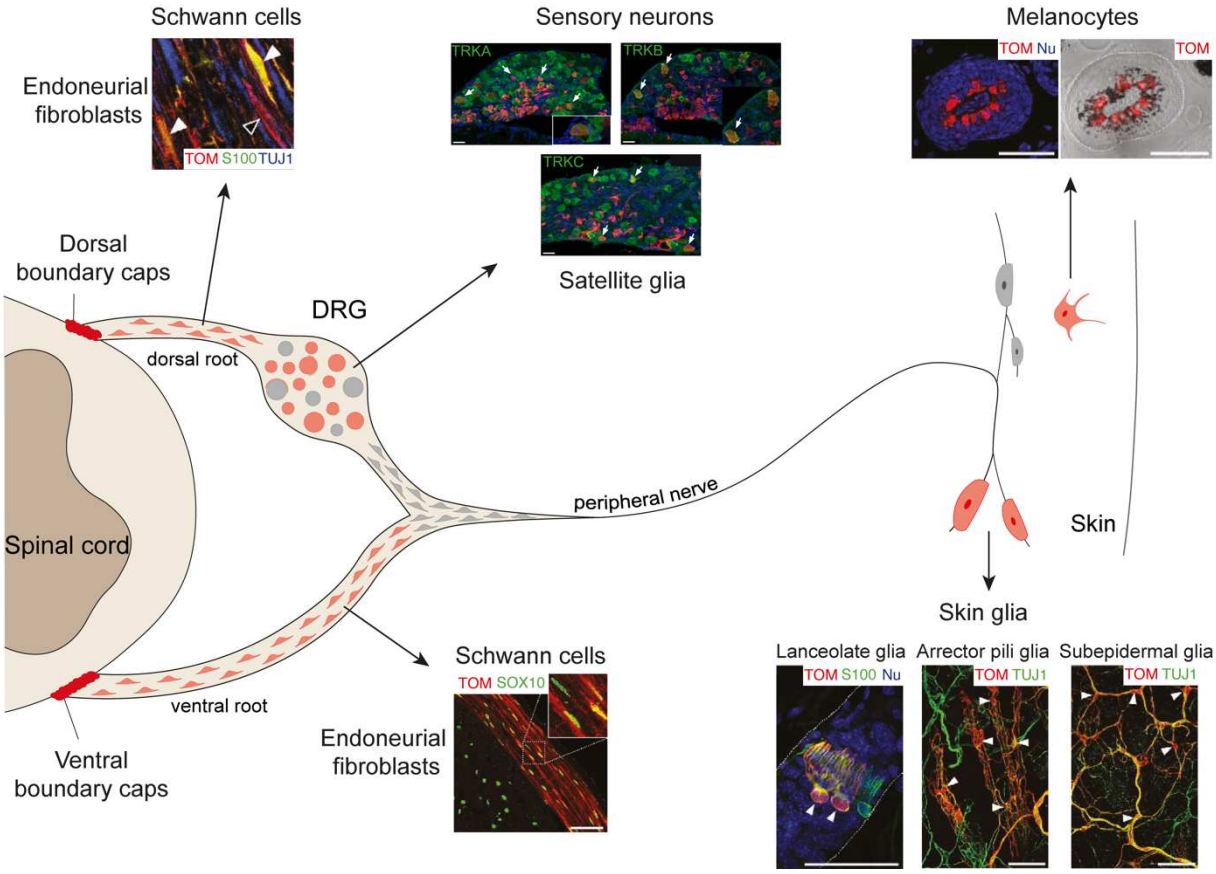

Figure 30: Fate of Prss56-expressing boundary cap cells during development. Adapted from [479,482,625]

The comparative analysis of Prss56- and Krox20-derived boundary caps cells suggests cellular heterogeneity within boundary caps (Figure 30). One hypothesis is that BCs contain 3 subpopulations of cells: (i) cells expressing both *Prss56* and *Krox20* and giving rise to Schwann cells in nerve roots, sensory neurons, and satellite glia, (ii) cells expressing only *Krox20*, migrating to the skin and reaching a perivascular location to become pericytes and (iii) cells expressing only *Prss56*, migrating to the skin and giving rise to Schwann cells, melanocytes, and dermal stem cells[625]. This model of heterogeneity of BC cells remains to be further demonstrated and the presence of BC-derived cells in other peripheral tissue remains unstudied.

2.2. Boundary caps as the cell of origin of NF1

BC derivatives contribute massively to the glial compartment of nerve roots and skin, two sites where glial cells lead to tumor formation in NF1. *Nf1* inactivation in Krox20-derived cells by using *Krox20^{Cre}, Nf1$^{fl/-}$* mice causes the formation of plexiform neurofibromas, but no dermatological manifestations were observed in this model[472]. Radomska *et al.* investigated the implication of Prss56-derived cells in NF1 by generating *Prss56-Nf1 KO* mice: *Prss56^{Cre}; R26^{tdTom}; Nf1$^{fl/fl}$* (*Prss56-Nf1$^{fl/fl}$*) and *Prss56^{Cre}; R26^{tdTom}; Nf1$^{fl/-}$* (*Prss56-Nf1$^{fl/-}$*) mice[479,625]. *Prss56-Nf1$^{fl/-}$* mice recapitulate *Nf1* biallelic inactivation in Prss56 expressing-BC cells and their derivatives in a heterozygote background as observed in patients, while

Prss56-Nf1$^{fl/fl}$ mice allow specific *Nf1* biallelic inactivation in the Prss56 lineage. Mutant mice develop NF1 symptoms at 10 ± 4.5 months and 13.1 ± 3.9 months for *Prss56-Nf1*$^{fl/fl}$ and *Prss56-Nf1*$^{fl/-}$ mice respectively. These symptoms include plexiform paraspinal neurofibroma in the thoracic and cervical region, rich in Prss56-derived nmSCs, as well as non-Prss56-derived immune cells, fibroblasts, and fibrotic tissue. Additionally, mutant mice develop cutaneous neurofibromas, with accumulation of Prss56-derived nmSCs, and non-Prss56-derived macrophages, mastocytes, and fibroblasts. Analysis of mutant skin from E11 to 12 months old mice showed the progressiveness of cNFs. No difference is observed in the skin of mutant mice at E15.5, but an increased number of Prss56-derived SCs is observed at birth, accompanied by morphological changes of traced Schwann cells at 3 months leading to micro-cNFs at 6 months of age and macroscopic cNFs, with pruritus at 12 months. The development of cNFs is stimulated by local skin injury when inflammation promotes tumor development. Comparative analysis of *Prss56-Nf1*$^{fl/fl}$ model with other NF1 models (*Krox20*^{Cre}, *Dhh*^{Cre}) showed that subepidermal glia is labeled only by *Prss56*^{Cre}, suggesting it could be the source of cNFs[479]. In this model, accumulation of Prss56-derived melanocytes in the dermal compartment, that can be reminiscent of CALMs is also observed (Figure 31)[479].

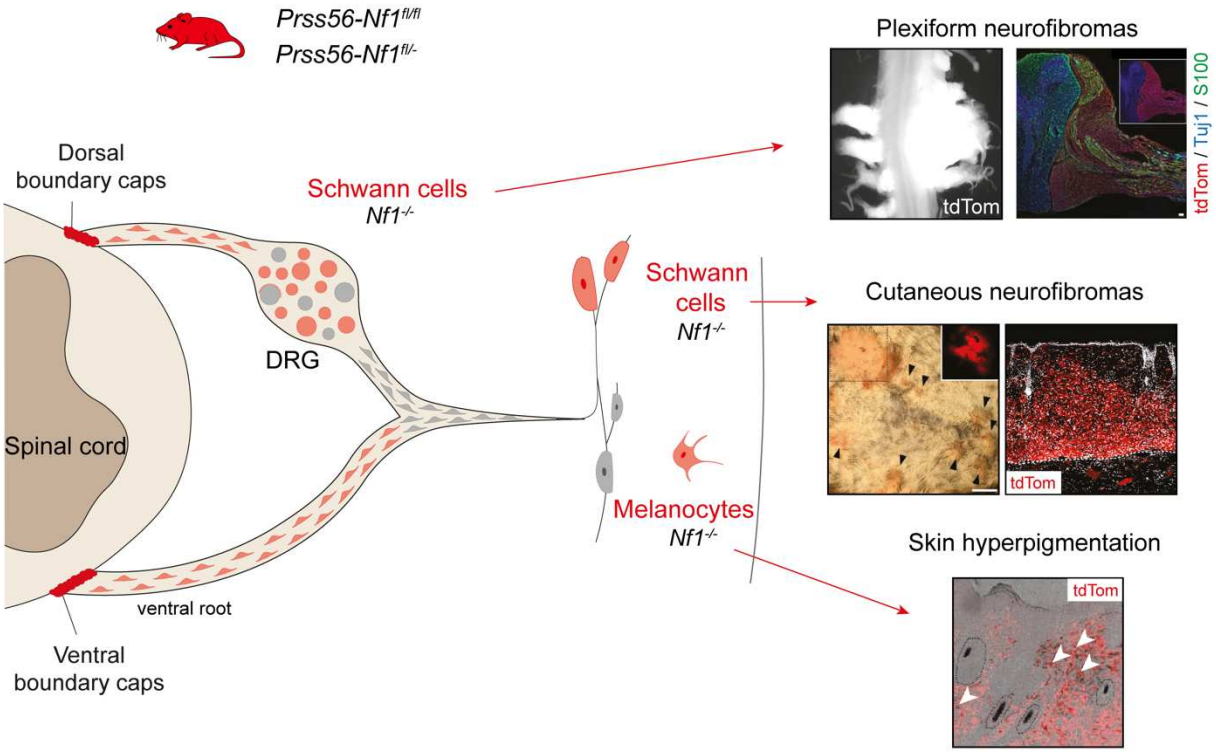

Figure 31: Prss56-expressing boundary cap cells as the cellular origin of NF1. *Prss56-Nf1*$^{fl/fl}$ and *Prss56-Nf1*$^{fl//-}$ mutant mice recapitulate several NF1 symptoms : (i) *Nf1*-deficient Schwann cells from the nerve root and DRG lead to paraspinal plexiform neurofibroma development, composed of tdTom+ Schwann cells, (ii) *Nf1*-deficient Schwann cells in the skin cause formation of cutaneous neurofibroma, macroscopically visible (black arrowhead) and composed of tdTom+ cells, (iii) TdTom+ *Nf1*-deficient melanocytes accumulates in the skin of mutant mice leading to skin hyperpigmentation. Adapted from[479,625]

The *Prss56-Nf1 KO* model is the first one to develop spontaneous cNFs and is a promising model to understand cNF development and perform pre-clinical studies. This model is highly interesting as it recapitulates several features of NF1, including plexiform and cutaneous neurofibromas, as well as skin hyperpigmentation, showing a common cellular origin of neurodermatological lesions of NF1. Additional studies from Dr. Topilko's group indicate that mutant mice display eye lesions reminiscent of Lisch nodules (unpublished data), suggesting that this model could develop multiple NF1 symptoms. The presence of bone phenotypes in this model, including congenital pseudarthrosis of the tibia, has not been studied yet and is the aim of the 3rd part of the thesis.

Aims of the thesis

Each year, around 180 million persons are impacted by a fracture worldwide. Bone repair is a highly efficient process, leading to scarless healing. However, around 10% of fracture present delay or unsuccessful healing, rising the need for therapeutical approaches to enhance bone healing[626,627]. Bone repair relies on the activation and differentiation of skeletal stem/progenitor cells (SSPCs) from the periosteum, the bone marrow and the skeletal muscle surrounding the fracture site. The periosteum is known to be a major source of cells for bone and cartilage formation after fracture, but the identity of periosteal SSPCs (pSSPCs), their mechanisms of activation and differentiation are poorly understood. Moreover, the involvement of the periosteum in bone repair defects is unknown. The goal of the thesis is to investigate the heterogeneity and function of pSSPCs during bone repair and their role in congenital pseudarthrosis of the tibia (CPT), a severe orthopedic condition linked to the disease Neurofibromatosis type 1 (NF1).

Aim 1: Heterogeneity and activation of periosteal stem/progenitor cells in response to bone fracture

In this aim, I assessed the heterogeneity of pSSPCs at steady state and their response to fracture at single cell level using the single-cell RNAseq technology. The pattern of pSSPCs activation was compared to that of SSPCs in skeletal muscle that contribute together to the endochondral ossification process during bone repair. The functional role of BMP signaling in this coordinated action of periosteal and skeletal muscle SSPCs was investigated. This work was published in Journal of Bone and Mineral Research in 2022 and correspond to article n°1: “Skeletal Stem/Progenitor Cells in Periosteum and Skeletal Muscle Share a Common Molecular Response to Bone Injury”.

Aim 2: Role of periosteal stem/progenitor cells in cartilage-to-bone transformation during bone repair

In this work, we determined the role of pSSPCs in a mouse model of pseudarthrosis due to overactivating mutation of the *Fgfr3* gene, known to be involved in dwarfism. Using cell grafting approaches, we studied the impact of *Fgfr3* overactivation on pSSPC chondrogenic differentiation, maturation and cartilage-to-bone transformation. We investigated the potential of pSSPCs for cell-based therapy to correct this pseudarthrosis phenotype. This work was published in Stem Cell Reports in 2020 and correspond to article n°2: “FGFR3 in Periosteal Cells Drives Cartilage-to-Bone Transformation in Bone Repair”.

Aim 3: Role of the periosteum in congenital pseudarthrosis of the tibia related to NF1

In this aim, I elucidated the role of the periosteum in CPT by combining the analysis of bone samples from CPT patients and the relevant *Prss56-Nf1 KO* mouse model. First, I

performedgenetic, transcriptomic and in vitro analyses of periosteum and periosteal cells from CPT patients to understand how *NF1* biallelic inactivation in the periosteum cause CPT. In parallel, I investigated the cellular origin of CPT in the *Prss56-Nf1 KO* mouse model to understand the cellular and molecular mechanisms leading to pseudarthrosis after fracture in this model. This work is presented in article n°3 (to be submitted): “Pro-fibrotic Schwann cells and skeletal stem/progenitor cells cause congenital pseudarthrosis of the tibia in NF1”.

Article 1

Skeletal Stem/Progenitor Cells in Periosteum and Skeletal Muscle Share a Common Molecular Response to Bone Injury

Anais Julien*, **Simon Perrin***, Ester Martinez-Sarra*, Anuya Kanagalingam, Caroline Carvalho, Marine Luka, Mickaël Ménager, and Céline Colnot (* co-first authors)

Research article

published in Journal of Bone and Mineral Research in 2022

Bone regeneration relies on the activation and differentiation of SSPCs recruited from the skeletal tissue, i.e., bone marrow compartment and periosteum, but also from the adjacent skeletal muscle. In addition to their difference of origin, SSPCs from various sources display differences in functions and potential. In this study, we aimed to compare the potential of SSPCs from bone marrow, periosteum and muscle and decipher the mechanisms of their activation following injury. We performed comparative analysis of the potential of primary SSPCs from the different sources and showed that only SSPCs from skeletal muscle and periosteum are contributing to the endochondral ossification process. We studied periosteal heterogeneity by using single-cell RNA sequencing of primary periosteal cells of *Prx1*^{Cre}*; R26*^{mTmG} mice. We detected 3 main cell populations, including SSPCs, macrophages and osteoclasts. By integrated analyses of primary cells of uninjured periosteum and periosteum 3 days post-fracture, we identified a population of fibrochondroprogenitors specific to injury response. This cell population express genes related to extracellular matrix production, skeletal development, proliferation and immune response, suggesting that they are injury-activated cells. Detailed analysis of the fibrochondroprogenitor population allowed us to decipher the pattern of pSSPCs activation. After injury, pSSPCs leave their stem/progenitor state to become fibrogenic cells before engaging into chondrogenic differentiation. This pattern of activation is identical between SSPCs from the periosteum and the skeletal muscle. Further analyses identified the Bone Morphogenetic Protein (BMP) signaling as one of the earliest signaling upregulated in both SSPC from periosteum and skeletal muscle after injury. Inactivation of the *Bmpr1a* gene in PDGFRA+ SSPCs using the mouse model *Pdgfra*^{CreERT} *; Bmpr1a*$^{fl/fl}$ led to a mild bone repair phenotype. Using tissue transplantation from *Pdgfra*^{CreERT} *; Bmpr1a*$^{fl/fl}$ mice at the fracture site of wild-type mice, we showed a reduced contribution of *Bmpr1a*-deficient SSPCs from periosteum and skeletal muscle to callus formation. This reduced contribution is due to reduced migration and proliferation of *Bmpr1a*-deficient SSPCs. Overall, this study uncovers the activation of pSSPCs after fracture and showed that pSSPCs and SSPCs from skeletal muscle share a common activation trajectory and are both regulated by the BMP signaling.

RESEARCH ARTICLE

JBMR®

Skeletal Stem/Progenitor Cells in Periosteum and Skeletal Muscle Share a Common Molecular Response to Bone Injury

Anais Julien,[1†] Simon Perrin,[1†] Ester Martínez-Sarrà,[1†] Anuya Kanagalingam,[1] Caroline Carvalho,[1] Marine Luka,[2,3] Mickaël Ménager,[2,3] and Céline Colnot[1]

[1]Univ Paris Est Creteil, INSERM, IMRB, Creteil, France
[2]Imagine Institute, Laboratory of Inflammatory Responses and Transcriptomic Networks in Diseases, Atip-Avenir Team, INSERM UMR 1163, Université de Paris, Paris, France
[3]Labtech Single-Cell@Imagine, Imagine Institute, INSERM UMR 1163, Paris, France

ABSTRACT

Bone regeneration involves skeletal stem/progenitor cells (SSPCs) recruited from bone marrow, periosteum, and adjacent skeletal muscle. To achieve bone reconstitution after injury, a coordinated cellular and molecular response is required from these cell populations. Here, we show that SSPCs from periosteum and skeletal muscle are enriched in osteochondral progenitors, and more efficiently contribute to endochondral ossification during fracture repair as compared to bone-marrow stromal cells. Single-cell RNA sequencing (RNAseq) analyses of periosteal cells reveal the cellular heterogeneity of periosteum at steady state and in response to bone fracture. Upon fracture, both periosteal and skeletal muscle SSPCs transition from a stem/progenitor to a fibrogenic state prior to chondrogenesis. This common activation pattern in periosteum and skeletal muscle SSPCs is mediated by bone morphogenetic protein (BMP) signaling. Functionally, *Bmpr1a* gene inactivation in *platelet-derived growth factor receptor alpha* (*Pdgfra*)-derived SSPCs impairs bone healing and decreases SSPC proliferation, migration, and osteochondral differentiation. These results uncover a coordinated molecular program driving SSPC activation in periosteum and skeletal muscle toward endochondral ossification during bone regeneration. © 2022 The Authors. *Journal of Bone and Mineral Research* published by Wiley Periodicals LLC on behalf of American Society for Bone and Mineral Research (ASBMR).

KEY WORDS: BONE REPAIR; SINGLE CELL RNA SEQUENCING; PERIOSTEUM; SKELETAL STEM/PROGENITOR CELLS; BMP PATHWAY

Introduction

Tissue regeneration is mediated by resident stem/progenitor cells that are activated locally within injured tissues or organs. During bone regeneration, skeletal stem/progenitor cells (SSPCs) are mobilized not only from bone compartments; ie, bone marrow and periosteum, but also from adjacent skeletal muscle.[1-10] These SSPC populations are diverse in their tissue origin and in their cellular composition, as revealed by single-cell RNAseq (scRNAseq).[2,11-16] Multiple markers have been used to identify SSPCs in bone marrow (ie, *Mx1*, *Grem1*, *LepR*, *Nes*, *Cxcl12*, *Pdgfra*, *Gli1*) or in periosteum (ie, *Ctsk*, *Acta2*),[12,17-23] but none of these markers is restricted to a single tissue.[11-18]

Despite the cellular diversity of SSPCs, functional analyses in adult tissues indicate unique regenerative potential of SSPCs according to their origin. Bone marrow SSPCs are osteogenic, support hematopoiesis and osteoclast formation, play paracrine and immunomodulatory roles, but show limited capacity to form cartilage during bone repair[19,24,25]. SSPCs within periosteum contribute efficiently to both cartilage and bone, and SSPCs from skeletal muscle mainly participate in cartilage formation.[1,2,10] Here, we assessed the activation pattern of SSPCs from periosteum and skeletal muscle after fracture to understand their role in the endochondral ossification process. Compared to bone marrow, SSPCs from periosteum and skeletal muscle are enriched in osteochondral progenitors and efficiently participate in endochondral ossification after transplantation. Using scRNA-seq analyses, we uncover the composition of the periosteal cell populations at steady state and compare their response to fracture with that of skeletal muscle-derived progenitors. We found

Received in original form September 3, 2021; revised form May 19, 2022; accepted May 28, 2022.
Address correspondence to: Céline Colnot, PhD, Univ Paris Est Creteil, INSERM, IMRB, F-94010, Creteil, France. Email: celine.colnot@inserm.fr
Additional Supporting Information may be found in the online version of this article.
[†]AJ, SP, and EMS contributed equally to this work.
Journal of Bone and Mineral Research, Vol. 00, No. 00, Month 2022, pp 1–17.
DOI: 10.1002/jbmr.4616

that bone morphogenetic protein (BMP) signaling is activated in periosteum-derived and skeletal muscle-derived progenitors after fracture. We investigated the consequences of *bmpr1a* gene inactivation in periosteum and skeletal muscle SSPCs marked by *platelet-derived growth factor receptor alpha* (*Pdgfra*) on proliferation, migration, and differentiation. These results reveal that independent of their tissue origin and heterogeneity, SSPCs from periosteum and skeletal muscle share a common molecular response after fracture to support endochondral ossification during bone repair.

Subjects and Methods

Mice

C57BL6/J, $Prx1^{Cre}$,[26] $Prx1^{CreERT}$ (Stock number #029211),[27] $Pdgfra^{CreERT}$ (Stock number # 018280),[28] Rosa-tdTomato-EGFP ($Rosa^{mTmG}$) and $Rosa^{LacZ}$ were obtained from The Jackson Laboratory (Bar Harbor, ME, USA). $Bmpr1a^{fl/fl}$ mice were provided by Dr. Yuji Mishina (University of Michigan, Ann Arbor, MI, USA).[29,30] All strains were maintained on a C57BL6/J background. Mice were bred and kept under controlled pathogen conditions in separated ventilated cages with controlled humidity and ambient temperature, with 12:12-hour light:dark cycles and free access to food and water in the animal facilities of IMRB, Creteil, and Imagine Institute, Paris. All experiments were performed in compliance with procedures approved by the Paris Est Creteil and Paris University Ethical Committees. Both males and females were used in all experiments. For in vitro experiments, 4-week-old to 8-week-old mice were used, and for in vivo experiments 12-week-old to 14-week-old mice were used. No specific randomization methods were used. Sample labeling allowed blind analyses.

Tamoxifen injection

Tamoxifen (TMX; Sigma-Aldrich, St. Louis, MO, USA; ref T5648) was dissolve at 10 mg/mL in corn oil (Sigma-Aldrich; ref C8267) at 60°C for 1 hour. Mice received 300 µL per intraperitoneally injection. To maximize recombination efficiency with the $Prx1^{CreERT}$ line, we tested two different tamoxifen induction protocols. $Prx1^{CreERT}$;$Rosa^{LacZ}$ and $Prx1^{CreERT}$;$Bmpr1a^{fl/fl}$ mice were injected three times a week from week 9 to week 11 post-birth, the day before fracture, and days 1 and 3 following fracture (Fig. S7*A*) or three times the week before fracture (Fig. S7*B*). For phenotypic characterization, $Pdgfra^{CreERT}$;$Bmpr1a^{fl/fl}$ and $Pdgfra^{CreERT}$;$Bmpr1a^{+/+}$ mice were injected once a week before fracture, the day before fracture, the day of fracture, and 1 day following fracture, to target stem/progenitor cells at the time of fracture (Fig. 6). $Pdgfra^{CreERT}$;$Rosa^{mTmG}$;$Bmpr1a^{+/+}$ ($Bmpr1a^{control}$) and $Pdgfra^{CreERT}$;$Rosa^{mTmG}$;$Bmpr1a^{fl/fl}$ ($Bmpr1a^{cKO}$) mice used as donors for extensor digitorum lengus (EDL) or periosteum grafts and for in vitro experiments were injected 3 consecutive days the week before harvest and the day before harvest (Fig. 7).

Non-stabilized tibial fracture

Mice were anesthetized with an intraperitoneal injection of Ketamine (50 mg/mL) and Medetomidine (1 mg/kg) and received a subcutaneous injection of Buprenorphine (0.1 mg/kg) for analgesia. The right leg was shaved and cleaned using Vetidine soap and solution (Vetoquinol, Lure Cedex, France; ref VET 001). The tibial surface was exposed, and the tibia was cut in the middiaphysis to create the fracture. At the end of the procedure, the skin was sutured using non-resorbable sutures (Harvard Apparatus, Holliston, MA, USA; ref 72-3318). Mice were revived with an intraperitoneal injection of atipamezole (1 mg/mL) and kept on heated plate. Two additional doses of analgesia were administrated within 24 hours post-surgery.

Isolation and primary culture of muscle mesenchymal progenitors, periosteal cells, and bone marrow stromal cells

Primary culture of skeletal muscle mesenchymal progenitors (muMPs) was performed as described.[2] Briefly, 4-week-old to 8-week-old mice were euthanized and hindlimbs were harvested. After removing skin and fascia, skeletal muscles surrounding the tibia were dissected. Only the middle part of the muscle tissue free of tendon was used for cell isolation. In a Petri dish with Dulbecco's modified Eagle medium (DMEM) (Life Technologies, Grand Island, NY, USA; ref 21063029) skeletal muscles were minced with scissors. Skeletal muscles were then digested in digesting medium composed of DMEM with 1% Trypsin (Life Technologies; ref 210234) and 1% collagenase D (Roche Diagnostics, Mannheim, Germany; ref 11088866001) and incubated at 37°C for 2 hours. Every 20 minutes individualized cells were removed and transferred into growth media on ice: α minimum essential medium (α-MEM) (Life Technologies; ref 32561029) with 1% penicillin–streptomycin (P/S) (Life Technologies; ref 15140122), 20% lot-selected non-heat-inactivated fetal bovine serum (FBS) (Life Technologies; ref 10270106) and 10 ng/mL basic fibroblast growth factor (bFGF; R&D Systems, Minneapolis, MN, USA; ref 3139-FB-025/CF) and digesting medium was renewed. This step was repeated until all skeletal muscle tissue was digested. After the digestion, cells were filtered sequentially through 100-µm (Dutscher, Bernolsheim, France; ref 352360) and 40-µm filters (Dutscher; ref 352340), centrifuged 10 minutes at 300 *g*, resuspended in growth medium and placed in culture in growth medium.

Primary cultures of periosteal cells (PCs) and bone marrow stromal cells (BMSCs) were performed as described.[10,31] Briefly, 4-week-old to 8-week-old mice were euthanized, and femurs and tibias were dissected to remove fat, adjacent skeletal muscles, and tendons. Epiphyses were then cut and removed. For BMSC culture, bone marrow was flushed out, collected in growth medium, and centrifuged 10 minutes at 300 *g*. Bone marrow cells were resuspended in growth medium and placed in culture. Growth medium was changed every day for 3 days to eliminate floating cells, and then every 3 days. For PC culture, flushed femurs and tibias were placed in 6-cm culture plates and covered with a drop of growth medium to allow PCs to migrate out of the bone explants. When PCs reached confluence, bone explants were removed and cells at passage 0 (P0) were directly subjected to scRNAseq analyses or expanded for subsequent analyses.

Cell sorting

For cell transplantation experiments, PCs, BMSCs, and muMPs were trypsinized (Life Technologies; ref 25200056) and resuspended in growth medium. After 10 minutes of centrifugation at 300 *g*, cells were resuspended in sorting medium containing α-MEM with 1% P/S and 2% lot-selected non-heat-inactivated FBS. Sytox blue (1/1000; Thermo Fisher Scientific, Waltham, MA, USA; ref S34857) was added just before sorting to stain dead cells. Sytox Blue-/*Prx1*-derived green fluorescent protein–positive (GFP+) cells were sorted from $Prx1^{Cre}$;$Rosa^{mTmG}$ mice.

For scRNAseq of muMPs, Sytox Blue-/*Prx1*-derived GFP+ cells were sorted after muscle digestion as described in 'Isolation of primary culture of muscle mesenchymal progenitors' section. For in vitro experiments, SytoxBlue-/*Pdgfra*-derived GFP+ cells were sorted directly after muscle digestion from *Bmpr1a*^{control} and *Bmpr1a*^{cKO} mice. Equivalent percentage of GFP+ cells in the muscle of *Bmpr1a*^{control} and *Bmpr1a*^{cKO} mice was observed (13.6 ± 1.2% and 13.9 ± 4.7%, respectively). Cell sorting was performed on BD FACS Aria II SORP (BD Biosciences, San Jose, CA, USA) for scRNAseq and cell transplantation experiments and Aria Fusion (BD Biosciences) for in vitro experiments.

Flow cytometry analyses

For flow cytometry analyses, PCs, BMSCs and muMPs at passage 0–1 were trypsinized and resuspended in growth medium. After 10 minutes of centrifugation at 300 *g*, cells were resuspended in sorting medium and counted. A total of 500,000 cells were incubated with 50 µL of BD Horizon Brilliant Stain Buffer (BD Biosciences; ref 563794), CD45-BV650 (Clone 30-F11, 1/300; BD Biosciences; ref 563410), TER-119-BV650 (Clone TER-119, 1/300; BD Biosciences; ref 747739), CD51-BV711 (Clone RMV-7, 1/300; BD Biosciences; ref 740755), TIE2-APC (1/300; BioLegend, San Diego, CA, USA; ref 124009), 6C3-PECy7 (1/300; Ozyme, Saint-Cyr-l'École, France; ref BLE108313), THY.2-BV786 (Clone 53–2.1, 1/300; BD Biosciences; ref 564365), CD105-BV421 (Clone MJ7/18, 1/300; BD Biosciences; ref 562760), CD200-BV605 (Clone OX-90, 1/300; BD Biosciences; ref 745255), PDGFRα-PECy7 (Clone APA5, 1/300; eBioscience, Santa Clara, CA, USA; ref 25-1401-80), SCA1-APC (Clone REA422, 1/200; Miltenyi Biotec, Bergisch Gladbach, Germany; ref 103-123-848), CD29-APC (Clone HMβ1-1, 1/400; Miltenyi Biotech; ref 130-102-557), or PDGFRα-BV711 (Clone APA5, 1/200; BD Biosciences; ref 740740) for 30 minutes on ice and protected from light. Cells were then washed by adding 1 mL of sorting medium and centrifuged for 10 minutes at 300 *g*. Supernatant was discarded and cell pellets were resuspended in 200 µL of sorting medium. Compensation beads (Thermo Fischer Scientific; ref 01-2222-42) were used for initial compensation set up and fluorescence minus one (FMO) controls were used for the gating. Analyses were performed on BD LSR Fortessa SORP (BD Biosciences) and results were analyzed using FlowJo software, version 10.2 (FlowJo, LLC, Ashland, OR, USA). The gating strategy used for the analyses is available in Fig. S1*A–C*.

In vitro differentiation

In vitro differentiation was performed as described.[31] Skeletal muscle from tamoxifen induced *Bmpr1a*^{control} and *Bmpr1a*^{cKO} mice were digested and *Pdgfra*-derived muMPs were sorted based on GFP+ expression. After cell sorting, *Pdgfra*-derived muMPs were expanded in six-well plates for in vitro differentiation. For osteogenic differentiation, cells at confluence were cultured in osteogenic medium containing αMEM supplemented with 10% lot-selected non-heat-inactivated FBS, 0.1µM dexamethasone (Sigma-Aldrich; ref D2915), 0.2mM L-ascorbic acid (Sigma-Aldrich; ref A8960) and 10mM glycerol 2-phosphate disodium salt hydrate (Sigma-Aldrich; ref G9422). Medium was changed every 3 days for 3 weeks. Mineralized particles were stained with 0.2% Alizarin red staining (Sigma-Aldrich; ref A5533). For chondrogenic differentiation, 1.5×10^5 cells were plated as micromass in 200 µL of growth media for 2 hours. Then, growth medium was replaced by chondrogenic medium composed of DMEM with 10% lot-selected non-heat-inactivated FBS, 0.1µM dexamethasone, 100 µg/mL sodium pyruvate (Sigma-Aldrich; ref P5280), 40 µg/mL L-proline (Sigma-Aldrich; ref P0380), 50 µg/mL L-ascorbic acid, 50 mg/mL Insulin-Transferrin-Selenium (Sigma-Aldrich; ref I1884), and 10 ng/mL transforming growth factor β1 (TGFβ1) (Sigma-Aldrich; ref T7039). Proteoglycans were stained with Alcian blue (Sigma-Aldrich; ref A5268). All pictures were obtained with a Leica DM IRB light microscope (Leica Microsystems, Inc., Buffalo Grove, IL, USA).

In vitro cell migration

A total of 100,000 cells resuspended in 200 µL of medium supplemented with 0.2% bovine serum albumin (Sigma-Aldrich; ref A2153) were seeded in the upper chamber of an 8-µm pore transwell plate (Thermo Fischer Scientific; ref 141082) and incubated with 800 µL of α-MEM at 1% P/S and 10% FBS in the lower chamber for 15 hours. Anti-mitotic Cytosine β-D-arabinofuranoside hydrochloride (Sigma-Aldrich; ref C6645) was added to synchronize cells. Cells were fixed with 4% paraformaldehyde (PFA) and nuclei were stained with 4′,6-diamidino-2-phenylindole (DAPI). Pictures were taken using EVOS Cell Imaging Systems (Thermo Fischer Scientific). Non-migrated cells were then removed from the upper side of the membrane with a cotton swap (VWR, Leicestershire, UK; ref PURJ896-PC) and migrated cells on the bottom side of the membrane were counted. DAPI+ nuclei were counted using ImageJ software (NIH, Bethesda, MD, USA; https://imagej.nih.gov/ij/).

In vitro cell proliferation

A total of 20,000 GFP+ sorted cells from *Bmpr1a*^{control} or *Bmpr1a*^{cKO} mice were plated in 12-well plates. Each sample was analyzed in duplicate. Cells were then manually counted at d2, d4 and d6 after plating. Growth curve was then generated and area under the curve (AUC) was used to determine cell proliferation using GraphPad Prism (GraphPad Software, Inc., La Jolla, CA, USA).

Genotyping of *Bmpr1a* mutant cells

GFP+ sorted cells from *Bmpr1a*^{control} or *Bmpr1a*^{cKO} mice were lysed in NaOH 50mM at 95°C for 10 minutes. The solution was then equilibrated with 23% Tris–HCl. *Bmpr1a* polymerase chain reaction (PCR) was performed with GoTaq G2 Hot Start Green Master Mix (Promega, San Luis Obispo, CA, USA; ref M7423) using the following primers: Fx2: 5′-GCA GCT GCT GCT GCA GCC TCC-3′, Fx4: 5′-TGG CTA CAA TTT GTC TCA TGC-3′, Fx1:5′-GGT TTG GAT CTT AAC CTT AGG-3′, according to Mishina and colleagues.[30] PCR products were then run on 4% agarose gel.

Tissue and cell transplantation

Tissue and cell transplantations were performed as described.[2,10,31,32] Tibial fracture was induced in the host mice as described in 'Non-stabilized tibial fracture' section. For EDL muscle transplantation, EDL muscle was dissected from tendon to tendon and grafted adjacent to the fracture site. EDL graft was positioned on the anterior surface of the tibia, free of endogenous skeletal muscle, and sutured to the host patellar and peroneus muscle tendons with nonresorbable sutures (Fine Science Tools, Foster, CA, USA; ref 12051-08). The skin was sutured and the mice revived. For periosteum transplantation, the tibia of donor mice was collected and a fragment of cortical bone of

approximately 2 mm in length and 1 mm in width was cut in the anterior-proximal area of each tibia. The endosteum and bone marrow were removed from the graft. Host mice were prepared by creating a cortical defect on the anterior-proximal surface of the tibia adjacent to a fracture. The graft was placed in the cortical defect. The muscle was sutured over the defect to hold the graft in place, and wounds were closed.

For cell transplantation, PCs, BMSCs, and muMPs at passage 1 were trypsinized, washed and resuspended in 1 mL of sorting medium. GFP+ cells were sorted as described in 'Cell sorting' section. The viability of MuMPs, PCs, and BMSCs was 99.8 ± 0.2%, 99.5 ± 0.2%, and 97.1 ± 2.3%, respectively. A total of 150,000 sorted cells were embedded in Tisseel Prima fibrin gel, composed of fibrinogen and thrombin (Baxter, Deerfield, IL, USA; ref 3400894252443), according to the manufacturer's instructions. Briefly, 1×10^5 cells were resuspended in 15 µL of fibrin (diluted at 1/4), 15 µL of thrombin (diluted at 1/4) was added and cells were placed on ice for at least 15 minutes to let the matrix polymerize. The cell pellet was transplanted at the fracture site and the wound was closed.

Sample processing, histology, and histomorphometric analyses

For Ki67 and phoshoSmad1/5/9 immunostaining, calluses were fixed in 4% PFA (Euromedex, Souffelweyersheim, France; ref 15714) for 4 hours and decalcified in 19% ethylenediamine tetraacetic acid (EDTA) (Euromedex; EU00084) for 3 to 4 days at 4°C under agitation in the dark. All other fractured tibias were harvested, fixed in 4% PFA for 24 hours and decalcified in 19% EDTA for 3 weeks at 4°C under agitation in the dark. Samples were embedded in paraffin or in optimal cutting temperature compound (OCT) (MM France, Brignais, France; ref F/62550–1). The entire callus was sectioned, and all consecutive sections were collected. After deparaffinization in NeoClear® (VWR; ref 1098435000) for 2 × 5 minutes, sections were rehydrated and rinsed in PBS for 5 minutes. Frozen sections were dried at room temperature for 30 minutes in the dark and rehydrated in PBS for 10 minutes. After staining, sections were dehydrated in series of graded alcohols and incubated in NeoClear® for 10 minutes. Slides were mounted with NeoMount® mounting medium (VWR; ref 1090160100).

Safranin-O staining

Sections were stained with Weigert's solution for 5 minutes, rinsed in tap running water for 3 minutes and stained with 0.02% Fast Green for 30s (Sigma-Aldrich; ref F7252), followed by 1% acetic acid for 30s and Safranin'O (SO) solution for 45 minutes (Sigma-Aldrich; ref S2255).

Masson's trichrome (TC) staining

Sections were stained with Harris hematoxylin (dilution ½) for 5 minutes (MM France; ref F/C0283), rinsed in running tap water 5 minutes, stained with Mallory red for 10 minutes, rinsed for 5 minutes, and then incubated with phosphomolybdic acid 1% for 10 minutes (Sigma-Aldrich; ref HT153). Collagen fibers were stained inu light green for 20 minutes (VWR; ref 720-0335) and fixed in 1% acetic acid.

Picrosirius staining

Sections were stained with Picrosirius solution (PS) (0.1 g of Direct Red 80; Sigma-Aldrich; ref 43665-25G; diluted into 100 mL of saturated solution of picric acid; Sigma-Aldrich; ref 80456) for 2 hours at room temperature, protected from light.

For histomorphometric analyses, every tenth slide throughout the entire callus was stained with SO, TC, or counterstained with DAPI to visualize fluorescent GFP and Tomato signals. Images were captured using a Zeiss Imager D1 AX10 light microscope (Carl Zeiss Microscopy GmbH, Jena, Germany). Areas of callus, cartilage, bone, and GFP or Tomato signal were determined using ZEN software v1.1.2.0 (Carl Zeiss Microscopy GmbH) and volumes were calculated via the following formula:

$$Volume = \tfrac{1}{3} h \sum_1^{n-1} \left(Ai + A(i+1) + \sqrt{Ai * A(i+1)} \right)$$

where Ai and Ai+1 were the areas of callus, cartilage, bone, or fluorescent signal in sequential sections, h was the distance between Ai and Ai+1 and equal to 300 µm, n was the total number of sections analyzed in the sample.

For transplanted cell and tissue contribution to cartilage and bone, GFP and Tomato signal surface were quantified throughout the entire callus on sections adjacent to SO and TC using a Zeiss Imager D1 AX10 light microscope and ZEN software. Volume of fluorescent signal was calculated as described for histomorphometric analyses above. For $Bmpr1^{control}$ and $Bmpr1a^{cKO}$ fracture calluses, the volume of GFP and Tomato signals were quantified on three sections 300 µm apart in the central part of the callus. GFP+ signal in each area was normalized over the total fluorescence signal (sum of GFP and Tomato fluorescent signals).

Immunofluorescence

GFP and Tomato signals were detected without immunofluorescence staining. Cryosections were dried at room temperature for 30 minutes, rehydrated in PBS for 10 minutes, and then mounted with Fluoromount (eBioscience, Santa Clara, CA, USA; ref 495952).

For Ki67 immunostaining, tissue sections were incubated in PBS supplemented with 5% normal goat serum for 30 minutes and with rabbit anti-mouse Ki67 antibody (dilution 1/200; Abcam, Cambridge, MA, USA; ref ab15580) overnight at 4°C. Secondary goat anti-rabbit AF647 antibody (Life Technologies; ref A-21245) was incubated for 1 hour at room temperature and slides were mounted with Fluoromount (ref 495952, eBioscience). For phospho-Smad1/5/9 immunostaining, citrate buffer antigen retrieval was used for 20 minutes at 95°C followed by 20 minutes at 4°C. Sections were incubated in PBS supplemented with 5% normal goat serum for 30 minutes, before incubation with rabbit anti-mouse phoshoSmad1/5/9 antibody (dilution 1/200; Cell Signaling Technology, Danvers, MA, USA; ref 13820 T) overnight at 4°C, and with secondary goat anti-rabbit AF647 antibody for 1 hour at room temperature. Slides were mounted with Fluoromount and images were acquired using a Zeiss LSM 800 confocal microscope.

X-Gal staining

Samples were harvested, fixed in 0.2% glutaraldehyde solution overnight at 4°C, cryoprotected in 30% sucrose solution and embedded in OCT. Sections were dried at room temperature for 30 minutes, rehydrated in PBS for 5 minutes and post-fixed in

0.2% glutaraldehyde solution for 15 minutes at room temperature. Slides were then washed 3 × 15 minutes in the washing buffer containing 1M $MgCl_2$ (Sigma-Aldrich; ref M8266), 1% Na-deoxycholate (Sigma-Aldrich; ref D6750), 2% NP40 (ref 74385, diluted in H_2O) in PBS. Sections were incubated overnight at 37°C in a humidified chamber in X-Gal solution containing X-Gal (Thermo Fisher Scientific; ref R0404; 50 mg/mL in DMSO), 1X potassium ferrocyanide, 1X potassium ferrocyanide, 1M Tris (pH 7.3–7.4) diluted in washing buffer. Sections were washed in PBS 3 × 5 minutes, counterstained with 1% eosin for 2 minutes, dehydrated, and mounted with NeoMount® mounting medium.

Quantification of cell migration and proliferation in vivo

In vivo cell migration was determined using ImageJ by measuring the minimal distance between each GFP+ cell in the callus and the border of the tissue graft. Every 30th section was used throughout the entire callus.

In vivo cell proliferation in the activated periosteum and skeletal muscle was measured by manual counting of Ki67 + GFP+ and total GFP+ in three independent regions per section. The results represent the mean of three different sections per sample.

Microarray analyses

For microarray analyses, datasets from Lu and colleagues[33] were reanalyzed. Wild-type fractured hindlimbs between knee and ankle were collected free of skin followed by RNA extraction at day 2 ($n = 3$) and day 7 ($n = 4$) and from uninjured limbs ($n = 4$) using Trizol (Invitrogen, Carlsbad, CA, USA). Microarrays were obtained using Agilent Mouse single-color 4 × 44 K arrays (Agilent Technologies, Santa Clara, CA, USA). Microarray feature extraction was performed using Agilent's Extraction 9.1 (Agilent Technologies).[33] Gene set enrichment analysis (GSEA) was performed using all normalized probes on "curated gene set" and "ontology gene set" collections of the Molecular Signatures Database v7 with gene sets between 15 and 5000 genes, 1000 permutations, FDR <0.25 and p value <0.05. Enrichment map was performed with Cytoscape software v3.8.1. using GSEA results with FDR cutoff <0.25, p value <0.05 and filtered by gene expression. Only clusters with more that five terms were retained for the analyses.

Single-cell RNAseq analyses

For skeletal muscle–derived muMPs, datasets from Julien and colleagues[2] were reanalyzed. Briefly, *Prx1*-derived skeletal muscle cells were isolated directly by enzymatic and mechanical digestion of skeletal muscles surrounding the tibia from $Prx1^{Cre}$; $Rosa^{mTmG}$ uninjured mice, and at day 3 and day 5 post–tibial fracture. Two mice were used per sample and only skeletal muscles adjacent to the fracture site were dissected. For PC scRNAseq, uninjured cells were isolated from three mice (ie, six uninjured tibias) by explant culture, and d3 post-fracture cells were isolated from five mice (ie, five injured tibias) as described.[10] PCs were then subjected to scRNAseq at passage 0 without further in vitro cell expansion. No specific analysis of the between-animal variance was conducted due to the design of the experiment. All scRNAseq libraries were generated using Chromium Single Cell 3′Library & Gel Bead Kit v.2 (10X Genomics, San Francisco, CA, USA; ref PN-120237) according to the manufacturer's protocol. Libraries were sequenced on NovaSeq 600 (Illumina, San Diego, CA, USA) with 26 cycles of read 1, eight cycles of i7 index, and 98 cycles of read 2. FastQ files from the scRNA 10X libraries were processed using the Cell Ranger Count pipeline with its default parameters (v5.0.1). Reads were aligned against the mm10 reference genome customized by adding GFP sequence.

Data analyses

Seurat v4.0.1 and RStudio v1.3.1073 were used for analysis of scRNA-seq data.[34,35]

As described in Julien and colleagues,[2] for muMPs, cells expressing between 350 and 8000 genes and expressing less that 20% of mitochondrial genes were retained for analysis, genes expressed in less than three cells were excluded from the analysis. For PCs, cells expressing between 100 and 8000 genes and expressing less that 10% of mitochondrial genes were retained for analysis. Genes expressed in less than three cells were excluded from the analysis. After quality control, 4458 uninjured PCs, 15726 PCs at d3, 4013 uninjured muMPs, 5313 muMPs at d3, and 1449 muMPs at d5 post-fracture were retained for the analysis.

Normalization was performed using sctransform pipeline to integrate datasets and raw counts were log normalized and scaled for gene expression. All datasets were regressed on mitochondrial content. Clustering was performed using the first 20 principal components and a resolution of 0.6 for muMPs, and the first 25 principal components and a resolution of 0.5 for PCs. The number of principal components was determined using the ElbowPlot function of Seurat package. Differentially expressed genes were determined using Wilcoxon rank sum test with p value <0.05. Gene ontology (GO) analyses were done using differentially upregulated genes and implemented in Enrichr interface (https://amp.pharm.mssm.edu/Enrichr/).[36] GO functions including less than five genes and with adjusted p value >0.05 were excluded. GO functions were classified into manually annotated general functions and the number of GO terms per general function was plotted.

Monocle analysis

Monocle3 v0.2.3.0 was used for pseudotime analysis.[37] Sctransform normalized data were used as matrix to perform pseudotime analyses. Starting points correspond to the highest expression of stem/progenitor genes (*Cd34*, *Ly6a*) and the lowest expression of chondrogenic genes (*Sox9/Acan*). Pseudotime values were then added as metadata into Seurat object and pseudotime was plotted as feature using Scatterplot function.

Cell cycle analysis

Cell Cycle Regression vignette from Seurat package was used to study cell cycle.

Lineage analysis

Signature score was calculated for each cell as arithmetic mean of the expression of the indicated genes (Table S1) and implemented as metadata in Seurat object.

Statistical analyses

Data are presented as mean ± standard deviation (SD) and were obtained from at least two independent experiments; n represents the number of samples used for the analysis. Two-sided Mann-Whitney test was used to compare two groups.

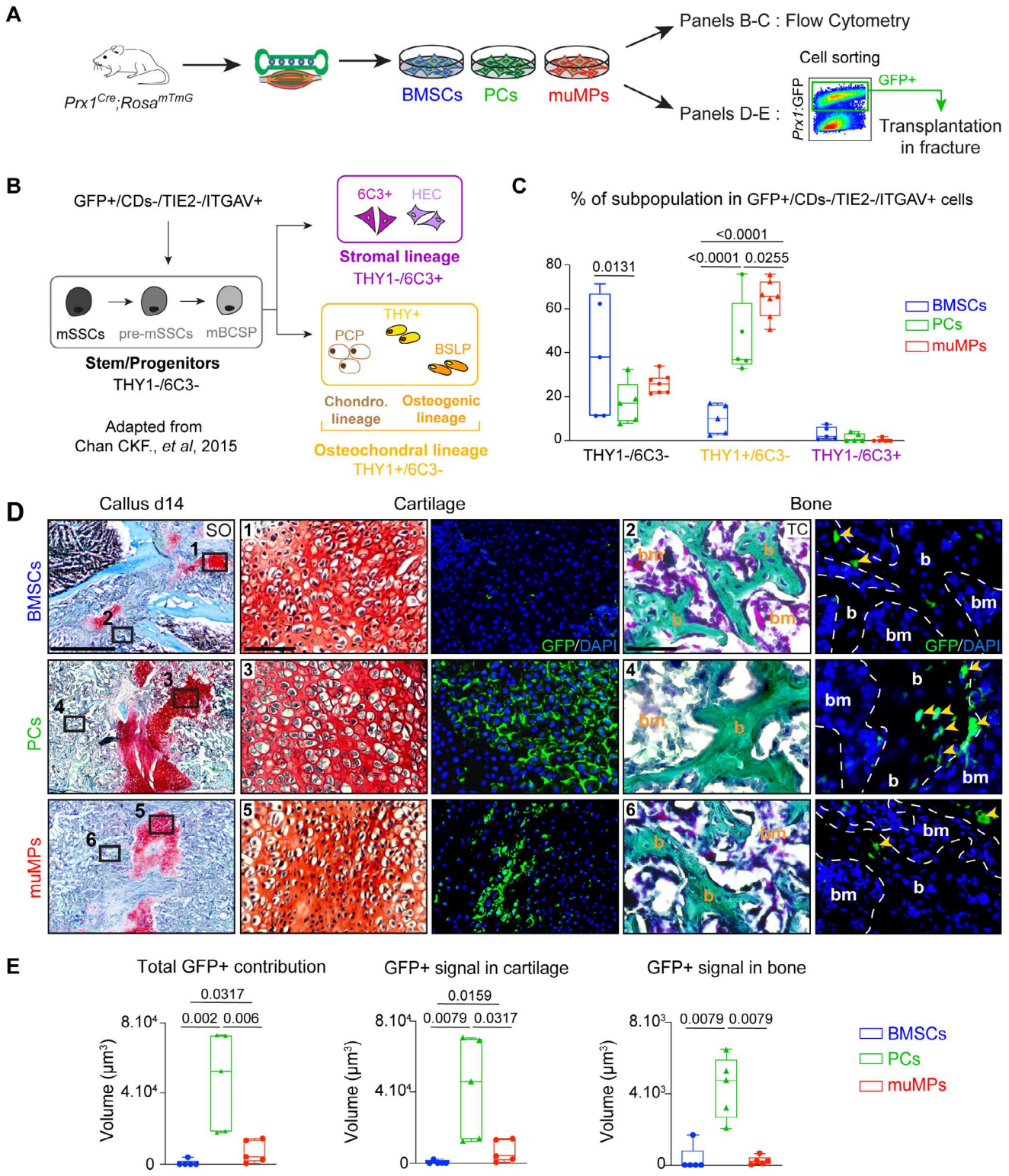

Fig. 1. Periosteum-derived and skeletal muscle-derived cells are enriched in osteochondral progenitors and contribute efficiently to endochondral ossification during bone repair. (*A*) Experimental design. BMSCs, PCs, and skeletal muMPs were isolated from *Prx1*^{Cre};*Rosa*^{mTmG} mice and cultured for one passage before flow cytometry analyses or cell sorting based on GFP expression prior to cell transplantation at the fracture site. (*B*) Schematic representation of hierarchical organization of skeletal stem/progenitor cells adapted from.[38] *Prx1*-derived GFP+ cells were gated first; hematopoietic and endothelial cells were excluded (CDs- = TER119−/CD45−/TIE2−) and ITGAV+ cells were included in the analysis. THY1 and 6C3 markers expression allow the identification of stem/progenitors (THY1−/6C3−), osteochondral (THY1+/6C3−) and stromal (THY1−/6C3+) subpopulations. (*C*) Percentage of skeletal stem/

(Figure legend continues on next page.)

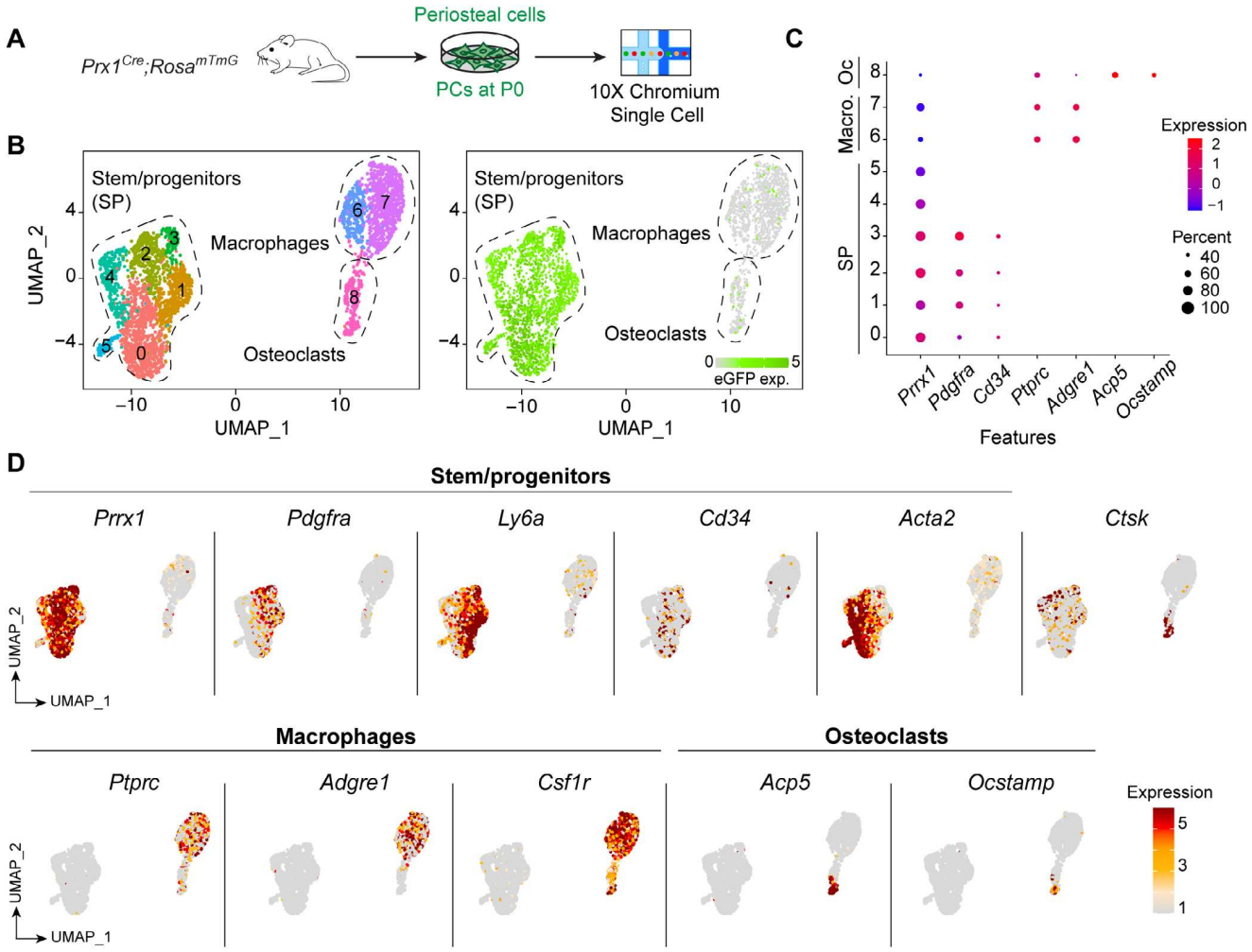

Fig. 2. Single-cell RNAseq of periosteal cells at steady state. (*A*) Experimental design of scRNAseq of PCs at steady state. PCs were isolated from uninjured tibia of *Prx1*^{Cre};*Rosa*^{mTmG} mice by explant culture without expansion and subjected to scRNAseq analyses at P0. (*B*) Left: clusterization of PCs. Right: Feature plot of *eGFP* expression. (*C*) Expression of markers used to define SP, Macro, and Oc clusters. (*D*) Representation of SP, Macro, and OC marker expression. Macro = macrophage; Oc = osteoclast; P0 = passage 0; PC = periosteal cell; SP = stem/progenitor.

For comparison of more than three groups, one-way or two-way analysis of variance (ANOVA) was used. One-way ANOVA was followed by two-sided Mann-Whitney test and two-way ANOVA was followed by Tukey test or Šídák's multiple comparison test as indicated in the legend. Statistical analyses were done using GraphPad Prism v6.0a. Differences were considered significant for p value <0.05. Statistical analyses are provided in the Table S2.

(Figure legend continued from previous page.)
progenitor, osteochondral, and stromal cells in *Prx1*-derived GFP+ BMSCs, PCs, and muMPs (n = 5–7 cell cultures per group). (*D*) Left, Longitudinal sections of fracture callus at d14 post-fracture stained by SO. Middle-right, High magnifications of boxed areas in cartilage and bone stained by SO and TC, respectively, and adjacent sections counterstained with DAPI (bone is delimited by a white dotted line). Boxed areas 1 and 2 showing limited contribution of BMSCs to cartilage and bone, boxed areas 3 and 4 showing robust contribution of PCs to cartilage and bone, and boxed areas 5 and 6 showing contribution of muMPs to cartilage and limited contribution to bone. Yellow arrowheads indicate contribution of transplanted cells to bone. (*E*) Histomorphometric quantification of total GFP+ signal and GFP+ signal in cartilage and bone, respectively. (*C*) Each dot represents an independent cell culture; (*E*) each dot represents a single animal. Values represent the median and interquartile range. (*C*) Exact p value calculated by two-way ANOVA followed by Tukey test. (*E*) n = 5 per group, exact p value calculated with one-way ANOVA followed by two-sided Mann-Whitney test. Scale bars: SO low magnification= 1 mm, cartilage high magnification = 200 µm, bone high magnification = 50 µm. b = bone; bm = bone marrow; BMSC = bone marrow stromal cell; muMP = muscle mesenchymal progenitor; PC = periosteal cell; SO = Safranin O; TC = trichrome.

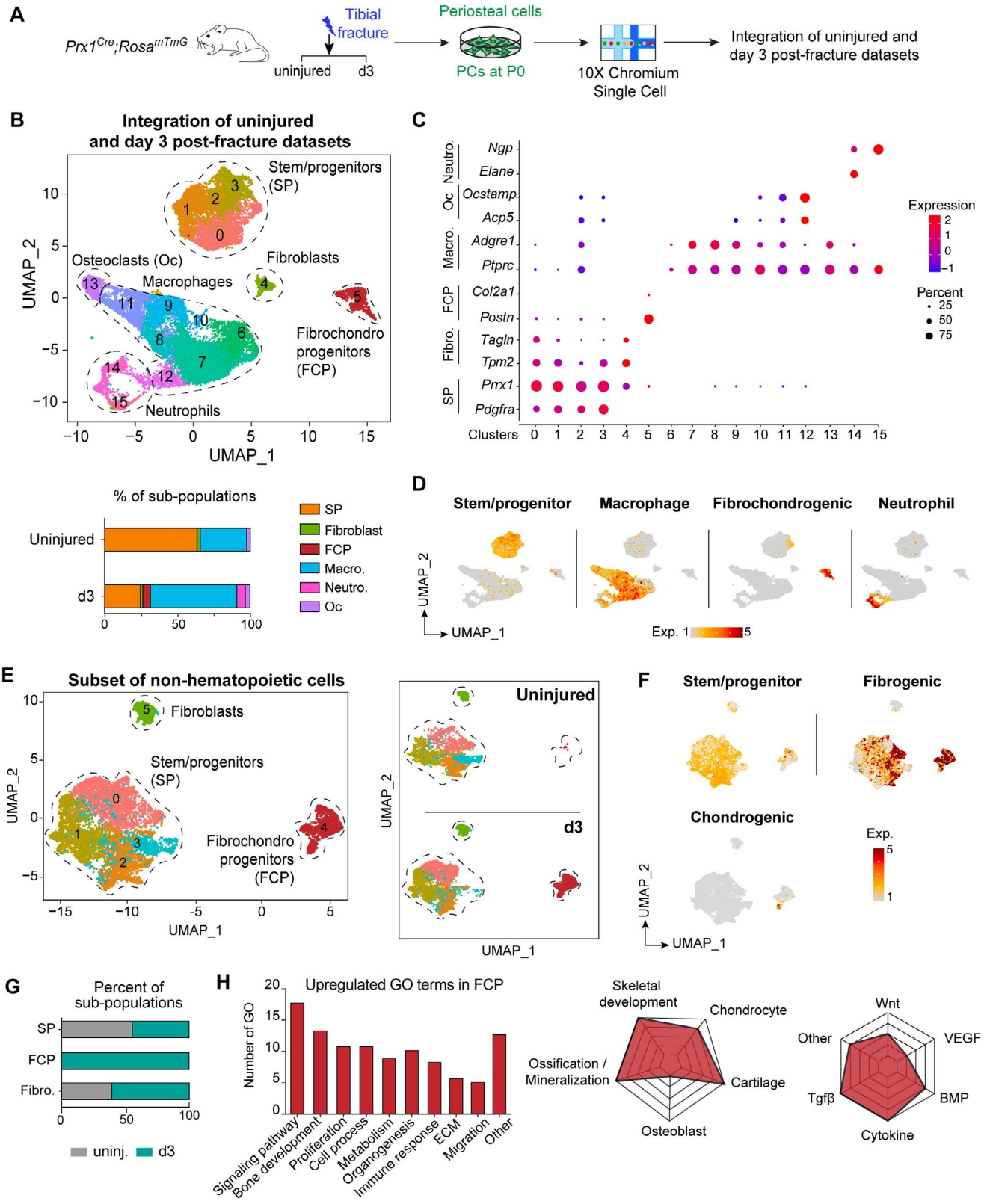

Fig. 3. Single-cell RNAseq of periosteal cells post-fracture. (*A*) Experimental design of scRNAseq. PCs were isolated from *Prx1*^{Cre};*Rosa*^{mTmG} mice by explant culture from uninjured tibia and from fractured tibia at d3 post-fracture and used at P0 for scRNAseq. (*B*) Top, Clusterization of integrated uninjured and d3 post-fracture datasets define six subpopulations (delimited by a black dotted line and named). Bottom, Percentage of subpopulations per sample. (*C*) Dot plot of markers used to define cell populations. (*D*) Feature plot of stem/progenitor, macrophage, fibrochondrogenic, and neutrophil lineage scores. (*E*)

(Figure legend continues on next page.)

Results

Periosteum and skeletal muscle are the sources of osteochondral progenitors

Prx1-derived SSPCs form cartilage and bone during bone regeneration, and are localized within periosteum, bone marrow and skeletal muscle.[2-4,10,23] To directly compare the expression profiles of SSPCs, we performed flow cytometry analyses of sorted *Prx1*-derived cultured cells isolated from bone marrow (BMSCs), periosteum (PCs), and skeletal muscle (muMPs) from $Prx1^{Cre}$;$Rosa^{mTmG}$ uninjured hindlimbs (Fig. 1*A*). We used the strategy proposed by Chan and colleagues,[38] a combination of cell surface markers that identify skeletal stem/progenitor, osteochondral, and stromal subpopulations from the entire bone. Hematopoietic and endothelial cells were excluded from the analyses and skeletal stem/progenitors were defined as ITGAV+/THY1−/6C3− cells, osteochondral progenitors as ITGAV+/THY1+/6C3− cells and stromal cells as ITGAV+/THY1−/6C3+ cells (Fig. 1*B*). We evaluated the proportions of each subpopulation isolated from bone marrow, periosteum, and skeletal muscle. We observed that BMSCs exhibit reduced proportions of non-hematopoietic and non-endothelial cells and increased proportions of ITGAV+/THY1−/6C3− cells compared to PCs and muMPs. However, PCs and muMPs were enriched in ITGAV+/THY1+/6C3− cells and were mostly *Prx1*-derived (Figs. 1*C* and S1). In vivo transplantation of *Prx1*-derived BMSCs, PCs, and muMPs at the fracture site showed that PCs have a higher capacity to integrate into the callus compared to BMSCs and muMPs, and both PCs and muMPs have an enhanced chondrogenic potential compared to BMSCs. Further, PCs were bi-potent because they also formed bone at d14 post-transplantation (Fig. 1*D*,*E*).

Heterogeneity of periosteal cells at steady state

Periosteum is a well-established source of SSPCs during bone repair[1,5,6,10,32]. To characterize the cellular composition of the periosteum, we performed scRNAseq analyses of primary PCs at P0 isolated from $Prx1^{Cre}$;$Rosa^{mTmG}$ uninjured hindlimbs (Fig. 2*A*). We identified nine clusters, grouped into three cell populations: stem/progenitors, encompassing clusters 0 to 5, expressing *Prrx1*, *Pdgfra*, *Ly6a*, *Cd34*, and *Acta2*; macrophages, corresponding to clusters 6 and 7, both expressing *Ptprc*, *Adgre1*, and *Csfr1*, and osteoclasts, ie, cluster 8, expressing *Acp5* and *Ocstamp* (Table S3). *Prx1*-driven GFP expression was detected almost exclusively in the stem/progenitor population (Fig. 2*B*, *C*). Within the stem/progenitor population, we observed regionalized expression of markers. *Ly6a and Pdgfra* were highly expressed in clusters 0, 1, 2, and 3, whereas *Acta2* was mainly expressed in clusters 0, 2, 4, and 5. In addition, we detected the expression of markers commonly defined as tenocyte (*Scx*, *Tnmd*) and pericyte (*Mylk*, *Cspg4*) markers, revealing heterogeneity within the periosteal stem/progenitor population (Figs. 2*D* and S2).

Periosteal cell response to bone injury at single-cell resolution

To characterize the cellular response of PCs to fracture, we performed scRNAseq analyses of PCs isolated at d3 post-fracture from $Prx1^{Cre}$;$Rosa^{mTmG}$ mice, and integrated uninjured and d3 post-fracture datasets (Fig. 3*A*). In addition to the stem/progenitor, macrophage and osteoclast populations described at steady state (Fig. 2), we identified neutrophils expressing *Ngp* and *Elane*, fibrochondro progenitors (FCPs) expressing *Col2a1* and *Postn*, and fibroblasts expressing *S100a4* and *Tpm2* (Figs. 3*B*–*D* and S3*A*,*B*, Table S3). *Prx1*-driven GFP expression was mainly detected in the non-hematopoietic populations, ie, stem/progenitor, FCP, and fibroblast populations (Fig. S3*C*). We then focused our analysis on these non-hematopoietic populations that form cartilage and bone in the callus. To assess the fate of the non-hematopoietic periosteal cells in response to fracture, we plotted the lineage score of stem/progenitor, fibrogenic (extracellular matrix [ECM]-producing cells) and chondrogenic gene expression. The FCP cluster, found exclusively at d3 post-fracture, was the only cluster containing cells with stem/progenitor, fibrogenic, and chondrogenic signatures (Fig. 3*E*–*G*). GO analysis of upregulated genes in the FCP cluster showed a high number of biological functions related to stem/progenitor cell activation upon injury (proliferation and migration categories) and ossification (bone development and ECM categories). Detailed analyses of GO terms highlighted an overrepresentation of GO terms related to skeletal development, cartilage/chondrocyte and ossification/mineralization, as well as signaling pathways related to cartilage/bone formation such as TGFβ and BMP (Fig. 3*H*). These results suggest that the FCP cluster contains the PC population specifically activated upon injury.

To better understand how PCs are activated upon fracture, we performed pseudotime analyses of FCPs as they correspond to cells engaging in chondrogenesis (Fig. 4*A*). The starting point of the pseudotime trajectory was defined by the least differentiated cells expressing the highest level of stem/progenitor genes (*Cd34/Ly6a*) and the lowest level of chondrogenic genes (*Sox9/Acan*). The pseudotime trajectory progressed through one main branch where PCs downregulated stem/progenitor genes and upregulated fibrogenic genes prior to engaging in chondrogenesis (Figs. 4*B* and S3*D*). Genes associated with cell migration were increased in parallel with fibrogenic genes, whereas genes associated with proliferation were upregulated in parallel with chondrogenic genes (Fig. 4*C*).

We previously reported the response to bone repair of *Prx1*-derived skeletal muscle progenitors using scRNAseq[2] (Fig. S4*A*–*D*). Within *Prx1*-derived skeletal muscle cells, the fibroadipogenic progenitor/mesenchymal progenitor (FAP/MP)

(Figure legend continued from previous page.)
Left, UMAP projection of uninjured and d3 post-fracture datasets subclusterized for non-hematopoietic cells. Right, Split UMAP visualization of non-hematopoietic cells from uninjured and d3 post-fracture datasets. (*F*) Feature plot of stem/progenitor, fibrogenic, and chondrogenic lineage scores in the non-hematopoietic cells. (*G*) Percentage of subpopulations per sample. (*H*) Left, GO analyses of upregulated genes in FCP subpopulation. Middle, Radar chart of skeletal related functions. Right, signaling pathways enriched in GO analyses. d3 = day 3; FCP = fibrochondro progenitor; Fibro. = fibroblast; GO = gene ontology; Macro. = macrophage; Neutro. = neutrophil; Oc = osteoclast; PC = periosteal cell; SP = stem/progenitor; UMAP = uniform manifold approximation and projection.

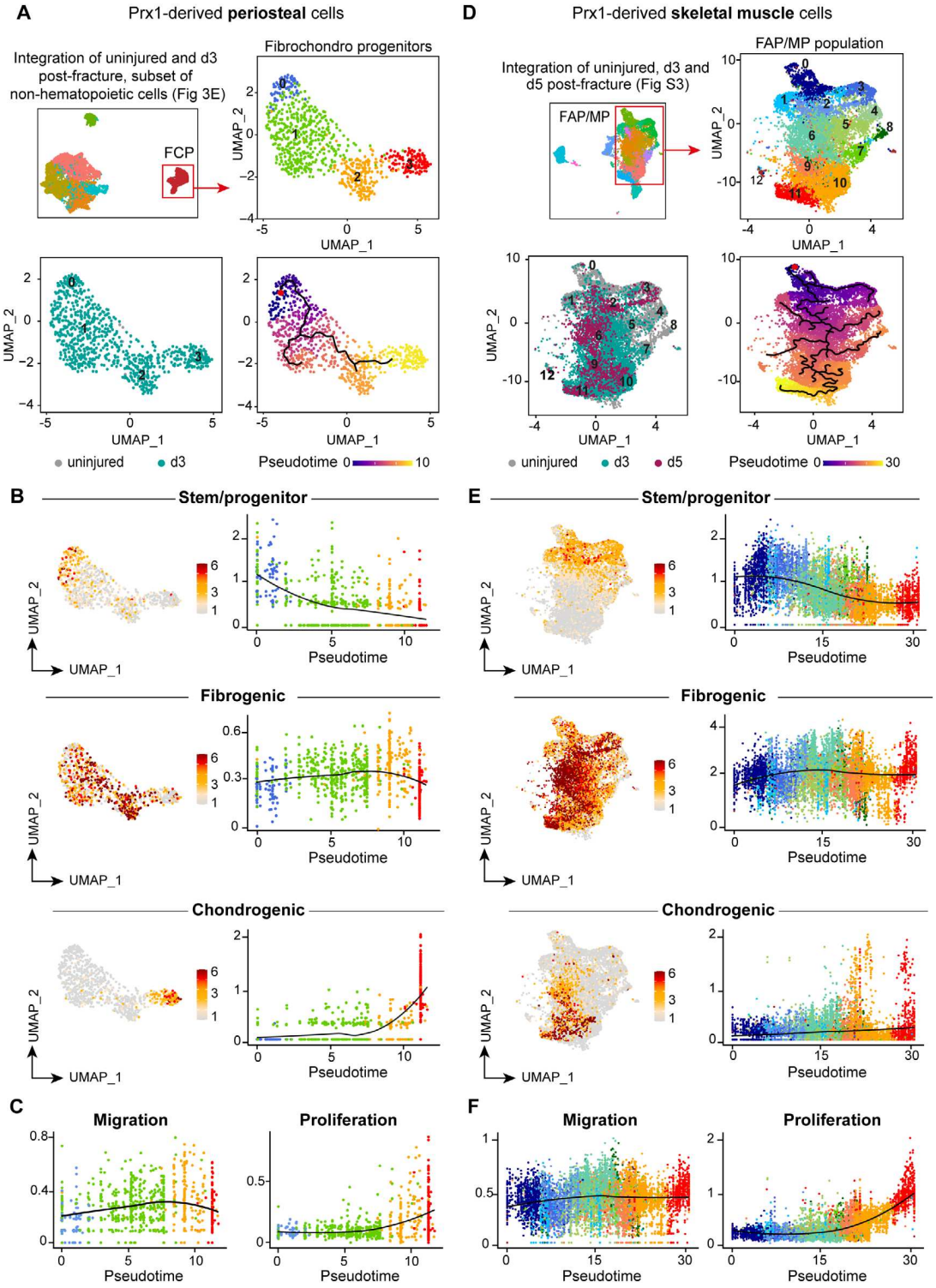

Fig. 4. Single-cell RNAseq reveals similar activation patterns of periosteum and muscle progenitors after bone fracture. (*A*) Top left, UMAP projection of subclusterization of non-hematopoietic PCs as in Fig. 3*E*. Top right, UMAP projection of FCPs used for the subsequent analyses. Bottom left, UMAP visualization of sample origin of FCPs (uninjured in gray and d3 post-fracture in green). Bottom right, Pseudotime trajectory analysis of periosteum-derived FCPs. (*B*) Feature plot and scatter plot of stem/progenitor (top), fibrogenic (middle), and chondrogenic (bottom) lineage scores along pseudotime in periosteum derived FCPs. (*C*) Scatter plot of migration and proliferation lineage scores along pseudotime in FCPs. (*D*) Top left, UMAP projection of Prx1-derived skeletal muscle cells from uninjured tissue and from d3 and d5 post-fracture samples as in Fig. S4. Top right, UMAP projection of subclusterization of *Prx1*-derived skeletal muscle FAP/MP used for the subsequent analyses. Bottom left, UMAP visualization of sample origin of *Prx1*-derived skeletal muscle FAP/MP (uninjured in gray, d3 post-fracture in green and d5 post-fracture in purple). Bottom right, Pseudotime trajectory analysis of *Prx1*-derived

(Figure legend continues on next page.)

population was the most responsive to injury[2] (Table S3). Activated muMPs displayed the same cellular response to bone injury as activated PCs by losing their stem/progenitor identity, engaging in fibrogenesis, prior to engaging in chondrogenesis and proliferating (Fig. 4D–F). However, in addition to the main trajectory, we observed multiple branches in the fibrogenic state for activated muMPs, suggesting that activated muMPs may not all engage in chondrogenesis and contain a subset of SSPCs (Fig. S4E). Chondrogenic-related and migration-related genes were not highly expressed by d5 post-fracture in activated muMPs because they were still localized in the skeletal muscle tissue prior to their migration into the fracture callus and only started expressing chondrogenic and migrating programs.

PC and muMP response to bone injury is mediated by BMP signaling

We then assessed the similarities in the molecular programs driving PC and muMP activation. Microarray datasets of uninjured, d2 and d7 post-fracture hindlimbs were reanalyzed.[33] We observed an overrepresentation of signaling pathways related to immune response such as Toll-like receptors (Toll-like R), chemokines, tumor necrosis factor (TNF), and interleukins, as well as Hedgehog (HH), platelet-derived growth factor receptor (PDGFR), epidermal growth factor (EGF), TGF, and BMP pathways at d2 post-fracture compared to uninjured samples (Fig. 5A,B). This correlated with the enrichment in GO terms related to immune response (Fig. S5A,B). At d7 post-fracture, GO terms related to immune response and HH, PDGFR, and EGF signaling pathways were downregulated, but not GO terms related to BMP signaling. In parallel, GO terms related to metabolism, signal transduction, neurotrophin, and Wnt signaling pathways were upregulated (Fig. 5B). This signature was associated with GO terms related to morphogenesis, skeletal development, and ECM secretion (Fig. S5C,D). BMP signaling, defined as the mean expression of BMP receptors and effectors, was overexpressed at d2 and d7 post-fracture, suggesting a role in the early stage of repair (Fig. 5C). In the PC and muMP scRNAseq datasets from Fig. 4, we observed that BMP signaling was upregulated in FCPs at d3 and in activated muMPs at d3 and d5 post-fracture (Figs. 5D,E and S6). Immunostaining for phoshoSMAD1/5/9 confirmed that the BMP pathway is active in *Prx1*-derived periosteal and skeletal muscle cells at d3 post-fracture in vivo (Fig. 5F).

BMP signaling is required for SSPC activation upon fracture

To functionally evaluate the role of BMP signaling in SSPCs during bone regeneration, we performed genetic inactivation of the *Bmpr1a* gene.[39] Due to the low efficiency of the $Prx1^{CreERT}$ mouse model (Fig. S7), we used the $Pdgfra^{CreERT}$ line to target periosteal and skeletal muscle progenitors expressing *Pdgfra* (Figs. 2 and 3C, and Fig. S4 and S8A,B).[2,10,14] We evaluated a 65.9% Cre recombination efficiency in $Pdgfra^{CreERT}$;$Rosa^{mTmG}$ mice and confirmed the presence of *Pdgfra*-derived skeletal progenitors contributing to fracture healing in both periosteum and skeletal muscle (Fig. S8C–E). Analysis of bone repair in tamoxifen-induced $Pdgfra^{CreERT}$; $Bmpr1a^{fl/fl}$ mice showed decreased callus and bone volumes at d14 post-fracture compared to $Bmpr1a^{fl/fl}$ controls and reduced contribution of *Bmpr1a*-deficient *Pdgfra*-derived cells within cartilage and bone as compared to control cells (Fig. 6A-D). However, the presence of non-recombined cells using this CRE model suggests that these cells may partially compensate for the phenotype using a systemic induction strategy.

To specifically trace *Bmpr1a*-deficient cells from periosteum and skeletal muscle, we used periosteum and EDL muscle graft transplantation. Grafts from tamoxifen-induced $Pdgfra^{CreERT}$; $Rosa^{mTmG}$; $Bmpr1a^{fl/fl}$ ($Bmpr1a^{cKO}$) and $Pdgfra^{CreERT}$;$Rosa^{mTmG}$; $Bmpr1a^{+/+}$ ($Bmpr1a^{control}$) mice were transplanted at the fracture site of wild-type hosts. We observed a reduced contribution to cartilage of *Bmpr1a*-deficient cells from periosteum and skeletal muscle, and reduced contribution to bone, of *Bmpr1a*-deficient cells from periosteum, as compared to controls (Fig. 7A,B). To determine whether abnormal cell migration could account for the impaired cellular contribution of periosteum and skeletal muscle to callus formation, we measured the distance between the graft and the *Pdgfra*-derived migrating cells within cartilage. We observed that *Bmpr1a*-deficient cells remained closer to the graft compared to control cells (Fig. 7C). We then assessed cell proliferation in vivo using Ki67 immunostaining on $Bmpr1a^{cKO}$ and $Bmpr1a^{control}$ calluses at d3 post-fracture. The percentage of proliferative *Pdgfra*-derived cells over the total *Pdgfra*-derived population was significantly reduced in the activated periosteum and adjacent skeletal muscle of $Bmpr1a^{cKO}$ mutant mice compared to control mice at day 3 post-fracture, suggesting that a decrease in the proliferation of skeletal muscle and periosteum progenitors in the absence of BMP signaling could also impact the phenotype (Fig. 7D,E). In vitro differentiation assays showed an abolition of the osteogenic potential of *Bmpr1a*-deficient cells, whereas early chondrogenic differentiation was not affected. In vitro migration and proliferation capacities of *Bmpr1a*-deficient cells were impaired, confirming in vivo observations (Fig. 7F). We verified Cre-mediated recombination in *Pdgfra*-derived cells by *Bmpr1a* genotyping and confirmed that *Bmpr1a* deletion did not affect the cellular identity of *Pdgfra*-derived cells by flow cytometry (Fig. S9). Altogether, these results highlight the role of BMP signaling as a common mediator of PC and muMP activation during the early stages of bone repair.

Discussion

Multiple markers have been proposed as specific for SSPC subpopulations in bone, but the diversity of these markers makes it challenging to investigate SSPC functions in skeletal growth, repair, and aging.[9,12,14,18-23,39] In addition, during bone regeneration, SSPCs originate not only from bone compartments; ie,

(Figure legend continued from previous page.)
skeletal muscle FAP/MP. (*E*) Feature plot and scatter plot of stem/progenitor (top), fibrogenic (middle), and chondrogenic (bottom) lineage scores along pseudotime in FAP/MP. (*F*) Scatter plot of migration and proliferation lineage scores along pseudotime in FAP/MP. Color scheme used in *B* and *C* corresponds to the color of clusters used in *A*, and color scheme used in and *E* and *F* corresponds to the color of clusters used in *D*. d3 = day 3; FAP = fibroadipogenic progenitor; FCP = fibrochondro progenitor; MP = mesenchymal progenitor; PC = periosteal cell; UMAP = uniform manifold approximation and projection.

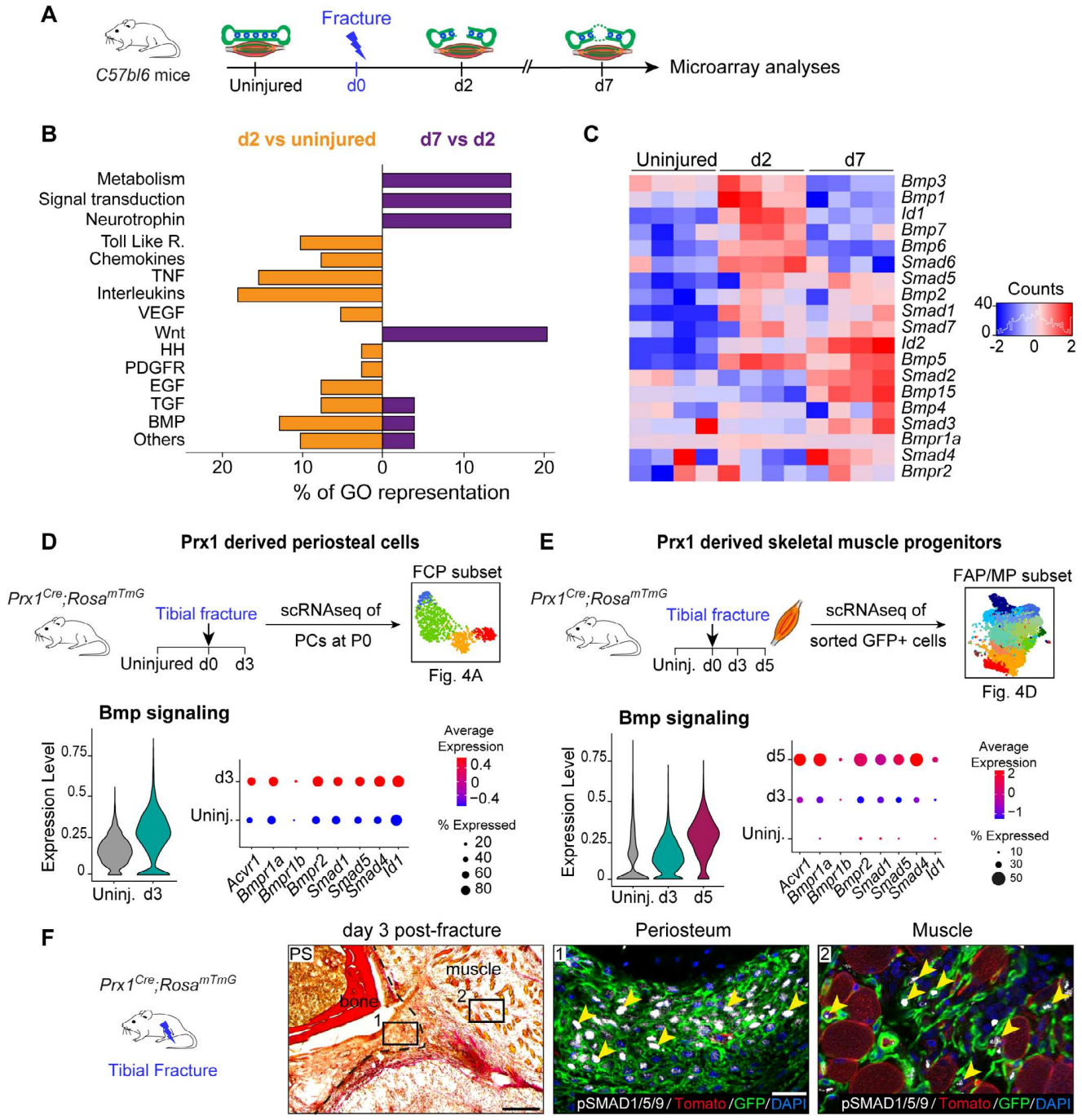

Fig. 5. BMP signaling is upregulated in injury-activated periosteum and muscle progenitors. (*A*) Experimental design of microarray analyses.[33] Tibia and adjacent skeletal muscle were harvested from uninjured hindlimbs at d2 and d7 post-fracture and used for microarray analyses. (*B*) Representation of upregulated signaling pathways from Gene Ontology analyses between d2 versus uninjured (in orange, left) and between d7 versus d2 (in purple, right). (*C*) Heat map of BMP signaling components from microarray dataset. (*D*,*E*) Experimental design of scRNAseq of *Prx1*-derived periosteal cells and skeletal muscle progenitors. Violin plot of BMP signaling pathway expression (left) and detailed visualization of receptor (*Acvr1*, *Bmpr1a*, *Bmpr1b*, *Bmpr2*), co-factor (*Smad1*, *Smad4*, *Smad5*), and target (*Id1*) gene expression (right) in *Prx1*-derived FCPs (*D*) and skeletal muscle FAP/MP (*E*). (*F*) Transverse section of d3 post-fracture $Prx1^{Cre};Rosa^{mTmG}$ hindlimb stained with PS showing activated periosteum (delimited by a black dotted line). High magnifications of boxed areas from adjacent section counterstained with DAPI show phosphoSMAD1/5/9 positive nuclei (white, pointed with yellow arrowhead) in GFP+ cells (in green) within periosteum (middle), and adjacent skeletal muscle (right). Scale bars: low magnification = 200 μm, high magnification = 50 μm. bm = bone-marrow; d2 = day 2; PS = Picrosirius.

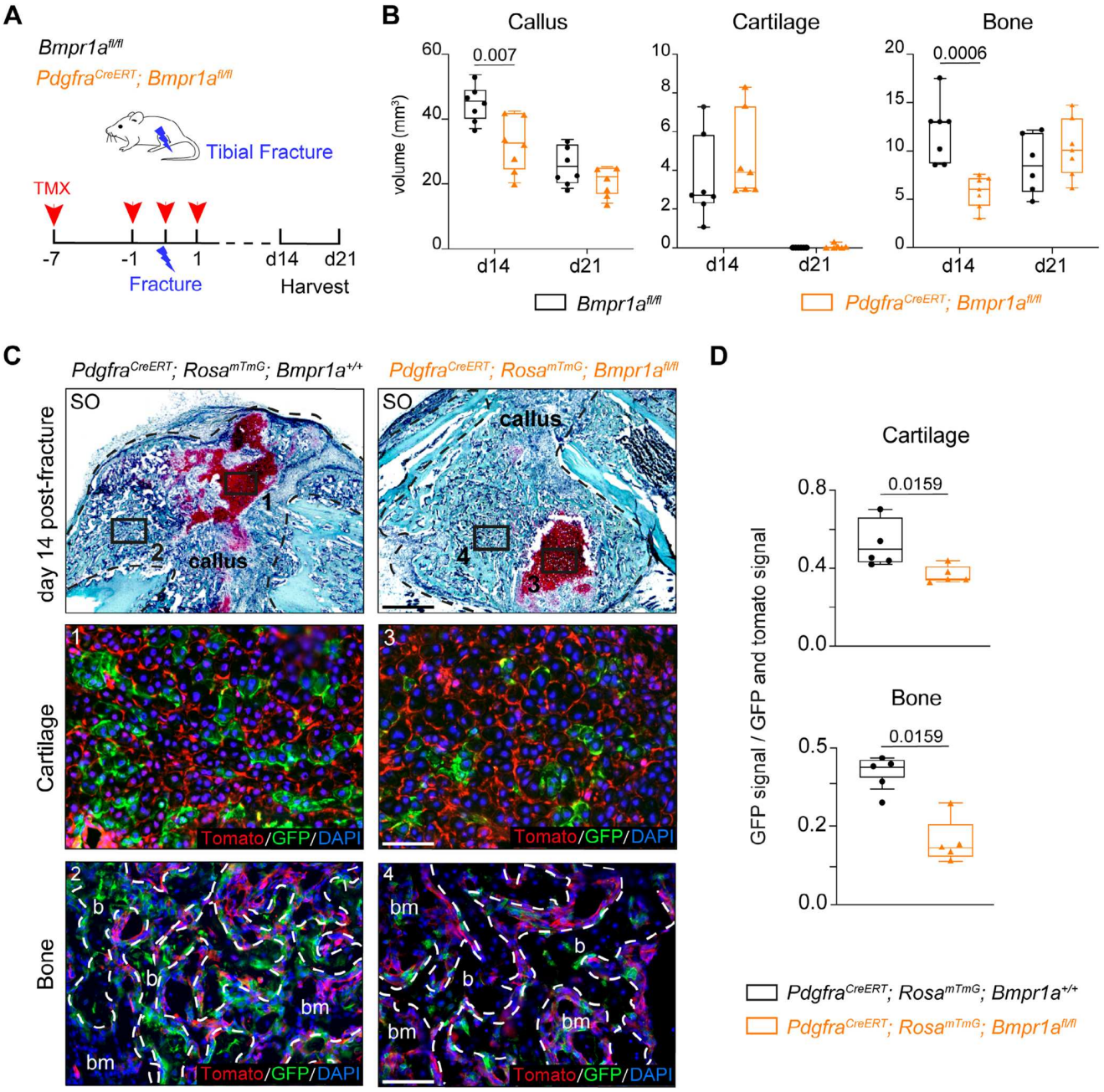

Fig. 6. Loss of *Bmpr1a* in *Pdgfra*-derived progenitors impairs bone healing. (*A*) Experimental design. *Bmpr1a*$^{fl/fl}$ (control) and *Pdgfra*^{CreERT};*Bmpr1a*$^{fl/fl}$ mice were induced with TMX at days 7 and 1 before fracture, day 0 and day 1 post-fracture. Tibial fractures were induced at d0 and calluses were harvested at d14 and d21 post-fracture. (*B*) Histomorphometric quantification of callus, cartilage, and bone volumes at d14 and d21 post-fracture in *Bmpr1a*$^{fl/fl}$ control and *Pdgfra*^{CreERT};*Bmpr1a*$^{fl/fl}$ mutant mice (in black and orange, respectively) ($n = 6$–7 animals per group). (*C*) Longitudinal callus sections from *Pdgfra*^{CreERT}; *Rosa*^{mTmG};*Bmpr1a*$^{+/+}$ control (left) and *Pdgfra*^{CreERT};*Rosa*^{mTmG};*Bmpr1a*$^{fl/fl}$ mutant (right) mice at d14 post-fracture stained with SO (callus delimited by a black dotted line). High magnifications of boxed areas of cartilage (1 and 3) and bone (2 and 4) show *Pdgfra*-derived cells in cartilage and bone. (*D*) Quantification of GFP+ signal normalized on total GFP+ and Tomato+ signal in cartilage and bone. $n = 4$–5 animals per group, each dot represents a single animal. Exact *p* value calculated with two-sided Mann-Whitney test, values represent median and interquartile range. Scale bars: low magnification = 1 mm, high magnification = 200 µm. b = bone; bm = bone-marrow; d0 = day 0; SO = Safranin O; TMX = tamoxifen.

bone marrow and periosteum, but also from adjacent skeletal muscle.[1-4,6,10,40] In skeletal muscle, the SSPC population overlaps with the non-myogenic cell population commonly termed "mesenchymal" cells.[2] These "mesenchymal" cells have fibrogenic, adipogenic, and osteochondrogenic potentials in muscle regeneration or pathological conditions.[41,42] More knowledge is needed to improve the nomenclature and better describe "mesenchymal" cells that share common cell surface

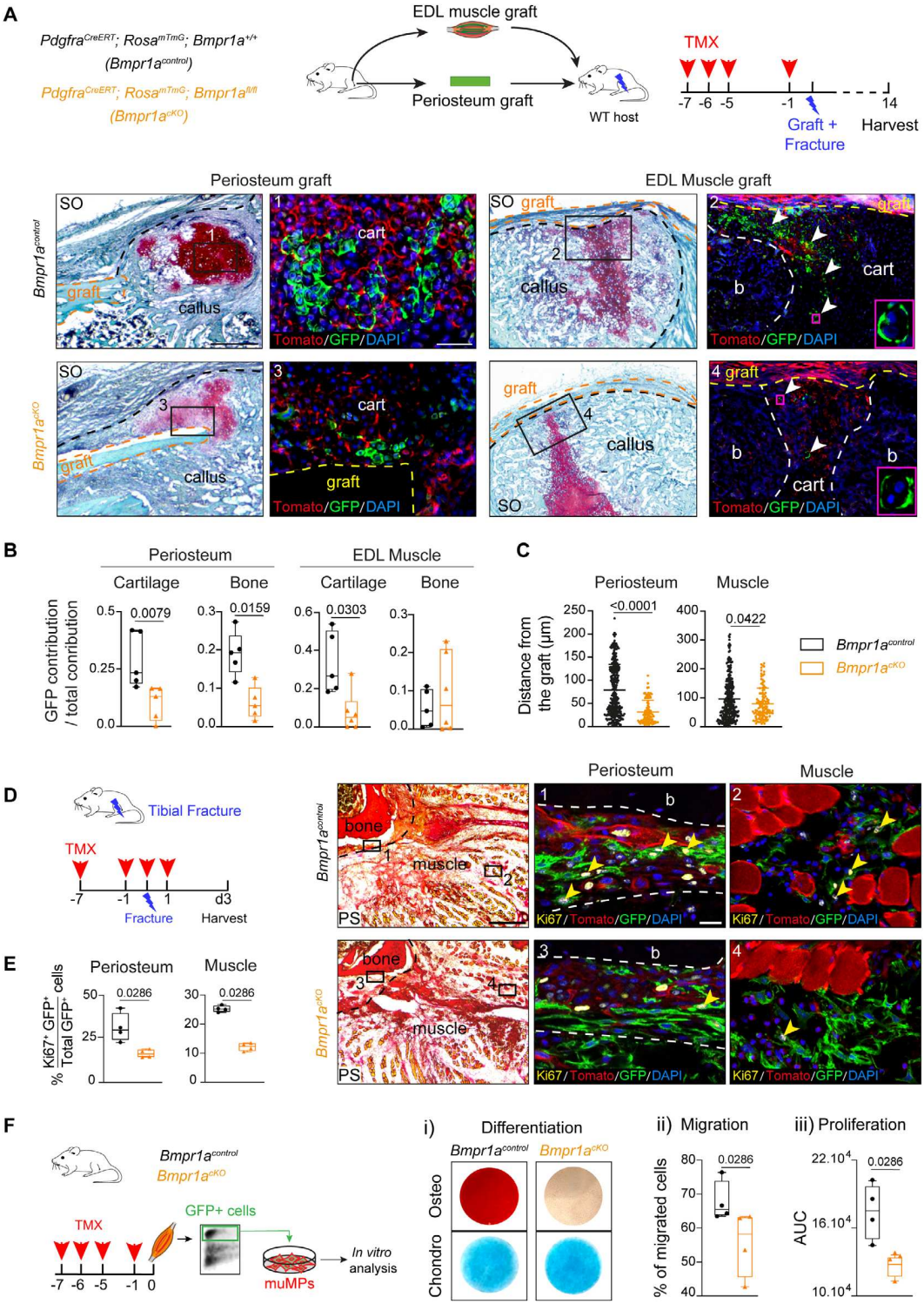

Fig. 7. *Bmpr1a* inactivation in *Pdgfra*-derived cells affects periosteum and muscle progenitors during bone repair. (*A*) Top, Experimental design of periosteum or EDL grafts from *Pdgfra*^{CreERT};*Rosa*^{mTmG};*Bmpr1a*$^{+/+}$ (*Bmpr1a*^{control}) or *Pdgfra*^{CreERT}; *Rosa*^{mTmG};*Bmpr1a*$^{fl/fl}$ (*Bmpr1a*^{cKO}) mice transplanted at the fracture site of wild-type hosts. Donor mice were induced with TMX at d7, d6, d5, and d1 prior to fracture. Fractures were induced at d0, and samples were collected at d14 post-fracture. Bottom, Longitudinal callus sections stained with SO at d14 post-fracture and periosteum (left) or EDL muscle (right) graft from *Bmpr1a*^{control} (top) and *Bmpr1a*^{cKO} (bottom) mice (callus delimited by a black dotted line, graft delimited by an orange/yellow dotted line). High magnifications of boxed areas of cartilage show reduced contribution to cartilage of *Pdgfra*-derived cells from *Bmpr1a*^{cKO} periosteal and EDL muscle grafts compared to *Bmpr1a*^{control}. Magenta boxed areas show GFP+ hypertrophic chondrocytes from EDL muscle grafts. (*B*) Quantification of GFP+ contribution normalized on total cellular contribution to cartilage and bone of periosteum and EDL muscle grafts. $n = 5$–6 animals per group, each dot represents a

(Figure legend continues on next page.)

markers yet may have distinct embryonic origins and functions in different tissues.[43,44] In this study we set out to compare SSPCs in bone marrow, periosteum, and skeletal muscle. In these three tissues, we identified skeletal stem/progenitor, osteochondral, and stromal cell populations expressing combinations of cell surface markers, as defined by Chan and colleagues.[38] Furthermore, our flow cytometry results indicate that periosteum-derived and skeletal muscle-derived cells are enriched in osteochondral progenitors, which may correlate with their in vivo differentiation potential. Transplanted PCs show efficient chondrogenic and osteogenic potential in vivo, whereas muMPs are mainly chondrogenic, and BMSCs have a limited osteochondral potential. These results reinforce that the periosteum is the major source of SSPCs for bone repair.

We then focused on periosteum-derived cells, which remain poorly characterized, and report here the cellular heterogeneity of periosteum-derived cells by scRNAseq at steady state and in response to fracture. None of the clusters identified by scRNAseq coincided with populations defined by the flow cytometry panel. Given the cooperation between PCs and muMPs during endochondral ossification, we compared their cellular and molecular response to fracture at the single cell level. We identified a similar response to bone fracture toward chondrogenesis through pseudotime analyses. After bone fracture, both activated muMPs and PCs leave their stem/progenitor state to undergo fibrogenesis prior to chondrogenesis. Thus, SSPCs from periosteum and skeletal muscle follow a common molecular program during the initiation of the endochondral ossification process. Single-cell analyses of freshly isolated SSPCs and from later time points post-injury will be helpful in the future to further characterize the cellular heterogeneity of SSCPs and the in vivo differentiation potential of various SSPC subpopulations. In particular, given the bipotentiality of SSPCs in periosteum for osteogenesis and chondrogenesis, whether this is due to the presence of a single lineage or multiple lineages within periosteum remains to be clarified.

We show that the shared molecular response within periosteum and skeletal muscle is mediated by early activation of the BMP pathway, known to play a central role during skeletal development, bone homeostasis, and fracture healing.[45] Genes associated with the BMP signaling pathway are expressed at early stages of bone repair from 3 days post-fracture and regulate chondrogenesis and osteogenesis.[46-51] Here, we combined lineage tracing, conditional knockout of *Bmpr1a* gene in *Pdgfra*-derived progenitors and tissue transplantation to assess the role of BMP signaling in SSPCs from periosteum and skeletal muscle. Notably, due to the current limitations in easily discriminating SSPCs derived from periosteum and skeletal muscle in vivo, which would entail the analysis of a combination of several markers and their expression levels, cell or tissue transplantation at the injury site remains an efficient way to discriminate the regenerative potential of SSCPs from different tissues. Using these approaches, we show that the contribution to endochondral ossification of *Bmpr1a* deficient SSPCs from periosteum and skeletal muscle is impaired. Loss of BMP signaling in SSPCs leads to a decrease in proliferation, migration, and chondrogenic and osteogenic differentiation of periosteum and skeletal muscle SSPCs in vitro and in vivo. These functional analyses confirm that BMP signaling is a critical mediator for the activation of periosteum and skeletal muscle SSPCs during bone regeneration. Although there are reports showing that PDGFRβ or CCL5-CCR5 signaling pathways are also essential[52,53], little is known about the molecular regulation of SSPC activation. More work is required to provide insight and understanding of the mechanisms driving SSPC activation and their interactions with the bone injury environment.

Acknowledgments

This work was supported by Foundation de l'Avenir, ANR-18-CE14-0033, NIAMS R01 AR072707 to CColnot, INSERM ATIP-Avenir to MM. AJ and SP were supported by a PhD fellowship from Paris University. The LabTech Single-Cell@Imagine is supported by the Paris Region and the "Investissements d'avenir" program 764 through the 2019 ATF funding – S same Filires PIA (Grant N 3877871) and the Agence National de la Recherche as part of the "Investment for the Future" program (Institut Hospitalo-Universitaire Imagine, grant ANR-10-IAHU-01). We thank C. Alms, R. Prota, A. Lermant, H. Mouigni and A. Henry for technical assistance. Flow cytometry and cell sorting were performed at the Flow Cytometry platforms of Imagine Institute and IMRB. Single-cell RNAseq were performed at the Genomic and Bioinformatic platforms of Imagine Institute.

(Figure legend continued from previous page.)

single animal. (*C*) Distance between GFP+ chondrocytes and the border of periosteum or EDL grafts (delimited by an orange dotted line) from *Bmpr1a*^{control} and *Bmpr1a*^{cKO} donors. Control periosteum: $n = 284$ cells, mutant periosteum: $n = 99$ cells, control EDL: $n = 302$ cells, and mutant EDL: $n = 120$ cells. Five animals were used per group. Each dot represents an individual cell. (*D*) Left, Experimental design. *Bmpr1a*^{control} and *Bmpr1a*^{cKO} mice were induced with TMX at d7 and d1 before fracture, d0 and d1 post-fracture. Samples were harvested at d3 post-fracture. Right, Transverse sections of fracture site at d3 post-fracture were stained with PS and adjacent sections were immunostained for Ki67 (Ki67 cells in yellow, pointed with yellow arrowhead). High magnifications of boxed areas in activated periosteum (delimited by a dotted line) and skeletal muscle adjacent to fracture site show less Ki67+/GFP+ cells in *Bmpr1a*^{cKO} mice compared to *Bmpr1a*^{control} *mice*. (*E*) Quantification of GFP + Ki67+ over the total GFP+ cells in activated periosteum and skeletal muscle at d3 post-fracture in tamoxifen induced *Bmpr1a*^{control} and *Bmpr1a*^{cKO} mice. $n = 3$–4 animals per group, each dot represents a single animal. (*F*) Left, Experimental design of in vitro cell differentiation, migration, and proliferation assays. *Bmpr1a*^{control} and *Bmpr1a*^{cKO} mice were induced with tamoxifen at d7, d6, d5, and d1 before experiment. *Pdgfra*-derived GFP+ cells were collected from skeletal muscles surrounding the tibia, sorted based on GFP expression and cultured in vitro prior analyses. (i) Representative images of osteogenic (top, osteo) and chondrogenic (bottom, chondro) differentiation assays of GFP+ cells isolated from *Bmpr1a*^{control} and *Bmpr1a*^{cKO} mice, (ii) Percentage of migrating cells assessed by in vitro transwell migration assay, (iii) AUC of proliferation. $n = 3$ independent primary cultures per group, each dot represents a primary culture. Statistical analyses: Exact *p* value calculated with two-sided Mann-Whitney test; values represent median and interquartile range. Scale bars: low magnification = 200 μm, high magnification = 50 μm. AUC = area under the curve; b = bone; bm = bone-marrow; cart = cartilage; chondro = chondrogenic; d0 = day 0; osteo = osteogenic; PS = Picrosirius; SO = Safranin O; TMX = tamoxifen.

Author Contributions

Anais Julien: Data curation; formal analysis; methodology; writing – original draft. **Simon Perrin:** Formal analysis; methodology; writing – review and editing. **Ester Martinez-Sarra:** Formal analysis; writing – review and editing. **Anuya Kanagalingam:** Formal analysis. **Caroline Carvalho:** Formal analysis. **Marine Luka:** Methodology. **Mickaël Menager:** Funding acquisition; methodology; resources. **Celine Colnot:** Conceptualization; funding acquisition; supervision; writing – original draft.

Authors' Roles

AJ, SP, and EMS performed the experiments and analyzed the data with the help of AK and CCarvalho. ML performed scRNAseq libraries and MM gave advice. AJ, SP, and CColnot designed the experiments. AJ and CColnot wrote the manuscript. SP and EMS reviewed the manuscript. CColnot conceived the project and supervised the study.

Conflicts of Interest

Authors declare no competing interests.

Data Availability

scRNAseq data from uninjured and d3 post-fracture PCs have been deposited in the Gene Expression Omnibus (GEO) database under the accession number GSE195940. scRNAseq data from Prx1-derived skeletal muscle cells are available through the accession number GSE164573. Microarray data are available upon request.

References

1. Colnot C. Skeletal cell fate decisions within periosteum and bone marrow during bone regeneration. J Bone Miner Res. 2009;24(2):274-282.
2. Julien A, Kanagalingam A, Martínez-Sarrà E, et al. Direct contribution of skeletal muscle mesenchymal progenitors to bone repair. Nat Commun. 2021;12(1):1-14.
3. Bianco P, Cao X, Frenette PS, et al. The meaning, the sense and the significance: translating the science of mesenchymal stem cells into medicine. Nat Med. 2013;19(1):35-42.
4. Crane JL, Cao X. Bone marrow mesenchymal stem cells and TGF-β signaling in bone remodeling. J Clin Invest. 2014;124(2):466-472.
5. Roberts SJ, van Gastel N, Carmeliet G, Luyten FP. Uncovering the periosteum for skeletal regeneration: the stem cell that lies beneath. Bone. 2015;70:10-18.
6. Ferretti C, Mattioli-Belmonte M. Periosteum derived stem cells for regenerative medicine proposals: boosting current knowledge. World J Stem Cells. 2014;6(3):266.
7. Shen B, Tasdogan A, Ubellacker JM, et al. A mechanosensitive periarteriolar niche for osteogenesis and lymphopoiesis. Nature. 2021;591(7850):438-444.
8. Sacchetti B, Funari A, Michienzi S, et al. Self-renewing osteoprogenitors in bone marrow sinusoids can organize a hematopoietic microenvironment. Cell. 2007;131(2):324-336.
9. Matsushita Y, Ono W, Ono N. Skeletal stem cells for bone development and repair: diversity matters. Curr Osteoporos Rep. 2020;18(3):189-198.
10. Duchamp De Lageneste O, Julien A, Abou-Khalil R, et al. Periosteum contains skeletal stem cells with high bone regenerative potential controlled by Periostin. Nat Commun. 2018;9(1):773.
11. Baccin C, Al-Sabah J, Velten L, et al. Combined single-cell and spatial transcriptomics reveal the molecular, cellular and spatial bone marrow niche organization. Nat Cell Biol. 2020;22(1):38-48.
12. Debnath S, Yallowitz AR, McCormick J, et al. Discovery of a periosteal stem cell mediating intramembranous bone formation. Nature. 2018;562(7725):133-139.
13. Matsushita Y, Nagata M, Kozloff KM, et al. A Wnt-mediated transformation of the bone marrow stromal cell identity orchestrates skeletal regeneration. Nat Commun. 2020;11(1):1-17.
14. Matthews BG, Novak S, Sbrana FV, et al. Heterogeneity of murine periosteum progenitors involved in fracture healing. Elife. 2021;10:e58534.
15. Sivaraj KK, Jeong H-W, Dharmalingam B, et al. Regional specialization and fate specification of bone stromal cells in skeletal development. Cell Rep. 2021;36(2):109352.
16. Tikhonova AN, Dolgalev I, Hu H, et al. The bone marrow microenvironment at single-cell resolution. Nature. 2019;569(7755):222-228.
17. Grcevic D, Pejda S, Matthews BG, et al. In vivo fate mapping identifies mesenchymal progenitor cells. Stem Cells. 2012;30(2):187-196.
18. Greenbaum A, Hsu YMS, Day RB, et al. CXCL12 in early mesenchymal progenitors is required for haematopoietic stem-cell maintenance. Nature. 2013;495(7440):227-230.
19. Méndez-Ferrer S, Michurina TV, Ferraro F, et al. Mesenchymal and haematopoietic stem cells form a unique bone marrow niche. Nature. 2010;466(7308):829-834.
20. Park D, Spencer JA, Koh BI, et al. Endogenous bone marrow MSCs are dynamic, fate-restricted participants in bone maintenance and regeneration. Cell Stem Cell. 2012;10(3):259-272.
21. Shi Y, He G, Lee W-C, McKenzie JA, Silva MJ, Long F. Gli1 identifies osteogenic progenitors for bone formation and fracture repair. Nat Commun. 2017;8(1):1-12.
22. Worthley DL, Churchill M, Compton JT, et al. Gremlin 1 identifies a skeletal stem cell with bone, cartilage, and reticular stromal potential. Cell. 2015;160(1-2):269-284.
23. Zhou BO, Yue R, Murphy MM, Peyer JG, Morrison SJ. Leptin-receptor-expressing mesenchymal stromal cells represent the main source of bone formed by adult bone marrow. Cell Stem Cell. 2014;15(2):154-168.
24. Calvi LM, Adams GB, Weibrecht KW, et al. Osteoblastic cells regulate the haematopoietic stem cell niche. Nature. 2003;425(6960):841-846.
25. Morrison SJ, Scadden DT. The bone marrow niche for haematopoietic stem cells. Nature. 2014;505(7483):327.
26. Logan M, Martin JF, Nagy A, Lobe C, Olson EN, Tabin CJ. Expression of Cre recombinase in the developing mouse limb bud driven by a Prxl enhancer. Genesis. 2002;33(2):77-80.
27. Kawanami A, Matsushita T, Chan YY, Murakami S. Mice expressing GFP and CreER in osteochondro progenitor cells in the periosteum. Biochem Biophys Res Commun. 2009;386(3):477-482.
28. Kang SH, Fukaya M, Yang JK, Rothstein JD, Bergles DE. NG2+ CNS glial progenitors remain committed to the oligodendrocyte lineage in postnatal life and following neurodegeneration. Neuron. 2010;68(4):668-681.
29. Mishina Y, Suzuki A, Ueno N, Behringer RR. Bmpr encodes a type I bone morphogenetic protein receptor that is essential for gastrulation during mouse embryogenesis. Genes Dev. 1995;9(24):3027-3037.
30. Mishina Y, Hanks MC, Miura S, Tallquist MD, Behringer RR. Generation of Bmpr/Alk3 conditional knockout mice. Genesis. 2002;32(2):69-72.
31. Perrin S, Julien A, Duchamp de Lageneste O, Abou-Khalil R, Colnot C. Mouse periosteal cell culture, in vitro differentiation, and in vivo transplantation in tibial fractures. Bio Protoc. 2021;11(15):e4107.
32. Julien A, Perrin S, Duchamp de Lageneste O, et al. FGFR3 in periosteal cells drives cartilage-to-bone transformation in bone repair. Stem Cell Reports. 2020;15(4):955-967.
33. Lu C, Saless N, Hu D, et al. Mechanical stability affects angiogenesis during early fracture healing. J Orthop Trauma. 2011;25(8):494-499.
34. Butler A, Hoffman P, Smibert P, Papalexi E, Satija R. Integrating single-cell transcriptomic data across different conditions, technologies, and species. Nat Biotechnol. 2018;36(5):411-420.

35. Stuart T, Butler A, Hoffman P, et al. Comprehensive integration of single-cell data. Cell. 2019;177(7):1888-1902.
36. Kuleshov MV, Jones MR, Rouillard AD, et al. Enrichr: a comprehensive gene set enrichment analysis web server 2016 update. Nucleic Acids Res. 2016;44(W1):W90-W97.
37. Cao J, Spielmann M, Qiu X, et al. The single-cell transcriptional landscape of mammalian organogenesis. Nature. 2019;566:496-502.
38. Chan CKF, Seo EY, Chen JY, et al. Identification and specification of the mouse skeletal stem cell. Cell. 2015;160(1-2):285-298.
39. Mizoguchi T, Ono N. The diverse origin of bone-forming osteoblasts. J Bone Miner Res. 2021;36(8):1432-1447.
40. Abou-Khalil R, Yang F, Lieu S, et al. Role of muscle stem cells during skeletal regeneration. Stem Cells. 2015;33(5):1501-1511.
41. Theret M, Rossi FMV, Contreras O. Evolving roles of muscle-resident fibro-adipogenic progenitors in health, regeneration, neuromuscular disorders, and aging. Front Physiol. 2021;20(12):481.
42. Lees-Shepard JB, Yamamoto M, Biswas AA, et al. Activin-dependent signaling in fibro/adipogenic progenitors causes fibrodysplasia ossificans progressiva. Nat Commun. 2018;9(1):1-14.
43. Lee JH, Tammela T, Hofree M, et al. Anatomically and functionally distinct lung mesenchymal populations marked by Lgr5 and Lgr6. Cell. 2017;170(6):1149-1163.e12.
44. Stzepourginski I, Nigro G, Jacob JM, et al. CD34+ mesenchymal cells are a major component of the intestinal stem cells niche at homeostasis and after injury. Proc Natl Acad Sci U S A. 2017;114(4):E506-E513.
45. Salazar VS, Gamer LW, Rosen V. BMP signalling in skeletal development, disease and repair. Nat Rev Endocrinol. 2016;12:203-221.
46. Tsuji K, Bandyopadhyay A, Harfe BD, et al. BMP2 activity, although dispensable for bone formation, is required for the initiation of fracture healing. Nat Genet. 2006;38(12):1424-1429.
47. Yoon BS, Ovchinnikov DA, Yoshii I, Mishina Y, Behringer RR, Lyons KM. Bmpr1a and Bmpr1b have overlapping functions and are essential for chondrogenesis in vivo. Proc Natl Acad Sci U S A. 2005;102(14):5062-5067.
48. Morgan EF, Pittman J, DeGiacomo A, et al. BMPR1A antagonist differentially affects cartilage and bone formation during fracture healing. J Orthop Res. 2016;34(12):2096-2105.
49. van Gastel N, Stegen S, Stockmans I, et al. Expansion of murine periosteal progenitor cells with fibroblast growth factor 2 reveals an intrinsic endochondral ossification program mediated by bone morphogenetic protein 2. Stem Cells. 2014;32(9):2407-2418.
50. Chappuis V, Gamer L, Cox K, Lowery JW, Bosshardt DD, Rosen V. Periosteal BMP2 activity drives bone graft healing. Bone. 2012;51(4):800-809.
51. Yu YY, Lieu S, Lu C, Miclau T, Marcucio RS, Colnot C. Immunolocalization of BMPs, BMP antagonists, receptors, and effectors during fracture repair. Bone. 2010;46(3):841-851.
52. Böhm AM, Dirckx N, Tower RJ, et al. Activation of skeletal stem and progenitor cells for bone regeneration is driven by PDGFRβ signaling. Dev Cell. 2019;51(2):236-254.e12.
53. Ortinau LC, Wang H, Lei K, et al. Identification of functionally distinct Mx1+αSMA+ periosteal skeletal stem cells. Cell Stem Cell. 2019;25(6):784-796.e5.

Skeletal stem/progenitor cells in periosteum and skeletal muscle share a common molecular response to bone injury

Anais Julien[1$], Simon Perrin[1$], Ester Martínez-Sarrà[1$], Anuya Kanagalingam[1], Caroline Carvalho[1], Marine Luka[2,3], Mickaël Ménager[2,3], and Céline Colnot[1, *]

Supplemental Material

Supplemental Figure S1

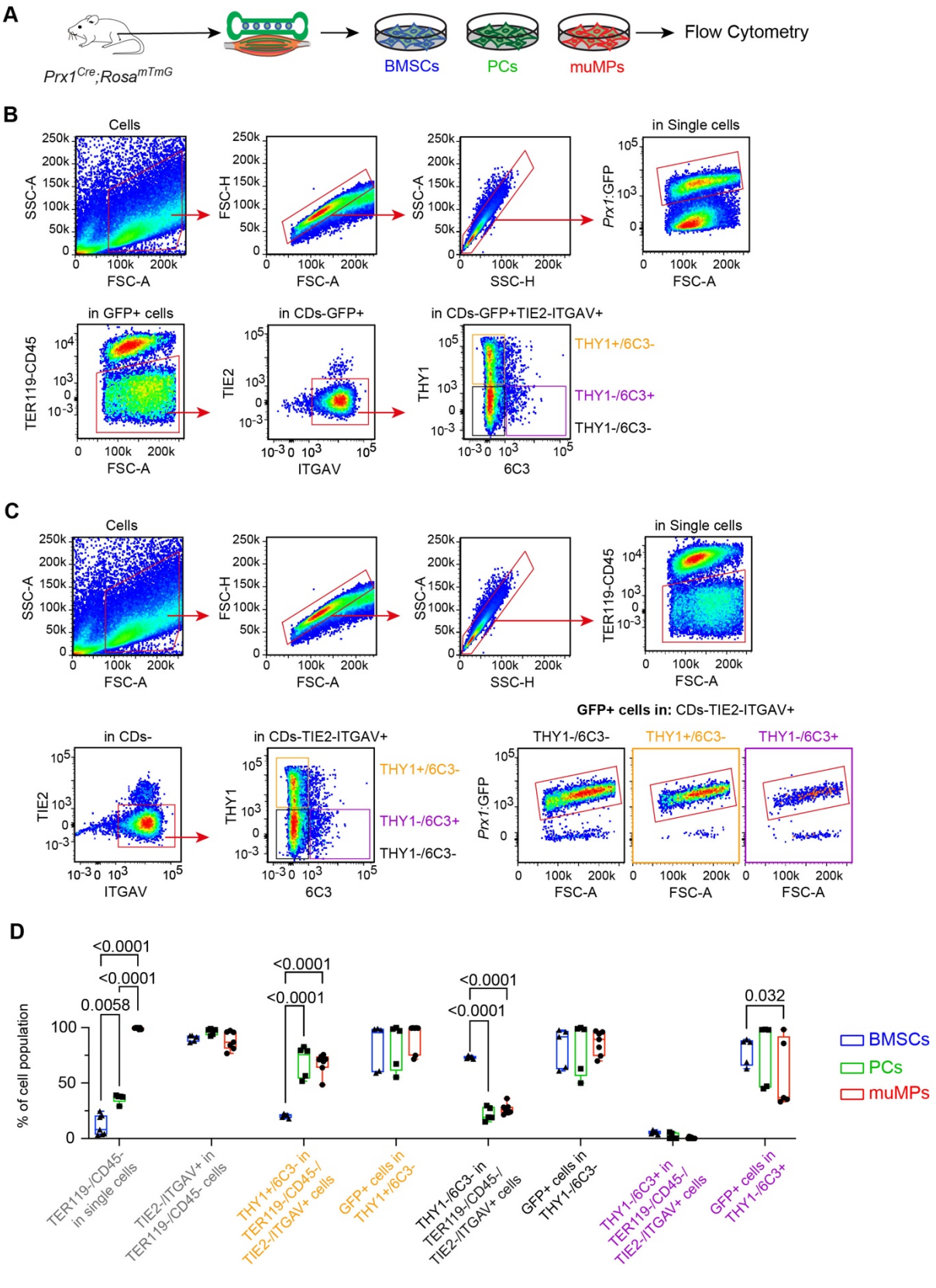

Supplemental Fig. S1: *Prx1*-derived cells encompass the majority of skeletal stem/progenitor sub-populations.

(A) Experimental design. Bone marrow stromal cells (BMSCs), periosteal cells (PCs) and skeletal muscle mesenchymal progenitors (muMPs) were isolated from *Prx1*^{Cre};*Rosa*^{mTmG} mice, amplified in culture and analysed by flow cytometry. **(B)** Gating strategy used in Fig. 1. *Prx1*-derived GFP+ cells were gated after doublet exclusion; hematopoietic cells (CDs=TER119+CD45+) and endothelial cells (TIE2+) were excluded and ITGAV+ cells were included in the analysis. THY1 and 6C3 marker expression allow the identification of THY1-/6C3-, THY1+/6C3- and THY1-/6C3+ sub-populations. Representative image of FACS plot. **(C)** Gating strategy used to analyze BMSCs, PCs and muMPs in panel D. After doublet exclusion, hematopoietic cells (TER119+CD45+) and endothelial cells (TIE2+) were excluded and ITGAV+ cells were analyzed. THY1 and 6C3 markers expression define the different sub-populations and GFP+ cells were assessed in the three sub-populations. Representative image of FACS plot. **(D)** Quantification of the proportion of TER119-/CD45- cells in the total single cell population; TIE2-/ITGAV+ cells in TER119-/CD45- population and each sub-population in TIE2-/ITGAV+ cells with the proportion of GFP+ cells in each sub-population. n=5-7 per group, each dot represents a primary culture. Values represent the median and interquartile range, exact p-value calculated by 2-way ANOVA followed by Tukey test.

Supplemental Figure S2

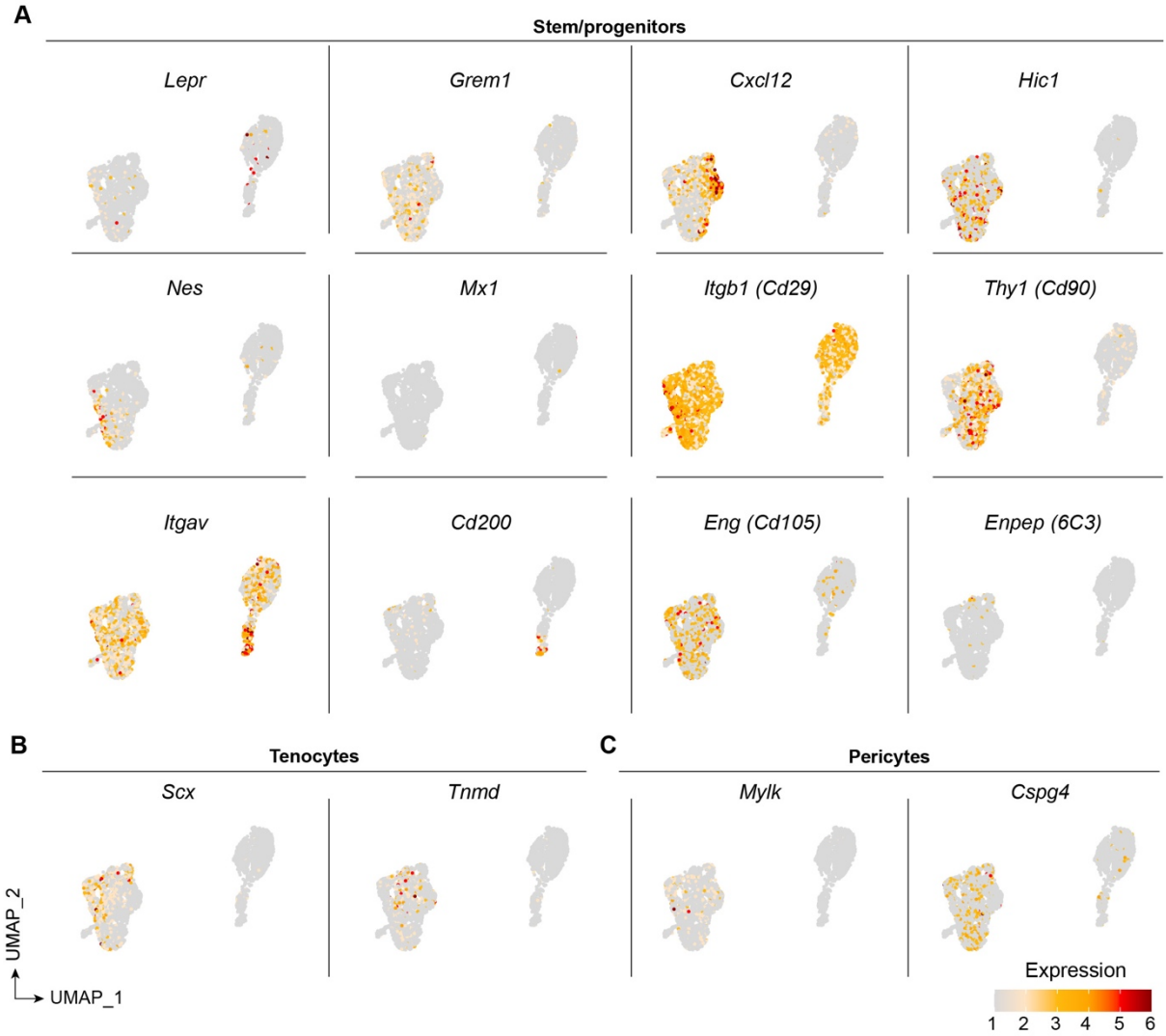

Supplemental Fig. S2: Marker expression in scRNAseq of periosteal cells at steady state.

(A-C) Feature plots of stem/progenitor (**A**), tenocyte (**B**) and pericyte (**C**) markers in periosteal cells at steady state.

Supplemental Figure S3

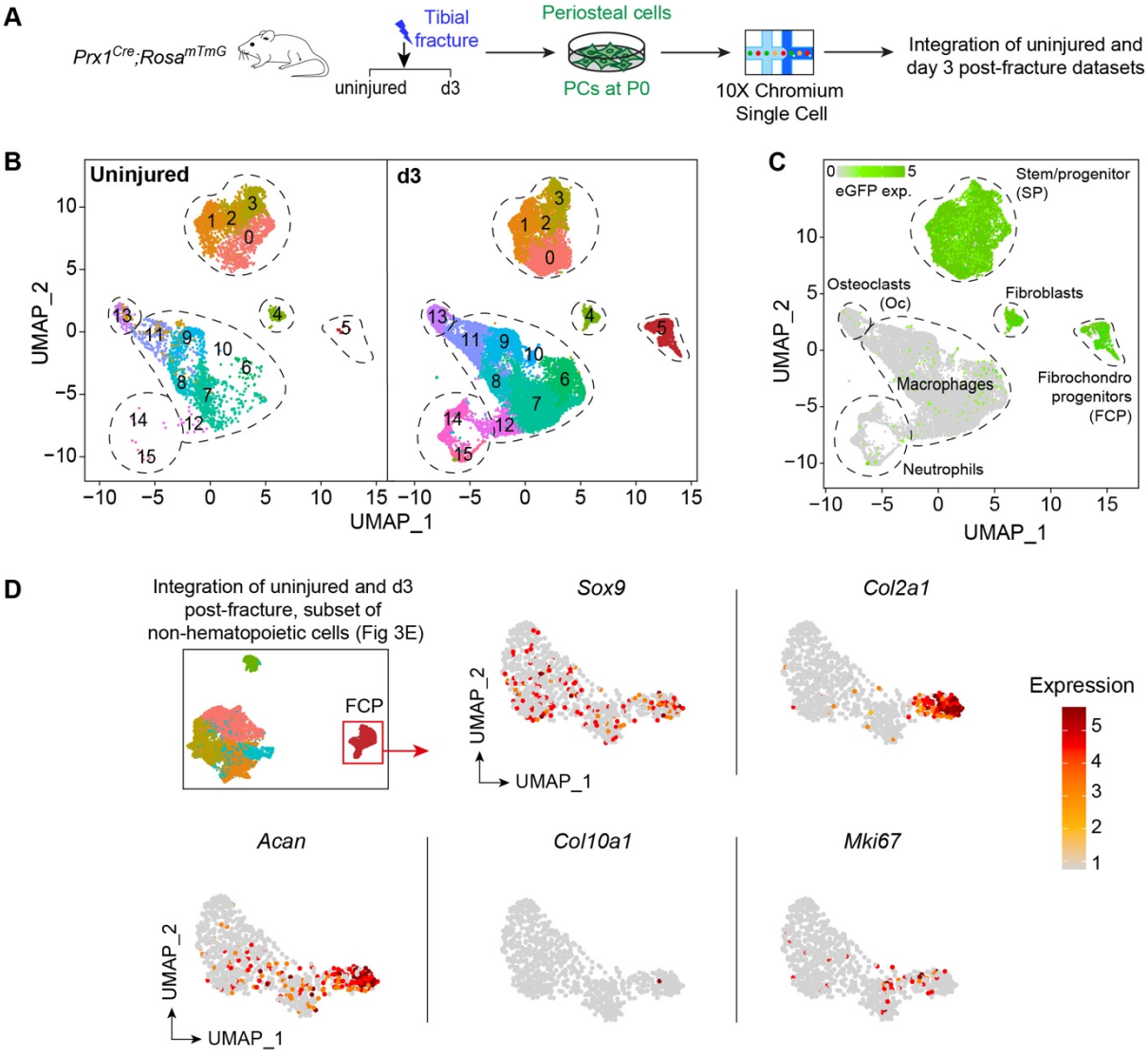

Supplemental Fig. S3: ScRNAseq analyses of periosteal cells at d3 post-fracture.

(A) Experimental design of scRNAseq. **(B)** Split UMAP visualization of uninjured (left) and d3 post-fracture (right) datasets. **(C)** Feature plot of *eGFP* expression. *eGFP* expression is mainly detected in non-hematopoietic sub-populations containing stem/progenitors, fibroblasts and fibrochondro progenitors. **(D)** Top left, UMAP projection of sub-clusterization of non-hematopoietic PCs as in Fig. 3E. Feature plots of chondrogenic (*Sox9, Acan, Col2a1, Col10a1*) and proliferative (*Mki67*) gene expression in fibro chondroprogenitors (FCP).

Supplemental Figure S4

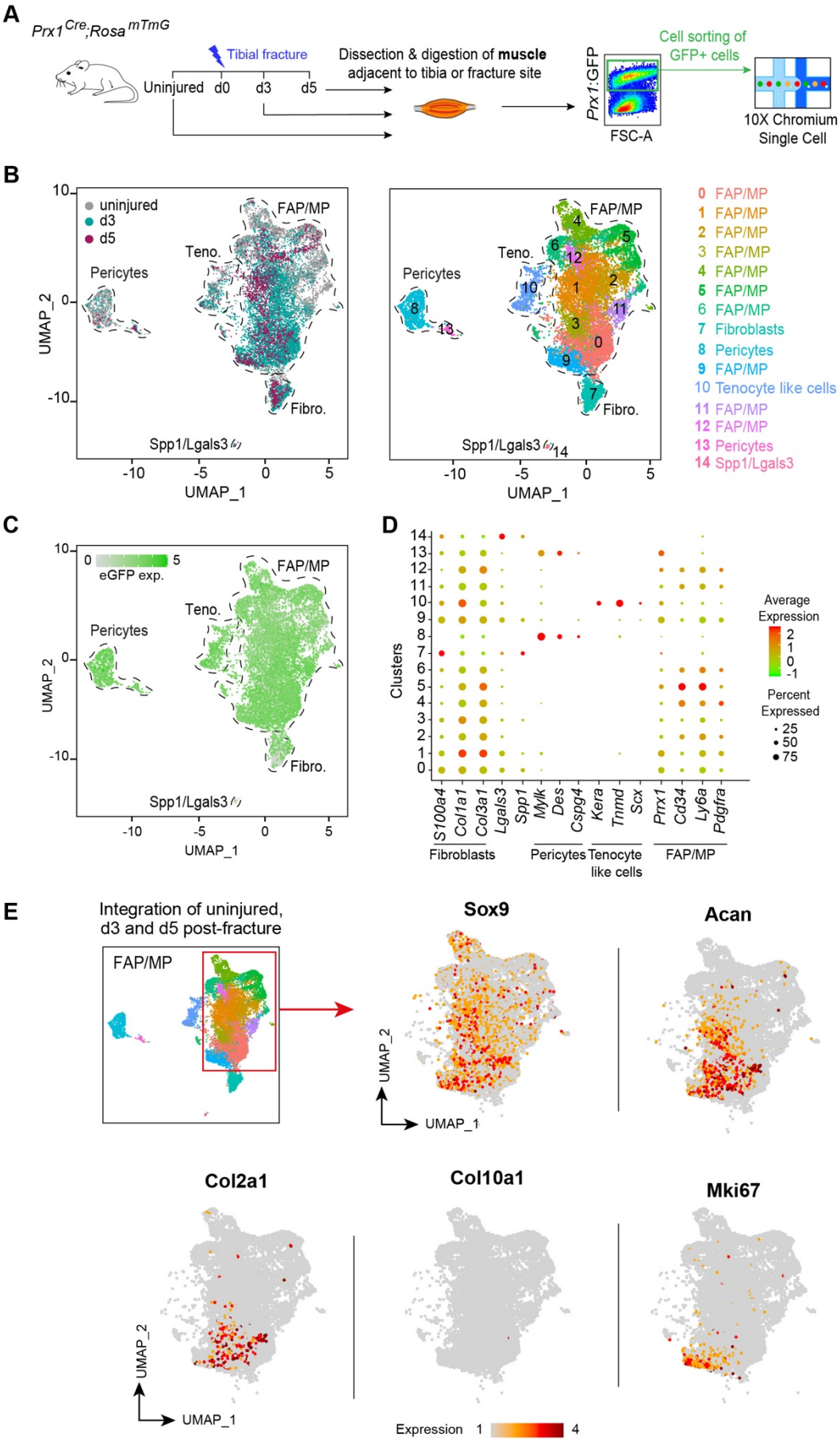

Supplemental Fig. S4: Single-cell RNAseq analysis of *Prx1*-derived skeletal muscle cells upon fracture.

(A) Experimental design. *Prx1*-derived skeletal muscle cells were isolated from skeletal muscles surrounding the tibia from uninjured tibias and at days 3 and 5 post-fracture, and sorted based on GFP-expression prior to scRNAseq. **(B)** UMAP projections of color-coded clustering of integrated uninjured (grey), d3 (green) and d5 (purple) cells represented by sample (left) or by cluster (right) show 14 clusters grouped in 5 cell populations named FAP/MP, pericytes, tenocyte-like cells (Teno.), fibroblasts (Fibro.) and *Spp1/Lgals3* cells, consistent with results described in [1]. Cell populations are delimited by a black dotted line and cluster identities are indicated on the right. **(C)** Feature plot of *eGFP* expression. **(D)** Dotplot of indicated genes expression identifying FAP/MP, tenocyte-like cell, pericyte, fibroblast and *Spp1/Lgals3* cell populations. **(E)** Feature plots of integrated uninjured, d3 and d5 post-fracture muMPs datasets showing chondrogenic (*Sox9, Acan, Col2a1, Col10a1*) and proliferative (*Mki67*) genes expression.

Supplemental Figure S5

Supplemental Fig. S5: Gene Ontology analyses of microarray samples identifies distinct gene signatures at d2 and d7 post-fracture.

(A, C) Enrichment map following GSEA analysis of microarray data from [2]. (A) Comparison of unfractured (green dots) vs d2 post-fracture samples (orange dots). (C) Comparison of d2 (orange dots) vs d7 (purple dots) post-fracture samples. Dots corresponding to the same function are surrounded by a black line and named accordingly with the gene ontology terms. **(B, D)** Analysis of molecular pathways enriched at d2 vs unfractured (B) and at d7 vs d2 post-fracture (D). Gene ontology names for a common molecular pathway are grouped by color.

Supplemental Figure S6

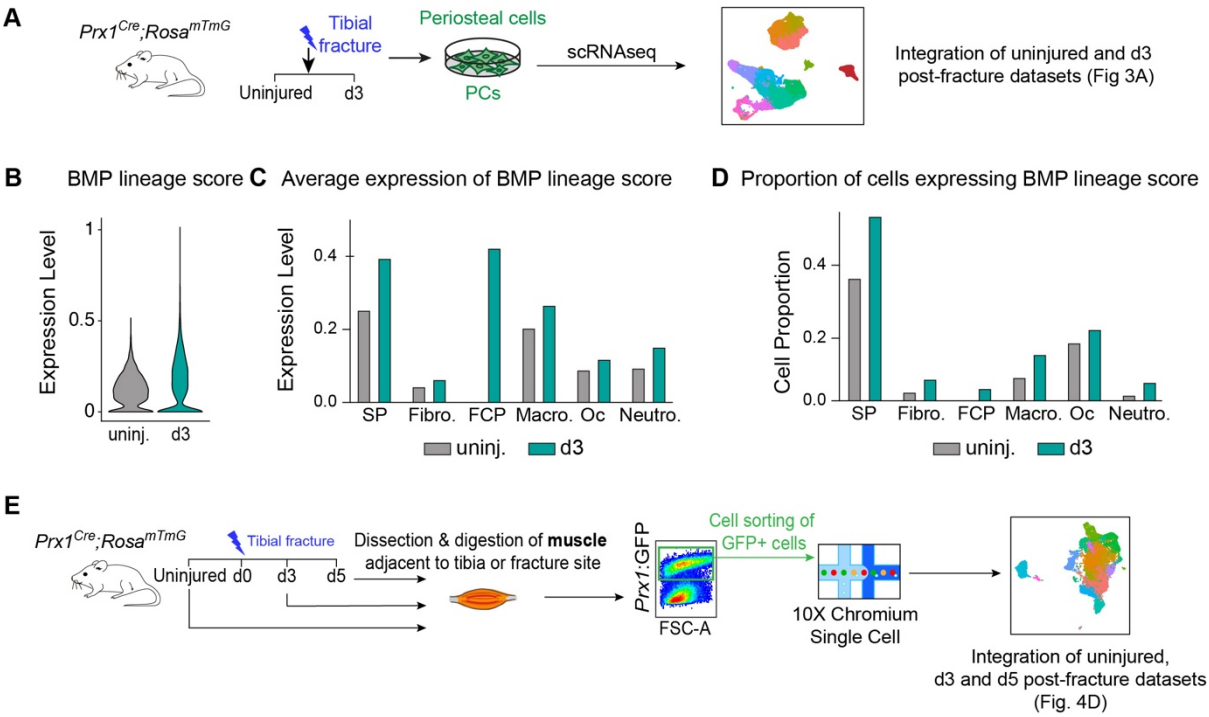

Supplemental Fig. S6: BMP related gene expression in response to fracture in PCs and muMPs.

(A) Experimental design of scRNAseq. PCs were isolated from *Prx1*^{Cre}*;Rosa*^{mTmG} mice by explant culture from uninjured tibia and from fractured tibias at day3 post-fracture (d3) and used at P0 for scRNAseq. The 2 datasets were integrated as in Fig. 3A. **(B)** BMP lineage score expression in uninjured and d3 post-fracture PCs. **(C)** BMP lineage score expression per cell population in uninjured and d3 post-fracture PCs. **(D)** Proportion of cell expressing BMP lineage score per cell population and per time points in PCs. **(E)** Experimental design. *Prx1*-derived skeletal muscle cells were isolated from skeletal muscles surrounding the tibia from uninjured tibias and at days 3 and 5 post-fracture, and sorted based on GFP-expression prior to scRNAseq. The 3 datasets were integrated, and the subsequent analyses were performed on the total muMPs population as in Supplemental Fig S3. **(F)** BMP lineage score expression in uninjured, d3 and d5 post-fracture muMPs. **(G)** BMP lineage score expression per cell population in uninjured, d3 and d5 post-fracture muMPs. **(H)** Proportion of cell expressing BMP lineage score per cell population and per time point in uninjured, d3 and d5 post-fracture muMPs. SSPCs: skeletal stem/progenitor cells, Macro.: macrophages, FCP: fibrochondroprogenitors, Oc: osteoclasts, Neutro.: neutrophils, Fibro.: fibroblasts, Teno.: tenocyte like cells, FAP/MP: Fibro-adipo progenitors/mesenchymal progenitors.

Supplemental Figure S7

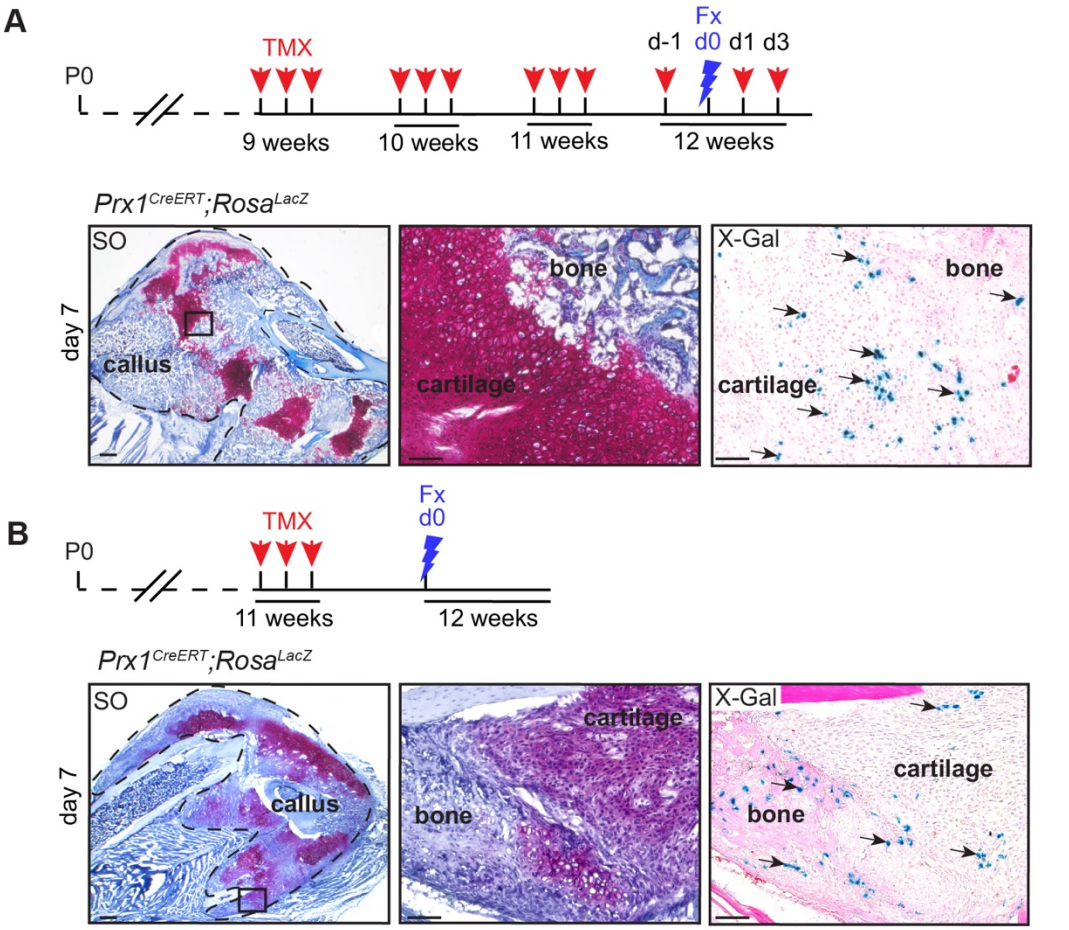

Supplemental Fig. S7: Inducible *Prx1*^{CreERT} mouse strain does not drive efficient Cre recombination in adult bone.

(A-B) Top, Experimental design of tamoxifen injection (TMX) in *Prx1*^{CreERT}*;Rosa*^{LacZ} mice. (A) TMX was injected 3 times a week for 4 consecutive weeks from week 9 after birth. Fractures were performed on week 12 and TMX was administrated the day before fracture and at days 1 and 3 post-fracture. (B) TMX was injected at days -7, -6 and -5 before fracture. **Bottom**, Longitudinal callus sections stained with safranin'O (SO) at d7 post-fracture. Callus is delimited by a black dotted line. High magnifications of cartilage area stained with SO and adjacent sections stained with X-Gal showing rare recombined blue cells pointed by black arrows. **(C)** Histomorphometric quantification of callus, cartilage and bone volumes at d14 post-fracture of *Bmpr1a*$^{fl/fl}$ control and *Prx1*^{CreERT}*;Bmpr1a*$^{fl/fl}$ mutant mice induced according to protocols (A) and (B). No significant differences between control and mutant groups in each condition. n=3-5 per group, each dot represents a single animal. Exact p-value calculated with two-sided Mann-Whitney test, values represent mean ± SD. Scale bars: low magnification 1mm, high magnification: 200µm.

Supplemental Figure S8

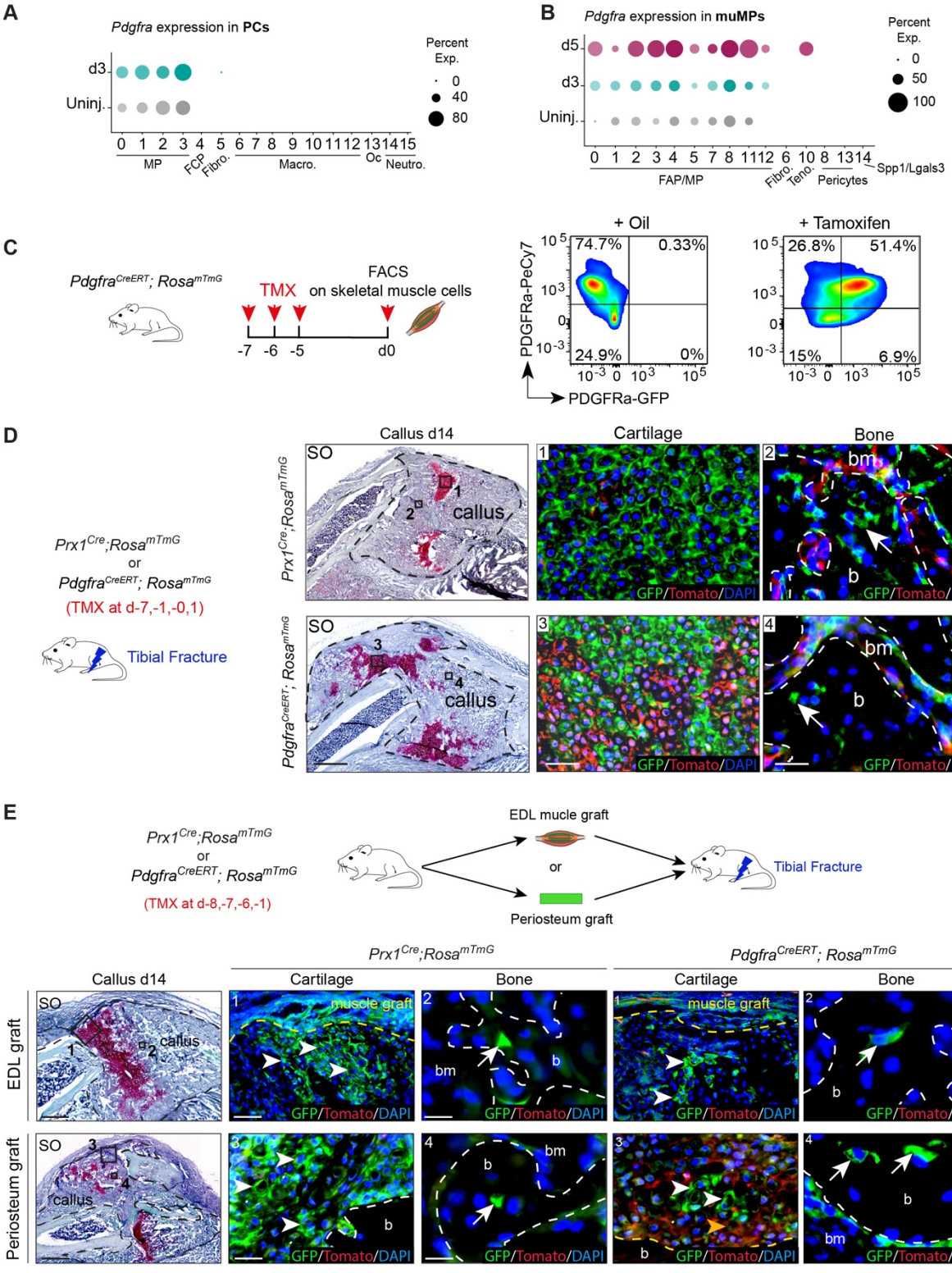

Supplemental Fig. S8: *Prx1*- and *Pdgfra*- lineages contribute to cartilage and bone after fracture.

(A) Expression of *Pdgfra* in uninjured and d3 post-fracture PCs from scRNAseq dataset in Fig.3. **(B)** Expression of *Pdgfra* in uninjured, d3 and d5 post-fracture muMPs from scRNAseq dataset in Fig. S3. **(C) Left**, Experimental design of flow cytometry analyses of skeletal muscle cells isolated from tamoxifen-induced $Pdgfra^{CreERT};Rosa^{mTmG}$ mice. **Right**, FACS plots show that the recombination efficiency is 65.9%, corresponding to the percentage of GFP+ cells in the total PDGFRa+ cells. **(D)** Localization of *Prx1*- and *Pdgfra*-derived cells in the fracture callus of $Prx1^{Cre};Rosa^{mTmG}$ or tamoxifen-induced $Pdgfra^{CreERT};Rosa^{mTmG}$ mice respectively at d14 post-fracture. Longitudinal callus sections stained with Safranin-O (SO, left) and adjacent sections counterstained with DAPI to visualize GFP and Tomato signals (right). High magnifications show that all chondrocytes in cartilage and osteocytes in bone (b, white arrows) are *Prx1*-derived GFP+. In $Pdgfra^{CreERT};Rosa^{mTmG}$ calluses, cartilage and bone contains *Pdgfra*-derived GFP+ chondrocytes and osteocytes, as well as Tomato+ cells that are not Cre-recombined. **(E) Top**, Experimental design of EDL muscle and periosteum grafts from $Prx1^{Cre};Rosa^{mTmG}$ or tamoxifen-induced $Pdgfra^{CreERT};Rosa^{mTmG}$ mice transplanted at the fracture site of wild-type hosts. **Bottom**, Longitudinal callus sections stained with SO at d14 post-fracture (left) and adjacent sections counterstained with DAPI at high magnification showing EDL- (top, yellow dotted line marks the limit between EDL muscle graft and callus) or periosteum-derived (bottom) cells within the callus. $Prx1^{Cre};Rosa^{mTmG}$ EDL and periosteum grafts (left) give rise exclusively to *Prx1*-derived GFP+ chondrocytes (white arrowheads) and osteocytes (white arrows) in the callus. $Pdgfra^{CreERT};Rosa^{mTmG}$ EDL and periosteum grafts (right) give rise to GFP+ *Pdgfra*-derived chondrocytes (white arrowheads) and osteocytes (white arrows) but also to non-recombined Tomato+ chondrocytes (orange arrowhead). b: bone, delimited by a white dotted line; bm: bone-marrow. Scale bars: low magnification 1mm, high magnification for cartilage: 200µm, for bone: 50µm.

Supplemental Figure S9

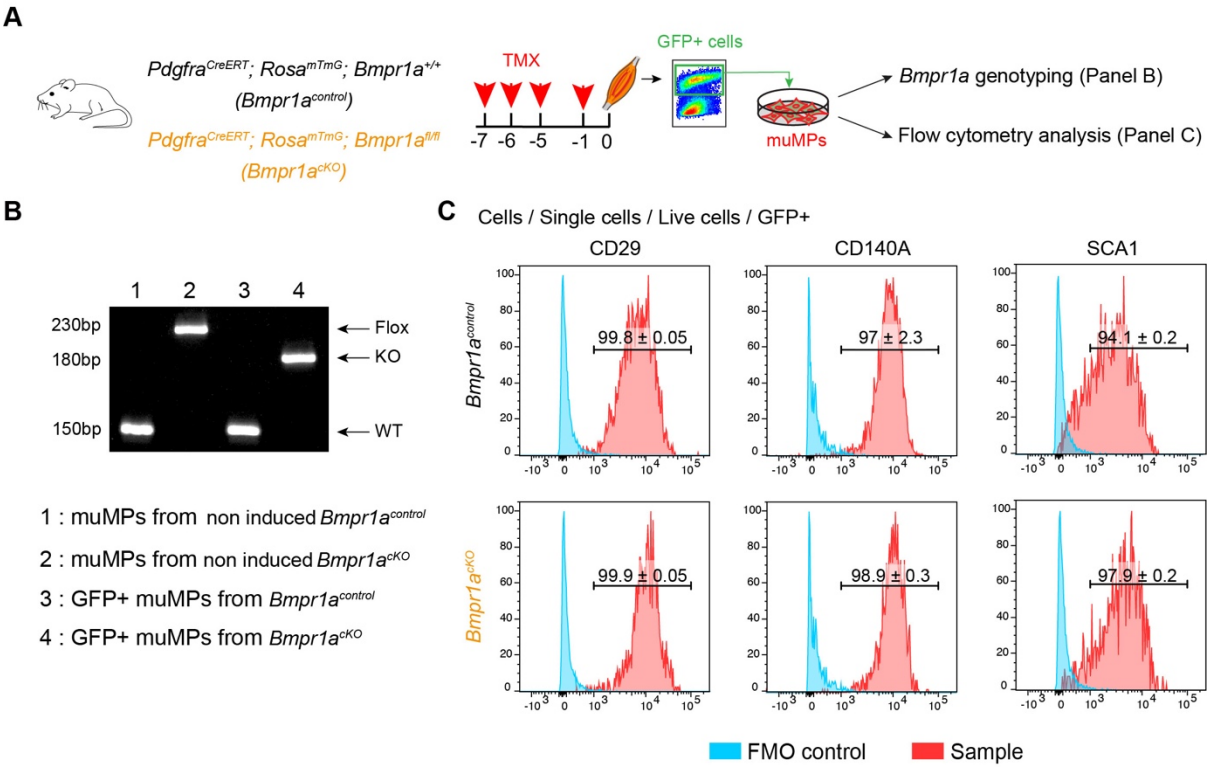

Supplemental Figure S9: *Bmpr1a* inactivation in *Pdgfra*-derived cells does not affect muMPs cellular identity. (A) Experimental design of *Pdgfra*-derived muMPs analyses by genotyping and flow cytometry. *Pdgfra*^{CreERT};*Rosa*^{mTmG};*Bmpr1a*$^{+/+}$ (*Bmpr1a*^{control}) and *Pdgfra*^{CreERT}; *Rosa*^{mTmG};*Bmpr1a*$^{fl/fl}$ (*Bmpr1a*^{cKO}) mice were induced at d7, d6, d5 and d1 before experiment. Skeletal muscle cells were isolated, sorted based on GFP expression and cultured in vitro prior to genotyping and flow cytometry analyses. **(B)** *Bmpr1a* genotyping confirmed that tamoxifen (TMX) induction leads to cre-mediated recombination of *Bmpr1a* gene in GFP+ *Pdgfra*-derived muMPs. **(C)** Flow cytometry analyses of GFP+ *Pdgfra*-derived muMPs isolated from *Bmpr1a*^{control} and *Bmpr1a*^{cKO} mice reveal comparable percentages of CD29+, CD140a+ and SCA1+ cells between control and mutant GFP+ *Pdgfra*-derived muMPs. n = 4 independent cultures per group.

Skeletal muscle mesenchymal progenitors/ Stem/progenitor cells	"Cd34", "Cxcl12", "Prrx1", "Ly6a", "Pdgfra", "Eng"
Fibrogenic	Abi3bp, 'Adam12', 'Anxa2', 'Aspn', 'Bgn', 'Cav1', 'Col12a1', 'Col1a1', 'Col5a1', 'Col5a2', 'Col5a3', 'Col6a1', 'Col6a2', 'Col6a3', 'Col8a1', 'Creb3l1', "Crispld2", "Dstn", 'Emilin1', 'Fbln5', 'Gpm6b', 'Lamb1', 'Lox', 'Loxl2', 'Pmp22', 'Postn', 'Ptn', 'Ptx3', 'Serp1', 'Serpinh1', 'Smoc2', 'Tagln', 'Tagln2', 'Tgfb2', 'Tgfbi', 'Tnn', 'Tsn', 'Vim', 'Col14a1', 'Fbln2', 'Mmp13', 'Fscn1', 'Ecm2', 'Loxl3', 'Lum', 'Mfap4', 'Mmp14', 'Mmp2', 'Ogn', 'Olfml2b', 'Pdpn', 'Aplp2', "Csgalnact1"
Chondrogenic	Col2a1, "Acan", "Sox9", "Pth1r", "Fgfr3", "Wnta", "Wnt5a", "Sox6"
Fibrochondrogenic	Col2a1, "Acan", "Sox9", "Postn", "Tagln", "Col5a1"
Macrophages	"Adgre1", "Ptprc", "Csf1r", "Ly76"
Neutrophils	"Elane", "S100a8", "Ngp"
Migration	Acta2, "Actr3", "Ager", "Akap12", "Akt1", "Bag4", "Dmtn", "Fgfr1", "Itgb1", "Itgb3", "Itgb3", "Pak1", "Pak3", "Prkce", "Ptk2", "Slc8a1", "Tgfb1", "Tgfbi", "Thbs1", "Tsc2", "Uts2", "Zfp640", "Cxcr4", "Fbxo5", "Abi3bp", "Col8a1", "Emilin1", "Lox", "Mfap4", "Pmp22", "Smoc2", "Pdpn", "Loxl2"
BMP signaling pathway	Bmpr1a, "Bmpr1b", "Bmpr2", "Smad4", "Smad1", "Smad5", "Smad9", "Acvr1"

Supplemental Table 1: List of genes used for lineage score analyses in scRNAseq analyses.

Supplemental Table 2			
	Cluster	Identity	Markers
Fig 2	0	Skeletal stem/progenitor cells	"Cd34", "Cxcl12", "Prrx1", "Ly6a", "Pdgfra", "Eng"
	1		
	2		
	3		
	4		
	5		
	6	Macrophages	"Adgre1","Ptprc", "Csf1r","Ly76"
	7		
	8	Osteoclasts	"Acp5", "Ctsk","Ocstamp"
Fig 3	0	Skeletal stem/progenitor cells	"Cd34", "Cxcl12", "Prrx1", "Ly6a", "Pdgfra", "Eng"
	1		
	2		
	3		
	4	Fibroblasts	"Tagln", "Lgals1", "Tpm4",
	5	Fibrochondro progenitors	"Col2a1", "Acan",
	6	Macrophages	"Adgre1","Ptprc", "Csf1r","Ly76"
	7		
	8		
	9		
	10		
	11		
	12		
	13	Osteoclasts	"Acp5", "Ctsk","Ocstamp"
	14	Neutrophils	Elane", "S100a8", "Ngp"
	15		
Fig 4A	0	Skeletal stem/progenitor	"Cd34", "Cxcl12", "Prrx1",
	1	Fibrogenic cells	"Aspn", "Postn", "Col1a1",
	2		"Col5a1", "Col6a1", "Ogn",
	3	Chondrogenic cells	"Col2a1", "Sox9", "Acan"
Supp Fig 3	0	FAP/MP	"Cd34", "Pdgfra", "Prrx1", "Ly6a"
	1		
	2		
	3		
	4		
	5		
	6		
	9		
	11		
	12		
	7	Fibroblasts	"S100a4", "Col1a1",
	8	Pericytes	"Mylk", "Des", "Cspg4"
	13		
	10	Tenocyte-like cells	"Kera", "Tnmd", "Scx"
	14	Spp1/Lgals3	"Spp1", "Lgals3"

Supplemental Table 2: List of markers used to define cell clusters in scRNAseq analyses.

Bibliography

1. Julien A, Kanagalingam A, Martínez-Sarrà E, Megret J, Luka M, Ménager M, et al. Direct contribution of skeletal muscle mesenchymal progenitors to bone repair. Nat Commun. 2021;12(1):2860.
2. Lu C, Saless N, Hu D, Wang X, Xing Z, Hou H, et al. Mechanical stability affects angiogenesis during early fracture healing. J Orthop Trauma. 2011;25(8):494–9.

Article 2

FGFR3 in Periosteal Cells Drives Cartilage-to-Bone Transformation in Bone Repair

Anais Julien*, **Simon Perrin***, Oriane Duchamp de Lageneste*, Caroline Carvalho, Morad Bensidhoum, Laurence Legeai-Mallet, and Céline Colnot (* co-first authors)

Research article
published in Stem Cell Reports in 2020

During endochondral ossification, the chondrocytes forming cartilage mature and enlarge to become hypertrophic. The cartilage is progressively resorbed and replaced by bone, either by apoptosis of the chondrocytes or by transdifferentiation of hypertrophic chondrocytes into osteoblasts. The presence of this process during bone regeneration has been shown, but its importance and the involvement of cells from the periosteum remain unknown. Many signaling pathways and growth factors are known to play a crucial role during chondrogenesis and chondrocyte maturation. Among them, the Fibroblast Growth Factor (FGF) family and their receptors FGFR1-3 are key players in skeletal development, and mutations in the *FGFR3* gene cause several forms of dwarfism. However, the role of the *FGFR3* gene during bone repair is still unknown. In this study, we aimed to investigate the role of FGFR3 in the activation and differentiation of SSPCs after fracture. We studied the phenotype of $Prx1^{Cre}; Fgfr3^{Y367C}$ mice, where the limb mesenchyme-derived cells carry an over activating mutation in the *Fgfr3* gene, known to be involved in a severe achondroplasia phenotype. This model showed reduced limb size with abnormal structure of the tibial growth plate. After fracture, we observed a complete absence of endochondral ossification and fracture consolidation one-month post-injury. Lineage and cell transplantation analyses showed that cells derived from the periosteum of *Fgfr3* mutant mice can differentiate into chondrocytes. However, *Fgfr3*-deficient chondrocytes are not able to mature into hypertrophic chondrocytes and transdifferentiate into osteoblasts. Instead, *Fgfr3*-deficient cells accumulate and form persistent fibrocartilage preventing bone repair. Periosteal intrinsic deficiency was sufficient to cause a pseudarthrosis phenotype. This severe repair phenotype can be corrected by transplantation of wild type pSSPCs at the fracture site of $Prx1^{Cre}; Fgfr3^{Y367C}$ mice. Overall, we demonstrated the requirement of the transdifferentiation process of periosteal-derived chondrocytes into osteoblasts during bone regeneration, and the role of the FGFR3 receptor in this process. This work also highlights the interest of studying pSSPCs as a source of cells for tissue engineering and the development of bone cell therapies.

Stem Cell Reports
Article

ISSCR

OPEN ACCESS

FGFR3 in Periosteal Cells Drives Cartilage-to-Bone Transformation in Bone Repair

Anais Julien,[1,5] Simon Perrin,[1,4,5] Oriane Duchamp de Lageneste,[1,5] Caroline Carvalho,[1] Morad Bensidhoum,[2] Laurence Legeai-Mallet,[3] and Céline Colnot[1,4,*]

[1]Paris University, *Imagine* Institute, INSERM UMR 1163, 75015, Paris, France
[2]Paris university, Laboratory of Osteoarticular Biology, Bioengineering and Bioimaging (B3OA), UMR CNRS 7052, INSERM 1271
[3]Paris University, *Imagine* Institute, Laboratory of Molecular and Physiopathological Bases of Osteochondrodysplasia, INSERM UMR 1163, 75015, Paris, France
[4]Present address: Univ Paris Est Creteil, INSERM, IMRB, 94010 Creteil, France
[5]Co-first author
*Correspondence: celine.colnot@inserm.fr
https://doi.org/10.1016/j.stemcr.2020.08.005

SUMMARY

Most organs and tissues in the body, including bone, can repair after an injury due to the activation of endogenous adult stem/progenitor cells to replace the damaged tissue. Inherent dysfunctions of the endogenous stem/progenitor cells in skeletal repair disorders are still poorly understood. Here, we report that $Fgfr3^{Y637C/+}$ over-activating mutation in Prx1-derived skeletal stem/progenitor cells leads to failure of fracture consolidation. We show that periosteal cells (PCs) carrying the $Fgfr3^{Y637C/+}$ mutation can engage in osteogenic and chondrogenic lineages, but following transplantation do not undergo terminal chondrocyte hypertrophy and transformation into bone causing pseudarthrosis. Instead, $Prx1^{Cre}$;$Fgfr3^{Y637C/+}$ PCs give rise to fibrocartilage and fibrosis. Conversely, wild-type PCs transplanted at the fracture site of $Prx1^{Cre}$;$Fgfr3^{Y637C/+}$ mice allow hypertrophic cartilage transition to bone and permit fracture consolidation. The results thus highlight cartilage-to-bone transformation as a necessary step for bone repair and FGFR3 signaling within PCs as a key regulator of this transformation.

INTRODUCTION

Bone fracture repair is an efficient regenerative process, which depends on a controlled inflammatory response, followed by the recruitment of skeletal stem/progenitor cells, deposition of cartilage and bone matrix and skeletal tissue remodeling. Skeletal stem/progenitor cells are recruited from multiple sources in the bone fracture environment, including the bone marrow, the periosteum, and the surrounding soft tissues but cannot be strictly distinguished using genetic lineage tracing (Abou-Khalil et al., 2015; Chan et al., 2015; Duchamp de Lageneste et al., 2018; Debnath et al., 2018; Matsushita et al., 2020; Ortinau et al., 2019; Van Gastel et al., 2012; Worthley et al., 2015; Zhang et al., 2005; Zhou et al., 2014a). However, several strategies have revealed that the periosteum comprises populations of skeletal stem/progenitor cells largely involved in callus formation through intramembranous and endochondral ossification (Debnath et al., 2018; Duchamp de Lageneste et al., 2018; Ortinau et al., 2019). These studies emphasized the periosteum as a key contributor to bone repair and likely affected in skeletal repair dysfunctions.

When bone repair is compromised by extensive injuries or pathological conditions, failure of the bone regenerative process can lead to delayed-union or non-union but the underlying cause of this failed healing is often undetermined. An adverse inflammatory environment or impaired revascularization of the fracture site may contribute to the bone repair deficit, but the role of the main players, the skeletal stem/progenitor cells, is less understood. Whether cells cannot be properly activated in response to injury or do not support the subsequent stages of skeletal tissue deposition and remodeling is difficult to assess *in vivo* due to the diversity of skeletal stem/progenitor cell populations that may participate in repair.

Here, we explored the role of periosteal cells (PCs) in bone repair and uncovered PC dysfunctions in $Prx1^{Cre}$;$Fgfr3^{Y367C/+}$ mice that exhibit a severe bone repair phenotype of pseudarthrosis. Fibroblast growth factor receptor 3 (FGFR3) is a key regulator of endochondral ossification during bone development. Gain-of-function point mutations in *FGFR3* gene causing upregulation of FGFR3 signaling are associated with the human genetic disease achondroplasia or dwarfism, affecting the cartilage growth plate in developing long bones with abnormal chondrocyte proliferation and differentiation, loss of columnar organization, and overall reduction in long bone growth (Bonaventure et al., 1996; Mugniery et al., 2012; Pannier et al., 2009; Rousseau et al., 1994). We report that mice carrying the $Fgfr3^{Y637C/+}$ activating mutation in the Prx1-derived skeletal stem/progenitor cells exhibit short limbs during postnatal growth and pseudarthrosis following a tibial fracture. The pseudarthrosis phenotype is marked by the accumulation of fibrotic tissue and un-resorbed cartilage in the center of the fracture callus. We show that impaired bone healing in $Prx1^{Cre}$;$Fgfr3^{Y367C/+}$ mice is correlated

with intrinsic deficiencies in PCs affecting the endochondral ossification process, and more specifically cartilage-to-bone transformation that is taking place at a critical time when cartilage replacement by bone is crucial to consolidate the fracture gap. The requirement of this transformation step for bone repair is still debated and our results reveal that this transformation is required for effective healing (Hu et al., 2017; Yang et al., 2014; Zhou et al., 2014b).

RESULTS

Impaired Bone Regeneration and Pseudarthrosis in *Prx1^{Cre};Fgfr3$^{Y367C/+}$* Mice

To investigate the role of FGFR3 in bone repair, we crossed *Fgfr3$^{Y637C/+}$* mice with the *Prx1^{Cre}* mouse line to target the mesenchymal lineage in the limb (Logan et al., 2002; Pannier et al., 2009). This mesenchymal lineage gives rise to the skeletal stem/progenitor cells in the periosteum that contributes to fracture repair in the adult (Duchamp de Lageneste et al., 2018). While mice expressing the heterozygous *Fgfr3$^{Y637C/+}$* mutation ubiquitously recapitulate a severe form of dwarfism and die within 2 months after birth, the *Prx1^{Cre};Fgfr3$^{Y367C/+}$* mice also displayed shorter long bones in the limbs but survived until adulthood. Adult *Prx1^{Cre};Fgfr3$^{Y367C/+}$* mice exhibited a 65% reduction in tibia length (Figure 1A). Consistent with the known dwarfism phenotype, we observed a strong disorganization of the epiphyseal cartilage in 1- and 3-month-old *Prx1^{Cre};Fgfr3$^{Y367C/+}$* mice with an abnormal shape and size of hypertrophic chondrocytes compared with control mice (Figure 1B). Immunofluorescence staining on epiphyseal cartilage of 3-month-old *Prx1^{Cre};Fgfr3$^{Y367C/+}$* mice showed absence of Collagen X (COLX) and Osterix (OSX) expression in the area below the cartilage where trabeculae are missing compared with controls (Figure 1C). We also observed a significant reduction of vascularization and an absence of CD31/Endomucin (EMCN) double-positive vessels at the cartilage-to-bone transition zone in *Prx1^{Cre};Fgfr3$^{Y367C/+}$* mice, indicating an impairment of endochondral ossification (Figures 1C and 1D).

We induced open non-stabilized tibial fractures in 3-month-old *Prx1^{Cre};Fgfr3$^{Y367C/+}$* mice and *Prx1^{Cre};Fgfr3$^{+/+}$* control mice. Histomorphometric analyses showed a severe impairment of bone healing as indicated by a marked reduction in callus and bone volumes in *Prx1^{Cre};Fgfr3$^{Y367C/+}$* mice throughout the stages of repair (Figure 2A). Cartilage volume was also reduced through to day 14 followed by cartilage accumulation from day 21 post-fracture. At 28 days post-fracture, micro-computed tomography (micro-CT) and histological analyses showed a complete absence of bone bridging of *Prx1^{Cre};Fgfr3$^{Y367C/+}$* calluses, whereas *Prx1^{Cre};Fgfr3$^{+/+}$* control mice displayed fully ossified calluses with reconstitution of the cortex to bridge the fracture gap. Although new bone formation was detected at the periphery of *Prx1^{Cre};Fgfr3$^{Y367C/+}$* calluses, there was a complete absence of bone deposition in the center of the callus (Figures 2B, 2C, and S1). Instead, we identified areas of unresorbed fibrocartilage with low Safranin O (SO) staining and abnormal COLX expression and areas of fibrous tissue deposition marked by the matrix protein Periostin in *Prx1^{Cre};Fgfr3$^{Y367C/+}$* mice that are characteristic of pseudarthrosis (Figures 2D and 2E). By day 56, micro-CT analyses showed partial bridging of the two ossified parts of the callus in *Prx1^{Cre};Fgfr3$^{Y367C/+}$* mice with a persistent decrease in bone volume (Figure S2).

Cartilage-to-Bone Transition Is Disrupted in *Prx1^{Cre};Fgfr3$^{Y367C/+}$* Fracture Callus

The pseudarthrosis phenotype in *Prx1^{Cre};Fgfr3$^{Y367C/+}$*mice indicated a lack of endochondral ossification during bone repair. Indeed, when we evaluated bone repair strictly through intramembranous ossification using a unicortical defect repair model in *Prx1^{Cre};Fgfr3$^{Y367C/+}$* mice, we did not observe delayed healing compared with *Prx1^{Cre};Fgfr3$^{+/+}$* mice (Figure S3). Endochondral ossification depends on proper chondrocyte differentiation, followed by maturation to hypertrophic chondrocytes and finally cartilage-to-bone transition to allow the replacement of the cartilaginous matrix by bone. The volume and percentage of hypertrophic cartilage were markedly decreased in the callus of *Prx1^{Cre};Fgfr3$^{Y367C/+}$* mice compared with controls (Figure 3A). At day 7 post-fracture, we observed the presence of SOX9-expressing cells in the cartilage of control and mutant mice (Figure 3B). By day 14 post-fracture, although chondrocytes expressed markers of hypertrophy, such as vascular endothelial growth factor (VEGF) and COLX, we observed a reduced amount of COLX$^+$ hypertrophic cartilage (Figure 3C). Hypertrophic chondrocytes also exhibited abnormal shape and reduced size in *Prx1^{Cre};Fgfr3$^{Y367C/+}$* mice that may also contribute to the reduced cartilage volume. These results suggest that mutant chondrocytes can initiate chondrogenic differentiation and maturation but failed to achieve hypertrophy. We then examined the crucial step of cartilage-to-bone transition in *Prx1^{Cre};Fgfr3$^{Y367C/+}$* mice. Further analyses of the transition zone at day 14 post-fracture showed no co-localization of COLX$^+$ cells and OSX$^+$ cells in the new bone area of the transition zone in *Prx1^{Cre};Fgfr3$^{Y367C/+}$* calluses. POSTN was undetected within cartilage but was highly expressed in the fibrotic area suggesting absence of terminal hypertrophy and fibrotic accumulation by day 14 in *Prx1^{Cre};Fgfr3$^{Y367C/+}$* calluses. This correlated with a poor vascularization as shown by the absence of CD31/EMCN double-positive vessels in *Prx1^{Cre};Fgfr3$^{Y367C/+}$* calluses compared

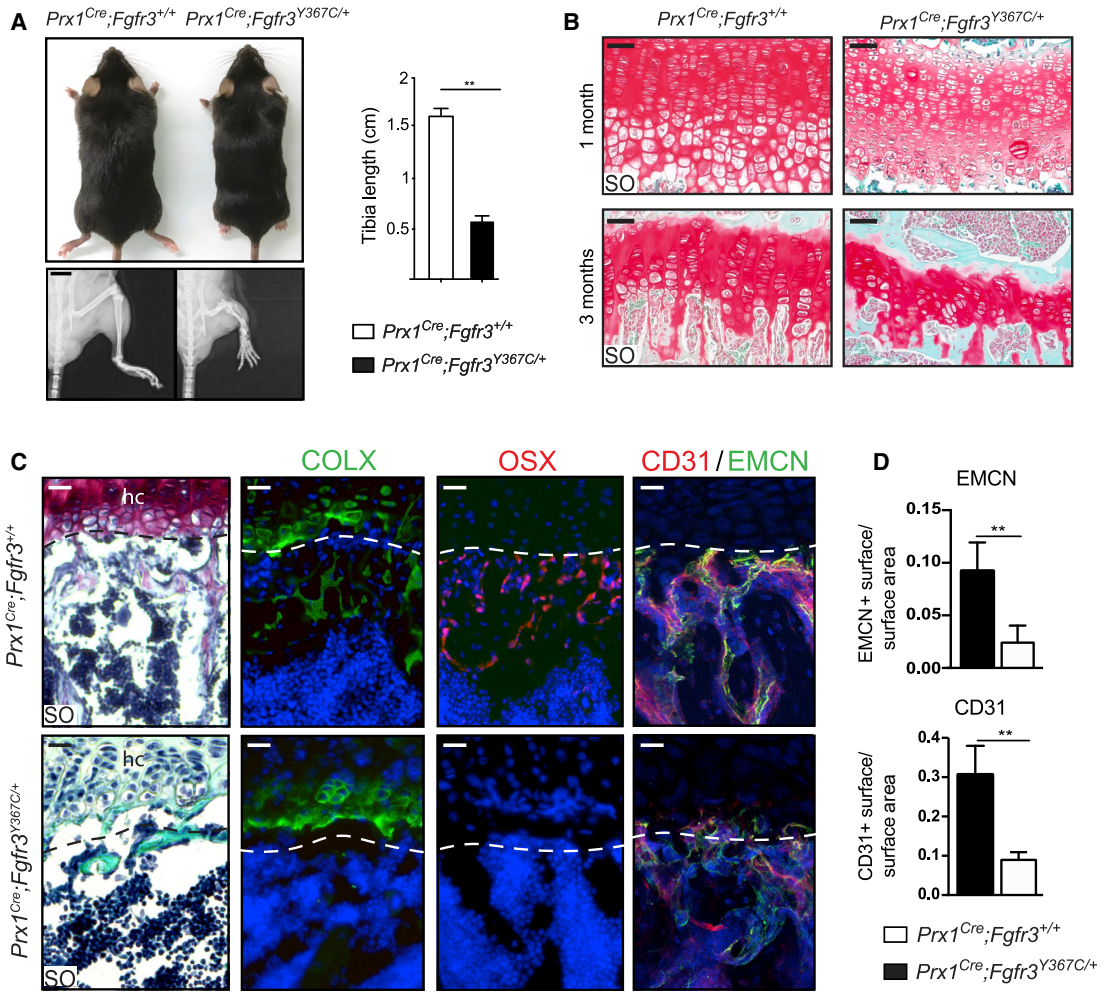

Figure 1. Reduced Tibia Length and Abnormal Tibial Epiphyseal Cartilage Organization in *Prx1^{Cre};Fgfr3$^{Y367C/+}$* Mice

(A) Three-month-old *Prx1^{Cre};Fgfr3$^{Y367C/+}$* and *Prx1^{Cre};Fgfr3$^{+/+}$* mice (top), radiographs of hindlimbs (bottom), and quantification of tibia length (right) (n = 5 per group). Scale bar, 0.5 cm.

(B) Representative Safranin O (SO) staining of epiphyseal cartilage of uninjured tibia from 1- to 3 month-old *Prx1^{Cre};Fgfr3$^{+/+}$* and *Prx1^{Cre};Fgfr3$^{Y367C/+}$* mice. Scale bar, 50 μm.

(C) Immunofluorescence of Collagen X (COLX), Osterix (OSX), and CD31/Endomucin (EMCN) at the transition zone between the epiphyseal hypertrophic cartilage (hc) and the metaphysis in uninjured tibia from 3 months old *Prx1^{Cre};Fgfr3$^{+/+}$* and *Prx1^{Cre};Fgfr3$^{Y367C/+}$* mice (n = 3). Scale bar, 50 μm.

(D) Quantification of CD31 and EMCN immunofluorescence at the transition zone between the epiphyseal cartilage and the metaphysis from *Prx1^{Cre};Fgfr3$^{+/+}$* and *Prx1^{Cre};Fgfr3$^{Y367C/+}$* mice (n = 6).

Values represent mean ± SD. **p < 0.01 using Mann-Whitney test.

with controls (Figure 3D). In previous studies, the presence of proliferating chondrocytes in the transition zone has been associated with the ability of terminal hypertrophic chondrocytes to transdifferentiate into osteoblasts (Hu et al., 2017; Yang et al., 2014; Zhou et al., 2014b). We observed a strong reduction in the number of KI67^{+} and SOX2^{+} chondrocytes in the transition zone of *Prx1^{Cre};Fgfr3$^{Y367C/+}$* calluses compared with controls (Figure 3E). These results indicate abnormal chondrocyte hypertrophy followed by lack of cartilage-to-bone transition that may lead to the pseudarthrosis phenotype in *Prx1^{Cre};Fgfr3$^{Y367C/+}$* mice.

Prx1^{Cre};Fgfr3$^{Y367C/+}$ PCs Fail to Undergo Cartilage-to-Bone Transformation

We sought to test the involvement of PCs in this defective endochondral ossification process during bone repair given their efficient contribution to this process (Duchamp de

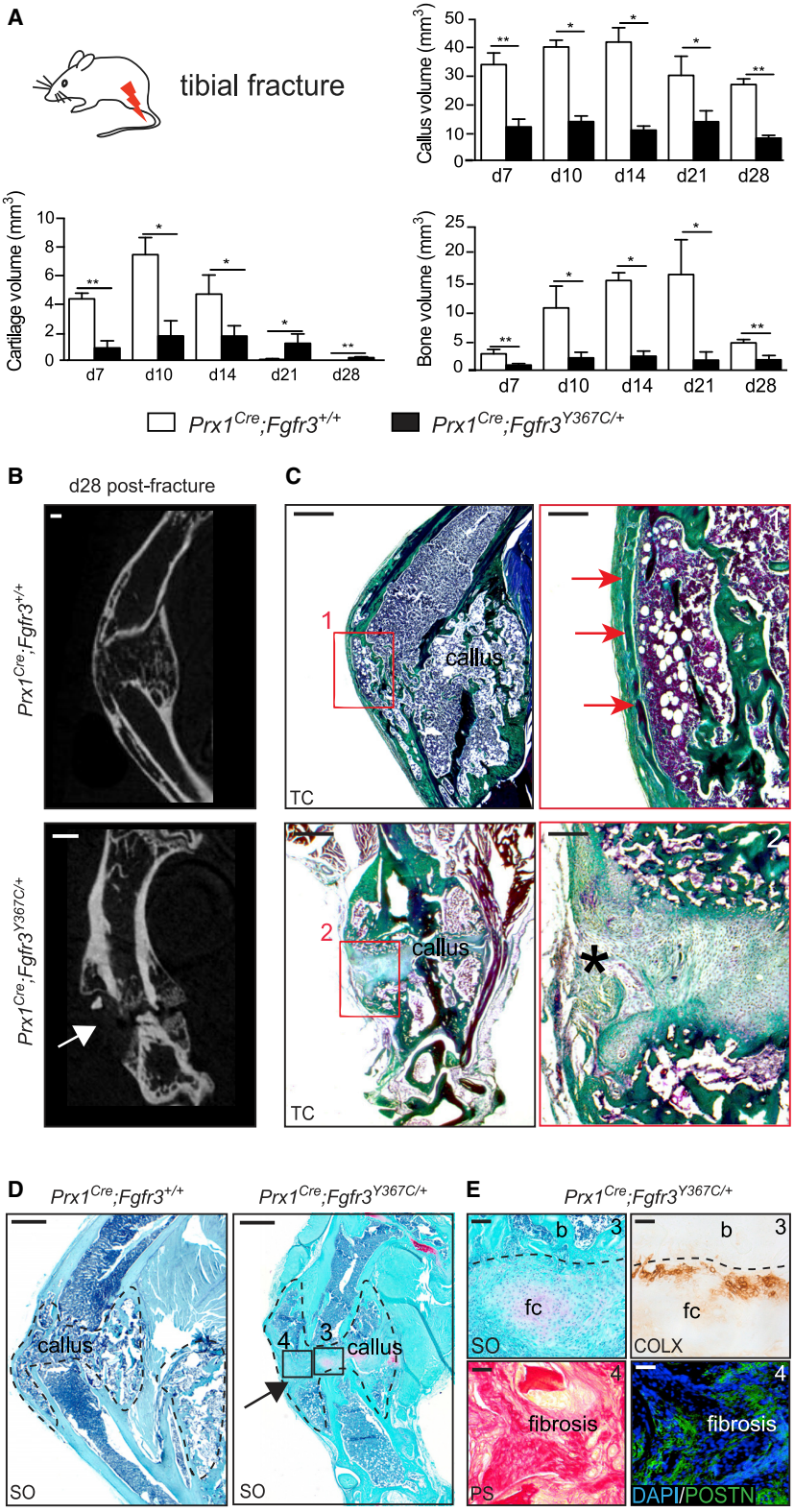

Figure 2. Altered Bone Regeneration and Pseudarthrosis in *Prx1^{Cre};Fgfr3$^{Y367C/+}$* Mice

(A) Histomorphometric analyses of callus, cartilage, and bone volumes at days 7, 10, 14, 21, and 28 post-fracture in *Prx1^{Cre};Fgfr3$^{+/+}$* and *Prx1^{Cre};Fgfr3$^{Y367C/+}$* mice (n = 4 or 5 per group).

(B) Representative micro-CT images of *Prx1^{Cre};Fgfr3$^{+/+}$* and *Prx1^{Cre};Fgfr3$^{Y367C/+}$* calluses at 28 days post-fracture. White arrow points to the absence of bone bridging in *Prx1^{Cre};Fgfr3$^{Y367C/+}$* callus (n = 4–5 per group). Scale bar, 1 mm.

(C) Longitudinal sections stained with Masson's trichrome (TC) of *Prx1^{Cre};Fgfr3$^{+/+}$* and *Prx1^{Cre};Fgfr3$^{Y367C/+}$* calluses 28 days post-fracture. High magnification showing continuity of the newly formed cortex in *Prx1^{Cre};Fgfr3$^{+/+}$* callus (box 1, red arrows) and absence of new bone in the center of *Prx1^{Cre};Fgfr3$^{Y367C/+}$* callus (box 2, asterisk). Scale bars, 1 mm (left) and 300 μm (right).

(D) Longitudinal sections stained with SO of *Prx1^{Cre};Fgfr3$^{+/+}$* and *Prx1^{Cre};Fgfr3$^{Y367C/+}$* calluses 28 days post-fracture (callus delimited with a black dotted line). Scale bar, 1 mm.

(E) High magnification of fibrocartilage (fc) stained with SO and COLX immunostaining showing few COLX^{+} cells adjacent to fibrocartilage and bone (b) in *Prx1^{Cre};Fgfr3$^{Y367C/+}$* callus (box 3, top). High magnification of fibrosis stained with Picrosirius (PS) and Periostin (POSTN) immunostaining in *Prx1^{Cre};Fgfr3$^{Y367C/+}$* callus (box 4, bottom). Scale bar, 100 μm. Values represent mean ± SD. *p < 0.05, **p < 0.01 using Mann-Whitney test.

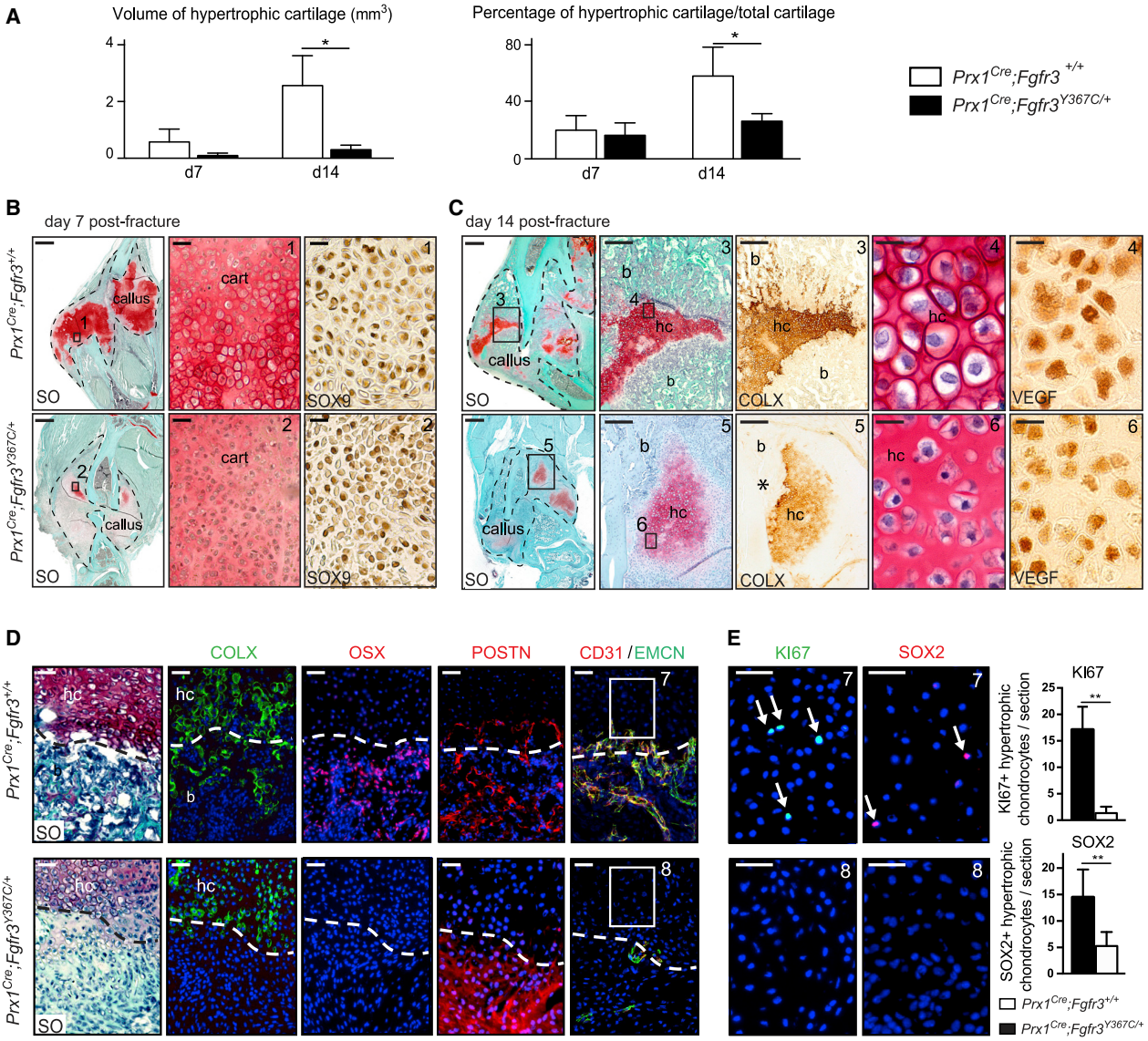

Figure 3. Impaired Cartilage Differentiation and Cartilage-to-Bone Transition in *Prx1^{Cre};Fgfr3$^{Y367C/+}$* Fracture Callus

(A) Histomorphometric quantification of hypertrophic cartilage volume and percentage of hypertrophic cartilage volume in total cartilage volume at days 7 and 14 post tibial fracture in *Prx1^{Cre};Fgfr3$^{+/+}$* and *Prx1^{Cre};Fgfr3$^{Y367C/+}$* mice (n = 4 or 5 per group).

(B) Longitudinal sections of *Prx1^{Cre};Fgfr3$^{+/+}$* (control) and *Prx1^{Cre};Fgfr3$^{Y367C/+}$* (mutant) calluses (delimited with a black dotted line) at day 7 post-fracture stained with SO. High magnification of cartilage area (box 1, 2) and SOX9 immunostaining showing the presence of chondrogenic cells in the callus of control and mutant mice. Scale bars, 1 mm and 50 μm (boxes 1 and 2).

(C) Longitudinal sections of *Prx1^{Cre};Fgfr3$^{+/+}$* and *Prx1^{Cre};Fgfr3$^{Y367C/+}$* calluses at day 14 post-fracture stained with SO. High magnification of hypertrophic cartilage (hc) area (box 3, 5) and COLX immunostaining on adjacent sections showing positive staining in control and mutant hc, and within new bone trabeculae (b) in control but not in mutant (asterisk). High magnification of hypertrophic chondrocytes (box 4, 6) and VEGF immunostaining showing abnormal cellular size and shape in mutant. Scale bars, 1 mm, 300 μm (boxes 3 and 5), and 25 μm (boxes 4 and 6).

(D) Immunostaining for COLX, OSX, Periostin (POSTN), and CD31/EMCN at the cartilage-to-bone transition zone in *Prx1^{Cre};Fgfr3$^{+/+}$* and *Prx1^{Cre};Fgfr3$^{Y367C/+}$* calluses 14 days post-fracture (n = 5 per group). Scale bar, 50 μm.

(E) High magnification of cartilage area next to bone and immunostaining for KI67 and SOX2 (box 7 and 8). Quantification of KI67^{+} and SOX2^{+} hypertrophic chondrocytes in day 14 post-fracture calluses from *Prx1^{Cre};Fgfr3$^{+/+}$* and *Prx1^{Cre};Fgfr3$^{Y367C/+}$* mice (n = 5 per group) Scale bar, 25 μm. Values represent the mean ± SD. **p < 0.01 using Mann-Whitney test.

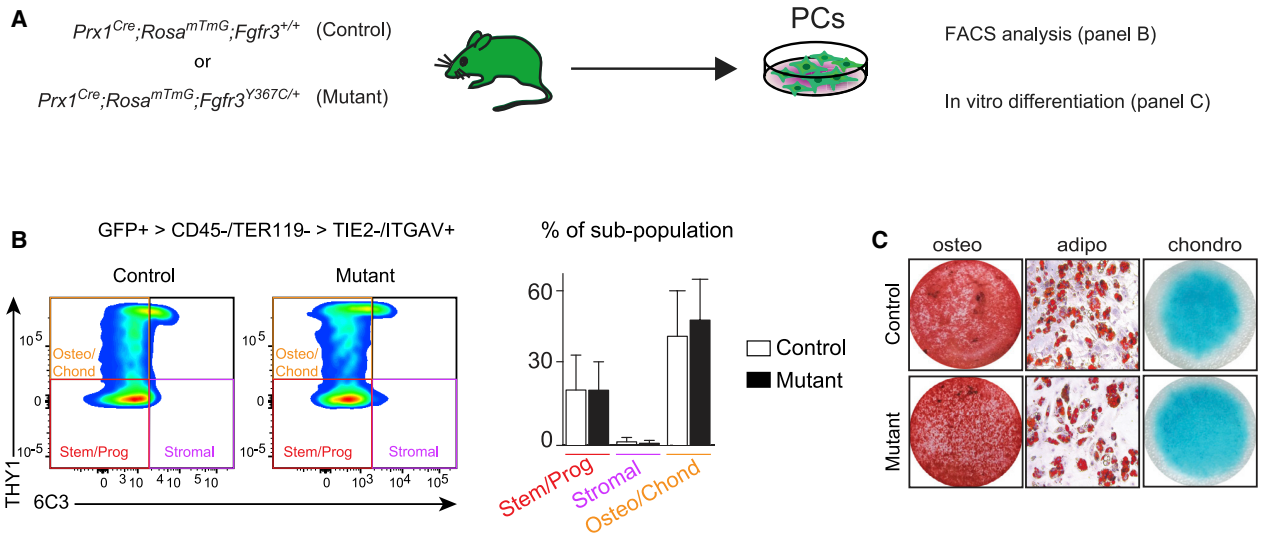

Figure 4. *In Vitro* Characterization of *Prx1^{Cre};Fgfr3$^{Y367C/+}$* Periosteal Cells

(A) Experimental design of *Prx1^{Cre};Rosa^{mTmG};Fgfr3$^{+/+}$* (control) and *Prx1^{Cre};Rosa^{mTmG};Fgfr3$^{Y367C/+}$* (mutant) PC analyses via flow cytometry and *in vitro* differentiation.

(B) Representative fluorescence-activated cell sorting plots of GFP+ (Prx1-derived) PCs negative for hematopoietic and endothelial markers, and positive for ITGAV marker (left). Percentage of stem/progenitor (THY1$^-$/6C3$^-$ cells), stromal (THY1$^-$/6C3$^+$ cells), and osteo/chondroprogenitor (THY1$^+$/6C3$^-$ cells) sub-populations in GFP$^+$ PCs as defined (Chan et al., 2015) (right) (n = 3 from 3 independent experiments per group). Values represent the mean ± SD.

(C) Osteogenic (alizarin red staining), adipogenic (oil red O staining), and chondrogenic (Alcian blue staining) *in vitro* differentiation of control and mutant PCs (n = 3 from 3 independent experiments per group). Values represent the mean ± SD.

Lageneste et al., 2018; Colnot, 2009). We did not identify changes in the proportions of skeletal stem/progenitor cells, osteo-chondroprogenitors and stromal cells in the GFP$^+$ PC populations from *Prx1^{Cre};Rosa^{mTmG};Fgfr3$^{Y367C/+}$* mutant mice compared with *Prx1^{Cre};Rosa^{mTmG};Fgfr3$^{+/+}$* control mice (Figures 4A and 4B) (Chan et al., 2015). Mutant PCs could engage into the osteogenic, adipogenic, and chondrogenic lineages *in vitro* as observed for control PCs (Figure 4C). When mutant PCs were transplanted at the fracture site of wild-type hosts, they integrated into the cartilage by differentiating into SOX9$^+$ chondrocytes at day 10 (Figures 5A and 5B). However, unlike control PCs they failed to mature and undergo chondrocyte hypertrophy by day 14. Mutant PCs gave rise to cells producing fibrocartilage in the center of the fracture callus in place of hypertrophic cartilage (Figure 5C). By day 21, cartilage-to-bone transformation had occurred and osteocytes derived from control PCs were localized within new bone trabeculae (Figure 5D, top). Mutant PCs were not detected within hypertrophic cartilage or new bone by day 21 but localized within fibrous tissue and caused a pseudarthrosis-like phenotype (Figure 5D, bottom). Histomorphometric analysis confirmed that the transplantation of mutant PCs at the fracture site of wild-type mice impaired healing as shown by decreased callus and bone volumes by day 14 and increased fibrosis by days 14 and 21 compared with wild-type callus transplanted with control PCs (Figure 5E). Thus, transplanted PCs carrying an over-activating mutation in FGFR3 cannot form hypertrophic cartilage or bone via endochondral ossification during bone repair but cause pseudarthrosis through a cell-autonomous mechanism.

Exogenous PCs Can Rescue Pseudarthrosis in *Prx1^{Cre};Fgfr3$^{Y367C/+}$* Mice

We next attempted to rescue the pseudarthrosis phenotype in *Prx1^{Cre};Fgfr3$^{Y367C/+}$* mice with the tyrosine kinase inhibitor PD173074 that can arrest the G0/G1 phase of the FGFR3-expressing cells (Jonquoy et al., 2012; Martin et al., 2018). Although PD173074 treatment increased cartilage and hypertrophic cartilage volumes in the fracture callus of mutant mice, the treatment did not stimulate cartilage-to-bone transition and did not affect callus and bone volumes (Figure S4). Given the cell-autonomous defect of mutant PCs, we turned to a cell-based approach to rescue the pseudarthrosis phenotype (Figure 6A). PCs isolated from *Prx1^{Cre};Rosa^{mTmG};Fgfr3$^{+/+}$* mice integrated into the fracture callus of mutant hosts and were able to differentiate into hypertrophic chondrocytes by day 14 and subsequently gave rise to osteocytes within new

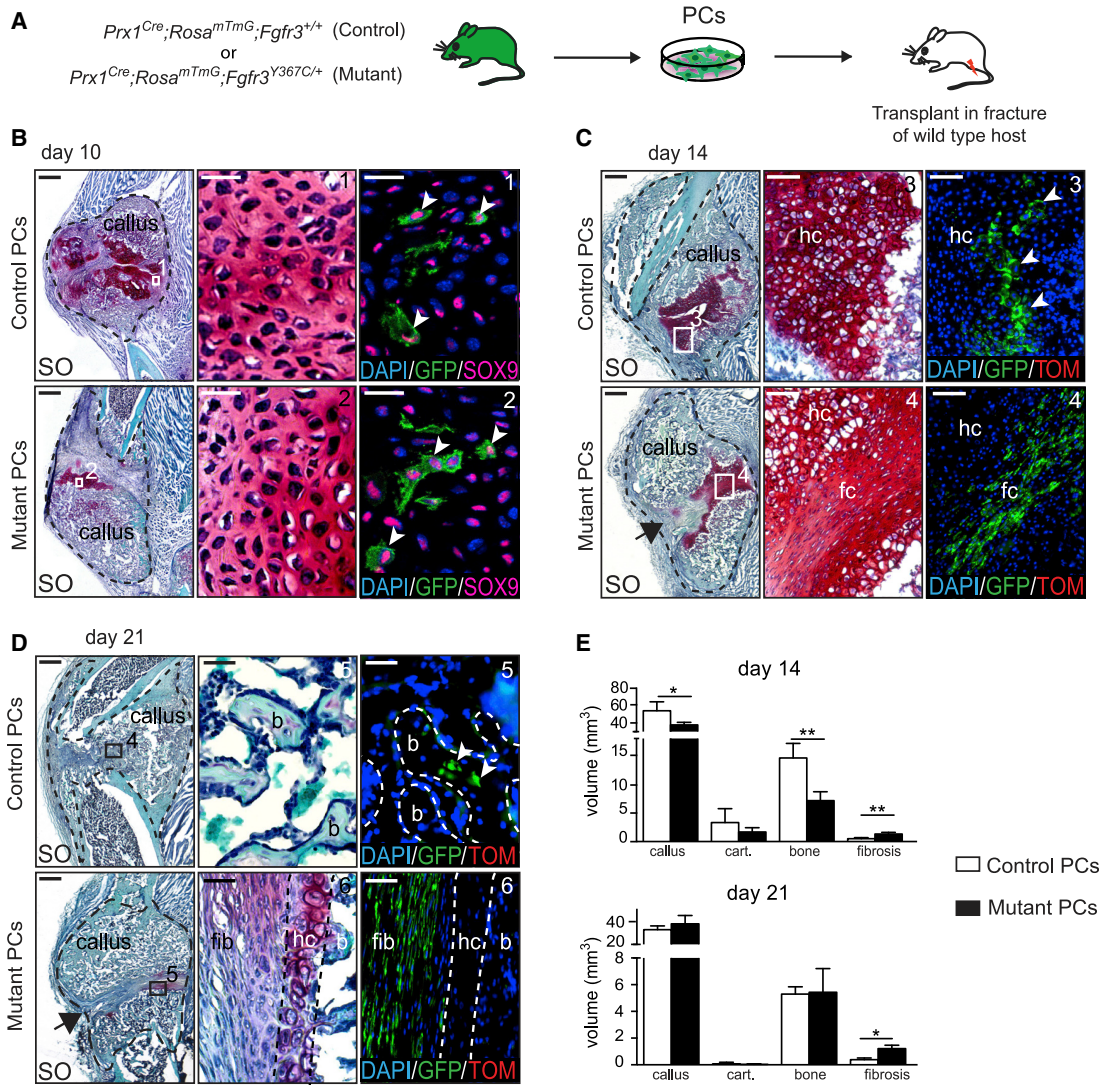

Figure 5. Transplantation of *Prx1^{Cre};Fgfr3$^{Y367C/+}$* Periosteal Cells Impairs Bone Healing

(A) Experimental design of *Prx1^{Cre};Rosa^{mTmG};Fgfr3$^{+/+}$* (control) and *Prx1^{Cre};Rosa^{mTmG};Fgfr3$^{Y367C/+}$* (mutant) PC isolation and transplantation at the fracture site of wild-type host.

(B) Lineage tracing of GFP^{+} control and mutant PCs at 10 days post-fracture. SO staining and SOX9 immunofluorescence on longitudinal sections of host calluses showing SOX9/GFP double-positive cells from control and mutant donor in the cartilage (box 1 and 2). Scale bars, 1 mm and 25 μm (high magnification).

(C and D) Lineage tracing of GFP^{+} control and mutant PCs at days 14 (C) and 21 (D) post-transplantation. SO staining and DAPI/GFP/Tomato fluorescence on longitudinal sections of host calluses (black dotted line). (C) Control PCs differentiate into hypertrophic chondrocytes (hc) (box 3, white arrowhead) but mutant PCs form elongated fibrocartilage cells by day 14 (fc, box 4). (D) Control PCs give rise to osteocytes within new bone trabeculae (b, box 5, white arrowhead) in the center of the callus, whereas mutant PCs form fibrotic (fib, box 6) cells by day 21 leading to pseudarthrosis (black arrow) (n = 5 per group). Scale bars: 1 mm, 100 μm (C, high magnification), and 25 μm (D, high magnification).

(E) Histomorphometric quantification of callus, cartilage, bone, and fibrosis volumes at days 14 and 21 post-fracture and PCs transplantation (n = 5 per group). Values represent mean ± SD. *p < 0.05, **p < 0.01 using Mann-Whitney test.

bone trabeculae by day 21 (Figure 6B, top). Conversely, in mutant hosts treated with Tisseel matrix carrier alone, we observed the pseudarthrosis phenotype of mutant mice (Figure 6B, bottom). By day 28, the transplantation of *Prx1^{Cre};Rosa^{mTmG};Fgfr3$^{+/+}$* PCs in mutant hosts had a significant impact on bone healing as shown by the decrease in

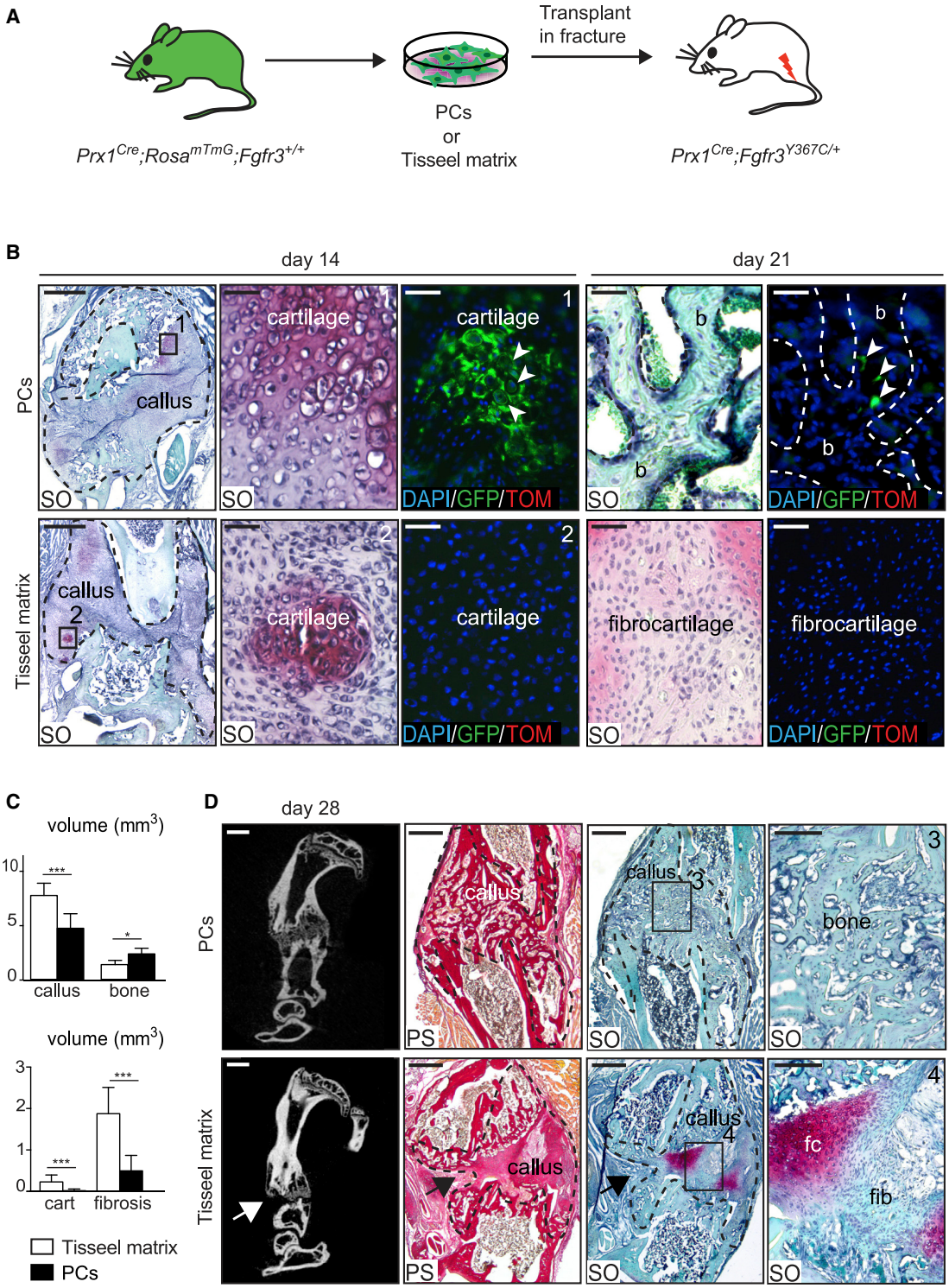

Figure 6. Transplantation of PCs Corrects the *Prx1*^{Cre};*Fgfr3*$^{Y367C/+}$ Pseudarthrosis Phenotype

(A) Experimental design of transplantation of Tisseel matrix or *Prx1*^{Cre};*Rosa*^{mTmG};*Fgfr3*$^{+/+}$ PCs at the fracture site of *Prx1*^{Cre};*Fgfr3*$^{Y367C/+}$ hosts.

(legend continued on next page)

callus, unresorbed cartilage and persistent fibrosis volumes, and by the increase in bone volume (Figure 6C). The callus was fully ossified with complete resorption of cartilage and fibrous tissue in 7 out of 11 cases (Figure 6D). Transplanted PCs in mutant hosts were sufficient to support endochondral ossification by compensating for the failure of mutant hypertrophic cartilage to transform into bone, and preventing fibrocartilage and fibrosis accumulation. All together, these data establish that the pseudarthrosis phenotype in *Prx1*^{Cre};*Fgfr3*$^{Y367C/+}$ mice is linked with an intrinsic deficiency of PCs to differentiate into late hypertrophic chondrocytes, leading to a defect in cartilage-to-bone transformation and absence of bone bridging, that can be prevented by exogenous PCs transplantation.

DISCUSSION

Here, we elucidate the underlying mechanisms of bone repair defect in the *Prx1*^{Cre};*Fgfr3*$^{Y367C/+}$ mouse model that exhibit a pseudarthrosis phenotype. We identify inherent deficiencies of PCs carrying the *Fgfr3*^{Y367C} heterozygous mutation and causing the pseudarthrosis phenotype after cell transplantation. These PCs deficiencies were not revealed using fluorescence-activated cell sorting analyses or *in vitro* differentiation assays that are classically used to identify functional impairment of skeletal stem/progenitor cells. Instead, we implanted mutant PCs into a bone fracture environment to study their behavior and to establish a correlation between the impaired regenerative potential of PCs *in vivo* and the bone repair deficit. Mutant PCs transplanted at the fracture site of wild-type hosts were detected in the cartilage within the fracture callus indicating that they did not exhibit deficiency in recruitment or migration. However, transplanted PCs could not differentiate into late hypertrophic chondrocytes and undergo cartilage-to-bone transformation, a process that cannot be evaluated *in vitro*. Mutant PCs were sufficient to impair bone healing in a wild-type host highlighting the cell-autonomous effect of exogenous PCs on bone repair and their involvement in the pseudarthrosis phenotype. The bone repair phenotype in *Prx1*^{Cre};*Fgfr3*$^{Y367C/+}$ mice mimics the severe human condition of pseudarthrosis that can be associated with trauma or disease, suggesting that deficient PCs may be correlated with other pseudarthrosis phenotypes.

We also report the ability of control PCs to consolidate the bone fracture by producing hypertrophic cartilage that can transform into bone independent of the disease environment. This suggests that PCs could be beneficial in cell-based approaches to treat pseudarthrosis, given their positive effect on the very dynamic process of bone healing. Furthermore, in a cell-based therapy setting, it is generally accepted that long-term integration of transplanted cells is needed for efficient treatment (O'Keefe et al., 2020b; O'Keefe et al., 2020a). Our results illustrate that transient integration of PCs may be sufficient to correct a skeletal repair disorder.

The results show that cartilage-to-bone transformation mediated by PCs during bone repair is regulated by FGFR3 signaling. Fibroblast growth factors and their receptors are important regulators of bone development and are re-expressed in hypertrophic cartilage after bone fracture (Du et al., 2012; Nakajima et al., 2001; Schmid et al., 2009; Su et al., 2008). In the FGFR3 model carrying the *Fgfr3*$^{G369C/+}$ gain-of-function mutation with milder achondroplasia phenotype, delayed healing of un-stabilized or semi-stabilized tibial fractures has been reported due to altered chondrogenesis and hypertrophic differentiation (Chen et al., 2017; Su et al., 2008). However, callus ossification was not inhibited in the *Fgfr3*$^{G369C/+}$ model suggesting that cartilage-to-bone transformation was not affected. Thus, our results using the *Fgfr3*$^{Y367C/+}$ model bring further insights on the essential role of FGFR3 during bone repair in regulating not only chondrocyte differentiation but also cartilage-to-bone transformation necessary for endochondral ossification. The functional requirement of this cartilage-to-bone transformation process for the success of bone repair is still underestimated. We provide evidence that when this process is disrupted bone healing fails. Although intramembranous ossification at the periphery

(B) SO staining and DAPI/GFP/Tomato fluorescence on longitudinal sections of *Prx1*^{Cre};*Fgfr3*$^{Y367C/+}$ calluses (delimited by a black dotted line) at days 14 and 21 post-fracture. GFP^{+} PCs form hypertrophic chondrocytes (box 1, white arrowheads) by day 14 and osteocytes (white arrow) within new bone (b, dotted line) by day 21 post-transplantation. By days 14 and 21, the center of mutant calluses transplanted with Tisseel matrix is composed of fibrocartilage (box 2, n = 4 or 5 per group). Scale bars, 1 mm, 100 μm (for d14, high magnification), and 25 μm (for d21, high magnification).

(C) Histomorphometric quantification of callus, cartilage, bone, and fibrosis volumes at day 28 post-fracture (n = 9 or 11 per group).

(D) Representative micro-CT images of *Prx1*^{Cre};*Fgfr3*$^{Y367C/+}$ calluses by day 28 post-fracture showing bone bridging after PCs transplantation and absence of bone bridging (white arrow) after transplantation with Tisseel matrix. SO and PS staining on callus sections after transplantation of PCs showing complete ossification and absence of fibrocartilage and fibrous tissue accumulation (box 3, n = 7 cases out of 11). Representative callus sections confirm the presence of pseudarthrosis (black arrows) and at high magnification of fibrocartilage (fc) and fibrous tissue (fib) in mice transplanted with Tisseel matrix (box 4, n = 9 cases out of 9). Scale bars, 1 mm and 100 μm (high magnification). Values represent mean ± SD. **p < 0.01, ***p < 0.005 using Mann-Whitney test.

of the callus is not delayed in the *Prx1*^{Cre};*Fgfr3*$^{Y367C/+}$ model, healing is halted due to absence of cartilage-to-bone transformation in the center of the callus. In addition, abnormal chondrocyte hypertrophy and transition to bone is associated with fibrocartilage and fibrous tissue accumulation that also interferes with bone bridging, revealing a central role of FGFR3 signaling in controlling the balance between ossification and fibrosis. These findings have major impacts on the management of patients affected with achondroplasia that may require surgery for limb lengthening as managing the level of stabilization and endochondral ossification may be crucial to allow successful healing (Chilbule et al., 2016; Kitoh et al., 2014). Beyond this specific clinical setting, the results bring fundamental insights on the mechanisms of bone repair defects in pseudarthrosis and the role of PCs and FGFR3 in the essential step of cartilage-to-bone transformation during bone repair.

EXPERIMENTAL PROCEDURES

Mice

C57BL/6ScNj, *Prx1*^{Cre}, and *Rosa-tdTomato-EGFP* (*Rosa*^{mTmG}) transgenic mice were obtained from Jackson Laboratory (Bar Harbor, ME). *Fgfr3*^{Y367C} mice were generated in Dr. Legeai-Mallet's laboratory (Pannier et al., 2009). In brief, the point mutation was inserted within exon 9 at position 367 of the *Fgfr3* gene, directly followed by a floxed *neo* cassette. Under Cre recombination, the *neo* cassette is removed, allowing expression of the mutated allele of the *Fgfr3* gene. Mice were bred and genotyped in our laboratory using primers purchased from Eurofins (Eurofins Scientific, Lux). Five- to 8-week-old mice were used for *in vitro* experiments and 3 month-old mice for *in vivo* experiments. Male and female mice were used and distributed homogenously within experimental groups. All procedures were approved by the Paris University and Creteil University Ethical Committees.

Primary Cultures of PCs

PCs were obtained as described previously (Duchamp de Lageneste et al., 2018). In brief, mouse hindlimbs (tibias and femurs) were harvested free of skin, and muscles were dissected using scissors and forceps, without damaging the periosteum. Epiphyses were cut and bone marrow was flushed using growth media (MEMα supplemented with 20% lot-selected non-heat-inactivated FBS, 1% penicillin-streptomycin, Life Technologies, Carlsbad, CA). The remaining flushed bones free of bone marrow were placed in culture and PCs migrated out of the explants after 3 days in growth medium. Explants were removed after 2 weeks and PCs were expanded after one passage in culture for *in vivo* and *in vitro* experiments.

In Vitro Differentiation

In vitro differentiation of PCs in the three mesenchymal lineages (osteoblasts, chondrocytes, and adipocytes) were performed as described previously (Duchamp de Lageneste et al., 2018). Osteogenic, adipogenic, and chondrogenic differentiation was performed for 4 weeks, 10 and 3 days, respectively. Cells were stained with alizarin red S, oil red O, or Alcian blue solutions to stain mineralization, lipid droplets, and glycosaminoglycans, respectively.

Flow Cytometry Analyses

PCs were isolated as described above and incubated with CD45-BV650 (563410, BD Biosciences), TER-119-BV650 (747739, BD Biosciences), TIE2-APC (124009, BioLegend), CD51-BV711 (740755, BD Biosciences), THY1-BV786 (564365, BD Biosciences), and 6C3-PeCy7 (BLE108313, BioLegend) in PBS-brilliant stain buffer (563794, BD Biosciences) for 15 min on ice protected from light. Cells were then washed by adding 1 mL of wash medium (MEMα supplemented with 2% lot-selected non-heat-inactivated FBS and 1% penicillin-streptomycin) and centrifuged for 10 min at 1,500 rpm. Supernatant was discarded and cell pellets were resuspended in 200 μL of wash medium and 7-AAD (559925, BD Biosciences) was added just before analysis as viability marker. Beads (01-2222-42, Thermo Fischer Scientific) were used for initial compensation set up and FMO (fluorescence minus one) controls were used to determine background level of each color. Analyses were performed on a BD LSRFortessa SORP (BD Biosciences) and results analyzed using FlowJo software, version 10.2.

Tibial Fracture, Unicortical Defect Injury, and Cell Transplantation

Open non-stabilized tibial fractures and unicortical defects were performed as previously described to study bone regeneration through endochondral and intramembranous ossification, respectively (Duchamp de Lageneste et al., 2018). For cell transplantation, 100,000 PCs were embedded in a fibrin gel (Baxter, France, Tisseel, composed of human fibrinogen 15 mg/mL and thrombin 9 mg/mL) and the cell pellet was transplanted at the time of fracture (Abou-Khalil et al., 2015; Duchamp de Lageneste et al., 2018).

PD173074 Treatment

Prx1^{Cre};*Fgfr3*$^{Y367C/+}$ mice received intraperitoneal injections of PD173074 (Sigma, St. Louis, MO, ref. P2499) at a concentration of 10 mg/kg per injection. One injection per day was performed on the day of tibial fracture and every day until harvesting at days 7 and 14 post-fracture. Control mice were injected daily with 5% DMSO in PBS.

Histomorphometry and *In Vivo* Cell Tracing

Mice were euthanized, and tibias were harvested and fixed for 24 h in 4% paraformaldehyde followed by decalcification in 19% EDTA for 3 weeks. Tibias were embedded in paraffin or O.C.T. compound. Ten-micron-thick cryosections or paraffin sections were stained with Safranin O (SO), Masson's trichrome (TC), or Picrosirius (PS) for histomorphometric analyses to determine callus, cartilage, bone, and fibrosis volumes as described previously (Abou-Khalil et al., 2014, 2015). In brief, images of the stained sections were captured and analyzed using ZEN software to determine the surface of callus and cartilage on SO sections, bone on TC sections, and fibrosis on PS sections. Total volume of each component was determined using the dedicated formula (Abou-Khalil et al.,

2014). Hypertrophic cartilage was quantified based on the cell morphology of hypertrophic chondrocytes (cells with a large cytoplasm in the SO^+ area and specific organization) (Su et al., 2008). For cell transplantation experiments, Prx1-derived cells expressing GFP were detected by analysis of GFP signal on cryosections adjacent to SO and TC. Images were captured using a Zeiss Imager D1 AX10 light microscope and ZEN software (Carl Zeiss Microscopy, Gottinger, Germany).

Vascularization at the cartilage-to-bone transition zone was quantified at three different regions per section and on two sections per sample. The surface of AF488 and AF546 signal per μm^2 was measured using ZEN software (Carl Zeiss Microscopy). Numbers of $KI67^+$ and $SOX2^+$ hypertrophic chondrocytes was determined by the average count of positive cells in three sections at the center of the callus per sample.

Immunofluorescence and Immunohistochemistry

For immunofluorescence, tibias and fracture calluses were processed as described previously (Kusumbe et al., 2015). Samples were fixed in ice-cold paraformaldehyde 4% for 4 h, decalcified in EDTA 19% at 4°C for 2–5 days and placed in sucrose 30% for 24 h before embedding in O.C.T. Thirty micron thick cryosections were collected for CD31/EMCN immunostaining and 10-μm-thick cryosections for the other markers. After blocking in 5% serum 0.25% Triton PBS for 1 h, sections were incubated with the primary antibody overnight at 4°C to label CD31 (AF3628, 1:100, BioTechne), EMCN (sc-65495, 1:100, Santa Cruz), COLX (ab58632, 1:200, Abcam), OSX (ab22552, 1:200, Abcam), SOX2 (ab97959, 1:400, Abcam), SOX9 (ab182530, 1:1,000, Abcam), KI67 (ab15580, 1:200, Abcam), and POSTN (AF2955,1:400, BioTechne). Sections were washed and incubated with secondary antibody Alexa Fluor 488 goat anti-rabbit (A11034, 1:1,000, Invitrogen), Alexa Fluor 488 donkey anti-goat (A11055, 1:1,000, Invitrogen), Alexa Fluor 546 goat anti-rabbit (A11056, 1:1,000, Invitrogen), Alexa Fluor 647 goat anti-rabbit (A-21245, 1:1,000, Invitrogen), and rhodamine donkey anti-rat (712-025-150, 1:400, Jackson ImmunoResearch). Sections were mounted with Fluoromount-G mounting medium with DAPI (00-4959-52, Life Technologies).

For immunohistochemistry staining, sections were rehydrated and incubated in 5% serum 0.25% Triton PBS for 1 h before incubation at 4°C overnight with primary antibody anti-VEGF (ab46154, 1:750, Abcam) and SOX9 (ab182530, 1:1,000, Abcam). Sections were incubated with biotin-coupled secondary antibody, followed by streptavidin-HRP (554066, 1:200, BD Biosciences) and staining was revealed using DAB-Plus Substrate Kit (002020, Invitrogen).

For COLX immunostaining a Dako EnVision Kit (N.2031501005; 1:50, BIOCYC) was used.

Micro-Computed Tomography Imaging

The injured tibia were dissected and micro-CT images were captured with a SkyScan 1172 micro-CT (Bruker, Hamburg, Germany) using the following settings: 80 kV, 100 μA, exposure time 100 ms, filter Al 0.5, and pixel size 19.98 μm. The scanned images were reconstructed as a stack of slices of each sample using Nrecon software (Bruker, Hamburg, Germany) and DataViewer software (Bruker, Hamburg, Germany). The callus bone volume was quantified by delimitating the callus area without the cortex using CTan software (Bruker, Hamburg, Germany).

Statistical Analyses

Statistical significance was determined with two-sided Mann-Whitney test and reported in GraphPad Prism v.6.0a. p values were determined as follows: $*p \leq 0.05$, $**p < 0.01$, $***p < 0.005$. All samples were included. All analyses were performed using a blind numbering system.

SUPPLEMENTAL INFORMATION

Supplemental Information can be found online at https://doi.org/10.1016/j.stemcr.2020.08.005.

AUTHOR CONTRIBUTIONS

C. Colnot conceived the project and wrote the paper. A.J., S.P., and O.D.d.L. performed the experiments, analyzed the data, and wrote the paper. C. Carvalho performed the experiments. M.B. assisted with micro-CT analyses. L.L.-M. provided the *Fgfr3*$^{Y367C/+}$ mice, provided help to generate immunostaining data, and reviewed the manuscript.

ACKNOWLEDGMENTS

We thank C. Benoit and T. Horville for technical assistance and advice, C. Cordier and J. Megret of the Imagine Institute Flow Cytometry Core, E. Panafieu and C. Dicu of the Imagine Institute Animal Facility. Micro-CT analyses were performed at the B3OA laboratory IMOSAR platform. This research was supported by Inserm ATIP-Avenir, France, Osteosynthesis and Trauma Care Foundation, Switzerland, Fondation de l'Avenir, France, Agence Nationale de la Recherche ANR-13-BSV1 and ANR-18-CE14-0033, France, NIAMS R01 AR072707, United States to C. Colnot. A.J., S.P., and O.D.d.L. were supported by PhD fellowships from Paris University.

Received: April 3, 2020
Revised: August 10, 2020
Accepted: August 11, 2020
Published: September 10, 2020

REFERENCES

Abou-Khalil, R., Yang, F., Lieu, S., Julien, A., Perry, J., Pereira, C., Relaix, F., Miclau, T., Marcucio, R., and Colnot, C. (2015). Role of muscle stem cells during skeletal regeneration. Stem Cells *33*, 1501–1511.

Abou-Khalil, R., Yang, F., Mortreux, M., Lieu, S., Yu, Y.Y., Wurmser, M., Pereira, C., Relaix, F., Miclau, T., Marcucio, R.S., and Colnot, C. (2014). Delayed bone regeneration is linked to chronic inflammation in murine muscular dystrophy. J. Bone Miner Res. *29*, 304–315.

Bonaventure, J., Rousseau, F., Legeai-Mallet, L., le Merrer, M., Munnich, A., and Maroteaux, P. (1996). Common mutations in the fibroblast growth factor receptor 3 (FGFR 3) gene account

for achondroplasia, hypochondroplasia, and thanatophoric dwarfism. Am. J. Med. Genet. *63*, 148–154.

Chan, C.K., Seo, E.Y., Chen, J.Y., Lo, D., Mcardle, A., Sinha, R., Tevlin, R., Seita, J., Vincent-Tompkins, J., Wearda, T., et al. (2015). Identification and specification of the mouse skeletal stem cell. Cell *160*, 285–298.

Chen, H., Sun, X., Yin, L., Chen, S., Zhu, Y., Huang, J., Jiang, W., Chen, B., Zhang, R., Chen, L., et al. (2017). PTH 1-34 ameliorates the osteopenia and delayed healing of stabilized tibia fracture in mice with achondroplasia resulting from gain-of-function mutation of FGFR3. Int. J. Biol. Sci. *13*, 1254–1265.

Chilbule, S.K., Dutt, V., and Madhuri, V. (2016). Limb lengthening in achondroplasia. Indian J. Orthop. *50*, 397–405.

Colnot, C. (2009). Skeletal cell fate decisions within periosteum and bone marrow during bone regeneration. J. Bone Miner Res. *24*, 274–282.

Debnath, S., Yallowitz, A.R., Mccormick, J., Lalani, S., Zhang, T., Xu, R., Li, N., Liu, Y., Yang, Y.S., Eiseman, M., et al. (2018). Discovery of a periosteal stem cell mediating intramembranous bone formation. Nature *562*, 133–139.

Du, X., Xie, Y., Xian, C.J., and Chen, L. (2012). Role of FGFs/FGFRs in skeletal development and bone regeneration. J. Cell Physiol. *227*, 3731–3743.

Duchamp de Lageneste, O., Julien, A., Abou-Khalil, R., Frangi, G., Carvalho, C., Cagnard, N., Cordier, C., Conway, S.J., and Colnot, C. (2018). Periosteum contains skeletal stem cells with high bone regenerative potential controlled by Periostin. Nat. Commun. *9*, 773.

Hu, D.P., Ferro, F., Yang, F., Taylor, A.J., Chang, W., Miclau, T., Marcucio, R.S., and Bahney, C.S. (2017). Cartilage to bone transformation during fracture healing is coordinated by the invading vasculature and induction of the core pluripotency genes. Development *144*, 221–234.

Jonquoy, A., Mugniery, E., Benoist-Lasselin, C., Kaci, N., le Corre, L., Barbault, F., Girard, A.L., le Merrer, Y., Busca, P., Schibler, L., et al. (2012). A novel tyrosine kinase inhibitor restores chondrocyte differentiation and promotes bone growth in a gain-of-function Fgfr3 mouse model. Hum. Mol. Genet. *21*, 841–851.

Kitoh, H., Mishima, K., Matsushita, M., Nishida, Y., and Ishiguro, N. (2014). Early and late fracture following extensive limb lengthening in patients with achondroplasia and hypochondroplasia. Bone Joint J. *96-B*, 1269–1273.

Kusumbe, A.P., Ramasamy, S.K., Starsichova, A., and Adams, R.H. (2015). Sample preparation for high-resolution 3D confocal imaging of mouse skeletal tissue. Nat. Protoc. *10*, 1904–1914.

Logan, M., Martin, J.F., Nagy, A., Lobe, C., Olson, E.N., and Tabin, C.J. (2002). Expression of Cre recombinase in the developing mouse limb bud driven by a Prxl enhancer. Genesis *33*, 77–80.

Martin, L., Kaci, N., Estibals, V., Goudin, N., Garfa-Traore, M., Benoist-Lasselin, C., Dambroise, E., and Legeai-Mallet, L. (2018). Constitutively-active FGFR3 disrupts primary cilium length and IFT20 trafficking in various chondrocyte models of achondroplasia. Hum. Mol. Genet. *27*, 1–13.

Matsushita, Y., Nagata, M., Kozloff, K.M., Welch, J.D., Mizuhashi, K., Tokavanich, N., Hallett, S.A., Link, D.C., Nagasawa, T., Ono, W., and Ono, N. (2020). A Wnt-mediated transformation of the bone marrow stromal cell identity orchestrates skeletal regeneration. Nat. Commun. *11*, 332.

Mugniery, E., Dacquin, R., Marty, C., Benoist-Lasselin, C., de Vernejoul, M.C., Jurdic, P., Munnich, A., Geoffroy, V., and Legeai-Mallet, L. (2012). An activating Fgfr3 mutation affects trabecular bone formation via a paracrine mechanism during growth. Hum. Mol. Genet. *21*, 2503–2513.

Nakajima, A., Nakajima, F., Shimizu, S., Ogasawara, A., Wanaka, A., Moriya, H., Einhorn, T.A., and Yamazaki, M. (2001). Spatial and temporal gene expression for fibroblast growth factor type I receptor (FGFR1) during fracture healing in the rat. Bone *29*, 458–466.

O'Keefe, R.J., Tuan, R.S., Lane, N.E., Awad, H.A., Barry, F., Bunnell, B.A., Colnot, C., Drake, M.T., Drissi, H., Dyment, N.A., et al. (2020a). American Society for Bone and Mineral Research—Orthopaedic Research Society joint task force report on cell-based therapies. J. Bone Miner Res. *35*, 3–17.

O'Keefe, R.J., Tuan, R.S., Lane, N.E., Awad, H.A., Barry, F., Bunnell, B.A., Colnot, C., Drake, M.T., Drissi, H., Dyment, N.A., et al. (2020b). American Society for Bone and Mineral Research—Orthopaedic Research Society joint task force report on cell-based therapies—secondary publication. J. Orthop. Res. *38*, 485–502.

Ortinau, L.C., Wang, H., Lei, K., Deveza, L., Jeong, Y., Hara, Y., Grafe, I., Rosenfeld, S.B., Lee, D., Lee, B., et al. (2019). Identification of functionally distinct Mx1+alphaSMA+ periosteal skeletal stem cells. Cell Stem Cell *25*, 784–796 e5.

Pannier, S., Couloigner, V., Messaddeq, N., Elmaleh-Berges, M., Munnich, A., Romand, R., and Legeai-Mallet, L. (2009). Activating Fgfr3 Y367C mutation causes hearing loss and inner ear defect in a mouse model of chondrodysplasia. Biochim. Biophys. Acta *1792*, 140–147.

Rousseau, F., Bonaventure, J., Legeai-Mallet, L., Pelet, A., Rozet, J.M., Maroteaux, P., le Merrer, M., and Munnich, A. (1994). Mutations in the gene encoding fibroblast growth factor receptor-3 in achondroplasia. Nature *371*, 252–254.

Schmid, G.J., Kobayashi, C., Sandell, L.J., and Ornitz, D.M. (2009). Fibroblast growth factor expression during skeletal fracture healing in mice. Dev. Dyn. *238*, 766–774.

Su, N., Yang, J., Xie, Y., Du, X., Lu, X., Yin, Z., Yin, L., Qi, H., Zhao, L., Feng, J., and Chen, L. (2008). Gain-of-function mutation of FGFR3 results in impaired fracture healing due to inhibition of chondrocyte differentiation. Biochem. Biophys. Res. Commun. *376*, 454–459.

Van Gastel, N., Torrekens, S., Roberts, S.J., Moermans, K., Schrooten, J., Carmeliet, P., Luttun, A., Luyten, F.P., and Carmeliet, G. (2012). Engineering vascularized bone: osteogenic and proangiogenic potential of murine periosteal cells. Stem Cells *30*, 2460–2471.

Worthley, D.L., Churchill, M., Compton, J.T., Tailor, Y., Rao, M., Si, Y., Levin, D., Schwartz, M.G., Uygur, A., Hayakawa, Y., et al. (2015). Gremlin 1 identifies a skeletal stem cell with bone, cartilage, and reticular stromal potential. Cell *160*, 269–284.

Yang, L., Tsang, K.Y., Tang, H.C., Chan, D., and Cheah, K.S. (2014). Hypertrophic chondrocytes can become osteoblasts and

osteocytes in endochondral bone formation. Proc. Natl. Acad. Sci. U S A *111*, 12097–12102.

Zhang, X., Xie, C., Lin, A.S., Ito, H., Awad, H., Lieberman, J.R., Rubery, P.T., Schwarz, E.M., O'keefe, R.J., and Guldberg, R.E. (2005). Periosteal progenitor cell fate in segmental cortical bone graft transplantations: implications for functional tissue engineering. J. Bone Miner Res. *20*, 2124–2137.

Zhou, B.O., Yue, R., Murphy, M.M., Peyer, J.G., and Morrison, S.J. (2014a). Leptin-receptor-expressing mesenchymal stromal cells represent the main source of bone formed by adult bone marrow. Cell Stem Cell *15*, 154–168.

Zhou, X., von der Mark, K., Henry, S., Norton, W., Adams, H., and de Crombrugghe, B. (2014b). Chondrocytes transdifferentiate into osteoblasts in endochondral bone during development, postnatal growth and fracture healing in mice. PLoS Genet. *10*, e1004820.

Stem Cell Reports, Volume *15*

Supplemental Information

FGFR3 in Periosteal Cells Drives Cartilage-to-Bone Transformation in Bone Repair

Anais Julien, Simon Perrin, Oriane Duchamp de Lageneste, Caroline Carvalho, Morad Bensidhoum, Laurence Legeai-Mallet, and Céline Colnot

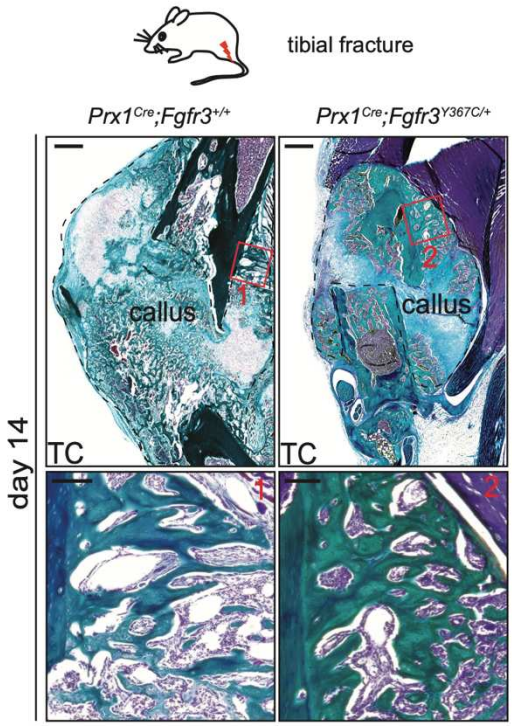

Figure S1. Direct bone formation at the periphery of the callus is not affected in *Prx1^{Cre};Fgfr3$^{Y367C/+}$* mice.

(A) Representative Masson's Trichrome (TC) staining of tibial fracture calluses from *Prx1^{Cre};Fgfr3$^{+/+}$* (control) and *Prx1^{Cre};Fgfr3$^{Y367C/+}$* (mutant) mice at day 14 post-fracture and high magnification of new bone area at the periphery of the callus showing normal bone deposition in mutant compared to control. Scale bar: 1mm, high magnification: 100 μm.

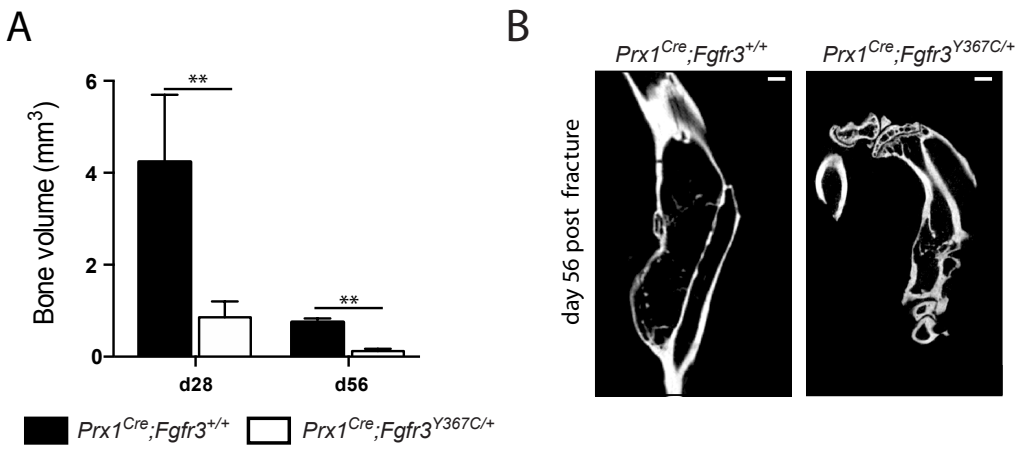

Figure S2. Reduced bone formation in *Prx1^{Cre};Fgfr3$^{Y367C/+}$* mutant calluses.

(A) Quantification of bone volume via µCT in the callus of *Prx1^{Cre};Fgfr3$^{+/+}$* control and *Prx1^{Cre};Fgfr3$^{Y367C/+}$* mutant mice at day 28 and 56 post-fracture (n=4-5 per group). (B) Representative µCT images of *Prx1^{Cre};Fgfr3$^{Y367C/+}$* and *Prx1^{Cre};Fgfr3$^{+/+}$* calluses at 56 days post-fracture. Values represent the mean ± SD. **p<0.01 using Mann-Whitney test. Scale bar: 1mm.

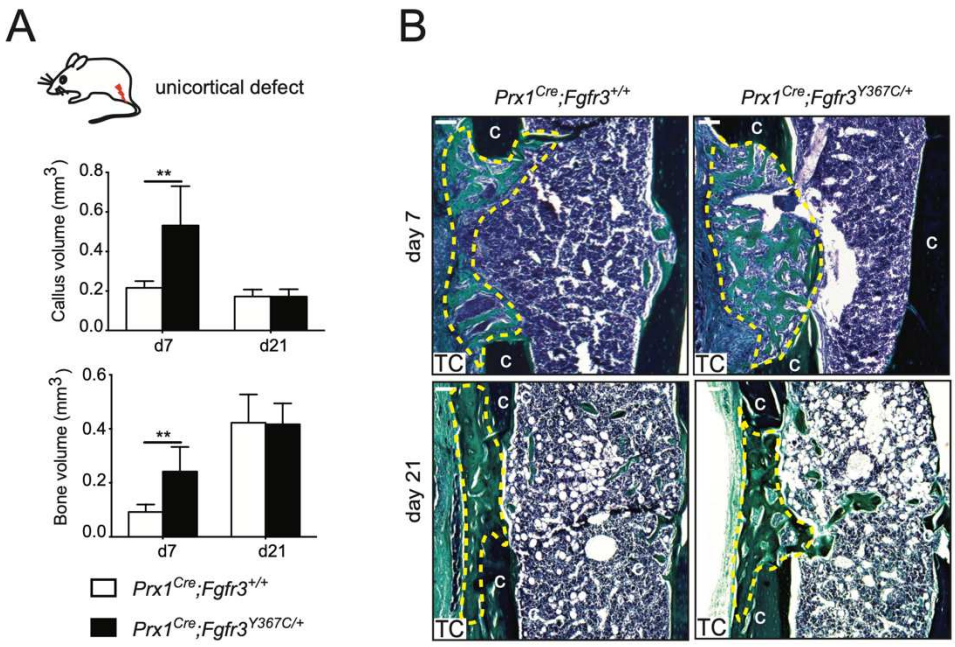

Figure S3. Healing via intramembranous ossification is unaltered in *Prx1^{Cre};Fgfr3$^{Y367C/+}$* mice.

(A) Histomorphometric analyses of callus and bone volumes at day 7 and 21 post-unicortical defect in the tibia of *Prx1^{Cre};Fgfr3$^{+/+}$* and *Prx1^{Cre};Fgfr3$^{Y367C/+}$* mice. n=5 per group. (B) Representative TC staining of cortical defect calluses from *Prx1^{Cre};Fgfr3$^{+/+}$* and *Prx1^{Cre};Fgfr3$^{Y367C/+}$* mice at day 7 (upper panels) and day 21 (lower panels). Scale bar: 0.1mm. Values represent the mean ± SD. **p<0.01 using Mann-Whitney test.

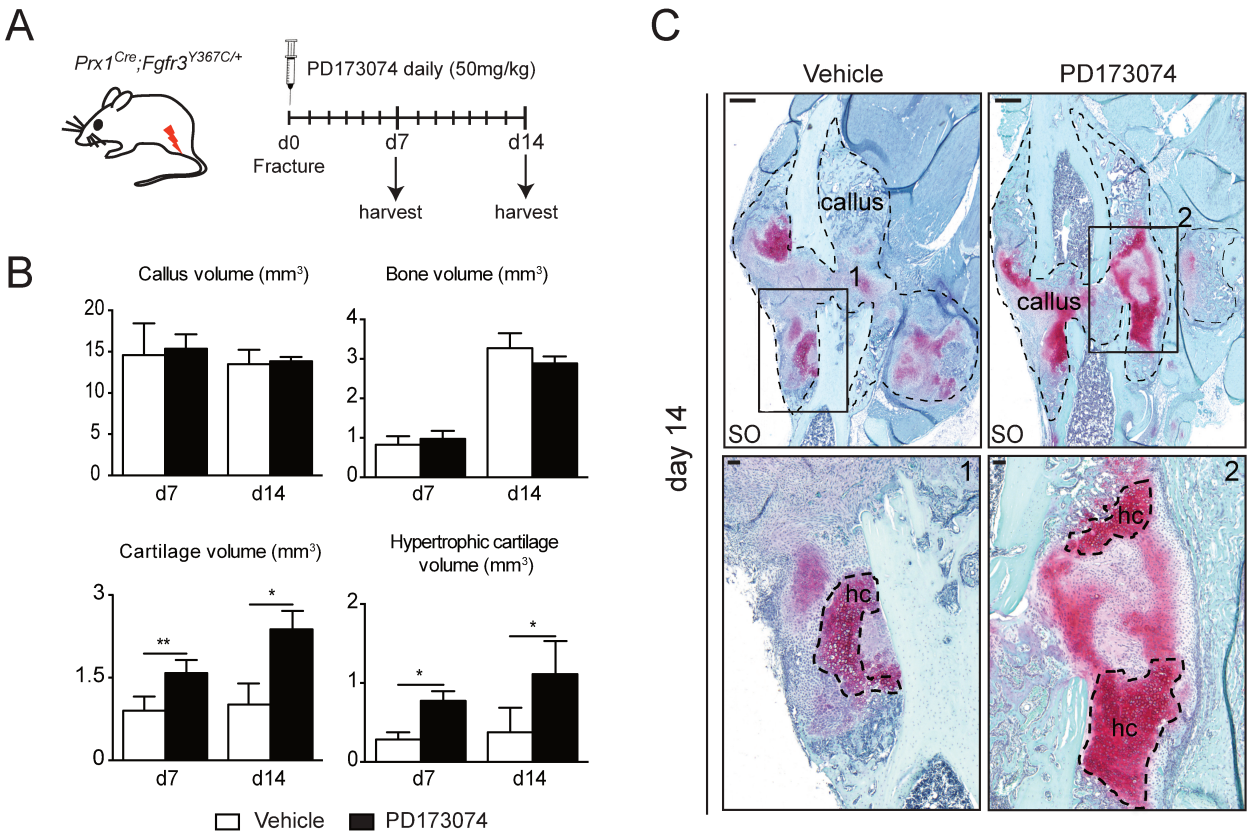

Figure S4. PD173074 treatment increases cartilage and hypertrophic cartilage in the callus of *Prx1^{Cre};Fgfr3$^{Y367C/+}$* mice.

(A) Experimental design of daily injection of PD173074 (50mg/kg) or vehicle (control) in *Prx1^{Cre};Fgfr3$^{Y367C/+}$* mice with tibial fracture. (B) Histomorphometric analysis of total callus, bone, cartilage and hypertrophic cartilage volumes of PD173074 treated and control mice at days 7 and 14 post-fracture. (n=4 or 5 per group). (C) Representative callus sections of *Prx1^{Cre};Fgfr3$^{Y367C/+}$* treated and control mice stained with Safranin'O (SO) at day 14 post-fracture and high magnification of hypertrophic cartilage area (Box 1-2). Scale bar: 1mm, high magnification: 150 µm.

Values represent the mean ± SD. **p<0.01 using Mann-Whitney test.

REAGENT or RESOURCE	SOURCE	IDENTIFIER
Antibodies		
Goat polyclonal anti-CD31	BioTechne	AF3628
Rat polyclonal anti-EMCN	Santa Cruz	sc-65495
Rabbit polyclonal anti-COLX	Abcam	ab58362
Rabbit polyclonal anti-OSX	Abcam	ab22552
Rabbit polyclonal anti-SOX2	Abcam	ab97959
Rabbit monoclonal anti-SOX9	Abcam	ab182530
Rabbit polyclonal anti-KI67	Abcam	ab15580
Rabbit polyclonal anti-VEGFA	Abcam	ab46154
Goat polyclonal anti-POSTN	BioTechne	AF2955
Mouse monoclonal anti-COLX	BIOCYC	N.2031501005
Alexa Fluor 488 goat anti-rabbit	Invitrogen	A11034
Alexa Fluor 488 donkey anti-goat	Invitrogen	A11055
Alexa Fluor 546 goat anti-rabbit	Invitrogen	A11056,
Alexa Fluor 647 goat anti-rabbit	Invitrogen	A-21245
Rhodamine donkey anti-rat	Jackson immunoresearch	712-025-150
streptavidin-HRP	BD Biosciences	554066
CD45-BV650	BD Biosciences	563410
TER119-BV650	BD Biosciences	747739
CD51-BV711	BD Biosciences	740755
THY1-BV786	BD Biosciences	564365
TIE2-APC	BioLegend	124009
6C3-PeCy7	BioLegend	BLE108313
Chemicals		
PD173074	Sigma	P2499
Experimental Models		
Mouse : C57BL/6ScNj, $Prx1^{Cre}$	Jackson Laboratory	005584
Mouse : Rosa-tdTomato-EGFP	Jackson Laboratory	007676
Mouse : $Fgfr3^{Y367C}$	Laurence Legeai Mallet Laboratory	
Softwares		
FlowJo, LLC software	FlowJo, LLC	
ZEN software	Carl Zeiss	
Ctan	Bruker	
GraphPad Prism	GraphPad	

Article 3

Pro-fibrotic Schwann Cells and Skeletal Stem/Progenitor Cells cause Congenital Pseudarthrosis of the Tibia in NF1

Simon Perrin, Sanela Protic, Ingrid Laurendeau, Oriane Duchamp de Lageneste, Nicolas Panara, Katarzyna Radomska, Odile Ruckebusch, Marine Luka, Cécile Masson, Stéphanie Pannier, Philippe Wicart, Smail Hadj-Rabia, Mohammed Zarhrate, Mickael Ménager, Dominique Vidaud, Piotr Topilko, Béatrice Parfait and Céline Colnot

Research article

to be submitted

Congenital pseudarthrosis of the tibia (CPT) is a severe pediatric bone repair disorder leading to spontaneous tibial fracture and fibrous non-union. CPT can be classified as isolated CPT or NF1-related CPT for patients affected with the genetic disorder Neurofibromatosis type 1 (NF1). NF1 is caused by mutation in the *NF1* gene encoding the RAS/MAPK regulator Neurofibromin. NF1 patients develop peripheral nerve tumors (neurofibromas), skin hyperpigmentation and orthopedic manifestations including CPT. Neurofibromas and skin hyperpigmentation are caused by *NF1* biallelic inactivation in Schwann cells and melanocytes respectively. *NF1* biallelic inactivation was detected at pseudarthrosis site but the cellular origin of CPT remains unknown. A new mouse model of NF1, the *Prss56-Nf1 KO* model, was recently developed by inactivating *Nf1* in boundary cap (BC) cells. This model is the first one to recapitulate several NF1 features, including neurofibromas and skin hyperpigmentation, rising the question of a common cellular origin of all NF1 manifestations. In this study, we aimed to elucidated the cellular origin and pathogenic mechanisms of CPT through the combined analysis of samples from patients with CPT and the *Prss56-Nf1 KO* mouse model. In humans, we investigated the localization of biallelic *NF1* inactivation by sequencing of bone samples from CPT patients. Our results showed that CPT is associated with *NF1* biallelic inactivation in periosteum and pSSPCs from the pseudarthrosis site. Biallelic inactivation of *NF1* was found in patients with NF1-related and isolated CPT, indicating that the majority of CPT is related to *NF1* biallelic inactivation. *NF1* loss induces overactivation of the MAPK pathway in the periosteum and pSSPCs at pseudarthrosis site. Transcriptomic analyses of pathological periosteum from the pseudarthrosis site and control periosteum from the iliac crest showed the presence of pro-fibrotic pSSPCs at the pseudarthrosis site. Periosteal SSPCs from the pseudarthrosis site display impaired fate and form fibrosis after transplantation at the fracture site of immunodeficient mice.

To elucidate the cellular and molecular mechanisms of CPT, we studied the *Prss56-Nf1 KO* mouse model. We showed that this model recapitulates a pseudarthrosis phenotype after fracture. By cell lineage analysis, we showed that BC derivatives correspond to a rare population of cells in bone, including a subpopulation of SSPCs and Schwann cells in the periosteum. After fracture, BC-derivatives are present in cartilage and bone of control mice. In *Prss56-Nf1 KO* mice, BC-derived cells are located in bone and fibrosis and their contribution to cartilage is strongly reduced. *Nf1*-mutated pSSPCs show an intrinsic differentiation defect, and form fibrosis after fracture. Analysis of the dynamic of MAPK pathway activation in pSSPCs after fracture showed reduced activation of this pathway as cells transition from fibrogenic to chondrogenic state. *Nf1*-mutated pSSPCs exhibit overactivation of the MAPK pathway blocking their transition to chondrogenesis and causing their retention in the fibrogenic stage. In addition to this impairment of *Nf1*-mutated pSSPCs, we demonstrated that the fracture environment of *Prss56-Nf1 KO* mutant mice affects the differentiation of wild-type pSSPCs, driving them to form fibrosis as well. The pro-fibrotic effect of the mutant environment is mediated by *Nf1*-deficient Schwann cells. We identified the pro-fibrotic factor TGFβ as one of the factors involved in the impaired differentiation of wild-type pSSPCs. Inhibition of TGFβ corrects the pseudarthrosis phenotype in *Prss56-Nf1 KO* mice. Overall, this study unravels the cellular origin of CPT and the mechanisms leading to the lack of bone repair following *NF1* inactivation in the periosteum. The understanding of the pathological mechanisms of CPT opens the way to the development of new specific therapeutic strategies, such as the use of anti-fibrotic agents targeting TGFβ.

Pro-fibrotic Schwann cells and skeletal stem/progenitor cells cause congenital pseudarthrosis of the tibia in NF1

Simon Perrin[1], Sanela Protic[1], Ingrid Laurendeau[2], Oriane Duchamp de Lageneste[1], Nicolas Panara[2], Odile Ruckebusch[3], Marine Luka[4,5], Cécile Masson[6,7], Stéphanie Pannier[8], Philippe Wicart[8], Smail Hadj-Rabia[9], Katarzyna Radomska[1], Mohammed Zarhrate[10,11], Mickael Ménager[4,5], Dominique Vidaud[2], Piotr Topilko[1], Béatrice Parfait[2] and Céline Colnot[1]

[1] Univ Paris Est Creteil, INSERM, IMRB, Creteil, France

[2] INSERM UMR S1016, Institut Cochin, Université de Paris, Paris, France

[3] Univ Paris Est Creteil, INSERM, IMRB, Plateforme de Cytométrie en flux, Creteil, France.

[4]Paris Cité University, Imagine Institute, Laboratory of Inflammatory Responses and Transcriptomic Networks in Diseases, Atip-Avenir Team, INSERM UMR 1163, Paris, France.

[5] Labtech Single-Cell@Imagine, Imagine Institute, INSERM UMR 1163, Paris, France.

[6] Bioinformatics Core Facility, Institut Imagine-Structure Fédérative de Recherche Necker, INSERM U1163

[7] INSERM US24/CNRS UAR3633, Paris Cité University, Paris, France

[8] Department of Pediatric Orthopedic Surgery and Traumatology, Necker-Enfants Malades Hospital, AP-HP, Paris Cité University, Paris, France

[9] Department of Dermatology, Reference Center for Rare Skin Diseases (MAGEC), Imagine Institute, Necker-Enfants Malades Hospital, AP-HP, Paris Cité University, Paris, France.

[10] Genomics Core Facility, Institut Imagine-Structure Fédérative de Recherche Necker, INSERM U1163

[11] INSERM US24/CNRS UAR3633, Paris Cité University, Paris, France

Summary

Congenital pseudarthrosis of the tibia (CPT) is a severe orthopedic condition marked by spontaneous tibial fractures and fibrous non-union. Half of CPT patients are affected by the multisystemic disorder Neurofibromatosis type 1 (NF1), due to mutations in the tumor suppressor gene NF1. Here, we uncover the cellular origin and pathogenic mechanisms of CPT in parallel analyses of CPT patients and *Prss56-Nf1 KO* mice carrying *Nf1* gene inactivation in Boundary Cap (BC) cells. We identify *NF1* biallelic inactivation and pro-fibrotic periosteal skeletal stem/progenitor cells (pSSPCs) in human periosteum. In mice, *Nf1* loss in BC-derived pSSPCs and Schwann cells (SCs) in periosteum leads to tibial pseudarthrosis. This phenotype is due to fibrotic accumulation at the injury site caused by *Nf1*-deficient pSSPCs that adopt a pro-fibrotic fate and *Nf1*-deficient SCs that induce fibrogenic differentiation of wild-type pSSPCs. TGFβ inhibition corrects the pseudarthrosis phenotype in mice, suggesting new therapeutic strategies targeting pro-fibrotic factors for CPT and other NF1 symptoms.

Keywords

periosteum – bone repair – Neurofibromatosis type 1 – Congenital Pseudarthrosis – Schwann cells – skeletal stem/progenitor cells

Introduction

Congenital pseudarthrosis of the tibia (CPT) is a very severe pediatric bone repair disorder characterized by tibial bowing at birth leading to spontaneous fracture and fibrous non-union. Despite progress in surgical procedures, CPT treatment remains highly challenging with a significant risk of amputation (Pannier, 2011). CPT can be classified as isolated CPT, of unknown etiology, or NF1-related CPT in patients also diagnosed with Neurofibromatosis type 1 (NF1). NF1 is one of the most common multisystemic genetic disorders that affects 1 in 3000 births. It predisposes patients to a variety of symptoms, including benign nerve sheath tumors, called cutaneous and plexiform neurofibromas (NFBs), skin hyperpigmentation (Café-au-lait macules, CALMs), learning disabilities, optic pathway glioma, and orthopedic manifestations (Gutmann et al., 2017). NF1 is caused by heterozygous mutations in the *NF1* gene encoding the tumor-suppressor neurofibromin, a negative regulator of RAS and the MAPK pathway. However, the cellular origin and spatio-temporal variability of NF1 symptoms are poorly understood. NFBs and CALMs have been shown to result from *NF1* biallelic inactivation in specific cell types, i.e., Schwann cells and melanocytes respectively (Kluwe et al., 1999; Maertens et al., 2006). The cell type(s) affected in other symptoms such as bone lesions are still unknown. Until now, most studies on NF1-related bone phenotypes have focused on the impact of *Nf1* inactivation in the skeletal lineage independent of other NF1 symptoms (de la Croix Ndong et al., 2014; El Khassawna et al., 2012; Kamiya et al., 2017; Sharma et al., 2013; Wang et al., 2011). However, other studies in the last decade have suggested that *NF1* second hit mutations occur in neural crest derivatives during development (Le et al., 2011; Wu et al., 2008; Zhu et al., 2002). Recent work by Radomska et al. demonstrated that *Prss56*-expressing boundary cap (BC) cells, a transient cell population of plastic neural crest derivatives, are the cellular origin of cutaneous and plexiform NFBs, as well as skin hyperpigmentation (Radomska et al., 2019). The common BC origin of NF1 dermatological and neurological lesions raises the question of a common cellular origin of all NF1 symptoms, including CPT. *NF1* biallelic inactivation has been detected in CPT, and clinical studies have reported pathological periosteum at pseudarthrosis sites, suggesting its involvement in CPT (Brekelmans et al., 2019; Hermanns-Sachweh et al., 2005; Stevenson et al., 2006). The periosteum, the tissue on the outer layer of bones, is a major source of skeletal stem/progenitor cells (SSPCs), forming cartilage and bone after fracture, as well as a source of immune, endothelial and neural cells for bone repair (Debnath et al., 2018; Duchamp de Lageneste et al., 2018; Julien et al., 2022; Li et al., 2019; Matthews et al., 2021;

Raggatt et al., 2014; van Gastel et al., 2020). In this study, we establish the cellular origin of CPT by the combined analysis of bone tissues from CPT patients and the *Prss56-Nf1* KO mouse model *(Prss56^{Cre}; R26^{tdTom}; Nf1$^{fl/fl}$* and *Prss56^{Cre}; R26^{tdTom}; Nf1$^{fl/-}$*). Using targeted *NF1* gene sequencing and single nuclei RNAseq (snRNAseq), we found that CPT is associated with *NF1* biallelic inactivation in human periosteum and that pathological periosteum contains pro-fibrotic periosteal SSPCs (pSSPCs). Tibial fracture in *Prss56-Nf1 KO* mice induced a pseudarthrosis-like phenotype with absence of bone bridging and fibrotic accumulation. We discover that BC-derived *Nf1*-deficient pSSPCs and Schwann cells (SCs) within periosteum contribute together to the pseudarthrosis phenotype. Using single nuclei RNAseq analyses of mouse periosteum, we elucidate the role of the MAPK pathway in pSSPCs activation and provide the molecular mechanism underlying the fibrotic fate of *Nf1*-deficient pSSPCs. We show that paracrine factors in the *Prss56-Nf1 KO* fracture environment switch the fate of wild type SSCPs toward fibrosis and that *Nf1*-deficient SCs play a central role in mediating this paracrine effect causing the pseudarthrosis phenotype. Furthermore, we identify the pro-fibrotic factor TGFβ as a driver of fibrotic accumulation in *Prss56-Nf1 KO* mice. BC derivatives are thus at the origin of CPT in NF1, in addition to NFBs and skin hyperpigmentation, showing that NF1 symptoms share a common cellular origin and common pathogenic mechanisms.

Results

Identification of *NF1* biallelic inactivation in pathological periosteum of CPT patients

To investigate the tissue specificity of *NF1* biallelic inactivation in CPT, we performed *NF1* targeted sequencing of tissues from the affected pseudarthrosis (PA) site, the unaffected iliac crest (IC) and blood of 17 patients undergoing surgical treatment for CPT (Fig. 1A-B, Table S1). We detected *NF1* biallelic inactivation primarly in the periosteum at PA site (13/17 patients, Fig. 1C) and in cultured pSSPCs of 8 of the 13 patients carrying 2 hits in the periosteum tissue (Fig. 1D). We also identified *NF1* biallelic inactivation in fibrous tissue (6/17 patients), in bone (6/17), and in bone marrow (4/17) at PA site and in skeletal muscle (3/14) and skin (2/14) adjacent to the PA site. *NF1* biallelic inactivation was not detected in the blood and IC. Interestingly, *NF1* biallelic inactivation was detected not only in patients with NF1-related CPT but also in patients with isolated CPT, suggesting that most CPTs are caused by *NF1* loss of function (Fig. 1E). In 4/5 patients affected by combined tibia and fibula CPT, the same *NF1* second hit was present in tibia and fibula, indicating that the second mutational event occurred early during embryogenic skeletal patterning (Fig. 1F). Additionally, we found that patients P3, P7 and P15, with isolated CPT, harbor an identical second *NF1* hit mutation in PA periosteum and in muscle and/or skin surrounding the PA site (Fig. 1G). This suggests that the second *NF1* hit mutation happened in a non-skeletal restricted lineage. *NF1* loss was associated with overactivation of the MAPK pathway as shown by increased pERK signal in periosteum and pSSPCs from PA site, as well as increased proliferation of pSSPCs (Fig. 1H-I). Overall, CPT is associated with *NF1* biallelic inactivation in the periosteum and pSSPCs. Yet, we detected 2 patients without *NF1* mutations in PA fibrous tissue although it was found in periosteum suggesting the contribution of non-*NF1* mutant cells to CPT.

Human periosteal SSPCs at pseudarthrosis site are pro-fibrotic

To explore the impact of *NF1* biallelic inactivation on the periosteum, we compared PA periosteum from patients P5 and P13 with IC periosteum from patient P13 using single nuclei RNAseq (snRNAseq) analyses (Fig 2A, Fig S1A-C). We identified 5 main cell populations: pericytes/smooth muscle cells (SMC), endothelial cells, adipocytes, immune cells, and SSPCs encompassing several subpopulations expressing *PDGFRA*, *ADAM12*, or osteochondral genes (Fig 2B-C, Fig S1D). The percentage of SSPCs, *ADAM12*+ SSPCs, and osteochondral SSPCs was increased in periosteum from PA site (Fig.

2D). In addition, PA periosteum displayed increased fibrogenic, osteogenic and chondrogenic lineage score, as well as increased MAPK activation and response to TGFβ compared to IC periosteum, revealing the pro-fibrotic phenotype of pSSPCs in PA periosteum (Fig. 2E). We performed RNAseq analyses of primary pSSPCs from PA site and IC. We confirmed the fibrotic phenotype of PA pSSPCs as they overexpress fibrogenic and MAPK-related genes and are enriched for Gene Ontology related to skeletal development and extracellular matrix (Fig. 2F-G). We observed impaired in vitro chondrogenic (5/6 patients) and osteogenic differentiation (4/6 patients) of pSSPCs from PA compared to IC pSSPCs (Fig. S1E-H). To investigate the impact of *NF1*-loss of function on the in vivo differentiation potential of pSSPCs, we grafted PA- or IC-derived pSSPCs at the fracture site of immunodeficient mice. PA-derived pSSPCs switched from a chondrogenic to a fibrogenic fate after fracture as they were detected within fibrotic tissue, while IC-derived pSSPCs mostly contributed to callus cartilage. In addition, PA pSSPCs increased callus fibrosis compared to IC pSSPCs confirming their pro-fibrotic properties in vivo (Fig. 2H-I).

Tibial pseudarthrosis in mice lacking *Nf1* gene in Prss56-derived boundary cap cells

To better understand the cellular bases of CPT, we investigated the *Prss56-Nf1* KO mouse model. At 3 months of age, we did not detect differences in cortical porosity and trabecular BV/TV parameters in *Prss56^{Cre}; R26^{tdTom}; Nf1$^{fl/fl}$ (Prss56-Nf1$^{fl/fl}$)* and *Prss56^{Cre}; R26^{tdTom}; Nf1$^{fl/-}$ (Prss56-Nf1$^{fl/-}$)* mutant tibia compared to *Prss56^{Cre}; R26^{tdTom}; Nf1$^{+/+}$ (Prss56-Nf1$^{+/+}$)* controls (Fig. S2A-B). After tibial fracture, reduced callus and bone volumes were detected in both *Prss56-Nf1$^{fl/fl}$* and *Prss56-Nf1$^{fl/-}$* mutant mice compared to *Prss56-Nf1$^{+/+}$* controls through all stages of repair, as well as delayed cartilage formation and resorption (Fig S2 C-D). From day 14 post-fracture, we observed persistence of fibrotic tissue in the callus (Fig 3A-B). Absence of bone bridging was striking by one month on microCT scans of *Prss56-Nf1$^{fl/fl}$* and *Prss56-Nf1$^{fl/-}$* mutant calluses (Fig 3C). Failed bone healing was marked by the presence of unresorbed cartilage and fibrotic tissue, composed of non-cartilaginous extracellular matrix, macrophages and blood vessels reminiscent of CPT (Fig 3E-F). *Nf1* inactivation in Prss56-derived BC cells thus leads to pseudarthrosis.

BC-derivatives give rise to pSSPCs and SCs in periosteum contributing to fracture repair and callus fibrosis

To determine the role of BC cells in the pseudarthrosis phenotype, we traced them from developmental stages through adulthood in the tibia. TdTom+ *Prss56*-expressing cells were restricted to BC at embryonic stage E12.5 (Fig. S3A). In the tibia, tdTom+ cells were localized in the perichondrium from E13.5 and in the cartilage template from E14.5, but no expression of *Prss56* was detected (Fig. S3A-B). These results indicate that tdTom+ traced cells were derived from *Prss56*-expressing BC cells that migrated into the skeletal element. Analysis of single cell RNAseq datasets of the developing hindlimbs from Kelly *et al.* confirmed the absence of *Prss56* expression in limb mesenchyme during development (Fig. S3C-E). In adult bone, lineage tracing showed that tdTom+ BC-derived cells represent a rare population of cells in uninjured tibia found predominantly within the periosteum. TdTom+ cells correspond to a population of PDGFRA+ pSSPCs and a population of SOX10+ Schwann cells (SCs, Fig. 4A). An increased number of tdTom+ was observed in the periosteum of *Prss56-Nf1*$^{fl/fl}$ mutant mice compared to controls, with equivalent proportions of pSSPCs and Schwann cells (Fig. 4B). We confirmed that the periosteum is only source of tdTom+ cells involved in the pseudarthrosis phenotype. Analyses of the other sources of cells contributing to bone repair showed that the bone marrow did not contain tdTom+ cells and tdTom+ SSPCs from the skeletal muscle did not contribute to callus formation (Fig. S4). In the fracture callus 14 days post-injury, Prss56-derived tdTom+ cells were detected in the cartilage and bone of *Prss56-Nf1*$^{+/+}$ control mice but their contribution to cartilage decreased in *Prss56-Nf1*$^{fl/fl}$ mice (Fig. 4C-D). Instead, tdTom+ cells were localized in fibrotic tissue of *Prss56-Nf1*$^{fl/fl}$ calluses and corresponded to PDGFRA+ fibrogenic cells and SOX10+ SCs (Fig. 4E). TdTom+ SCs in callus fibrosis exhibit a repair Schwann cell phenotype as they are positive for the stemness marker SOX2, are negative for the differentiation marker Myelin Basic Protein (MBP) and are not along TH+ nerves (Fig. 4E). By 28 days post-fracture, the newly formed periosteum was enriched in tdTom+ cells in *Prss56-Nf1*$^{fl/fl}$ mice (Fig 4F).

***Nf1*-deficient periosteal SSPCs fail to transition from fibrogenic to chondrogenic state**

To functionally assess the impact of *Nf1* inactivation on periosteal cell fate, we grafted periosteum or cultured pSSPCs from *Prss56-Nf1*$^{fl/fl}$ mutant or *Prss56-Nf1*$^{+/+}$ control mice at the fracture site of wild-type hosts (Fig. 5A). We observed a reduced contribution to cartilage of mutant tdTom+ periosteum-

derived cells or pSSPCs. These tdTom+ mutant cells were present in callus fibrosis, indicating an impaired fate of *Nf1*-deficient pSSPCs following fracture (Fig. 5A, Fig. S5A-E). To characterize the molecular mechanisms controlling periosteal cell fate impairment, we generated snRNAseq datasets from uninjured periosteum, and periosteum and hematoma at days 5 and 7 post-fracture (Fig 5B, Fig S6A). In the integrated dataset, we identified 10 cell populations: endothelial cells, pericytes/smooth muscle cells (SMC), Schwann cells, SSPCs, osteoblasts, fibrogenic cells, chondrocytes, adipocytes, osteoclasts and immune cells (Fig. S6B-D). Pseudotime analyses of the subset of SSPCs, fibrogenic cells, osteoblasts and chondrocytes revealed the pattern of pSSPC activation in 4 successive phases : (i) stem/progenitor phase marked by the expression of stemness markers (*Ly6a, Cd34*), predominant in uninjured dataset, (ii) immune response marked by the expression of inflammatory related-genes (*Cxcl5, Il33*), (iii) fibrogenic stage marked by active expression of extracellular matrix proteins (*Postn, Aspn*), predominant at 5 days post-fracture and (iv) a bifurcation between osteogenesis and chondrogenesis, predominant at day 7 post-fracture (Fig. 5C-D, Fig. S6E-F). Since *Nf1* is a master regulator of MAPK pathway, we assessed the MAPK pathway activation using a lineage score based on the expression of MAPK target and related genes. We observed that MAPK score increased between uninjured periosteum and day 5 post-fracture, before decreasing at day 7 (Fig. 5E). Along pseudotime, we observed an increase of MAPK score between SSPC stage and fibrogenic stage, followed by a decrease when cells engage into osteochondral lineages. In details, MAPK score was reduced in cells with high chondrogenic lineage score and *Acan* expression, but remained constant in cells with high osteogenic lineage score (Fig. 5F). This suggests that pSSPCs specifically downregulate the activation of MAPK pathway to transition from the fibrogenic stage to the chondrogenic stage. SOX9 and phosphoERK (pERK) co-immunostaining in day 7 post-fracture wild-type calluses confirmed a negative correlation between SOX9 and pERK signals (Fig 5G). Analyses of SOX9 and pERK signal in tdTom+ cells showed higher pERK signal and reduced SOX9 expression in *Prss56-Nf1*$^{fl/fl}$ compared to *Prss56-Nf1*$^{+/+}$ calluses. Negative correlation between pERK and SOX9 signal was observed in *Prss56-Nf1*$^{+/+}$ calluses while *Prss56-Nf1*$^{fl/fl}$ cells only exhibited high pERK and low SOX9 signals (Fig 5H). Overall, *Nf1*-deficient pSSPCs fail to downregulate MAPK activation preventing them from transitioning from the fibrogenic and the chondrogenic stage required for callus formation.

Nf1-deficient Schwann cells drive fibrosis accumulation and pseudarthrosis

Since the fibrotic tissue at pseudarthrosis site is mainly composed of non-Prss56-derived cells, we explored the role of environmental factors influencing SSPC fate after fracture. We transplanted sorted wild-type GFP+ pSSPCs from *Prx1^{Cre}; R26^{mTmG}* mice at the fracture site of *Prss56-Nf1$^{fl/fl}$* or *Prss56-Nf1$^{+/+}$* hosts. GFP+ cells formed cartilage in the control *Prss56-Nf1$^{+/+}$* environment and fibrosis in the mutant *Prss56-Nf1$^{fl/fl}$* environment 14 days post-fracture, showing the influence of the mutant callus environment on pSSPC fate (Fig. 6A). We generated snRNAseq datasets of day 7 post-fracture periosteum and hematoma of *Prss56-Nf1$^{fl/fl}$* mice and integrated with day 7 dataset *Prss56-Nf1$^{+/+}$* mice from Fig. 5 (Fig. 6B). Integrated datasets identified 8 cell populations composed of non-traced cells: endothelial cells, pericytes/SMC, SSPCs, osteoblasts, fibrogenic cells, chondrocytes, osteoclasts and immune cells (Fig S7A-E). We focused our analysis on the subset of pSSPCs, fibrogenic cells, osteoblasts and chondrocytes and observed a reduced percentage of cells in chondrogenic clusters and increased percentage of cells in fibrogenic clusters in *Prss56-Nf1$^{fl/fl}$* compared to *Prss56-Nf1$^{+/+}$* dataset (Fig. 6C-D). Thus, the mutant environment affects chondrogenic differentiation of wild-type pSSPCs and promotes accumulation of fibrogenic cells. To identify the cell type responsible for this deleterious effect in the mutant environment, we first investigated the role of *Nf1*-deficient pSSPCs. Transplanted pSSPCs from *Prss56-Nf1$^{fl/fl}$* mice induced callus fibrosis in wild-type hosts 14 days post-fracture compared to *Prss56-Nf1$^{+/+}$* pSSPCs. By 28 days post-fracture, the fibrosis was resorbed and bone bridging was apparent indicating that *Nf1*-deficient pSSPCs alone did not cause pseudarthrosis (Fig. S5F-G). Hence, we considered *Nf1*-deficient SCs, the other BC-derivatives localized within periosteum. Transplantation at the fracture site of wild-type hosts of SCs isolated from *Prss56-Nf1$^{fl/fl}$* mice induced pseudarthrosis as displayed by the absence of bone bridging at 28 days and fibrous accumulation at both 14- and 28-days post-fracture (Fig. 6E). *Nf1*-deficient SCs are therefore the main source of paracrine factors switching wild-type SSPC fate in the pseudarthrosis phenotype.

Fibrotic fate of periosteal SSPCs is mediated by TGFβ signaling

To identify the pro-fibrotic factors in the mutant environment, we proceeded with in depth analyses of pSSPCs in our snRNAseq datasets. We focused on cluster 6 that corresponds to cells transitioning from the fibrogenic to the chondrogenic stage, marked by an increasing chondrogenic lineage score and expression of specific genes such as *Col12a1* and *Itga11* (Fig. 7A-C). Gene Ontology (GO) analyses

showed upregulation of GO linked to calcium transport, cellular process and migration specifically in *Prss56-Nf1*$^{+/+}$ cells and GO linked to proliferation specifically in *Prss56-Nf1*$^{fl/fl}$ cells (Fig. 7C). GO related to the profibrotic factor TGFβ was upregulated specifically in cluster 6 of *Prss56-Nf1*$^{fl/fl}$ dataset, suggesting TGFβ as a paracrine factor affecting the fate of pSSPCs (Fig. 7D-E, Fig S7F). We observed increased *Tgfb1* expression and percentage of phospho-SMAD2 (TGFβ downstream effector) positive cells in day 7 *Prss56-Nf1*$^{fl/fl}$ calluses compared to *Prss56-Nf1*$^{+/+}$ (Fig. 7F-G). To test functionally the role of TGFβ, we inhibited TGFβ signaling by IP injection of TGFβ blocking antibody in *Prss56-Nf1*$^{fl/fl}$ mice at days 5, 8 and 11 post-fracture. Mice treated with TGFβ blocking antibody exhibited bone bridging and improved union score, as well as reduced fibrosis accumulation at day 28 post-fracture (Fig 7H), indicating that TGFβ is a key paracrine factor involved in the pseudarthrosis phenotype.

Discussion

In this study, we uncover the cellular origin of CPT in parallel analyses of CPT patients and *Prss56-Nf1 KO* mice. We identified *NF1* biallelic inactivation in human pathological periosteum, and specifically in periosteal SSPCs that exhibit a pro-fibrotic phenotype. These findings correlate with the localization of BC-derived *Nf1*-deficient pSSPCs in the periosteum of *Prss56-Nf1 KO* mice. Functionally, both human and murine *NF1*-deficient pSSPCs contribute to fibrous tissue in CPT due to a fate switch from chondrogenesis to fibrogenesis after fracture. Using snRNAseq, we described the temporal dynamics of the MAPK pathway during pSSPC activation and differentiation. The MAPK pathway is first up-regulated in pSSPCs that transition from a stem / progenitor stage to fibrogenesis in response to bone injury and is then down-regulated during the transition from fibrogenesis to chondrogenesis. These results provide the molecular mechanism explaining the retention of *Nf1*-deficient pSSPC in the fibrogenic stage as they fail to downregulate MAPK signaling due to the loss of neurofibromin inhibitory action. Fibrogenic pSSPCs in the center of the callus then interfere with the endochondral ossification process and prevent fracture consolidation. The results may have a larger impact in understanding other bone repair disorders, associated with periosteum defect and callus fibrosis, and that may share similar mechanisms with CPT.

Most surprisingly, our results highlight the role of SCs, a neural cell type, in promoting callus fibrosis in CPT. Data from CPT patients and *Prss56-Nf1 KO* mice support that *Nf1*-deficient pSSPCs are not the only cell type involved in CPT. Indeed, in 3 patients, we identified *NF1* loss in periosteum but not in pSSPCs. In *Prss56-Nf1 KO* mice, we detected *Nf1*-deficient SCs in the periosteum and the fibrous tissue. These *Nf1*-deficient SCs cause pseudarthrosis and are the major source of deleterious paracrine factors driving wild type pSSPCs toward fibrosis. Thus, both wild type and *Nf1*-deficient pSSPCs together contribute to fibrotic accumulation. The involvement of non-mutated cells in CPT is confirmed in 2 patients where *NF1* loss was identified in pathological periosteum but not in fibrous tissue. SCs in the fibrotic tissue of *Prss56-Nf1 KO* mice exhibit a repair SC phenotype. Previous studies showed that the MAPK pathway regulates the transition from SCs to repair SCs suggesting that *Nf1*-deficient SCs are blocked as repair SCs and maintain the secretion of pro-fibrotic factors in CPT (Cervellini et al., 2018; Harrisingh et al., 2004; Napoli et al., 2012). We identified the profibrotic factor TGFβ1 as a critical driver of fibrotic accumulation in CPT and inhibiting TGFβ led to improved healing in *Prss56-Nf1 KO*

mice. This paves the way for the use of anti-fibrotic treatment such as TGFβ inhibitors, for CPT. This study also provides the first evidence that SCs can impair non-nervous peripheral tissue repair. Previous studies reported the key paracrine role of SCs in skin and digit tip regeneration, but the role of SCs in bone repair remains elusive and further studies are needed to understand the role of SC in adult tissue regeneration (Johnston et al., 2016, 2013; Parfejevs et al., 2018).

The involvement of both pSSPCs and SCs in CPT suggests new mechanisms for NF1 bone manifestations. CPT and other NF1 bone phenotypes have been investigated independent of other NF1 symptoms, presumably since the cell types involved have distinct embryonic origins. SCs and melanocytes, responsible for NFBs and CALMs, are neural-crest derived, while axial and appendicular bones are derived from the mesoderm. Our genetic analysis of the *NF1* mutational landscape in CPT revealed that *NF1* 2nd hit mutation occurs early during embryonic development and is not restricted to the skeletal lineage. We identified boundary caps (BCs) as a source of neural crest-derived cells in long bones and as the cellular origin of CPT. BC give rise to both pSSPCs and SCs causing the CPT phenotype. CPT thus shares a common cellular origin with NF1 neurodermatological features and particularly NFBs that are due to *NF1* loss in BCs and their derivatives in peripheral nerves (Radomska et al., 2019). The *Prss56-Nf1 KO* model carrying *Nf1* inactivation in BCs is the first relevant model to faithfully recapitulate NF1 features, suggesting that several if not all NF1 symptoms may be due to loss of *Nf1* in BC-derivatives. The presence of other bone phenotypes in this model, including spine deformities or cranial abnormalities, remains to be determined. In addition, to sharing a common cellular origin, we further show that NFBs and CPTs share common pathogenic mechanisms. In NFBs, SCs secrete profibrotic factors, including TGFβ and SCF, to promote fibroblast accumulation and proliferation involved in tumor progression (Badache et al., 1998; Mashour et al., 2001; Patmore et al., 2012). *Nf1*-deficient SCs exert a similar pro-fibrotic role during bone repair causing CPT. NF1 pathology is also characterized by a heterogeneity of symptoms and variability in their severity, which could be partly explained by location and timing of *NF1* mutations in BC cells. Overall, this study calls from a more integrated analysis of NF1 features and suggests the use of common therapeutical approaches such as anti-fibrotic agents to treat NF1 manifestations.

Data availability

All RNAseq and single nuclei RNAseq datasets will be deposited in the Gene Expression Omnibus (GEO) at time of submission.

Acknowledgements

This work was supported by Association Neurofibromatoses et Recklinghausen to C.C and B.P., Osteosynthesis and Trauma Care Foundation to C.C. and St.P., ANR-18-CE14-0033 and ANR-21-CE18-007-01 to C.C, P.T. and B.P., and NIAMS R01 AR072707 to C. C. and Ted Miclau. S. Perrin and O. Duchamp de Lageneste were supported by a PhD fellowship from Paris Cité University.

We thank A. Henry, A. Guigan and O. Pellé from the Flow Cytometry platforms of IMRB and Imagine Institute, L. Slimani and K. Henri from Life Imaging Facility of Paris Cité University (Plateforme Imagerie du Vivant “Micro-CT platform”), all the staff from the Imagine genomic core facility at Imagine Institute and N. Cagnard from Bioinformatics Platform at Imagine Institute for advice and technical assistance. We thank A. Julien, C.-A. Wotawa, F. Coulpier, S. Berger, E. Tacu, E. Paniel and M. Mansour for technical assistance or advice.

Competing interests

Authors declare no competing interests.

Figures and legends

Figure 1: Congenital pseudarthrosis of the tibia is linked to *NF1* biallelic inactivation in human periosteum.

A. X-ray of the pseudarthrosis of the tibia and the fibula of patient P15 (white arrows). **B.** Experimental design. DNA was extracted from tissues or periosteal SSPCs (pSSPCs) collected at the pseudarthrosis (PA) site, the iliac crest (IC) and from blood of CPT patients undergoing surgery, and *NF1* targeted sequencing was performed. **C.** *NF1* genotyping of tissues from 17 CPT patients shows the absence of *NF1* biallelic inactivation in blood and IC and the presence of *NF1* biallelic inactivation in the periosteum at PA site in 13/17 patients. *NF1* biallelic inactivation in detected in 6/14 patients in the fibrous tissue and bone, in 4/17 in the bone marrow, in 3/17 in the muscle and in 2/17 in the skin from the PA site. **D.** *NF1* genotyping of periosteum and SSPCs from PA site shows the presence of *NF1* biallelic inactivation in pSSPCs from PA site in 8/13 patients. **E.** Number of patients with NF1-related CPT and isolated CPT carrying *NF1* biallelic inactivation. **F.** *NF1* sequencing of 5 patients with combined tibia and fibula pseudarthrosis. The presence of the same second *NF1* hit mutation in the tibia and fibula PA is detected in 4/5 patients. *Imbalance in informative SNP rs146315101 suggests a cnLOH. **cnLOH was determined using informative SNPs. **G.** *NF1* sequencing of patients P3, P7 and P15 shows the presence of the same 2nd *NF1* point mutation in the periosteum, muscle and skin at the PA site in patients P3 and P7 and in periosteum and muscle in patient P15. **H.** phospho-ERK (pERK) immunofluorescence on periosteum sections shows an increased number of pERK+ cells in the periosteum from PA site compared to the periosteum from IC (white arrows). Quantification of the percentage of pERK+ cells in the periosteum from PA and IC (n=4 per group). **I.** Increased MAPK pathway activation in pSSPCs from PA site compared to pSSPCs from IC measured by the ratio of pERK/ERK on Western Blot (n=6 per group, each symbol represents a patient from Fig. S1G). **H.** Increased in vitro proliferation of PA pSSPCs compared to IC pSSPCs. (n=6 per group). p-value: * $p < 0.05$. NS: not sampled, cnLOH: copy neutral loss of heterozygosity, BM: Bone marrow, Spongy b.: spongy bone, Fibrous t.: fibrous tissue, WT: wild-type. Scale bar: 50µm.

Figure 1

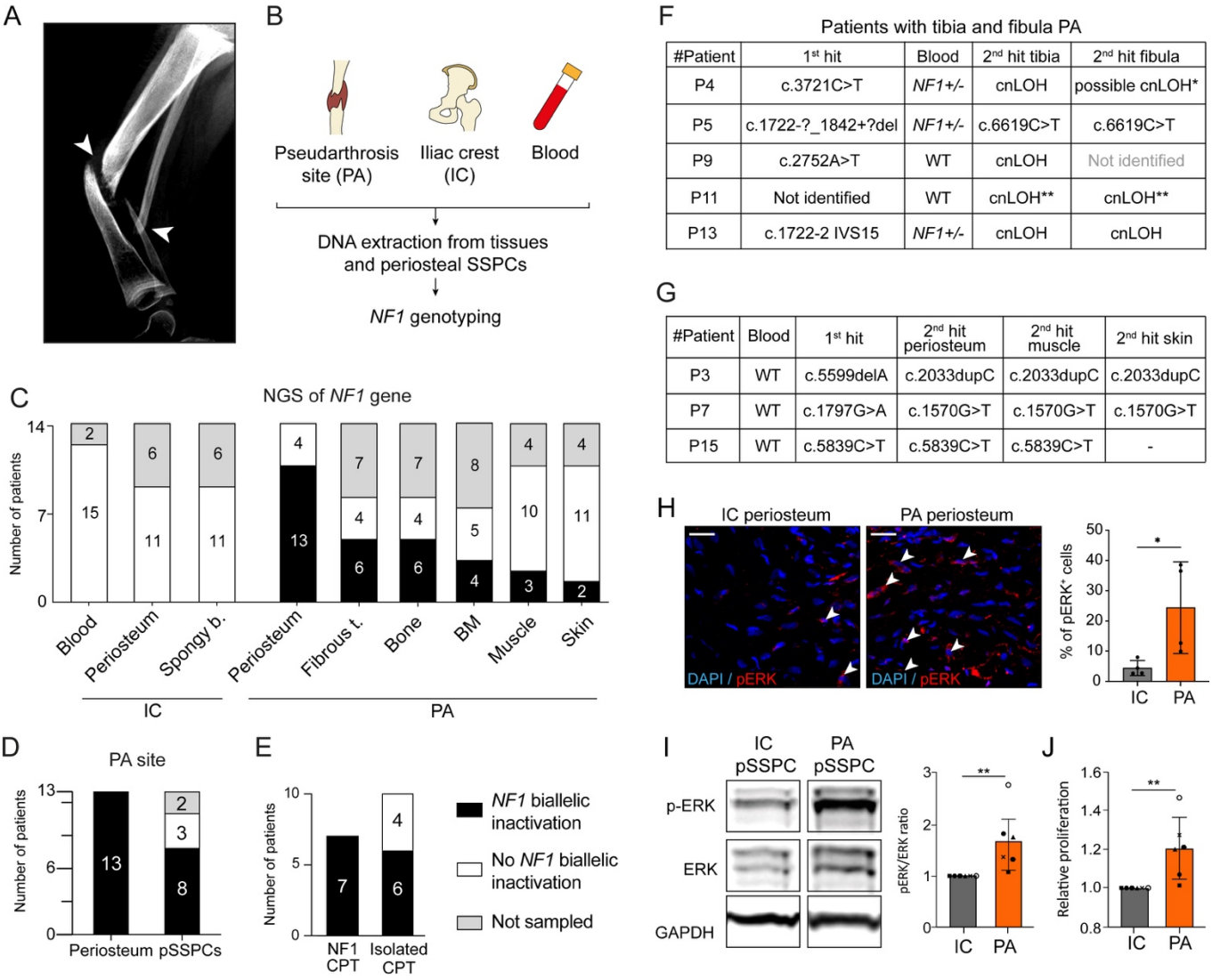

#Patient	1st hit	Blood	2nd hit tibia	2nd hit fibula
P4	c.3721C>T	*NF1*+/-	cnLOH	possible cnLOH*
P5	c.1722-?_1842+?del	*NF1*+/-	c.6619C>T	c.6619C>T
P9	c.2752A>T	WT	cnLOH	Not identified
P11	Not identified	WT	cnLOH**	cnLOH**
P13	c.1722-2 IVS15	*NF1*+/-	cnLOH	cnLOH

#Patient	Blood	1st hit	2nd hit periosteum	2nd hit muscle	2nd hit skin
P3	WT	c.5599delA	c.2033dupC	c.2033dupC	c.2033dupC
P7	WT	c.1797G>A	c.1570G>T	c.1570G>T	c.1570G>T
P15	WT	c.5839C>T	c.5839C>T	c.5839C>T	-

Figure 2: Human pathological periosteum contains pro-fibrotic SSPCs

A. Experimental design. Nuclei were extracted from periosteum of PA site or IC, sorted and processed for single-nuclei RNAseq. The datasets were integrated for analyses. **B.** UMAP projection of color-coded clustering (top) and sampling (bottom) of the integration of the datasets of IC periosteum from P13 (IC-P13, green), PA periosteum from P13 (PA-P13, blue) and PA periosteum from P5 (PA-P5, orange). **C.** Feature plots of the SSPC lineage score and the expression of *ADAM12*, *PDGFRA*, *ACAN* and *RUNX2*. **D.** Percentage of the cells per dataset in SSPC populations, *ADAM12*+ SSPCs, *PDGFRA*+ SSPCs, and osteochondral SSPCs. **E.** Violin plots of the fibrogenic, osteogenic, chondrogenic, cellular response to TGFβ and MAPK activation lineage score per dataset. **F.** Venn diagram and list of genes upregulated in PA pSSPCs (left) and IC pSSPCs (right) in only patient P3 (blue), only patient P7 (red) and both patients (purple). **G.** Gene ontology of the upregulated genes in pSSPCs from IC (left) and PA site (right) of patients P3 and P7.**H.** Experimental design: PA or IC pSSPCs from patients P3 and P4 were transplanted at the fracture site of immunodeficient mice. Volume of fibrosis in day 14 post-fracture callus of immunodeficient mice grafted with human pSSPCs from IC and PA, showing increased fibrosis in the callus of mice grafted with PA cells (n=7-8 per group).

I. Representative callus section stained with Picrosirius (PS). High magnification of cartilage stained in Safranin'O and fibrosis stained in PS and immunofluorescence of the human KU80 protein at day 14 post-fracture showing that IC pSSPC-derived cells are located mostly in cartilage while PA pSSPC-derived cells are located in fibrosis (white arrow). VAF: variant allele frequency, WT: wild-type, cnLOH: copy neutral loss of heterozygosity, point mut.: point mutation, cal: callus, fib: fibrosis, cart: cartilage. p-value: * $p < 0.05$, ** $p < 0.01$. Scale bars: Low magnification: 1mm. High magnification: 100µm.

Figure 2

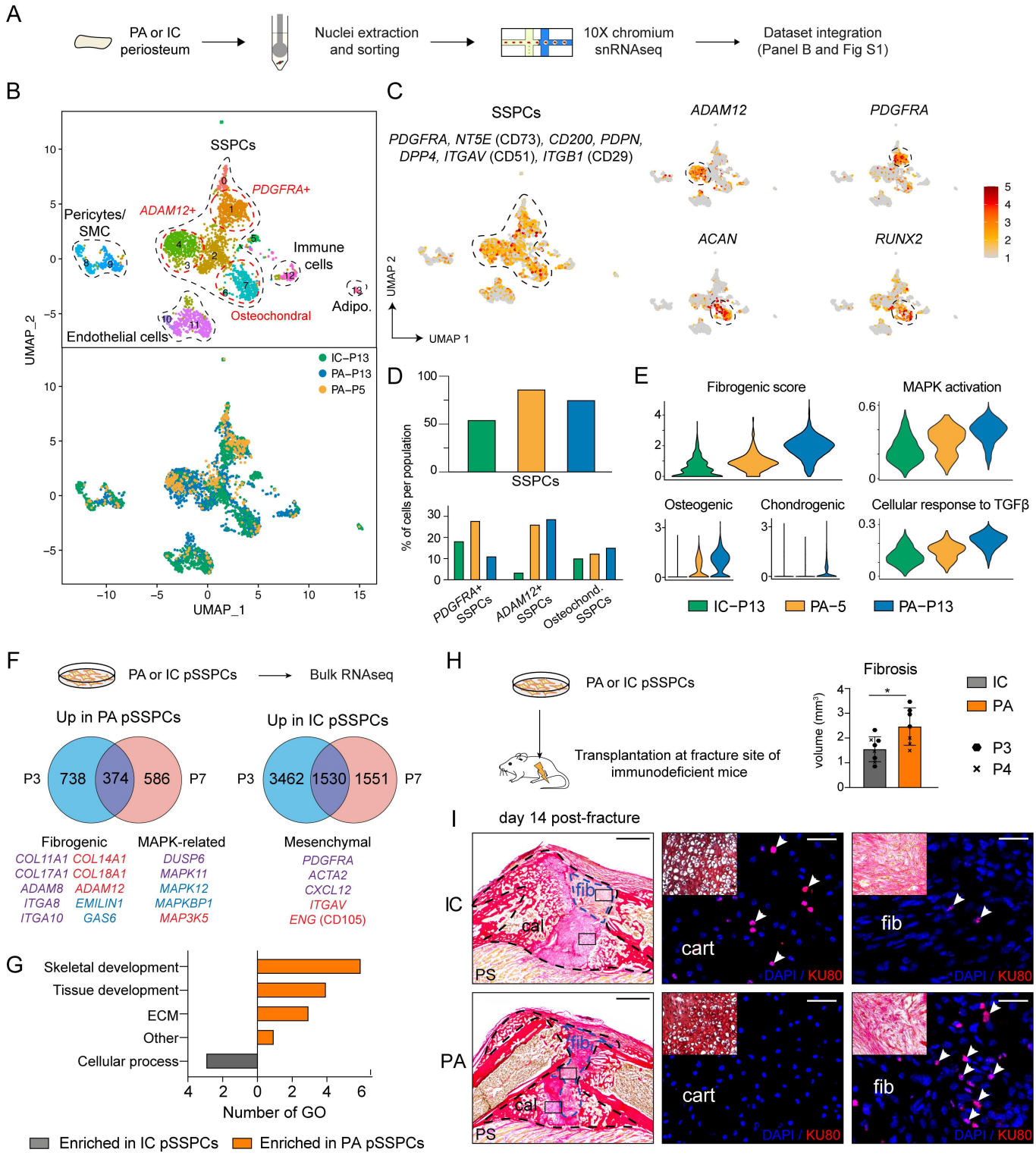
A
PA or IC periosteum
Nuclei extraction and sorting
10X chromium snRNAseq
Dataset integration (Panel B and Fig S1)
B
SSPCs
PDGFRA+
ADAM12+
Pericytes/ SMC
Immune cells
Adipo.
Osteochondral
Endothelial cells
UMAP_2
UMAP_1
IC–P13
PA–P13
PA–P5
C
SSPCs
PDGFRA, NT5E (CD73), CD200, PDPN, DPP4, ITGAV (CD51), ITGB1 (CD29)
ADAM12
PDGFRA
ACAN
RUNX2
UMAP 2
UMAP 1
D
% of cells per population
SSPCs
PDGFRA+ SSPCs
ADAM12+ SSPCs
Osteochond. SSPCs
E
Fibrogenic score
MAPK activation
Osteogenic
Chondrogenic
Cellular response to TGFβ
IC–P13
PA–5
PA–P13
F
PA or IC pSSPCs
Bulk RNAseq
Up in PA pSSPCs
P3 738 374 586 P7
Up in IC pSSPCs
P3 3462 1530 1551 P7
Fibrogenic
COL11A1 COL14A1
COL17A1 COL18A1
ADAM8 ADAM12
ITGA8 EMILIN1
ITGA10 GAS6
MAPK-related
DUSP6
MAPK11
MAPK12
MAPKBP1
MAP3K5
Mesenchymal
PDGFRA
ACTA2
CXCL12
ITGAV
ENG (CD105)
G
Skeletal development
Tissue development
ECM
Other
Cellular process
Number of GO
Enriched in IC pSSPCs
Enriched in PA pSSPCs
H
PA or IC pSSPCs
Transplantation at fracture site of immunodeficient mice
Fibrosis
volume (mm³)
IC
PA
P3
P4
I
day 14 post-fracture
IC
PA
fib
cal
PS
cart
DAPI / KU80

Figure 3: Tibial pseudarthrosis in *Prss56-Nf1 KO* mice

A. Experimental design of tibial fracture in *Prss56^{Cre}; R26^{tdTom}; Nf1$^{+/+}$* (*Prss56-Nf1$^{+/+}$*) control, *Prss56^{Cre}; R26^{tdTom}; Nf1$^{fl/fl}$* (*Prss56-Nf1$^{fl/fl}$*) and *Prss56^{Cre}; R26^{tdTom}; Nf1$^{fl/-}$* (*Prss56-Nf1$^{fl/-}$*) mutant mice. **B.** Histomorphometric quantification of the volume of callus fibrosis at days 7, 14, 21 and 28 post-fracture in *Prss56-Nf1$^{+/+}$*, *Prss56-Nf1$^{fl/fl}$* and *Prss56-Nf1$^{fl/-}$* mice (n=5-6 per group). **C.** Representative microCT images of callus from *Prss56-Nf1$^{+/+}$, Prss56-Nf1$^{fl/fl}$* and *Prss56-Nf1$^{fl/-}$* mice at 28 days post-fracture, showing absence of bone bridging in *Prss56-Nf1$^{fl/fl}$* and *Prss56-Nf1$^{fl/-}$* mutant mice (white arrows). **D.** Top, representatives callus sections of *Prss56-Nf1$^{+/+}$, Prss56-Nf1$^{fl/fl}$* and *Prss56-Nf1$^{fl/-}$* mice at 28 days post-fracture stained with Picrosirius (PS). Bottom, high magnification of callus periphery showing bone bridging (box 1, black arrows) in *Prss56-Nf1$^{+/+}$* control mice, and presence of fibrosis (box 2 and 4) and unresorbed cartilage (stained with Safranin'O, box 3) in *Prss56-Nf1$^{fl/fl}$* and *Prss56-Nf1$^{fl/-}$* mutant mice. **E.** Percentage of calluses from *Prss56-Nf1$^{+/+}$, Prss56-Nf1$^{fl/fl}$* and *Prss56-Nf1$^{fl/-}$* mice showing bone union (white), semi-union (grey) or non-union (black) on microCT scan at day 28 post-fracture (n=6 per group). **F.** Immunofluorescence on fibrotic callus tissue at day 28 post-fracture in *Prss56-Nf1$^{fl/fl}$* mice showing expression of the extracellular matrix proteins periostin (POSTN), but not Collagen II (COL2), Collagen X (COLX), expression of the immune marker CD68 and the endothelial marker PECAM1 but no expression of the nerve marker TH (n=3). cal: callus, b: bone, bm: bone marrow, fib: fibrosis, cart: cartilage. p-value: * $p < 0.05$, ** $p < 0.01$. Scale bars: Panel C: 1mm, Panel D: low magnification: 1mm, high magnification: 100µm. Panel F: 50µm.

Figure 3

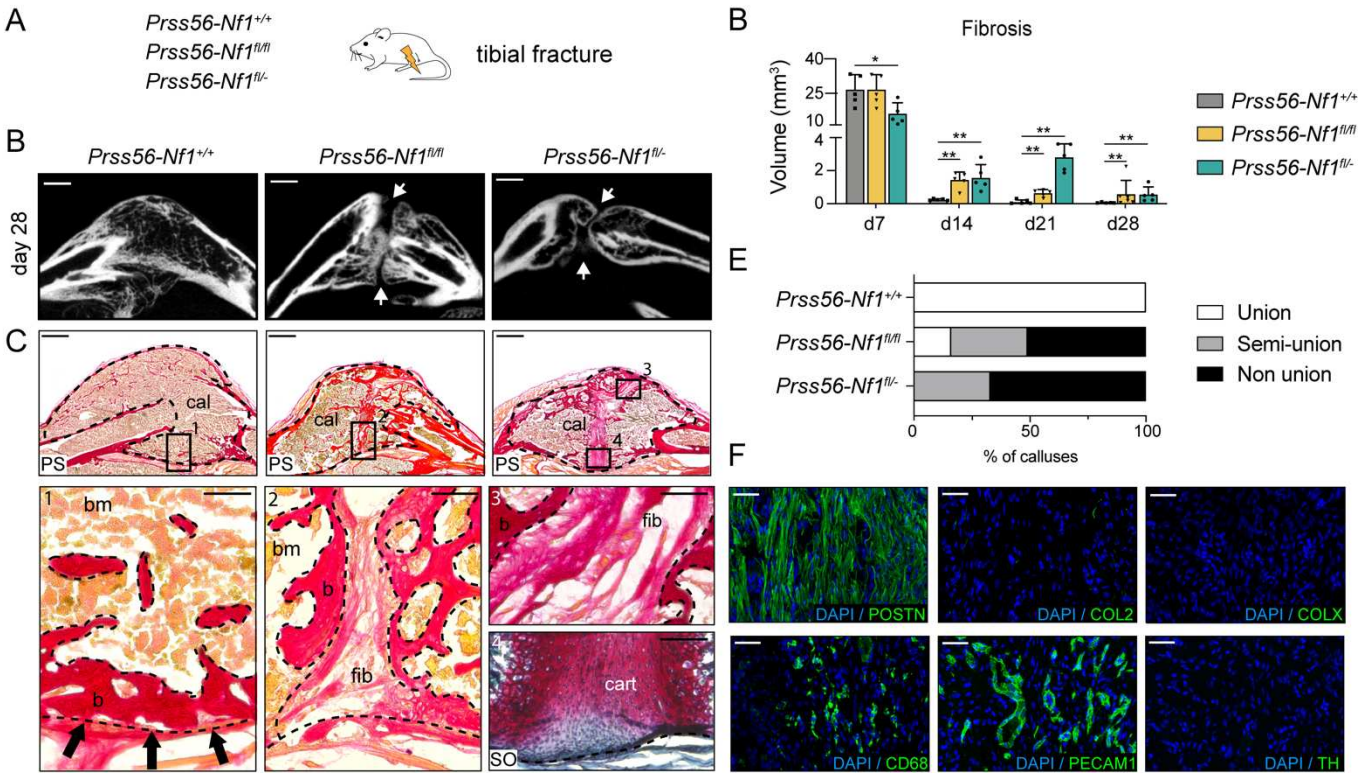
A
Prss56-Nf1+/+
Prss56-Nf1fl/fl
Prss56-Nf1fl/-
tibial fracture
B
Prss56-Nf1+/+
Prss56-Nf1fl/fl
Prss56-Nf1fl/-
day 28
C
cal
PS
bm
b
fib
cart
SO
B
Fibrosis
Volume (mm3)
d7
d14
d21
d28
E
Union
Semi-union
Non union
% of calluses
F
DAPI / POSTN
DAPI / COL2
DAPI / COLX
DAPI / CD68
DAPI / PECAM1
DAPI / TH

Figure 4: Boundary cap-derived periosteal SSPCs and SCs are traced in adult periosteum and callus fibrosis

A. Longitudinal sections of uninjured tibia of 3-month-old *Prss56-Nf1*$^{+/+}$ mice stained with Hematoxylin-Eosin showing the periosteum (po) and immunofluorescence on adjacent sections showing tdTom+ periosteal skeletal stem/progenitor cells (pSSPCs) expressing PDGFRα and tdTom+ Schwann cells (SCs) expressing SOX10 along TH+ nerves within the periosteum (orange box: transverse imaging). **B.** Percentage of total tdTom+ cells and of pSSPCs (PDGFRα^{+}) and SCs (p75-NTR^{+}) in the tdTom+ population in uninjured periosteum of *Prss56-Nf1*$^{+/+}$ and *Prss56-Nf1*$^{fl/fl}$ mice determined by flow cytometry (n=5 per group). **C.** Lineage tracing of Prss56-expressing Boundary Cap (BC)-derived tdTom+ cells (white arrows) in callus cartilage (labelled by SOX9), bone (labelled by OSX) and fibrosis (labelled by POSTN) of *Prss56-Nf1*$^{+/+}$ and *Prss56-Nf1*$^{fl/fl}$ mice 14 days after fracture. **D.** Quantification of tdTom+ signal in callus, cartilage, bone and fibrosis of *Prss56-Nf1*$^{+/+}$ and *Prss56-Nf1*$^{fl/fl}$ mice 14- and 28-days post-fracture (n=5 per group). **E.** Immunofluorescence on callus sections of *Prss56-Nf1*$^{fl/fl}$ mice day 14 post-fracture shows the presence of PDGFRα+ fibroblasts and SOX10+ SCs in fibrotic tissue. SCs are expressing SOX2 but not Myelin Basic Protein (MBP) and are not located along TH+ nerves. **F.** Lineage tracing of Prss56-derived tdTom+ cells in the new periosteum of day 28 post-fracture calluses in *Prss56-Nf1*$^{+/+}$ and *Prss56-Nf1*$^{fl/fl}$ mice showing an increased number of tdTom+ cells in *Prss56-Nf1*$^{fl/fl}$ mutant. Percentage of tdTom+ cells and of PDGFRα+ pSSPCs in the tdTom+ population in digested periosteum 28 days post-fracture of *Prss56-Nf1*$^{+/+}$ and *Prss56-Nf1*$^{fl/fl}$ mice determined by flow cytometry (n=4-6 per group). po: periosteum, b: bone, fib: fibrosis, cart: cartilage. p-value: * $p < 0.05$, ** $p < 0.01$, *** $p < 0.001$. Scale bars: Panel A: 50µm. Panel B: 25µm. Panel F: Low magnification: 1mm. High magnification: 25µm. Panel H: 10µm. Panel I: 50µm.

Figure 4

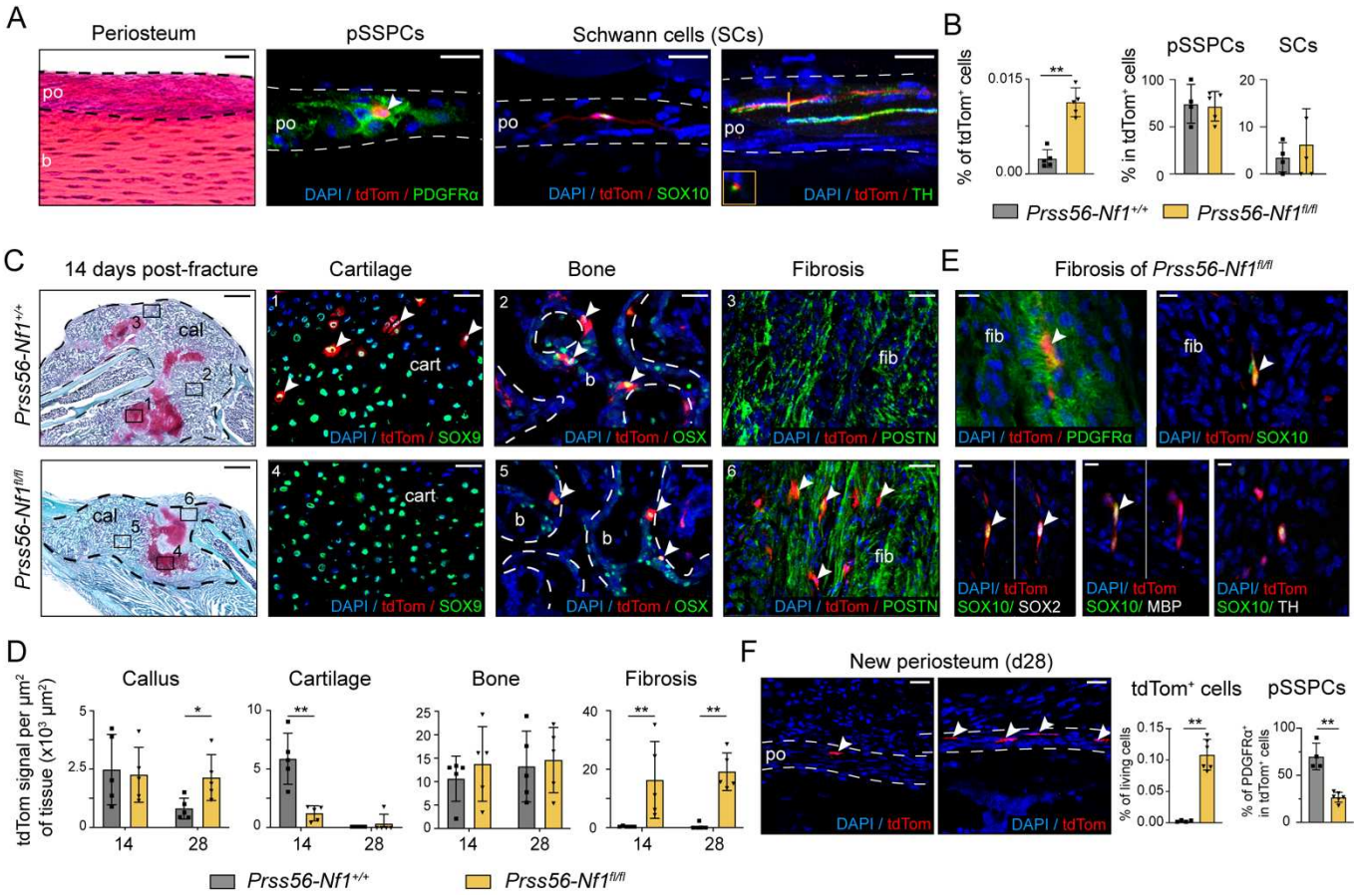
A
Periosteum
pSSPCs
Schwann cells (SCs)
po
b
DAPI / tdTom / PDGFRα
DAPI / tdTom / SOX10
DAPI / tdTom / TH
B
% of tdTom+ cells
% in tdTom+ cells
pSSPCs
SCs
Prss56-Nf1+/+
Prss56-Nf1fl/fl
C
14 days post-fracture
Cartilage
Bone
Fibrosis
Prss56-Nf1+/+
Prss56-Nf1fl/fl
cal
cart
fib
DAPI / tdTom / SOX9
DAPI / tdTom / OSX
DAPI / tdTom / POSTN
E
Fibrosis of Prss56-Nf1fl/fl
DAPI / tdTom / PDGFRα
DAPI/ tdTom/ SOX10
DAPI/ tdTom SOX10/ SOX2
DAPI/ tdTom SOX10/ MBP
DAPI/ tdTom SOX10/ TH
D
tdTom signal per µm² of tissue (x10³ µm²)
Callus
Cartilage
Bone
Fibrosis
14
28
Prss56-Nf1+/+
Prss56-Nf1fl/fl
F
New periosteum (d28)
tdTom+ cells
pSSPCs
% of living cells
% of PDGFRα+ in tdTom+ cells
DAPI / tdTom

Figure 5: Fibrogenic fate of *Nf1*-deficient periosteal cells during bone repair

A. Left: Experimental design. Periosteum or cultured tdTom^{+} periosteal skeletal stem/progenitor cells (pSSPCs) were isolated from *Prss56-Nf1*$^{+/+}$ or *Prss56-Nf1*$^{fl/fl}$ mice and transplanted at the fracture site of wild-type hosts. Middle: Representative images of the contribution of grafted tdTom+ cells (white arrows) showing that cells from *Prss56-Nf1*$^{+/+}$ mice are detected in cartilage (labelled by SOX9) and cells from *Prss56-Nf1*$^{fl/fl}$ mice are detected in fibrosis (labelled by POSTN). Right: Percentage of grafted tdTom+ cells in cartilage and fibrosis (n=5 per group). **B.** Experimental design of single nuclei RNAseq (snRNAseq) experiment. Nuclei were isolated from uninjured periosteum, or periosteum and hematoma at day 5 and 7 post-fracture of wild type mice, sorted and processed for snRNAseq. **C.** UMAP projection of color-coded clustering and monocle pseudotime trajectory of the subset of SSPCs, fibrogenic cells, osteoblasts and chondrocytes from integrated uninjured, day 5 and day 7 post-fracture samples. The four populations are delimited by black dashed lines. **D.** Violin plots of SSPC, fibrogenic and chondrogenic lineage scores in uninjured (uninj.), day 5 and day 7 post-fracture datasets. **E.** Violin plot of the MAPK score in uninjured, day 5 and day 7 post-fracture datasets. **F.** Scatter plots of MAPK score along pseudotime, chondrogenic lineage score, *Acan* expression, fibrogenic and osteogenic lineage scores. **G.** Immunofluorescence of SOX9 and phospho-ERK (pERK) in day 7 post-fracture callus section of wild type (WT) mice. Quantification of SOX9 and pERK signal per cell show negative correlation between pERK and SOX9 signals (red line) (n = 397 cells from 8 callus sections of 4 mice). **H.** Left: Quantification of SOX9 and pERK fluorescent signal per tdTom+ cells in day 7 post-fracture callus of *Prss56-Nf1*$^{+/+}$ and *Prss56-Nf1*$^{fl/fl}$ mice. Right: Correlation analysis of pERK and SOX9 signals in tdTom+ cells in *Prss56-Nf1*$^{+/+}$ (top) and *Prss56-Nf1*$^{fl/fl}$ (bottom) mice (n = 209 to 238 cells from 9 sections of 3 mice per group). cart: cartilage, fib: fibrosis. Scale bars: Panel B: Low magnification: 1mm, High magnification: 100µm. Panel I: Low magnification: 150µm, High magnification: 25µm.

Figure 5

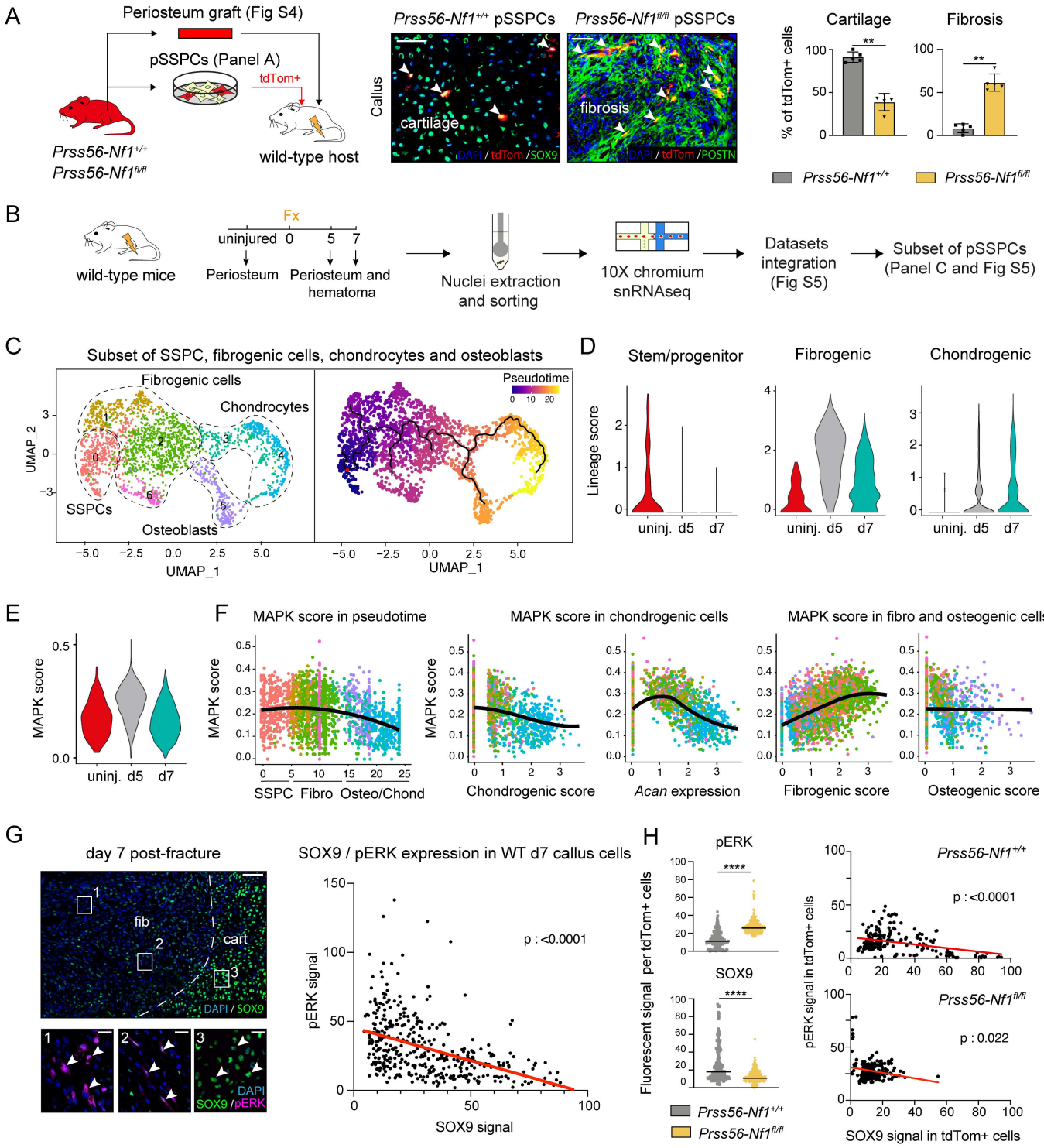
A
Periosteum graft (Fig S4)
pSSPCs (Panel A)
tdTom+
Prss56-Nf1+/+
Prss56-Nf1fl/fl
wild-type host
Prss56-Nf1+/+ pSSPCs
Prss56-Nf1fl/fl pSSPCs
Callus
cartilage
fibrosis
DAPI / tdTom /SOX9
DAPI / tdTom /POSTN
Cartilage
Fibrosis
% of tdTom+ cells
B
wild-type mice
Fx
uninjured 0 5 7
Periosteum
Periosteum and hematoma
Nuclei extraction and sorting
10X chromium snRNAseq
Datasets integration (Fig S5)
Subset of pSSPCs (Panel C and Fig S5)
C
Subset of SSPC, fibrogenic cells, chondrocytes and osteoblasts
Fibrogenic cells
Chondrocytes
SSPCs
Osteoblasts
Pseudotime
UMAP_1
UMAP_2
D
Stem/progenitor
Fibrogenic
Chondrogenic
Lineage score
uninj. d5 d7
E
MAPK score
F
MAPK score in pseudotime
MAPK score in chondrogenic cells
MAPK score in fibro and osteogenic cells
SSPC Fibro Osteo/Chond
Chondrogenic score
Acan expression
Fibrogenic score
Osteogenic score
G
day 7 post-fracture
fib
cart
DAPI / SOX9
SOX9 /pERK
SOX9 / pERK expression in WT d7 callus cells
pERK signal
SOX9 signal
p : <0.0001
H
pERK
SOX9
Fluorescent signal per tdTom+ cells
Prss56-Nf1+/+
Prss56-Nf1fl/fl
pERK signal in tdTom+ cells
SOX9 signal in tdTom+ cells
p : <0.0001
p : 0.022

Figure 6: Pro-fibrotic effect of the fracture environment and *Nf1*-deficient Schwann cells in *Prss56-Nf1* KO mice

A. Left: Experimental design. Cultured GFP$^+$ pSSPCs were isolated from *Prx1^{Cre}; R26^{mTmG}* mice and transplanted at the fracture site of *Prss56-Nf1$^{+/+}$* control or *Prss56-Nf1$^{fl/fl}$* mutant hosts. Middle: Representative images of the contribution of GFP+ pSSPCs to cartilage (labelled by SOX9) in *Prss56-Nf1$^{+/+}$* hosts and to fibrosis (labelled by POSTN) in *Prss56-Nf1 $^{fl/fl}$* hosts. Right: Percentage of the contribution of grafted GFP+ pSSPCs to cartilage and fibrosis in *Prss56-Nf1$^{+/+}$* and *Prss56-Nf1 $^{fl/fl}$* hosts (n=4 per group). **B.** Experimental design. Nuclei were isolated from the periosteum and hematoma at day 7 post-fracture of *Prss56-Nf1$^{+/+}$* or *Prss56-Nf1$^{fl/fl}$* mice, sorted and processed for snRNAseq. Both datasets were integrated for analysis. **C.** UMAP projection of color-coded clustering of the subset of SSPCs, fibrogenic, chondrogenic and osteogenic cells from the integration of day 7 post-fracture *Prss56-Nf1$^{+/+}$* and *Prss56-Nf1$^{fl/fl}$* datasets. Lineage score of the 4 populations. **D.** UMAP projection of color-coded sampling of the subset of SSPCs, fibrogenic, chondrogenic and osteogenic cells from the integration of day 7 post-fracture *Prss56-Nf1$^{+/+}$* and *Prss56-Nf1$^{fl/fl}$* datasets. Violon plot of the lineage score of chondrogenic and fibrogenic score per dataset. Percentage of cells per cluster in *Prss56-Nf1$^{+/+}$* and *Prss56-Nf1$^{fl/fl}$* datasets. **E.** Top: Experimental design. tdTom+ Schwann cells (SCs) were isolated from *Prss56-Nf1$^{+/+}$* or *Prss56-Nf1$^{fl/fl}$* mice and transplanted at the fracture site of a wild type hosts. Middle: Representative microCT images of 28 days post-fracture calluses of wild type mice grafted with tdTom+ SCs from *Prss56-Nf1$^{+/+}$* or *Prss56-Nf1$^{fl/fl}$* mice, showing absence of bridging in mice grafted with *Nf1*-deficient SCs (white arrow). Bottom: percentage of day 28 post-fracture calluses showing union (white), semi-union (grey) or non-union (black) on microCT scan. Histomorphometric quantification of the volume of callus fibrosis at 14- and 28-days post-fracture (n=4-5 per group). cart: cartilage, fib: fibrosis. p-value: * $p < 0.05$, ** $p < 0.01$. Scale bars: Panel A: 100µm. Panel E: 1mm.

Figure 6

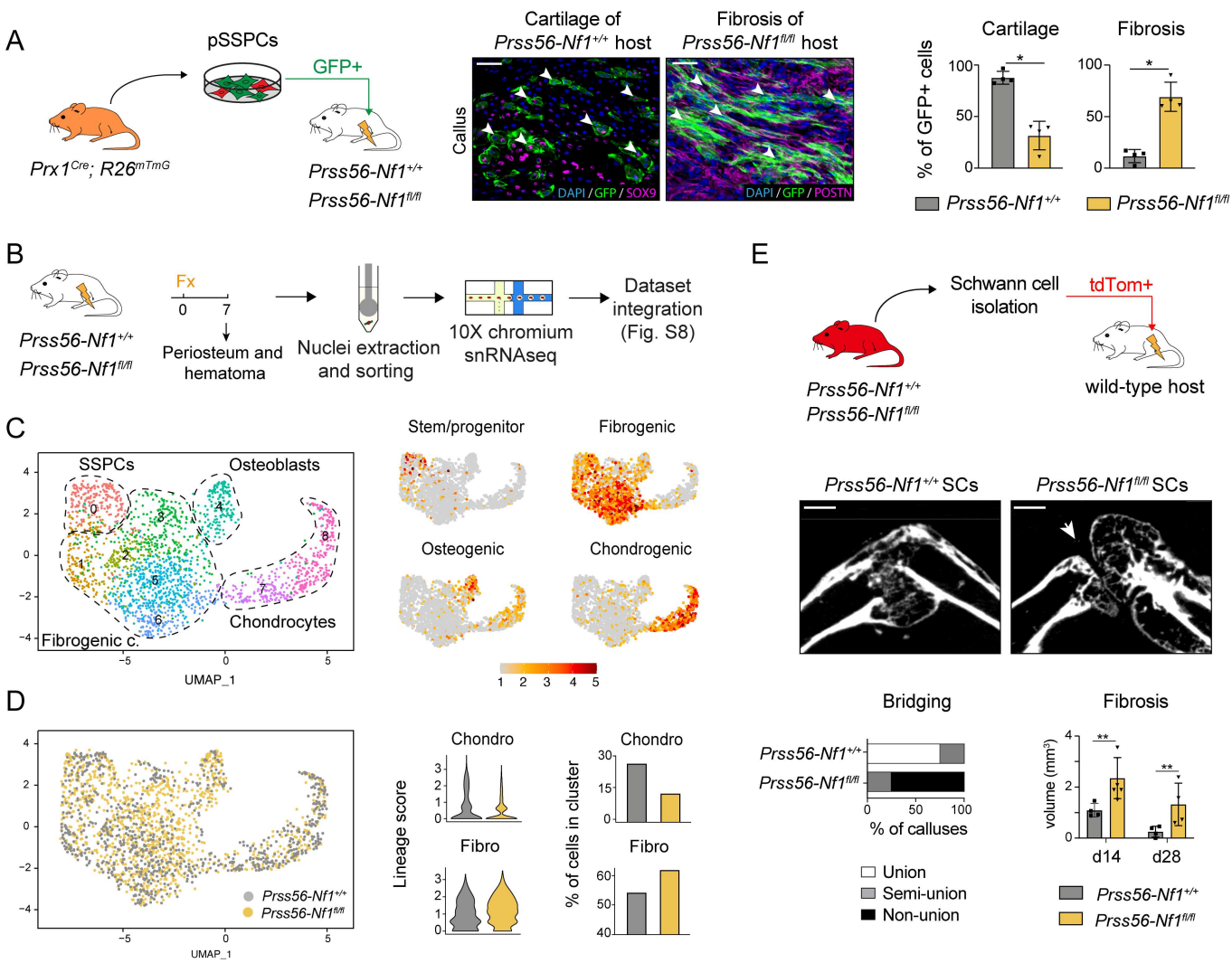
A
pSSPCs
GFP+
Prx1Cre; R26mTmG
Prss56-Nf1+/+
Prss56-Nf1fl/fl
Cartilage of Prss56-Nf1+/+ host
Fibrosis of Prss56-Nf1fl/fl host
Callus
DAPI / GFP / SOX9
DAPI / GFP / POSTN
Cartilage
Fibrosis
% of GFP+ cells
B
Fx
0 7
Periosteum and hematoma
Nuclei extraction and sorting
10X chromium snRNAseq
Dataset integration (Fig. S8)
C
SSPCs
Osteoblasts
Chondrocytes
Fibrogenic c.
UMAP_1
Stem/progenitor
Fibrogenic
Osteogenic
Chondrogenic
D
Prss56-Nf1+/+
Prss56-Nf1fl/fl
Lineage score
Chondro
Fibro
% of cells in cluster
E
Schwann cell isolation
tdTom+
wild-type host
Prss56-Nf1+/+ SCs
Prss56-Nf1fl/fl SCs
Bridging
% of calluses
Union
Semi-union
Non-union
Fibrosis
volume (mm3)
d14
d28

Figure 7: TGFβ mediates the pro-fibrotic effect of the fracture environment in *Prss56-Nf1* KO mice

A. Left: UMAP projection of monocle pseudotime trajectory of the subset of SSPCs, fibrogenic, chondrogenic and osteogenic cells from the integration of day 7 post-fracture *Prss56-Nf1*$^{+/+}$ and *Prss56-Nf1*$^{fl/fl}$ datasets. Right: UMAP projection of the integrated datasets with cluster 6 labelled in red. **B.** Scatter plot of the chondrogenic score along pseudotime. Cells from cluster 6 are in red and are located at the beginning of the chondrogenic differentiation. **C.** Violin plots of *Col12a1* and *Itga11* expression. **D.** Top: Gene Ontology of upregulated genes in cluster 6 of *Prss56-Nf1*$^{+/+}$ and *Prss56-Nf1*$^{fl/fl}$ datasets. Bottom: Gene Ontology of upregulated genes in cluster 6 of *Prss56-Nf1*$^{fl/fl}$ dataset in "Signaling pathways" category. **E.** TGFβ score in cluster 6 from *Prss56-Nf1*$^{+/+}$ and *Prss56-Nf1*$^{fl/fl}$ datasets. **F.** Relative expression of *Tgfb1* in day 7 post-fracture callus of *Prss56-Nf1*$^{+/+}$ or *Prss56-Nf1*$^{fl/fl}$ mice (n=5 per group). **G.** Percentage of phospho-SMAD2 positive (pSMAD2+) cells in the day 7 post-fracture callus of *Prss56-Nf1*$^{+/+}$ or *Prss56-Nf1*$^{fl/fl}$ mice (n=4 per group). **H.** Left: Experimental design. *Prss56-Nf1*$^{fl/fl}$ mice were treated with blocking TGFβ antibody or IgG1control isotype at day 5, 8 and 11 post-fracture. Representative microCT images of callus of *Prss56-Nf1*$^{fl/fl}$ mice treated with TGFβ blocking antibody or IgG1 isotype control at 28 days post-fracture, showing absence of bridging in mice grafted with *Nf1*-deficient Schwann cells (white arrows). Right: Histomorphometric quantification of the volume of callus fibrosis of *Prss56-Nf1*$^{fl/fl}$ mice treated with blocking TGFβ antibody or IgG1 isotype control at 28 days post-fracture. (n=4 per group). Scale bars: Panel G: 50μm, Panel I: 1mm.

Figure 7

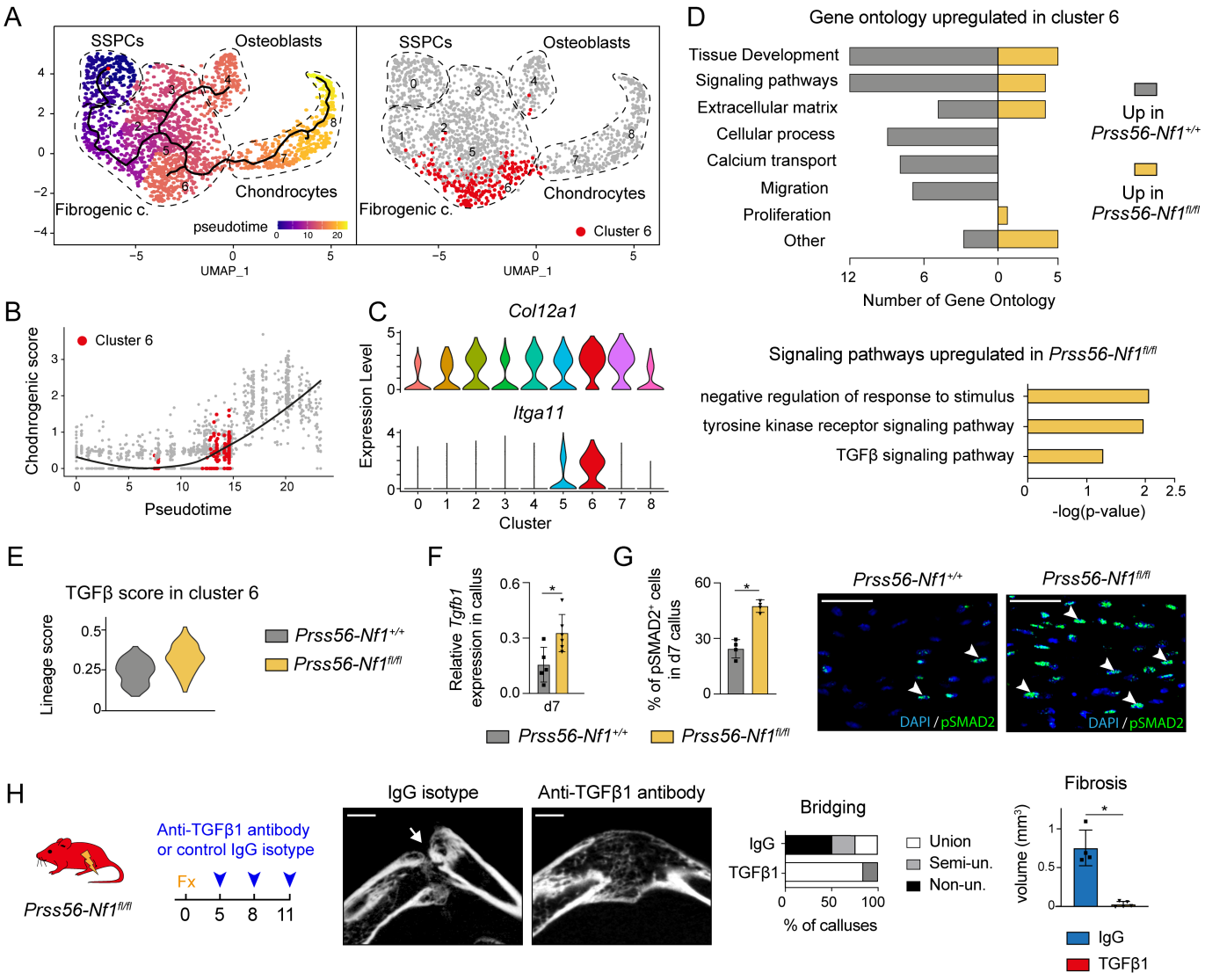
A
SSPCs
Osteoblasts
Chondrocytes
Fibrogenic c.
pseudotime
Cluster 6
UMAP_1
B
Cluster 6
Chodnrogenic score
Pseudotime
C
Col12a1
Itga11
Expression Level
Cluster
D
Gene ontology upregulated in cluster 6
Tissue Development
Signaling pathways
Extracellular matrix
Cellular process
Calcium transport
Migration
Proliferation
Other
Up in Prss56-Nf1+/+
Up in Prss56-Nf1fl/fl
Number of Gene Ontology
Signaling pathways upregulated in Prss56-Nf1fl/fl
negative regulation of response to stimulus
tyrosine kinase receptor signaling pathway
TGFβ signaling pathway
-log(p-value)
E
TGFβ score in cluster 6
Lineage score
Prss56-Nf1+/+
Prss56-Nf1fl/fl
F
Relative Tgfb1 expression in callus
d7
G
% of pSMAD2+ cells in d7 callus
Prss56-Nf1+/+
Prss56-Nf1fl/fl
DAPI / pSMAD2
H
Prss56-Nf1fl/fl
Anti-TGFβ1 antibody or control IgG isotype
Fx
IgG isotype
Anti-TGFβ1 antibody
Bridging
IgG
TGFβ1
Union
Semi-un.
Non-un.
% of calluses
Fibrosis
volume (mm3)
IgG
TGFβ1

Figure S1: Analyses of human pathological periosteum and PA pSSPCs (related to Figure 1 and 2).

A. Experimental design. Nuclei were extracted from periosteum of IC of P13 and PA site of P13 and P15, sorted and processed for snRNAseq. **B.** Sorting strategy of nuclei stained with Sytox-7AAD for snRNAseq. Sorted nuclei are delimited by a red box. **C.** Violin plots of the UMI counts, detected genes, percentage of mitochondrial and ribosomal genes in each snRNAseq dataset. UMAP projection of the three datasets independently. Cell populations are delimited by dashed lines. **D.** Feature plots of the lineage score of pericytes / smooth muscle cells (SMC), endothelial cells, immune cells and adipocytes in the integrated datasets. **E.** Experimental design. Periosteum collected at the pseudarthrosis (PA) site or iliac crest (IC) was cultured to isolate periosteal skeletal stem/progenitor cells (pSSPCs), for *NF1* genotyping, in vitro proliferation and differentiation. **F.** Flow cytometry analyses of cultured pSSPCs from PA site and IC, showing that they express mesenchymal markers (CD73, CD105) but not immune and endothelial markers (CD14, CD31, CD45). Samples are in red and Fluorescent Minus One (FMO) controls are in blue. **G.** *NF1* sequencing of pSSPCs from IC and PA site of patients P3, P4, P7, P9, P11 and P13, used for in vitro characterization. (n=6 per group). **H.** Chondrogenic, osteogenic and adipogenic differentiation of pSSPCs from PA and IC. Relative expression of *Sox9, Runx2,* and *Pparg* by in vitro differentiated pSSPCs from IC and PA into the chondrogenic, osteogenic and adipogenic lineage respectively. (n=6 per group). VAF: variant allele frequency, WT: wild-type, cnLOH: copy neutral loss of heterozygosity. p-value: ** $p < 0.01$.

Figure S1 (related to Fig. 1-2)

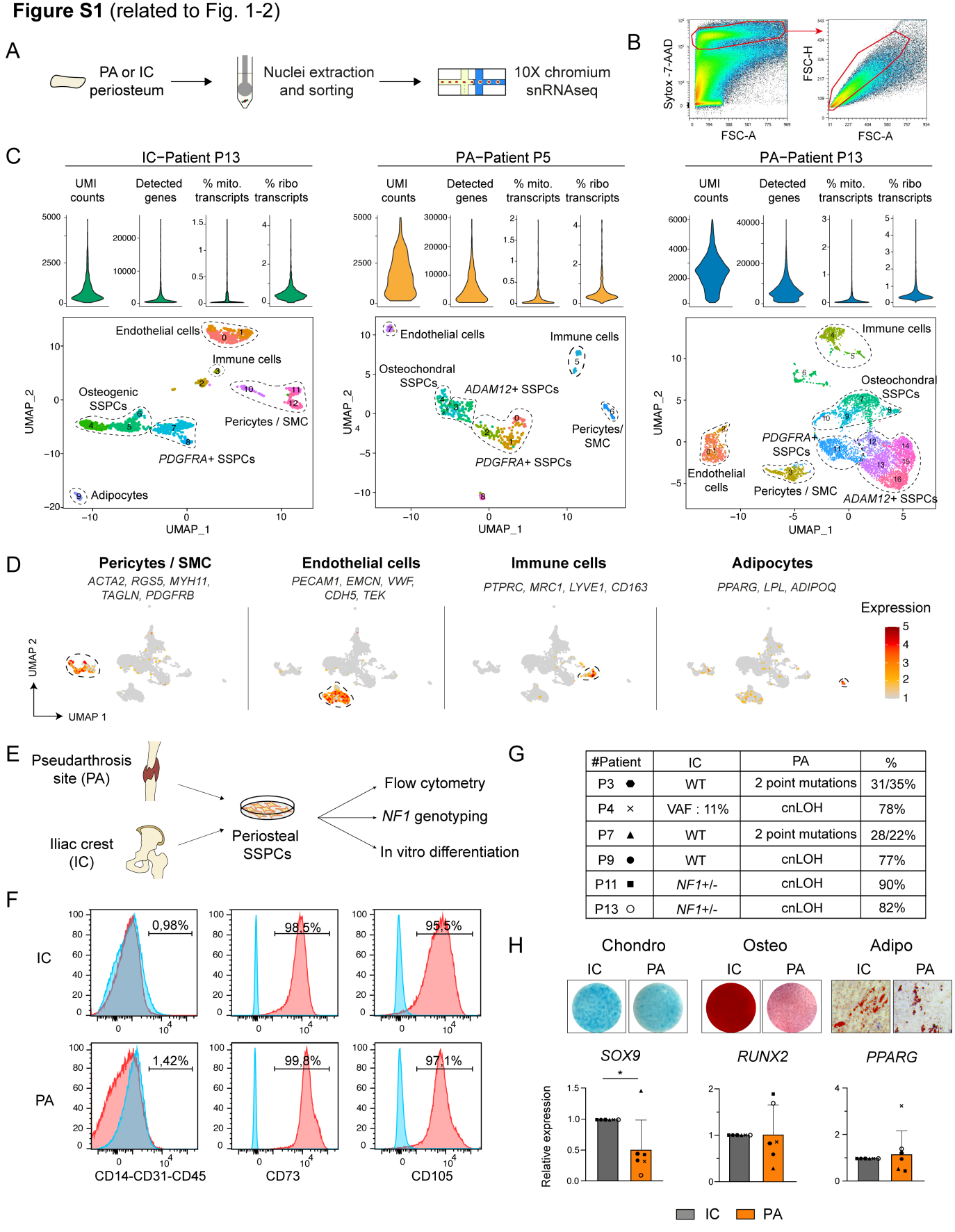

#Patient	IC	PA	%
P3 ⬣	WT	2 point mutations	31/35%
P4 ×	VAF : 11%	cnLOH	78%
P7 ▲	WT	2 point mutations	28/22%
P9 ●	WT	cnLOH	77%
P11 ■	*NF1*+/-	cnLOH	90%
P13 ○	*NF1*+/-	cnLOH	82%

Figure S2: Bone and bone repair phenotype of *Prss56-Nf1* KO mice (related to Figure 3)

A. Cortical porosity and bone volume/total volume (BV/TV) of trabecular bone of uninjured tibia from 3 month-*Prss56-Nf1*$^{+/+}$, *Prss56-Nf1*$^{fl/fl}$ and *Prss56-Nf1*$^{fl/-}$ mice (n = 5-7 per group).

B. Representative longitudinal and transverse microCT images of uninjured tibia from 3 month-*Prss56-Nf1*$^{+/+}$, *Prss56-Nf1*$^{fl/fl}$ and *Prss56-Nf1*$^{fl/-}$ mice. n.s.: non-significant. Scale bar: 500µm. **C**. Representatives callus sections of *Prss56-Nf1*$^{+/+}$, *Prss56-Nf1*$^{fl/fl}$ and *Prss56-Nf1*$^{fl/-}$ mice at 28 days post-fracture stained with Safrarnin'O (SO). **D.** Histomorphometric quantification of the volume of callus, cartilage, and bone at days 7, 14, 21 and 28 post-fracture of *Prss56-Nf1*$^{+/+}$, *Prss56-Nf1*$^{fl/fl}$ and *Prss56-Nf1*$^{fl/-}$ mice. (n=5-6 per group).

Figure S2 (related to Fig. 3)

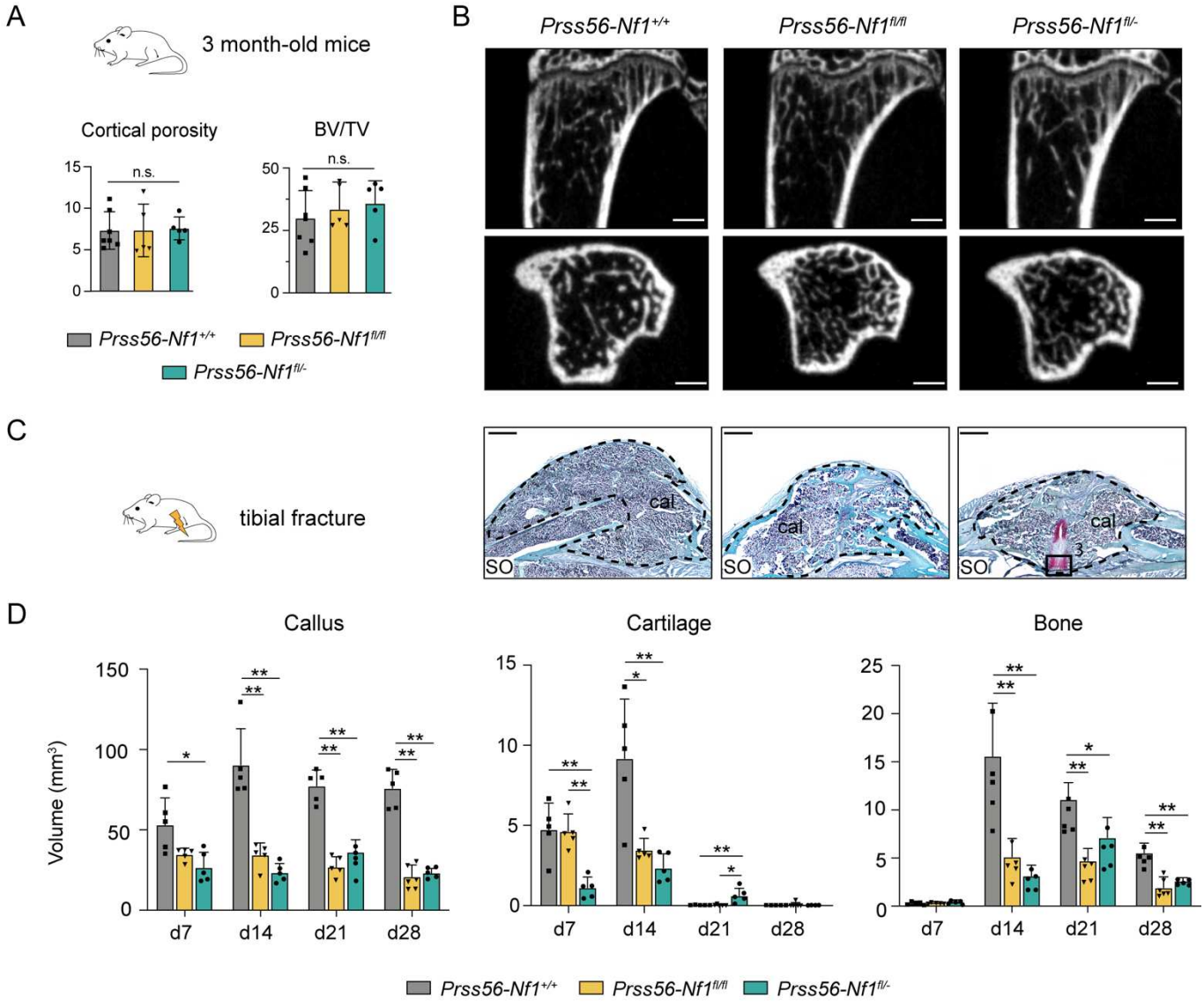

Figure S3: Absence of *Prss56* expression in tibia during bone development (related to Figure 4)

A. RNAscope experiments using *tdTom* and *Prss56* probes on boundary cap and tibia sections from E12.5, E13.5 and E14.5 *Prss56-Nf1*$^{+/+}$ embryos. tdTom+ cells are detected within the perichondrium (p) from E13.5 and the cartilaginous matrix (cart) from E14.5 (white arrowheads). **B.** Number of *tdTom* and *Prss56* expressing cells per tibia sections of E12.5, E13.5 and E14.5 *Prss56-Nf1*$^{+/+}$ embryos (n=5-6 embryos per group). **C.** UMAP projection of integrated scRNAseq datasets from digested hindlimbs at E11.5, E13.5, E15.5 and E18.5 from (Kelly et al., 2020) **D.** Dot plot of genes identifying endothelial cells (*Pecam1, Cdh5*), myogenic cells (*Myog, Tnnt1*), pericytes (*Acta2, Rgs5*), chondrogenic cells (*Col2a1, Acan*), mesenchymal cells (*Prrx1, Prrx2*), skin cells (*Krt14, Epcam*), and immune cells (*Lyz2, Ptprc*). **E.** Feature plot of *Prss56* gene expression.

Figure S3 (related to Fig. 4)

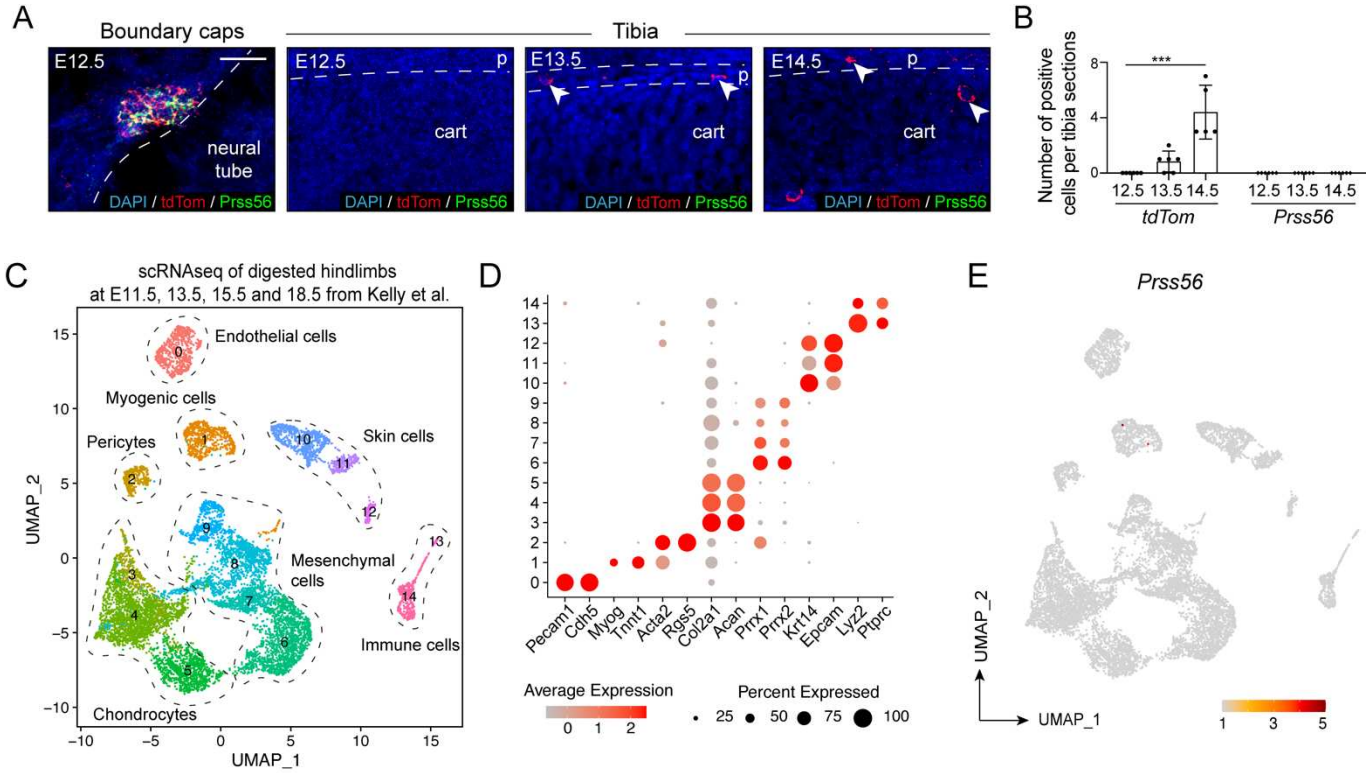

Figure S4: The periosteum is the only source of Prss56-derived SSPCs and Schwann cells for bone healing. (related to Figure 4)

A. Experimental design. Periosteum, bone marrow, and skeletal muscle were collected from *Prss56-Nf1*$^{+/+}$and *Prss56-Nf1*$^{fl/fl}$ mice and digested for flow cytometry analysis. **B.** Percentage of tdTom+ cells in periosteum (Po), skeletal muscle (Mu) and bone marrow (BM) from *Prss56-Nf1*$^{+/+}$and *Prss56-Nf1*$^{fl/fl}$ mice (n=5-7 per group). **C.** Flow cytometry analysis of tdTom+ cells isolated from periosteum, bone marrow and skeletal muscle of *Prss56-Nf1*$^{+/+}$and *Prss56-Nf1*$^{fl/fl}$ mice showing the presence of tdTom+ Lin- (CD11b-, CD31-, CD45-) SSPCs in the periosteum and skeletal muscle and tdTom+ Lin- Schwann cells (SC) in the periosteum. (n=5-7 per group). **D.** Experimental design. EDL muscles or periosteum were collected from *Prss56-Nf1*$^{+/+}$and *Prss56-Nf1*$^{fl/fl}$ mice and grafted at the fracture site of a wild-type host. **E.** Volume of tdTom signal in the callus of wild-type host at 14 days post-fracture and periosteum (Po) or skeletal muscle (Mu) graft isolated from *Prss56-Nf1*$^{+/+}$or *Prss56-Nf1*$^{fl/fl}$ mice. **F.** Representative Safranin'O (SO) staining of transverse callus section at day 14 post-fracture and EDL muscle graft from *Prss56-Nf1*$^{+/+}$or *Prss56-Nf1*$^{fl/fl}$ mice (grafted delimited by orange dashed line). High magnification of the cartilage in adjacent section showing the absence of contribution of Prss56-derived cells from the skeletal muscle of *Prss56-Nf1*$^{+/+}$and *Prss56-Nf1*$^{fl/fl}$ mice to the host callus. Cart: cartilage. * $p < 0.05$, *** $p < 0.001$. Scale bars: Low magnification: 1mm. High magnification: 50 µm.

Figure S4 (related to Fig. 4)

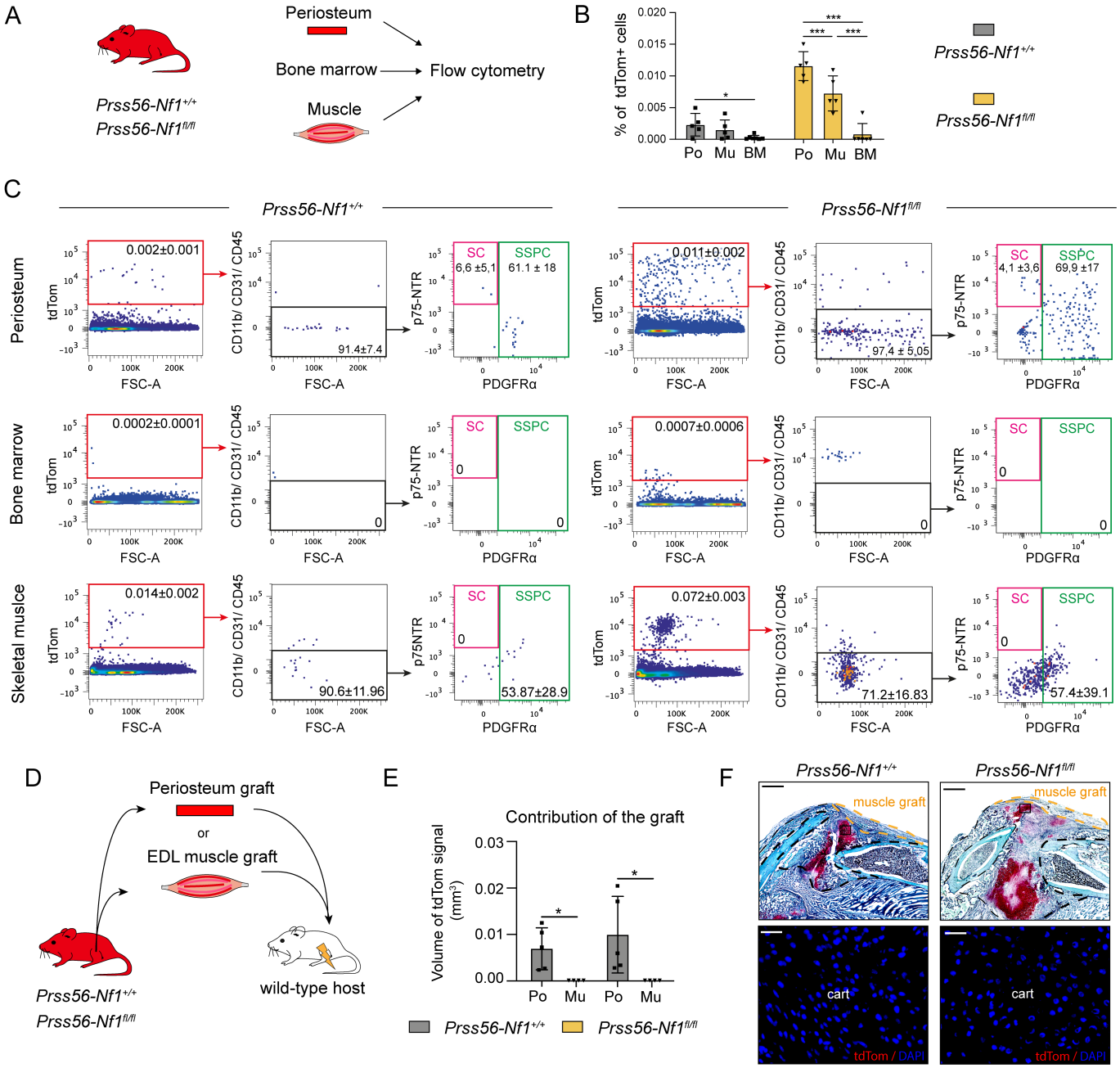

Figure S5: Intrinsic deficiency of Prss56-derived periosteal cells is not sufficient to induce pseudarthrosis phenotype. (related to Figure 5 and 6)

A. Experimental design. Periosteum was isolated from *Prss56-Nf1*$^{+/+}$ or *Prss56-Nf1*$^{fl/fl}$ mice and transplanted at the fracture site of a wild-type host. **B.** Representative Safranin'O (SO) staining of longitudinal day 14 post-fracture callus section of wild-type host grafted with periosteum from *Prss56-Nf1*$^{+/+}$ or *Prss56-Nf1*$^{fl/fl}$ mice (graft is delimited by red dashed line). Representative images of the contribution of tdTom+ cells showing that cells from *Prss56-Nf1*$^{+/+}$ graft are located in cartilage (labelled by SOX9) and cells from *Prss56-Nf1*$^{fl/fl}$ graft are located in fibrosis (labelled by POSTN). **C.** Percentage of the contribution of control and mutant tdTom+ cells to cartilage and fibrosis (n = 5-6 per group). **D.** Experimental design. Cultured tdTom^{+} periosteal skeletal stem/progenitor cells (pSSPCs) were isolated from *Prss56-Nf1*$^{+/+}$ or *Prss56-Nf1*$^{fl/fl}$ mice and analyzed by flow cytometry or transplanted at the fracture site of a wild-type host. **E.** Flow cytometry analysis of *Prss56-Nf1*$^{+/+}$ or *Prss56-Nf1*$^{fl/fl}$ cultured periosteal cells showing that cultured tdTom^{+} are PDGFRa+ SSPCs (97.4% ± 4.6 for *Prss56-Nf1*$^{+/+}$ mice and 98 % ± 2.4 for *Prss56-Nf1*$^{fl/fl}$ mice) (n= 5-6 per group). **F.** Histomorphometric quantification of the volume of cartilage and fibrosis at days 14 and 28 post-fracture of wild-type mice grafted with pSSPCs from *Prss56-Nf1*$^{+/+}$ or *Prss56-Nf1*$^{fl/fl}$ mice. (n= 3-5 per group). **G.** Representative Picrosirius (PS) staining of sections of day 28 post-fracture callus grafted with pSSPCs from *Prss56-Nf1*$^{+/+}$or *Prss56-Nf1*$^{fl/fl}$ mice showing bone bridging in both groups. (n = 3 – 5 per group). * $p < 0.05$, ** $p < 0.005$. Scale bars: Low magnification: 1mm. Panel B: 50µm for SOX9 and 100µm for POSTN. Panel G: High magnification: 200µm.

Figure S5 (related to Fig. 5-6)

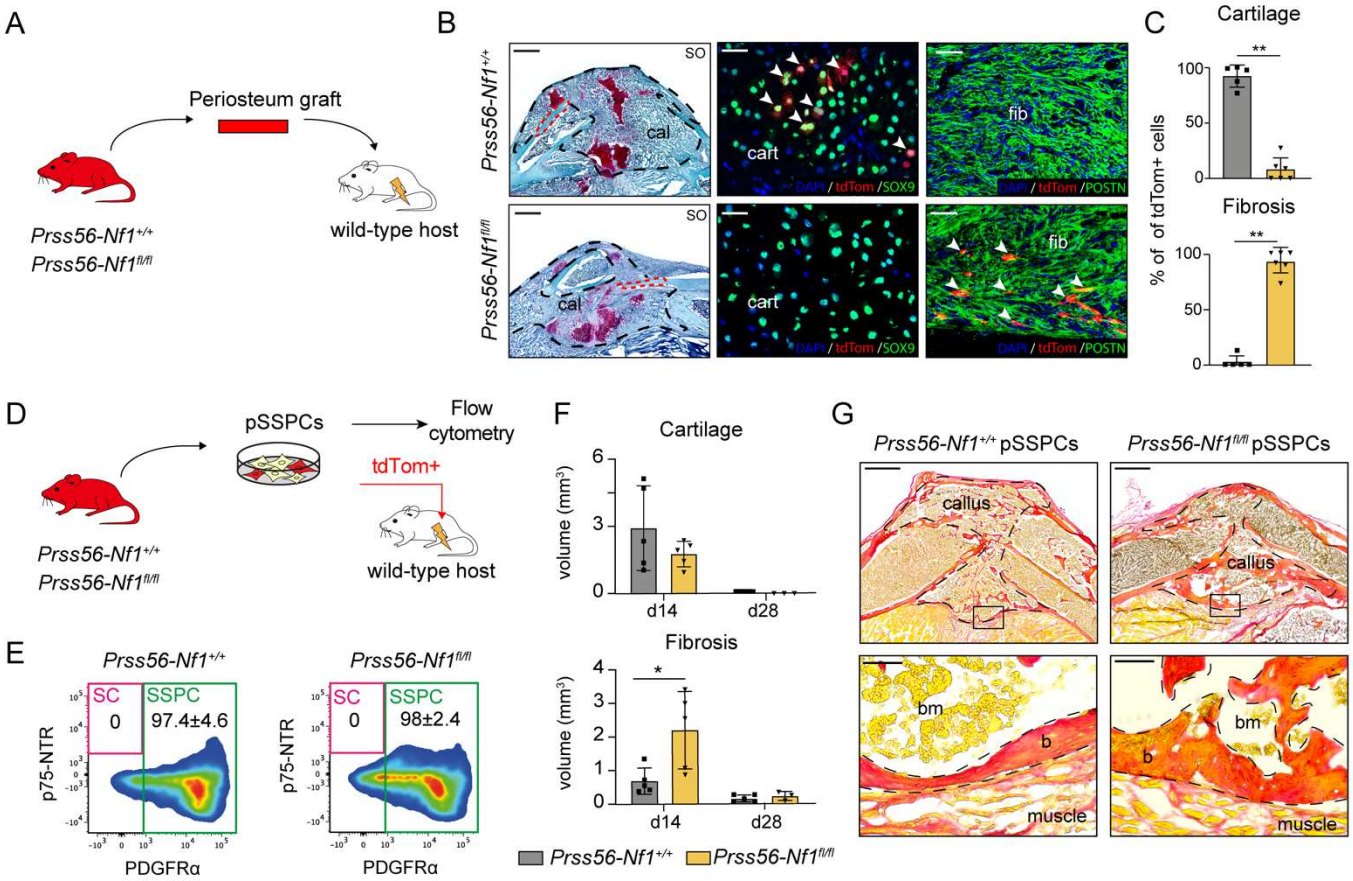

Figure S6: Periosteal response to fracture at single-nuclei resolution (related to Figure 5)

A. Experimental design. Nuclei were extracted from the periosteum of uninjured tibias and the periosteum and hematoma at day 5 and day 7 post-fracture of wild-type mice and processed for single-nuclei RNAseq. **B.** UMAP projection of color-coded clustering (top) and sampling (bottom) of the integration of uninjured, day 5 and day 7 datasets. 10 populations are identified (delimited by black dashed lines): pericytes, endothelial cells, Schwann cells, skeletal/stem progenitor cells (SSPCs), fibrogenic cells (Fibrog.), chondrocytes (Chondro), osteoblasts (Osteo), immune cells, adipocytes and osteoclasts. **C.** Lineage score of the different cell populations identified. **D.** Percentage of cells in SSPC, fibrogenic cell, osteoblast, chondrocyte and immune cell clusters in uninjured, day 5 and day 7 datasets. **E.** UMAP projection of color-coded clustering (left), color-coded sampling (middle) and monocle pseudotime trajectory (bottom) of the subset of skeletal stem/progenitor cells (SSPCs), fibrogenic cells, osteoblasts and chondrocytes from integrated uninjured, day 5 and day 7 post-fracture samples. The four populations are delimited by black dashed lines. **F.** Feature plot (top) and Scatter plot (bottom) of stem/progenitor, immune response, fibrogenic chondrogenic and osteogenic lineage scores along pseudotime in pSSPCs and their derivatives.

Figure S6 (related to Fig. 5)

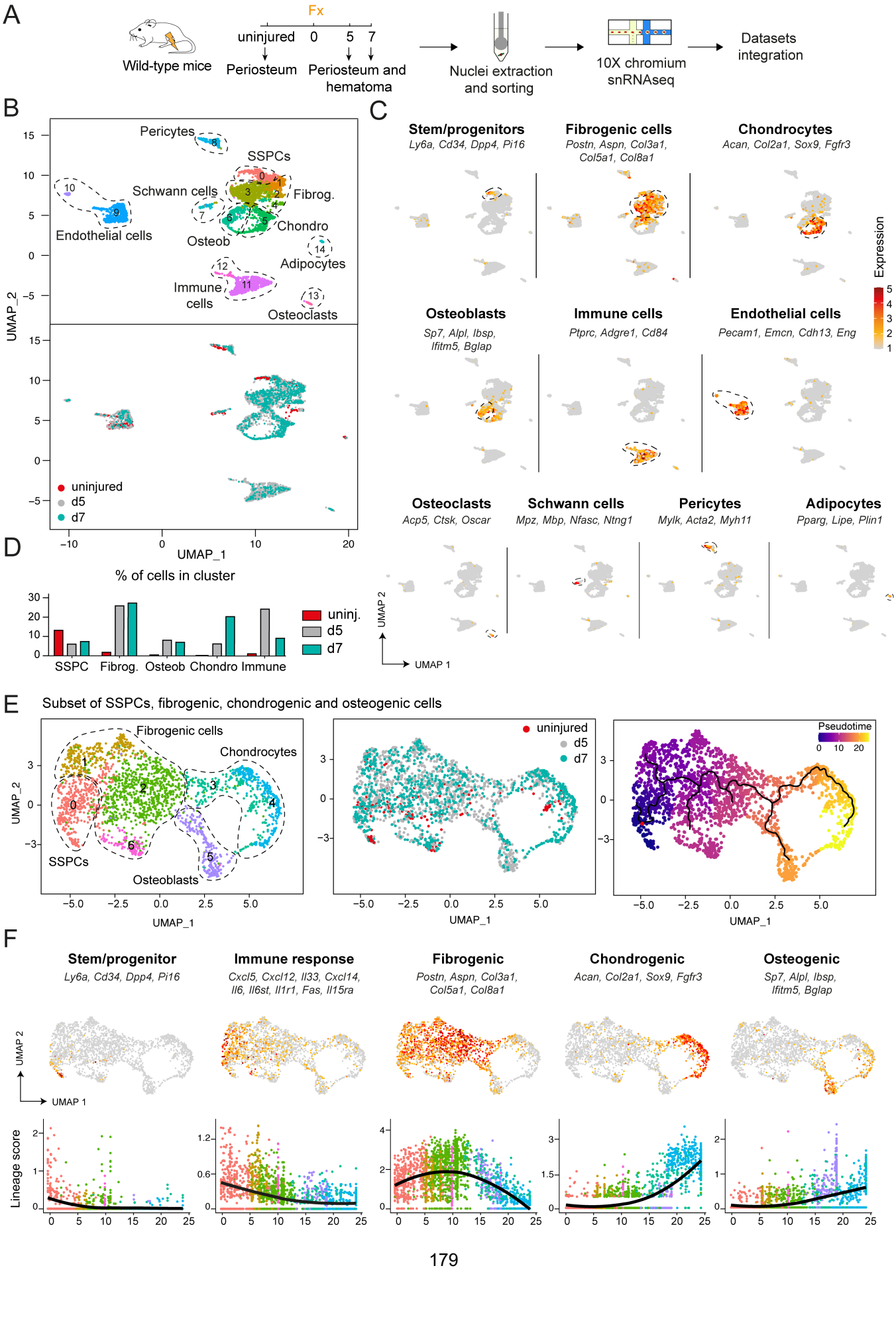

Figure S7: Integration of snRNAseq datasets from day 7 post-fracture callus of *Prss56-Nf1*$^{+/+}$ and *Prss56-Nf1*$^{fl/fl}$ mice. (related to Figure 6 and 7)

A. Experimental design. Nuclei were extracted from the periosteum and hematoma at day 7 post-fracture of *Prss56-Nf1*$^{+/+}$ and *Prss56-Nf1*$^{fl/fl}$ mice and processed for single-nuclei RNAseq.

B-C. UMAP projection of color-coded clustering (B) and color-coded sampling (C) of the integration of the day 7 post-fracture callus of *Prss56-Nf1*$^{+/+}$ and *Prss56-Nf1*$^{fl/fl}$ mice datasets. 8 populations are identified (delimited by black dashed lines): pericytes, endothelial cells, skeletal/stem progenitor cells (SSPCs), fibrogenic cells (Fibrog.), chondrocytes (Chondro), osteoblasts (Osteo), immune cells and osteoclasts. **D.** Lineage score of the different cell populations identified. **E.** Feature plot of *tdTomato* and *Prss56* expression. **F.** Ratio of TGFβ lineage score per cluster in *Prss56-Nf1*$^{fl/fl}$ cells on *Prss56-Nf1*$^{+/+}$cells in the subset of pSSPCs, fibrogenic, chondrogenic and osteogenic cells.

Figure S7 (related to Fig. 6-7)

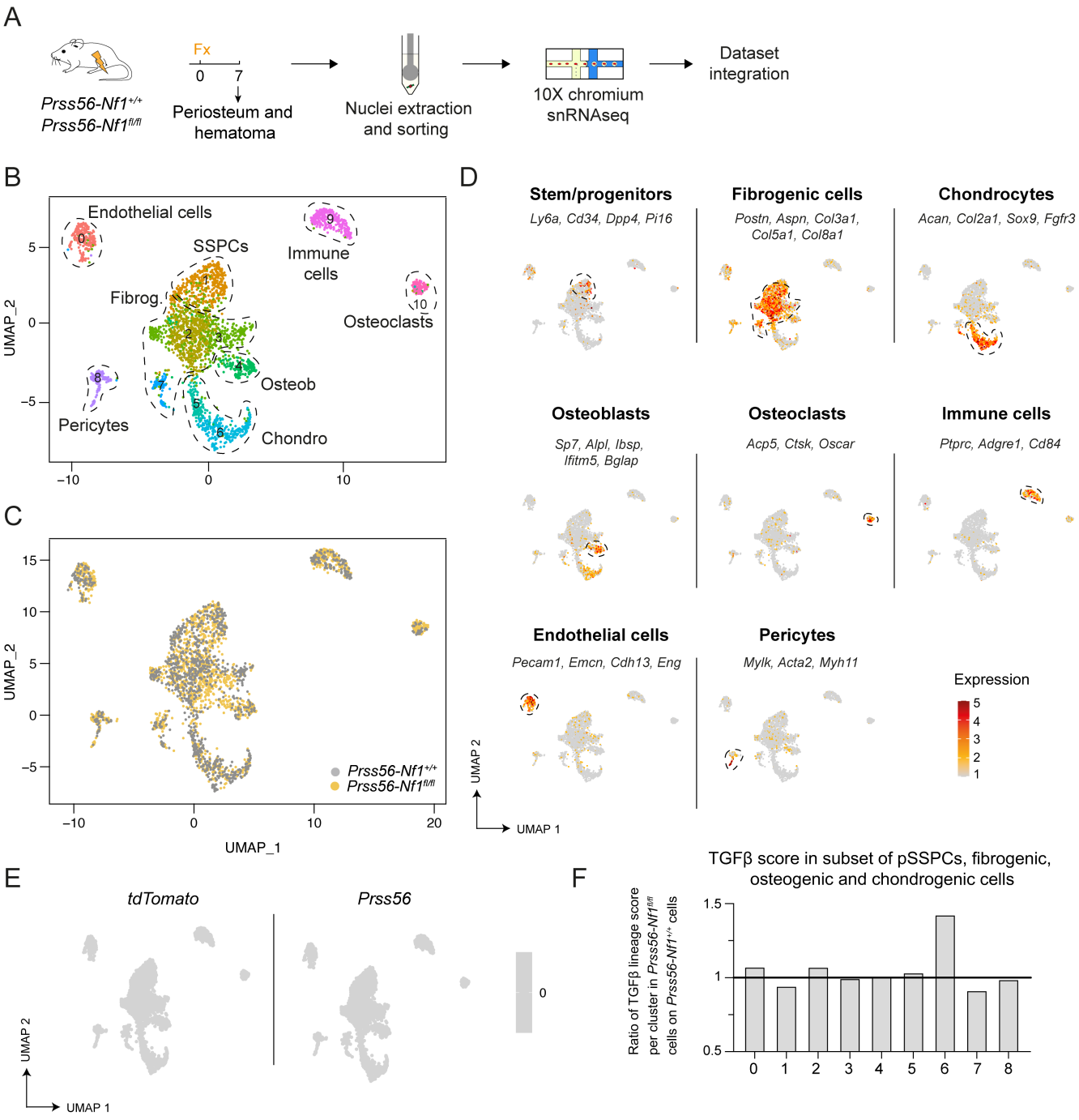

Table S1: Detailed information on the 17 patients of our CPT cohort and *NF1* sequencing results of the different tissues from IC and PA site (related to Figure 1).

Second *NF1* hit mutations were predominantly copy-neutral loss of heterozygosity (cnLOH, 7/13 patients), as well as point mutations (5/13) and *NF1* gene deletion (1/13). M: male, F: female, cnLOH: copy neutral loss of heterozygosity, Reinterv: reintervention, PO: periosteum, BM: Bone marrow, Fibrous tiss.: Fibrous tissue, Spong. bone: spongy bone, NS: Not sampled.

										Iliac crest		Pseudarthrosis site							Pseudarthrosis - 2nd bone		
Patient	Age	Gender	CPT type	Operation	Affected bone	1st event	2nd event	Comments	Blood	PO	Spong. Bone	PO	pSSPC	BM	Bone	Fibrous tis.	Skin	Muscle	PO	Bone	Fibrous tis.
P1	3	M	NF1	Primary	Tibia	Exon 1 - c.31C>T = p.(Gln11*)	*NF1* locus deletion		52	51	52	67	54	NS	74	75	50	50			
P2	3	M	NF1	Primary	Tibia	Intron 37 - c.4773-1G>T = p.Phe1592Leufs*7	cnLOH		50	51	49	75	72	55	NS	69	50	50			
P3	2	F	Isolated	Primary	Tibia	Exon 16 - c.1797G>A = p.Trp599*	Exon 14 - c.1570G>T = p.Glu524*		0 / 0	01 / 0	0 / 0	21 / 19	31/35	0 / 0	04 / 01	38 / 38	02/01	08 / 06			
P4	4	F	mosaic NF1	Primary	Tibia + Fibula	Exon 21 - c.2752A>T = p.(Lys918*)	cnLOH	* : possible cnLOH : allelic ratio of informative SNP : 58%	38	16	33	61	78	27	31*	23	14	24	NS	NS	32*
P5	4	F	NF1	Primary	Tibia + Fibula	Exon 16 - c.1722-?_1842+?del = p.(?)	Exon 44 - c.6619C>T = p.Gln2207*		50 / 0	NS	50 / 0	50 / 43	4	50 / 12	50 / 28	NS	50 / 0	50 / 0	50 / 32	50 / 08	50/02
P6	3	M	Isolated	Primary	Tibia	Exon 37 to 52 - c.4773-?_7675+?del	cnLOH		0	0	NS	80	0	0	0	NS	0	0			
P7	4	M	Isolated	Primary	Fibula	Exon 39 - c.5599delA = p.(Ile1867Serfs*6)	Exon 18 - c.2033dupC = p.Ile679Aspfs*21		0 / 0	0 / 0	0 / 0	21 / 14.5	27.5 / 22	NS	NS	34 / 33	03 / 02	01 / 01			
P8	2	M	Isolated	Primary	Tibia + Fibula	Exon 5 - c.525T>C = p.His175His	-	undetected ponctual variation LOH by deletion and cnLOH excluded	47/.	49/.	NS	48/.	0	NS	49/.	NS	50/.	49/.	49/.	49/.	NS
P9	3	F	Isolated	Primary	Tibia + Fibula	Ex28 - c.3721C>T = p.Arg1241*	cnLOH	**: cnLOH can't be determined due to the absence of informative SNP	0	0,2	0	71	77	60	37	7	1	1	NS	11**	NS
P10	3	F	Isolated	Primary	Tibia + Fibula	-	-	undetected ponctual variation LOH by deletion and cnLOH excluded	0	0	0	0	0	NS	NS	0	NS	NS	0	NS	NS
P11	10	F	Isolated	Reinterv.	Tibia + Fibula	Not identified	cnLOH	1st event not identified but cnLOH detected by informative SNP	SNP: 50%	NS	SNP: 48%	SNP: 90%	SNP: 78%	NS	NS	NS	NS	NS	SNP : 83%	NS	NS
P12	10	F	NF1	Reinterv.	Tibia	Exon 32 - c.4117_4118insCTTAAC = p.(Val1372_Ser1373insThr*)	Exon 38 - c.5242C>T = p.Arg1748*		50 / 0	50 / 0	NS	50 / 11	NS	NS	NS	NS	NS	NS			
P13	11	M	NF1	Reinterv.	Tibia + Fibula	c.1722-2A>T, p.	cnLOH	*** VAF from pSSPCs isolated from the periosteum of the 2nd bone	54	NS	46	51	82***	49	64	70	46	49	86	64	NS
P14	3	M	NF1	Primary	Tibia (tibial bowing	c.5752delA, p.(Ile1918Leufs*3)	cnLOH		53	49	48	81	53	60	51	NS	48	50			
P15	2	F	Isolated	Primary	Tibia	Exon 40 - c.5839C>T = p.Arg1947*	Exon 5 - c.574C>T = p.Arg192*		NS	NS	NS	28 / 26	NS	19 / 18	6/4	19 / 18	0/0	7/7			
P16	6	M	Isolated	Primary	Tibia	-	-	undetected ponctual variation LOH by deletion and cnLOH excluded	NS	NS	NS	0	NS	NS	NS	0	0	0			
P17	2	M	Isolated	Primary	Tibia (cystic CPT)	-	-	undetected ponctual variation LOH by deletion excluded Absence of informative SNP	0	NS	NS	0	NS	NS	NS	NS	NS	NS			

Materials and Methods

Human tissue sample collection

Cohort and Ethical approval

Sample collection from patients affected by congenital pseudarthrosis of the tibia (CPT) was performed at Necker-Enfants Malades Hospital, Paris. This study was approved by the Ethics Committee CPP-IDF-2 (#ID-RCB/EUDRACT: 2014- A01420-47; IMNIS2014-03). Informed consent of legal representatives of patients was obtained prior to sample collection. The cohort is composed of 17 patients, 7 with NF1-associated CPT and 10 with isolated CPT. NF1 diagnosis was performed by the Dermatology department at Necker-Enfants Malades Hospital, following guidelines from International Consensus Group on Neurofibromatosis Diagnostic Criteria (Legius et al., 2021). Isolated CPT was defined by the absence of additional NF1 clinical feature and the absence of *NF1* mutation in blood sample. 14 patients were treated for the first time (named “Primary” operation in Table S1) and 3 were undergoing surgery following initial treatment (named “Reintervention”). Two patients undergoing reintervention were excluded from the cohort as original PA tissues from the first resection were not accessible and we did not detect *NF1* biallelic inactivation. Therefore, we could not definitely conclude on the absence of *NF1* mutation.

Surgical procedure and sample collection

Tissues were collected during CPT treatment surgery using the induced membrane technique typically performed in 2 steps(Masquelet et al., 2000). The first surgical procedure consists of pseudarthrosis tissue resection, intramedullary nailing and insertion of a cement spacer to fill the gap. During this procedure, diseased periosteum, bone marrow, bone, fibrous tissue, muscle and skin from the pseudarthrosis site (PA) were collected. For patients undergoing surgery as secondary treatment, the primary pseudarthrosis tissues were unavailable but were collected away from the primary PA site when possible. After 6 to 8 weeks, a second surgical procedure was performed to remove the cement spacer and graft autologous iliac crest periosteum and cancellous bone in the induced membrane that formed around the cement. During this second procedure, unaffected periosteum and spongy bone from the iliac crest (IC) were harvested. Blood sample was also collected during surgery. Tissue dissection and identification was performed by orthopedic surgeons. Collected tissues were immediately placed in DMEM (21063029, ThermoFischer Scientific, USA) with 10% HEPES (15630056, ThermoFischer

Scientific) and 1% Penicillin-Streptomycin (15140122, ThermoFischer Scientific) at 4°C, and processed for *NF1* genotyping, single-nuclei RNAseq, primary culture and histological analyses as described below.

DNA extraction and *NF1* genotyping

Collected tissue samples were snap frozen in liquid nitrogen and stored at -80°C until processing for DNA extraction. Tissue disruption was performed using TissueLyser system (Qiagen). DNA was isolated from disrupted tissues or primary culture of periosteal cells using standard proteinase K digestion followed by phenol-chloroform extraction. DNA concentrations were assessed by spectrophotometry using Qubit 2.0 Fluorometer (ThermoFisher Scientific). Sequencing was performed at the NGS facility of Cochin Hospital, Paris. *NF1* genotyping was performed using targeted next generation sequencing (NGS) allowing *NF1* point mutations and copy number variation detection, as previously described (Pasmant et al., 2015). Briefly, targeted regions were sequenced using Ion Torrent PGM/S5 or Illumina MiSeq technologies after multiplex PCR amplification including the coding exons and the flanking intronic regions (25 bp) of *NF1* gene and *SPRED1* gene as copy number reference. Sequence alignment was performed with the Torrent Mapping Alignment Program (TMAP, Ion Torrent, Thermo Fisher Scientific) or BWA Aligner (Illumina). Aligned reads from BAM files were visualized using the Integrative Genomics Viewer v2.3 from the Broad Institute (Cambridge, MA, USA). SNVs and short Indels were annotated, ranked, and interpreted using the Polydiag suite (Bioinformatics Department, Paris-Descartes University). Structural variants (single and multi-exon deletion/duplication) were also investigated. *NF1* amplicon reads were first internally normalized by *SPRED1* amplicon reads. Subsequently, normalized reads obtained for each amplicon of a sample were then divided by the average normalized reads of control samples for the corresponding amplicon. Copy number ratios of 0,9 to 1,1 allowed the exclusion of a deletion. Copy number ratios under 0.8 were considered deleted.

Mice

C57BL/6ScNj, *Prx1*^{Cre} (Logan et al., 2002), *Rosa26-mtdTomato-mEGFP* (*R26*^{mTmG}) (Muzumdar et al., 2007), *R26tdTomato* (*R26*^{tdTom}) (Madisen et al., 2010), *Nf1*^{flox} (*Nf1*^{fl}), *Nf1*-knock out (*Nf1*$^{-}$) (Zhu et al., 2001) were obtained from Jackson Laboratory (Bar Harbor, ME). *Prss56*^{Cre} mice were generated by Piotr Topilko (Gresset et al., 2015; Radomska et al., 2019). Immunodeficient nude CD1 mice were

purchased from Janvier Labs. Mice were bred in animal facilities at IMRB, Creteil and Imagine Institute, Paris. Mice were kept in separated ventilated cages, in pathogen-controlled environment and ad libitum access to water and food. All procedures performed were approved by Paris University or Paris Est Creteil University Ethical Committees. Males and females were mixed in experimental groups. Bone injury and tissue collection for graft and digestion were performed on 10- to 14-week-old mice. Six- to 8-week-old mice were used for primary periosteum culture. Controlled breeding was performed to collect embryonic tissues at 12.5, 13.5 and 14.5 days of development.

Tibial fracture and tissue transplantation

For all surgical procedures, mice were anesthetized with an intraperitoneal injection of Ketamine (50 mg/mL) and Metedomidine (1 mg/kg) and received a subcutaneous injection of Buprenorphine (0.1 mg/kg) for analgesia. Mice were kept on a 37°C heating pad during anesthesia. Closed non-stabilized fracture was performed in mid-diaphysis of the right tibia by three-point bending (Duchamp de Lageneste et al., 2018). Briefly, the tibia was placed on a fracture jig, and a 470g weight was dropped from 11.5 cm to induce the fracture. For cell and tissue grafting, open non-stabilized tibial fracture was performed (Duchamp de Lageneste et al., 2018). The right hindlimb was shaved and sanitized. The skin was incised to expose the tibia and osteotomy was performed in the mid-diaphysis by cutting the bone. The wound was sutured, the mice were revived with an intraperitoneal injection of atipamezole (1 mg/kg) and received two additional analgesic injections in the 24 hours following surgery.

Tissue transplantation was performed as previously described (Duchamp de Lageneste et al., 2018; Julien et al., 2021). Grafted tissues were collected from *Prss56*^{Cre}*, R26*^{tdTom}*, Nf1*$^{+/+}$ or *Prss56*^{Cre}*, R26*^{tdTom}*, Nf1*$^{fl/fl}$ mice. For periosteum transplantation, a piece of cortical bone was collected from the anterior-proximal area of the donor tibia. The endosteum and bone marrow were removed. A cortical defect was performed on the anterior-proximal surface of the tibia of the host, adjacent to a fracture site. The graft was placed within the cortical defect. The muscle was sutured over the defect to hold the graft in position. For muscle transplantation, EDL (Extensor digitorum longus) muscle was dissected from tendon to tendon and grafted on the anterior surface of the tibia of the host wild-type mice. The grafted EDL was sutured to the host patellar and peroneus muscle tendons with non-resorbable sutures (12051-08, Fine Science Tool, Germany). After tissue grafting, a non-stabilized fracture was induced as described above.

TGFβ blocking antibody treatment

InVivoMAb antimouse/human/rat/monkey/hamster/canine/bovine TGF-β, Clone 1D11 (BX-BE0057) was purchased from Euromedex. Mice were treated at days 5, 8 and 11 post-fracture by intraperitoneal injection of 5 mg/kg of TGF-β blocking antibody diluted in PBS. Control mice were treated with 5 mg/kg InVivoMAb mouse IgG1 isotype control antibody (BX-BE0083, Euromedex).

MicroCT et bone union scoring

Callus samples or tibias were scanned at the Small Animal Platform of Paris Cité University (EA2496, Paris Cité) using X-ray micro- CT device (Quantum FXCaliper, Life Sciences, Perkin Elmer, Waltham, MA) with the X-ray source at 90 kV and 160 µA. A 10 mm field of view and µm voxel size was used. Images were processed using Horos software. Bone parameters (cortical porosity and bone volume/ total volume (BV/TV)) were determined on 1mm sections using CTan software v1.17.7.2 (Bruker, Hamburg, Germany). Callus bridging was determined in sagittal and longitudinal axes and the number of bridged sides was evaluated. A callus bridged in 3 or 4 sides was considered as union, 2 sides as semi-union, and 1 or 0 side as non-union (Julien et al., 2021).

Tissue sample processing and histology

Human periosteum samples were fixed in ice-cold 4% PFA (sc-281692, CliniSciences) for 24 hours, before embedding in paraffin. Mouse samples were processed as previously described (Perrin et al., 2021). Mice were euthanized and the uninjured or fractured tibias were collected and fixed in ice-cold 4% paraformaldehyde for 4 or 24 hours upon agitation. Samples were decalcified in 19% EDTA (EU00084, Euromedex) for 1 to 3 weeks at 4°C under constant agitation, placed in 30% sucrose (200-301-B, Euromedex) gradient for 24h before embedding in cryoprotectant. Samples were cryosectionned throughout the entire callus in 10µm thick sections. Every thirtieth sections were defrosted, rehydrated and stained with Picrosirius, Masson's Trichrome or Safranin'O staining. After staining, sections were dehydrated with successive ethanol and NeoClear incubations. Slides were mounted using NeoMount medium (1.09016.0100, VWR, USA). Stained sections were pictured using a Zeiss Imager D1 AX10 light microscope (Carl Zeiss Microscopy GmbH).

Picrosirius staining (PS)

Sections were stained in PicroSirius solution (0.1% of Direct Red 80 (43665-25G, Merck) in picric acid (80456, Merck)) for 2 hours protected from light.

Masson's trichrome staining (TC)

Sections were first stained in Harris hematoxylin diluted ½ (ref F/C0283, MMFrance) for 5 min, washed in tap water for 5 min, stained with Red Mallory for 10 min, washed for 5 min and then placed 10 min in phosphomolybdic acid 1% (HT153, Merck). Finally, sections were stained 20 min in light green (720-0335, VWR) and fixed in 1% acetic acid.

Safranin'O staining (SO)

Sections were stained with Weigert's solution for 5 min, rinsed in running tap water for 3 min and stained with 0.02% Fast Green for 30 seconds (F7252, Merck), followed by 1% acetic acid for 30 seconds and Safranin'O solution for 45 min (S2255, Merck).

Histomorphometric analysis

Histomorphometric analysis was performed on every thirtieth sections throughout the entire callus as described in (Duchamp de Lageneste et al., 2018). Areas of callus, cartilage, bone and fibrosis were determined using ZEN software v1.1.2.0 (Carl Zeiss Microscopy GmbH) on SO, TC and PS staining respectively. Volumes were calculated using the formula: $volume = \frac{1}{3} h \sum_{1}^{n-1} (A_i + A_{i+1} + \sqrt{A_i * A_{i+1}})$ with A_i and A_{i+1} being the areas of callus, cartilage, bone and fibrosis in following sections, h was the distance between Ai and Ai + 1 and equal to 300 µm and n the total number of sections analyzed in the sample.

Immunostaining

Cryosections were defrosted at room temperature protected from light and rehydrated in PBS. Paraffin sections were deparaffinized by successive Neo-Clear and alcohol incubations and rehydrated in PBS. For phosho-ERK, OSX, SOX10 and KU80 immunofluorescence, an antigen retrieval step was performed by incubating the slides in citrate buffer at 95°C for 20 min, followed by 20 min at 4°C. Sections were incubated 1 hour at room temperature in 5% serum, 0.25% Triton PBS before incubation

with primary antibodies listed in Table S2 overnight at 4°C. Secondary antibody incubation was performed at room temperature for 1 hour. Slides were mounted with Fluoromount-G mounting medium with DAPI (00-4959-52, Life Technologies). All immunostainings were validated using positive controls.

Quantification of fluorescent signal

Quantification of tdTom signal in the callus. The surface of tdTom signal in the callus, cartilage, bone and fibrosis of *Prss56^{Cre}-Nf1$^{+/+}$* or *Prss56^{Cre}-Nf1$^{fl/fl}$* mice was measured on three central-callus sections 300 µm apart as described in (Duchamp de Lageneste et al., 2018). The sections were pictured using Zeiss Imager D1 AX10 microscope and tdTom surface was measured using Zen Software.

Quantification of tissue or cell graft contribution. For graft contribution, tdTom or GFP signal was measured every 300 µm through the entire callus. The tdTom or GFP signal was pictured using Zeiss Imager D1 AX10 microscope and tdTom or GFP surface was measured using Zen Software.

Quantification of pERK+ and pSMAD2+ cells. The percentage of phospho-ERK+ and phosho-SMAD2+ cells was calculated by the number of pERK+ or pSMAD2+ cells compared to the number of DAPI+ nuclei using QuPath. For each sample, the percentage of pERK+ and pSMAD2+ cells were determined by the mean of 2 sections 300µm apart. For each section, the number of positive cells was determined in 3 areas of the callus.

Quantification of pERK and SOX9 fluorescent signal per cell. Two sections of day 7 post-fracture callus per sample were immunostained with both SOX9 and pERK antibody. Three pictures were taken per section and cells or tdTom+ cells were manually delimited using ImageJ. SOX9 and pERK signal was quantified for each cell and values were plotted using GraphPad Prism to determine the correlation between SOX9 and pERK fluorescence.

RNAscope in situ hybridation

The expression of *Prss56* and *tdTom* at E12.5, 13.5 and 14.5 was visualized using the RNAscope® Multiplex Fluorescent Assay V2 (Biotechne). Embryos were dissected and the hindlimbs were fixed in ice-cold 4% PFA for 24 hours, before progressive sucrose incubation and cryoembedding. Twenty µm thick sections were cut and processed according to the manufacturer's protocol: 15 min of post-fixation in 4% PFA, ethanol dehydration, 10 min of H_2O_2 treatment, 5 min of target retrieval at 95°C, and 30 min of protease III treatment. After hybridization and revelation, the sections were mounted under a glass

coverslip with Prolong Gold Antifade (P10144, ThermoFischer). Sections were pictured and analyzed using Zeiss LSM800 and the number of tdTom$^+$ and Prss56$^+$ cells per tibia per section was manually counted.

Primary periosteal cell culture

Mouse periosteal cell culture

Primary culture of murine periosteal cells was performed as previously described (Duchamp de Lageneste et al., 2018; Perrin et al., 2021). Six- to 8-week-old mice were euthanized and tibias were dissected free of muscle and surrounding tissue. Epiphyses were cut and bone marrow flushed. Flushed bones were placed in a culture-dish for explant culture with drops of culture medium composed of MEMα (32561094, ThermoFischer Scientific), supplemented with 20% of lot-selected Fetal Bovine Serum (10270106, ThermoFischer Scientific), 1% of Penicillin-Streptomycin and 10 ng/ml basic Fibroblast Growth Factor (bFGF, 3139-FB-025/CF, Biotechne). After cell migration, bone explants were removed. As previously reported, this protocol allows specific amplification of periosteal derived stem/progenitor cells, macrophages and osteoclasts (Julien et al., 2022). Cells were trypsinized and used at passage 1 to 3. For in vivo cell transplantation of Prss56-derived cells, periosteal cells were cultured to passage 2, trypsinized and living tdTom+ were sorted using FACS Aria Fusion. Sorted tdTom+ cells were cultured one passage for cell amplification, trypsinized, counted and used for transplantation as described above.

Human periosteal cell culture

Primary culture of human periosteal cells was performed as described for murine periosteal cells. Periosteum collected at the pseudarthrosis site or the iliac crest was divided in several pieces and placed in a culture dish for explant culture with drops of culture medium composed of MEMα, supplemented with 20% of FBS, 1% of Penicillin-Streptomycin and 10 ng/ml bFGF. Drops of medium were replaced every day until the tissue attached to the culture dish. Periosteal cells progressively migrated in the dish. After one to two weeks, periosteum explants were removed and periosteal cells were trypsinised for further analysis. *NF1* genotyping and RNAseq analysis were performed at passage 1, in vivo transplantation at passage 2, in vitro proliferation, differentiation and MAPK pathway activation between passages 2 and 4.

Schwann cell and periosteal stem/progenitor cell transplantation

Schwann cell isolation

Prss56-derived Schwann cells were isolated from intercostal nerves (Clements et al., 2017). Mice were euthanized and the back skin was incised. Nerves were collected free of surrounding tissues, minced and digested under constant agitation at 37°C in digestion buffer composed of Hanks Balanced Salt Solution (HBSS, 24020117, ThermoFischer Scientific) with 0,04% of Hyaluronidase (WOLS05474, Serlabo), 0,3% of Collagenase II, 0,15% of Trypsin and 100U/mL of DNAse I for 20 to 40 min. Digestion was stopped with MEMα medium supplemented with 20% of FBS. Cells were filtered, centrifuged, resuspended in MEMα with 20% FBS. Sytox Blue (S34857, Thermo Fisher Scientific) was added to stain dead cells and living $tdTom^+$ were sorted using Influx Cell Sorter.

Cell transplantation

Cell transplantation was performed as described in (Perrin et al., 2021). 100,000 cultured murine or human periosteal cells, isolated as described in the "Primary periosteal cell culture" section, or 3000 to 4000 tdTom+ Schwann cells were embedded in Tisseel Prima fibrin gel, composed of fibrinogen and thrombin (3400894252443, Baxter S.A.S, USA), according to manufacturer's instructions. Briefly, the cells were resuspended in 15 µl of fibrin (diluted at 1/4), before adding 15 µL of thrombin (diluted at 1/4) and mixing. The pellet was then placed on ice at least 15 min for polymerization. The cell pellet was transplanted at the fracture site between the bone cortex.

In vitro proliferation

Cell proliferation was determined by cell counting every two days from day 2 to 10 after passage. 10,000 cells were plated in 24-well dish. The number of cells in each well was determined using the luminescent cell viability buffer CellTiter-Glo® (G7571, Promega, USA) according to the manufacturer's recommendation. Culture medium was removed and replaced by 0.7 ml of CellTiter-Glo® Buffer and 0.7 mL of fresh culture medium. After 30 min, the luminescence was measured using Tecan Infinite M200 Pro (Tecan, Switzerland). Each sample was analyzed in duplicates at each time point. Standard curve was used to determine the number of cells from absorbance values. Growth curve was drawn and area under curve (AUC) was calculated using GraphPad Prism. AUC of periosteal cells from PA and IC was normalized on the AUC of the IC of each patient.

In vitro differentiation

In vitro differentiation was performed as described in (Perrin et al., 2021). For osteogenic and adipogenic differentiation, cells were plated and amplified in growth medium. At confluency, cells were cultured in osteogenic medium, containing MEMα with 10% lot selected FBS, 0.2mM L-ascorbic acid (A8960, Merck), 10mM glycerol 2- phosphate disodium salt hydrate (G9422, Merck) and 0.1 µM dexamethasone (D8893, Merck), or adipogenic medium, containing MEMα with 10% lot selected FBS, 10 ug/mL insulin (I3536, Merck), 100µM indomethacin (I7378, Merck), 0.5 mM 3-isobutyl-methylxanthine (I5879, Merck) and 0.1 µM dexamethasone (D8893, Merck). The medium was changed twice a week. After 21 days, cells were resuspended in Trizol (12034977, Thermo Fisher Scientific) and frozen for RNA analysis or fixed in ethanol for staining. Fixed cells were stained with Oil Red O solution (O0625, Merck) or Alizarin Red solution (A5533, Merck) for adipogenic and osteogenic differentiation respectively.

For chondrogenic differentiation, cells were plated as micromass of 5.10^5 cells in 200 µL of growth medium. After 4 hours, growth medium was replaced by chondrogenic medium containing high glucose DMEM with 10% FBS, 0.1 µM dexamethasone, 100 µg/mL sodium pyruvate (P5280, Merck), 40 µg/mL L-proline (P0380, Merck), 50 µg/mL L-ascorbic acid, 50 mg/mL Insulin-Transferrin-Selenium (I1884, Merck), and 10 ng/mL TGFβ1 (T7039, Merck). After 3 days, micromasses were resuspended in Trizol and frozen for RNA analysis or fixed in glutaraldehyde before staining with Alcian Blue solution (A5268, Merck).

RNA extraction and qPCR

For qPCR analyses of *SOX9, RUNX2* and *PPARG* from differentiated human pSSPCS, cells were collected in Trizol (15596026, Thermofisher) and RNAs were extracted following the manufacturer's instructions. After reverse transcription of 50ng to 1µg of RNA with Superscript II® (18064022, Thermofisher), cDNAs were amplified with Power SYBR Green System (4368706, Thermofischer) in 384 wells optical plates with the Roche LightCycler 480 Real -Time PCR System. Analyses were performed with the ΔΔCT method using *RPLP0* used as calibrator gene. The values of each sample were normalized on the iliac crest of the same patient. RT-qPCR were performed twice with duplicates for each data point.

To assess the expression of *Tgfb1* in *Prss56-Nf1* KO mice, the periosteum and hematoma from day 7 post-fracture callus were collected and snap frozen in liquid nitrogen. RNA extraction was performed using RNAeasy Plus Kit (74134, Qiagen) following manufacturer's instructions. RNA concentration was quantified using NanoDrop spectrophotometer (Thermo Scientific). Reverse transcription was performed using Superscript III RT® (18080-044, Life Technologies) following manufacturer's instructions. qPCR was performed by mixing 10 µL of SYBR green Master Mix, 5 µL of cDNA, 1 µL of primers and 4 µL of RNAse free H2O using StepOnePlus Real-Time PCR system (ThermoFischer). Analyses were performed with the ΔΔCT method using *Gapdh* as calibrator gene. Primers sequences are provided in Table S3.

Western Blot

Cultured human periosteal cells were washed with 1X phosphate-buffered saline (PBS) and lysed on ice in RIPA buffer, 1X protease inhibitors (P8340, Merck) and 1X phosphatase inhibitors (4906845001, Merck). After 20 minutes of centrifugation at 17400 g and 4°C, protein concentrations were determined using the BCA protein assay kit (J63283.QA, ThermoFisher Scientific). Protein lysates (50µg) were migrated in SDS-polyacrylamide (Sodium Dodecyl Sulfate) 4-12% gel (Biorad) and transferred to nitrocellulose membranes (GE Healthcare). TBS-Tween was used for blocking solutions and to dilute the antibody solutions. Membranes were blocked for 1h with 5% BSA (Bovine Serum Albumin) and incubated at 4°C overnight with primary antibodies listed in Table S3. Proteins were visualized using secondary antibodies conjugated to horseradish peroxidase. Images were obtained with the FusionFX imager (Vilbert) and chemiluminescence solutions (ECL, enhanced chemiluminescent, ThermoFisherScientific). Semi-quantitative analysis was done with ImageJ tools and signals were normalized on GAPDH signal. pERK signal on ERK signal was calculated for each sample, and each sample were normalized on the pERK/ERK signal of the IC of the same patient.

Bulk RNA sequencing of human primary periosteal cells

RNAs were extracted from primary periosteal cells from IC and PA site of patients 3 and 7 using the RNeasy Kit (Qiagen) use a DNA removal step accordingly to manufacturer's recommendation. RNA qualities were assessed by capillary electrophoresis using High Sensitivity RNA reagents with the Fragment Analyzer (Agilent Technologies) and the RNA concentrations were measured by using

spectrophometry using Xpose (Trinean) and Fragment Analyzer capillary electrophoresis. RNAseq libraries were prepared from 1 µg of total RNA using the Universal Plus mRNA-Seq kit (Nugen) as recommended by the manufacturer. The oriented cDNAs produced from the poly-A+ fraction were sequenced on a NovaSeq6000 from Illumina (Paired-End reads 100 bases + 100 bases). A total of ~22 millions of passing filter paired-end reads was produced per library. FASTQ files were mapped to the ENSEMBL Human (GRCh38/hg38) reference using HISAT2 and counted by featureCounts from the Subread R package. Read count normalization and group comparisons were performed by three independent and complementary statistical methods: Deseq2, edgeR, LimmaVoom. Flags were computed from counts normalized to the mean coverage. All normalized counts <20 were considered as background. The results of the three methods were filtered at pvalue<0.05 and folds 1.2 compared and grouped by Venn diagram. Principal component analysis was performed using Rstudio v1.4.1717 and Gene Ontology analyses using EnrichR (maayanlab.cloud/Enrichr/).

Flow Cytometry analyses of periosteal, bone marrow and skeletal muscle cells

Periosteal cell isolation

To isolate periosteal cells, uninjured tibia or tibia 28 days after fracture were collected from *Prss56*^{Cre}-*Nf1*$^{+/+}$ and *Prss56*^{Cre}-*Nf1*$^{fl/fl}$ mice, by carefully removing all surrounding soft tissues (van Gastel et al., 2012). Epiphyses were embedded in low melting agarose and tibias were placed for 30 min at 37°C in digestion medium composed of PBS with 3mg/ml of Collagenase B (C6885, Merck), 4mg/ml of Dispase (D4693, Merck) and 100U/mL of DNAse I (WOLS02007, Serlabo, France). After digestion, tibias were removed and the suspension was filtered, centrifuged and resuspend in the appropriate buffer for subsequent analysis.

Bone marrow cell isolation

The bone marrow was flushed using MEMα with 10% FBS. The flushed bone marrow was centrifuged and resuspend in ACK buffer (A1049201, Thermo Fisher Scientific) for red blood cells lysis for 5 min at room temperature. After centrifugation, the bone marrow was resuspended in digestion medium composed of PBS with 3mg/ml of Collagenase B, 4mg/ml of Dispase and 100U/mL of DNAse I and placed at 37°C for 30 min. After digestion, the suspension was filtered, centrifuged and resuspend in PBS with 0,5% BSA et 2mM EDTA (EU00084, Euromedex). A step of hematopoietic cell depletion was

performed to increase the mesenchymal fraction of the cell suspension using lineage cell depletion kit following the manufacturer's instructions. Bone marrow cells were incubated with primary biotinylated antibodies specific to hematopoietic lineage (CD5, CD45R (B220), CD11b, Gr-1 (Ly-6G/C), 7-4, and Ter-119) followed by an incubation with Anti-Biotin microbeads and magnetic column filtering (130-090-858, Milteny Biotec, Germany). After depletion, cells were centrifuged and resuspend in the appropriate buffer for subsequent analysis.

Skeletal muscle mononucleated cell isolation

Skeletal muscle mononucleated cells were isolated as described (Julien et al., 2021). The skeletal muscles surrounding the tibia were dissected free of fascia, tendon and fat. Tissues were minced and digested at 37°C for 2 hours in DMEM (21063029, Life Technologies) with 1% Trypsin (15090046, Life Technologies) and 1% collagenase D (11088866001, Roche). Cells in suspension were removed every 20 min and digestion medium was replaced. After 2 hours, the cell suspension was filtered, centrifuged and resuspended in the appropriate buffer for subsequent analysis.

Flow cytometry analysis

For flow cytometry analyses of digested tissues, cell suspensions were prepared as described above. For cultured cells, cells were trypsinised, centrifuged and resuspended in FACS buffer, composed of PBS with 0,5% BSA et 2mM EDTA. Cells were incubated with antibodies listed in Table S3 for 30 min, on ice and protected from light. After washing, cells were resuspended in FACS buffer and Sytox Blue (S34857, Thermo Fisher Scientific) was added before analysis to stain dead cells. Analyses were performed using a BD Fortessa X20 (BD Biosciences). Compensation matrix was designed using Compensation Beads (01-2222-42, Thermo Fischer Scientific) and appropriate controls were used to delimitate the gating strategy. Data were analyzed using FlowJo v10.8.1.

Nuclei extraction and single nuclei RNAseq

Nuclei extraction from murine periosteum

Nuclei extraction protocol was adapted from (G Martelotto, 2019; Santos et al., 2021). Four datasets were generated for this study: (i) uninjured periosteum from wild-type mice, (ii) periosteum and hematoma 5 days post-fracture from wild-type mice, (iii) periosteum and hematoma 7 days post-fracture from *Prss56-Nf1*$^{+/+}$ mice, considered wild type equivalent and (iv) periosteum and hematoma 7 days post-fracture from *Prss56-Nf1*$^{fl/fl}$ mice. For uninjured periosteum, tibias from 4 mice were dissected free of muscle and surrounding tissues. The epiphyses were cut and the bone marrow flushed. The periosteum was scraped from the cortex using Dissecting Chisel (10095-12, Fine Science Tools). For day 5 and 7 post fracture, injured tibias from 4 to 9 mice were collected and the surrounded tissues were removed. The activated periosteum was scraped and collected with the hematoma. Collected tissues were minced and placed 5 min in ice-cold Nuclei Buffer (NUC101, Merck) before mechanical nuclei extraction using a glass douncer. Extraction was performed by 20 strokes of pestle A followed by 20 of pestle B. Nuclei suspension was filtered, centrifuged and resuspensed in RNAse-free PBS (AM9624, ThermoFischer Scientific) with 2% Bovine Serum Albumin (A2153, Merck) and 0.2 U/µL RNAse inhibitor (3335399001, Roche). A second step of centrifugation was performed to reduce contamination by cytoplasmic RNA. Sytox™ AADvanced™ (S10349, ThermoFischer Scientific) was added (1/200) to label nuclei and Sytox-AAD+ nuclei were sorted using Sony SH800.

Nuclei extraction from human periosteum

Nuclei extraction was performed on frozen human periosteum samples from PA site and IC of patient P13 and from PA site of patient P5. RNA integrity was checked beforehand on identical tissue samples (RIN > 6.5). Periosteum samples were briefly defrosted in nuclei extraction buffer before mincing and nuclei extraction as described above for murine periosteum.

Single nuclei RNA sequencing

The snRNA-seq libraries were generated using Chromium Single Cell Next GEM 3′ Library & Gel Bead Kit v.3.1 (10x Genomics) according to the manufacturer's protocol. Briefly, 10 000 to 20 000 nuclei were loaded in the 10x Chromium Controller to generate single-nuclei gel- beads in emulsion. After reverse transcription, gel-beads in emulsion were disrupted. Barcoded complementary DNA was isolated and

amplified by PCR. Following fragmentation, end repair and A-tailing, sample indexes were added during index PCR. The purified libraries were sequenced on a Novaseq (Illumina) with 28 cycles of read 1, 8 cycles of i7 index and 91 cycles of read 2. Sequencing data were processed using the Cell Ranger Count pipeline and reads were mapped on the mm10 reference mouse genome or HG38 2020-A reference human genome, with intronic and exonic sequences.

Single nuclei RNA sequencing analysis

Single-nuclei RNAseq analyses were performed using Seurat v4.1.0(Butler et al., 2018; Stuart et al., 2019) and Rstudio v1.4.1717.

Filtering and clustering

Aligned snRNAseq datasets were filtered to retain only nuclei expressing between 200 et 5000 genes and expressing less than 0,5% of mitochondrial genes and 2.5% of ribosomal genes. Contamination from myogenic cells were removed from the analyses. After filtering, the datasets of murine samples were composed of 471 cells for uninjured dataset, 2114 nuclei for day 5 post-fracture dataset, 1058 nuclei for *Prss56-Nf1*$^{+/+}$ day 7 post-fracture dataset and 1113 nuclei for *Prss56-Nf1*$^{fl/fl}$ day 7 post-fracture dataset.

Uninjured, d5 and *Prss56-Nf1*$^{+/+}$ d7 datasets were integrated using Seurat. The integrated dataset was regressed using sctransform on cell cycle, mitochondrial and ribosomal content. Clustering was performed using the first 30 principal components and a resolution of 0.6. SSPC, fibrogenic, chondrogenic and osteogenic clusters from the integration were isolated to perform subset analysis. The subset was reclustered using the first 10 principal components and a resolution of 0.6.

Day 7 post-fracture datasets from *Prss56-Nf1*$^{+/+}$ and *Prss56-Nf1*$^{fl/fl}$ mice were integrated. The integrated dataset was regressed on mitochondrial and ribosomal content. Clustering was performed using the first 35 principal components and a resolution of 0.8. SSPC, fibrogenic, chondrogenic and osteogenic clusters from the integration were isolated to perform subset analysis. The subset was reclustered using the first 25 principal components and a resolution of 1. Gene ontology analyses were performed using EnrichR.

Human periosteum samples were filtered to retain only nuclei expressing between 200 et 6000 genes and expressing less than 3% of mitochondrial genes and 5% of ribosomal genes. Contamination from

myogenic cells were removed from the analyses. After filtering, the datasets of human samples were composed of 395 nuclei for the PA periosteum of P5, 1216 nuclei for the PA periosteum of P13, and 8011 nuclei for the IC periosteum of P13. To allow comparison between datasets, the number of nuclei in the dataset of PA periosteum of P13 was reduced to 1500 nuclei using random selection. Datasets were integrated with regression on mitochondrial and ribosomal content and clustering using the first 25 principal components and a resolution of 0.8.

Pseudotime analysis

Monocle3 v1.0.0 was used for pseudotime analysis (Cao et al., 2019). Single-cell trajectories were determined using monocle3 default parameters. The starting point of the pseudotime trajectory was determined as the cells from the uninjured dataset with the highest expression of stem/progenitor marker genes *(Ly6a, Cd34, Dpp4, Pi16)*.

Lineage and MAPK score

Lineage score was calculated by the mean of the expression of specific markers listed in Table S4. For cell type identification, common markers from the literature were used. To assess the migration, activation of the MAPK pathway and cellular response to TGFβ, the list of genes from the Gene Ontology "positive regulation of fibroblast migration", "positive regulation of MAPK cascade" and "Cellular response to TGFβ stimulus" were used respectively. To compare the cellular response to TGFβ of the different clusters between *Prss56-Nf1*$^{+/+}$ and *Prss56-Nf1*$^{fl/fl}$ datasets, the average lineage score per cluster per dataset was calculated, and the lineage score in *Prss56-Nf1*$^{fl/fl}$ dataset were normalized on the lineage score of *Prss56-Nf1*$^{+/+}$ dataset.

Analysis of published datasets from Kelly *et al.*

To assess the expression of Prss56 in developing limb, we analyzed a single cell-RNAseq dataset from (Kelly et al., 2020) (GSE142425). Murine limbs from E11.5, E13.5, E15.5 and E18.5 embryos were digested and living cells were processed for single cell RNA-sequencing using the 10X genomics platform. A total of 9939 cells were obtained. The provided data were reanalyzed and clustered using UMAP projection.

Statistical analyses

Data are reported as mean +/- standard deviation. n represents the number of samples used for the analysis. For human experiment, each sample corresponds to a different patient. For mouse experiment, samples correspond to an individual mouse. Statistical differences between experimental groups were evaluated using GraphPad Prism. For comparison between 2 groups, two-side Mann-Whitney test was used. For comparison between 3 groups, one-way ANOVA followed by Holm-Šídák s multiple comparisons post-hoc test was used. For SOX9/pERK signal correlation, each value corresponds to an individual cell. Correlation analysis and simple linear regression were performed to assess the correlation between both signals. Significance was determined as *$p < 0.05$, **$p < 0.01$, ***$p < 0.001$. All experiments were performed in at least 2 independent experiments.

Antibody type	Use	Antigen	Reference	Dilution
Primary	IF	Mouse monoclonal to human phospho-MAPK1/2	05-481, Merck	1:100
Primary	IF	Rabbit polyclonal to mouse phospho-ERK	9101S, Ozyme	1:200
Primary	IF	Rabbit polyclonal to mouse phosho-SMAD2	3101, Cell signaling	1:200
Primary	IF	Rabbit monoclonal to mouse SOX9	ab185230, Abcam	1:1000
Primary	IF	Rabbit polyclonal to mouse Osterix/Sp7	ab22552, Abcam	1:200
Primary	IF	Goat polyclonal to mouse Periostin	AF2955, R&D Systems	1:400
Primary	IF	Rabbit monoclonal to human KU80	2180T, Ozyme	1:200
Primary	IF	Goat polyclonal to mouse PDGFRα	AF1062, RD Systems	1:200
Primary	IF	Rabbit monoclonal to mouse SOX10	BSB2583, BioSB	1:200
Primary	IF	Rabbit polyclonal to mouse Tyrosine Hydroxylase	AB152, Merck	1:400
Primary	IF	Rabbit polyclonal to mouse SOX2	ab97959, Abcam	1:200
Primary	IF	Rabbit monoclonal to mouse MBP	HL1033, GeneTex	1:200
Primary	IF	Rabbit polyclonal to mouse Collagen II	ab34712, Abcam	1:200
Primary	IF	Rabbit polyclonal to mouse Collagen X	ab58632, Abcam	1:200
Primary	IF	Rat monoclonal to mouse CD68	137002, BioLegend	1:200
Primary	IF	Goat polyclonal to mouse PECAM1	AF3628, Biotechne	1:100
Secondary	IF	FITC - Goat anti mouse Ig	115-095-166, Jackson ImmunoResearch	1:200
Secondary	IF	Alexa Fluor 647 goat anti rabbit Ig	A-21245, Invitrogen	1:200
Secondary	IF	Alexa Fluor 488 goat anti rabbit Ig	A-11034, Invitrogen	1:1000
Secondary	IF	Alexa Fluor 647 donkey anti goat Ig	A-21447, Invitrogen	1:1000
Secondary	IF	Alexa Fluor 488 donkey anti goat Ig	A11055, Invitrogen	1:200
Primary	FC	anti-human CD31-PeCy7	563651, BD Biosciences	1:400
Primary	FC	anti-human CD45-PeCy7	60915, BD Biosciences	1:400
Primary	FC	anti-human CD14-PeCy7	557742, BD Biosciences	1:400
Primary	FC	anti-human CD73-BV711	742634, BD Biosciences	1:200
Primary	FC	anti-human CD105-APC	562408, BD Biosciences	1:200
Primary	FC	anti-mouse CD31-PeCy7	561410, BD Biosciences	1:400
Primary	FC	anti-mouse CD45- PeCy7	552848, BD Bioscience	1:400
Primary	FC	anti-mouse CD11b- PeCy7	552850, BD Biosciences	1:400
Primary	FC	anti-mouse CD140A-BV711	740740, BD Biosciences	1:200
Primary	FC	anti-mouse p75-NGFR-FITC	130-110-115, Milteny	1:200
Primary	WB	Rabbit monoclonal to human p44 MAPK (ERK1)	9101, Cell signaling	1:1000
Primary	WB	Mouse monoclonal to human GAPDH	sc-47724, Santa Cruz	1:5000
Primary	WB	Rabbit polyclonal to human p44/42 MAPK (Erk1/2)	9102, Cell signaling	1:1000

Secondary	WB	Mouse IgG HRP Linked Whole Ab	GENXA931-1ML, Merck	1:2500
Secondary	WB	Rabbit IgG HRP Linked F(ab′)2	GENA9340-1ML, Merck	1:2500

Table S2: List of antibodies used for this study. IF: immunofluorescence. FC: Flow cytometry. WB: Western Blot

Gene	Primers	
TBP	5’ TGCACAGGAGCCAAGAGTGAA 3’	5’ CACATCACAGCTCCCCACCA 3’
SOX9	5' GCCACGGAGCAGACGCACAT 3'	5' CCCTGGGATTGCCCCGAGT 3'
RUNX2	5' CGGAATGCCTCTGCTGTTATGAA 3'	5' ACTCTTGCCTCGTCCACTCCG 3'
PPARG	5' GCCACGGAGCAGACGCACAT 3'	5' CCCTGGGATTGCCCCGAGT 3'
Tgfb1	5' ACTGGAGTTGTACGGCAGTG 3'	5' GGCTGATCCCGTTGATTTCC 3'

Table S3: List of qPCR primers used for this study.

Lineage	Genes
Skeletal stem/progenitor cells (SSPC)	*Ly6a, Cd34, Dpp4, Pi16*
Fibrogenic cells	*Postn, Aspn, Col3a1, Col5a1, Col8a1*
Chondrocytes	*Acan, Col2a1, Sox9, Fgfr3*
Osteoblasts	*Sp7, Alpl, Ibsp, Ifitm5, Bglap*
Endothelial cells	*Pecam1, Emcn, Cdh13, Eng*
Pericytes	*Mylk, Acta2, Myh11*
Osteoclasts	*Acp5, Ctsk, Oscar*
Immune cells	*Ptprc, Adgre1, Cd84*
Schwann cells	*Mpz, Mbp, Nfasc, Ntng1*
Adipocytes	*Pparg, Lipe, Plin1*
Immune response	*Cxcl5, Cxcl12, Il33, Cxcl14, Il6, Il6st, Il1r1, Fas, Il15ra*
Migration	*Acta2, Actr3, Ager, Akap12, Akt1, Bag4, Dmtn, Fgfr1, Itgb1, Itgb3, Pak1, Pak3, Prkce, Ptk2, Slc8a1, Tgfb1, Tgfbi, Thbs1, Tsc2, Uts2, Zfp640, Cxcr4, Fbxo5, Abi3bp, Col8a1, Emilin1, Lox, Mfap4, Pmp22, Smoc2, Pdpn, Loxl2*
MAPK pathway activation	*Epgn , Gpr39 , Mst1r , Zeb2 , Pdgfc , Nek10 , Rps3 , Fgd4 , Nox4 , Bcl10 , Ccr7 , Flt1 , Fgfr1 , Fgf2 , Fgf1 , Fgd2 , Pdcd10 , Fzd10 , Syk , Ghr , Ceacam1 , Pik3r5 , Erbb2 , Src , Egf , Edn3 , Ror2 , Tnf , Pdgfd , Adam8 , Dusp19 , Mif , Kitl , Tlr9 , Irak1 , Igh-7 , Tlr6 , Map3k13 , Tnfrsf11a , Ntrk3 , Erp29 , Ajuba , Kras , Kit , Ezh2 , Dusp6 , Ptprc , Ptpn1 , Pdgfrb , Pdgfb , Pdgfa , Dab2ip , Map2k4 , Map2k6 , Ccl19 , Vangl2 , Fgf18 , Lrrk2 , Magi3 , Dkk1 , Pik3cg , Il34 , Ilk , Drd4 , Adra2a , Ern2 , Adam9 , Pak1 , P2rx7 , Cd40 , Cd24a , Wnt5a , Dvl2 , Tdgf1 , Csk , Tgfb1 , Tgfa , Arhgef5 , Htr2b , Axin1 , Egfr , Htr2a , Map4k2 , Map3k12 , Map3k11 , Map3k10 , Map3k7 , Tab1 , Map2k5 , Tirap , Taok3 , Mapk8ip3 , Edn1 , Epha4 , Ager , Robo1 , Fcer1a , Map3k4 , Map3k1 , Map2k7 , Nod2 , Tpd52l1 , Sash1 , Tenm1 , Psen1 , Tlr4 , Fzd5 , Traf2 , Fzd4 , Dvl3 , Pik3r6 , Traf6 , Akap13 , Ptk2b , Ntf3 , Prkcd , Tnfsf11 , Fzd8 , Pde5a , Gab1 , Hras , Rasgrp1 , Insr , Il1rn , Il1b*
Cellular response to TGFβ stimulus	*Sox9, Sox6, Sox5, Trp53, Eid2, Apaf1, Cited2, Bmp2, Crk, Skil, Tgfbr2, Tgfb3, Tgfb1, Creb1, Col1a2, Col4a2, Col3a1, Spi1, Ccl2, Dab2, Dnmt1, Dlx1, Appl1, Tab1, Mapk7, Ptprk, Mstn, Eng, Fut8, Scx, Zyx, Map3k7, Map3k1, Smad1, Itga8, Cav1, Acvr1, Npnt, Onecut2, Dcp1a, Stk16, Pdcd5, Ppargc1a, Flcn, Mir145b, Acvr1c, Gcnt2, Actr3, Parp1, Fermt2, Usp9x, Zmiz1, Smad3, Yes1, Cav2, Gdnf, Appl2, Cilp, Jun, Zfyve9, Itgb1, Dbn1, Smad9, Onecut1, Hyal2, Nlk, Ankrd1, Dusp22, Igf1r, Arrb2, Mef2c, Cldn5, Crkl, Mir21a, Mir192, Mir155, Mir145a, Usp15, Hpgd, Acvrl1, Glg1, Ltbp4, Lpxn, Nrros, Smad7, Itgb5, Itgb6, Pxn, Nos3, Nodal, Serpine1, Amhr2, Cdh5, Pml, Tgfbr3, Xcl1, Bmp8a, Twsg1, Foxh1, Nr3c1, Fyn, Mtmr4, Stat3, Epb41l5, Fos, Ptk2, Zfp36l1, Zfp36l2, Wfikkn2, Ovol2, Itgb8, Bmp8b, Ppm1a, Runx1, Smad2, Lrrc32, Sirt1, Bambi, Tgfbr3l, Akr1c18, Mir143, Smad5, Cited1, Smad6, Src, Tgfb2, Tgfbr1, Smad4, Adam9, Hipk2, Wwox*

Table S4: Lists of genes used for lineage score analyses of murine snRNAseq.

Lineage	Genes
Skeletal stem/progenitor cells	*PDGFRA, NT5E, CD200, PDPN, DPP4, ITGB1, ITGAV*
Fibrogenic score	*POSTN, ASPN, COL1A1, COL1A2, COL6A3, COL3A1*
Chondrogenic score	*ACAN, FGFR3*
Osteogenic score	*ALPL, RUNX2*
Endothelial cells	*PECAM1, EMCN, VWF, CDH5, TEK*
Pericytes / SMC	*ACTA2, RGS5, MYH11, TAGLN, PDGFRB*
Immune cells	*PTPRC, MRC1, LYVE1, CD163*
Adipocytes	*PPARG, LPL, ADIPOQ*
MAPK pathway activation	*EDN1, TAOK3, HIPK2, RASGRP1, GADD45G, MT3, BANK1, GPR55, FERMT2, PTPN22, LAMTOR2, CCL3, MAPKBP1, CD40, ZC3H12A, CDH2, VEGFA, PSEN1, LPAR3, IL6, FGF1, KDR, FZD4, ALK, FZD10, FLT4, PYCARD, FGF20, EZH2, NOX1, CD36, PRMT1, CCL3L1, MYD88, CIB1, TIRAP, SOX2, FGF10, FZD5, ROCK1, TAOK2, DNAJC27, CD74, ADAM9, RYK, HAND2, TREM2, DENND2B, PTPRC, PRKD2, TGFBR1, ERBB4, FLT3, ALKAL2, TRAF5, DOK4, DKK1, SCIMP, GPER1, FZD8, CRKL, CRK, HGF, NODAL, FGF23, STK3, PDGFD, MAP2K5, PAK1, ERN2, PDE6H, WWC1, PROK1, FFAR4, P2RY6, TRAF3, RAMP3, MIF, EDN3, GLIPR2, HMGB1, AXIN1, CCL16, TLR3, CCL25, SPHK1, AVPI1, SRC, CRACR2A, NENF, FGG, FGB, FGA, APOE, ITGA1, KLHDC10, PDGFRB, IGFBP6, GPR37, TP73, MID1, PDGFA, GADD45A, RAF1, GRM1, CCL22, CCL19, GDF15, GFRAL, ABCA7, TRAF7, LGALS9, CSK, NPY, CCL24, WNT5A, KSR1, NOD2, ALOX15, MAP2K2, NTRK1, CX3CL1, HLA-DRB1, NOTCH1, NEK10, WNT7B, CHI3L1, DOK6, SH3RF3, EPGN, SH3RF2, GNAI2, RB1CC1, CSPG4, PDGFRA, GPBAR1, CCL11, SDCBP, MAP3K4, LTBR, STK25, NPNT, SSTR4, MAP4K1, DUSP19, SYK, FRS2, CXCL17, NPY5R, MADD, TAB1, KISS1, GATA4, XCL1, RAP1B,HAVCR2, CAV2, S100A7,IRAK1, IQGAP1, AGER, TGFB2, RIPK1, ADAM8, NCF1, PLA2G2A, C1QTNF1, GDF6, SYT14P1, CD4, TRPV4, IQGAP3, CASR, LEP, OPRK1, EDA2R, RELL1, PELI2, CCL20, MAP3K3, DIXDC1, ROR1, WNT7A, NTF3, NPTN, ARRB2, PRDX2, AVPR1B, P2RY1, MAGED1, CALCR, RAP1A,NOTCH2, FGF19, TNIK, ALOX12B, DIRAS2, LAMTOR1, SLC30A10, CCL26, CARD9, DAB2IP, C5AR2, MAP3K11, CARTPT, CSF1R, NDST1, PTPN11, HCRTR1, SOD1, EFNA1, NAIP, MST1R, MFHAS1, CCL4L1, ERN1, TGFB3, LAMTOR3, GPR183, CCR7, CCR1, MARCO, STK39, NTRK3, IL11, TLR6,SPRY2 ANKRD6, ARRB1, GPNMB, MAP2K6, MAP3K7, MAPK3, MOS, EGFR, ABL1, PPIA, ROBO1, PRKCA, SEMA7A, ACTA2, BIRC7, NPSR1, GHR, MAP3K13, XDH, KIT, DOK5, CCN2, ARL6IP5, ADRB2, MBIP, GAREM1, DHX33, IL34, DSTYK, EIF2AK2, PDE8A, FCRL3, XIAP, TLR9, SORBS3, CDC42, PLA2G5, THBS1, SHC2, BMP4, BMP2, FGF21, PIK3R6, IGFBP4, ICAM1, SPAG9, SHC1, FGFR3, FLT1, SPI1, NDRG4, RIPK2, FGFR4, BCAR3, GADD45B, MEF2C, APELA, TENM1, PDGFC, RASSF2, RET, EPHA4, MMP8, GSDME, FGF2, MAP3K10, AJUBA, TBX1, CCL14, NTRK2, IAPP, CCL1, TPD52L1, TNFAIP8L3, DDR2, JUN, TNF, ANGPT1, HTR2B, GRM5, KLB, HTR2C, TGFB1, TGFA, EGF, CD27, PDGFB, HRAS, CDON, KL, PIK3R5, P2RX7, RIT2, TRAF6, FGFR1, ADRA2B, PTPN1, DRD4, RAPGEF2, PRXL2C, CCL17, KITLG, PLCG2, PIK3CG, HTR2A,PHB2,PRKCZ, FGF18, ARHGAP8, DVL3,*

	PDE5A, ALKAL1, NELFE, TPBG, CHRNA7, SASH1, INAVA, PDE6G, MINK1, TMEM106A, CCL7, CCL8, TAOK1, IGF2, FGFR2, IGF1R, CDK10, INS, LPAR1, LRRK2, INSR, GCG, C5AR1, GCNT2, CCL13, GH1, FCGR2B, MAP3K5, ADCYAP1, EPO, IL1B, IL1A, ELANE, F2RL1, FGF8, CCL21, CCL4, TLR4, S100A12, CD81, CTNNB1, UNC5CL, DRD2, NRG1, ADRB3,THPO, ROCK2, GRM4, TNFRSF11A, AR, FZD7, WNT16, GHRL, NOD1, CCL15, ADORA1, IGFBP3, EPHA8, SEMA3A, XCL2, RELL2, MAPK8IP3,BRAF, MAP3K12, MAP4K2, LIF, AKAP13, MAP2K3, ERBB2,MAPK8IP1,ZNF622, ITGB3,CD44, CCL5, CCL2, PJA2,LILRA5, SLAMF1, PDCD10, BMPER, PRKCE, TRAF4, GAS6, JAK2, NOX4, IL26, AKAP12, PLCB1, APP, DIRAS1, EDAR, PTK2B, TRIM5, IGF1, SEMA4C, MAP2K4, ARHGEF5, MYDGF, FBXW7, CAVIN3,F2R, OSM, ACKR3, ADRA1D, CFLAR, TNFSF11, NRP1, OPRM1, ADRA1B, PLA2G1B, ADRA1A, MAP2K7, FSHR, ROR2, MAPK8IP2, TDGF1, JCAD, SERPINF2, PLCE1, FGF4, ADRA2C, TEK, GPR37L1, MAP2K1, OR2AT4, TNFRSF19, DUSP22, TRAF2, PTPRJ, DDT, ERP29, TRAF1, FPR2, CD24, PTEN, CCL18, CCL23, ADRA2A, DVL2, PHB1, FGD2, SH3RF1, NECAB2, LAPTM5, INHBA, RPS3, MTURN
Cellular response to TGFβ stimulus	*ABL1, ACVR1, ACVRL1, ADAM9, AMHR2, ANKRD1, APAF1, APOA1, APPL1, APPL2, ARG1, ARRB2, BAMBI, BMPR1A, CAV1, CAV2, CDH5, CDKN2B, CHST11, CILP, CITED1, CITED2, CLDN1, CLDN5, CLEC3B, COL1A1, COL1A2, COL3A1, COL4A2, CRK, CRKL, CTSK, CX3CR1, DAB2, DCSTAMP, DDR2, DLX1, DUSP22, EDN1, EID2, ENG, EPB41L5, FBN1, FERMT2, FGFR2, FLCN, FMOD, FNTA, FOXH1, FSHB, FURIN, FUT8, FYN, GCNT2, GDF10, GDF15, GDF5, GDF9, GLG1, HDAC2, HIPK2, HPGD, HYAL2, ID1, IGF1R, ITGA8, ITGB1, ITGB5, ITGB6, ITGB8, LEFTY1, LIMS1, LPXN, LRRC32, LTBP2, LTBP3, LTBP4, MAP3K7, MAPK7, MEF2C, MSTN, MTMR4, NFATC1, NLK, NODAL, NPNT, NR3C1, NRROS, ONECUT1, ONECUT2, OVOL2, PAK2, PARP1, PDCD5, PDE2A, PDE3A, PDGFA, PDGFD, PENK, PML, PPM1A, PSG9, PTK2, PTPRK, PXN, SCX, SFRP1, SIRT1, SKIL, SMAD1, SMAD2, SMAD3, SMAD4, SMAD5, SMAD6, SMAD7, SMAD9, SOX5, SOX6, SOX9, SPI1, SRC, STK16, TAB1, TGFB1, TGFB2, TGFB3, TGFBR1, TGFBR2, TGFBR3, TGFBR3L, TGFBRAP1, TP53, TWSG1, USP15, USP9X, USP9Y, WFIKKN2, WNT10A, WNT2, WNT4, WNT5A, WNT7A, WWOX, XCL1, YES1, ZEB1, ZFP36L1, ZFP36L2, ZFYVE9, ZMIZ1, ZMIZ2, ZYX*

Table S5: Lists of genes used for lineage score analyses in analyses of human snRNAseq.

References

Badache, A., Muja, N., De Vries, G.H., 1998. Expression of Kit in neurofibromin-deficient human Schwann cells: role in Schwann cell hyperplasia associated with type 1 neurofibromatosis. Oncogene 17, 795–800. https://doi.org/10.1038/sj.onc.1201978

Brekelmans, C., Hollants, S., De Groote, C., Sohier, N., Maréchal, M., Geris, L., Luyten, F.P., Ginckels, L., Sciot, R., de Ravel, T., De Smet, L., Lammens, J., Legius, E., Brems, H., 2019. Neurofibromatosis type 1-related pseudarthrosis: Beyond the pseudarthrosis site. Hum Mutat 40, 1760–1767. https://doi.org/10.1002/humu.23783

Butler, A., Hoffman, P., Smibert, P., Papalexi, E., Satija, R., 2018. Integrating single-cell transcriptomic data across different conditions, technologies, and species. Nat Biotechnol 36, 411–420. https://doi.org/10.1038/nbt.4096

Cao, J., Spielmann, M., Qiu, X., Huang, X., Ibrahim, D.M., Hill, A.J., Zhang, F., Mundlos, S., Christiansen, L., Steemers, F.J., Trapnell, C., Shendure, J., 2019. The single-cell transcriptional landscape of mammalian organogenesis. Nature 566, 496–502. https://doi.org/10.1038/s41586-019-0969-x

Cervellini, I., Galino, J., Zhu, N., Allen, S., Birchmeier, C., Bennett, D.L., 2018. Sustained MAPK/ERK Activation in Adult Schwann Cells Impairs Nerve Repair. J Neurosci 38, 679–690. https://doi.org/10.1523/JNEUROSCI.2255-17.2017

Clements, M.P., Byrne, E., Camarillo Guerrero, L.F., Cattin, A.-L., Zakka, L., Ashraf, A., Burden, J.J., Khadayate, S., Lloyd, A.C., Marguerat, S., Parrinello, S., 2017. The Wound Microenvironment Reprograms Schwann Cells to Invasive Mesenchymal-like Cells to Drive Peripheral Nerve Regeneration. Neuron 96, 98-114.e7. https://doi.org/10.1016/j.neuron.2017.09.008

de la Croix Ndong, J., Makowski, A.J., Uppuganti, S., Vignaux, G., Ono, K., Perrien, D.S., Joubert, S., Baglio, S.R., Granchi, D., Stevenson, D.A., Rios, J.J., Nyman, J.S., Elefteriou, F., 2014. Asfotase-α improves bone growth, mineralization and strength in mouse models of neurofibromatosis type-1. Nat Med 20, 904–910. https://doi.org/10.1038/nm.3583

Debnath, S., Yallowitz, A.R., McCormick, J., Lalani, S., Zhang, T., Xu, R., Li, N., Liu, Y., Yang, Y.S., Eiseman, M., Shim, J.-H., Hameed, M., Healey, J.H., Bostrom, M.P., Landau, D.A., Greenblatt, M.B., 2018. Discovery of a periosteal stem cell mediating intramembranous bone formation. Nature 562, 133–139. https://doi.org/10.1038/s41586-018-0554-8

Duchamp de Lageneste, O., Julien, A., Abou-Khalil, R., Frangi, G., Carvalho, C., Cagnard, N., Cordier, C., Conway, S.J., Colnot, C., 2018. Periosteum contains skeletal stem cells with high bone regenerative potential controlled by Periostin. Nat Commun 9, 773. https://doi.org/10.1038/s41467-018-03124-z

El Khassawna, T., Toben, D., Kolanczyk, M., Schmidt-Bleek, K., Koennecke, I., Schell, H., Mundlos, S., Duda, G.N., 2012. Deterioration of fracture healing in the mouse model of NF1 long bone dysplasia. Bone 51, 651–660. https://doi.org/10.1016/j.bone.2012.07.011

G Martelotto, L., 2019. 'Frankenstein' protocol for nuclei isolation from fresh and frozen tissue for snRNAseq v2 (preprint). https://doi.org/10.17504/protocols.io.3fkgjkw

Gresset, A., Coulpier, F., Gerschenfeld, G., Jourdon, A., Matesic, G., Richard, L., Vallat, J.-M., Charnay, P., Topilko, P., 2015. Boundary Caps Give Rise to Neurogenic Stem Cells and Terminal Glia in the Skin. Stem Cell Reports 5, 278–290. https://doi.org/10.1016/j.stemcr.2015.06.005

Gutmann, D.H., Ferner, R.E., Listernick, R.H., Korf, B.R., Wolters, P.L., Johnson, K.J., 2017. Neurofibromatosis type 1. Nat Rev Dis Primers 3, 17004. https://doi.org/10.1038/nrdp.2017.4

Harrisingh, M.C., Perez-Nadales, E., Parkinson, D.B., Malcolm, D.S., Mudge, A.W., Lloyd, A.C., 2004. The Ras/Raf/ERK signalling pathway drives Schwann cell dedifferentiation. EMBO J 23, 3061–3071. https://doi.org/10.1038/sj.emboj.7600309

Hermanns-Sachweh, B., Senderek, J., Alfer, J., Klosterhalfen, B., Büttner, R., Füzesi, L., Weber, M., 2005. Vascular changes in the periosteum of congenital pseudarthrosis of the tibia. Pathol Res Pract 201, 305–312. https://doi.org/10.1016/j.prp.2004.09.013

Johnston, A.P.W., Naska, S., Jones, K., Jinno, H., Kaplan, D.R., Miller, F.D., 2013. Sox2-mediated regulation of adult neural crest precursors and skin repair. Stem Cell Reports 1, 38–45. https://doi.org/10.1016/j.stemcr.2013.04.004

Johnston, A.P.W., Yuzwa, S.A., Carr, M.J., Mahmud, N., Storer, M.A., Krause, M.P., Jones, K., Paul, S., Kaplan, D.R., Miller, F.D., 2016. Dedifferentiated Schwann Cell Precursors Secreting

Paracrine Factors Are Required for Regeneration of the Mammalian Digit Tip. Cell Stem Cell 19, 433–448. https://doi.org/10.1016/j.stem.2016.06.002

Julien, A., Kanagalingam, A., Martínez-Sarrà, E., Megret, J., Luka, M., Ménager, M., Relaix, F., Colnot, C., 2021. Direct contribution of skeletal muscle mesenchymal progenitors to bone repair. Nature Communications 12, 2860. https://doi.org/10.1038/s41467-021-22842-5

Julien, A., Perrin, S., Martínez-Sarrà, E., Kanagalingam, A., Carvalho, C., Luka, M., Ménager, M., Colnot, C., 2022. Skeletal stem/progenitor cells in periosteum and skeletal muscle share a common molecular response to bone injury. J of Bone & Mineral Res jbmr.4616. https://doi.org/10.1002/jbmr.4616

Kamiya, N., Yamaguchi, R., Aruwajoye, O., Kim, A.J., Kuroyanagi, G., Phipps, M., Adapala, N.S., Feng, J.Q., Kim, H.K., 2017. Targeted Disruption of *NF1* in Osteocytes Increases FGF23 and Osteoid With Osteomalacia-like Bone Phenotype: NF1 DISRUPTION IN OSTEOCYTES CAUSES A MINERALIZATION DEFECT. J Bone Miner Res 32, 1716–1726. https://doi.org/10.1002/jbmr.3155

Kelly, N.H., Huynh, N.P.T., Guilak, F., 2020. Single cell RNA-sequencing reveals cellular heterogeneity and trajectories of lineage specification during murine embryonic limb development. Matrix Biology 89, 1–10. https://doi.org/10.1016/j.matbio.2019.12.004

Kluwe, L., Friedrich, R., Mautner, V.F., 1999. Loss of NF1 allele in Schwann cells but not in fibroblasts derived from an NF1-associated neurofibroma. Genes Chromosomes Cancer 24, 283–285. https://doi.org/10.1002/(sici)1098-2264(199903)24:3<283::aid-gcc15>3.0.co;2-k

Le, L.Q., Liu, C., Shipman, T., Chen, Z., Suter, U., Parada, L.F., 2011. Susceptible stages in Schwann cells for NF1-associated plexiform neurofibroma development. Cancer Res 71, 4686–4695. https://doi.org/10.1158/0008-5472.CAN-10-4577

Legius, E., Messiaen, L., Wolkenstein, P., Pancza, P., Avery, R.A., Berman, Y., Blakeley, J., Babovic-Vuksanovic, D., Cunha, K.S., Ferner, R., Fisher, M.J., Friedman, J.M., Gutmann, D.H., Kehrer-Sawatzki, H., Korf, B.R., Mautner, V.-F., Peltonen, S., Rauen, K.A., Riccardi, V., Schorry, E., Stemmer-Rachamimov, A., Stevenson, D.A., Tadini, G., Ullrich, N.J., Viskochil, D., Wimmer, K., Yohay, K., Gomes, A., Jordan, J.T., Mautner, V., Merker, V.L., Smith, M.J., Stevenson, D., Anten, M., Aylsworth, A., Baralle, D., Barbarot, S., Barker, F., Ben-Shachar, S., Bergner, A., Bessis, D., Blanco, I., Cassiman, C., Ciavarelli, P., Clementi, M., Frébourg, T., Giovannini, M., Halliday, D., Hammond, C., Hanemann, C.O., Hanson, H., Heiberg, A., Joly, P., Kalamarides, M., Karajannis, M., Kroshinsky, D., Larralde, M., Lázaro, C., Le, L., Link, M., Listernick, R., MacCollin, M., Mallucci, C., Moertel, C., Mueller, A., Ngeow, J., Oostenbrink, R., Packer, R., Papi, L., Parry, A., Peltonen, J., Pichard, D., Poppe, B., Rezende, N., Rodrigues, L.O., Rosser, T., Ruggieri, M., Serra, E., Steinke-Lange, V., Stivaros, S.M., Taylor, A., Toelen, J., Tonsgard, J., Trevisson, E., Upadhyaya, M., Varan, A., Wilson, M., Wu, H., Zadeh, G., Huson, S.M., Evans, D.G., Plotkin, S.R., 2021. Revised diagnostic criteria for neurofibromatosis type 1 and Legius syndrome: an international consensus recommendation. Genetics in Medicine 23, 1506–1513. https://doi.org/10.1038/s41436-021-01170-5

Li, Zhu, Meyers, C.A., Chang, L., Lee, S., Li, Zhi, Tomlinson, R., Hoke, A., Clemens, T.L., James, A.W., 2019. Fracture repair requires TrkA signaling by skeletal sensory nerves. Journal of Clinical Investigation 129, 5137–5150. https://doi.org/10.1172/JCI128428

Logan, M., Martin, J.F., Nagy, A., Lobe, C., Olson, E.N., Tabin, C.J., 2002. Expression of Cre recombinase in the developing mouse limb bud driven by aPrxl enhancer. genesis 33, 77–80. https://doi.org/10.1002/gene.10092

Madisen, L., Zwingman, T.A., Sunkin, S.M., Oh, S.W., Zariwala, H.A., Gu, H., Ng, L.L., Palmiter, R.D., Hawrylycz, M.J., Jones, A.R., Lein, E.S., Zeng, H., 2010. A robust and high-throughput Cre reporting and characterization system for the whole mouse brain. Nat Neurosci 13, 133–140. https://doi.org/10.1038/nn.2467

Maertens, O., Prenen, H., Debiec-Rychter, M., Wozniak, A., Sciot, R., Pauwels, P., De Wever, I., Vermeesch, J.R., de Raedt, T., De Paepe, A., Speleman, F., van Oosterom, A., Messiaen, L., Legius, E., 2006. Molecular pathogenesis of multiple gastrointestinal stromal tumors in NF1 patients. Hum Mol Genet 15, 1015–1023. https://doi.org/10.1093/hmg/ddl016

Mashour, G.A., Ratner, N., Khan, G.A., Wang, H.L., Martuza, R.L., Kurtz, A., 2001. The angiogenic factor midkine is aberrantly expressed in NF1-deficient Schwann cells and is a mitogen for neurofibroma-derived cells. Oncogene 20, 97–105. https://doi.org/10.1038/sj.onc.1204026

Masquelet, A.C., Fitoussi, F., Begue, T., Muller, G.P., 2000. [Reconstruction of the long bones by the induced membrane and spongy autograft]. Ann Chir Plast Esthet 45, 346–353.

Matthews, B.G., Novak, S., Sbrana, F.V., Funnell, J.L., Cao, Y., Buckels, E.J., Grcevic, D., Kalajzic, I., 2021. Heterogeneity of murine periosteum progenitors involved in fracture healing. eLife 10, e58534. https://doi.org/10.7554/eLife.58534

Muzumdar, M.D., Tasic, B., Miyamichi, K., Li, L., Luo, L., 2007. A global double-fluorescent Cre reporter mouse. Genesis 45, 593–605. https://doi.org/10.1002/dvg.20335

Napoli, I., Noon, L.A., Ribeiro, S., Kerai, A.P., Parrinello, S., Rosenberg, L.H., Collins, M.J., Harrisingh, M.C., White, I.J., Woodhoo, A., Lloyd, A.C., 2012. A central role for the ERK-signaling pathway in controlling Schwann cell plasticity and peripheral nerve regeneration in vivo. Neuron 73, 729–742. https://doi.org/10.1016/j.neuron.2011.11.031

Pannier, S., 2011. Congenital pseudarthrosis of the tibia. Orthopaedics & Traumatology: Surgery & Research 97, 750–761. https://doi.org/10.1016/j.otsr.2011.09.001

Parfejevs, V., Debbache, J., Shakhova, O., Schaefer, S.M., Glausch, M., Wegner, M., Suter, U., Riekstina, U., Werner, S., Sommer, L., 2018. Injury-activated glial cells promote wound healing of the adult skin in mice. Nat Commun 9, 236. https://doi.org/10.1038/s41467-017-01488-2

Pasmant, E., Parfait, B., Luscan, A., Goussard, P., Briand-Suleau, A., Laurendeau, I., Fouveaut, C., Leroy, C., Montadert, A., Wolkenstein, P., Vidaud, M., Vidaud, D., 2015. Neurofibromatosis type 1 molecular diagnosis: what can NGS do for you when you have a large gene with loss of function mutations? Eur J Hum Genet 23, 596–601. https://doi.org/10.1038/ejhg.2014.145

Patmore, D.M., Welch, S., Fulkerson, P.C., Wu, J., Choi, K., Eaves, D., Kordich, J.J., Collins, M.H., Cripe, T.P., Ratner, N., 2012. *In Vivo* Regulation of TGF-β by R-Ras2 Revealed through Loss of the RasGAP Protein NF1. Cancer Research 72, 5317–5327. https://doi.org/10.1158/0008-5472.CAN-12-1972

Perrin, S., Julien, A., Duchamp de Lageneste, O., Abou-Khalil, R., Colnot, C., 2021. Mouse Periosteal Cell Culture, in vitro Differentiation, and in vivo Transplantation in Tibial Fractures. BIO-PROTOCOL 11. https://doi.org/10.21769/BioProtoc.4107

Radomska, K.J., Coulpier, F., Gresset, A., Schmitt, A., Debbiche, A., Lemoine, S., Wolkenstein, P., Vallat, J.-M., Charnay, P., Topilko, P., 2019. Cellular Origin, Tumor Progression, and Pathogenic Mechanisms of Cutaneous Neurofibromas Revealed by Mice with Nf1 Knockout in Boundary Cap Cells. Cancer Discov 9, 130–147. https://doi.org/10.1158/2159-8290.CD-18-0156

Raggatt, L.J., Wullschleger, M.E., Alexander, K.A., Wu, A.C.K., Millard, S.M., Kaur, S., Maugham, M.L., Gregory, L.S., Steck, R., Pettit, A.R., 2014. Fracture Healing via Periosteal Callus Formation Requires Macrophages for Both Initiation and Progression of Early Endochondral Ossification. The American Journal of Pathology 184, 3192–3204. https://doi.org/10.1016/j.ajpath.2014.08.017

Santos, M.D., Gioftsidi, S., Backer, S., Machado, L., Relaix, F., Maire, P., Mourikis, P., 2021. Extraction and sequencing of single nuclei from murine skeletal muscles. STAR Protocols 2, 100694. https://doi.org/10.1016/j.xpro.2021.100694

Sharma, R., Wu, X., Rhodes, S.D., Chen, S., He, Y., Yuan, J., Li, J., Yang, X., Li, X., Jiang, L., Kim, E.T., Stevenson, D.A., Viskochil, D., Xu, M., Yang, F.-C., 2013. Hyperactive Ras/MAPK signaling is critical for tibial nonunion fracture in neurofibromin-deficient mice. Human Molecular Genetics 22, 4818–4828. https://doi.org/10.1093/hmg/ddt333

Stevenson, D.A., Zhou, H., Ashrafi, S., Messiaen, L.M., Carey, J.C., D'Astous, J.L., Santora, S.D., Viskochil, D.H., 2006. Double inactivation of NF1 in tibial pseudarthrosis. Am J Hum Genet 79, 143–148. https://doi.org/10.1086/504441

Stuart, T., Butler, A., Hoffman, P., Hafemeister, C., Papalexi, E., Mauck, W.M., Hao, Y., Stoeckius, M., Smibert, P., Satija, R., 2019. Comprehensive Integration of Single-Cell Data. Cell 177, 1888-1902.e21. https://doi.org/10.1016/j.cell.2019.05.031

van Gastel, N., Stegen, S., Eelen, G., Schoors, S., Carlier, A., Daniëls, V.W., Baryawno, N., Przybylski, D., Depypere, M., Stiers, P.-J., Lambrechts, Dennis, Van Looveren, R., Torrekens, S., Sharda, A., Agostinis, P., Lambrechts, Diether, Maes, F., Swinnen, J.V., Geris, L., Van Oosterwyck, H., Thienpont, B., Carmeliet, P., Scadden, D.T., Carmeliet, G., 2020. Lipid availability determines fate of skeletal progenitor cells via SOX9. Nature 579, 111–117. https://doi.org/10.1038/s41586-020-2050-1

van Gastel, N., Torrekens, S., Roberts, S.J., Moermans, K., Schrooten, J., Carmeliet, P., Luttun, A., Luyten, F.P., Carmeliet, G., 2012. Engineering vascularized bone: osteogenic and proangiogenic potential of murine periosteal cells. Stem Cells 30, 2460–2471. https://doi.org/10.1002/stem.1210

Wang, W., Nyman, J.S., Ono, K., Stevenson, D.A., Yang, X., Elefteriou, F., 2011. Mice lacking Nf1 in osteochondroprogenitor cells display skeletal dysplasia similar to patients with neurofibromatosis type I. Human Molecular Genetics 20, 3910–3924. https://doi.org/10.1093/hmg/ddr310

Wu, J., Williams, J.P., Rizvi, T.A., Kordich, J.J., Witte, D., Meijer, D., Stemmer-Rachamimov, A.O., Cancelas, J.A., Ratner, N., 2008. Plexiform and dermal neurofibromas and pigmentation are caused by Nf1 loss in desert hedgehog-expressing cells. Cancer Cell 13, 105–116. https://doi.org/10.1016/j.ccr.2007.12.027

Zhu, Y., Ghosh, P., Charnay, P., Burns, D.K., Parada, L.F., 2002. Neurofibromas in NF1: Schwann cell origin and role of tumor environment. Science 296, 920–922. https://doi.org/10.1126/science.1068452

Zhu, Y., Romero, M.I., Ghosh, P., Ye, Z., Charnay, P., Rushing, E.J., Marth, J.D., Parada, L.F., 2001. Ablation of NF1 function in neurons induces abnormal development of cerebral cortex and reactive gliosis in the brain. Genes Dev 15, 859–876. https://doi.org/10.1101/gad.862101

General discussion

Bone repair relies on the activation and differentiation of tissue-resident SSPCs to form a fibrocartilaginous callus progressively ossified and remodeled. The periosteum is a critical source of SSPCs during bone repair and is required for bone healing. In this thesis, we investigated the heterogeneity and fate of pSSPCs after fracture and the role of the periosteum in congenital pseudarthrosis of the tibia.

Heterogeneity of skeletal stem/progenitor cells for bone repair

To investigate the cellular heterogeneity of pSSPCs, we performed scRNAseq experiment of primary cultured pSSPCs and identified several clusters of stem/progenitor cells with mild differences in transcriptomics profiles. Different populations were previously described in the periosteum, such as CTSK+ pSSPCs, aSMA+ pSSPCs, and SSPCs from Chan et al., but these different populations were not detected in our scRNAseq datasets. Further analyses of the snRNAseq datasets generated in the third article from freshly isolated nuclei will allow us to investigate the cellular heterogeneity of the periosteum in vivo.

After injury, callus-forming SSPCs are recruited from the periosteum, skeletal muscle, and bone marrow[27,28,112,113]. While analyses of the different tissues independently were performed, there is a lack of comprehensive analysis to understand the overall dynamic of SSPCs after fracture. One limitation of such studies is the challenge of labeling and tracing each source independently. PRX1 and PDGFRα can be used to mark all SSPCs but do not allow tissue-specific labeling. Many markers were described in the bone marrow (LepR, CXCL12, NESTIN, GREM1), the periosteum (CTSK, αSMA, MX1), and the skeletal muscle (HIC1, CD34, SCA1), but analysis from our group and others showed that those markers are not tissue-specific and can be express by SSPCs from the other tissues[28,112–114,141,143,148,191,195]. As SSPCs from different tissue can share common markers, the question of the identity and heterogeneity of these cells between tissues remains. Detailed transcriptomics analyses will further describe the differences between SSPCs to understand their differences of potential following injury, and maybe identify tissue-specific markers. Due to the current lack of specific markers, the relative contribution of each compartment remains to be evaluated. In the first article, we compared the potential of cultured SSPCs from bone marrow, skeletal muscle, and periosteum to integrate the fracture callus after grafting. We observed that periosteal SSPCs display the highest capacity to integrate the callus compared to other SSPC populations. These results are consistent with previous in vivo and in vitro observations performed in mouse models and with human cells[27,265,266] While these experiments allow comparison of the intrinsic potential of SSPCs from various tissues, it may not reflect the actual contribution to bone repair, as the number of SSPCs, activation, and regulation may vary between sources.

Understanding the activation and regulation of pSSPCs after fracture

In this thesis, we aimed to investigate the function and activation of pSSPCs after fracture. As shown in Article 1, pSSPCs are the only population of SSPCs showing bipotent potential after fracture, as they can differentiate into both bone and cartilage. However, the origin of this bipotency remains unknown. Several hypotheses are considered, including that the periosteum encompasses distinct populations of SSPCs with an osteogenic or chondrogenic fate after injury, or that cell fate decision in the periosteum is regulated by environmental factors.

In the first article, we also investigated the pSSPCs response to fracture. scRNAseq analyses of primary cultured pSSPCs from uninjured periosteum and periosteum at 3 days post-fracture demonstrated that pSSPCs activate in 3 steps: first, pSSPCs leave their stem/progenitor state, to engage into a fibrogenic step marked by the expression of ECM-related genes and finally chondrogenesis. However, these analyses are limited by the absence of osteogenic differentiation, likely due to the presence of a culture step. To overcome this issue, we decided to perform snRNAseq from freshly isolated tissue in the third article. This work allowed a better description of pSSPC activation with the presence of a phase of immune response while cells start engaging in the fibrogenic step. It also showed that cells are undergoing osteogenic differentiation after the fibrogenic step, common with the cells undergoing chondrogenesis (Figure 32). The presence of a common activation trajectory for pSSPCs undergoing osteogenesis and chondrogenesis supports the hypothesis of a unique bipotent pSSPC population within the periosteum. Further studies will allow us to better understand how cell fate decision is regulated during the fibrogenic step and decipher the importance of the intrinsic potential of the cells, the environmental factors, and the metabolic regulation in fate decision. It is intriguing to see that both SSPCs from periosteum and skeletal muscle undergo the same pattern of activation but that only pSSPCs form osteoblasts. Comparative analysis of the activation of pSSPCs and muscle SSPCs would be of interest to decipher mechanisms or pathways specific to pSSPCs that allow osteogenesis.

In addition to bone formation via osteogenesis after the fibrogenic step, pSSPCs can also form bone via cartilage-to-bone transformation of hypertrophic chondrocytes. In the second article, we showed that pSSPC-derived chondrocytes can transdifferentiate into bone, and that failure in this step alters bone healing and cause pseudarthrosis. This shows that there are multiple ways to form bone after injury. Additionally, Matsushita et al. described the steps of osteogenic differentiation of CXCL12+ bone marrow cells after bone marrow ablation injury. The process was characterized by a pre-osteogenic step marked by the expression of stemness-related genes and increased Wnt signaling[113]. The presence of this osteogenic process after bone fracture remains to be confirmed but it is highly interesting that multiple osteogenic paths occur simultaneously after fracture and unravel increased complexity in understanding how bone forms after injury and how it is regulated.

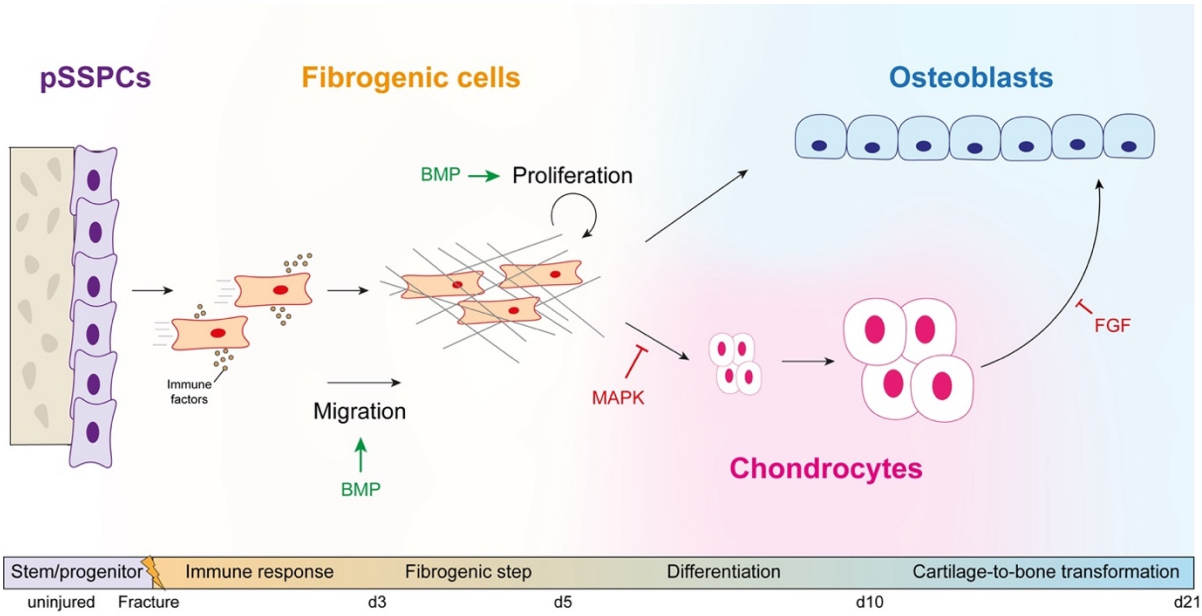

Figure 32: Pattern of activation of periosteal skeletal stem/progenitor cells after fracture.

Periosteal SSPC activation is known to be regulated by many signaling pathways and their action can differ between the different steps of activation. BMP signaling is active in the early phase of repair, from day 2 post-fracture, and plays a role in regulating migration and proliferation during the fibrogenic step and osteogenic differentiation. The MAPK pathway, which acts downstream of tyrosine kinase receptors such as EGFR, TrkA, and PDGFR, shows a tight regulation. Increased MAPK activation is required for pSSPC activation and transition to fibrogenic step. Inhibition of the MAPK from the time of fracture leads to the absence of callus formation (data not shown). After the fibrogenic step, downregulation of the MAPK is required for chondrogenesis but not osteogenesis. In contrast, signaling via FGFR3 is not involved in the early phase of pSSPCs differentiation but is critical for cartilage-to-bone transition. These results show the importance of the timing and regulation of signaling pathways regulating pSSPC activation and differentiation.

Overall, bone regeneration is a highly complex process relying on a multistep activation process of several populations of SSPCs, regulated by various signaling pathways and multiple interactions between SSPCs and the fracture environment. While this thesis and recent studies have increased our understanding of the steps and mechanisms of bone repair, there is still a lot of work needed to fully understand bone regeneration.

Role of the periosteum in congenital pseudarthrosis of the tibia

While risk factors affecting bone repair are known such as age, mechanical instability, smoking, or injury of adjacent soft tissues, an important part of bone repair defects are still of unknown etiology[627–629]. Children possess an extraordinary capacity to regenerate bones, thus the presence of a complete absence of bone healing in patients with CPT is surprising.

Around half of CPT cases are linked to Neurofibromatosis type 1 (41% in our cohort). Several NF1 manifestations develop due to *NF1* biallelic inactivation. In our cohort, all NF1 patients were carrying *NF1* biallelic at PA site, and we also identified *NF1* biallelic inactivation in 60% of patients with isolated CPT. This reinforces the link between NF1 and CPT, even in patients non-affected with systemic NF1 disease. Still, we did not identify *NF1* mutations in 4 patients of our cohort. We are currently using other techniques to determine whether mutations may be detected in the non-coding regions of the *NF1* gene in these patients. We are also performing exome sequencing to investigate the presence of mutations in other genes responsible for CPT. It will be interesting to see if the mutated genes are related to the MAPK pathway or if the mechanisms are MAPK independent. While neurofibromas are mostly associated with NF1, cases of sporadic dermal NFs were described. Genomic analysis on these tumors showed that only a part of them is due to *NF1* loss, some are due to mutations in other genes, including *KIR2DL5*, leading to overactivation of the RAS/MAPK[630]. The presence of a similar genetic basis in isolated CPT can be considered.

In previous studies, CPT was considered as a bone-specific lesion[462,464,465,504,508]. The presence of a common genetic pattern with other NF1 manifestations raised the question of a link between CPT and NFs or CALMs. In patients of our cohort, we identified the same *NF1* second hit at PA site from tibia and fibula, and the same *NF1* second hit in periosteum, muscle, and skin at PA site. This shows that the second *NF1* mutation occurred early during embryogenesis and not in a bone-specific lineage. Identifying the timing and location of *NF1* second hit mutation in humans is extremely challenging. The presence of a common lineage origin between CALMs and NFBs was demonstrated in patients by sequencing cNF and CALMs at closed locations and identifying the same *NF1* mutation in both symptoms[631]. This type of analysis between CPT and cNFs or CALMs would allow to confirm the common origin of these symptoms in patients. Yet, as patients undergoing CPT treatment are usually around 3 years old, CALMs and cNF are rarely developed making this type of study unlikely. Studies using animal models enable the analysis of the origin of NF1 symptoms. Mouse models to study NF1 bone manifestations were mostly using bone-specific CRE models, and mouse models to study NFs were mostly Schwann cell-specific CRE models. Bone phenotypes were not described or assessed in most SC-specific animal models. Spine alterations were identified using PLP^{CreERT} and $Postn^{Cre}$, but those models also target bone cells ([357,632] and S. Perrin, data not shown). Thus, until now, the question of the common cellular origin of NF1 skeletal and neurodermatological symptoms was never assessed. The *Prss56-Nf1 KO* mouse model that recapitulates cNFs, pNFs, and CALMs, also displays pseudarthrosis as described in the third article. This is the first evidence that a cell lineage can be the cellular origin of pNFs, cNFs, CALMs, and CPT[479]. Current analysis from Dr. Topilko's group and our group demonstrate the presence of pNF transformation into MPNST, eye lesions reminiscent of Lisch nodules, and spine deformities in this model (data not shown). This indicates that boundary cap cells can be the cellular origin of most NF1 manifestations, making this model the best one to investigate NF1 features.

Our NGS analyses of tissues from CPT showed that the periosteum is the only tissue mutated in all patients with *NF1* biallelic inactivation, highlighting its role in CPT. In bones of *Prss56-Nf1 KO* mice, boundary cap-derived cells are also located within the periosteum and our analysis showed that both *Nf1*-deficient SSPCs and Schwann cells within periosteum are involved in the pseudarthrosis phenotype (Figure 33). In patients, we identified the presence of *NF1* biallelic inactivation in periosteal SSPCs. We are currently investigating the presence of *NF1* second hit mutation in periosteal Schwann cells, by sorting cells populations from freshly digested PA periosteum (i.e. SSPCs, Schwann cells, immune cells, endothelial cells, pericytes) and performing *NF1* sequencing.

Analysis of the composition of the pathological periosteum from CPT patients using snRNAseq showed a strong increase in fibrogenic cells compared to IC periosteum. We specifically observed increased proportion of fibroblasts expressing *ADAM12* and osteochondrogenic markers. Cultured pSSPCs from PA also display a post-fracture fibrogenic phenotype. Using grafting approaches, we showed that *NF1*-deficient pSSPCs in CPT patients and in the *Prss56-Nf1 KO* mice display impaired fate after fracture and form fibrosis. Using snRNAseq technology, we described the molecular mechanism leading to fibrogenic fate of mutated murine pSSPCs. Downregulation of the MAPK pathway is required for the switch from fibrogenic to chondrogenic stages, and cannot occur in *Nf1*-deficient cells. Thus, cells are blocked in a post-fracture fibrogenic state and finally accumulate in the callus and the newly formed periosteum at late stages of repair. We are currently investigated the identity of the *Nf1*-deficient cells accumulating within the newly-formed periosteum of *Prss56-Nf1 KO* mice after fracture. This analysis will determine if they express common markers with the populations identified in the snRNAseq datasets of human PA periosteum.

Fibrotic tissue at PA site in the *Prss56-Nf1 KO* model is not only composed of *Nf1*-deficient cells. We also observed 2 patients in our cohort with *NF1* biallelic inactivation in the periosteum but not in the fibrous tissue composing the PA site, showing similarity with human CPT. Unexpectedly, we identified *Nf1*-deficient Schwann cells as the cells responsible for the deleterious mutant environment. While recent studies showed the role of SCs in tissue regeneration, it is to our knowledge the first disorder where SC dysfunction alters non-nervous tissue regeneration[612–614]. Little is known about the role of SCs in bone healing and studies are needed to understand the fate of SCs following fracture and their interactions with SSPCs. In NFs, *NF1*-deficient SCs are also responsible for the accumulation of fibrotic tissue, due to their ability to secrete profibrotic factors, such as TGFβ1, Midkine, and SCF, to stimulate the recruitment and proliferation of wild-type fibroblasts[633–637]. This shows that, in the *Prss56-Nf1 KO* model, in addition to the common origin of NFs and CPT, there are common cellular and molecular mechanisms between those symptoms. We identified TGFβ as the paracrine factor in the mutant environment affecting the fate of wild-type pSSPCs. Based on the role of SC in the pseudarthrosis phenotype and the known potential of *NF1*-deficient SCs to secrete TGFβ, we suspect TGFβ to be the factor produced by SCs in the callus environment. To demonstrate this, we are currently performing in situ hybridation to assess the expression of *Tgfb1* by Prss56-derived SCs. In addition, we are performing TGFβ inhibition in mice grafted with Nf1-deficient SCs to determine whether blocking TGFβ signaling

can prevent fibrosis accumulation and pseudarthrosis, and thus determine whether TGFβ is the main paracrine factor secreted by SCs causing pseudarthrosis.

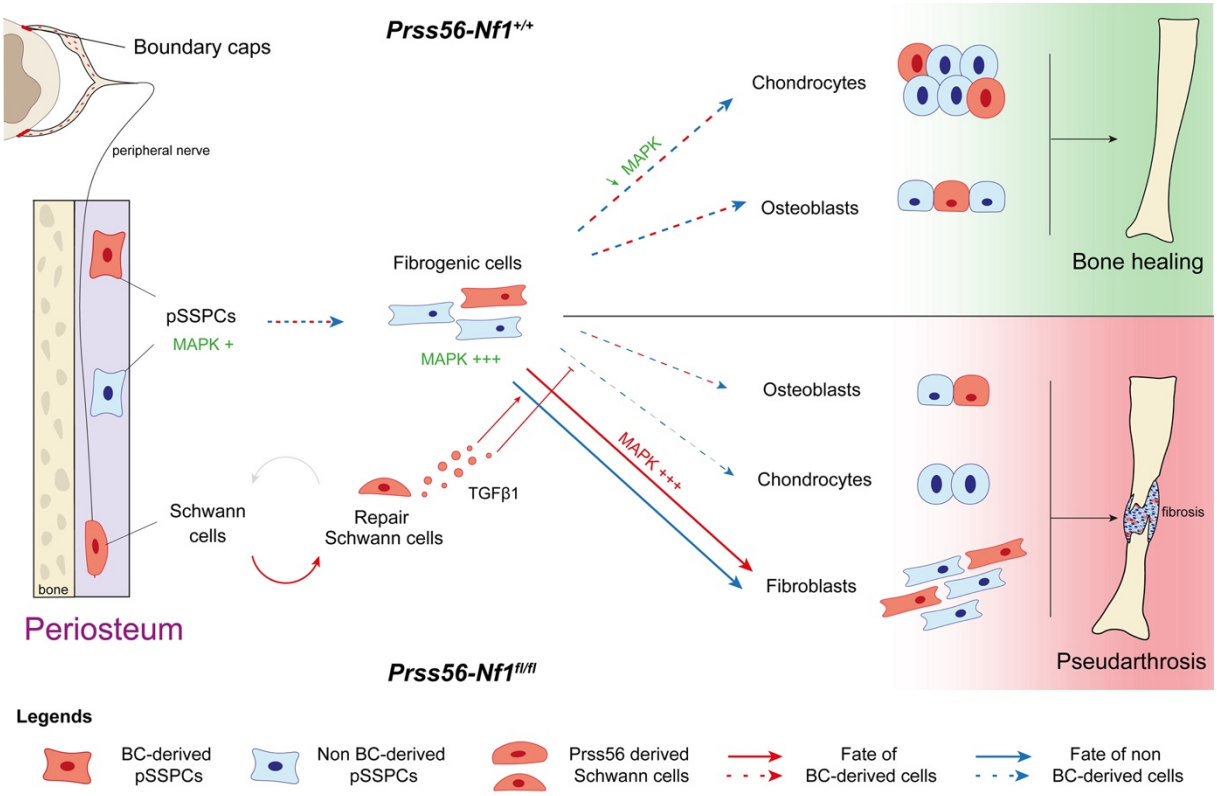

Figure 33: Model of bone repair defect in the *Prss56-Nf1 KO* mouse model.

The identification of TGFβ as a profibrotic factor involved in the pathogenesis of CPT suggests new therapeutical approaches. Antifibrotic treatment in *Prss56-Nf1 KO* mice using TGFβ blocking antibody allowed improved healing and bone bridging. TGFβ inhibition has been shown to improve bone healing in a model of *Nf1* inactivation in bone cells (using *Col1a1*^{Cre}*; Nf1*$^{fl/-}$ mice)[501]. In addition to the effect on TGFβ from SC, TGFβ inhibition can improve pseudarthrosis phenotype by acting on *Nf1*-deficient osteoblasts and heterozygous overactive osteoclasts[501]. As a factor involved in many disorders including cancer, molecules were developed to target TGFβ, including blocking antibodies, antisense oligonucleotides, and small molecule inhibitors[638]. Yet, current clinical trials show poor and inconsistent results[639]. Additionally, TGFβ1 treatment can lead to adverse effects including hemorrhagic lesions, chronic skin and gut inflammation, and squamous cell carcinoma[638,640–642]. It would be of interest to identify new profibrotic factors secreted by SCs in CPT to offer new therapeutical perspectives, that might be more specific to CPT. Another approach is the use of MEK inhibitors. Even if trials of MEK inhibitions on previous NF1 bone models had limited success, MEK inhibition can efficiently target *Nf1*-deficient SC in neurofibromas, leading to FDA approval of Selumetinib for the treatment of inoperable plexiform neurofibromas[460–462,464]. We combined Selumetinib with an inhibitor of SHP2, acting upstream of the neurofibromin, to treat *Prss56-Nf1 KO* mice after fracture and observed bone bridging (data not shown). Several challenges persist for the use of MEK inhibitors in CPT. While combining MEK and

SHP2 inhibition can provide a synergic effect and could allow the use of reduced dosage of these molecules, inhibition of the MAPK pathway remains at risk for pediatric cohorts. A second limitation is the timing of treatment, as the MAPK activation is dynamic and is required for several steps of bone repair. An inappropriate inhibition of the MAPK pathway could have a deleterious effect and reduce the chance of bridging and healing.

Another therapeutical approach considered to enhance bone healing is cell-based therapies. In this thesis, we investigated the FGFR3 induced-pseudarthrosis model and showed that this phenotype can be corrected by grafting wild-type SSPCs. However, in the *Prss56-Nf1 KO* model, grafting wild-type cells at the fracture site of mutant mice does not correct the phenotype, as grafted cells form fibrosis. It is interesting to compare the differences between the FGFR3 model, whose phenotype is due to pSSPC intrinsic deficiency, and the *Prss56-Nf1 KO* mouse model, whose phenotype is due to combined intrinsic deficiency of pSSPCs and alteration of the fracture environment. This highlights that cell-based approaches to treat bone repair defects, while promising, may not be optimal in all cases. While repair defects due to intrinsic cell deficiency can strongly benefit from adding effective SSPCs such as the FGFR3 model, cases when environmental factors are perturbed may not be responsive to this type of approach. This shows that understanding the origin and pathogenic mechanisms of bone repair defects in patients is critical in order to develop and provide appropriate therapeutical strategies.

Future perspectives

The thesis opens several perspectives:

In response to fracture, periosteal SSPCs form bone and cartilage by first transitioning through an initial fibrogenic state. This fibrogenic response of pSSPCs was firstly described in this thesis and will require further studies to understand its role and how cell fate decision towards osteogenesis and chondrogenesis is regulated. This fibrogenic step is also observed during the activation of muscle SSPCs that contribute mostly to cartilage and do not engage in osteogenesis. Despite sharing a common pattern of activation with muscle SSPCs, only pSSPCs can form cartilage and bone. Further studies will allow to decipher if the bipotentiality of pSSPCs is due to intrinsic cellular differences with muscle SSPCs and/or changes in the fracture environment.

The fracture environment is a complex dynamic multicellular environment. Interactions between SSPCs and other cell populations are crucial for bone healing, but are still not fully described. In depth analyses of the snRNAseq datasets of the periosteal response to fracture generated during the thesis will allow to better describe and understand the interactions of pSSPCs and the fracture environment, including immune cells, endothelial cells, pericytes and osteoclasts.

Analysis of the pseudarthrosis phenotype in the *Prss56-Nf1 KO* model revealed an unexpected role of *Nf1*-deficient Schwann cells (SCs) in causing this phenotype, suggesting that SCs may also play a role

during the normal bone repair process. Yet, the physiological role of Schwann cells in bone homeostasis and repair is unknown. This work opens new perspectives to study the role of the peripheral nervous system and Schwann cells in regulating bone physiology and bone regeneration.

The study of NF1-related CPT unraveled the pathogenic mechanisms leading to fibrous non-union following fracture. The results elucidate the consequences of *Nf1*-loss on pSSPCs from their early stage of activation. The work shows that *Nf1*-loss prevents the fibrogenic to chondrogenic transition leading to persistent fibrosis and pseudarthrosis. In addition, we identified SC dysfunction that play a pro-fibrotic role on wild-type SSPCs through TGFβ, reminiscent of their role in other NF1 symptoms. These analyses pave the way for the development of new targeted therapies to improve bone healing in CPT patients. We showed the potential of using anti-fibrotic treatment such as TGFβ inhibition to improve the pseudarthrosis phenotype in *Prss56-Nf1 KO* mice. Other options can be considered including MEK inhibitors.

Appendixes

Appendix 1: Résumé détaillé de la thèse

Appendix 2: List of conferences attended during the thesis

Appendix 3:

Periosteal skeletal stem and progenitor cells in bone regeneration

Simon Perrin and Céline Colnot

Review
published in Current Osteoporosis report in 2022

Appendix 4:

Mouse Periosteal Cell Culture, in vitro Differentiation, and in vivo Transplantation in Tibial Fractures

Simon Perrin, Anais Julien, Oriane Duchamp de Lageneste, Rana Abou-Khalil and Céline Colnot

Protocol
published in Bio-protocol in 2021

Appendix 5:

Renal Capsule Transplantation to Assay Angiogenesis in Skeletal Development and Repair

Anais Julien, **Simon Perrin**, Rana Abou-Khalil, and Céline Colnot

Technical book chapter
published in “Skeletal Development and Repair: Methods and Protocols, Methods in Molecular Biology, vol. 2230” in 2021

Appendix 1

Rôle du périoste dans la régénération osseuse et la pseudarthrose congénitale de jambe

Chaque année, environ 180 millions de personnes sont affectées par une fracture dans le monde. La régénération osseuse est un processus très efficace permettant aux os de se réparer suite à une fracture. Pourtant, environ 10% des fractures présentent un retard ou défaut de réparation, nécessitant le développement d'approches thérapeutiques pour améliorer la régénération osseuse. Ce processus repose sur l'activation de cellules souches/progénitrices osseuses (CSPOs) qui se différencient pour former une matrice cartilagineuse, progressivement remplacée par de l'os afin de permettre l'union des fragments osseux. Les CSPOs sont recrutées localement depuis différentes sources, dont le périoste, la moelle osseuse, et les muscles adjacents à la fracture. Le périoste, la membrane fibreuse entourant les os, est une source majeure de CSPOs formant de l'os et du cartilage après une fracture. Bien que des études récentes aient démontré le potentiel accru des CSPOs du périoste (pCSPOs) en réponse à la fracture, leur identité et leur hétérogénéité restent encore peu décrites. Les mécanismes de recrutement et de maturation des CSPOs du périoste après une fracture restent également à élucider.

Bien que son implication dans la régénération osseuse soit établie, le rôle du périoste dans les défauts de réparation osseuse est peu décrit. Il est toutefois suspecté dans le cas des pseudarthroses congénitales de jambe (PCJ), une atteinte osseuse sévère caractérisée par une fracture tibiale spontanée et une absence de consolidation due à l'accumulation de tissu fibrotique au site de fracture. Malgré le progrès des techniques chirurgicales utilisées pour traiter les PCJ, sa prise en charge reste un challenge et le risque d'amputation est élevé. La PCJ peut être classifiée comme isolée, dont l'étiologie est inconnue, ou comme associée à la Neurofibromatose de type 1 (NF1). NF1 est une maladie génétique causée par des mutations hétérozygotes du gène suppresseur de tumeur *NF1,* codant pour la neurofibromine, un régulateur des voies RAS et MAPK. NF1 est marqué par une grande variabilité de symptômes, dont des tumeurs de la gaine des nerfs périphériques, nommées neurofibromes et localisées sur la peau (neurofibromes cutanées, cNF) ou le long des nerfs périphériques (neurofibromes plexiformes, pNF), des hyperpigmentations cutanées, des défauts cognitifs et des atteintes osseuses, dont la PCJ et des déformations de la colonne vertébrale. Certains symptômes de NF1, dont les neurofibromes et les hyperpigmentations cutanées, sont dues à la perte biallélique de *NF1* dans des types cellulaires spécifiques i.e. les cellules de Schwann et les mélanocytes respectivement. L'inactivation biallélique de *NF1* a été identifiée dans les PCJ mais le(s) type(s) cellulaire(s) atteints restent à déterminer. De nombreux modèles murins ont été développés pour étudier les atteintes de NF1, sans toutefois récapituler la variabilité des symptômes observés chez les patients. Un nouveau modèle murin a été récemment développé, le modèle *Prss56-Nf1 KO*, portant une inactivation du gène *Nf1* dans une population spécifique de cellules de crêtes neurales, les capsules frontières (CP), et leurs dérivés. Ce modèle est le premier récapitulant différents symptômes de NF1, dont les neurofibromes plexiformes, cutanés et les hyperpigmentations cutanées. Cela suggère une

origine commune des différentes atteintes de NF1. La présence des atteintes osseuses dont la PCJ chez ce modèle n'a pas encore étudié.
L'objectif de la thèse est d'étudier l'hétérogénéité et le rôle des cellules souches/progénitrices osseuses du périoste au cours de la régénération osseuse ainsi que l'implication du périoste dans la pseudarthrose congénitale de jambe liée à la Neurofibromatose de type 1.

Dans la première partie de la thèse, j'ai utilisé la technique de séquençage de l'ARN en cellule unique pour décrire l'hétérogénéité des pCSPOs et leur réponse à la fracture. L'analyse de cellules primaires de périoste non blessé de souris *Prx1*^{Cre} *; R26*^{mTmG} a mis en évidence la présence de 3 populations cellulaires, des cellules souches/progénitrices, des macrophages et des ostéoclastes. L'analyse intégrée de cellules primaires issues de périoste non blessé et de périoste 3 jours post-fracture a permis d'identifier une population de cellules fibrochondrogéniques, spécifique de la réponse à la fracture. Ce cluster cellulaire exprime de nombreux gènes liés à la production de matrice extracellulaire, au développement osseux, à la prolifération cellulaire et à la réponse immunitaire, suggérant qu'il correspond à des cellules activées par la fracture. Une analyse détaillée de la population fibrochondrogénique a permis d'identifier les étapes d'activation des pCSPOs vers la chondrogenèse. En s'activant, les pCSPOs quittent leur état souche/progénitrice pour entrer en fibrogenèse puis en chondrogenèse. Ce schéma d'activation est équivalent à celui des CSPOs du muscle. Nous avons identifié la voie de signalisation BMP (Bone Morphogenetic Protein), comme une des premières cascades de signalisation activées dans les CSPOs après la fracture. L'inactivation du gène codant pour le récepteur BMPR1A (Bone Morphogenetic Protein Receptor type 1A) dans les CSPOs marquées par PDGFRα (Platelet-Derived Growth Factor Receptor Alpha) en utilisant le modèle murin *Pdgfra*^{CreERT} *; Bmpr1a*$^{fl/fl}$ conduit à un léger retard de régénération osseuse. La transplantation de périoste de souris *Pdgfra*^{CreERT} *; Bmpr1a*$^{fl/fl}$ au site de fracture de souris sauvages a permis de démontrer une diminution de la contribution des cellules déficientes pour le récepteur BMPR1A. Cette réduction est notamment liée à une diminution de la migration cellulaire et de la prolifération des pCSPOs aux étapes précoces de la régénération. Dans l'ensemble, la première partie de la thèse a permis d'élucider les étapes de différentiation précoce des pCSPOs vers la chondrogenèse et de montrer le rôle de la voie BMP dans la régulation de ces étapes.

Au cours de l'ossification endochondrale, les chondrocytes formant le cartilage maturent en s'hypertrophiant. Le cartilage est progressivement résorbé et remplacé par de l'os, soit par apoptose des chondrocytes soit par transdifférenciation des chondrocytes hypertrophiques en ostéoblastes. La présence de ce processus au cours de la régénération osseuse a été montré mais son importance et l'implication des cellules issues du périoste restent inconnues. **Dans la seconde partie de la thèse**, nous avons étudié le phénotype des souris *Prx1*^{Cre}*; Fgfr3*^{Y367C}*,* où les cellules dérivées du mésenchyme des membres portent une mutation suractivant le récepteur FGFR3 (Fibroblast growth factor receptor 3), impliquée dans certaines formes de nanisme. Ce modèle présente des membres de taille réduite et une absence complète de réparation osseuse un mois post-fracture. Des analyses de lignage et de transplantation cellulaire ont mis en évidence que les cellules issues du périoste de souris mutantes

pour *Fgfr3* se différencient en chondrocytes mais ne sont pas capables de maturer en chondrocytes hypertrophiques et de se transdifférencier en ostéoblastes. Cela conduit à la production de fibrocartilage persistant et bloquant la réparation osseuse. Ce phénotype sévère de réparation peut être corrigé par la transplantation de pCSPOs sauvages au site de fracture de souris $Prx1^{Cre}$; $Fgfr3^{Y367C}$. La seconde partie de la thèse a donc permis de démontrer la nécessité du processus de transdifférenciation des chondrocytes issus du périoste en ostéoblastes au cours de la régénération osseuse, et le rôle du récepteur FGFR3 dans ce processus. Ce travail met également en avant l'intérêt de l'étude des pCSPOs comme source de cellules pour l'ingénierie tissulaire et le développement de thérapies cellulaires osseuses.

Dans la troisième partie de la thèse, j'ai élucidé l'origine cellulaire de la pseudarthrose congénitale de jambe (PCJ) grâce à l'analyse combinée d'échantillons de patients atteints de PCJ et du modèle murin *Prss56-Nf1 KO*. Chez l'homme, nous avons étudié la localisation de l'inactivation biallélique de *NF1* par des analyses de séquençage de prélèvements osseux de patients opérés pour une PCJ. Nos résultats montrent que la PCJ est associée à l'inactivation biallélique de *NF1* au niveau du périoste et des pCSPOs du site de pseudarthrose. L'inactivation biallélique de *NF1* est retrouvé chez les patients atteints de PCJ lié à NF1 et isolée, indiquant que la majorité des PCJ sont liées à des mutations du gène *NF1*. Cela induit une suractivation de la voie MAPK dans le périoste et les pCSPOs du site de pseudarthrose. Des analyses transcriptomiques du périoste pathologique issu du site de pseudarthrose et de périoste témoin issu de la crête iliaque ont permis de montrer la présence de pCSPOs pro-fibrotiques au site de pseudarthrose. Les pCSPOs issus du site de pseudarthrose ont une capacité de différenciation altérée après transplantation au site de fracture de souris immunodéficientes et forment des cellules fibrotiques au lieu de former des chondrocytes. Afin d'élucider les mécanismes cellulaires et moléculaires de la PCJ, nous avons ensuite étudié le modèle murin *Prss56-Nf1 KO*. Nous avons montré que ce modèle récapitule un phénotype de pseudarthrose après fracture. Par analyse de lignage cellulaire, nous avons montré que les dérivés des capsules frontières correspondent à une population rare de cellules dans l'os, dont une sous-population de pCSPOs et de cellules de Schwann dans le périoste. Après fracture, les dérivés des CPs sont présents dans le cartilage et l'os de souris témoins. Chez les souris *Prss56-Nf1 KO*, leur contribution au cartilage est fortement réduite et les cellules dérivées des CPs sont situées dans l'os et la fibrose. Les pCSPOs mutées pour *Nf1* présentent un défaut intrinsèque de différenciation, et forme de la fibrose après fracture. L'analyse de la dynamique de l'activation de la voie MAPK dans les pCSPOs en réponse à la fracture a montré la diminution de l'activation de cette voie quand les cellules transitionnent du stade fibrogénique au stade chondrogénique. Les pCSPOS mutées pour le gène *Nf1* présentent une suractivation de la voie MAPK bloquant leur transition en chondrogenèse et conduisant à leur persistance au stade fibrogénique. En plus de cette déficience des pCSPOs mutées pour *Nf1*, nous avons démontré que l'environnement de fracture des souris mutantes *Prss56-Nf1 KO* affecte la différentiation des pCSPOs non mutées, les poussant vers la voie fibrogénique également. Cet effet de l'environnement est médié par les cellules de Schwann mutantes qui ont un effet paracrine pro-fibrotique sur les CSPOs non-mutées. Nous avons identifié le facteur pro-fibrotique TGFβ comme un des facteurs impliqués dans la différentiation altérée

des CSPOs non-mutées. L'inhibition de TGFβ permet de corriger le phénotype de pseudarthrose chez les souris *Prss56-Nf1 KO*. Dans l'ensemble, la troisième partie de la thèse a permis d'élucider l'origine cellulaire de la PCJ et les mécanismes conduisant à l'absence de réparation osseuse suite à une inactivation de *NF1* dans le périoste. La compréhension des mécanismes pathologiques de la PCJ ouvre la voie au développement de nouvelles stratégies thérapeutiques spécifiques, comme l'utilisation d'agents anti-fibrotiques visant TGFβ.

Cette thèse apporte une meilleure compréhension du rôle clé des pCSPO au cours de la régénération osseuse et les étapes d'activation et de maturation des pCSPOs. Cette thèse démontre également qu'une déficience du périoste, liée à une déficience intrinsèque des CSPOs du périoste ou à une perturbation de l'environnement de fracture, conduit à un défaut de régénération osseuse sévère, notamment dans le cas de la pseudarthrose congénitale de jambe liée à NF1. Cela met en avant l'importance de la compréhension des mécanismes physiologiques de la régénération osseuse afin de comprendre les déficiences de réparation et proposer des approches thérapeutiques ciblées et efficaces.

Appendix 2

List of conferences attended during the thesis

Webinar organized by the French Society of Biology of Mineralized Tissues (SFBTM)

June 9th 2021

Selected oral presentation - Award for best presentation

Role of Prss56-lineage in bone repair defect associated with Neurofibromatosis type 1

Simon Perrin, Oriane Duchamp de Lageneste, Anais Julien, Katarzyna Radomska, Piotr Topilko and Céline Colnot

Forum of BIOSPC Doctoral School

Ferrières-en-Brie – October 14 -15 2021

Selected oral presentation

Role of neural crest derivatives in bone repair defect associated with Neurofibromatosis type 1

Simon Perrin, Oriane Duchamp de Lageneste, Anais Julien, Katarzyna Radomska, Piotr Topilko and Céline Colnot

French Days of Biology of Mineralized Tissues

La Baule – April 27 - 29, 2022

Selected oral presentation

NF1 biallelic inactivation in periosteum causes congenital pseudarthrosis of the tibia

Simon Perrin, Sanela Protic, Ingrid Laurendeau, Oriane Duchamp de Lageneste, Elena Tacu, Katarzyna Radomska, Stéphanie Pannier, Philippe Wicart, Smail Hadj-Rabia, Dominique Vidaud, Piotr Topilko, Béatrice Parfait and Céline Colnot

NF Conference – Children's Tumor Foundation

Philadelphia, USA – June 18 – 21, 2022

Poster presentation - Top 5 of the best posters in Basic Science

NF1 biallelic inactivation in periosteum causes congenital pseudarthrosis of the tibia

Simon Perrin, Sanela Protic, Ingrid Laurendeau, Oriane Duchamp de Lageneste, Elena Tacu, Katarzyna Radomska, Stéphanie Pannier, Philippe Wicart, Smail Hadj-Rabia, Dominique Vidaud, Piotr Topilko, Béatrice Parfait and Céline Colnot

Gordon Research Seminar & Conference - Bone & Teeth

Ventura, USA – September 17 - 23 2022

Poster presentation - Travel grant for best poster presentation

NF1 biallelic inactivation in periosteum causes congenital pseudarthrosis of the tibia

Simon Perrin, Sanela Protic, Ingrid Laurendeau, Oriane Duchamp de Lageneste, Elena Tacu, Katarzyna Radomska, Stéphanie Pannier, Philippe Wicart, Smail Hadj-Rabia, Dominique Vidaud, Piotr Topilko, Béatrice Parfait and Céline Colnot

Appendix 3

Periosteal skeletal stem and progenitor cells in bone regeneration

Simon Perrin and Céline Colnot

Review
published in Current Osteoporosis report in 2022

Current Osteoporosis Reports
https://doi.org/10.1007/s11914-022-00737-8

SKELETAL BIOLOGY AND REGULATION (M MCDONALD AND E SCHIPANI, SECTION EDITORS)

Periosteal Skeletal Stem and Progenitor Cells in Bone Regeneration

Simon Perrin[1] · Céline Colnot[1]

Accepted: 24 June 2022

Abstract

Purpose of Review The periosteum, the outer layer of bone, is a major source of skeletal stem/progenitor cells (SSPCs) for bone repair. Here, we discuss recent findings on the characterization, role, and regulation of periosteal SSPCs (pSSPCs) during bone regeneration.

Recent Findings Several markers have been described for pSSPCs but lack tissue specificity. In vivo lineage tracing and transcriptomic analyses have improved our understanding of pSSPC functions during bone regeneration. Bone injury activates pSSPCs that migrate, proliferate, and have the unique potential to form both bone and cartilage. The injury response of pSSPCs is controlled by many signaling pathways including BMP, FGF, Notch, and Wnt, their metabolic state, and their interactions with the blood clot, nerve fibers, blood vessels, and macrophages in the fracture environment.

Summary Periosteal SSPCs are essential for bone regeneration. Despite recent advances, further studies are required to elucidate pSSPC heterogeneity and plasticity that make them a central component of the fracture healing process and a prime target for clinical applications.

Keywords Periosteum · Skeletal stem/progenitor cells · Bone regeneration · In vivo lineage tracing

Introduction

The periosteum is a thin fibrous membrane covering the outer surface of bone. It is organized in 2 layers: the outer fibrous layer, mostly composed of fibroblasts and extracellular matrix, and the inner cambium layer, composed of osteoblasts and skeletal stem/progenitor cells (SSPCs). The periosteum is highly vascularized and innervated by sensory and sympathetic fibers, and hosts resident and osteal macrophages (osteomacs) [1–3]. In long bones, the periosteum is derived from the limb mesenchyme that forms the cartilage template and the surrounding perichondrium during development [4, 5]. The periosteum plays crucial roles in bone physiology during development, growth, and remodeling. Periosteal cells directly contribute to cortical bone formation and control bone growth by secreting paracrine factors such as osteocrin [6, 7]. Extrinsic factors including mechanical loading stimulate bone formation in the periosteum during bone growth and remodeling [8–10].

The capacity of the periosteum to form bone after a fracture was first described in 1845 by Alexander Watson [11]. The periosteum displays a remarkable ability to regenerate bone and is indispensable to achieve bone healing [12]. Periosteum removal or damage at the time of fracture causes altered healing and non-union in experimental models [13–17]. The periosteum is a key source of SSPCs for bone repair in addition to SSPCs localized within the bone marrow compartment and the adjacent skeletal muscle [18–25••]. Following a bone injury, SSPCs are activated during the inflammatory phase of repair and differentiate into osteoblasts and chondrocytes. SSPC differentiation is regionalized in the fracture callus. Osteogenesis leading to intramembranous ossification occurs primarily at the periphery of the callus while chondrogenesis leading to endochondral ossification occurs in the center of the callus. The mechanical environment also influences cell differentiation as fracture stability favors intramembranous ossification and fracture instability favors endochondral ossification. The role of periosteal SSPCs in coordinating these events is still poorly understood.

This article is part of the Topical Collection on *Skeletal Biology and Regulation*

✉ Céline Colnot
celine.colnot@inserm.fr

[1] Univ Paris Est Creteil, INSERM, IMRB, F-94010 Creteil, France

Published online: 13 July 2022

understand the endogenous role and fate of pSSPCs during bone regeneration (Table 1). Due to their mesenchymal origin, pSSPCs in long bones can be tracked from developmental stages using the limb bud mesenchymal marker PRX1. The non-inducible *Prrx1*^{Cre} model labels not only SSPCs in the periosteum but also in bone marrow and skeletal muscle [20••, 21]. In adult bone, pSSPCs still express *Prrx1* but the inducible *Prrx1*^{CreERT} model does not allow efficient labeling of pSSPCs [20••, 37••, 46]. The platelet-derived growth factor-α (PDGFRα) has been described as a marker of mesenchymal cells from various tissue origins. Studies using the *Pdgfra*^{CreERT} model showed that PDGFRα marks pSSPCs with osteochondral potential during bone healing but is not restricted to the periosteum [24•, 25••, 47–49].

Debnath and colleagues combined the markers described by Chan et al. with the marker cathepsin K (CTSK) and identified a population of pSSPCs involved in intramembranous ossification [22••]. CTSK$^+$ pSSPCs, traced in the non-inducible *Ctsk*^{Cre} model, display self-renewing capacity and osteochondral potential in calvarial or femoral injury models. scRNAseq analysis of sorted CTSK$^+$ pSSPCs showed heterogeneity within this population, with clusters expressing chondrogenic genes (*Col2a1*, *Sox9*), osteogenic markers (*Kera*, *Alpl*), stemness markers (*Ly6a*, *Cd34*), and *Acta2* [22••]. CTSK$^+$ and CD200$^+$ periosteal cells were also detected in human periosteum [22••].

The protein alpha-smooth muscle actin (αSMA), encoded by the *Acta2* gene, labels cells in the periosteum [24•, 50]. αSMA$^+$ periosteal cells, traced using the *Acta2*^{CreERT} mouse line, are an heterogenous population of osteochondroprogenitors, with self-renewing potential and required for efficient bone healing [24•]. Ortinau and colleagues described a subpopulation of αSMA$^+$ cells, using the pIpC-inducible *Mx1*^{Cre} line [51••]. αSMA$^+$ Mx1$^+$ pSSPCs display self-renewal potential and are required for callus formation after tibial and calvarial injury [51••].

Several other markers have been identified, such as the Wnt signaling downstream target AXIN2, the receptor PDGFRβ, and HOX11 [52–54]. Markers, such as leptin receptor and Nestin, used to characterize bone marrow self-renewing SSPCs also label cells in the periosteum [42, 55]. Tournaire et al. reported that Nestin-GFP$^+$ periosteal cells in *Nestin-GFP* transgenic mice correspond to unipotent osteoprogenitors, with limited contribution to callus formation

Table 1 Markers and mouse lines labeling pSSPCs

Markers	Mouse model	Injury model	Contribution	Comment	Used in
PRX1	*Prrx1*^{Cre}	Non-stabilized tibial fracture	Cartilage/bone	Labels all SSPCs	Duchamp et al. [20••]
	Prrx1^{CreERT}	Non-stabilized ulna fracture	Cartilage/bone	Low cell labeling	Kawanami et al. [46]
PDGFRα	*Pdgfra*^{CreERT}	Non-stabilized tibial fracture	Bone/cartilage	Labels mesenchymal cells from various tissues	Julien et al. [25••]
		Non-stabilized forelimb fracture	Bone/cartilage		Xu et al. [47]
CTSK	*Ctsk*^{Cre}	Semi-stabilized femoral fracture Calvarial cortical defect	Bone/cartilage Bone	Marks osteoclasts	Debnath et al. [22••]
αSMA	*aSMA*^{CreERT}	Semi-stabilized tibial fracture	Bone/cartilage		Matthews et al. [24•]
	aSMA-GFP	Calvarial cortical defect	Bone		Ortinau et al. [51••]
MX1	*Mx1*^{Cre}	Non-stabilized tibial fracture Tibial periosteal defect	Bone/cartilage Bone	Requires pIpC injection to induce Cre recombination	Ortinau et al. [51••]
		Tibial cortical defect	Bone		
		Calvarial cortical defect	Bone		
Axin2	*Axin2*^{CreERT}	Tibial cortical defect	Bone		Ransom et al. [52]
PDGFRβ	*Pdgfrb*^{Cre}	Semi-stabilized femoral fracture	Bone/cartilage		Bohm et al. [53]
HOX11	*Hoxa11*^{CreERT2}	Non-stabilized ulnar fracture	Bone/cartilage	Restricted to zeugopod bone	Pineault et al. [54]
GLI1	*Gli1*^{CreERT1}	Semi-stabilized femoral fracture	Bone/cartilage	Marks bone marrow SSPCs	Shi et al. [56]
		Semi-stabilized tibial fracture	Bone/cartilage		Xia et al. [57]
Nestin	*Nes-GFP*	Semi-stabilized tibial fracture	Bone	Marks bone marrow SSPCs	Tournaire et al. [55]
	Nes^{CreERT}	Tibial cortical defect	Bone	Marks bone marrow SSPCs	Gao et al. [42]
LEPR	*Lepr*^{Cre}	Tibial cortical defect	Bone	Marks bone marrow SSPCs	Gao et al. [42]
SOX9	*Sox9*^{CreERT}	Semi-stabilized femoral fracture	Bone/cartilage		He et al. [58]
		Rib bone resection	Bone/cartilage	Labeling is increased when induced after fracture	Kuwahara et al. [17]
OSX	*Osx*^{Cre}	Semi-stabilized tibial fracture	Bone/cartilage	Labels osteogenic progenitors	Bohm et al. [53]

and no stemness properties. Lineage tracing in the Nes^{CreERT} model revealed an osteogenic and self-renewing potential of Nestin^{+} periosteal cells [42, 55]. GLI1 labels populations of SSPCs, including in the periosteum, forming chondrocytes and osteoblasts after fracture [56, 57]. Osteochondrogenic markers such as SOX9 ($Sox9^{CreERT}$ model) and osterix (Osx^{Cre} model) both label populations of periosteal progenitors contributing to cartilage and bone formation after fracture [53, 58].

Overall, periosteal SSPC populations defined by these various CRE models exhibit similar proprieties, such as the expression of stem/progenitor markers, osteochondral fate after fracture, and self-renewing capacity. It remains unclear how these populations overlap and differ in their identity and potential, and whether the periosteum encompasses several populations of pSSPCs. Moreover, no marker currently used to characterize pSSPC is fully specific to the periosteum as most of them are expressed also by cells localized in the bone marrow, skeletal muscle, or by stromal cells in other tissues [21, 25••, 49, 59]. Thus, marker expression is not sufficient to specifically trace periosteum-derived SSPCs and exclude the contribution of traced cells from other bone compartments during bone repair. Specifying the tissue of origin and using protocols to isolate periosteal cells without contamination from other tissues remain essential to identify pSSPCs and investigate their role in bone repair.

Molecular Regulation of Periosteal Stem and Progenitor Cells

During bone repair, pSSPC proliferation, migration, and differentiation are governed by several signaling pathways including bone morphogenic protein (BMP), Wnt, Notch, fibroblast growth factor (FGF), platelet-derived growth factor (PDGF), transforming growth factor-β (TGFβ), and Hedgehog (HH) signaling (Fig. 1). BMP signaling is one of the earliest pathway upregulated after fracture [25••]. Increased BMP ligand and receptor expression as well as activated downstream SMAD effectors are observed in the activated periosteum at day 3 post-fracture [25••, 60]. The role of BMP signaling during the early stage of bone healing was evaluated by inactivating *Bmpr1a* using the $Pdgfra^{CreERT}$ model. *Bmpr1a*-deficient periosteal SSPCs display reduced proliferation, migration, and osteochondrogenic differentiation after fracture [25••]. While endogenous BMP2 is required for bone healing, BMP4 and BMP7 are dispensable [61–63]. BMP2 plays a role in pSSPC fate decision, and *Bmp2* gene inactivation prevents periosteal activation and bone healing [64–66].

Notch signaling also plays a role in the early steps of bone healing before pSSPCs commit to the chondrogenic or osteogenic lineage. Notch inactivation in *Prx1*-derived cells, using $Prx1^{Cre}$ mice, causes bone non-union but Notch inactivation in chondrocytes using $Acan^{Cre}$ mice, or osteoblasts using $Col1.1^{Cre}$ mice, does not impact healing [67]. The crosstalk between Notch and Wnt signaling pathways is essential for the progression of the bone healing process. Whereas Notch signaling is active early to promote pSSPC activation and proliferation, the expression of Wnt pathway and target genes peaks between 5 and 10 days post-fracture [68, 69]. Inhibition of Notch signaling by Wnt signaling marks the end of the pSSPC activation phase and the initiation of osteogenic differentiation [67, 70, 71]. Wnt regulates the differentiation of pSSPCs by promoting osteogenic differentiation over chondrogenesis through SOX9 repression [72]. Wnt overactivation, in Sostdc1 knock-out mice, causes premature activation of periosteal cells and overmineralized callus formation [73]. The factors regulating Wnt expression and activation remain poorly understood.

FGFs are expressed not only during pSSPC activation (FGF2, FGF5, FGF9), but also during cartilage formation and maturation (FGF16, FGF18), and during ossification (FGF1, FGF17), suggesting their involvement through all stages of repair [74]. FGF2 promotes the proliferation and chondrogenic differentiation of pSSPCs through BMP2 signaling [75, 76]. By overactivating FGF receptor 3 (FGFR3) signaling in $Prx1^{Cre}$ mice, Julien et al. showed that FGFR3 is crucial for the differentiation of periosteum-derived chondrocytes and their ability to support cartilage-to-bone transformation during endochondral ossification [37•].

In addition, PDGF-BB, TGFβ, and Hedgehog are required for pSSPC proliferation and differentiation [57, 77–81]. PDGF-BB stimulates pSSPC migration and angiotropism while inhibiting apoptosis [42, 82]. Cyclooxygenase 2 (COX2) is essential for the initiation of the periosteal response to cortical bone injury by modulating several key pathways such as HIF, PI3K-Akt, and Wnt [83–85]. In sum, many signaling pathways and growth factors must act in coordination to control pSSPC activation and subsequent steps of differentiation. Whether several pSSPC subpopulations respond to distinct molecular signals and whether regulatory networks specific to pSSPCs define their unique osteochondral potential after fracture remain to be investigated.

Influence of the Fracture Environment on Periosteal Stem and Progenitor Cells

Bone fracture creates a major perturbation of bone tissue homeostasis with the rupture of blood vessels and nerve fibers initiating an acute inflammatory response shortly after fracture. This complex multicellular environment influences the activation and fate of pSSPCs (Fig. 1). The disruption of blood vessels causes immediate bleeding and subsequent blood clot formation. The blood clot is then progressively degraded by

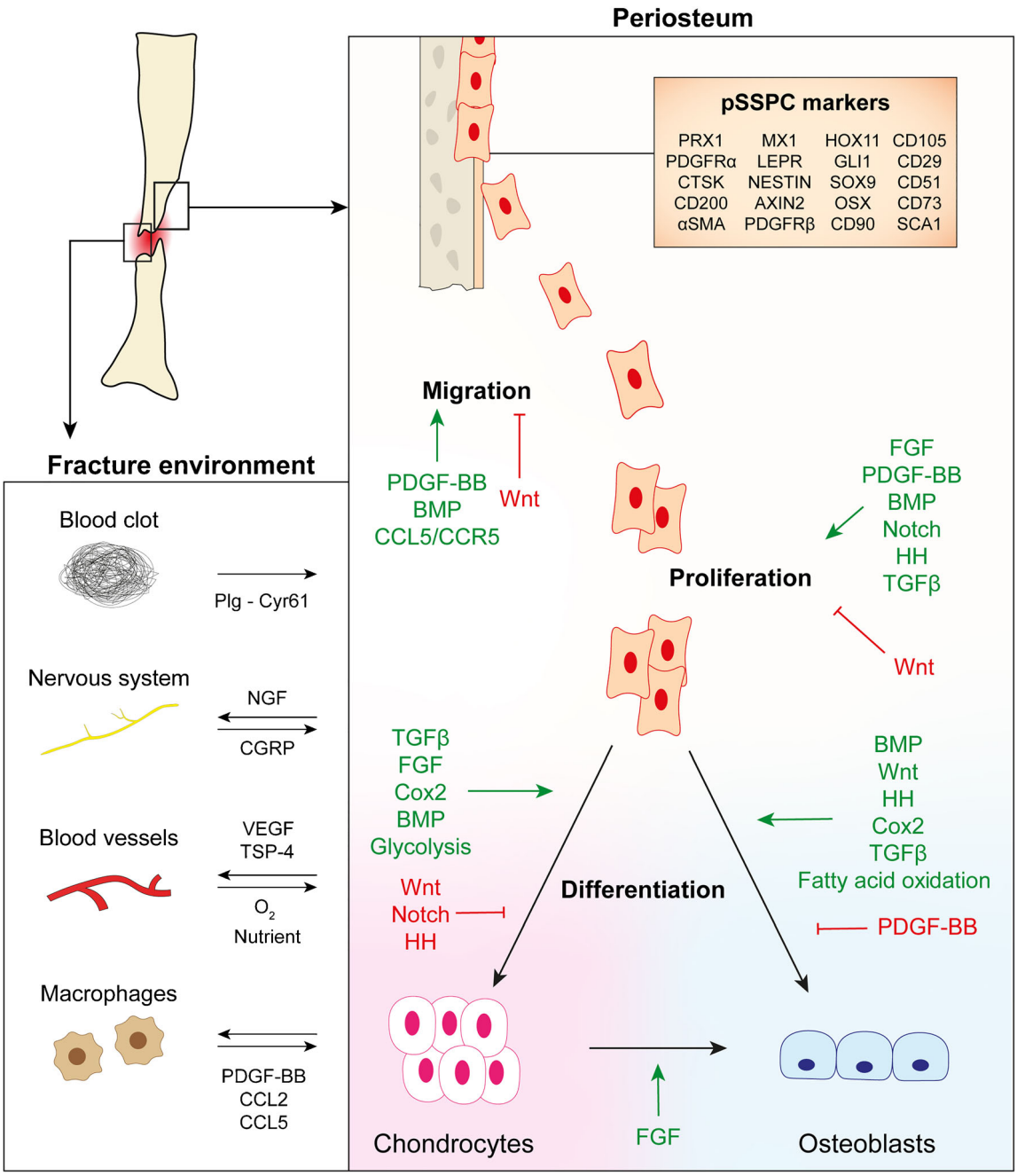

Fig. 1 Fate and regulation of periosteal stem/progenitor cells during bone repair. After fracture, periosteal stem/progenitor cells (pSSPCs), labeled by several markers (orange box), migrate to the site of injury, proliferate, and differentiate into chondrocytes or osteoblasts. These steps are controlled by several signaling pathways (activation in green and inhibition in red). The fate of pSSPCs is also influenced by their interactions with the fracture environment, including the blood clot, nerve fibers, blood vessels, and macrophages (left box)

the action of enzymes such as plasminogen (Plg) [86, 87]. Plg knock-out mice display impaired bone healing, with reduced callus, cartilage, and bone formation. Plg plays a paracrine role in the activation of pSSPCs. By cleaving the inactivated form of the matrix-associated growth factor Cyr61 secreted by pSSPCs, Plg can stimulate pSSPC proliferation and migration [87]. Periosteum is essential for the revascularization of the fracture site as periosteum removal reduces blood vessel density [43••]. Vascular disruption at the fracture site also causes hypoxia in the first days after injury [88]. The hypoxic environment stimulates HIF1α expression by pSSPCs and the secretion of the proangiogenic factors VEGF and TSP-4 required for angiogenesis and bone healing [27, 89–91]. More research is needed to elucidate the role of the periosteum and the interplay between blood vessels and pSSPCs during fracture revascularization.

During the inflammatory phase of bone repair, immune cells are recruited at the injury site. The periosteum becomes

invaded with osteomacs and activated macrophages [3]. Macrophages play a critical role in bone healing, and their depletion, using the Mafia inducible system, reduces periosteal callus formation [92]. Macrophages remove necrotic tissue at the fracture site and secrete factors involved in the recruitment and activation of pSSPCs. Gao et al. showed that $TRAP^+$ periosteal macrophages secrete PDGF-BB that binds to PDGFRβ expressed by pSSPCs to activate the Pi3K-Akt-CREB pathway and stimulate periostin expression [42]. Periostin is a critical regulator of pSSPC response to injury and self-renewal [20••]. Periosteal SSPCs are responsive to different chemokines. Chemokine ligand 2 (CCL2/MCP-1) is expressed in the periosteum during the first 3 days following fracture [93]. Inactivation or inhibition of CCL2 and his receptor CCR2 delays fracture healing [93, 94]. The CCL5-CCR5 axis is necessary to induce the migration of murine and human pSSPCs [51••]. In vitro osteogenic induction of periosteal cells can modulate macrophage polarization and promote M2 phenotype by secreting chemokines suggesting a crosstalk between macrophages and pSSPCs [95, 96].

The disruption of nerve fibers in the periosteum triggers rapid nerve sprouting from both sympathetic and sensory fibers in the first day post-bone injury. Nerve sprouting is concomitant with NGF expression in periosteal cells and macrophages, and occurs prior to revascularization [97]. Nerves subsequently regulate pSSPC activation by releasing neuropeptide calcitonin gene-related peptide (CGRP) that binds to the CALCRL-RAMP1 receptor and stimulates *Osterix* expression [98]. Overall, the perturbations in the microenvironment of the periosteum following bone injury generate unique cell-cell interactions and specific signals. This environment can vary depending on the type of injury, the mechanical stimuli, and additional interactions with the adjacent skeletal muscle, bone marrow, and systemic factors. How changes in this complex tissue environment influence the fate of pSSPCs remains to be explored.

Clinical Applications of Periosteal Stem and Progenitor Cells for Bone Repair

As the periosteum is an essential actor of bone healing, pSSPC deficiencies can have direct consequences on repair. Metabolic dysregulation in mice with induced type 1 diabetes reduces callus formation, correlated with decreased pSSPC proliferation and osteogenic differentiation [99]. Mice with diet-induced obesity (DIO) and subsequent type 2 diabetes also exhibit impaired fracture healing [100, 101]. Periosteal SSPCs isolated from DIO mice show reduced osteochondral and adipogenic differentiation potential in vitro [100]. Aging is a long-known factor affecting bone repair in human and animal models partially due to a reduction of pSSPC potential and number [102, 103]. Two reports indicate abnormal extracellular matrix deposition and proliferation of periosteal cells isolated from 1-year-old mice and reduced chondrogenic potential when isolated from 2-year-old mice [104, 105]. Aging is frequently linked to osteoporosis [106]. Mice with estrogen or glucocorticoid-induced osteoporosis display an abnormal periosteal response to scratch injury, with reduced cartilage formation and maturation [107]. Overall, dysfunctions of pSSPCs are still poorly described, but could be of major interest to understand bone healing impairment.

Periosteum flap or allograft is frequently used in orthopedic surgery to promote bone repair with convincing results in animal models and in human [108–110]. Periosteal SSPCs are therefore considered for cell-based therapies. Transplanted pSSPCs can improve bone healing in aged mice, genetically induced pseudarthrosis, and critical size defects [37•, 108, 111]. Bone tissue engineering aims to replace autograft approaches, by using cultured SSPCs embedded in a 3D matrix containing growth factors. The choice of the optimal cell source is key for successful bone tissue engineering and the periosteum rise as a promising source of cells. Compared to other cell sources, such as bone marrow, adipose, or dental pulp-derived cells, pSSPCs display higher clonogenicity, proliferation, osteogenic, and chondrogenic differentiation [20••, 112, 113]. Moreover, the potential of pSSPCs can be increased depending on the harvesting site and by using pre-treatment with BMP2 or FGF2 [38, 114, 115]. The development of periosteum-like matrix that mimics the structural organization and cellular composition of the periosteum is also explored with encouraging results [116]. Growth factors can be added to the scaffold in order to stimulate endogenous pSSPCs or promote angiogenesis of the grafted bioengineered tissue (VEGF) [113, 117]. To exploit pSSPCs as an alternative source of cells for orthopedic cell-based therapies, a better understanding of their identity and the factors regulating their fate is needed.

Conclusions

The first studies describing periosteal SSPCs in vitro provided limited relevance for endogenous pSSPC functions. In vivo lineage tracing, using transgenic mouse models, is a valuable tool to characterize pSSPCs in their periosteal niche and study their behavior in the complex fracture environment. Different subpopulations of pSSPCs have been identified using markers such as PRX1, CTSK, and αSMA. These pSSPCs share common features, including multipotency after fracture and self-renewal. It remains to be elucidated whether distinct subpopulations differ in their identity and potency or if they overlap and exhibit great plasticity based on their tissue localization and environmental signals in the fracture vicinity. Additionally, the absence of a specific marker to distinguish pSSPCs from the other SSPC sources remains a challenge.

While SSPCs from the bone marrow and skeletal muscle are mostly unipotent in vivo, pSSPCs are bi-potent differentiating into osteoblasts or chondrocytes. The origin of this bi-potentiality is unknown. The heterogeneity of pSSPC populations with distinct osteochondral potential is one hypothesis. pSSPCs also evolve in a unique fracture environment at the interface of bone and skeletal muscle, exposing them to numerous biological and mechanical stimuli. Advances in single-cell transcriptomics will provide new insights in the heterogeneity of pSSPCs and their responses to bone injury. The complementarity of in vitro, in vivo, and transcriptomic approaches will enhance our understanding of pSSPCs and pave the way for new orthopedic cell-based therapies.

Acknowledgements We thank A. Julien and R. Marcucio for critical reading and comments.

Funding This work was supported by ANR-18-CE14-0033, ANR-21-CE18-007-01, and NIAMS R01 AR072707 to C. Colnot. S. Perrin was supported by a PhD fellowship from Paris University.

Declarations

Conflict of Interest Authors declare no competing interests.

Human and Animal Rights and Informed Consent This article does not contain any studies with human or animal subjects performed by any of the authors.

References

Papers of particular interest, published recently, have been highlighted as:
- • Of importance
- •• Of major importance

1. Chartier SR, Mitchell SAT, Majuta LA, Mantyh PW. The changing sensory and sympathetic innervation of the young, adult and aging mouse femur. Neuroscience. 2018;387:178–90.
2. Lorenz MR, Brazill JM, Beeve AT, Shen I, Scheller EL. A neuroskeletal atlas: spatial mapping and contextualization of axon subtypes innervating the long bones of C3H and B6 mice. J Bone Miner Res. 2021;36:1012–25.
3. Alexander KA, Raggatt L, Millard S, Batoon L, Chiu-Ku Wu A, Chang M, Hume DA, Pettit AR. Resting and injury-induced inflamed periosteum contain multiple macrophage subsets that are located at sites of bone growth and regeneration. Immunol Cell Biol. 2017;95:7–16.
4. Colnot C, Lu C, Hu D, Helms JA. Distinguishing the contributions of the perichondrium, cartilage, and vascular endothelium to skeletal development. Dev Biol. 2004;269:55–69.
5. Akiyama H, Kim J-E, Nakashima K, et al. Osteochondroprogenitor cells are derived from Sox9 expressing precursors. Proc Natl Acad Sci U S A. 2005;102:14665–70.
6. Kaneko S, Matsushita M, Mishima K, Takegami Y, Imagama S, Kitoh H. Effect of periosteal resection on longitudinal bone growth in a mouse model of achondroplasia. Bone Reports. 2020;13:100708.
7. Watanabe-Takano H, Ochi H, Chiba A, Matsuo A, Kanai Y, Fukuhara S, Ito N, Sako K, Miyazaki T, Tainaka K, Harada I, Sato S, Sawada Y, Minamino N, Takeda S, Ueda HR, Yasoda A, Mochizuki N. Mechanical load regulates bone growth via periosteal osteocrin. Cell Reports. 2021;36:109380.
8. Moore ER, Zhu YX, Ryu HS, Jacobs CR. Periosteal progenitors contribute to load-induced bone formation in adult mice and require primary cilia to sense mechanical stimulation. Stem Cell Res Ther. 2018;9:190.
9. Zannit HM, Silva MJ. Proliferation and activation of osterix-lineage cells contribute to loading-induced periosteal bone formation in mice. JBMR Plus. 2019;3:e10227. https://doi.org/10.1002/jbm4.10227.
10. Cabahug-Zuckerman P, Liu C, Cai C, Mahaffey I, Norman SC, Cole W, Castillo AB. Site-specific load-induced expansion of Sca-1 $^{+}$ Prrx1 $^{+}$ and Sca-1 $^{-}$ Prrx1 $^{+}$ cells in adult mouse long bone is attenuated with age. JBMR Plus. 2019;3:e10199. https://doi.org/10.1002/jbm4.10199.
11. Watson A. Observations on the formation of bone by the periosteum. Edinb Med Surg J. 1845;63:302–7.
12. Sales de Gauzy J, Fitoussi F, Jouve J-L, Karger C, Badina A, Masquelet A-C. Traumatic diaphyseal bone defects in children. Orthopaedics & Traumatology: Surgery & Research. 2012;98:220–6.
13. Garcia P, Holstein JH, Maier S, Schaumlöffel H, Al-Marrawi F, Hannig M, Pohlemann T, Menger MD. Development of a reliable non-union model in mice. Journal of Surgical Research. 2008;147:84–91.
14. Wu X-Q, Wang D, Liu Y, Zhou J-L. Development of a tibial experimental non-union model in rats. J Orthop Surg Res. 2021;16:261.
15. Sharun K, Pawde AM, Banu SA, Manjusha KM, Kalaiselvan E, Kumar R, Kinjavdekar P, Amarpal. Development of a novel atrophic non-union model in rabbits: a preliminary study. Annals of Medicine and Surgery. 2021;68:102558.
16. Gröngröft I, Wissing S, Meesters DM, Poeze M, Matthys-Mark R, Ito K, Zeiter S. Development of a novel murine delayed secondary fracture healing in vivo model using periosteal cauterization. Arch Orthop Trauma Surg. 2019;139:1743–53.
17. Kuwahara ST, Serowoky MA, Vakhshori V, Tripuraneni N, Hegde NV, Lieberman JR, Crump JG, Mariani FV. Sox9+ messenger cells orchestrate large-scale skeletal regeneration in the mammalian rib. eLife. 2019;8:e40715.
18. Colnot C. Skeletal cell fate decisions within periosteum and bone marrow during bone regeneration. Journal of Bone and Mineral Research. 2009;24:274–82.
19. Murao H, Yamamoto K, Matsuda S, Akiyama H. Periosteal cells are a major source of soft callus in bone fracture. J Bone Miner Metab. 2013;31:390–8.
20.•• Duchamp de Lageneste O, Julien A, Abou-Khalil R, Frangi G, Carvalho C, Cagnard N, Cordier C, Conway SJ, Colnot C. Periosteum contains skeletal stem cells with high bone regenerative potential controlled by Periostin. Nat. Commun. 2018;9:773. **This study provides the first evidence of the presence of skeletal stem cells within the periosteum and their enhanced contribution to bone repair compared to bone marrow stromal cells**
21. Julien A, Kanagalingam A, Martínez-Sarrà E, Megret J, Luka M, Ménager M, Relaix F, Colnot C. Direct contribution of skeletal muscle mesenchymal progenitors to bone repair. Nature Communications. 2021;12:2860.
22.•• Debnath S, Yallowitz AR, McCormick J, et al. Discovery of a periosteal stem cell mediating intramembranous bone formation.

Nature. 2018;562:133–9. **This study identifies CTSK as a marker of pSSPCs supporting intramembranous ossification**

23. Matsushita Y, Nagata M, Kozloff KM, Welch JD, Mizuhashi K, Tokavanich N, Hallett SA, Link DC, Nagasawa T, Ono W, Ono N. A Wnt-mediated transformation of the bone marrow stromal cell identity orchestrates skeletal regeneration. Nat Commun. 2020;11:332.
24.• Matthews BG, Novak S, Sbrana FV, Funnell JL, Cao Y, Buckels EJ, Grcevic D, Kalajzic I. Heterogeneity of murine periosteum progenitors involved in fracture healing. eLife. 2021;10:e58534. **This study characterizes the αSMA$^+$ population within the periosteum**
25.•• Julien A, Perrin S, Martínez-Sarrà E, Kanagalingam A, Carvalho C, Luka M, Ménager M, Colnot C (2022) Skeletal stem/progenitor cells in periosteum and skeletal muscle share a common molecular response to bone injury. J of Bone & Mineral Res. https://doi.org/10.1002/jbmr.4616. **This study uses single-cell transcriptomics to describe how pSSPCs respond to bone injury.**
26. Roberts SJ, van Gastel N, Carmeliet G, Luyten FP. Uncovering the periosteum for skeletal regeneration: the stem cell that lies beneath. Bone. 2015;70:10–8.
27. van Gastel N, Torrekens S, Roberts SJ, Moermans K, Schrooten J, Carmeliet P, Luttun A, Luyten FP, Carmeliet G. Engineering vascularized bone: osteogenic and proangiogenic potential of murine periosteal cells. Stem Cells. 2012;30:2460–71.
28. Perrin S, Julien A, Duchamp de Lageneste O, Abou-Khalil R, Colnot C. Mouse periosteal cell culture, in vitro differentiation, and in vivo transplantation in tibial fractures. Bio-Protocol. 2021; https://doi.org/10.21769/BioProtoc.4107.
29. Declercq HA, De Ridder LI, Cornelissen MJ. Isolation and osteogenic differentiation of rat periosteum-derived cells. Cytotechnology. 2005;49:39–50.
30. Wang Q, Huang C, Zeng F, Xue M, Zhang X. Activation of the Hh pathway in periosteum-derived mesenchymal stem cells induces bone formation in vivo. The American Journal of Pathology. 2010;177:3100–11.
31. Bianco P. "Mesenchymal" stem cells. Annu Rev Cell Dev Biol. 2014;30:677–704.
32. Dominici M, Le Blanc K, Mueller I, Slaper-Cortenbach I, Marini FC, Krause DS, Deans RJ, Keating A, Prockop DJ, Horwitz EM. Minimal criteria for defining multipotent mesenchymal stromal cells. The International Society for Cellular Therapy position statement. Cytotherapy. 2006;8:315–7.
33. Sacchetti B, Funari A, Michienzi S, di Cesare S, Piersanti S, Saggio I, Tagliafico E, Ferrari S, Robey PG, Riminucci M, Bianco P. Self-renewing osteoprogenitors in bone marrow sinusoids can organize a hematopoietic microenvironment. Cell. 2007;131:324–36.
34. De Bari C, Dell'Accio F, Vanlauwe J, et al. Mesenchymal multipotency of adult human periosteal cells demonstrated by single-cell lineage analysis. Arthritis Rheum. 2006;54:1209–21.
35. Stich S, Loch A, Park S-J, Häupl T, Ringe J, Sittinger M. Characterization of single cell derived cultures of periosteal progenitor cells to ensure the cell quality for clinical application. PLoS ONE. 2017;12:e0178560.
36. Chan CKF, Seo EY, Chen JY, Lo D, McArdle A, Sinha R, Tevlin R, Seita J, Vincent-Tompkins J, Wearda T, Lu WJ, Senarath-Yapa K, Chung MT, Marecic O, Tran M, Yan KS, Upton R, Walmsley GG, Lee AS, et al. Identification and specification of the mouse skeletal stem cell. Cell. 2015;160:285–98.
37.• Julien A, Perrin S, Duchamp de Lageneste O, Carvalho C, Bensidhoum M, Legeai-Mallet L, Colnot C. FGFR3 in periosteal cells drives cartilage-to-bone transformation in bone repair. Stem Cell Reports. 2020;15:955–67. **This study reveals the important role of periosteum-derived chondrocyte transdifferentiation into osteoblasts during bone healing., 2020**
38. Groeneveldt LC, Herpelinck T, Maréchal M, Politis C, WFJ v IJ, Huylebroeck D, Geris L, Mulugeta E, Luyten FP. The bone-forming properties of periosteum-derived cells differ between harvest sites. Front Cell Dev Biol. 2020;8:554984.
39. Choi Y-S, Noh S-E, Lim S-M, Lee C-W, Kim C-S, Im M-W, Lee M-H, Kim D-I. Multipotency and growth characteristic of periosteum-derived progenitor cells for chondrogenic, osteogenic, and adipogenic differentiation. Biotechnol Lett. 2008;30:593–601.
40. Isogai N, Landis WJ, Mori R, Gotoh Y, Gerstenfeld LC, Upton J, Vacanti JP. Experimental use of fibrin glue to induce site-directed osteogenesis from cultured periosteal cells. Plast Reconstr Surg. 2000;105:953–63.
41. Eyckmans J, Luyten FP. Species specificity of ectopic bone formation using periosteum-derived mesenchymal progenitor cells. Tissue Eng. 2006;12:2203–13.
42. Gao B, Deng R, Chai Y, Chen H, Hu B, Wang X, Zhu S, Cao Y, Ni S, Wan M, Yang L, Luo Z, Cao X. Macrophage-lineage TRAP+ cells recruit periosteum-derived cells for periosteal osteogenesis and regeneration. Journal of Clinical Investigation. 2019;129:2578–94.
43.•• van Gastel N, Stegen S, Eelen G, et al. Lipid availability determines fate of skeletal progenitor cells via SOX9. Nature. 2020;579:111–7. **This study highlights the role of revascularization and the involvement of cell metabolism in pSSPC fate decision.**
44. Zhou X, von der Mark K, Henry S, Norton W, Adams H, de Crombrugghe B. Chondrocytes transdifferentiate into osteoblasts in endochondral bone during development, postnatal growth and fracture healing in mice. PLoS Genet. 2014;10:e1004820.
45. Hu DP, Ferro F, Yang F, Taylor AJ, Chang W, Miclau T, Marcucio RS, Bahney CS. Cartilage to bone transformation during fracture healing is coordinated by the invading vasculature and induction of the core pluripotency genes. Development. 2017;144:221–34.
46. Kawanami A, Matsushita T, Chan YY, Murakami S. Mice expressing GFP and CreER in osteochondro progenitor cells in the periosteum. Biochemical and Biophysical Research Communications. 2009;386:477–82.
47. Xu J, Wang Y, Li Z, Tian Y, Li Z, Lu A, Hsu CY, Negri S, Tang C, Tower RJ, Morris C, James AW. PDGFRα reporter activity identifies periosteal progenitor cells critical for bone formation and fracture repair. Bone Res. 2022;10:7.
48. Uezumi A, Ikemoto-Uezumi M, Tsuchida K. Roles of nonmyogenic mesenchymal progenitors in pathogenesis and regeneration of skeletal muscle. Front Physiol. 2014;5:68.
49. O'Rourke M, Cullen CL, Auderset L, Pitman KA, Achatz D, Gasperini R, Young KM. Evaluating tissue-specific recombination in a Pdgfrα-CreERT2 transgenic mouse line. PLoS ONE. 2016;11:e0162858.
50. Matthews BG, Grcevic D, Wang L, Hagiwara Y, Roguljic H, Joshi P, Shin D-G, Adams DJ, Kalajzic I. Analysis of αSMA-labeled progenitor cell commitment identifies notch signaling as an important pathway in fracture healing. J Bone Miner Res. 2014;29:1283–94.
51.•• Ortinau LC, Wang H, Lei K, et al. Identification of functionally distinct Mx1+αSMA+ periosteal skeletal stem cells. Cell Stem Cell. 2019;25:784–796.e5. **This study identifies αSMA+ Mx1+ cells as a population of pSSPCs required for bone healing**
52. Ransom RC, Hunter DJ, Hyman S, Singh G, Ransom SC, Shen EZ, Perez KC, Gillette M, Li J, Liu B, Brunski JB, Helms JA. Axin2-expressing cells execute regeneration after skeletal injury. Sci Rep. 2016;6:36524.

53. Böhm A-M, Dirckx N, Tower RJ, et al. Activation of skeletal stem and progenitor cells for bone regeneration is driven by PDGFRβ signaling. Dev. Cell. 2019;51:236–254.e12.
54. Pineault KM, Song JY, Kozloff KM, Lucas D, Wellik DM. Hox11 expressing regional skeletal stem cells are progenitors for osteoblasts, chondrocytes and adipocytes throughout life. Nat Commun. 2019;10:3168.
55. Tournaire G, Stegen S, Giacomini G, Stockmans I, Moermans K, Carmeliet G, van Gastel N. Nestin-GFP transgene labels skeletal progenitors in the periosteum. Bone. 2020;133:115259.
56. Shi Y, He G, Lee W-C, McKenzie JA, Silva MJ, Long F. Gli1 identifies osteogenic progenitors for bone formation and fracture repair. Nat Commun. 2017;8:2043.
57. Xia C, Ge Q, Fang L, Yu H, Zou Z, Zhang P, Lv S, Tong P, Xiao L, Chen D, Wang PE, Jin H. TGF-β/Smad2 signalling regulates enchondral bone formation of Gli1 $^{+}$ periosteal cells during fracture healing. Cell Prolif. 2020;53:e12904. https://doi.org/10.1111/cpr.12904.
58. He X, Bougioukli S, Ortega B, Arevalo E, Lieberman JR, McMahon AP. Sox9 positive periosteal cells in fracture repair of the adult mammalian long bone. Bone. 2017;103:12–9.
59. Kramann R, Schneider RK, DiRocco DP, Machado F, Fleig S, Bondzie PA, Henderson JM, Ebert BL, Humphreys BD. Perivascular Gli1+ progenitors are key contributors to injury-induced organ fibrosis. Cell Stem Cell. 2015;16:51–66.
60. Yu YY, Lieu S, Lu C, Miclau T, Marcucio RS, Colnot C. Immunolocalization of BMPs, BMP antagonists, receptors, and effectors during fracture repair. Bone. 2010;46:841–51.
61. Tsuji K, Cox K, Bandyopadhyay A, Harfe BD, Tabin CJ, Rosen V. BMP4 is dispensable for skeletogenesis and fracture-healing in the limb. Journal of Bone and Joint Surgery. 2008;90:14–8.
62. Tsuji K, Cox K, Gamer L, Graf D, Economides A, Rosen V. Conditional deletion of BMP7 from the limb skeleton does not affect bone formation or fracture repair. J Orthop Res. 2010;28:384–9.
63. Salazar VS, Capelo LP, Cantù C, Zimmerli D, Gosalia N, Pregizer S, Cox K, Ohte S, Feigenson M, Gamer L, Nyman JS, Carey DJ, Economides A, Basler K, Rosen V. Reactivation of a developmental Bmp2 signaling center is required for therapeutic control of the murine periosteal niche. eLife. 2019;8:e42386.
64. Chappuis V, Gamer L, Cox K, Lowery JW, Bosshardt DD, Rosen V. Periosteal BMP2 activity drives bone graft healing. Bone. 2012;51:800–9.
65. Tsuji K, Bandyopadhyay A, Harfe BD, Cox K, Kakar S, Gerstenfeld L, Einhorn T, Tabin CJ, Rosen V. BMP2 activity, although dispensable for bone formation, is required for the initiation of fracture healing. Nat Genet. 2006;38:1424–9.
66. Wang Q, Huang C, Xue M, Zhang X. Expression of endogenous BMP-2 in periosteal progenitor cells is essential for bone healing. Bone. 2011;48:524–32.
67. Wang C, Inzana JA, Mirando AJ, Ren Y, Liu Z, Shen J, O'Keefe RJ, Awad HA, Hilton MJ. NOTCH signaling in skeletal progenitors is critical for fracture repair. Journal of Clinical Investigation. 2016;126:1471–81.
68. Zhong N, Gersch RP, Hadjiargyrou M. Wnt signaling activation during bone regeneration and the role of dishevelled in chondrocyte proliferation and differentiation. Bone. 2006;39:5–16.
69. Kim J-B, Leucht P, Lam K, Luppen C, Ten Berge D, Nusse R, Helms JA. Bone regeneration is regulated by wnt signaling. J Bone Miner Res. 2007;22:1913–23.
70. Novak S, Roeder E, Sinder BP, Adams DJ, Siebel CW, Grcevic D, Hankenson KD, Matthews BG, Kalajzic I. Modulation of Notch1 signaling regulates bone fracture healing. J Orthop Res. 2020;38:2350–61.
71. Lee S, Remark LH, Josephson AM, et al. Notch-Wnt signal crosstalk regulates proliferation and differentiation of osteoprogenitor cells during intramembranous bone healing. npj. Regen. Med. 2021;6:29.
72. Minear S, Leucht P, Miller S, Helms JA. rBMP represses Wnt signaling and influences skeletal progenitor cell fate specification during bone repair. J Bone Miner Res. 2010;25:1196–207.
73. Collette NM, Yee CS, Hum NR, Murugesh DK, Christiansen BA, Xie L, Economides AN, Manilay JO, Robling AG, Loots GG. Sostdc1 deficiency accelerates fracture healing by promoting the expansion of periosteal mesenchymal stem cells. Bone. 2016;88:20–30.
74. Schmid GJ, Kobayashi C, Sandell LJ, Ornitz DM. Fibroblast growth factor expression during skeletal fracture healing in mice. Dev Dyn. 2009;238:766–74.
75. Nakajima F, Nakajima A, Ogasawara A, Moriya H, Yamazaki M. Effects of a single percutaneous injection of basic fibroblast growth factor on the healing of a closed femoral shaft fracture in the rat. Calcif Tissue Int. 2007;81:132–8.
76. van Gastel N, Stegen S, Stockmans I, Moermans K, Schrooten J, Graf D, Luyten FP, Carmeliet G. Expansion of murine periosteal progenitor cells with fibroblast growth factor 2 reveals an intrinsic endochondral ossification program mediated by bone morphogenetic protein 2. Stem Cells. 2014;32:2407–18.
77. Moore ER, Mathews OA, Yao Y, Yang Y. Prx1-expressing cells contributing to fracture repair require primary cilia for complete healing in mice. Bone. 2021;143:115738.
78. Wang Q, Huang C, Zeng F, Xue M, Zhang X. Activation of the Hh pathway in periosteum-derived mesenchymal stem cells induces bone formation in vivo: implication for postnatal bone repair. Am J Pathol. 2010;177:3100–11.
79. Huang C, Tang M, Yehling E, Zhang X. Overexpressing sonic hedgehog peptide restores periosteal bone formation in a murine bone allograft transplantation model. Molecular Therapy. 2014;22:430–9.
80. Miyaji T, Nakase T, Iwasaki M, Kuriyama K, Tamai N, Higuchi C, Myoui A, Tomita T, Yoshikawa H. Expression and distribution of transcripts for sonic hedgehog in the early phase of fracture repair. Histochem Cell Biol. 2003;119:233–7.
81. Doherty L, Yu J, Wang X, Hankenson KD, Kalajzic I, Sanjay A. A PDGFRβ-PI3K signaling axis mediates periosteal cell activation during fracture healing. PLoS ONE. 2019;14:e0223846.
82. Wang X, Matthews BG, Yu J, Novak S, Grcevic D, Sanjay A, Kalajzic I. PDGF modulates BMP2-induced osteogenesis in periosteal progenitor cells. JBMR Plus. 2019;3:e10127.
83. Huang C, Xue M, Chen H, Jiao J, Herschman HR, O'Keefe RJ, Zhang X. The spatiotemporal role of COX-2 in osteogenic and chondrogenic differentiation of periosteum-derived mesenchymal progenitors in fracture repair. PLoS ONE. 2014;9:e100079.
84. Xie C, Ming X, Wang Q, Schwarz EM, Guldberg RE, O'Keefe RJ, Zhang X. COX-2 from the injury milieu is critical for the initiation of periosteal progenitor cell mediated bone healing. Bone. 2008;43:1075–83.
85. Yukata K, Xie C, Li T-F, Brown ML, Kanchiku T, Zhang X, Awad HA, Schwarz EM, Beck CA, Jonason JH, O'Keefe RJ. Teriparatide (human PTH1–34) compensates for impaired fracture healing in COX-2 deficient mice. Bone. 2018;110:150–9.
86. Bravo D, Josephson AM, Bradaschia-Correa V, Wong MZ, Yim NL, Neibart SS, Lee SN, Huo J, Coughlin T, Mizrahi MM, Leucht P. Temporary inhibition of the plasminogen activator inhibits periosteal chondrogenesis and promotes periosteal osteogenesis during appendicular bone fracture healing. Bone. 2018;112:97–106.
87. Wang L, Yao L, Duan H, Yang F, Lin M, Zhang R, He Z, Ahn J, Fan Y, Qin L, Gong Y. Plasminogen regulates fracture repair by promoting the functions of periosteal mesenchymal progenitors. J Bone Miner Res. 2021;36:2229–42.
88. Lu C, Saless N, Hu D, Wang X, Xing Z, Hou H, Williams B, Swartz HM, Colnot C, Miclau T, Marcucio RS. Mechanical

stability affects angiogenesis during early fracture healing. Journal of Orthopaedic Trauma. 2011;25:494–9.
89. Stegen S, Deprez S, Eelen G, Torrekens S, Van Looveren R, Goveia J, Ghesquière B, Carmeliet P, Carmeliet G. Adequate hypoxia inducible factor 1α signaling is indispensable for bone regeneration. Bone. 2016;87:176–86.
90. Andrés Sastre E, Maly K, Zhu M, Witte-Bouma J, Trompet D, Böhm AM, Brachvogel B, van Nieuwenhoven CA, Maes C, van Osch GJVM, Zaucke F, Farrell E. Spatiotemporal distribution of thrombospondin-4 and -5 in cartilage during endochondral bone formation and repair. Bone. 2021;150:115999.
91. Street J, Bao M, deGuzman L, Bunting S, Peale FV Jr, Ferrara N, Steinmetz H, Hoeffel J, Cleland JL, Daugherty A, van Bruggen N, Redmond HP, Carano RAD, Filvaroff EH. Vascular endothelial growth factor stimulates bone repair by promoting angiogenesis and bone turnover. Proc Natl Acad Sci U S A. 2002;99:9656–61.
92. Raggatt LJ, Wullschleger ME, Alexander KA, Wu ACK, Millard SM, Kaur S, Maugham ML, Gregory LS, Steck R, Pettit AR. Fracture healing via periosteal callus formation requires macrophages for both initiation and progression of early endochondral ossification. The American Journal of Pathology. 2014;184:3192–204.
93. Ishikawa M, Ito H, Kitaori T, Murata K, Shibuya H, Furu M, Yoshitomi H, Fujii T, Yamamoto K, Matsuda S. MCP/CCR2 signaling is essential for recruitment of mesenchymal progenitor cells during the early phase of fracture healing. PLoS ONE. 2014;9:e104954.
94. Xing Z, Lu C, Hu D, Yu Y, Wang X, Colnot C, Nakamura M, Wu Y, Miclau T, Marcucio RS. Multiple roles for CCR2 during fracture healing. Disease Models & Mechanisms. 2010;3:451–8.
95. He F, Umrath F, Reinert S, Alexander D. Jaw periosteum-derived mesenchymal stem cells regulate THP-1-derived macrophage polarization. IJMS. 2021;22:4310.
96. He F, Umrath F, von Ohle C, Reinert S, Alexander D. Analysis of the influence of jaw periosteal cells on macrophages phenotype using an innovative horizontal coculture system. Biomedicines. 2021;9:1753.
97. Li Z, Meyers CA, Chang L, Lee S, Li Z, Tomlinson R, Hoke A, Clemens TL, James AW. Fracture repair requires TrkA signaling by skeletal sensory nerves. Journal of Clinical Investigation. 2019;129:5137–50.
98. Zhang Y, Xu J, Ruan YC, Yu MK, O'Laughlin M, Wise H, Chen D, Tian L, Shi D, Wang J, Chen S, Feng JQ, Chow DHK, Xie X, Zheng L, Huang L, Huang S, Leung K, Lu N, et al. Implant-derived magnesium induces local neuronal production of CGRP to improve bone-fracture healing in rats. Nat Med. 2016;22:1160–9.
99. Doherty L, Wan M, Kalajzic I, Sanjay A. Diabetes impairs periosteal progenitor regenerative potential. Bone. 2021;143:115764.
100. Marin C, Tuts J, Luyten FP, Vandamme K, Kerckhofs G. Impaired soft and hard callus formation during fracture healing in diet-induced obese mice as revealed by 3D contrast-enhanced computed tomography imaging. Bone. 2021;150:116008.
101. Brown ML, Yukata K, Farnsworth CW, Chen D-G, Awad H, Hilton MJ, O'Keefe RJ, Xing L, Mooney RA, Zuscik MJ. Delayed fracture healing and increased callus adiposity in a C57BL/6J murine model of obesity-associated type 2 diabetes mellitus. PLoS ONE. 2014;9:e99656.
102. Lu C, Miclau T, Hu D, Hansen E, Tsui K, Puttlitz C, Marcucio RS. Cellular basis for age-related changes in fracture repair. J Orthop Res. 2005;23:1300–7.
103. Clark D, Nakamura M, Miclau T, Marcucio R. Effects of aging on fracture healing. Curr Osteoporos Rep. 2017;15:601–8.
104. O'Driscoll SWM, Saris DBF, Ito Y, Fitzimmons JS. The chondrogenic potential of periosteum decreases with age. J Orthop Res. 2001;19:95–103.
105. Yukata K, Xie C, Li T-F, Takahata M, Hoak D, Kondabolu S, Zhang X, Awad HA, Schwarz EM, Beck CA, Jonason JH, O'Keefe RJ. Aging periosteal progenitor cells have reduced regenerative responsiveness to bone injury and to the anabolic actions of PTH 1-34 treatment. Bone. 2014;62:79–89.
106. Demontiero O, Vidal C, Duque G. Aging and bone loss: new insights for the clinician. Therapeutic Advances in Musculoskeletal. 2012;4:61–76.
107. Zhang H, Shi X, Wang L, Li X, Zheng C, Gao B, Xu X, Lin X, Wang J, Lin Y, Shi J, Huang Q, Luo Z, Yang L. Intramembranous ossification and endochondral ossification are impaired differently between glucocorticoid-induced osteoporosis and estrogen deficiency-induced osteoporosis. Sci Rep. 2018;8:3867.
108. Barastegui D, Gallardo-Calero I, Rodriguez-Carunchio L, Barrera-Ochoa S, Knorr J, Rivas-Nicolls D, Soldado F. Effect of vascularized periosteum on revitalization of massive bone isografts: an experimental study in a rabbit model. Microsurgery. 2021;41:157–64.
109. Harhaus L, Huang J-J, Kao S-W, Wu Y-L, Mackert GA, Höner B, Cheng M-H, Kneser U, Cheng C-M. The vascularized periosteum flap as novel tissue engineering model for repair of cartilage defects. J Cell Mol Med. 2015;19:1273–83.
110. Abed PF, El Chaar E, Boltchi F, Bassir SH. The novel periosteal flap stretch technique: a predictable method to achieve and maintain primary closure in augmentative procedures. J Int Acad Periodontol. 2020;22:11–20.
111. Hassibi H, Farsinejad A, Dabiri S, Vosough D, Mortezaeizadeh A, Kheirandish R, Azari O. Allogenic bone graft enriched by periosteal stem cell and growth factors for osteogenesis in critical size bone defect in rabbit model: histopathological and radiological evaluation. Iran J Pathol. 2020;15:205–16.
112. Amler A-K, Dinkelborg PH, Schlauch D, Spinnen J, Stich S, Lauster R, Sittinger M, Nahles S, Heiland M, Kloke L, Rendenbach C, Beck-Broichsitter B, Dehne T. Comparison of the translational potential of human mesenchymal progenitor cells from different bone entities for autologous 3D bioprinted bone grafts. IJMS. 2021;22:796.
113. Ho-Shui-Ling A, Bolander J, Rustom LE, Johnson AW, Luyten FP, Picart C. Bone regeneration strategies: engineered scaffolds, bioactive molecules and stem cells current stage and future perspectives. Biomaterials. 2018;180:143–62.
114. Bolander J, Herpelinck T, Chaklader M, Gklava C, Geris L, Luyten FP. Single-cell characterization and metabolic profiling of in vitro cultured human skeletal progenitors with enhanced in vivo bone forming capacity. Stem Cells Translational Medicine. 2020;9:389–402.
115. Bolander J, Ji W, Leijten J, Teixeira LM, Bloemen V, Lambrechts D, Chaklader M, Luyten FP. Healing of a large long-bone defect through serum-free in vitro priming of human periosteum-derived cells. Stem Cell Reports. 2017;8:758–72.
116. Dai K, Deng S, Yu Y, Zhu F, Wang J, Liu C. Construction of developmentally inspired periosteum-like tissue for bone regeneration. Bone Res. 2022;10:1.
117. Wu L, Gu Y, Liu L, Tang J, Mao J, Xi K, Jiang Z, Zhou Y, Xu Y, Deng L, Chen L, Cui W. Hierarchical micro/nanofibrous membranes of sustained releasing VEGF for periosteal regeneration. Biomaterials. 2020;227:119555.

Appendix 4

Mouse Periosteal Cell Culture, in vitro Differentiation, and in vivo Transplantation in Tibial Fractures

Simon Perrin, Anais Julien, Oriane Duchamp de Lageneste, Rana Abou-Khalil and Céline Colnot

Protocol
published in Bio-protocol in 2021

bio-protocol www.bio-protocol.org/e4107 Bio-protocol 11(15): e4107. DOI:10.21769/BioProtoc.4107

Mouse Periosteal Cell Culture, *in vitro* Differentiation, and *in vivo* Transplantation in Tibial Fractures

Simon Perrin[1, #], Anais Julien[1, #], Oriane Duchamp de Lageneste[1], Rana Abou-Khalil[2] and Céline Colnot[1, *]

[1]Univ Paris Est Creteil, INSERM, IMRB, F-94010 Creteil, France; [2]Center of Excellence for Biomedicine, Joint Centers of Excellence Program, King Abdulaziz City for Science and Technology (KACST), Riyadh, Saudi Arabia

*For correspondence: celine.colnot@inserm.fr

[#]Contributed equally to this work

[Abstract] The periosteum covering the outer surface of bone contains skeletal stem/progenitor cells that can efficiently form cartilage and bone during bone repair. Several methods have been described to isolate periosteal cells based on bone scraping and/or enzymatic digestion. Here, we describe an explant culture method to isolate periosteum-derived stem/progenitor cells for subsequent *in vitro* and *in vivo* analyses. Periosteal cells (PCs) isolated using this protocol express mesenchymal markers, can be expanded *in vitro*, and exhibit high regenerative potential after *in vivo* transplantation at a fracture site, suggesting that this protocol can be employed for PC production to use in new cell-based therapies.

Keywords: Periosteum, Bone regeneration, Skeletal stem/progenitor cell, *In vivo* cell transplantation, *In vitro* differentiation

[Background] Bone regeneration is a highly efficient process. After bone fracture, skeletal stem/progenitor cells are activated and differentiate into chondrocytes and osteoblasts that form cartilage and bone to consolidate the fracture. Skeletal stem/progenitor cells originate from the bone itself including bone-marrow and periosteum, as well as from adjacent soft tissue. The diverse origins of skeletal stem/progenitor cells during bone regeneration suggest that these cells can be obtained from various sources for stem cell therapies. Due to their accessibility, bone marrow stromal cells (BMSCs) are the most studied (Arthur and Gronthos, 2020); however, their variable osteogenic potential highlights the need for new sources of cells capable of contributing efficiently to the repair process. Recent studies have revealed the role of the periosteum as an essential source of stem/progenitor cells during bone regeneration (Debnath *et al.*, 2018; Duchamp de Lageneste *et al.*, 2018; Ortinau *et al.*, 2019). When transplanted to a bone fracture site, periosteal cells (PCs) display a higher regenerative potential than BMSCs and have the ability to correct a bone repair failure (Duchamp de Lageneste *et al.*, 2018; Julien *et al.*, 2020). Isolating mouse PCs is challenging since the periosteum is a very thin layer of tissue on the outer surface of bone. Several methods have been previously described to isolate PCs in mice, relying on enzymatic digestion and periosteum scraping or peeling (Brownlow *et al.*, 2000; Arnsdorf *et al.*, 2009; Wang *et al.*, 2010; Chang and Knothe Tate, 2012; van Gastel *et al.*, 2012). Here, we describe a method to isolate PCs based on cell migration from bone explants without digestion or periosteum

Bio-protocol 11(15): e4107.
DOI:10.21769/BioProtoc.4107

separation from the bone (Figure 1). We developed this method to analyze PC properties for direct comparison with BMSCs that are usually isolated by direct bone marrow flushing and plating. Long bones free of skeletal muscle, epiphyses, and bone-marrow are placed in culture to allow PC migration and proliferation. PCs isolated using this protocol express mesenchymal markers (Figure 2), display *in vitro* adipogenic, osteogenic, and chondrogenic differentiation capacities (Figure 3), and are able to form cartilage and bone upon *in vivo* transplantation at the site of a tibial fracture (Figure 4). PCs therefore maintain their osteochondrogenic capacities, offering new potential perspectives for the study of PCs and their use in cell-based therapies.

Materials and Reagents

1. Falcon® 5-ml round-bottomed polystyrene test tubes (Corning, catalog number: 352235)
2. 40-µm cell strainer (Fisher Scientific, catalog number: 352340)
3. Conical tubes, 15-ml and 50-ml (Falcon, catalog numbers: 352097 [15 ml] and 352070 [50 ml] or equivalent)
4. 25 G needles (Terumo, catalog number: AN*2516R1)
5. 1-ml syringes (Terumo, catalog number: SS+01H1)
6. 60-mm TPP culture dishes (TPP, catalog number: 93060)
7. 100-mm TPP culture dishes (TPP, catalog number: 93100)
8. 6-well plates (TPP, catalog number: 009206)
9. Greiner Bio-One Petri dishes (bacterial dish; Dutscher, catalog number: 633185)
10. 10-ml and 25-ml pipets (Dutscher, catalog numbers: 357551 [10 ml] and 357535 [25 ml] or equivalent)
11. Cell scrapers (TPP, catalog number: 99010 or equivalent)
12. Kova® slides (Fisher Scientific, catalog number: 22-270141)
13. Falcon® 5-ml round-bottomed polystyrene test tubes (Corning, catalog number: 352235)
14. Glass slides, Superfrost Plus (Thermo Fisher, catalog number: J1800AMNZ)
15. Coverslips (Labellians, catalog number: LCO2460M)
16. For periosteum-derived cell culture: 4 to 8-week-old mice in the C57BL/6J background (see Note 1)
17. Hosts for *in vivo* cell transplantation: 10 to 14-week-old mice in the C57BL/6J background (see Note 2)
18. DMEM (Life Technologies, catalog number: 11966-025)
19. Penicillin-streptomycin (P/S; Life Technologies, catalog number:15140-122)
20. α-Modified Eagle's Medium (α-MEM with GlutaMAX; Life Technologies, catalog number: 32561-029)
21. Lot-selected fetal bovine serum (FBS; Life Technologies, catalog number:10270-106)
22. Recombinant mouse basic fibroblast growth factor (bFGF; R&D, catalog number: 3139FB/CF)
23. Trypan Blue stain (Life Technologies, catalog number: 15250-061)

Bio-protocol 11(15): e4107.
DOI:10.21769/BioProtoc.4107

24. Trypsin-EDTA (0.25%), phenol red (Life Technologies, catalog number: 25200056)
25. Dexamethasone (Sigma-Aldrich, catalog number: D8893)
26. Human insulin solution (Sigma-Aldrich, catalog number: I9278)
27. Indomethacin (Sigma-Aldrich, catalog number: I7378)
28. 3-Isobutyl-1-methylxantine (IBMX, Sigma-Aldrich, catalog number: I5879)
29. Oil Red O (Sigma-Aldrich, catalog number: O0625)
30. Isopropanol (Sigma-Aldrich, catalog number: I9516)
31. L-ascorbic acid (Sigma-Aldrich, catalog number: A8960)
32. Beta-glycerophosphate (Sigma-Aldrich, catalog number: G9422)
33. Alizarin Red S (Sigma-Aldrich, catalog number: A5533)
34. DMEM high glucose (Life Technologies, catalog number: 31966-021)
35. Sodium pyruvate (Sigma-Aldrich, catalog number: P5280)
36. L-proline (Sigma-Aldrich, catalog number: P5607)
37. Insulin-transferrin-sodium selenite (ITS; Sigma-Aldrich, catalog number: I1884)
38. TGF-β1 (Sigma-Aldrich, catalog number: T7039)
39. Alcian Blue (Sigma-Aldrich, catalog number: A5268)
40. Glutaraldehyde (Merck, catalog number:1-04239-0250)
41. Hydrochloric acid (Sigma-Aldrich, catalog number:H1758)
42. Phosphate-buffered saline (PBS; Life Technologies, catalog number: 14190-094)
43. Ethanol (Ethanol absolute ≥99.8%; VWR, catalog number: 20821.365)
44. Hematoxylin (Sigma-Aldrich, Hematoxylin Solution, Harris Modified, catalog number: HHS32-1L)
45. Sytox Blue dead cell stain (Life Technologies, catalog number: S34857)
46. Tisseel matrix (Thrombin and Fibrin solution, Baxter, catalog number: 3400894252443)
47. Sterile distilled water (Life Technologies, catalog number: 15230162)
48. Buprenorphine (Centravet, catalog number: BUP001)
49. Atipamezole (Centravet, catalog number: ANT201)
50. Ketamine (Centravet, catalog number: KET205)
51. Medetomidine (Centravet, catalog number: DOM003)
52. Vetedine Savon (Vetoquinol, catalog number: 2608436 7/1992)
53. Vetedine solution (Vetoquinol, catalog number: 4576889 5/1992)
54. Paraformaldehyde 4% (PFA; Clinisciences, catalog number: sc-281692)
55. Sucrose (VWR, catalog number: 443815S)
56. EDTA solution 0.5 M (Euromedex, catalog number: EU0084)
57. Tissue Freezing Medium (MMFrance, catalog number:F/TFM-C)
58. Neo-Clear (Sigma-Aldrich, catalog number: 109843)
59. Hematoxylin anhydrous (Sigma-Aldrich, catalog number: 109843)
60. Iron(III) chloride, 97% (Sigma-Aldrich, catalog number: 157740)
61. Fast Green (Sigma-Aldrich, catalog number: F7252)

Bio-protocol 11(15): e4107.
DOI:10.21769/BioProtoc.4107

62. Safranin O (Sigma-Aldrich, catalog number: S2255)
63. Neo-mount (Sigma-Aldrich, catalog number: 109016)
64. Fluoromount-G Mounting medium with DAPI (Thermo Fisher, catalog number: 00-4959-52)
65. PE-Cy™7 Rat Anti-Mouse CD31 Antibody (dilution 1/400; BD Bioscience, catalog number: 561410)
66. PE-Cy™7 Rat Anti-Mouse CD45 Antibody (dilution 1/400; BD Bioscience, catalog number: 552848)
67. PE-Cy™7 Rat Anti-Mouse CD11b Antibody (dilution 1/400; BD Bioscience, catalog number: 552850)
68. BV650 Rat Anti-Mouse Ly-6A/E Antibody (dilution 1/200; BD Bioscience, catalog number: 740450)
69. PE Hamster Anti-MouseCD29 Antibody (dilution 1/200; Miltenyi, catalog number: 130-102-994)
70. Washing medium (see Recipes)
71. Growth medium (see Recipes)
72. FACS medium (see Recipes)
73. Adipogenic medium (see Recipes)
74. Oil Red O stock solution (see Recipes)
75. Osteogenic medium (see Recipes)
76. Alizarin Red S staining solution (see Recipes)
77. Chondrogenic medium (see Recipes)
78. 1% Alcian Blue staining solution (see Recipes)
79. Cryoprotection solution (see Recipes)
80. Weigert's solution (see Recipes)
81. Fast Green solution (see Recipes)
82. Safranin O solution (see Recipes)

Equipment

1. Surgical forceps (×4) (Dumont AA Forceps; FST, catalog number: 11210-20, or equivalent)
2. Surgical scissors (×4) (Fine Scissors-ToughCut® 11 mm; FST, catalog number: 14058-11, or equivalent)
3. BD LSRFortessa machine (Becton Dickinson)
4. Sterile hood for cell culture
5. Centrifuge with temperature control
6. Water bath with temperature control
7. CO_2 incubator set at 5% CO_2 and 33°C or 37°C
8. Shaker (VWR, model: Mini nutating, 3D mixer)
9. Drill (Dremel, catalog number: 8050-15)
10. Drill bits (0.4 mm)

Bio-protocol 11(15): e4107.
DOI:10.21769/BioProtoc.4107

11. W/C3 NDL Silk BL Braid sutures (Havard Apparatus, catalog number: 72-3318)
12. Heating pad (Harvard Apparatus, catalog number: 55-7033)
13. Mouse mower (Kerbl, catalog number: GT416)
14. Sterile scalpels (Dutscher, catalog number: 132622)
15. Cryostat (Leica Biosystems)
16. MM35P blade (MMFrance, F/MM35P)
17. Zeiss Imager D1 AX10 light microscope (Carl Zeiss Microscopy)

Procedures

A. Bone explant culture
   1. Prepare washing and growth media before mouse sacrifice.
   2. Keep 10 ml washing medium on ice to keep the bones in until culture.
   3. Place the growth medium in a 37°C water bath.
   4. Sacrifice the mice by cervical dislocation (or any other appropriate method).
   5. Rinse the animal thoroughly with 10 ml 70% ethanol.
   6. Bone isolation (Time: 10 min/mouse, requires 2 scissors and 2 forceps)
      a. Incise the skin of the inguinal region using scissors and remove it entirely from the hindlimbs. Disconnect the hindlimbs (femur with attached tibia) from the trunk by cutting at the femoral head with scissors. Place the hindlimbs in a sterile 100-mm Petri dish (Note 3, see Figure 1A).
      b. Cut at the knee junction to separate the tibia from the femur. Remove the soft tissue using forceps and scissors. Avoid taking hair and fat (see Figure 1A).
      c. Place the bones (femurs and tibias) in a 50-ml conical tube containing 15 ml washing medium on ice until all the bones have been isolated (see Notes 4 and 5).
   7. Bone marrow cell removal (Time: 2 min/bone, requires 2 scissors and 2 forceps)
      a. Under a cell culture hood, place the bones into a dish containing 10 ml washing medium.
      b. Cut the epiphyses just below the end of the marrow cavity using sterile scissors.
      c. Place the diaphysis into an empty Petri dish.
      d. Insert a 25 G needle with a 1-ml syringe filled with 1 ml growth medium into the bone marrow cavity and flush out the bone marrow. Repeat this step at least 3 times, until the bone becomes white (Notes 6 and 7, see Figure 1A).
      e. Place the flushed bones into a 50-ml tube containing 5 ml ice-cold growth medium for periosteal cell isolation.
   8. Periosteal cell culture
      a. Remove the growth medium and wash the bones by rinsing 3 times with fresh growth medium.
      b. Place all 12 bones into a 60-mm TPP culture dish (in the center of the dish, each bone separated by 0.3 cm, see Figure 1B).

Bio-protocol 11(15): e4107.
DOI:10.21769/BioProtoc.4107

c. Cover the bones by adding drops of growth medium at 37°C (around 1 ml in total, see Note 8).
d. Place the bones in a humid CO_2 incubator at 33℃ or 37℃ and 5% CO_2 (see Note 9).
e. Change the medium daily. Carefully aspirate the medium and replace with fresh growth medium. Place the dish back at 33°C or 37℃ (see Notes 10 and 11). Cell migration usually starts after 2 or 3 days.

9. When cell migration is observed (Figure 1C), add 2-3 ml growth medium. Change the medium daily.
10. When PCs have sufficiently migrated from the explant (usually after 2 weeks), gently remove the explants from the dish using sterile forceps, wash once with 1× PBS, and add 5 ml fresh growth medium to cover the cells (Figure 1C).
11. Allow the cells to grow for 4-5 more days. Change the medium daily.
12. When PCs reach 80% confluence around the explant site, remove the medium and add 3 ml trypsin. Place the plate back into the incubator for 3 min. Detach PCs using a cell scraper and transfer the cells to a 50-ml Falcon tube containing 10 ml growth medium.
13. Centrifuge at 300 × *g* for 10 min.
14. Discard the supernatant and resuspend the cells in 10 ml growth medium. Plate the cells into a 100-mm TPP plate.
15. Replace the medium every 2-3 days with fresh growth medium.
16. When PCs reach 80% confluence, cells can be trypsinized for further passage (Figure 1D). For experiments, PCs can be used from P0 (Notes 12, 13, and 14).

Bio-protocol 11(15): e4107.
DOI:10.21769/BioProtoc.4107

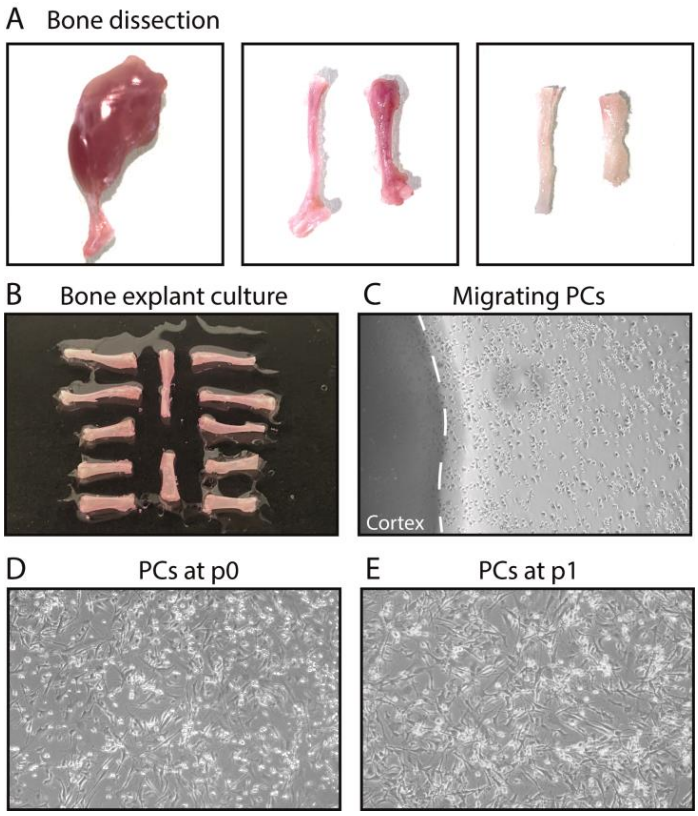

Figure 1. Steps of bone explant culture. (A) Steps of bone dissection. Left, hindlimb free of skin. Middle, tibia, and femur free of muscle. Right, tibia and femur after cutting the epiphyses and flushing the bone marrow. (B) Tibias and femurs plated in a culture dish. (C) After a few days, periosteal cells (PCs) migrate out of the bone explants into the dish. (D-E) PCs at P0 and P1.

B. Flow cytometry analysis of PCs

1. When PCs reach 80% confluence, remove medium and add 3 ml trypsin. Place the plate back into the incubator for 3 min. Detach PCs using a cell scraper, and transfer the cells into a 50-ml Falcon tube containing 10 ml growth medium.
2. Centrifuge at 300 × *g* for 10 min.
3. Resuspend cells in 10 ml growth medium.
4. Filter through a 40-μm cell strainer.
5. Count the living cells using Trypan Blue and process the number of cells needed for the experiment: 1.5×10^5 cells per tube.
6. Centrifuge at 300 × *g* for 10 min.
7. Resuspend the cells in 200 μl FACS medium per 1.5×10^5 cells.
8. Split the cells into FACS tubes.
9. Add antibody mix according to each tube and mix well (Notes 15 and 16).
10. Incubate for 15 min on ice in the dark.
11. Add 1 ml FACS medium to each tube.

Bio-protocol 11(15): e4107.
DOI:10.21769/BioProtoc.4107

12. Centrifuge at 300 × *g* for 10 min.
13. Remove the supernatant and resuspend the cells in 200 µl FACS medium.
14. Add 0.5 µl Sytox Blue per tube immediately before analysis.
15. Perform flow cytometry analysis using a BD LSR Fortessa (Figure 2).

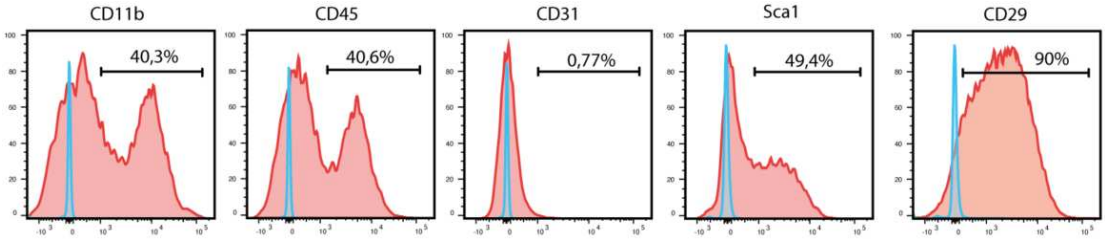

Figure 2. Flow cytometry analysis of periosteum-derived cells at P1. Blue curves represent FMO controls, and red curves represent experimental samples.

C. *In vitro* differentiation

1. *In vitro* adipogenesis
   a. Plate 1.5 × 10^5 PCs in a 6-well plate in duplicate.
   b. Allow the cells to reach 100% confluence in growth medium.
   c. When confluency is reached, induce adipogenesis by covering the cells with adipogenic medium.
   d. Incubate the cells at 37°C for up to 3 weeks; change adipogenesis medium twice a week.
   e. After 3 weeks of differentiation, proceed to Oil Red O staining for lipid droplets:
      Discard medium.
      Rinse gently twice with PBS.
      Fix cells with 3 ml 70% ethanol for 30 min at room temperature.
      Rinse gently twice with H_2O.
      Cover the cells with 3 ml 60% isopropanol for 5 min.
      Discard isopropanol and stain with 3 ml filtered Oil Red O staining solution for 50 min at room temperature.
      Rinse twice with H_2O.
      Counterstain nuclei with 3 ml hematoxylin for 1 min.
      Rinse twice with H_2O.
      Leave H_2O and take an image within 2 h using an inverted microscope (Figure 3).
2. *In vitro* osteogenesis
   a. Plate 1.5 × 10^5 PCs in a 6-well plate in duplicate.
   b. Allow the cells to reach 100% confluence in growth medium.
   c. When confluency is reached, induce osteogenesis by covering the cells with osteogenic medium.
   d. Incubate the cells at 37°C for up to 3 weeks; change the osteogenic medium twice a week.
   e. After 3 weeks of differentiation, proceed to Alizarin Red staining for hydroxyapatite crystals.

Bio-protocol 11(15): e4107.
DOI:10.21769/BioProtoc.4107

Discard medium.

Rinse twice with PBS.

Fix cells with 3 ml 70% ethanol for 30 min at room temperature.

Rinse twice with H_2O.

Stain with 3 ml Alizarin Red S solution for 45 min at room temperature, under agitation and protected from light.

Rinse twice with H_2O.

Allow the plate to dry before taking images (Figure 3).

3. *In vitro* chondrogenesis
   a. Resuspend the cells at a concentration of 5×10^5 cells in 200 µl growth medium.
   b. Using a 200-µl pipet, seed the PCs in drops of 200 µl containing 5×10^5 cells. Place 3 drops in a 60-mm TPP culture dish.
   c. Carefully place the plates at 37°C (Note 17).
   d. Allow the cells to attach to the plate for 6-8 h.
   e. Check cell attachment before starting differentiation (leave longer if necessary).
   f. Remove growth medium and induce chondrogenesis by covering the cell drops with chondrogenic medium.
   g. Incubate the cells at 37°C for 3 days.
   h. Proceed to Alcian Blue staining for sulfated GAG:

      Discard medium.

      Rinse twice with PBS.

      Fix cells with 2% glutaraldehyde in H_2O for 1 h at room temperature.

      Rinse with 0.1 M HCl.

      Stain with 1% Alcian Blue for 2 h at room temperature.

      Rinse twice with 0.1 M HCl.

      Allow the plate to dry before taking images (Figure 3).

Bio-protocol 11(15): e4107.
DOI:10.21769/BioProtoc.4107

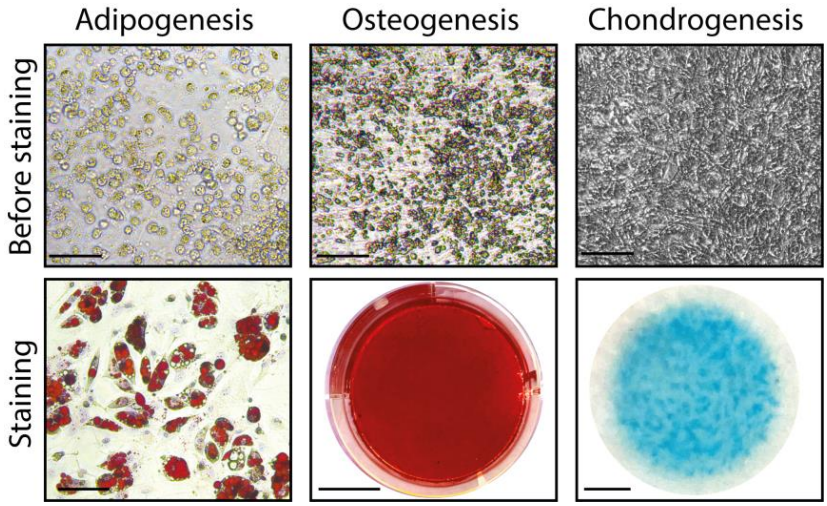

Figure 3. *In vitro* adipogenic, osteogenic, and chondrogenic differentiation of PCs before and after staining. Scale bars: before staining: 200 μm; staining: 50 μm (adipogenesis), 1 cm (osteogenesis), 2.5 mm (chondrogenesis).

D. *In vivo* PC transplantation at the fracture site (Note 18)

1. Tisseel matrix pellet formation
   a. When PCs reach 80% confluence, remove the medium and add 3 ml trypsin. Place the plate back into the incubator for 3 min. Detach PCs using a cell scraper and transfer the cells to a 50-ml Falcon tube containing 10 ml growth medium.
   b. Centrifuge at 300 × *g* for 10 min.
   c. Count the cells and keep only the number of cells needed for the experiment: 10^5 cells per host animal.
   d. Place 10^5 cells in a 1.5-ml sterile Eppendorf tube (one tube for each host animal). Centrifuge for 10 min at 300 × *g* and remove as much medium as possible.
   e. Prepare appropriate volumes of fibrin (F) and thrombin (T) diluted 1:4 in distilled water: 10^5 cells are resuspended in 15 μl F (diluted 1:4) + 15 μl T (diluted 1:4) per host animal (see Note 19).
   f. Add 15 μl diluted fibrin to the tubes containing cells. Resuspend by pipetting without forming bubbles.
   g. Add 15 μl diluted thrombin to form a solid gel (see Note 20).
   h. Allow the matrix to polymerize for 15 min on ice. If the pellet is well formed, it can be easily grabbed with the tip of forceps (Figure 4E).
   i. Keep the tubes at 4℃ on ice until transplantation.
2. Surgery for *in vivo* transplantation
   a. Anesthetize mice with intraperitoneal injection of 50 mg/kg ketamine and 1 mg/kg medetomidine (Note 21).
   b. Inject 0.1 mg/kg buprenorphine subcutaneously for analgesia.
   c. After 15 min, check the quality of anesthesia by foot pinching.

Bio-protocol 11(15): e4107.
DOI:10.21769/BioProtoc.4107

d. Shave the right limb and sanitize using vetedine soap and solution or any other skin disinfectant solution (Figure 4A).
e. Perform a 2-cm incision on the skin above the tibia using a sterile scalpel (Figure 4B).
f. Expose the anterior tibial surface by carefully separating the muscle from the bone surface (Figure 4C).
g. Create 3 holes at the mid-diaphysis perpendicular to the longitudinal axis of the tibia using a drill and a 0.4-mm drill bit.
h. Induce an osteotomy by cutting the bone along the 3 holes with scissors (see Note 22) (Figure 4D).
i. Gently position the Tisseel matrix pellet containing PCs at the fracture site between the two bone cortices (Figure 4F).
j. Close the skin wound using 5-0 non-resorbable sutures.
k. Revive the mice with an intraperitoneal injection of 1 mg/kg atipamezole.
l. Place the mice on a 37°C heating pad until revived.
m. Perform two additional subcutaneous injections of buprenorphine 0.1 mg/kg at 12 h and 24 h post-surgery.

3. Histological analysis of the PC contribution to the callus
   a. Sacrifice the mice by cervical dislocation (or any other appropriate method) and rinse the limb with 70% ethanol (Note 23).
   b. Incise the skin and remove it entirely from the hindlimbs. Disconnect the femur and the tibia by cutting at the knee junction and at the feet. Remove the soft tissue around the callus using forceps and scissors (Note 24).
   c. Place the sample in a 15-ml Falcon tube containing 8 ml 4% ice-cold PFA for 24 h with constant shaking at 4°C.
   d. Remove the PFA solution, wash the sample with ice-cold PBS, and add 8 ml EDTA solution. Place at 4°C with constant shaking for 21 days; change the EDTA solution every other day (see Note 25).
   e. Remove the EDTA solution, wash the sample with ice-cold PBS, and add 8 ml cryoprotection solution. Place at 4°C for 24 h without shaking.
   f. Remove the cryoprotection solution and wash 3 times with ice-cold PBS.
   g. On dry ice, fill a plastic mold with Tissue Freezing Medium, embed the bone, and place the sample at -80°C.
   h. Cut the sample into 10 µm-thick sections using a cryostat.
   i. Stain the sections with Safranin O to allow cartilage visualization (Figure 4G):
      Allow the slides to dry for 30 min at room temperature.
      Hydrate the slides in PBS for 5 min.
      Place the slides in Weigert's solution for 5 min.
      Wash in tap water for 3 min.
      Place the slides in Fast Green solution for 30 s.

Bio-protocol 11(15): e4107.
DOI:10.21769/BioProtoc.4107

Place the slides in 1% acetic acid for 30 s.

Place the slides in Safranin O solution for 30 min.

Wash in distilled water for 3 min.

Place the slides in 70% ethanol for 3 min.

Place the slides in 95% ethanol for 3 min.

Place the slides in 100% ethanol for 5 min, twice.

Place the slides in Neo-Clear for 3 min, twice.

Mount the slides with Neo-mount.

Take images using a brightfield microscope.

j. Mount the slides with DAPI to visualize the PC contribution to the callus (Figure 4H):

Allow the slides to dry for 30 min at room temperature.

Hydrate the slides in PBS for 5 min.

Mount the slides with Fluoromount-G with DAPI.

Take images using a fluorescence microscope.

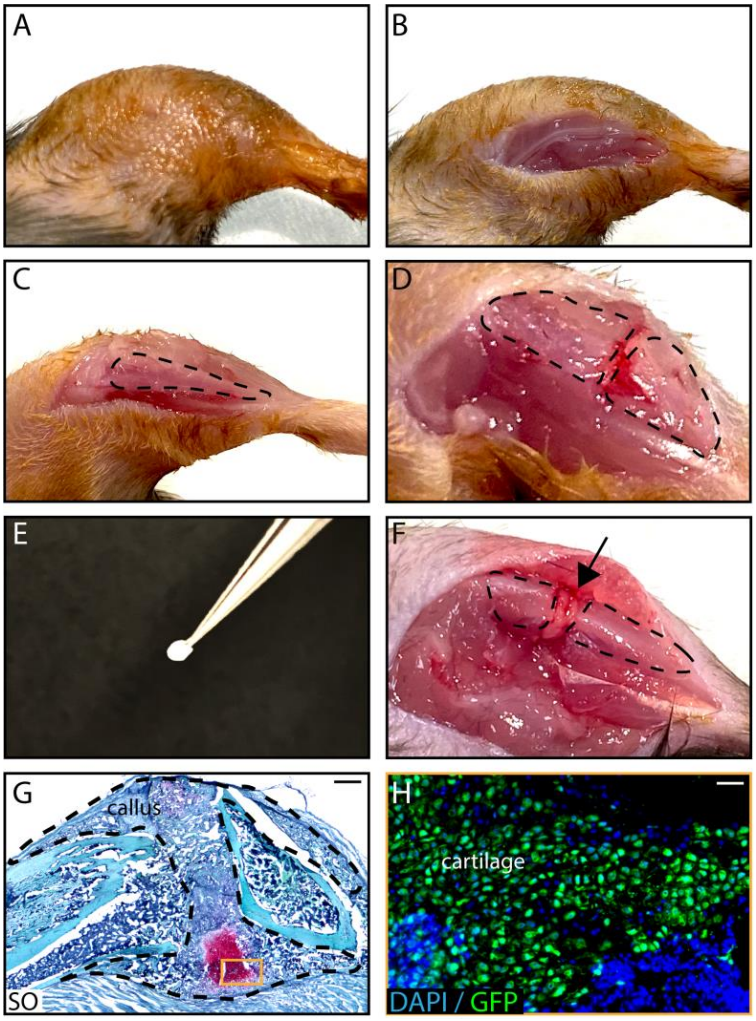

Figure 4. *In vivo* transplantation of PCs isolated from GFP-actin donors at the fracture site of wild-type hosts. After shaving and sanitizing the limb (A), an incision in the skin is

Bio-protocol 11(15): e4107.
DOI:10.21769/BioProtoc.4107

performed (B) and the tibia is exposed (C, tibia is delineated by a dotted line) to induce a fracture (D). A Tisseel matrix pellet containing PCs (E) is transplanted at the fracture site (F, black arrow). (G) Representative image of a longitudinal callus section on day 14 post-fracture stained with SO. (H) GFP+ chondrocytes derived from PCs on an adjacent section of the callus. Scale bars: 1 mm (G) and 100 µm (H).

Notes

1. We recommend using the hindlimbs (femur and tibia bones) of at least 3 mice per culture. Donor mice for PC culture should carry a reporter transgene in the C57BL/6J background in order to perform cell tracing following *in vivo* transplantation in C57BL/6J hosts.
2. All procedures must be approved by the local Ethics Committee.
3. Two sets of sterilized surgical tools (2 scissors and 2 forceps per set) are needed for bone explant culture: one for bone dissection and one for bone marrow removal under a culture hood. To avoid contamination, tools used to cut and remove the skin should not be used to touch bones and soft tissue. Bones should only be handled using forceps to avoid any contamination.
4. Remove soft tissue gently along the bone using scissors, instead of pulling out tissues, to avoid detaching the periosteum from the cortex.
5. Isolated bones can be kept on ice in washing medium for up to 2 h.
6. Be careful not to drop the bones into the Petri dish containing the bone marrow cells in order to avoid contamination of PC cultures with BMSCs. Any bone dropped in the plate containing BMSCs should be discarded.
7. BMSCs can be cultured from the flushed bone marrow. Centrifuge the medium containing the flushed bone marrow at 300 × *g* for 10 min, resuspend the pellet in growth medium, and plate in a 100-mm TPP culture dish. On subsequent days, wash the cells with PBS once a day to eliminate floating hematopoietic cells and obtain adherent bone marrow cells.
8. When covering the bones with medium, drops covering each bone can touch and merge. However, be careful that the bones are not floating or detaching, as it is critical for bones to be in contact with the plate to allow for cell migration.
9. The protocol was initially optimized using a 33°C incubator, but PC migration and growth are also observed when cultured in a 37°C incubator.
10. Do not wash the bones and proceed gently to avoid moving bones that have started to attach to the bottom of the dish.
11. Change the medium daily to avoid bone explant drying.
12. We recommend using PCs between passages 0 and 2 for optimal cell growth.
13. PCs can be frozen down for later use. For optimal cell viability after thawing, we recommend freezing cells in growth medium supplemented with 10% DMSO.

Bio-protocol 11(15): e4107.
DOI:10.21769/BioProtoc.4107

14. As observed in Figure 2, primary cultures of PCs also contain hematopoietic cells. An additional step of cell sorting or antibody-based column depletion can be used to discard hematopoietic cells and increase the purity of periosteal stem/progenitor populations.
15. Each antibody has to be titrated prior to the experiment.
16. For each experiment, FMO (Fluorescence Minus One) controls can be included to determine positive vs. negative signals, and isotype controls can be used to check the specificity of the antibodies.
17. After plating cell drops for chondrogenesis, handle the plates with caution, as the drop should remain intact to allow cell deposition at the right confluency to mimic a 3D environment.
18. For tracing of PC contribution to the fracture callus, donor mice should express a reporter gene. As an example, we use GFP-actin mice in this protocol.
19. Fibrin is a highly viscous solution; be careful to pipet the right volume of fibrin when diluting. If needed, cut the extremity of the tip for easier pipetting of the viscous solution.
20. Coagulation is very fast. After adding thrombin, remove the tip from the gel within 2 s.
21. Anesthetized mice should be kept on a 37°C heating pad to avoid temperature loss and improve well-being.
22. Tibia can be cut without drilling holes, but drilling holes prevents bone fragments.
23. The time of sacrifice should be decided according to the biological question. We recommend choosing days 7-14 post-fracture to observe the contribution to cartilage and days 14-21 to observe the contribution to bone.
24. Be careful to remove enough soft tissue without affecting the callus structure, especially when collecting on days 3, 5, and 7 post-fracture.
25. The pH of the EDTA solution must be between 7.4 and 7.6 to allow for proper decalcification.

Recipes

1. Washing medium
   DMEM
   1% penicillin/streptomycin
2. Growth medium
   α-MEM with GlutaMAX
   1% penicillin/streptomycin
   20% lot-selected fetal bovine serum
   10 ng/ml bFGF
3. FACS medium
   PBS
   1% penicillin/streptomycin
   2% fetal bovine serum
4. Adipogenic medium (make fresh)

Bio-protocol 11(15): e4107.
DOI:10.21769/BioProtoc.4107

α-MEM with GlutaMAX
1% penicillin/streptomycin
10% fetal bovine serum
0.1 μM dexamethasone
100 μM indomethacin
0.5 mM IBMX
10 μg/ml insulin

5. Oil Red O stock solution
   Stock solution: 300 mg Oil Red O powder in 100 ml 99% isopropanol
   Ready-to-use solution (make fresh):
   Mix 3 parts Oil Red O stock solution with 2 parts H_2O
   Allow to sit at room temperature for 10 min
   Filter the staining solution through coffee filter paper
6. Osteogenic medium (make fresh)
   α-MEM with GlutaMAX
   1% penicillin/streptomycin
   10% fetal bovine serum
   0.1 μM dexamethasone
   0.05 mM L-ascorbic acid
   10 mM β-glycerophosphate
7. Alizarin Red S staining solution
   Alizarin Red S 0.2% in distilled water
   Adjust the pH to 4.1-4.3.
   The pH is critical; make fresh or check the pH if the solution is more than one month old.
   Store at 4°C.
8. Chondrogenic medium (make fresh)
   DMEM high glucose
   1% penicillin/streptomycin
   10% fetal bovine serum
   0.1 μM dexamethasone
   100 μg/ml sodium pyruvate
   40 μg/ml L-proline
   50 μg/ml L-ascorbic acid
   50 mg/ml ITS
   10 ng/ml TGFβ1
9. 1% Alcian Blue staining solution
   Prepare 5% Alcian Blue solution in PBS
   Dilute 5% Alcian Blue stock solution in 0.1 M HCl to obtain 1% Alcian Blue
10. Cryoprotection solution

Bio-protocol 11(15): e4107.
DOI:10.21769/BioProtoc.4107

30 g sucrose

100 ml H_2O

11. Weigert's solution (make fresh)

100 ml solution A and 100 ml solution B

Solution A:

5.0 g hematoxylin

500 ml ethanol 95%

Solution B:

20 ml 29% aqueous iron(III) chloride

5 ml HCl

475 ml distilled water

12. Fast Green solution

0.2 g Fast Green

1 L distilled water

13. Safranin O solution

1 g Safranin O

1 L distilled water

Acknowledgments

This work was supported by Fondation de l'Avenir, Osteosynthesis and Trauma Care Foundation, ANR-18-CE14-0033, NIAMS R01 AR072707 to C.C. A.J., S.P., and O.D.L were supported by Ph.D. fellowships from Paris University. This protocol was first described in Duchamp de Lageneste *et al.* (2018) and in Julien *et al.* (2020).

Competing interests

The authors declare no competing interests.

Ethics

All procedures involving animals were approved by the Creteil University (agreement #19295-2019052015468705) Ethical Committee.

References

1. Arnsdorf, E. J., Luis M. J., Dennis, R. C. and Christopher, R. J. (2009). The periosteum as a cellular source for functional tissue engineering. *Tissue Eng Part A* 15(9): 2637-2642.

2. Arthur, A. and Gronthos, S. (2020). Clinical Application of Bone Marrow Mesenchymal Stem/Stromal Cells to Repair Skeletal Tissue. *Int J Mol Sci* 21(24): 9759.
3. Brownlow, H. C., Reed, A., Joyner, C., Simpson, A.H. (2000). Anatomical effects of periosteal elevation. *J Orthop Res* 18(3): 500-502.
4. Chang, H. and Knothe Tate, M. L. (2012) Concise review: the periosteum: tapping into a reservoir of clinically useful progenitor cells. *Stem Cells Transl Med* 1(6): 480-491.
5. Debnath, S., Yallowitz, A.R., McCormick, J., Lalani, S., Zhang, T., Xu, R., Li, N., Liu, Y. F., Yang, Y. S., Eiseman, M., Shim, J. H., Hameed, M., Healey, J. H., Bostrom, M. P., Landau, D. A., Greenblatt, M. B. (2018). Discovery of a periosteal stem cell mediating intramembranous bone formation. *Nature* 562(7725): 133-139.
6. Duchamp de Lageneste, O., Julien, A., Abou-Khalil, R., Frangi, G., Carvalho, C., Cagnard, N., Cordier, C., Conway, S. J., Colnot, C. (2018). Periosteum contains skeletal stem cells with high bone regenerative potential controlled by Periostin. *Nat Commun* 9(1): 773.
7. van Gastel, N., Torrekens, S., Roberts, S. J., Moermans, K., Schrooten, J., Carmeliet, P., Luttun, A., Luyten, F. P., Carmeliet, G. (2012). Engineering vascularized bone: osteogenic and proangiogenic potential of murine periosteal cells. *Stem Cells* 30(11): 2460-2471.
8. Julien, A. Perrin, S., Duchamp de Lageneste, O., Carvalho, C., Bensidhoum, M., Legeai-Mallet, L., Colnot, C. (2020). FGFR3 in Periosteal Cells Drives Cartilage-to-Bone Transformation in Bone Repair. *Stem Cell Reports* 15(4): 955-967.
9. Ortinau, L. C., Wang, H., Lei, K., Deveza, L., Jeong, Y., Hara, Y., Grafe, I., Rosenfeld, S. B., Lee, D., Lee, D., Scadden, D. T., Park, D. (2019). Identification of Functionally Distinct Mx1+αSMA+ Periosteal Skeletal Stem Cells. *Cell Stem Cell* 25(6): 784-796.e5.
10. Wang, Q., Huang, C., Zeng, F., Xue, M., Zhang, X. (2010). Activation of the Hh pathway in periosteum-derived mesenchymal stem cells induces bone formation *in vivo*: implication for postnatal bone repair. *Am J Pathol* 177(6): 3100-3111.

Appendix 5

Renal Capsule Transplantation to Assay Angiogenesis in Skeletal Development and Repair

Anais Julien, **Simon Perrin**, Rana Abou-Khalil, and Céline Colnot

Technical book chapter
published in “Skeletal Development and Repair: Methods and Protocols, Methods in Molecular Biology, vol. 2230” in 2021

Chapter 10

Renal Capsule Transplantation to Assay Angiogenesis in Skeletal Development and Repair

Anais Julien, Simon Perrin, Rana Abou-Khalil, and Céline Colnot

Abstract

Renal capsule transplantation is a very helpful method to grow embryonic tissues or tumors in a vascular environment, allowing for long-term engraftment and biological analyses. This chapter describes the surgical procedure for the transplantation of embryonic skeletal elements in the renal capsule of adult mice and points out the manipulations that can be applied for assaying the role of angiogenesis during bone development and repair.

Key words Skeletal development, Skeletal repair, Angiogenesis, Renal capsule transplantation

1 Introduction

Bone is a highly vascularized tissue with tight connections between blood vessels, bone marrow, and bone cells to maintain skeletal integrity. Angiogenesis plays a pivotal role in skeletal development and particularly during endochondral ossification as an angiogenic switch is required for the replacement of cartilage by bone marrow and bone [1–3]. Numerous tools and methodologies have been used to study the impact of angiogenesis on osteogenesis both in vitro and in vivo [4–8]. Although in vitro angiogenesis assays have provided direct evidence for bidirectional interactions between osteoblasts and endothelial cells, which are crucial for osteogenesis, other cell types, circulating factors, and extracellular matrix proteins are involved in bone vascularization. Therefore, in vivo angiogenic assays are also essential to study the role of supporting cells (smooth muscle cells, pericytes, and fibroblastic cells) and other factors in the tissue environment. Moreover, in vitro assays do not allow the development of the hematopoietic compartment of bone, which is required for establishing the stromal compartment of bone and providing osteoclasts that are together necessary for bone formation and remodeling. Since the

Matthew J. Hilton (ed.), *Skeletal Development and Repair: Methods and Protocols*, Methods in Molecular Biology, vol. 2230, https://doi.org/10.1007/978-1-0716-1028-2_10,

kidney is one of the most vascularized organs in the body, the renal capsule constitutes a permissive environment to grow cells, tumors, or embryonic tissues [9–13]. The renal capsule of adult mice has been used as a host environment to dissect the role of angiogenesis in skeletal development [13, 14]. With the growing number of genetically modified mouse models, this approach can help distinguish the effects of specific gene mutations in skeletal tissues versus blood vessels and their impact on angiogenesis and subsequent bone development [15, 16]. Any skeletal element from the developing embryo can potentially be collected prior to its vascularization in vivo and transplanted in the adult host renal capsule. More recently, this model was used to grow human embryonic skeletal elements [17]. Vascularization of the grafts occurs within 3 days, and the renal capsule environment can support normal bone development and growth, including establishment of the bone marrow, cortical bone, and surrounding periosteum (Fig. 1). Finally, skeletal stem/progenitors within bone marrow and periosteum can be isolated from long bones grown in the renal capsule and mobilized to repair bone after skeletal injury thus extending the use of this system to study bone repair mechanisms (Fig. 2) [18].

2 Materials

2.1 Anesthetics and Analgesic

1. Anesthetics: Prepare the solution of ketamine–medetomidine by mixing 1 volume of ketamine with 1 volume of medetomidine.
2. Anesthetic reversal solution: Atipamezole comes as a ready to use reagent.
3. Analgesics: Prepare the solution of buprenorphine in NaCl 0.09%.

2.2 Isolation of E14–E14.5 Mouse Femora

1. Pregnant female mice with embryos at E14–E14.5 (*see* **Note 1**).
2. Surgical instruments (Fine forceps Dumont #5 and #55, scissors, Fine Science Tools).
3. Ice-cold phosphate buffer saline solution (1× PBS).
4. 70% ethanol.
5. 24-well plate.
6. Petri dish 100 mm diameter.
7. Binocular microscope.

2.3 Renal Capsule Transplantation

1. 24-well plate.
2. Insulin micro-fine syringe (30G).
3. Wound clipper.

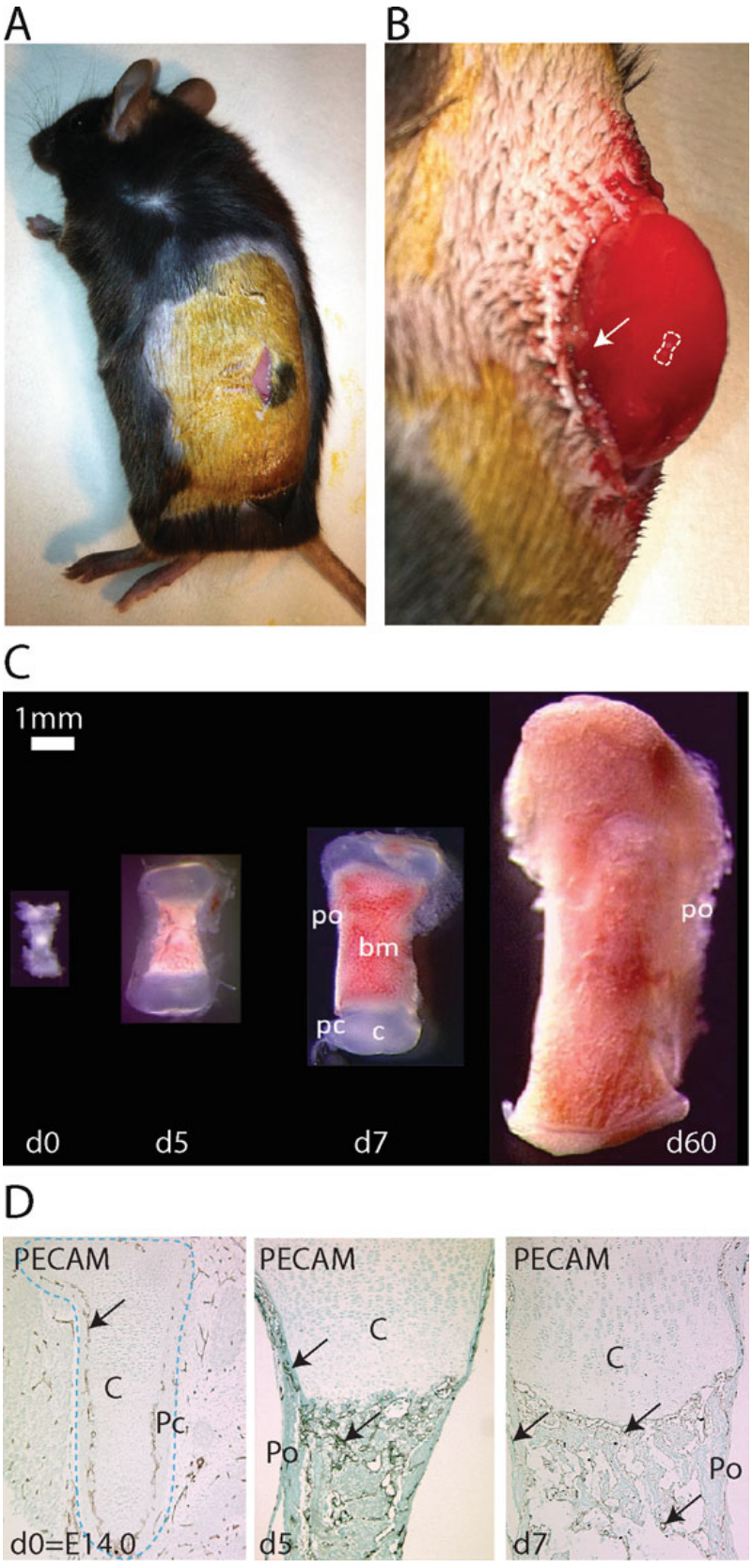

Fig. 1 Steps of the surgical procedure and development of skeletal elements in the renal capsule. (**a**) Anesthetized host mouse prior to transplantation; note the

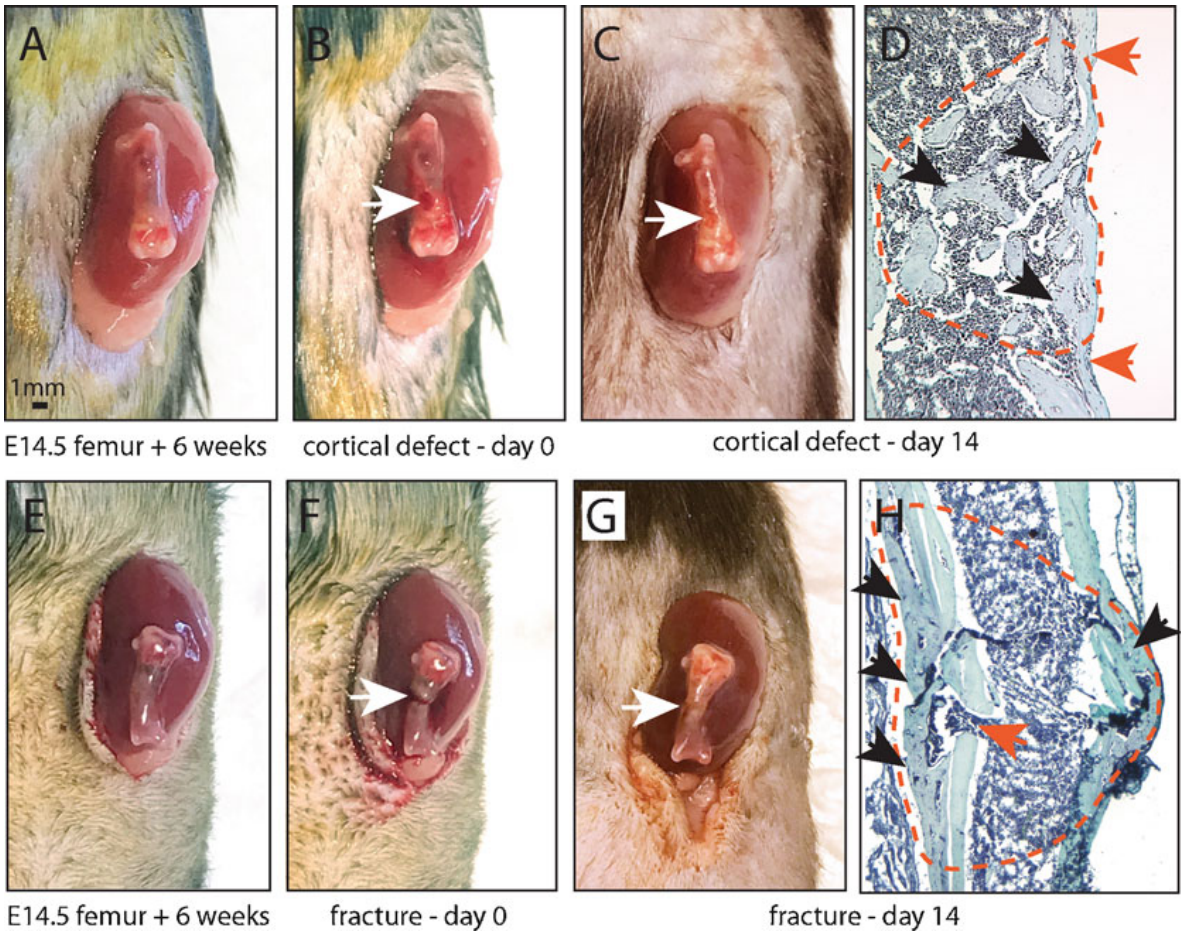

Fig. 2 Steps of the surgical procedure and repair after cortical defect or fracture in long bones grown under the renal capsule. (**a**–**d**) Steps of cortical defect repair and (**e**–**h**) steps of fracture repair. (**a**, **e**) Exteriorized kidney 6 weeks posttransplantation of an E14.5 femoral skeletal element. (**b**, **f**) Cortical defect (**b**) and bone fracture (**f**) at the time of procedure (white arrows point to the injury site). (**c**, **g**) Healing cortical defect (**c**) and bone fracture (**g**) 2 weeks after the procedure (white arrows indicate the repair site). (**d**, **h**) Longitudinal sections of cortical defect (**d**) and fracture (**h**) stained with Safranin-O showing a fully ossified callus (orange dotted line) composed of newly formed bone (black arrows)

Fig. 1 (continued) position of the skin incision. (**b**) Exteriorized kidney post-transplantation of one E14.5 femoral skeletal element (denoted by a white dotted line). The white arrow indicates the incision in the renal capsule. (**c**) Femoral skeletal elements at days 0 (d0), 5 (d5), 7 (d7), and 60 (d60) posttransplantation. By day 60, the skeletal element is fully ossified and has grown to reach almost the size of a two-month-old mouse femur (approximately 1 cm in length). (**d**) PECAM immunostaining reveals blood vessels (black arrows) on longitudinal sections of femoral skeletal elements at d0 (E14.0), d5, and d7 posttransplantation. At the time of transplantation (d0), the perichondrium (pc) is vascularized but not the cartilage (**c**). The cartilage becomes vascularized by day 5 to form the primary ossification center. The bone marrow (bm) and periosteum (po) are well developed by day 7; the epiphyseal cartilage (**c**) is not yet invaded by blood vessels to form the secondary ossification center

4. Male mice (8–12 weeks old) (*see* **Note 1**).
5. Pregnant mouse female (E14–E14.5).
6. Binocular microscope.
7. Betadine soap and Betadine solution.
8. Cotton swab.
9. 1× PBS.
10. Plastic Pasteur pipette.
11. "L"-shape glass rod (Home made): Using a fire, separate the narrow end of a glass Pasteur pipette (4–5 cm in length); make a thin "L"-shaped glass rod with a rounded closed end of approximately 1 mm in diameter.
12. Surgical instruments (Fine forceps, Fine Vanna Scissors, tweezers, hemostatic forceps, scissors) (Fine Science Tools) (*see* **Note 2**).
13. 4-0 absorbable sutures.
14. Clips and wound clipper.

2.4 Bone Fracture and Cortical Defect in the Renal Capsule

1. Wound clipper.
2. Binocular microscope.
3. Betadine soap and Betadine solution.
4. Surgical instruments (Fine forceps, Fine Vanna Scissors, tweezers, scissors) (Fine Science Tools) (*see* **Note 2**).
5. Drill with 0.8 mm drill bit.
6. 4-0 absorbable sutures.
7. Clips and wound clipper.

2.5 Analysis of Vascularization and Angiogenesis

1. Glass jar.
2. 4% paraformaldehyde (PFA) fixative solution.
3. 0.5 M ethylenediaminetetraacetic acid (EDTA) pH 7.4.
4. 70% ethanol.
5. 95% ethanol.
6. 100% ethanol.
7. Xylene.
8. Paraffin.
9. Superfrost microscope slides.
10. Histoclear.
11. 1× PBS.
12. Rotary microtome.
13. Deionized water.

14. Hydrophobic pen.
15. Hydrogen peroxidase (H_2O_2).
16. Methanol.
17. Ficin solution.
18. Glycine.
19. Ovalbumin.
20. Nonfat powdered milk.
21. Normal goat serum.
22. Rat anti-PECAM primary antibody (BD Biosciences).
23. Goat biotinylated anti-Rat secondary antibody (BD Biosciences).
24. Horseradish peroxidase (HRP)-conjugated Streptavidin (BD Biosciences).
25. Diaminobenzidine (DAB): Prepare working solution according to supplier manual (Life Technologies).
26. Fast Green.
27. Permount.
28. Cover slides.

3 Methods

3.1 Isolation of Mouse Embryonic Femora

Prepare the cartilage grafts by finely dissecting the skeletal elements of E14-E14.5 mouse embryos using 2 pairs of fine forceps (*see* **Note 3**).

1. Sacrifice pregnant mouse by cervical dislocation under anesthesia (IP injection of ketamine–medetomidine: 50 mg of ketamine and 0.5 mg of medetomidine per kg of body weight) and position the mouse in a supine posture.
2. Soak the abdomen with 70% ethanol, and make a small incision at the midline. Continue with a V-shaped incision through the skin and pull the skin toward the head to expose the abdomen.
3. Cut the peritoneum to expose the abdominal cavity.
4. Locate the 2 uterine horns, the uterus and oviduct in the dorsal region of the abdomen cavity.
5. Explant the uterus by cutting the mesometrium and the surrounding fat tissue. Place the uterus in ice-cold 1× PBS (*see* **Note 4**).
6. Discard the pregnant mouse and proceed for embryo dissection.

7. Separate each embryo by cutting between implantation sites along the uterine explant.
8. Make a small incision through the decidua tissue surrounding each embryo and with a pair of fine forceps, tear decidua apart and the embryo can be shelled out.
9. Once embryo is removed, Reichert's membrane may still be attached as well as the ectoplacental cone (*see* **Note 5**).
10. Place the embryo in a clean petri dish with clean ice-cold 1× PBS and proceed to carefully dissecting the embryo under the binocular microscope.
11. Using fine forceps, carefully separate the upper and bottom parts of the embryo body by cutting through the abdomen. Discard the upper body.
12. Carefully peel the skin to visualize the femora.
13. Use the surrounding soft tissue to hold the hindlimb with the forceps and separate the hindlimb from the hip.
14. Using a pair of fine forceps, pinch the soft tissue on both sides of the femora and the soft tissue on both sides of the tibia. Pull to separate the femora and the tibia. Discard tibia.
15. Take off the surrounding soft tissue. Keep some to be used to grasp the femoral cartilage (*see* **Note 6**).
16. Place the femoral cartilage grafts in ice-cold 1× PBS or DMEM medium in a 24-well plate on ice for no longer than 2 h for optimal development after transplantation.

3.2 Renal Capsule Transplantation

1. Weigh male (8–12 week old) mice and induce general anesthesia with an IP injection of ketamine–medetomidine (50 mg of ketamine and 0.5 mg of Medetomidine per kg of body weight).
2. Perform a subcutaneous injection of analgesics solution (0.1 mg buprenorphine in NaCl 0.09% per kg of body weight) (*see* **Note 7**).
3. With the mouse under anesthesia, shave the left flank with the electric clipper.
4. Position the mouse on its side with the left shaved flank facing up under the binocular microscope (Fig. 1).
5. Swab the shaved area center-out with Betadine soap followed by Betadine solution.
6. Locate the left kidney and make a small longitudinal incision of approximately 1–1.5 cm through the skin and the body wall (Fig. 1) (*see* **Note 8**).
7. Expose the kidney outside the body by pulling with forceps the fat located at the distal pole of the kidney and simultaneously applying a slight pressure to both sides of the incision with the

forefinger and thumb to pop the kidney out of the abdominal cavity. The exteriorized kidney will rest on the body wall. Keep the kidney moist by applying a PBS solution with a Pasteur pipette (*see* **Note 9**).

8. Prepare the graft site by making a small 2 mm hole in the renal capsule at the base of the kidney using small Vanna scissors (Fig. 1, arrow) (*see* **Note 10**).
9. Insert the "L"-shape glass rod into the hole and carefully slide it in between the capsule and the kidney parenchyma to make a small pouch for the graft (*see* **Note 11**).
10. Transfer the graft to the surface of the kidney using a pair of fine forceps (*see* **Notes 12–14**).
11. Insert the graft into the pouch by gently lifting the capsule with one pair of fine forceps and by placing the graft under the capsule with another pair of forceps. Once the graft is entirely covered with the capsule, guide it with the forceps to position it in the mid-axial part of the kidney (Fig. 1, white dotted line).
12. Reposition the kidney into the body cavity and close the body wall layer with 2 stiches using a 4-0 silk absorbable suture.
13. Align both sides of the skin incision together and close the skin with 2 or 3 clips using a wound clipper.
14. If needed, clean the skin of the mouse using a Betadine solution swab.
15. Inject the anesthetic reversal solution (0.1 mg atipamezole per kg body weight) via IP injection and place the mouse on a heating blanket set at approximately 37 °C for recovery. Monitor the mice closely until fully awake. Let the mice ambulate freely to access food and water.
16. Monitor mice daily and remove skin staples after 2 weeks (*see* **Note 15**).

3.3 Bone Fracture and Cortical Defect in the Renal Capsule

1. Six to eight weeks after transplantation of E14–E14.5 femora in the renal capsule, weight and anesthetize the host mice as described in Subheading 3.2.
2. Shave the left flank of the mice and clean the shaved area with Betadine soap then Betadine solution.
3. At the level of the left kidney, make an incision (approximately 1–1.5 cm) longitudinally within the skin and the body wall.
4. Expose the kidney with the bone transplant to make it accessible as described in Subheading 3.2 (*see* **Note 16**) (Fig. 2a, e).
5. To induce a cortical defect, drill a hole of 0.8 mm in diameter into one cortex in the diaphysis (Fig. 2b).

   To induce a bone fracture, cut the bone in the mid diaphysis with scissors (*see* **Note 17**) (Fig. 2f).

6. Reposition the kidney into the body cavity and suture the body wall using a 4-0 silk absorbable suture.
7. Close the skin incision with 2 or 3 clips using a wound clipper.
8. If needed, clean the skin of the mouse using a Betadine solution swab.
9. Inject the anesthetic reversal solution (0.1 mg atipamezole per kg body weight) via IP injection and place the mouse on a heating blanket set at approximately 37 °C for recovery. Monitor the mice closely until fully awake. Let the mice ambulate freely to access food and water.
10. Monitor mice daily and remove skin staples after 2 weeks (*see* **Note 15**).

3.4 Analysis of Vascularization and Angiogenesis

Blood vessels are visualized with anti-PECAM (CD31) immunostaining (*see* **Notes 18** and **19**).

1. Harvest renal capsule transplanted femora and fix the tissue with 4% PFA fixative solution for 24 h (*see* **Notes 20** and **21**).
2. Decalcify samples in 0.5 M EDTA for 24 h—7 days on a rocking platform shaker at 4 °C. Change EDTA solution every day (*see* **Notes 22** and **23**).
3. Dehydrate skeletal tissues by immersing tissue in graded ethanol series followed by xylene three times for 20 min each at room temperature (*see* **Note 24**).
4. Embed the tissue in paraffin at 58 °C.
5. Cut 5–7 μm thick tissue sections using a rotary microtome. Float the sections in a 56 °C water bath and mount the sections onto microscope slides.
6. Dry the slides at room temperature for 1 h and proceed with anti-PECAM immunostaining (*see* **Notes 25** and **26**).
7. Rehydrate sections by immersing the slides in Histoclear two times for 5 min each.
8. Immerse the slides in 100% ethanol two times for 5 min each.
9. Immerse the slides in 95% ethanol for 5 min.
10. Immerse the slides in 70% ethanol for 5 min.
11. Immerse the slides with deionized H_2O for 5 min.
12. Rehydrate the slides with 1× PBS for 5 min using a glass jar with lid.
13. Surround the tissue with a hydrophobic barrier using a barrier pen.
14. Block endogenous peroxidase activity with fresh 0.3% of hydrogen peroxide (H_2O_2) diluted in methanol for 45 min at room temperature (*see* **Notes 27** and **28**).

15. Proceed for enzymatic antigen retrieval step by incubating sections with ready to use Ficin solution for 5 min at room temperature (*see* **Notes 29**).
16. Wash slides three times for 5 min each in 1× PBS.
17. Block non-specific staining by incubating sections with 0.1 M glycine solution diluted in 1× PBS for 60 s at room temperature (*see* **Note 30**).
18. Wash slides three times for 5 min each in 1× PBS.
19. Block nonspecific staining by incubating sections with 5% non-fat powdered milk solution diluted in 1× PBS for 10 min at room temperature.
20. Wash slides three times for 5 min each in 1× PBS.
21. Block nonspecific staining by incubating sections with 0.1% ovalbumin solution diluted in 1× PBS for 10 min at room temperature.
22. Wash slides three times for 5 min each in 1× PBS.
23. Block nonspecific staining by incubating sections with 5% normal goat serum diluted in 1× PBS for 30 min at room temperature (*see* **Note 31**).
24. Apply rat anti-PECAM primary antibodies solution at 1:50 diluted in serum blocking solution (5% normal goat serum diluted in 1× PBS) and incubate overnight at 4 °C (*see* **Notes 32** and **33**).
25. Rinse one time with 1× PBS to drain the excess of primary antibodies.
26. Wash slides three times for 5 min each in 1× PBS.
27. Block non-specific staining by incubating sections with 5% normal goat serum diluted in 1× PBS for 30 min at room temperature (*see* **Note 31**).
28. Apply goat biotinylated anti- rat secondary antibodies solution at 1:200 diluted in serum blocking solution (5% normal goat serum diluted in 1× PBS) and incubate for 1 h at room temperature.
29. Rinse the slides once with 1× PBS to remove excess secondary antibody.
30. Wash the slides three times for 5 min each in 1× PBS.
31. Apply HRP-conjugated streptavidin solution at 1:100 diluted in serum blocking solution (5% normal goat serum diluted in 1× PBS) and incubate for 45 min at room temperature.
32. Rinse the slides once with 1× PBS to remove excess HRP-streptavidin solution.
33. Wash the slides three times for 10 min each in 1× PBS.

34. Apply DAB substrate working solution and develop for 30 s to 1 min (*see* **Notes 34–36**).
35. Rinse the slides for 2 min with ddH_2O.
36. Wash the slides three times for 5 min each in ddH_2O.
37. Proceed to counterstaining by incubating sections with 0.01% Fast Green solution diluted in deionized H_2O for 15 s at room temperature.
38. Dehydrate the sections by immersing tissue in 70% ethanol for 3 min at room temperature.
39. Immerse the slides in 95% ethanol for 3 min at room temperature.
40. Immerse the slides in 100% ethanol for 3 min at room temperature.
41. Immerse the slides in Histoclear solution for 5 min at room temperature.
42. Apply a drop of Permount and coverslip.
43. Let slides dry at room temperature.

4 Notes

1. Use donor and host mice from the same genetic background to avoid graft rejection. Host mice should be preferably male as remodeling of the graft is accelerated in female hosts.
2. All surgical instruments and reagents must be sterile to avoid any risks of infection.
3. For the transplantation of stylopods and zeugopods, E14–E14.5 embryonic stage is the ideal time point as hypertrophic cartilage is well differentiated and will efficiently attract host blood vessels, but endogenous blood vessels have not invaded the cartilage yet and will not for another 24 h. For other skeletal elements that are less advanced in their development, such as autopods, later embryonic stages may be more appropriate.
4. Avoid excessive compression on the uterine explant, which could deform and compromise the embryonic tissues.
5. Embryo can be handled by grasping the attached Reichert's membrane as well as the ectoplacental cone using fine forceps.
6. Use the soft tissue surrounding the stylopod (cartilage femoral graft) to handle the embryonic tissue. At E14–E14.5 embryonic stage, the stylopod is very soft. Excessive compression may deform and compromise the normal development under the renal capsule.

7. At least one additional injection of analgesic is performed the day following the surgery. Please refer to your institutional guidelines concerning animal care and welfare. All of our procedures received approval from the Paris Descartes University Ethical committee.
8. The kidney is retroperitoneal. It is not necessary to cut into the peritoneum. The cut through the body wall should start just above the hip level and should be long enough (1–1.5 cm) for the kidney to be "popped out" but not longer to avoid the risk of it falling back into the body cavity during the procedure (Fig. 1). Avoid cutting major vessels and nerves.
9. It is important to keep the capsule moist during the entire process; otherwise it will be easily torn.
10. The size of the incision in the capsule is determined by the size of the graft, but it should not exceed 4 mm as it may cause a loss of the graft (Fig. 1).
11. The L-shape glass should be manipulated under the capsule tangential to the surface of the kidney to avoid tearing the capsule. Great care should be taken while creating the pouch to not damage the kidney parenchyma which if damaged will bleed.
12. The skeletal elements should be transplanted with intact perichondrium to allow optimal vascularization and development. Some remaining soft tissues can be kept around the graft, as it will not interfere with bone development and growth.
13. Numerous treatments and manipulations can be applied to the graft prior to transplantation or at the time of transplantation (for example incubation in a solution of blocking antibody, or placing beads soaked in a protein solution adjacent to the graft under the kidney capsule) [16].
14. Several grafts can be transplanted in one kidney capsule depending on the length of the study (3 grafts for up to 1 week of development in the renal capsule, 2 grafts for up to 2 weeks, one graft for longer time points). Bilateral grafting is not recommended.
15. Potential adverse effects include infection, parenchyma bleeding and graft rejection. Although these effects occur very rarely, mice should be monitored daily following the transplantation.
16. Avoid pulling on bone transplant to expose the kidney.
17. These procedures are performed through the outer layer of the kidney. Make a small incision and maintain one extremity of the bone with forceps to create fracture or cortical defect. This will not affect the attachment of the bone to the kidney surface.

18. Femurs or other long bones grown under the renal capsule repair after a cortical defect or a fracture (Fig. 2c, d, g–h, respectively) following a similar regeneration process as observed in adult bone [18].
19. PECAM immunostaining can be realized on uninjured transplanted embryonic femur (Fig. 1d) or after a cortical defect or fracture (data not shown) following the same protocol.
20. The volume of fixative solution should be 50 times greater than the size of the immersed tissue to ensure a proper fixation of the tissue.
21. Avoid fixing the tissue for more than 24 h since tissue antigens may either be masked or destroyed.
22. Decalcification using chelator reagents such as EDTA works by capturing the calcium ions from the bone. EDTA acts slowly but is compatible with many immunostaining protocols.
23. The time of decalcification varies from 24 h to 7 days depending on the mineral density of the sample determined by the size of the skeletal element and the time point of harvest.
24. Paraffin is immiscible with water. Tissue must be dehydrated before adding paraffin wax.
25. Slides with paraffin-embedded sections can be stored either at room temperature or at 2–8 °C for several years in slide storage boxes. However, PECAM immunostaining should be performed within a week after sectioning for optimum results.
26. This PECAM immunostaining protocol can also be performed on cryo-embedded tissues (starting the procedure at **step 12**).
27. Some cells or tissues contain endogenous peroxidase. Using HRP conjugated antibody may result in high, non-specific background staining. Incubation with Peroxide (H_2O_2) suppresses endogenous peroxidase activity and therefore reduces background staining.
28. Hydrogen peroxide should be stored in the refrigerator and protected from sunlight in order to slow its thermal decomposition. Always use fresh H_2O_2 working solution.
29. The Ficin enzymatic antigen retrieval method serves as a proteolytic digestion to expose the antigenic sites that are covered when the tissue is fixed, making antibody-antigen binding easier during the staining procedure.
30. The non-specific staining blocking step is most often performed just prior to incubating the sample with the primary and secondary antibodies. Non-specific staining blocking solution reduces the background signal produced by non-specific interaction of primary and secondary antibodies with proteins in the tissue section.

31. Serum is required in the blocking solution to block immunoglobulin Fc receptors present on cells in the section. The serum should be of the same species as the secondary antibody.
32. Overnight incubation at 4 °C with primary antibodies allows proper and optimal specific binding of antibodies to tissue targets and reduces nonspecific background staining.
33. A negative control is critical for an accurate interpretation of the immunostaining results. A negative control could be using the incubation buffer with no primary antibody to identify non-specific staining of the secondary reagents. Additional controls can be employed to support the specificity of staining generated by the primary antibody. These include absorption controls, isotype-matched controls (for monoclonal primary antibodies), and tissue-type controls.
34. Upon reaction with HRP, DAB substrate will produce a brown colored deposit. Signal development should be monitored under microscope.
35. DAB is extremely carcinogenic. Necessary precautions should be taken (wear gloves and use only glass containers).
36. DAB is photosensitive: Keep the DAB working solution away from light and always use freshly prepared DAB working solution.

Acknowledgments

This work was supported by INSERM ATIP-AVENIR, Osteosynthesis and Trauma Care Foundation, ANR-18-CE14-0033 and NIH-NIAMS R01AR072707 grants to CC.

References

1. Vu TH, Shipley JM, Bergers G, Berger JE, Helms JA, Hanahan D, Shapiro SD, Senior RM, Werb Z (1998) MMP-9/gelatinase B is a key regulator of growth plate angiogenesis and apoptosis of hypertrophic chondrocytes. Cell 93(3):411–422
2. Gerber HP, Hillan KJ, Ryan AM, Kowalski J, Keller GA, Rangell L, Wright BD, Radtke F, Aguet M, Ferrara N (1999) VEGF is required for growth and survival in neonatal mice. Development 126(6):1149–1159
3. Gerber HP, Vu TH, Ryan AM, Kowalski J, Werb Z, Ferrara N (1999) VEGF couples hypertrophic cartilage remodeling, ossification and angiogenesis during endochondral bone formation. Nat Med 5(6):623–628
4. Gerber HP, Ferrara N (2000) Angiogenesis and bone growth. Trends Cardiovasc Med 10 (5):223–228
5. Zelzer E, Mamluk R, Ferrara N, Johnson RS, Schipani E, Olsen BR (2004) VEGFA is necessary for chondrocyte survival during bone development. Development 131 (9):2161–2171
6. Maes C, Kobayashi T, Selig MK, Torrekens S, Roth SI, Mackem S, Carmeliet G, Kronenberg HM (2010) Osteoblast precursors, but not mature osteoblasts, move into developing and fractured bones along with invading blood vessels. Dev Cell 19(2):329–344
7. Grellier M, Ferreira-Tojais N, Bourget C, Bareille R, Guillemot F, Amedee J (2009) Role of vascular endothelial growth factor in

the communication between human osteoprogenitors and endothelial cells. J Cell Biochem 106(3):390–398

8. Schipani E, Maes C, Carmeliet G, Semenza GL (2009) Regulation of osteogenesis-angiogenesis coupling by HIFs and VEGF. J Bone Miner Res 24(8):1347–1353
9. Vu TH, Alemayehu Y, Werb Z (2003) New insights into saccular development and vascular formation in lung allografts under the renal capsule. Mech Dev 120(3):305–313
10. Wiesen JF, Young P, Werb Z, Cunha GR (1999) Signaling through the stromal epidermal growth factor receptor is necessary for mammary ductal development. Development 126(2):335–344
11. Wang Y, Revelo MP, Sudilovsky D, Cao M, Chen WG, Goetz L, Xue H, Sadar M, Shappell SB, Cunha GR, Hayward SW (2005) Development and characterization of efficient xenograft models for benign and malignant human prostate tissue. Prostate 64(2):149–159
12. Szot GL, Koudria P, Bluestone JA (2007) Transplantation of pancreatic islets into the kidney capsule of diabetic mice. J Vis Exp 9:404
13. Chan CK, Seo EY, Chen JY, Lo D, McArdle A, Sinha R, Tevlin R, Seita J, Vincent-Tompkins J, Wearda T, Lu WJ, Senarath-Yapa K, Chung MT, Marecic O, Tran M, Yan KS, Upton R, Walmsley GG, Lee AS, Sahoo D, Kuo CJ, Weissman IL, Longaker MT (2015) Identification and specification of the mouse skeletal stem cell. Cell 160(1-2):285–298
14. Colnot C, Lu C, Hu D, Helms JA (2004) Distinguishing the contributions of the perichondrium, cartilage, and vascular endothelium to skeletal development. Dev Biol 269 (1):55–69
15. Colnot C (2005) Cellular and molecular interactions regulating skeletogenesis. J Cell Biochem 95(4):688–697
16. Colnot C, de la Fuente L, Huang S, Hu D, Lu C, St-Jacques B, Helms JA (2005) Indian hedgehog synchronizes skeletal angiogenesis and perichondrial maturation with cartilage development. Development 132 (5):1057–1067
17. Chan CKF, Gulati GS, Sinha R, Tompkins JV, Lopez M et al (2018) Identification of the human skeletal stem cell. Cell 175(1):43–56. e21
18. Duchamp de Lageneste O, Julien A, Abou-Khalil R, Frangi G, Carvalho C, Cagnard N, Cordier C, Conway SJ, Colnot C (2018) Periosteum contains skeletal stem cells with high bone regenerative potential controlled by Periostin. Nat Commun 9(1):773

References

1. Clarke, B. Normal Bone Anatomy and Physiology. *CJASN* **3**, S131–S139 (2008).
2. Marieb, E. N. *Human Anatomy & Physiology (7th Edition).* vols 2006-01–14 (2006).
3. Gordon Betts, J. *et al. Anatomy and Physiology*. (OpenStax, 2013).
4. Comazzetto, S., Shen, B. & Morrison, S. J. Niches that regulate stem cells and hematopoiesis in adult bone marrow. *Developmental Cell* **56**, 1848–1860 (2021).
5. Lucas, D. Structural organization of the bone marrow and its role in hematopoiesis. *Current Opinion in Hematology* **28**, 36–42 (2021).
6. Lin, X., Patil, S., Gao, Y.-G. & Qian, A. The Bone Extracellular Matrix in Bone Formation and Regeneration. *Front. Pharmacol.* **11**, 757 (2020).
7. Ansari, N. & Sims, N. A. The Cells of Bone and Their Interactions. in *Bone Regulators and Osteoporosis Therapy* (ed. Stern, P. H.) vol. 262 1–25 (Springer International Publishing, 2019).
8. Saito, M. & Marumo, K. Effects of Collagen Crosslinking on Bone Material Properties in Health and Disease. *Calcif Tissue Int* **97**, 242–261 (2015).
9. Garnero, P. The Role of Collagen Organization on the Properties of Bone. *Calcif Tissue Int* **97**, 229–240 (2015).
10. Moorehead, C., Prudnikova, K. & Marcolongo, M. The regulatory effects of proteoglycans on collagen fibrillogenesis and morphology investigated using biomimetic proteoglycans. *Journal of Structural Biology* **206**, 204–215 (2019).
11. Kalamajski, S., Aspberg, A., Lindblom, K., Heinegård, D. & Oldberg, Å. Asporin competes with decorin for collagen binding, binds calcium and promotes osteoblast collagen mineralization. *Biochemical Journal* **423**, 53–59 (2009).
12. Rosset, E. M. & Bradshaw, A. D. SPARC/osteonectin in mineralized tissue. *Matrix Biology* **52–54**, 78–87 (2016).
13. Delany, A. M. *et al.* Osteopenia and decreased bone formation in osteonectin-deficient mice. *J. Clin. Invest.* **105**, 915–923 (2000).
14. Delany, A. M. & Hankenson, K. D. Thrombospondin-2 and SPARC/osteonectin are critical regulators of bone remodeling. *J. Cell Commun. Signal.* **3**, 227–238 (2009).
15. Singh, A., Gill, G., Kaur, H., Amhmed, M. & Jakhu, H. Role of osteopontin in bone remodeling and orthodontic tooth movement: a review. *Prog Orthod.* **19**, 18 (2018).
16. Marinovich, R. *et al.* The role of bone sialoprotein in the tendon–bone insertion. *Matrix Biology* **52–54**, 325–338 (2016).
17. Mizokami, A., Kawakubo-Yasukochi, T. & Hirata, M. Osteocalcin and its endocrine functions. *Biochemical Pharmacology* **132**, 1–8 (2017).
18. Ramesh, N., Moratti, S. C. & Dias, G. J. Hydroxyapatite-polymer biocomposites for bone regeneration: A review of current trends: HYDROXYAPATITE/POLYMER BIOCOMPOSITES FOR BONE REGENERATION: A REVIEW. *J. Biomed. Mater. Res.* **106**, 2046–2057 (2018).
19. Tavafoghi, M. & Cerruti, M. The role of amino acids in hydroxyapatite mineralization. *J. R. Soc. Interface.* **13**, 20160462 (2016).
20. Stilwell, D. L. & Gray, D. J. The microscopic structure of periosteum in areas of tendinous contact. *Anat. Rec.* **120**, 663–677 (1954).
21. Benjamin, M. *et al.* Where tendons and ligaments meet bone: attachment sites ('entheses') in relation to exercise and/or mechanical load. *J Anatomy* **208**, 471–490 (2006).
22. Cohn, S. A. A re-examination of Sharpey's fibres in alveolar bone of the mouse. *Archives of Oral Biology* **17**, 255-IN4 (1972).
23. Jones, S. J. & Boyde, A. The organization and gross mineralization patterns of the collagen fibres in sharpey fibre bone. *Cell Tissue Res.* **148**, (1974).
24. Nahian, A. & Chauhan, P. R. Histology, Periosteum And Endosteum. in *StatPearls* (StatPearls Publishing, 2022).
25. Squier, C. A., Ghoneim, S. & Kremenak, C. R. Ultrastructure of the periosteum from membrane bone. *J Anat* **171**, 233–239 (1990).
26. Dwek, J. R. The periosteum: what is it, where is it, and what mimics it in its absence? *Skeletal Radiol* **39**, 319–323 (2010).
27. Duchamp de Lageneste, O. *et al.* Periosteum contains skeletal stem cells with high bone regenerative potential controlled by Periostin. *Nat Commun* **9**, 773 (2018).
28. Debnath, S. *et al.* Discovery of a periosteal stem cell mediating intramembranous bone formation. *Nature* **562**, 133–139 (2018).
29. Chanavaz, M. Anatomy and histophysiology of the periosteum: quantification of the periosteal blood supply to the adjacent bone with 85Sr and gamma spectrometry. *J Oral Implantol* **21**, 214–219

(1995).
30. Simpson, A. H. R. W. The blood supply of the periosteum: *Plastic and Reconstructive Surgery* **78**, 548 (1986).
31. Grüneboom, A. *et al.* A network of trans-cortical capillaries as mainstay for blood circulation in long bones. *Nat Metab* **1**, 236–250 (2019).
32. Ritchlin, C. & Adamopoulos, I. E. Go with the flow—hidden vascular passages in bone. *Nat Metab* **1**, 173–174 (2019).
33. Chartier, S. R., Mitchell, S. A. T., Majuta, L. A. & Mantyh, P. W. The Changing Sensory and Sympathetic Innervation of the Young, Adult and Aging Mouse Femur. *Neuroscience* **387**, 178–190 (2018).
34. Lorenz, M. R., Brazill, J. M., Beeve, A. T., Shen, I. & Scheller, E. L. A Neuroskeletal Atlas: Spatial Mapping and Contextualization of Axon Subtypes Innervating the Long Bones of C3H and B6 Mice. *J Bone Miner Res* **36**, 1012–1025 (2021).
35. Alexander, K. A. *et al.* Resting and injury-induced inflamed periosteum contain multiple macrophage subsets that are located at sites of bone growth and regeneration. *Immunol Cell Biol* **95**, 7–16 (2017).
36. Xie, M. *et al.* Schwann cell precursors contribute to skeletal formation during embryonic development in mice and zebrafish. *Proc. Natl. Acad. Sci. U.S.A.* **116**, 15068–15073 (2019).
37. Kawane, T. *et al.* Dlx5 and Mef2 Regulate a Novel Runx2 Enhancer for Osteoblast-Specific Expression: OSTEOBLAST-SPECIFIC ENHANCER OF RUNX2. *J Bone Miner Res* **29**, 1960–1969 (2014).
38. Baek, W.-Y., Kim, Y.-J., de Crombrugghe, B. & Kim, J.-E. Osterix is required for cranial neural crest-derived craniofacial bone formation. *Biochemical and Biophysical Research Communications* **432**, 188–192 (2013).
39. Franz-Odendaal, T., A. Induction and patterning of intramembranous bone. *Front Biosci* **16**, 2734 (2011).
40. Yuan, Y. & Chai, Y. Regulatory mechanisms of jaw bone and tooth development. in *Current Topics in Developmental Biology* vol. 133 91–118 (Elsevier, 2019).
41. Bi, W., Deng, J. M., Zhang, Z., Behringer, R. R. & de Crombrugghe, B. Sox9 is required for cartilage formation. *Nat Genet* **22**, 85–89 (1999).
42. Akiyama, H., Chaboissier, M.-C., Martin, J. F., Schedl, A. & de Crombrugghe, B. The transcription factor Sox9 has essential roles in successive steps of the chondrocyte differentiation pathway and is required for expression of *Sox5* and *Sox6*. *Genes Dev.* **16**, 2813–2828 (2002).
43. Duan, X. *et al.* Vegfa regulates perichondrial vascularity and osteoblast differentiation in bone development. *Development* **142**, 1984–1991 (2015).
44. Tomlinson, R. E., Christiansen, B. A., Giannone, A. A. & Genetos, D. C. The Role of Nerves in Skeletal Development, Adaptation, and Aging. *Front. Endocrinol.* **11**, 646 (2020).
45. Heffner, M. A., Anderson, M. J., Yeh, G. C., Genetos, D. C. & Christiansen, B. A. Altered bone development in a mouse model of peripheral sensory nerve inactivation. *J Musculoskelet Neuronal Interact* **14**, 1–9 (2014).
46. Tomlinson, R. E. *et al.* NGF-TrkA Signaling by Sensory Nerves Coordinates the Vascularization and Ossification of Developing Endochondral Bone. *Cell Reports* **16**, 2723–2735 (2016).
47. Mizoguchi, T. & Ono, N. The diverse origin of bone-forming osteoblasts. *J Bone Miner Res* **36**, 1432–1447 (2021).
48. Colnot, C., Lu, C., Hu, D. & Helms, J. A. Distinguishing the contributions of the perichondrium, cartilage, and vascular endothelium to skeletal development. *Dev Biol* **269**, 55–69 (2004).
49. Kronenberg, H. M. The Role of the Perichondrium in Fetal Bone Development. *Annals of the New York Academy of Sciences* **1116**, 59–64 (2007).
50. Maes, C. *et al.* Osteoblast Precursors, but Not Mature Osteoblasts, Move into Developing and Fractured Bones along with Invading Blood Vessels. *Developmental Cell* **19**, 329–344 (2010).
51. Mizoguchi, T. *et al.* Osterix Marks Distinct Waves of Primitive and Definitive Stromal Progenitors during Bone Marrow Development. *Developmental Cell* **29**, 340–349 (2014).
52. Ono, N. *et al.* Vasculature-Associated Cells Expressing Nestin in Developing Bones Encompass Early Cells in the Osteoblast and Endothelial Lineage. *Developmental Cell* **29**, 330–339 (2014).
53. Shapiro, I. M., Adams, C. S., Freeman, T. & Srinivas, V. Fate of the hypertrophic chondrocyte: Microenvironmental perspectives on apoptosis and survival in the epiphyseal growth plate. *Birth Defect Res C* **75**, 330–339 (2005).
54. Adams, C. S. & Shapiro, I. M. The fate of the terminally differentiated chondrocyte: evidence

for microenvironmental regulation of chondrocyte apoptosis. *Critical Reviews in Oral Biology & Medicine* **13**, 465–473 (2002).
55. Yang, L., Tsang, K. Y., Tang, H. C., Chan, D. & Cheah, K. S. E. Hypertrophic chondrocytes can become osteoblasts and osteocytes in endochondral bone formation. *Proc. Natl. Acad. Sci. U.S.A.* **111**, 12097–12102 (2014).
56. Zhou, X. *et al.* Chondrocytes Transdifferentiate into Osteoblasts in Endochondral Bone during Development, Postnatal Growth and Fracture Healing in Mice. *PLoS Genet* **10**, e1004820 (2014).
57. Aghajanian, P. & Mohan, S. The art of building bone: emerging role of chondrocyte-to-osteoblast transdifferentiation in endochondral ossification. *Bone Res* **6**, 19 (2018).
58. Wolff, L. I. & Hartmann, C. A Second Career for Chondrocytes—Transformation into Osteoblasts. *Curr Osteoporos Rep* **17**, 129–137 (2019).
59. Ono, N., Ono, W., Nagasawa, T. & Kronenberg, H. M. A subset of chondrogenic cells provides early mesenchymal progenitors in growing bones. *Nat Cell Biol* **16**, 1157–1167 (2014).
60. Newton, P. T. *et al.* A radical switch in clonality reveals a stem cell niche in the epiphyseal growth plate. *Nature* **567**, 234–238 (2019).
61. Blumer, M. J. F. Bone tissue and histological and molecular events during development of the long bones. *Annals of Anatomy - Anatomischer Anzeiger* **235**, 151704 (2021).
62. Hallett, S. A., Ono, W. & Ono, N. Growth Plate Chondrocytes: Skeletal Development, Growth and Beyond. *IJMS* **20**, 6009 (2019).
63. Mizuhashi, K. *et al.* Resting zone of the growth plate houses a unique class of skeletal stem cells. *Nature* **563**, 254–258 (2018).
64. Muruganandan, S. *et al.* A FoxA2+ long-term stem cell population is necessary for growth plate cartilage regeneration after injury. *Nat Commun* **13**, 2515 (2022).
65. Mizuhashi, K., Nagata, M., Matsushita, Y., Ono, W. & Ono, N. Growth Plate Borderline Chondrocytes Behave as Transient Mesenchymal Precursor Cells. *J Bone Miner Res* **34**, 1387–1392 (2019).
66. Mackie, E. J. Growth Plate Borderline Chondrocytes: A New Source of Metaphyseal Mesenchymal Precursors. *J Bone Miner Res* **34**, 1385–1386 (2019).
67. Kenkre, J. & Bassett, J. The bone remodelling cycle. *Ann Clin Biochem* **55**, 308–327 (2018).
68. Raggatt, L. J. & Partridge, N. C. Cellular and Molecular Mechanisms of Bone Remodeling. *Journal of Biological Chemistry* **285**, 25103–25108 (2010).
69. Tatsumi, S. *et al.* Targeted Ablation of Osteocytes Induces Osteoporosis with Defective Mechanotransduction. *Cell Metabolism* **5**, 464–475 (2007).
70. Nakashima, T. *et al.* Evidence for osteocyte regulation of bone homeostasis through RANKL expression. *Nat Med* **17**, 1231–1234 (2011).
71. Xiong, J. *et al.* Matrix-embedded cells control osteoclast formation. *Nat Med* **17**, 1235–1241 (2011).
72. Swarthout, J. T., D'Alonzo, R. C., Selvamurugan, N. & Partridge, N. C. Parathyroid hormone-dependent signaling pathways regulating genes in bone cells. *Gene* **282**, 1–17 (2002).
73. Wein, M. N. & Kronenberg, H. M. Regulation of Bone Remodeling by Parathyroid Hormone. *Cold Spring Harb Perspect Med* **8**, a031237 (2018).
74. Delaissé, J.-M. *et al.* Matrix metalloproteinases (MMP) and cathepsin K contribute differently to osteoclastic activities: MMPS and Cathepsin in Osteoclastic Activity. *Microsc. Res. Tech.* **61**, 504–513 (2003).
75. Burgess, T. L. *et al.* The Ligand for Osteoprotegerin (OPGL) Directly Activates Mature Osteoclasts. *Journal of Cell Biology* **145**, 527–538 (1999).
76. McHugh, K. P. *et al.* Mice lacking β3 integrins are osteosclerotic because of dysfunctional osteoclasts. *J. Clin. Invest.* **105**, 433–440 (2000).
77. Delaisse, J.-M. The reversal phase of the bone-remodeling cycle: cellular prerequisites for coupling resorption and formation. *BoneKEy Reports* **3**, (2014).
78. Everts, V. *et al.* The Bone Lining Cell: Its Role in Cleaning Howship's Lacunae and Initiating Bone Formation. *J Bone Miner Res* **17**, 77–90 (2002).
79. Manolagas, S. C. Sex Steroids and Bone. *Recent Progress in Hormone Research* **57**, 385–409 (2002).
80. Boyce, B. F. & Xing, L. Biology of RANK, RANKL, and osteoprotegerin. *Arthritis Res Ther* **9**, S1 (2007).
81. Baron, R. & Kneissel, M. WNT signaling in bone homeostasis and disease: from human mutations to treatments. *Nat Med* **19**, 179–192 (2013).
82. Lips, P. & van Schoor, N. M. The effect of vitamin D on bone and osteoporosis. *Best Practice & Research Clinical Endocrinology & Metabolism* **25**, 585–591 (2011).

83. Sözen, T., Özışık, L. & Başaran, N. Ç. An overview and management of osteoporosis. *Eur J Rheumatol* **4**, 46–56 (2017).
84. Coughlan, T. & Dockery, F. Osteoporosis and fracture risk in older people. *Clin Med* **14**, 187–191 (2014).
85. Bahney, C. S. *et al.* Cellular biology of fracture healing. *J Orthop Res* **37**, 35–50 (2019).
86. Kolar, P. *et al.* The Early Fracture Hematoma and Its Potential Role in Fracture Healing. *Tissue Engineering Part B: Reviews* **16**, 427–434 (2010).
87. Schell, H. *et al.* The haematoma and its role in bone healing. *J EXP ORTOP* **4**, 5 (2017).
88. Ishikawa, M. *et al.* MCP/CCR2 Signaling Is Essential for Recruitment of Mesenchymal Progenitor Cells during the Early Phase of Fracture Healing. *PLoS ONE* **9**, e104954 (2014).
89. Xing, Z. *et al.* Multiple roles for CCR2 during fracture healing. *Disease Models & Mechanisms* **3**, 451–458 (2010).
90. Kovtun, A. *et al.* The crucial role of neutrophil granulocytes in bone fracture healing. *eCM* **32**, 152–162 (2016).
91. Wallace, A., Cooney, T. E., Englund, R. & Lubahn, J. D. Effects of Interleukin-6 Ablation on Fracture Healing in Mice. *J. Orthop. Res.* **29**, 1437–1442 (2011).
92. Lange, J. *et al.* Action of IL-1β during fracture healing: ACTION OF IL-1β DURING FRACTURE HEALING. *J. Orthop. Res.* **28**, 778–784 (2010).
93. Gerstenfeld, L. *et al.* Impaired Fracture Healing in the Absence of TNF-α Signaling: The Role of TNF-α in Endochondral Cartilage Resorption. *J Bone Miner Res* **18**, 1584–1592 (2003).
94. Yang, X. *et al.* Callus mineralization and maturation are delayed during fracture healing in interleukin-6 knockout mice. *Bone* **41**, 928–936 (2007).
95. Prystaz, K. *et al.* Distinct Effects of IL-6 Classic and Trans -Signaling in Bone Fracture Healing. *The American Journal of Pathology* **188**, 474–490 (2018).
96. Silfverswärd, C. *et al.* Bone formation in interleukin-4 and interleukin-13 depleted mice. *Acta Orthopaedica* **79**, 410–420 (2008).
97. Zhu, L., Zhao, Q., Yang, T., Ding, W. & Zhao, Y. Cellular Metabolism and Macrophage Functional Polarization. *International Reviews of Immunology* **34**, 82–100 (2015).
98. Bosurgi, L. *et al.* Macrophage function in tissue repair and remodeling requires IL-4 or IL-13 with apoptotic cells. *Science* **356**, 1072–1076 (2017).
99. Junttila, I. S. Tuning the Cytokine Responses: An Update on Interleukin (IL)-4 and IL-13 Receptor Complexes. *Front. Immunol.* **9**, 888 (2018).
100. Hebb, J. H. *et al.* Bone healing in an aged murine fracture model is characterized by sustained callus inflammation and decreased cell proliferation: FRACTURE HEALING IN AGED MICE. *J. Orthop. Res.* (2017) doi:10.1002/jor.23652.
101. Loi, F. *et al.* Inflammation, fracture and bone repair. *Bone* **86**, 119–130 (2016).
102. Claes, L., Recknagel, S. & Ignatius, A. Fracture healing under healthy and inflammatory conditions. *Nat Rev Rheumatol* **8**, 133–143 (2012).
103. Pirraco, R. P., Reis, R. L. & Marques, A. P. Effect of monocytes/macrophages on the early osteogenic differentiation of hBMSCs: Effect of monocytes/macrophages on the early osteogenic differentiation of hBMSCs. *J Tissue Eng Regen Med* **7**, 392–400 (2013).
104. Champagne, C. M., Takebe, J., Offenbacher, S. & Cooper, L. F. Macrophage cell lines produce osteoinductive signals that include bone morphogenetic protein-2. *Bone* **30**, 26–31 (2002).
105. Kitaori, T. *et al.* Stromal cell-derived factor 1/CXCR4 signaling is critical for the recruitment of mesenchymal stem cells to the fracture site during skeletal repair in a mouse model. *Arthritis Rheum* **60**, 813–823 (2009).
106. Xu, J. *et al.* NGF-p75 signaling coordinates skeletal cell migration during bone repair. *Sci Adv* **8**, eabl5716 (2022).
107. Gao, B. *et al.* Macrophage-lineage TRAP+ cells recruit periosteum-derived cells for periosteal osteogenesis and regeneration. *Journal of Clinical Investigation* **129**, 2578–2594 (2019).
108. Majidinia, M., Sadeghpour, A. & Yousefi, B. The roles of signaling pathways in bone repair and regeneration. *J Cell Physiol* **233**, 2937–2948 (2018).
109. Fei, Y., Gronowicz, G. & M. Hurley, M. Fibroblast Growth Factor-2, Bone Homeostasis and Fracture Repair. *CPD* **19**, 3354–3363 (2013).
110. Tsuji, K. *et al.* BMP2 activity, although dispensable for bone formation, is required for the initiation of fracture healing. *Nat Genet* **38**, 1424–1429 (2006).
111. Colnot, C. Skeletal Cell Fate Decisions Within Periosteum and Bone Marrow During Bone Regeneration. *Journal of Bone and Mineral Research* **24**, 274–282 (2009).
112. Julien, A. *et al.* Direct contribution of skeletal muscle mesenchymal progenitors to bone repair. *Nature Communications* **12**, 2860 (2021).

113. Matsushita, Y. *et al.* A Wnt-mediated transformation of the bone marrow stromal cell identity orchestrates skeletal regeneration. *Nat Commun* **11**, 332 (2020).
114. Matthews, B. G. *et al.* Heterogeneity of murine periosteum progenitors involved in fracture healing. *eLife* **10**, e58534 (2021).
115. Colnot, C., Thompson, Z., Miclau, T., Werb, Z. & Helms, J. A. Altered fracture repair in the absence of MMP9. *Development* **130**, 4123–4133 (2003).
116. Behonick, D. J. *et al.* Role of Matrix Metalloproteinase 13 in Both Endochondral and Intramembranous Ossification during Skeletal Regeneration. *PLoS ONE* **2**, e1150 (2007).
117. Ota, N. *et al.* Accelerated Cartilage Resorption by Chondroclasts during Bone Fracture Healing in Osteoprotegerin-Deficient Mice. *Endocrinology* **150**, 4823–4834 (2009).
118. Bando, Y. *et al.* Origin and development of septoclasts in endochondral ossification of mice. *Histochem Cell Biol* **149**, 645–654 (2018).
119. Sivaraj, K. K. *et al.* Mesenchymal stromal cell-derived septoclasts resorb cartilage during developmental ossification and fracture healing. *Nat Commun* **13**, 571 (2022).
120. Scammell, B. E. & Roach, H. I. A new role for the chondrocyte in fracture repair: Endochondral ossification includes direct bone formation by former chondrocytes. *J Bone Miner Res* **11**, 737–745 (2009).
121. Hu, D. P. *et al.* Cartilage to bone transformation during fracture healing is coordinated by the invading vasculature and induction of the core pluripotency genes. *Development* **144**, 221–234 (2017).
122. Schindeler, A., McDonald, M. M., Bokko, P. & Little, D. G. Bone remodeling during fracture repair: The cellular picture. *Seminars in Cell & Developmental Biology* **19**, 459–466 (2008).
123. Stefańska, K. *et al.* Mesenchymal stem cells – a historical overview. *Medical Journal of Cell Biology* **8**, 83–87 (2020).
124. Caplan, A. I. Mesenchymal stem cells. *J. Orthop. Res.* **9**, 641–650 (1991).
125. Dominici, M. *et al.* Minimal criteria for defining multipotent mesenchymal stromal cells. The International Society for Cellular Therapy position statement. *Cytotherapy* **8**, 315–317 (2006).
126. Bianco, P., Robey, P. G. & Simmons, P. J. Mesenchymal Stem Cells: Revisiting History, Concepts, and Assays. *Cell Stem Cell* **2**, 313–319 (2008).
127. Viswanathan, S. *et al.* Mesenchymal stem versus stromal cells: International Society for Cell & Gene Therapy (ISCT®) Mesenchymal Stromal Cell committee position statement on nomenclature. *Cytotherapy* **21**, 1019–1024 (2019).
128. Caplan, A. I. Mesenchymal Stem Cells: Time to Change the Name! *Stem Cells Translational Medicine* **6**, 1445–1451 (2017).
129. Kolios, G. & Moodley, Y. Introduction to Stem Cells and Regenerative Medicine. *Respiration* **85**, 3–10 (2013).
130. Buechler, M. B. *et al.* Cross-tissue organization of the fibroblast lineage. *Nature* **593**, 575–579 (2021).
131. Baccin, C. *et al.* Combined single-cell and spatial transcriptomics reveal the molecular, cellular and spatial bone marrow niche organization. *Nat Cell Biol* **22**, 38–48 (2020).
132. Dolgalev, I. & Tikhonova, A. N. Connecting the Dots: Resolving the Bone Marrow Niche Heterogeneity. *Front Cell Dev Biol* **9**, 622519 (2021).
133. Tikhonova, A. N., Lasry, A., Austin, R. & Aifantis, I. Cell-by-Cell Deconstruction of Stem Cell Niches. *Cell Stem Cell* **27**, 19–34 (2020).
134. Muhl, L. *et al.* Single-cell analysis uncovers fibroblast heterogeneity and criteria for fibroblast and mural cell identification and discrimination. *Nat Commun* **11**, 3953 (2020).
135. Chan, C. K. F. *et al.* Identification and Specification of the Mouse Skeletal Stem Cell. *Cell* **160**, 285–298 (2015).
136. Chan, C. K. F. *et al.* Identification of the Human Skeletal Stem Cell. *Cell* **175**, 43-56.e21 (2018).
137. Ono, N., Balani, D. H. & Kronenberg, H. M. Stem and progenitor cells in skeletal development. in *Current Topics in Developmental Biology* vol. 133 1–24 (Elsevier, 2019).
138. Kumagai, K., Vasanji, A., Drazba, J. A., Butler, R. S. & Muschler, G. F. Circulating cells with osteogenic potential are physiologically mobilized into the fracture healing site in the parabiotic mice model: OSTEOGENIC CTPs MOBILIZED TO FRACTURE SITE. *J. Orthop. Res.* **26**, 165–175 (2008).
139. Greenbaum, A. *et al.* CXCL12 in early mesenchymal progenitors is required for haematopoietic stem-cell maintenance. *Nature* **495**, 227–230 (2013).
140. Méndez-Ferrer, S. *et al.* Mesenchymal and haematopoietic stem cells form a unique bone marrow niche. *Nature* **466**, 829–834 (2010).
141. Worthley, D. L. *et al.* Gremlin 1 identifies a skeletal stem cell with bone, cartilage, and reticular stromal potential. *Cell* **160**, 269–284 (2015).

142. Park, D. *et al.* Endogenous Bone Marrow MSCs Are Dynamic, Fate-Restricted Participants in Bone Maintenance and Regeneration. *Cell Stem Cell* **10**, 259–272 (2012).
143. Zhou, B. O., Yue, R., Murphy, M. M., Peyer, J. G. & Morrison, S. J. Leptin-receptor-expressing mesenchymal stromal cells represent the main source of bone formed by adult bone marrow. *Cell Stem Cell* **15**, 154–168 (2014).
144. Tikhonova, A. N. *et al.* The bone marrow microenvironment at single-cell resolution. *Nature* **569**, 222–228 (2019).
145. Zhong, L. *et al.* Single cell transcriptomics identifies a unique adipose lineage cell population that regulates bone marrow environment. *Elife* **9**, e54695 (2020).
146. Baryawno, N. *et al.* A Cellular Taxonomy of the Bone Marrow Stroma in Homeostasis and Leukemia. *Cell* **177**, 1915-1932.e16 (2019).
147. Shen, B. *et al.* A mechanosensitive peri-arteriolar niche for osteogenesis and lymphopoiesis. *Nature* **591**, 438–444 (2021).
148. Shu, H. S. *et al.* Tracing the skeletal progenitor transition during postnatal bone formation. *Cell Stem Cell* **28**, 2122-2136.e3 (2021).
149. Caplan, A. I. & Correa, D. The MSC: an injury drugstore. *Cell Stem Cell* **9**, 11–15 (2011).
150. Caplan, A. I. & Dennis, J. E. Mesenchymal stem cells as trophic mediators. *J. Cell. Biochem.* **98**, 1076–1084 (2006).
151. Chen, L., Tredget, E. E., Wu, P. Y. G. & Wu, Y. Paracrine factors of mesenchymal stem cells recruit macrophages and endothelial lineage cells and enhance wound healing. *PLoS One* **3**, e1886 (2008).
152. Jones, B. J. & McTaggart, S. J. Immunosuppression by mesenchymal stromal cells: From culture to clinic. *Experimental Hematology* **36**, 733–741 (2008).
153. Gao, X. *et al.* Role of donor and host cells in muscle-derived stem cell-mediated bone repair: differentiation *vs.* paracrine effects. *FASEB j.* **28**, 3792–3809 (2014).
154. Kellum, E. *et al.* Myostatin (GDF-8) deficiency increases fracture callus size, Sox-5 expression, and callus bone volume. *Bone* **44**, 17–23 (2009).
155. Abou-Khalil, R. *et al.* Role of Muscle Stem Cells During Skeletal Regeneration. *Stem Cells* **33**, 1501–1511 (2015).
156. Blecher, R. *et al.* The Proprioceptive System Regulates Morphologic Restoration of Fractured Bones. *Cell Reports* **20**, 1775–1783 (2017).
157. Rot, C., Stern, T., Blecher, R., Friesem, B. & Zelzer, E. A Mechanical Jack-like Mechanism Drives Spontaneous Fracture Healing in Neonatal Mice. *Developmental Cell* **31**, 159–170 (2014).
158. Asakura, A., Rudnicki, M. A. & Komaki, M. Muscle satellite cells are multipotential stem cells that exhibit myogenic, osteogenic, and adipogenic differentiation. *Differentiation* **68**, 245–253 (2001).
159. Sondag, G. R. *et al.* Osteoactivin Induces Transdifferentiation of C2C12 Myoblasts Into Osteoblasts: OSTEOACTIVIN INDUCES TRANSDIFFERENTIATION. *J. Cell. Physiol* **229**, 955–966 (2014).
160. Meyers, C. *et al.* Heterotopic Ossification: A Comprehensive Review. *JBMR Plus* **3**, (2019).
161. Nelson, E. R., Wong, V. W., Krebsbach, P. H., Wang, S. C. & Levi, B. Heterotopic Ossification Following Burn Injury: The Role of Stem Cells. *Journal of Burn Care & Research* **33**, 463–470 (2012).
162. Watson, A. Observations on the Formation of Bone by the Periosteum. *Edinb Med Surg J* **63**, 302–307 (1845).
163. Garcia, P. *et al.* Development of a Reliable Non-Union Model in Mice. *Journal of Surgical Research* **147**, 84–91 (2008).
164. Wu, X.-Q., Wang, D., Liu, Y. & Zhou, J.-L. Development of a tibial experimental non-union model in rats. *J Orthop Surg Res* **16**, 261 (2021).
165. Sharun, K. *et al.* Development of a novel atrophic non-union model in rabbits: A preliminary study. *Annals of Medicine and Surgery* **68**, 102558 (2021).
166. Gröngröft, I. *et al.* Development of a novel murine delayed secondary fracture healing in vivo model using periosteal cauterization. *Arch Orthop Trauma Surg* **139**, 1743–1753 (2019).
167. Kuwahara, S. T. *et al.* Sox9+ messenger cells orchestrate large-scale skeletal regeneration in the mammalian rib. *eLife* **8**, e40715 (2019).
168. Roberts, S. J., van Gastel, N., Carmeliet, G. & Luyten, F. P. Uncovering the periosteum for skeletal regeneration: the stem cell that lies beneath. *Bone* **70**, 10–18 (2015).
169. van Gastel, N. *et al.* Engineering vascularized bone: osteogenic and proangiogenic potential of murine periosteal cells. *Stem Cells* **30**, 2460–2471 (2012).
170. Perrin, S., Julien, A., Duchamp de Lageneste, O., Abou-Khalil, R. & Colnot, C. Mouse Periosteal Cell Culture, in vitro Differentiation, and in vivo Transplantation in Tibial Fractures. *BIO-PROTOCOL* **11**, (2021).

171. Declercq, H. A., De Ridder, L. I. & Cornelissen, M. J. Isolation and Osteogenic Differentiation of Rat Periosteum-derived Cells. *Cytotechnology* **49**, 39–50 (2005).
172. Wang, Q., Huang, C., Zeng, F., Xue, M. & Zhang, X. Activation of the Hh pathway in periosteum-derived mesenchymal stem cells induces bone formation in vivo: implication for postnatal bone repair. *Am J Pathol* **177**, 3100–3111 (2010).
173. Nakahara, H. *et al.* Bone and cartilage formation in diffusion chambers by subcultured cells derived from the periosteum. *Bone* **11**, 181–188 (1990).
174. Bruder, S. P. & Caplan, A. I. Osteogenic cell lineage analysis is facilitated by organ cultures of embryonic chick periosteum. *Dev Biol* **141**, 319–329 (1990).
175. Koshihara, Y., Kawamura, M., Oda, H. & Higaki, S. In vitro calcification in human osteoblastic cell line derived from periosteum. *Biochem Biophys Res Commun* **145**, 651–657 (1987).
176. Thorogood, P. In vitro studies on skeletogenic potential of membrane bone periosteal cells. *J Embryol Exp Morphol* **54**, 185–207 (1979).
177. Sacchetti, B. *et al.* Self-Renewing Osteoprogenitors in Bone Marrow Sinusoids Can Organize a Hematopoietic Microenvironment. *Cell* **131**, 324–336 (2007).
178. De Bari, C. *et al.* Mesenchymal multipotency of adult human periosteal cells demonstrated by single-cell lineage analysis. *Arthritis Rheum* **54**, 1209–1221 (2006).
179. Stich, S. *et al.* Characterization of single cell derived cultures of periosteal progenitor cells to ensure the cell quality for clinical application. *PLoS ONE* **12**, e0178560 (2017).
180. Groeneveldt, L. C. *et al.* The Bone-Forming Properties of Periosteum-Derived Cells Differ Between Harvest Sites. *Front. Cell Dev. Biol.* **8**, 554984 (2020).
181. Choi, Y.-S. *et al.* Multipotency and growth characteristic of periosteum-derived progenitor cells for chondrogenic, osteogenic, and adipogenic differentiation. *Biotechnol Lett* **30**, 593–601 (2008).
182. Isogai, N. *et al.* Experimental use of fibrin glue to induce site-directed osteogenesis from cultured periosteal cells. *Plast Reconstr Surg* **105**, 953–963 (2000).
183. Eyckmans, J. & Luyten, F. P. Species specificity of ectopic bone formation using periosteum-derived mesenchymal progenitor cells. *Tissue Eng* **12**, 2203–2213 (2006).
184. van Gastel, N. *et al.* Lipid availability determines fate of skeletal progenitor cells via SOX9. *Nature* **579**, 111–117 (2020).
185. Kawanami, A., Matsushita, T., Chan, Y. Y. & Murakami, S. Mice expressing GFP and CreER in osteochondro progenitor cells in the periosteum. *Biochemical and Biophysical Research Communications* **386**, 477–482 (2009).
186. Xu, J. *et al.* PDGFRα reporter activity identifies periosteal progenitor cells critical for bone formation and fracture repair. *Bone Res* **10**, 7 (2022).
187. Uezumi, A., Ikemoto-Uezumi, M. & Tsuchida, K. Roles of nonmyogenic mesenchymal progenitors in pathogenesis and regeneration of skeletal muscle. *Front Physiol* **5**, 68 (2014).
188. O'Rourke, M. *et al.* Evaluating Tissue-Specific Recombination in a Pdgfrα-CreERT2 Transgenic Mouse Line. *PLoS ONE* **11**, e0162858 (2016).
189. Matthews, B. G. *et al.* Analysis of αSMA-Labeled Progenitor Cell Commitment Identifies Notch Signaling as an Important Pathway in Fracture Healing. *J Bone Miner Res* **29**, 1283–1294 (2014).
190. Kalajzic, Z. *et al.* Use of an alpha-smooth muscle actin GFP reporter to identify an osteoprogenitor population. *Bone* **43**, 501–510 (2008).
191. Ortinau, L. C. *et al.* Identification of Functionally Distinct Mx1+αSMA+ Periosteal Skeletal Stem Cells. *Cell Stem Cell* **25**, 784-796.e5 (2019).
192. Ransom, R. C. *et al.* Axin2-expressing cells execute regeneration after skeletal injury. *Sci Rep* **6**, 36524 (2016).
193. Böhm, A.-M. *et al.* Activation of Skeletal Stem and Progenitor Cells for Bone Regeneration Is Driven by PDGFRβ Signaling. *Developmental Cell* **51**, 236-254.e12 (2019).
194. Pineault, K. M., Song, J. Y., Kozloff, K. M., Lucas, D. & Wellik, D. M. Hox11 expressing regional skeletal stem cells are progenitors for osteoblasts, chondrocytes and adipocytes throughout life. *Nat Commun* **10**, 3168 (2019).
195. Tournaire, G. *et al.* Nestin-GFP transgene labels skeletal progenitors in the periosteum. *Bone* **133**, 115259 (2020).
196. Shi, Y. *et al.* Gli1 identifies osteogenic progenitors for bone formation and fracture repair. *Nat Commun* **8**, 2043 (2017).
197. Xia, C. *et al.* TGF-β/Smad2 signalling regulates enchondral bone formation of Gli1 $^{+}$ periosteal cells during fracture healing. *Cell Prolif* **53**, (2020).
198. He, X. *et al.* Sox9 positive periosteal cells in fracture repair of the adult mammalian long bone. *Bone* **103**, 12–19 (2017).
199. Perrin, S. & Colnot, C. Periosteal Skeletal Stem and Progenitor Cells in Bone Regeneration.

Curr Osteoporos Rep (2022) doi:10.1007/s11914-022-00737-8.
200. Kramann, R. *et al.* Perivascular Gli1+ Progenitors Are Key Contributors to Injury-Induced Organ Fibrosis. *Cell Stem Cell* **16**, 51–66 (2015).
201. Wan, M. & Cao, X. BMP signaling in skeletal development. *Biochemical and Biophysical Research Communications* **328**, 651–657 (2005).
202. Lowery, J. W. & Rosen, V. The BMP Pathway and Its Inhibitors in the Skeleton. *Physiological Reviews* **98**, 2431–2452 (2018).
203. Yu, Y. Y. *et al.* Immunolocalization of BMPs, BMP antagonists, receptors, and effectors during fracture repair. *Bone* **46**, 841–851 (2010).
204. Wang, Q., Huang, C., Xue, M. & Zhang, X. Expression of endogenous BMP-2 in periosteal progenitor cells is essential for bone healing. *Bone* **48**, 524–532 (2011).
205. Tsuji, K. *et al.* BMP4 Is Dispensable for Skeletogenesis and Fracture-Healing in the Limb. *Journal of Bone and Joint Surgery* **90**, 14–18 (2008).
206. Tsuji, K. *et al.* Conditional deletion of BMP7 from the limb skeleton does not affect bone formation or fracture repair. *J. Orthop. Res.* **28**, 384–389 (2010).
207. Chappuis, V. *et al.* Periosteal BMP2 activity drives bone graft healing. *Bone* **51**, 800–809 (2012).
208. Wang, C. *et al.* NOTCH signaling in skeletal progenitors is critical for fracture repair. *Journal of Clinical Investigation* **126**, 1471–1481 (2016).
209. Zhong, N., Gersch, R. P. & Hadjiargyrou, M. Wnt signaling activation during bone regeneration and the role of Dishevelled in chondrocyte proliferation and differentiation. *Bone* **39**, 5–16 (2006).
210. Kim, J.-B. *et al.* Bone regeneration is regulated by wnt signaling. *J Bone Miner Res* **22**, 1913–1923 (2007).
211. Novak, S. *et al.* Modulation of Notch1 signaling regulates bone fracture healing. *J Orthop Res* **38**, 2350–2361 (2020).
212. Lee, S. *et al.* Notch-Wnt signal crosstalk regulates proliferation and differentiation of osteoprogenitor cells during intramembranous bone healing. *npj Regen Med* **6**, 29 (2021).
213. Minear, S., Leucht, P., Miller, S. & Helms, J. A. rBMP represses Wnt signaling and influences skeletal progenitor cell fate specification during bone repair. *J Bone Miner Res* **25**, 1196–1207 (2010).
214. Farooq, M., Khan, A. W., Kim, M. S. & Choi, S. The Role of Fibroblast Growth Factor (FGF) Signaling in Tissue Repair and Regeneration. *Cells* **10**, 3242 (2021).
215. Tahara, N. *et al.* The FGF-AKT pathway is necessary for cardiomyocyte survival for heart regeneration in zebrafish. *Developmental Biology* **472**, 30–37 (2021).
216. Guzy, R. D., Stoilov, I., Elton, T. J., Mecham, R. P. & Ornitz, D. M. Fibroblast Growth Factor 2 Is Required for Epithelial Recovery, but Not for Pulmonary Fibrosis, in Response to Bleomycin. *Am J Respir Cell Mol Biol* **52**, 116–128 (2015).
217. Akita, S., Akino, K., Imaizumi, T. & Hirano, A. Basic fibroblast growth factor accelerates and improves second-degree burn wound healing: bFGF in second-degree burn scar quality. *Wound Repair and Regeneration* **16**, 635–641 (2008).
218. Su, N. FGF signaling: its role in bone development and human skeleton diseases. *Front Biosci* **13**, 2842 (2008).
219. Marie, P. J., Miraoui, H. & Sévère, N. FGF/FGFR signaling in bone formation: Progress and perspectives. *Growth Factors* **30**, 117–123 (2012).
220. Bonaventure, J. *et al.* Common mutations in the fibroblast growth factor receptor 3 (FGFR3) gene account for achondroplasia, hypochondroplasia, and thanatophoric dwarfism. *Am. J. Med. Genet.* **63**, 148–154 (1996).
221. Rousseau, F. *et al.* Mutations of the Fibroblast Growth Factor Receptor-3 Gene in Achondroplasia. *Horm Res* **45**, 108–110 (1996).
222. Pannier, S. *et al.* Activating Fgfr3 Y367C mutation causes hearing loss and inner ear defect in a mouse model of chondrodysplasia. *Biochimica et Biophysica Acta (BBA) - Molecular Basis of Disease* **1792**, 140–147 (2009).
223. Schmid, G. J., Kobayashi, C., Sandell, L. J. & Ornitz, D. M. Fibroblast growth factor expression during skeletal fracture healing in mice. *Dev. Dyn.* **238**, 766–774 (2009).
224. Nakajima, F., Nakajima, A., Ogasawara, A., Moriya, H. & Yamazaki, M. Effects of a Single Percutaneous Injection of Basic Fibroblast Growth Factor on the Healing of a Closed Femoral Shaft Fracture in the Rat. *Calcif Tissue Int* **81**, 132–138 (2007).
225. van Gastel, N. *et al.* Expansion of Murine Periosteal Progenitor Cells with Fibroblast Growth Factor 2 Reveals an Intrinsic Endochondral Ossification Program Mediated by Bone Morphogenetic Protein 2. *Stem Cells* **32**, 2407–2418 (2014).
226. Kim, K. K., Sheppard, D. & Chapman, H. A. TGF-β1 Signaling and Tissue Fibrosis. *Cold*

Spring Harb Perspect Biol **10**, a022293 (2018).
227. Plikus, M. V. *et al.* Fibroblasts: Origins, definitions, and functions in health and disease. *Cell* **184**, 3852–3872 (2021).
228. Denton, C. P. *et al.* Inducible Lineage-Specific Deletion of TβRII in Fibroblasts Defines a Pivotal Regulatory Role during Adult Skin Wound Healing. *Journal of Investigative Dermatology* **129**, 194–204 (2009).
229. Sonnylal, S. *et al.* Postnatal induction of transforming growth factor β signaling in fibroblasts of mice recapitulates clinical, histologic, and biochemical features of scleroderma. *Arthritis Rheum* **56**, 334–344 (2007).
230. Nakajima, H. *et al.* Atrial but Not Ventricular Fibrosis in Mice Expressing a Mutant Transforming Growth Factor-β $_1$ Transgene in the Heart. *Circulation Research* **86**, 571–579 (2000).
231. Munger, J. S. *et al.* A Mechanism for Regulating Pulmonary Inflammation and Fibrosis: The Integrin αvβ6 Binds and Activates Latent TGF β1. *Cell* **96**, 319–328 (1999).
232. Poniatowski, Ł. A., Wojdasiewicz, P., Gasik, R. & Szukiewicz, D. Transforming Growth Factor Beta Family: Insight into the Role of Growth Factors in Regulation of Fracture Healing Biology and Potential Clinical Applications. *Mediators of Inflammation* **2015**, 1–17 (2015).
233. Cho, T.-J., Gerstenfeld, L. C. & Einhorn, T. A. Differential Temporal Expression of Members of the Transforming Growth Factor β Superfamily During Murine Fracture Healing. *J Bone Miner Res* **17**, 513–520 (2002).
234. Moore, E. R., Mathews, O. A., Yao, Y. & Yang, Y. Prx1-expressing cells contributing to fracture repair require primary cilia for complete healing in mice. *Bone* **143**, 115738 (2021).
235. Huang, C., Tang, M., Yehling, E. & Zhang, X. Overexpressing Sonic Hedgehog Peptide Restores Periosteal Bone Formation in a Murine Bone Allograft Transplantation Model. *Molecular Therapy* **22**, 430–439 (2014).
236. Miyaji, T. *et al.* Expression and distribution of transcripts for sonic hedgehog in the early phase of fracture repair. *Histochem Cell Biol* **119**, 233–237 (2003).
237. Doherty, L. *et al.* A PDGFRβ-PI3K signaling axis mediates periosteal cell activation during fracture healing. *PLoS ONE* **14**, e0223846 (2019).
238. Wang, X. *et al.* PDGF Modulates BMP2-Induced Osteogenesis in Periosteal Progenitor Cells. *JBMR Plus* **3**, e10127 (2019).
239. Huang, C. *et al.* The Spatiotemporal Role of COX-2 in Osteogenic and Chondrogenic Differentiation of Periosteum-Derived Mesenchymal Progenitors in Fracture Repair. *PLoS ONE* **9**, e100079 (2014).
240. Xie, C. *et al.* COX-2 from the injury milieu is critical for the initiation of periosteal progenitor cell mediated bone healing. *Bone* **43**, 1075–1083 (2008).
241. Yukata, K. *et al.* Teriparatide (human PTH1–34) compensates for impaired fracture healing in COX-2 deficient mice. *Bone* **110**, 150–159 (2018).
242. Bravo, D. *et al.* Temporary inhibition of the plasminogen activator inhibits periosteal chondrogenesis and promotes periosteal osteogenesis during appendicular bone fracture healing. *Bone* **112**, 97–106 (2018).
243. Wang, L. *et al.* Plasminogen Regulates Fracture Repair by Promoting the Functions of Periosteal Mesenchymal Progenitors. *J Bone Miner Res* **36**, 2229–2242 (2021).
244. Lu, C. *et al.* Mechanical Stability Affects Angiogenesis During Early Fracture Healing. *Journal of Orthopaedic Trauma* **25**, 494–499 (2011).
245. Stegen, S. *et al.* Adequate hypoxia inducible factor 1α signaling is indispensable for bone regeneration. *Bone* **87**, 176–186 (2016).
246. Andrés Sastre, E. *et al.* Spatiotemporal distribution of thrombospondin-4 and -5 in cartilage during endochondral bone formation and repair. *Bone* **150**, 115999 (2021).
247. He, F., Umrath, F., Reinert, S. & Alexander, D. Jaw Periosteum-Derived Mesenchymal Stem Cells Regulate THP-1-Derived Macrophage Polarization. *IJMS* **22**, 4310 (2021).
248. He, F., Umrath, F., von Ohle, C., Reinert, S. & Alexander, D. Analysis of the Influence of Jaw Periosteal Cells on Macrophages Phenotype Using an Innovative Horizontal Coculture System. *Biomedicines* **9**, 1753 (2021).
249. Li, Z. *et al.* Fracture repair requires TrkA signaling by skeletal sensory nerves. *Journal of Clinical Investigation* **129**, 5137–5150 (2019).
250. Zhang, Y. *et al.* Implant-derived magnesium induces local neuronal production of CGRP to improve bone-fracture healing in rats. *Nat Med* **22**, 1160–1169 (2016).
251. Jones, R. E. *et al.* Skeletal Stem Cell-Schwann Cell Circuitry in Mandibular Repair. *Cell Reports* **28**, 2757-2766.e5 (2019).
252. Doherty, L., Wan, M., Kalajzic, I. & Sanjay, A. Diabetes impairs periosteal progenitor

regenerative potential. *Bone* **143**, 115764 (2021).
253. Marin, C., Tuts, J., Luyten, F. P., Vandamme, K. & Kerckhofs, G. Impaired soft and hard callus formation during fracture healing in diet-induced obese mice as revealed by 3D contrast-enhanced computed tomography imaging. *Bone* **150**, 116008 (2021).
254. Brown, M. L. *et al.* Delayed Fracture Healing and Increased Callus Adiposity in a C57BL/6J Murine Model of Obesity-Associated Type 2 Diabetes Mellitus. *PLoS ONE* **9**, e99656 (2014).
255. Clark, D., Nakamura, M., Miclau, T. & Marcucio, R. Effects of Aging on Fracture Healing. *Curr Osteoporos Rep* **15**, 601–608 (2017).
256. Lu, C. *et al.* Cellular basis for age-related changes in fracture repair. *J. Orthop. Res.* **23**, 1300–1307 (2005).
257. O'Driscoll, S. W. M., Saris, D. B. F., Ito, Y. & Fitzimmons, J. S. The chondrogenic potential of periosteum decreases with age. *J. Orthop. Res.* **19**, 95–103 (2001).
258. Yukata, K. *et al.* Aging periosteal progenitor cells have reduced regenerative responsiveness to bone injury and to the anabolic actions of PTH 1-34 treatment. *Bone* **62**, 79–89 (2014).
259. Zhang, H. *et al.* Intramembranous ossification and endochondral ossification are impaired differently between glucocorticoid-induced osteoporosis and estrogen deficiency-induced osteoporosis. *Sci Rep* **8**, 3867 (2018).
260. Barastegui, D. *et al.* Effect of vascularized periosteum on revitalization of massive bone isografts: An experimental study in a rabbit model. *Microsurgery* **41**, 157–164 (2021).
261. Harhaus, L. *et al.* The vascularized periosteum flap as novel tissue engineering model for repair of cartilage defects. *J. Cell. Mol. Med.* **19**, 1273–1283 (2015).
262. Abed, P. F., El Chaar, E., Boltchi, F. & Bassir, S. H. The Novel Periosteal Flap Stretch Technique: A Predictable Method to Achieve and maintain Primary Closure in Augmentative Procedures. *J Int Acad Periodontol* **22**, 11–20 (2020).
263. Hassibi, H. *et al.* Allogenic Bone Graft Enriched by Periosteal Stem Cell and Growth Factors for Osteogenesis in Critical Size Bone Defect in Rabbit Model: Histopathological and Radiological Evaluation. *Iran J Pathol* **15**, 205–216 (2020).
264. Xiao, H. *et al.* Periosteum progenitors could stimulate bone regeneration in aged murine bone defect model. *J. Cell. Mol. Med.* **24**, 12199–12210 (2020).
265. Ho-Shui-Ling, A. *et al.* Bone regeneration strategies: Engineered scaffolds, bioactive molecules and stem cells current stage and future perspectives. *Biomaterials* **180**, 143–162 (2018).
266. Amler, A.-K. *et al.* Comparison of the Translational Potential of Human Mesenchymal Progenitor Cells from Different Bone Entities for Autologous 3D Bioprinted Bone Grafts. *IJMS* **22**, 796 (2021).
267. Bolander, J. *et al.* Single-cell characterization and metabolic profiling of in vitro cultured human skeletal progenitors with enhanced in vivo bone forming capacity. *Stem Cells Translational Medicine* **9**, 389–402 (2020).
268. Bolander, J. *et al.* Healing of a Large Long-Bone Defect through Serum-Free In Vitro Priming of Human Periosteum-Derived Cells. *Stem Cell Reports* **8**, 758–772 (2017).
269. Dai, K. *et al.* Construction of developmentally inspired periosteum-like tissue for bone regeneration. *Bone Res* **10**, 1 (2022).
270. Wu, L. *et al.* Hierarchical micro/nanofibrous membranes of sustained releasing VEGF for periosteal regeneration. *Biomaterials* **227**, 119555 (2020).
271. Gutmann, D. H. *et al.* Neurofibromatosis type 1. *Nat Rev Dis Primers* **3**, 17004 (2017).
272. Cimino, P. J. & Gutmann, D. H. Neurofibromatosis type 1. in *Handbook of Clinical Neurology* vol. 148 799–811 (Elsevier, 2018).
273. Charlier, P., Benmoussa, N., Froesch, P., Huynh-Charlier, I. & Balzeau, A. Did Cro-Magnon 1 have neurofibromatosis type 1? *The Lancet* **391**, 1259 (2018).
274. Madigan, P. & Masello, M. J. Report of a neurofibromatosis-like case: Monstrorum Historia, 1642. *Neurofibromatosis* **2**, 53–56 (1989).
275. Madigan, P. & Shaw, R. V. Neurofibromatosis in 13th century Austria? *Neurofibromatosis* **1**, 339–341 (1988).
276. Antonio, J. R., Goloni-Bertollo, E. M. & Tridico, L. A. Neurofibromatosis: chronological history and current issues. *An. Bras. Dermatol.* **88**, 329–343 (2013).
277. von Recklinghausen, F. D. Uber die multiplen Fibome der Haut und ihre Beziehung zu den multiplen Neuromen. *Berlin Virchows Hirschward* 1–41 (1882).
278. Neurofibromatosis. Conference statement. National Institutes of Health Consensus Development Conference. *Arch Neurol* **45**, 575–578 (1988).
279. Legius, E. *et al.* Revised diagnostic criteria for neurofibromatosis type 1 and Legius syndrome: an international consensus recommendation. *Genetics in Medicine* **23**, 1506–1513 (2021).

280. Uusitalo, E. *et al.* Incidence and mortality of neurofibromatosis: a total population study in Finland. *J Invest Dermatol* **135**, 904–906 (2015).
281. Evans, D. G. R. *et al.* Mortality in neurofibromatosis 1: in North West England: an assessment of actuarial survival in a region of the UK since 1989. *Eur J Hum Genet* **19**, 1187–1191 (2011).
282. Rasmussen, S. A., Yang, Q. & Friedman, J. M. Mortality in neurofibromatosis 1: an analysis using U.S. death certificates. *Am J Hum Genet* **68**, 1110–1118 (2001).
283. Masocco, M. *et al.* Mortality associated with neurofibromatosis type 1: a study based on Italian death certificates (1995-2006). *Orphanet J Rare Dis* **6**, 11 (2011).
284. Wallace, M. R. *et al.* Type 1 neurofibromatosis gene: identification of a large transcript disrupted in three NF1 patients. *Science* **249**, 181–186 (1990).
285. Li, Y. *et al.* Genomic organization of the neurofibromatosis 1 gene (NF1). *Genomics* **25**, 9–18 (1995).
286. Anastasaki, C., Le, L. Q., Kesterson, R. A. & Gutmann, D. H. Updated nomenclature for human and mouse neurofibromatosis type 1 genes. *Neurol Genet* **3**, e169 (2017).
287. Barron, V. A. & Lou, H. Alternative splicing of the neurofibromatosis type I pre-mRNA. *Biosci Rep* **32**, 131–138 (2012).
288. Metheny, L. J., Cappione, A. J. & Skuse, G. R. Genetic and epigenetic mechanisms in the pathogenesis of neurofibromatosis type I. *J Neuropathol Exp Neurol* **54**, 753–760 (1995).
289. Skuse, G. R., Cappione, A. J., Sowden, M., Metheny, L. J. & Smith, H. C. The neurofibromatosis type I messenger RNA undergoes base-modification RNA editing. *Nucleic Acids Res* **24**, 478–485 (1996).
290. Daston, M. M. *et al.* The protein product of the neurofibromatosis type 1 gene is expressed at highest abundance in neurons, Schwann cells, and oligodendrocytes. *Neuron* **8**, 415–428 (1992).
291. Kuorilehto, T., Nissinen, M., Koivunen, J., Benson, M. D. & Peltonen, J. NF1 Tumor Suppressor Protein and mRNA in Skeletal Tissues of Developing and Adult Normal Mouse and NF1-Deficient Embryos. *J Bone Miner Res* **19**, 983–989 (2004).
292. Kuorilehto, T. *et al.* NF1 Gene Expression in Mouse Fracture Healing and in Experimental Rat Pseudarthrosis. *J Histochem Cytochem.* **54**, 363–370 (2006).
293. Abramowicz, A. & Gos, M. Neurofibromin in neurofibromatosis type 1 - mutations in NF1gene as a cause of disease. *Dev Period Med* **18**, 297–306 (2014).
294. Abdel-Aziz, N. *et al.* Mutational spectrum of *NF1* gene in 24 unrelated Egyptian families with neurofibromatosis type 1. *Molec Gen & Gen Med* **9**, (2021).
295. Gutmann, D. H., Wood, D. L. & Collins, F. S. Identification of the neurofibromatosis type 1 gene product. *Proc. Natl. Acad. Sci. U.S.A.* **88**, 9658–9662 (1991).
296. DeClue, J. E., Cohen, B. D. & Lowy, D. R. Identification and characterization of the neurofibromatosis type 1 protein product. *Proc. Natl. Acad. Sci. U.S.A.* **88**, 9914–9918 (1991).
297. Bergoug, M. *et al.* Neurofibromin Structure, Functions and Regulation. *Cells* **9**, E2365 (2020).
298. Sherekar, M. *et al.* Biochemical and structural analyses reveal that the tumor suppressor neurofibromin (NF1) forms a high-affinity dimer. *J Biol Chem* **295**, 1105–1119 (2020).
299. Rad, E. & Tee, A. R. Neurofibromatosis type 1: Fundamental insights into cell signalling and cancer. *Seminars in Cell & Developmental Biology* **52**, 39–46 (2016).
300. Feng, L. *et al.* PKA phosphorylation and 14-3-3 interaction regulate the function of neurofibromatosis type I tumor suppressor, neurofibromin. *FEBS Letters* **557**, 275–282 (2004).
301. Tokuo, H. *et al.* Phosphorylation of neurofibromin by cAMP-dependent protein kinase is regulated via a cellular association of N^G , N^G -dimethylarginine dimethylaminohydrolase. *FEBS Letters* **494**, 48–53 (2001).
302. Izawa, I., Tamaki, N. & Saya, H. Phosphorylation of neurofibromatosis type 1 gene product (neurofibromin) by cAMP-dependent protein kinase. *FEBS Letters* **382**, 53–59 (1996).
303. Mangoura, D. *et al.* Phosphorylation of neurofibromin by PKC is a possible molecular switch in EGF receptor signaling in neural cells. *Oncogene* **25**, 735–745 (2006).
304. Gregory, P. E. *et al.* Neurofibromatosis type 1 gene product (neurofibromin) associates with microtubules. *Somat Cell Mol Genet* **19**, 265–274 (1993).
305. Xu, H. & Gutmann, D. H. Mutations in the GAP-related domain impair the ability of neurofibromin to associate with microtubules. *Brain Res* **759**, 149–152 (1997).
306. Bollag, G., McCormick, F. & Clark, R. Characterization of full-length neurofibromin: tubulin inhibits Ras GAP activity. *EMBO J* **12**, 1923–1927 (1993).
307. Martin, G. A. *et al.* The GAP-related domain of the neurofibromatosis type 1 gene product interacts with ras p21. *Cell* **63**, 843–849 (1990).
308. Xu, G. *et al.* The catalytic domain of the neurofibromatosis type 1 gene product stimulates ras GTPase and complements ira mutants of S. cerevisiae. *Cell* **63**, 835–841 (1990).

309. Xu, G. *et al.* The neurofibromatosis type 1 gene encodes a protein related to GAP. *Cell* **62**, 599–608 (1990).
310. Buchberg, A. M., Cleveland, L. S., Jenkins, N. A. & Copeland, N. G. Sequence homology shared by neurofibromatosis type-1 gene and IRA-1 and IRA-2 negative regulators of the RAS cyclic AMP pathway. *Nature* **347**, 291–294 (1990).
311. Simanshu, D. K., Nissley, D. V. & McCormick, F. RAS Proteins and Their Regulators in Human Disease. *Cell* **170**, 17–33 (2017).
312. Cargnello, M. & Roux, P. P. Activation and Function of the MAPKs and Their Substrates, the MAPK-Activated Protein Kinases. *Microbiol Mol Biol Rev* **75**, 50–83 (2011).
313. Kim, E. K. & Choi, E.-J. Pathological roles of MAPK signaling pathways in human diseases. *Biochimica et Biophysica Acta (BBA) - Molecular Basis of Disease* **1802**, 396–405 (2010).
314. Sun, Y. *et al.* Signaling pathway of MAPK/ERK in cell proliferation, differentiation, migration, senescence and apoptosis. *Journal of Receptors and Signal Transduction* **35**, 600–604 (2015).
315. Porta, C., Paglino, C. & Mosca, A. Targeting PI3K/Akt/mTOR Signaling in Cancer. *Front Oncol* **4**, 64 (2014).
316. Asati, V., Mahapatra, D. K. & Bharti, S. K. PI3K/Akt/mTOR and Ras/Raf/MEK/ERK signaling pathways inhibitors as anticancer agents: Structural and pharmacological perspectives. *Eur J Med Chem* **109**, 314–341 (2016).
317. Schaefer, I.-M. & Fletcher, C. D. M. Malignant peripheral nerve sheath tumor (MPNST) arising in diffuse-type neurofibroma: clinicopathologic characterization in a series of 9 cases. *Am J Surg Pathol* **39**, 1234–1241 (2015).
318. Tucker, T. *et al.* Longitudinal study of neurofibromatosis 1 associated plexiform neurofibromas. *Journal of Medical Genetics* **46**, 81–85 (2008).
319. Friedrich, R. E., Hartmann, M. & Mautner, V. F. Malignant peripheral nerve sheath tumors (MPNST) in NF1-affected children. *Anticancer Res* **27**, 1957–1960 (2007).
320. Tucker, T., Wolkenstein, P., Revuz, J., Zeller, J. & Friedman, J. M. Association between benign and malignant peripheral nerve sheath tumors in NF1. *Neurology* **65**, 205–211 (2005).
321. Legius, E. *et al.* TP53 mutations are frequent in malignant NF1 tumors. *Genes Chromosomes Cancer* **10**, 250–255 (1994).
322. De Raedt, T. *et al.* PRC2 loss amplifies Ras-driven transcription and confers sensitivity to BRD4-based therapies. *Nature* **514**, 247–251 (2014).
323. Lee, W. *et al.* PRC2 is recurrently inactivated through EED or SUZ12 loss in malignant peripheral nerve sheath tumors. *Nat Genet* **46**, 1227–1232 (2014).
324. Sohier, P. *et al.* Confirmation of mutation landscape of NF1-associated malignant peripheral nerve sheath tumors. *Genes Chromosomes Cancer* **56**, 421–426 (2017).
325. Farid, M. *et al.* Malignant peripheral nerve sheath tumors. *Oncologist* **19**, 193–201 (2014).
326. Uusitalo, E. *et al.* Distinctive Cancer Associations in Patients With Neurofibromatosis Type 1. *J Clin Oncol* **34**, 1978–1986 (2016).
327. Gutmann, D. H. *et al.* Gliomas presenting after age 10 in individuals with neurofibromatosis type 1 (NF1). *Neurology* **59**, 759–761 (2002).
328. Walker, L. *et al.* A prospective study of neurofibromatosis type 1 cancer incidence in the UK. *Br J Cancer* **95**, 233–238 (2006).
329. Seminog, O. O. & Goldacre, M. J. Risk of benign tumours of nervous system, and of malignant neoplasms, in people with neurofibromatosis: population-based record-linkage study. *Br J Cancer* **108**, 193–198 (2013).
330. Sharif, S. *et al.* Women with neurofibromatosis 1 are at a moderately increased risk of developing breast cancer and should be considered for early screening. *J Med Genet* **44**, 481–484 (2007).
331. Miles, D. K. *et al.* Patterns of hematopoietic lineage involvement in children with neurofibromatosis type 1 and malignant myeloid disorders. *Blood* **88**, 4314–4320 (1996).
332. Miraglia, E. *et al.* Cutaneous manifestations in neurofibromatosis type 1. *Clin Ter* **171**, e371–e377 (2020).
333. Bernier, A., Larbrisseau, A. & Perreault, S. Café-au-lait Macules and Neurofibromatosis Type 1: A Review of the Literature. *Pediatr Neurol* **60**, 24-29.e1 (2016).
334. Senthilkumar, V. A. & Tripathy, K. Lisch Nodules. in *StatPearls* (StatPearls Publishing, 2022).
335. Anguita, R. & Veas, R. Lisch Nodules. *N Engl J Med* **386**, 478–478 (2022).
336. Campen, C. J. & Gutmann, D. H. Optic Pathway Gliomas in Neurofibromatosis Type 1. *J Child Neurol* **33**, 73–81 (2018).
337. Freret, M. E. & Gutmann, D. H. Insights into optic pathway glioma vision loss from mouse models of neurofibromatosis type 1. *J Neuro Res* **97**, 45–56 (2019).

338. Dalla Via, P. *et al.* Visual outcome of a cohort of children with neurofibromatosis type 1 and optic pathway glioma followed by a pediatric neuro-oncology program. *Neuro Oncol* **9**, 430–437 (2007).
339. Hyman, S. L., Shores, A. & North, K. N. The nature and frequency of cognitive deficits in children with neurofibromatosis type 1. *Neurology* **65**, 1037–1044 (2005).
340. Hyman, S. L., Arthur Shores, E. & North, K. N. Learning disabilities in children with neurofibromatosis type 1: subtypes, cognitive profile, and attention-deficit-hyperactivity disorder. *Dev Med Child Neurol* **48**, 973–977 (2006).
341. Mautner, V.-F., Granström, S. & Leark, R. A. Impact of ADHD in adults with neurofibromatosis type 1: associated psychological and social problems. *J Atten Disord* **19**, 35–43 (2015).
342. Isenberg, J. C., Templer, A., Gao, F., Titus, J. B. & Gutmann, D. H. Attention skills in children with neurofibromatosis type 1. *J Child Neurol* **28**, 45–49 (2013).
343. Garg, S. *et al.* Neurofibromatosis type 1 and autism spectrum disorder. *Pediatrics* **132**, e1642-1648 (2013).
344. Morris, S. M. *et al.* Disease Burden and Symptom Structure of Autism in Neurofibromatosis Type 1: A Study of the International NF1-ASD Consortium Team (INFACT). *JAMA Psychiatry* **73**, 1276–1284 (2016).
345. Wolkenstein, P. *et al.* Impact of neurofibromatosis 1 upon quality of life in childhood: a cross-sectional study of 79 cases. *Br J Dermatol* **160**, 844–848 (2009).
346. North, K. N. *et al.* Cognitive function and academic performance in neurofibromatosis. 1: consensus statement from the NF1 Cognitive Disorders Task Force. *Neurology* **48**, 1121–1127 (1997).
347. North, K., Joy, P., Yuille, D., Cocks, N. & Hutchins, P. Cognitive function and academic performance in children with neurofibromatosis type 1. *Dev Med Child Neurol* **37**, 427–436 (1995).
348. Sorrentino, U. *et al.* Epilepsy in NF1: Epidemiologic, Genetic, and Clinical Features. A Monocentric Retrospective Study in a Cohort of 784 Patients. *Cancers (Basel)* **13**, 6336 (2021).
349. Ostendorf, A. P., Gutmann, D. H. & Weisenberg, J. L. Z. Epilepsy in individuals with neurofibromatosis type 1. *Epilepsia* **54**, 1810–1814 (2013).
350. Licis, A. K. *et al.* Prevalence of Sleep Disturbances in Children With Neurofibromatosis Type 1. *J Child Neurol* **28**, 1400–1405 (2013).
351. Leschziner, G. D., Golding, J. F. & Ferner, R. E. Sleep disturbance as part of the neurofibromatosis type 1 phenotype in adults. *Am J Med Genet A* **161A**, 1319–1322 (2013).
352. Sivasubramanian, R. & Meyers, K. E. Hypertension in Children and Adolescents with Turner Syndrome (TS), Neurofibromatosis 1 (NF1), and Williams Syndrome (WS). *Curr Hypertens Rep* **23**, 18 (2021).
353. Jutant, E.-M. *et al.* Pulmonary hypertension associated with neurofibromatosis type 1. *Eur Respir Rev* **27**, 180053 (2018).
354. Afifi, A. K., Dolan, K. D., Van Gilder, J. C. & Fincham, R. W. Ventriculomegaly in neurofibromatosis-1. Association with Chiari type I malformation. *Neurofibromatosis* **1**, 299–305 (1988).
355. Huson, S. M., Harper, P. S. & Compston, D. A. S. VON RECKLINGHAUSEN NEUROFIBROMATOSIS: A CLINICAL AND POPULATION STUDY IN SOUTH-EAST WALES. *Brain* **111**, 1355–1381 (1988).
356. Hernández-Martín, A. & Duat-Rodríguez, A. An Update on Neurofibromatosis Type 1: Not Just Café-au-Lait Spots, Freckling, and Neurofibromas. An Update. Part I. Dermatological Clinical Criteria Diagnostic of the Disease. *Actas Dermosifiliogr* **107**, 454–464 (2016).
357. Rhodes, S. D. *et al.* Dystrophic spinal deformities in a neurofibromatosis type 1 murine model. *PLoS One* **10**, e0119093 (2015).
358. Chauvel-Picard, J. *et al.* Craniofacial bone alterations in patients with neurofibromatosis type 1. *Childs Nerv Syst* **36**, 2391–2399 (2020).
359. Al Kabbani, A. & Haghighi, S. Neurofibromatosis type 1 - with optic glioma. in *Radiopaedia.org* (Radiopaedia.org, 2018). doi:10.53347/rID-64709.
360. Elefteriou, F. *et al.* Skeletal abnormalities in neurofibromatosis type 1: Approaches to therapeutic options. *Am. J. Med. Genet.* **149A**, 2327–2338 (2009).
361. Schindeler, A. & Little, D. G. Recent insights into bone development, homeostasis, and repair in type 1 neurofibromatosis (NF1). *Bone* **42**, 616–622 (2008).
362. Heervä, E. *et al.* Neurofibromatosis 1-related osteopenia often progresses to osteoporosis in 12 years. *Calcif Tissue Int* **92**, 23–27 (2013).
363. Lammert, M. *et al.* Decreased bone mineral density in patients with neurofibromatosis 1. *Osteoporos Int* **16**, 1161–1166 (2005).
364. Kuorilehto, T. *et al.* Decreased bone mineral density and content in neurofibromatosis type 1:

lowest local values are located in the load-carrying parts of the body. *Osteoporos Int* **16**, 928–936 (2005).
365. Stevenson, D. A. *et al.* Bone mineral density in children and adolescents with neurofibromatosis type 1. *J Pediatr* **150**, 83–88 (2007).
366. Stevenson, D. A. *et al.* Evidence of increased bone resorption in neurofibromatosis type 1 using urinary pyridinium crosslink analysis. *Pediatr Res* **63**, 697–701 (2008).
367. Tucker, T. *et al.* Bone health and fracture rate in individuals with neurofibromatosis 1 (NF1). *J Med Genet* **46**, 259–265 (2009).
368. Seitz, S. *et al.* High bone turnover and accumulation of osteoid in patients with neurofibromatosis 1. *Osteoporos Int* **21**, 119–127 (2010).
369. Virdis, R. *et al.* Growth and pubertal disorders in neurofibromatosis type 1. *J Pediatr Endocrinol Metab* **16 Suppl 2**, 289–292 (2003).
370. Szudek, J., Birch, P. & Friedman, J. M. Growth in North American white children with neurofibromatosis 1 (NF1). *J Med Genet* **37**, 933–938 (2000).
371. Vitale, M. G., Guha, A. & Skaggs, D. L. Orthopaedic manifestations of neurofibromatosis in children: an update. *Clin Orthop Relat Res* 107–118 (2002) doi:10.1097/00003086-200208000-00013.
372. Durrani, A. A., Crawford, A. H., Chouhdry, S. N., Saifuddin, A. & Morley, T. R. Modulation of spinal deformities in patients with neurofibromatosis type 1. *Spine (Phila Pa 1976)* **25**, 69–75 (2000).
373. Crawford, A. H., Parikh, S., Schorry, E. K. & Von Stein, D. The immature spine in type-1 neurofibromatosis. *J Bone Joint Surg Am* **89 Suppl 1**, 123–142 (2007).
374. Toro, G. *et al.* Natural History of Scoliosis in Children with NF1: An Observation Study. *Healthcare (Basel)* **9**, 881 (2021).
375. He, Z. *et al.* Classification of neurofibromatosis-related dystrophic or nondystrophic scoliosis based on image features using Bilateral CNN. *Med Phys* **48**, 1571–1583 (2021).
376. Khong, P.-L., Goh, W. H. S., Wong, V. C. N., Fung, C.-W. & Ooi, G.-C. MR imaging of spinal tumors in children with neurofibromatosis 1. *AJR Am J Roentgenol* **180**, 413–417 (2003).
377. Alwan, S., Tredwell, S. J. & Friedman, J. M. Is osseous dysplasia a primary feature of neurofibromatosis 1 (NF1)? *Clin Genet* **67**, 378–390 (2005).
378. Friedman, J. M. & Birch, P. H. Type 1 neurofibromatosis: a descriptive analysis of the disorder in 1,728 patients. *Am J Med Genet* **70**, 138–143 (1997).
379. Jacquemin, C., Bosley, T. M., Liu, D., Svedberg, H. & Buhaliqa, A. Reassessment of sphenoid dysplasia associated with neurofibromatosis type 1. *AJNR Am J Neuroradiol* **23**, 644–648 (2002).
380. Jacquemin, C., Bosley, T. M. & Svedberg, H. Orbit deformities in craniofacial neurofibromatosis type 1. *AJNR Am J Neuroradiol* **24**, 1678–1682 (2003).
381. Lammert, M., Friedrich, R. E., Friedman, J. M., Mautner, V.-F. & Tucker, T. Early primary tooth eruption in neurofibromatosis 1 individuals. *Eur J Oral Sci* **115**, 425–426 (2007).
382. Tucker, T., Birch, P., Savoy, D. M. & Friedman, J. M. Increased dental caries in people with neurofibromatosis 1. *Clin Genet* **72**, 524–527 (2007).
383. Lee, H.-C. & Cho, D.-Y. Assessment of sacrum scalloping in neurofibromatosis type 1 caused by a giant cell lesion of the sacrum. *Surg Neurol* **65**, 194–198; discussion 198 (2006).
384. Pannier, S. Congenital pseudarthrosis of the tibia. *Orthop Traumatol Surg Res* **97**, 750–761 (2011).
385. Vander Have, K. L., Hensinger, R. N., Caird, M., Johnston, C. & Farley, F. A. Congenital pseudarthrosis of the tibia. *J Am Acad Orthop Surg* **16**, 228–236 (2008).
386. Sulaiman, A. R., Nordin, S., Faisham, W. I., Zulmi, W. & Halim, A. S. Residual nonunion following vascularised fibular graft treatment for congenital pseudarthrosis of the tibia: a report of two cases. *J Orthop Surg (Hong Kong)* **14**, 64–66 (2006).
387. Ruggieri, M. & Huson, S. M. The clinical and diagnostic implications of mosaicism in the neurofibromatoses. *Neurology* **56**, 1433–1443 (2001).
388. Kjell, V. R., Hilde, B., Eric, L., Johan, L. & Armand, L. Prevalence of neurofibromatosis type 1 in congenital pseudarthrosis of the tibia. *Eur J Pediatr* **175**, 1193–1198 (2016).
389. Crawford, A. H. & Bagamery, N. Osseous manifestations of neurofibromatosis in childhood. *J Pediatr Orthop* **6**, 72–88 (1986).
390. Aegerter, E. E. The possible relationship of neurofibromatosis, congenital pseudarthrosis, and fibrous dysplasia. *J Bone Joint Surg Am* **32-A**, 618–626 (1950).
391. Ippolito, E., Corsi, A., Grill, F., Wientroub, S. & Bianco, P. Pathology of bone lesions associated with congenital pseudarthrosis of the leg. *J Pediatr Orthop B* **9**, 3–10 (2000).
392. Morrissy, R. T. Congenital pseudarthrosis of the tibia. Factors that affect results. *Clin Orthop Relat Res* 21–27 (1982).
393. Zhu, G. *et al.* Identification and characterization of NF1 and non-NF1 congenital

pseudarthrosis of the tibia based on germline NF1 variants: genetic and clinical analysis of 75 patients. *Orphanet J Rare Dis* **14**, 221 (2019).
394. Berkshire, S. B., Maxwell, E. N. & Sams, B. F. Bilateral symmetrical pseudarthrosis in a newborn. *Radiology* **97**, 389–390 (1970).
395. Andersen, K. S. Radiological Classification of Congenital Pseudarthrosis of the Tibia. *Acta Orthopaedica Scandinavica* **44**, 719–727 (1973).
396. Boyd, H. B. Pathology and natural history of congenital pseudarthrosis of the tibia. *Clin Orthop Relat Res* 5–13 (1982).
397. Apoil, A. [Congenital pseudarthrosis of the leg. 13 cases]. *Rev Chir Orthop Reparatrice Appar Mot* **56**, 120–138 (1970).
398. Shah, H., Rousset, M. & Canavese, F. Congenital pseudarthrosis of the tibia: Management and complications. *Indian J Orthop* **46**, 616–626 (2012).
399. Cho, T.-J. *et al.* Biologic characteristics of fibrous hamartoma from congenital pseudarthrosis of the tibia associated with neurofibromatosis type 1. *J Bone Joint Surg Am* **90**, 2735–2744 (2008).
400. Hefti, F. *et al.* Congenital pseudarthrosis of the tibia: history, etiology, classification, and epidemiologic data. *J Pediatr Orthop B* **9**, 11–15 (2000).
401. Stevenson, D. A. *et al.* Double inactivation of NF1 in tibial pseudarthrosis. *Am J Hum Genet* **79**, 143–148 (2006).
402. Hermanns-Sachweh, B. *et al.* Vascular changes in the periosteum of congenital pseudarthrosis of the tibia. *Pathol Res Pract* **201**, 305–312 (2005).
403. Charnley, J. Congenital pseudarthrosis of the tibia treated by intramedullary nail. *J Bone Joint Surg Am* **38-A**, 283–290 (1956).
404. Coleman, S. S. & Coleman, D. A. Congenital pseudarthrosis of the tibia: treatment by transfer of the ipsilateral fibula with vascular pedicle. *J Pediatr Orthop* **14**, 156–160 (1994).
405. Paley, D. *et al.* Treatment of congenital pseudoarthrosis of the tibia using the Ilizarov technique. *Clin Orthop Relat Res* 81–93 (1992).
406. Masquelet, A. C., Fitoussi, F., Begue, T. & Muller, G. P. [Reconstruction of the long bones by the induced membrane and spongy autograft]. *Ann Chir Plast Esthet* **45**, 346–353 (2000).
407. Pannier, S., Pejin, Z., Dana, C., Masquelet, A. C. & Glorion, C. Induced membrane technique for the treatment of congenital pseudarthrosis of the tibia: Preliminary results of five cases. *Journal of Children's Orthopaedics* **7**, 477–485 (2013).
408. Giannoudis, P. V., Harwood, P. J., Tosounidis, T. & Kanakaris, N. K. Restoration of long bone defects treated with the induced membrane technique: protocol and outcomes. *Injury* **47 Suppl 6**, S53–S61 (2016).
409. Chadayammuri, V., Hake, M. & Mauffrey, C. Innovative strategies for the management of long bone infection: a review of the Masquelet technique. *Patient Saf Surg* **9**, 32 (2015).
410. Aurégan, J.-C. & Bégué, T. Induced membrane for treatment of critical sized bone defect: a review of experimental and clinical experiences. *Int Orthop* **38**, 1971–1978 (2014).
411. Masquelet, A. C. Induced Membrane Technique: Pearls and Pitfalls. *J Orthop Trauma* **31 Suppl 5**, S36–S38 (2017).
412. Henrich, D. *et al.* Establishment and characterization of the Masquelet induced membrane technique in a rat femur critical-sized defect model. *J Tissue Eng Regen Med* **10**, E382–E396 (2016).
413. Aho, O.-M. *et al.* The mechanism of action of induced membranes in bone repair. *J Bone Joint Surg Am* **95**, 597–604 (2013).
414. Klein, C. *et al.* The Masquelet technique: Current concepts, animal models, and perspectives. *J Tissue Eng Regen Med* term.3097 (2020) doi:10.1002/term.3097.
415. Pelissier, P., Martin, D., Baudet, J., Lepreux, S. & Masquelet, A.-C. Behaviour of cancellous bone graft placed in induced membranes. *British Journal of Plastic Surgery* **55**, 596–598 (2002).
416. Christou, C., Oliver, R. A., Yu, Y. & Walsh, W. R. The Masquelet technique for membrane induction and the healing of ovine critical sized segmental defects. *PLoS One* **9**, e114122 (2014).
417. Viateau, V. *et al.* Induction of a barrier membrane to facilitate reconstruction of massive segmental diaphyseal bone defects: an ovine model. *Vet Surg* **35**, 445–452 (2006).
418. Gaio, N. *et al.* Masquelet technique: The effect of altering implant material and topography on membrane matrix composition, mechanical and barrier properties in a rat defect model. *J Biomech* **72**, 53–62 (2018).
419. Gindraux, F. *et al.* Similarities between induced membrane and amniotic membrane: Novelty for bone repair. *Placenta* **59**, 116–123 (2017).
420. Gouron, R. *et al.* Osteoclasts and their precursors are present in the induced-membrane during bone reconstruction using the Masquelet technique. *J Tissue Eng Regen Med* **11**, 382–389 (2017).

421. Gruber, H. E. *et al.* Osteogenic, stem cell and molecular characterisation of the human induced membrane from extremity bone defects. *Bone Joint Res* **5**, 106–115 (2016).
422. Pelissier, P., Masquelet, A. C., Bareille, R., Pelissier, S. M. & Amedee, J. Induced membranes secrete growth factors including vascular and osteoinductive factors and could stimulate bone regeneration. *J Orthop Res* **22**, 73–79 (2004).
423. Bosemark, P., Perdikouri, C., Pelkonen, M., Isaksson, H. & Tägil, M. The masquelet induced membrane technique with BMP and a synthetic scaffold can heal a rat femoral critical size defect. *J Orthop Res* **33**, 488–495 (2015).
424. Ma, Y.-F. *et al.* Calcium sulfate induced versus PMMA-induced membrane in a critical-sized femoral defect in a rat model. *Sci Rep* **8**, 637 (2018).
425. Viateau, V. *et al.* Use of the induced membrane technique for bone tissue engineering purposes: animal studies. *Orthop Clin North Am* **41**, 49–56; table of contents (2010).
426. Tudisco, C. *et al.* Functional results at the end of skeletal growth in 30 patients affected by congenital pseudoarthrosis of the tibia. *J Pediatr Orthop B* **9**, 94–102 (2000).
427. Eisenberg, K. A. & Vuillermin, C. B. Management of Congenital Pseudoarthrosis of the Tibia and Fibula. *Curr Rev Musculoskelet Med* 356–368 (2019) doi:10.1007/s12178-019-09566-2.
428. Westberry, D. E., Carpenter, A. M., Tisch, J. & Wack, L. I. Amputation Outcomes in Congenital Pseudarthrosis of the Tibia. *Journal of Pediatric Orthopaedics* **38**, e475–e481 (2018).
429. Stenson, P. D. *et al.* The Human Gene Mutation Database: towards a comprehensive repository of inherited mutation data for medical research, genetic diagnosis and next-generation sequencing studies. *Hum Genet* **136**, 665–677 (2017).
430. Sabbagh, A. *et al.* NF1 molecular characterization and neurofibromatosis type I genotype-phenotype correlation: the French experience. *Hum Mutat* **34**, 1510–1518 (2013).
431. Sabbagh, A. *et al.* Unravelling the genetic basis of variable clinical expression in neurofibromatosis 1. *Hum Mol Genet* **18**, 2768–2778 (2009).
432. Pasmant, E., Vidaud, M., Vidaud, D. & Wolkenstein, P. Neurofibromatosis type 1: from genotype to phenotype. *J Med Genet* **49**, 483–489 (2012).
433. Easton, D. F., Ponder, M. A., Huson, S. M. & Ponder, B. A. An analysis of variation in expression of neurofibromatosis (NF) type 1 (NF1): evidence for modifying genes. *Am J Hum Genet* **53**, 305–313 (1993).
434. Kluwe, L. *et al.* Screening 500 unselected neurofibromatosis 1 patients for deletions of the NF1 gene. *Hum Mutat* **23**, 111–116 (2004).
435. De Raedt, T. *et al.* Genomic organization and evolution of the NF1 microdeletion region. *Genomics* **84**, 346–360 (2004).
436. Pacot, L. *et al.* Severe Phenotype in Patients with Large Deletions of NF1. *Cancers (Basel)* **13**, 2963 (2021).
437. Upadhyaya, M. *et al.* An absence of cutaneous neurofibromas associated with a 3-bp inframe deletion in exon 17 of the NF1 gene (c.2970-2972 delAAT): evidence of a clinically significant NF1 genotype-phenotype correlation. *Am J Hum Genet* **80**, 140–151 (2007).
438. Banerjee, S. *et al.* A novel mutation in NF1 is associated with diverse intra-familial phenotypic variation and astrocytoma in a Chinese family. *J Clin Neurosci* **31**, 182–184 (2016).
439. Szudek, J., Joe, H. & Friedman, J. M. Analysis of intrafamilial phenotypic variation in neurofibromatosis 1 (NF1). *Genet Epidemiol* **23**, 150–164 (2002).
440. Ejerskov, C., Raundahl, M., Gregersen, P. A. & Handrup, M. M. Clinical features and disease severity in patients with mosaic neurofibromatosis type 1: a single-center study and literature review. *Orphanet J Rare Dis* **16**, 180 (2021).
441. García-Romero, M. T., Parkin, P. & Lara-Corrales, I. Mosaic Neurofibromatosis Type 1: A Systematic Review. *Pediatr Dermatol* **33**, 9–17 (2016).
442. Knudson, A. G. Mutation and cancer: statistical study of retinoblastoma. *Proc Natl Acad Sci U S A* **68**, 820–823 (1971).
443. Chernoff, J. The two-hit theory hits 50. *Mol Biol Cell* **32**, rt1 (2021).
444. Laycock-van Spyk, S., Thomas, N., Cooper, D. N. & Upadhyaya, M. Neurofibromatosis type 1-associated tumours: their somatic mutational spectrum and pathogenesis. *Hum Genomics* **5**, 623–690 (2011).
445. Serra, E. *et al.* Schwann cells harbor the somatic NF1 mutation in neurofibromas: evidence of two different Schwann cell subpopulations. *Hum Mol Genet* **9**, 3055–3064 (2000).
446. Serra, E. *et al.* Confirmation of a double-hit model for the NF1 gene in benign neurofibromas. *Am J Hum Genet* **61**, 512–519 (1997).
447. Upadhyaya, M. *et al.* Germline and somatic NF1 gene mutation spectrum in NF1-associated malignant peripheral nerve sheath tumors (MPNSTs). *Hum Mutat* **29**, 74–82 (2008).

448. Sawada, S. *et al.* Identification of NF1 mutations in both alleles of a dermal neurofibroma. *Nat Genet* **14**, 110–112 (1996).
449. Maertens, O. *et al.* Molecular pathogenesis of multiple gastrointestinal stromal tumors in NF1 patients. *Hum Mol Genet* **15**, 1015–1023 (2006).
450. Brems, H. *et al.* Glomus tumors in neurofibromatosis type 1: genetic, functional, and clinical evidence of a novel association. *Cancer Res* **69**, 7393–7401 (2009).
451. Kluwe, L., Friedrich, R. & Mautner, V. F. Loss of NF1 allele in Schwann cells but not in fibroblasts derived from an NF1-associated neurofibroma. *Genes Chromosomes Cancer* **24**, 283–285 (1999).
452. Eisenbarth, I., Assum, G., Kaufmann, D. & Krone, W. Evidence for the presence of the second allele of the neurofibromatosis type 1 gene in melanocytes derived from café au laitmacules of NF1 patients. *Biochem Biophys Res Commun* **237**, 138–141 (1997).
453. Maertens, O. *et al.* Molecular Dissection of Isolated Disease Features in Mosaic Neurofibromatosis Type 1. *The American Journal of Human Genetics* **81**, 243–251 (2007).
454. Margraf, R. L. *et al.* NF1 Somatic Mutation in Dystrophic Scoliosis. *J Mol Neurosci* **68**, 11–18 (2019).
455. Margraf, R. L. *et al.* Utilization of Whole-Exome Next-Generation Sequencing Variant Read Frequency for Detection of Lesion-Specific, Somatic Loss of Heterozygosity in a Neurofibromatosis Type 1 Cohort with Tibial Pseudarthrosis. *The Journal of Molecular Diagnostics* **19**, 468–474 (2017).
456. Paria, N. *et al.* Neurofibromin Deficiency-Associated Transcriptional Dysregulation Suggests a Novel Therapy for Tibial Pseudoarthrosis in NF1: TRANSCRIPTIONAL DYSREGULATION IN NEUROFIBROMIN DEFICIENT PSEUDOARTHROSIS. *J Bone Miner Res* **29**, 2636–2642 (2014).
457. Sant, D. W. *et al.* Evaluation of somatic mutations in tibial pseudarthrosis samples in neurofibromatosis type 1. *J Med Genet* **52**, 256–261 (2015).
458. Brekelmans, C. *et al.* Neurofibromatosis type 1-related pseudarthrosis: Beyond the pseudarthrosis site. *Hum Mutat* **40**, 1760–1767 (2019).
459. Steinmann, K. *et al.* Mechanisms of Loss of Heterozygosity in Neurofibromatosis Type 1-Associated Plexiform Neurofibromas. *Journal of Investigative Dermatology* **129**, 615–621 (2009).
460. Anderson, M. K., Johnson, M., Thornburg, L. & Halford, Z. A Review of Selumetinib in the Treatment of Neurofibromatosis Type 1-Related Plexiform Neurofibromas. *Ann Pharmacother* **56**, 716–726 (2022).
461. Solares, I., Viñal, D., Morales-Conejo, M., Rodriguez-Salas, N. & Feliu, J. Novel molecular targeted therapies for patients with neurofibromatosis type 1 with inoperable plexiform neurofibromas: a comprehensive review. *ESMO Open* **6**, 100223 (2021).
462. Wang, W. *et al.* Local low-dose lovastatin delivery improves the bone-healing defect caused by Nf1 loss of function in osteoblasts. *J Bone Miner Res* **25**, 1658–1667 (2010).
463. El-Hoss, J. *et al.* A Combination of rhBMP-2 (Recombinant Human Bone Morphogenetic Protein-2) and MEK (MAP Kinase/ERK Kinase) Inhibitor PD0325901 Increases Bone Formation in a Murine Model of Neurofibromatosis Type I Pseudarthrosis. *The Journal of Bone and Joint Surgery* **96**, e117 (2014).
464. de la Croix Ndong, J. *et al.* Combined MEK Inhibition and BMP2 Treatment Promotes Osteoblast Differentiation and Bone Healing in *Nf1* $_{Osx}$ $^{-/-}$ Mice: RAS/ERK SIGNALING IN OSTEOPROGENITORS. *J Bone Miner Res* **30**, 55–63 (2015).
465. de la Croix Ndong, J. *et al.* Asfotase-α improves bone growth, mineralization and strength in mouse models of neurofibromatosis type-1. *Nat Med* **20**, 904–910 (2014).
466. Bok, S. *et al.* MEKK2 mediates aberrant ERK activation in neurofibromatosis type I. *Nat Commun* **11**, 5704 (2020).
467. Shin, J. *et al.* Zebrafish neurofibromatosis type 1 genes have redundant functions in tumorigenesis and embryonic development. *Dis Model Mech* **5**, 881–894 (2012).
468. Isakson, S. H. *et al.* Genetically engineered minipigs model the major clinical features of human neurofibromatosis type 1. *Commun Biol* **1**, 158 (2018).
469. Osum, S. H., Watson, A. L. & Largaespada, D. A. Spontaneous and Engineered Large Animal Models of Neurofibromatosis Type 1. *Int J Mol Sci* **22**, 1954 (2021).
470. Brannan, C. I. *et al.* Targeted disruption of the neurofibromatosis type-1 gene leads to developmental abnormalities in heart and various neural crest-derived tissues. *Genes Dev* **8**, 1019–1029 (1994).
471. Jacks, T. *et al.* Tumour predisposition in mice heterozygous for a targeted mutation in Nf1. *Nat Genet* **7**, 353–361 (1994).
472. Zhu, Y., Ghosh, P., Charnay, P., Burns, D. K. & Parada, L. F. Neurofibromas in NF1: Schwann cell origin and role of tumor environment. *Science* **296**, 920–922 (2002).

473. Zheng, H. *et al.* Induction of abnormal proliferation by nonmyelinating schwann cells triggers neurofibroma formation. *Cancer Cell* **13**, 117–128 (2008).
474. Wu, J. *et al.* Plexiform and dermal neurofibromas and pigmentation are caused by Nf1 loss in desert hedgehog-expressing cells. *Cancer Cell* **13**, 105–116 (2008).
475. Chen, Z. *et al.* Cells of origin in the embryonic nerve roots for NF1-associated plexiform neurofibroma. *Cancer Cell* **26**, 695–706 (2014).
476. Le, L. Q. *et al.* Susceptible stages in Schwann cells for NF1-associated plexiform neurofibroma development. *Cancer Res* **71**, 4686–4695 (2011).
477. Le, L. Q., Shipman, T., Burns, D. K. & Parada, L. F. Cell of origin and microenvironment contribution for NF1-associated dermal neurofibromas. *Cell Stem Cell* **4**, 453–463 (2009).
478. Li, S., Chen, Z. & Le, L. Q. New insights into the neurofibroma tumor cells of origin. *Neurooncol Adv* **2**, i13–i22 (2020).
479. Radomska, K. J. *et al.* Cellular Origin, Tumor Progression, and Pathogenic Mechanisms of Cutaneous Neurofibromas Revealed by Mice with Nf1 Knockout in Boundary Cap Cells. *Cancer Discov* **9**, 130–147 (2019).
480. Chen, Z. *et al.* Spatiotemporal Loss of NF1 in Schwann Cell Lineage Leads to Different Types of Cutaneous Neurofibroma Susceptible to Modification by the Hippo Pathway. *Cancer Discov* **9**, 114–129 (2019).
481. López, S. L., Dono, R., Zeller, R. & Carrasco, A. E. Differential effects of retinoic acid and a retinoid antagonist on the spatial distribution of the homeoprotein Hoxb-7 in vertebrate embryos. *Dev Dyn* **204**, 457–471 (1995).
482. Gresset, A. *et al.* Boundary Caps Give Rise to Neurogenic Stem Cells and Terminal Glia in the Skin. *Stem Cell Reports* **5**, 278–290 (2015).
483. Fletcher, J. S., Pundavela, J. & Ratner, N. After Nf1 loss in Schwann cells, inflammation drives neurofibroma formation. *Neuro-Oncology Advances* **2**, i23–i32 (2020).
484. Liao, C.-P. *et al.* Contributions of inflammation and tumor microenvironment to neurofibroma tumorigenesis. *J Clin Invest* **128**, 2848–2861 (2018).
485. Yang, F.-C. *et al.* Nf1-dependent tumors require a microenvironment containing Nf1+/-- and c-kit-dependent bone marrow. *Cell* **135**, 437–448 (2008).
486. Choi, K. *et al.* An inflammatory gene signature distinguishes neurofibroma Schwann cells and macrophages from cells in the normal peripheral nervous system. *Sci Rep* **7**, 43315 (2017).
487. Yang, F.-C. *et al.* Neurofibromin-deficient Schwann cells secrete a potent migratory stimulus for Nf1+/- mast cells. *J Clin Invest* **112**, 1851–1861 (2003).
488. Yang, F.-C. *et al.* Nf1+/- mast cells induce neurofibroma like phenotypes through secreted TGF-beta signaling. *Hum Mol Genet* **15**, 2421–2437 (2006).
489. Monk, K. R. *et al.* Mast cells can contribute to axon-glial dissociation and fibrosis in peripheral nerve. *Neuron Glia Biol* **3**, 233–244 (2007).
490. Ribeiro, S. *et al.* Injury signals cooperate with Nf1 loss to relieve the tumor-suppressive environment of adult peripheral nerve. *Cell Rep* **5**, 126–136 (2013).
491. Hegedus, B. *et al.* Neurofibromatosis-1 regulates neuronal and glial cell differentiation from neuroglial progenitors in vivo by both cAMP- and Ras-dependent mechanisms. *Cell Stem Cell* **1**, 443–457 (2007).
492. Solga, A. C. *et al.* The cell of origin dictates the temporal course of neurofibromatosis-1 (Nf1) low-grade glioma formation. *Oncotarget* **8**, 47206–47215 (2017).
493. Bajenaru, M. L. *et al.* Optic nerve glioma in mice requires astrocyte Nf1 gene inactivation and Nf1 brain heterozygosity. *Cancer Res* **63**, 8573–8577 (2003).
494. Anastasaki, C. *et al.* Neuronal hyperexcitability drives central and peripheral nervous system tumor progression in models of neurofibromatosis-1. *Nat Commun* **13**, 2785 (2022).
495. Pan, Y. *et al.* NF1 mutation drives neuronal activity-dependent initiation of optic glioma. *Nature* **594**, 277–282 (2021).
496. Wu, X. *et al.* The Haploinsufficient Hematopoietic Microenvironment Is Critical to the Pathological Fracture Repair in Murine Models of Neurofibromatosis Type 1. *PLoS ONE* **6**, e24917 (2011).
497. Yang, F.-C. *et al.* Hyperactivation of p21ras and PI3K cooperate to alter murine and human neurofibromatosis type 1–haploinsufficient osteoclast functions. *J. Clin. Invest.* **116**, 2880–2891 (2006).
498. Yan, J. *et al.* Rac1 mediates the osteoclast gains-in-function induced by haploinsufficiency of Nf1. *Human Molecular Genetics* **17**, 936–948 (2007).
499. Yu, X. *et al.* Neurofibromin and its inactivation of Ras are prerequisites for osteoblast functioning. *Bone* **36**, 793–802 (2005).

500. Kolanczyk, M. *et al.* Multiple roles for neurofibromin in skeletal development and growth. *Human Molecular Genetics* **16**, 874–886 (2007).
501. Rhodes, S. D. *et al.* Hyperactive Transforming Growth Factor-β1 Signaling Potentiates Skeletal Defects in a Neurofibromatosis Type 1 Mouse Model: TGF-β1 SIGNALING POTENTIATES SKELETAL DEFECTS IN A NF1 MOUSE MODEL. *J Bone Miner Res* **28**, 2476–2489 (2013).
502. Elefteriou, F. *et al.* ATF4 mediation of NF1 functions in osteoblast reveals a nutritional basis for congenital skeletal dysplasiae. *Cell Metabolism* **4**, 441–451 (2006).
503. Kamiya, N. *et al.* Targeted Disruption of *NF1* in Osteocytes Increases FGF23 and Osteoid With Osteomalacia-like Bone Phenotype: NF1 DISRUPTION IN OSTEOCYTES CAUSES A MINERALIZATION DEFECT. *J Bone Miner Res* **32**, 1716–1726 (2017).
504. Wang, W. *et al.* Mice lacking Nf1 in osteochondroprogenitor cells display skeletal dysplasia similar to patients with neurofibromatosis type I. *Human Molecular Genetics* **20**, 3910–3924 (2011).
505. Schindeler, A. *et al.* Models of tibial fracture healing in normal and Nf1-deficient mice. *J. Orthop. Res.* **26**, 1053–1060 (2008).
506. Ghadakzadeh, S., Kannu, P., Whetstone, H., Howard, A. & Alman, B. A. β-Catenin modulation in neurofibromatosis type 1 bone repair: therapeutic implications. *FASEB j.* **30**, 3227–3237 (2016).
507. Baht, G. S., Nadesan, P., Silkstone, D. & Alman, B. A. Pharmacologically targeting beta-catenin for NF1 associated deficiencies in fracture repair. *Bone* **98**, 31–36 (2017).
508. El Khassawna, T. *et al.* Deterioration of fracture healing in the mouse model of NF1 long bone dysplasia. *Bone* **51**, 651–660 (2012).
509. Sharma, R. *et al.* Hyperactive Ras/MAPK signaling is critical for tibial nonunion fracture in neurofibromin-deficient mice. *Human Molecular Genetics* **22**, 4818–4828 (2013).
510. His, W. *Untersuchungen über die erste Anlage des Wirbelthierleibes : die erste Entwickelung des Hühnchens im Ei / von Wilhelm His.* (F.C.W. Vogel, 1868). doi:10.5962/bhl.title.15288.
511. Rothstein, M., Bhattacharya, D. & Simoes-Costa, M. The molecular basis of neural crest axial identity. *Developmental Biology* **444**, S170–S180 (2018).
512. Le Douarin, N. M. & Dupin, E. The “beginnings” of the neural crest. *Developmental Biology* **444**, S3–S13 (2018).
513. Pla, P. & Monsoro-Burq, A. H. The neural border: Induction, specification and maturation of the territory that generates neural crest cells. *Developmental Biology* **444**, S36–S46 (2018).
514. Artinger, K. B. & Monsoro-Burq, A. H. Neural crest multipotency and specification: power and limits of single cell transcriptomic approaches. *Fac Rev* **10**, (2021).
515. Theveneau, E. & Mayor, R. Neural crest delamination and migration: From epithelium-to-mesenchyme transition to collective cell migration. *Developmental Biology* **366**, 34–54 (2012).
516. Kengaku, M. & Okamoto, H. Basic fibroblast growth factor induces differentiation of neural tube and neural crest lineages of cultured ectoderm cells from Xenopus gastrula. *Development* **119**, 1067–1078 (1993).
517. Milet, C. & Monsoro-Burq, A. H. Neural crest induction at the neural plate border in vertebrates. *Developmental Biology* **366**, 22–33 (2012).
518. Groves, A. K. & LaBonne, C. Setting appropriate boundaries: fate, patterning and competence at the neural plate border. *Dev Biol* **389**, 2–12 (2014).
519. García-Castro, M. I., Marcelle, C. & Bronner-Fraser, M. Ectodermal Wnt function as a neural crest inducer. *Science* **297**, 848–851 (2002).
520. Aybar, M. J., Nieto, M. A. & Mayor, R. Snail precedes slug in the genetic cascade required for the specification and migration of the Xenopus neural crest. *Development* **130**, 483–494 (2003).
521. Khudyakov, J. & Bronner-Fraser, M. Comprehensive spatiotemporal analysis of early chick neural crest network genes. *Dev Dyn* **238**, 716–723 (2009).
522. Kos, R., Reedy, M. V., Johnson, R. L. & Erickson, C. A. The winged-helix transcription factor FoxD3 is important for establishing the neural crest lineage and repressing melanogenesis in avian embryos. *Development* **128**, 1467–1479 (2001).
523. Chalpe, A. J., Prasad, M., Henke, A. J. & Paulson, A. Regulation of cadherin expression in the chicken neural crest by the Wnt/ β-catenin signaling pathway. *Cell Adhesion & Migration* **4**, 431–438 (2010).
524. Nakagawa, S. & Takeichi, M. Neural crest emigration from the neural tube depends on regulated cadherin expression. *Development* **125**, 2963–2971 (1998).
525. Burstyn-Cohen, T., Stanleigh, J., Sela-Donenfeld, D. & Kalcheim, C. Canonical Wnt activity regulates trunk neural crest delamination linking BMP/noggin signaling with G1/S transition. *Development* **131**, 5327–5339 (2004).
526. Sela-Donenfeld, D. & Kalcheim, C. Regulation of the onset of neural crest migration by coordinated activity of BMP4 and Noggin in the dorsal neural tube. *Development* **126**, 4749–4762

(1999).
527. Collazo, A., Bronner-Fraser, M. & Fraser, S. E. Vital dye labelling of Xenopus laevis trunk neural crest reveals multipotency and novel pathways of migration. *Development* **118**, 363–376 (1993).
528. Erickson, C. A. & Goins, T. L. Avian neural crest cells can migrate in the dorsolateral path only if they are specified as melanocytes. *Development* **121**, 915–924 (1995).
529. Szabó, A. & Mayor, R. Mechanisms of Neural Crest Migration. *Annu. Rev. Genet.* **52**, 43–63 (2018).
530. Golding, J. P., Trainor, P., Krumlauf, R. & Gassmann, M. Defects in pathfinding by cranial neural crest cells in mice lacking the neuregulin receptor ErbB4. *Nat Cell Biol* **2**, 103–109 (2000).
531. Gammill, L. S., Gonzalez, C. & Bronner-Fraser, M. Neuropilin 2/semaphorin 3F signaling is essential for cranial neural crest migration and trigeminal ganglion condensation. *Devel Neurobio* **67**, 47–56 (2007).
532. Schwarz, Q., Maden, C. H., Vieira, J. M. & Ruhrberg, C. Neuropilin 1 signaling guides neural crest cells to coordinate pathway choice with cell specification. *Proc. Natl. Acad. Sci. U.S.A.* **106**, 6164–6169 (2009).
533. Kirby, M. L., Gale, T. F. & Stewart, D. E. Neural Crest Cells Contribute to Normal Aorticopulmonary Septation. *Science* **220**, 1059–1061 (1983).
534. Burns, A. J., Champeval, D. & Le Douarin, N. M. Sacral Neural Crest Cells Colonise Aganglionic Hindgut in Vivo but Fail to Compensate for Lack of Enteric Ganglia. *Developmental Biology* **219**, 30–43 (2000).
535. Graham, A., Begbie, J. & McGonnell, I. Significance of the cranial neural crest. *Dev. Dyn.* **229**, 5–13 (2004).
536. Lwigale, P. Y., Conrad, G. W. & Bronner-Fraser, M. Graded potential of neural crest to form cornea, sensory neurons and cartilage along the rostrocaudal axis. *Development* **131**, 1979–1991 (2004).
537. Jessen, K. R., Mirsky, R. & Lloyd, A. C. Schwann Cells: Development and Role in Nerve Repair. *Cold Spring Harb Perspect Biol* **7**, a020487 (2015).
538. Monk, K. R., Feltri, M. L. & Taveggia, C. New insights on schwann cell development: Schwann Cell Development. *Glia* **63**, 1376–1393 (2015).
539. Mirsky, R. *et al.* Novel signals controlling embryonic Schwann cell development, myelination and dedifferentiation. *Journal of the Peripheral Nervous System* **13**, 122–135 (2008).
540. Balakrishnan, A. *et al.* Insights Into the Role and Potential of Schwann Cells for Peripheral Nerve Repair From Studies of Development and Injury. *Front. Mol. Neurosci.* **13**, 608442 (2021).
541. Winseck, A. K. & Oppenheim, R. W. An in vivo analysis of Schwann cell programmed cell death in embryonic mice: the role of axons, glial growth factor, and the pro-apoptotic gene Bax. *Eur J Neurosci* **24**, 2105–2117 (2006).
542. Woldeyesus, M. T. *et al.* Peripheral nervous system defects in erbB2 mutants following genetic rescue of heart development. *Genes Dev* **13**, 2538–2548 (1999).
543. Wanner, I. B. *et al.* Role of N-cadherin in Schwann cell precursors of growing nerves. *Glia* **54**, 439–459 (2006).
544. Wanner, I. B. *et al.* Invariant mantling of growth cones by Schwann cell precursors characterize growing peripheral nerve fronts. *Glia* **54**, 424–438 (2006).
545. Solovieva, T. & Bronner, M. Schwann cell precursors: Where they come from and where they go. *Cells & Development* **166**, 203686 (2021).
546. Furlan, A. & Adameyko, I. Schwann cell precursor: a neural crest cell in disguise? *Developmental Biology* **444**, S25–S35 (2018).
547. Joseph, N. M. *et al.* Neural crest stem cells undergo multilineage differentiation in developing peripheral nerves to generate endoneurial fibroblasts in addition to Schwann cells. *Development* **131**, 5599–5612 (2004).
548. Adameyko, I. *et al.* Schwann cell precursors from nerve innervation are a cellular origin of melanocytes in skin. *Cell* **139**, 366–379 (2009).
549. Furlan, A. *et al.* Multipotent peripheral glial cells generate neuroendocrine cells of the adrenal medulla. *Science* **357**, eaal3753 (2017).
550. Kastriti, M. E. *et al.* Schwann Cell Precursors Generate the Majority of Chromaffin Cells in Zuckerkandl Organ and Some Sympathetic Neurons in Paraganglia. *Front Mol Neurosci* **12**, 6 (2019).
551. Kaukua, N. *et al.* Glial origin of mesenchymal stem cells in a tooth model system. *Nature* **513**, 551–554 (2014).
552. Uesaka, T., Nagashimada, M. & Enomoto, H. Neuronal Differentiation in Schwann Cell Lineage Underlies Postnatal Neurogenesis in the Enteric Nervous System. *J Neurosci* **35**, 9879–9888

(2015).
553. Espinosa-Medina, I. *et al.* Neurodevelopment. Parasympathetic ganglia derive from Schwann cell precursors. *Science* **345**, 87–90 (2014).
554. Dyachuk, V. *et al.* Neurodevelopment. Parasympathetic neurons originate from nerve-associated peripheral glial progenitors. *Science* **345**, 82–87 (2014).
555. Isern, J. *et al.* The neural crest is a source of mesenchymal stem cells with specialized hematopoietic stem cell niche function. *Elife* **3**, e03696 (2014).
556. Mukouyama, Y., Shin, D., Britsch, S., Taniguchi, M. & Anderson, D. J. Sensory nerves determine the pattern of arterial differentiation and blood vessel branching in the skin. *Cell* **109**, 693–705 (2002).
557. Li, W. *et al.* Peripheral Nerve-Derived CXCL12 and VEGF-A Regulate the Patterning of Arterial Vessel Branching in Developing Limb Skin. *Developmental Cell* **24**, 359–371 (2013).
558. Newbern, J. & Birchmeier, C. Nrg1/ErbB signaling networks in Schwann cell development and myelination. *Semin Cell Dev Biol* **21**, 922–928 (2010).
559. Woodhoo, A. *et al.* Notch controls embryonic Schwann cell differentiation, postnatal myelination and adult plasticity. *Nat Neurosci* **12**, 839–847 (2009).
560. Jessen, K. R. & Mirsky, R. The origin and development of glial cells in peripheral nerves. *Nat Rev Neurosci* **6**, 671–682 (2005).
561. Meier, C., Parmantier, E., Brennan, A., Mirsky, R. & Jessen, K. R. Developing Schwann cells acquire the ability to survive without axons by establishing an autocrine circuit involving insulin-like growth factor, neurotrophin-3, and platelet-derived growth factor-BB. *J Neurosci* **19**, 3847–3859 (1999).
562. Mukouyama, Y.-S., Gerber, H.-P., Ferrara, N., Gu, C. & Anderson, D. J. Peripheral nerve-derived VEGF promotes arterial differentiation via neuropilin 1-mediated positive feedback. *Development* **132**, 941–952 (2005).
563. Parmantier, E. *et al.* Schwann cell-derived Desert hedgehog controls the development of peripheral nerve sheaths. *Neuron* **23**, 713–724 (1999).
564. Feltri, M. L., Poitelon, Y. & Previtali, S. C. How Schwann Cells Sort Axons: New Concepts. *Neuroscientist* **22**, 252–265 (2016).
565. Webster, H. D., Martin, R. & O'Connell, M. F. The relationships between interphase Schwann cells and axons before myelination: a quantitative electron microscopic study. *Dev Biol* **32**, 401–416 (1973).
566. Bunge, R. P., Bunge, M. B. & Eldridge, C. F. Linkage between axonal ensheathment and basal lamina production by Schwann cells. *Annu Rev Neurosci* **9**, 305–328 (1986).
567. Berti, C. *et al.* Non-redundant function of dystroglycan and β1 integrins in radial sorting of axons. *Development* **138**, 4025–4037 (2011).
568. Taveggia, C. *et al.* Neuregulin-1 type III determines the ensheathment fate of axons. *Neuron* **47**, 681–694 (2005).
569. Nave, K.-A. & Salzer, J. L. Axonal regulation of myelination by neuregulin 1. *Curr Opin Neurobiol* **16**, 492–500 (2006).
570. Jaegle, M. *et al.* The POU proteins Brn-2 and Oct-6 share important functions in Schwann cell development. *Genes Dev* **17**, 1380–1391 (2003).
571. Salzer, J. L. Schwann cell myelination. *Cold Spring Harb Perspect Biol* **7**, a020529 (2015).
572. Topilko, P. *et al.* Krox-20 controls myelination in the peripheral nervous system. *Nature* **371**, 796–799 (1994).
573. Torii, T., Miyamoto, Y. & Yamauchi, J. Cellular Signal-Regulated Schwann Cell Myelination and Remyelination. *Adv Exp Med Biol* **1190**, 3–22 (2019).
574. Reiprich, S., Kriesch, J., Schreiner, S. & Wegner, M. Activation of Krox20 gene expression by Sox10 in myelinating Schwann cells. *J Neurochem* **112**, 744–754 (2010).
575. Ioghen, O., Manole, E., Gherghiceanu, M., O. Popescu, B. & Cristina Ceafalan, L. Non-Myelinating Schwann Cells in Health and Disease. in *Demyelination Disorders* (eds. J. Baloyannis, S., H. Rossi, F. & Liu, W.) (IntechOpen, 2022). doi:10.5772/intechopen.91930.
576. Meyer Zu Horste, G. *et al.* Expression of antigen processing and presenting molecules by Schwann cells in inflammatory neuropathies. *Glia* **58**, 80–92 (2010).
577. Ydens, E. *et al.* The neuroinflammatory role of Schwann cells in disease. *Neurobiol Dis* **55**, 95–103 (2013).
578. Yamazaki, S. *et al.* Nonmyelinating Schwann cells maintain hematopoietic stem cell hibernation in the bone marrow niche. *Cell* **147**, 1146–1158 (2011).
579. Nocera, G. & Jacob, C. Mechanisms of Schwann cell plasticity involved in peripheral nerve repair after injury. *Cell. Mol. Life Sci.* **77**, 3977–3989 (2020).

580. Jessen, K. R. & Mirsky, R. The repair Schwann cell and its function in regenerating nerves: Repair Schwann cell and its function in regenerating nerves. *J Physiol* **594**, 3521–3531 (2016).
581. Stierli, S., Imperatore, V. & Lloyd, A. C. Schwann cell plasticity-roles in tissue homeostasis, regeneration, and disease. *Glia* **67**, 2203–2215 (2019).
582. Chen, Z.-L., Yu, W.-M. & Strickland, S. Peripheral Regeneration. *Annu. Rev. Neurosci.* **30**, 209–233 (2007).
583. Jessen, K. R. & Mirsky, R. Negative regulation of myelination: Relevance for development, injury, and demyelinating disease. *Glia* **56**, 1552–1565 (2008).
584. Fontana, X. *et al.* c-Jun in Schwann cells promotes axonal regeneration and motoneuron survival via paracrine signaling. *Journal of Cell Biology* **198**, 127–141 (2012).
585. Gordon, T. The role of neurotrophic factors in nerve regeneration. *Neurosurg Focus* **26**, E3 (2009).
586. Taskinen, H. S. & Röyttä, M. Increased expression of chemokines (MCP-1, MIP-1alpha, RANTES) after peripheral nerve transection. *J Peripher Nerv Syst* **5**, 75–81 (2000).
587. Cámara-Lemarroy, C. R., Guzmán-de la Garza, F. J. & Fernández-Garza, N. E. Molecular inflammatory mediators in peripheral nerve degeneration and regeneration. *Neuroimmunomodulation* **17**, 314–324 (2010).
588. Madduri, S. & Gander, B. Schwann cell delivery of neurotrophic factors for peripheral nerve regeneration. *Journal of the Peripheral Nervous System* **15**, 93–103 (2010).
589. Beirowski, B. *et al.* The progressive nature of Wallerian degeneration in wild-type and slow Wallerian degeneration (Wld(S)) nerves. *BMC Neurosci* **6**, 6 (2005).
590. Wong, K., Babetto, E. & Beirowski, B. Axon degeneration: make the Schwann cell great again. *Neural Regen Res* **12**, 518 (2017).
591. Vaquié, A. *et al.* Injured Axons Instruct Schwann Cells to Build Constricting Actin Spheres to Accelerate Axonal Disintegration. *Cell Reports* **27**, 3152-3166.e7 (2019).
592. Gomez-Sanchez, J. A. *et al.* Schwann cell autophagy, myelinophagy, initiates myelin clearance from injured nerves. *Journal of Cell Biology* **210**, 153–168 (2015).
593. Hirata, K. & Kawabuchi, M. Myelin phagocytosis by macrophages and nonmacrophages during Wallerian degeneration. *Microsc Res Tech* **57**, 541–547 (2002).
594. Cattin, A.-L. *et al.* Macrophage-Induced Blood Vessels Guide Schwann Cell-Mediated Regeneration of Peripheral Nerves. *Cell* **162**, 1127–1139 (2015).
595. Arthur-Farraj, P. J. *et al.* c-Jun Reprograms Schwann Cells of Injured Nerves to Generate a Repair Cell Essential for Regeneration. *Neuron* **75**, 633–647 (2012).
596. De Felipe, C. & Hunt, S. P. The differential control of c-jun expression in regenerating sensory neurons and their associated glial cells. *J Neurosci* **14**, 2911–2923 (1994).
597. Shy, M. E., Shi, Y., Wrabetz, L., Kamholz, J. & Scherer, S. S. Axon-Schwann cell interactions regulate the expression of c-jun in Schwann cells. *J Neurosci Res* **43**, 511–525 (1996).
598. Napoli, I. *et al.* A central role for the ERK-signaling pathway in controlling Schwann cell plasticity and peripheral nerve regeneration in vivo. *Neuron* **73**, 729–742 (2012).
599. Harrisingh, M. C. *et al.* The Ras/Raf/ERK signalling pathway drives Schwann cell dedifferentiation. *EMBO J* **23**, 3061–3071 (2004).
600. Monje, P. V., Soto, J., Bacallao, K. & Wood, P. M. Schwann cell dedifferentiation is independent of mitogenic signaling and uncoupled to proliferation: role of cAMP and JNK in the maintenance of the differentiated state. *J Biol Chem* **285**, 31024–31036 (2010).
601. Kato, N. *et al.* Critical role of p38 MAPK for regeneration of the sciatic nerve following crush injury in vivo. *J Neuroinflammation* **10**, 1 (2013).
602. Cervellini, I. *et al.* Sustained MAPK/ERK Activation in Adult Schwann Cells Impairs Nerve Repair. *J Neurosci* **38**, 679–690 (2018).
603. Carr, M. J. & Johnston, A. P. Schwann cells as drivers of tissue repair and regeneration. *Current Opinion in Neurobiology* **47**, 52–57 (2017).
604. Johnston, A. P. W. & Miller, F. D. The Contribution of Innervation to Tissue Repair and Regeneration. *Cold Spring Harb Perspect Biol* a041233 (2022) doi:10.1101/cshperspect.a041233.
605. Joven, A., Elewa, A. & Simon, A. Model systems for regeneration: salamanders. *Development* **146**, dev167700 (2019).
606. Kumar, A., Godwin, J. W., Gates, P. B., Garza-Garcia, A. A. & Brockes, J. P. Molecular Basis for the Nerve Dependence of Limb Regeneration in an Adult Vertebrate. *Science* **318**, 772–777 (2007).
607. Brockes, J. P. The nerve dependence of amphibian limb regeneration. *J Exp Biol* **132**, 79–91 (1987).
608. Takeo, M. *et al.* Wnt activation in nail epithelium couples nail growth to digit regeneration.

Nature **499**, 228–232 (2013).
609. Storer, M. A. & Miller, F. D. A finger on the pulse of regeneration: insights into the cellular mechanisms of adult digit tip regeneration. *Current Opinion in Genetics & Development* **70**, 1–6 (2021).
610. Storer, M. A. & Miller, F. D. Cellular and molecular mechanisms that regulate mammalian digit tip regeneration. *Open Biol.* **10**, 200194 (2020).
611. Lehoczky, J. A., Robert, B. & Tabin, C. J. Mouse digit tip regeneration is mediated by fate-restricted progenitor cells. *Proc. Natl. Acad. Sci. U.S.A.* **108**, 20609–20614 (2011).
612. Johnston, A. P. W. *et al.* Dedifferentiated Schwann Cell Precursors Secreting Paracrine Factors Are Required for Regeneration of the Mammalian Digit Tip. *Cell Stem Cell* **19**, 433–448 (2016).
613. Parfejevs, V. *et al.* Injury-activated glial cells promote wound healing of the adult skin in mice. *Nat Commun* **9**, 236 (2018).
614. Johnston, A. P. W. *et al.* Sox2-mediated regulation of adult neural crest precursors and skin repair. *Stem Cell Reports* **1**, 38–45 (2013).
615. Niederländer, C. & Lumsden, A. Late emigrating neural crest cells migrate specifically to the exit points of cranial branchiomotor nerves. *Development* **122**, 2367–2374 (1996).
616. Golding, J. P. & Cohen, J. Border Controls at the Mammalian Spinal Cord: Late-Surviving Neural Crest Boundary Cap Cells at Dorsal Root Entry Sites May Regulate Sensory Afferent Ingrowth and Entry Zone Morphogenesis. *Molecular and Cellular Neuroscience* **9**, 381–396 (1997).
617. Dickinson, D. P., Machnicki, M., Ali, M. M., Zhang, Z. & Sohal, G. S. Ventrally emigrating neural tube (VENT) cells: a second neural tube-derived cell population. *J Anat* **205**, 79–98 (2004).
618. Yaneza, M., Gilthorpe, J. D., Lumsden, A. & Tucker, A. S. No evidence for ventrally migrating neural tube cells from the mid- and hindbrain. *Dev Dyn* **223**, 163–167 (2002).
619. Coulpier, F. *et al.* Novel features of boundary cap cells revealed by the analysis of newly identified molecular markers. *Glia* **57**, 1450–1457 (2009).
620. Vermeren, M. *et al.* Integrity of Developing Spinal Motor Columns Is Regulated by Neural Crest Derivatives at Motor Exit Points. *Neuron* **37**, 403–415 (2003).
621. Bron, R. *et al.* Boundary cap cells constrain spinal motor neuron somal migration at motor exit points by a semaphorin-plexin mechanism. *Neural Dev* **2**, 21 (2007).
622. Mauti, O., Domanitskaya, E., Andermatt, I., Sadhu, R. & Stoeckli, E. T. Semaphorin6A acts as a gate keeper between the central and the peripheral nervous system. *Neural Dev* **2**, 28 (2007).
623. Garrett, A. M. *et al.* Analysis of Expression Pattern and Genetic Deletion of Netrin5 in the Developing Mouse. *Front Mol Neurosci* **9**, 3 (2016).
624. Maro, G. S. *et al.* Neural crest boundary cap cells constitute a source of neuronal and glial cells of the PNS. *Nat Neurosci* **7**, 930–938 (2004).
625. Radomska, K. J. & Topilko, P. Boundary cap cells in development and disease. *Curr Opin Neurobiol* **47**, 209–215 (2017).
626. Tzioupis, C. & Giannoudis, P. V. Prevalence of long-bone non-unions. *Injury* **38 Suppl 2**, S3-9 (2007).
627. Westgeest, J. *et al.* Factors Associated With Development of Nonunion or Delayed Healing After an Open Long Bone Fracture: A Prospective Cohort Study of 736 Subjects. *J Orthop Trauma* **30**, 149–155 (2016).
628. Sloan, A., Hussain, I., Maqsood, M., Eremin, O. & El-Sheemy, M. The effects of smoking on fracture healing. *Surgeon* **8**, 111–116 (2010).
629. Ensrud, K. E. Epidemiology of fracture risk with advancing age. *J Gerontol A Biol Sci Med Sci* **68**, 1236–1242 (2013).
630. Anastasaki, C., Dahiya, S. & Gutmann, D. H. *KIR2DL5* mutation and loss underlies sporadic dermal neurofibroma pathogenesis and growth. *Oncotarget* **8**, 47574–47585 (2017).
631. De Schepper, S. *et al.* Somatic mutation analysis in NF1 café au lait spots reveals two NF1 hits in the melanocytes. *J Invest Dermatol* **128**, 1050–1053 (2008).
632. Ma, Y. *et al.* A molecular basis for neurofibroma-associated skeletal manifestations in NF1. *Genet Med* **22**, 1786–1793 (2020).
633. Mashour, G. A. *et al.* Aberrant cutaneous expression of the angiogenic factor midkine is associated with neurofibromatosis type-1. *J Invest Dermatol* **113**, 398–402 (1999).
634. Mashour, G. A. *et al.* The angiogenic factor midkine is aberrantly expressed in NF1-deficient Schwann cells and is a mitogen for neurofibroma-derived cells. *Oncogene* **20**, 97–105 (2001).
635. Badache, A., Muja, N. & De Vries, G. H. Expression of Kit in neurofibromin-deficient human Schwann cells: role in Schwann cell hyperplasia associated with type 1 neurofibromatosis. *Oncogene* **17**, 795–800 (1998).

636. Carroll, S. L. & Stonecypher, M. S. Tumor Suppressor Mutations and Growth Factor Signaling in the Pathogenesis of NF1-Associated Peripheral Nerve Sheath Tumors: II. The Role of Dysregulated Growth Factor Signaling. *J Neuropathol Exp Neurol* **64**, 1–9 (2005).
637. Patmore, D. M. *et al. In Vivo* Regulation of TGF-β by R-Ras2 Revealed through Loss of the RasGAP Protein NF1. *Cancer Research* **72**, 5317–5327 (2012).
638. Huang, C.-Y. *et al.* Recent progress in TGF-β inhibitors for cancer therapy. *Biomedicine & Pharmacotherapy* **134**, 111046 (2021).
639. Teixeira, A. F., ten Dijke, P. & Zhu, H.-J. On-Target Anti-TGF-β Therapies Are Not Succeeding in Clinical Cancer Treatments: What Are Remaining Challenges? *Front. Cell Dev. Biol.* **8**, 605 (2020).
640. Lahn, M. *et al.* Clinical development of galunisertib (LY2157299 monohydrate), a small molecule inhibitor of transforming growth factor-beta signaling pathway. *DDDT* 4479 (2015) doi:10.2147/DDDT.S86621.
641. Lacouture, M. E. *et al.* Cutaneous keratoacanthomas/squamous cell carcinomas associated with neutralization of transforming growth factor β by the monoclonal antibody fresolimumab (GC1008). *Cancer Immunol Immunother* **64**, 437–446 (2015).
642. Hong, S. Connection between inflammation and carcinogenesis in gastrointestinal tract: Focus on TGF-β signaling. *WJG* **16**, 2080 (2010).

Role of periosteum in bone regeneration and congenital pseudarthrosis of the tibia

Bone repair is a highly efficient process allowing bones to fully regenerate without scarring after fracture. It relies on the activation and differentiation of skeletal stem/progenitor cells (SSPCs) recruited locally from the periosteum, the bone marrow, and the skeletal muscle adjacent to bone. The periosteum, the outer layer of bones, is a major source of SSPCs contributing to cartilage formation after bone injury. The identity of periosteal SSPCs (pSSPCs) and their mechanisms of activation after fracture remains poorly described. Moreover, the role of the periosteum in bone repair defects is unknown, but is suspected in congenital pseudarthrosis of the tibia (CPT), a severe disorder characterized by spontaneous tibial fracture and fibrous non-union. CPT is associated with the genetic disorder Neurofibromatosis Type 1 (NF1), caused by heterozygous mutations in the tumor suppressor gene *NF1*. NF1 symptoms such as nerve sheath tumors and skin hyperpigmentation are due to *NF1* biallelic inactivation in specific cell types i.e. Schwann cells and melanocytes respectively. *NF1* biallelic inactivation was also reported in CPT but the cellular origin of the disease remains to be determined. In the thesis, I investigated the mechanisms of pSSPCs recruitment and maturation, and the role of periosteum in CPT.

In the first part of the thesis, I used single-cell RNAseq technology to characterize pSSPC response to fracture. Upon activation, periosteal SSPCs leave their stem/progenitor stage to become fibrogenic before undergoing chondrogenic differentiation. This activation pattern, common with skeletal muscle SSPCs, is regulated by BMP signaling.

During endochondral ossification, cartilage undergoes maturation, hypertrophy and is replaced by bone, via chondrocyte apoptosis or cartilage-to-bone transformation. **In the second part of the thesis**, the phenotype of mice carrying an overactivating mutation of FGF Receptor 3 was analyzed and showed that this step of cartilage-to-bone transformation is essential for bone repair. Periosteum-derived chondrocytes in *Fgfr3*-mutant fail to transdifferentiate into osteoblasts and produce fibrocartilage, thus leading to callus fibrosis and fracture non-union.

In the third part of the thesis, I combined analyses of bone samples from CPT patients and *Prss56-Nf1 KO* mice carrying *Nf1* inactivation in neural crest-derived boundary cap (BC) cells and their derivatives. The results show that CPT is linked to *NF1* biallelic inactivation in human pathological periosteum and the presence of profibrotic pSSPCs. I identified a fibrous pseudarthrosis phenotype following tibial fracture in *Prss56-Nf1 KO* mice. BC derivatives are located in adult periosteum, where they give rise to pSSPCs and Schwann cells. *Nf1*-deficient pSSPCs have an intrinsic differentiation impairment and fail to transition from fibrogenesis to chondrogenesis, thus forming fibrosis. Additionally, *Nf1*-deficient Schwann cells exert a profibrotic paracrine effect on wild type SSPCs, which can be prevented by TGFβ inhibition to allow bone union. Overall, the thesis provides new insights into the role of pSSPCs during bone repair and how periosteum dysfunction can lead to severe bone repair deficiencies.